N-57606

COPY 626

NATIONAL ADVISORY COMMITTEE FOR AERONAUTICS

CLASSIFICATION CHANGED
TO UNCLASSIFIED
By Authority of TM-67 Date 10/5/71

NACA CONFERENCE ON AIRCRAFT LOADS, STRUCTURES, AND FLUTTER

(46)

A COMPILATION OF THE PAPERS PRESENTED

Langley Aeronautical Laboratory
Langley Field, Virginia

MARCH 5, 6, and 7, 1957

Declassified by authority of NASA
Classification Change Notices No. 215
Dated ** 12/31/71

NACA

N71-75382 N71-75427
(ACCESSION NUMBER) (THRU)
614 None
(PAGES) (CODE)
TMX-67367
(NASA CR OR TMX OR AD NUMBER) (CATEGORY)
FACILITY FORM 602

FA

NACA CONFERENCE ON

AIRCRAFT LOADS, STRUCTURES, AND FLUTTER

A Compilation of the Papers Presented

Langley Aeronautical Laboratory
Langley Field, Va.

March 5, 6, and 7, 1957

[redacted]

TABLE OF CONTENTS

INTRODUCTION

LIST OF CONFEREES

TECHNICAL PAPERS PRESENTED

AIRCRAFT LOADS

Session Chairman: Philip Donely

Loads on Lifting Surfaces and Bodies

Factors Affecting Loads at Hypersonic Speeds . . . by Arthur Henderson, Jr., and Mitchel H. Bertram

Span Loadings Due to Wing Twist at Transonic and Supersonic Speeds . . . by Frederick C. Grant and John P. Mugler, Jr.

Flight Measurements and Calculations of Wing Loads and Load Distributions at Subsonic, Transonic, and Supersonic Speeds . . . by Frank S. Malvestuto, Thomas V. Cooney, and Earl R. Keener

Air Load Distributions on a Flapped Wing Resulting From Leading-Edge and Trailing-Edge Blowing . . . by H. Clyde McLemore

Calculation of External-Store Loads and Correlation With Experiment . . . by Percy J. Bobbitt, Harry W. Carlson, and Albin O. Pearson

Steady Loads Due to Jet Interference on Wings, Tails, and Fuselages at Transonic Speeds . . . by John M. Swihart and Norman L. Crabill

Effects on Adjacent Surfaces From the Firing of Rocket Jets . . . by Walter E. Bressette and Abraham Leiss

Loads on Stabilizing and Control Surfaces

Influence of Automatic Control of Roll Coupling and Pitch-Up on Tail Loads . . . by Ralph W. Stone, Jr.

Aerodynamic Loads on Tails at High Angles of Attack and Sideslip . . . by J. Richard Spahr and Edward C. Polhamus

Loads Due to Controls at Transonic and Low Supersonic Speeds . . . by F. E. West, Jr., and K. R. Czarnecki 2

[redacted]

Gust Loads

Experimental Results on Wing Loads Due to Blasts . . . by Harold B. Pierce and Donald R. McFarland

Airplane Motions and Loads Induced by Flying Through the Flow Field Generated by an Airplane at Low Supersonic Speeds . . . by Gareth H. Jordan, Earl R. Keener, and Stanley P. Butchart

Effects of Airplane Flexibility on Wing Bending Strains in Rough Air . . . by Thomas L. Coleman, Harry Press, and C. C. Shufflebarger

Loads Implications of Gust-Alleviation Systems . . . by William H. Phillips

Ground Loads

Recent Data on Tire Friction During Landing . . . by Sidney A. Batterson

A Summary of Ground-Loads Statistics . . . by John R. Westfall, Benjamin Milwitzky, Norman S. Silsby, and Robert C. Dreher

STRUCTURES

Session Chairman: Richard R. Heldenfels

Aerodynamic Heating

Aerodynamic Heat Transfer to Wing Surfaces and Wing Leading Edges . . . by Aleck C. Bond, William V. Feller, and William M. Bland, Jr.

Total Heat Transfer to Blunt-Nose Shapes With Laminar Boundary Layers at High Supersonic Speeds . . . by John O. Reller, Jr.

Local Heat Transfer to Blunt Noses at High Supersonic Speeds . . . by William E. Stoney, Jr.

Heat Transfer to Bodies at Angles of Attack . . . by William V. Feller

Heat Transfer in Regions of Separated and Reattached Flows . . . by Davis H. Crawford and Charles B. Rumsey

Structures at Elevated Temperatures

Flight Measurements of Airplane Structural Temperatures at Supersonic Speeds . . . by Richard D. Banner

Two Factors Influencing Temperature Distributions and Thermal Stresses in Structures . . . by William A. Brooks, Jr., George E. Griffith, and H. Kurt Strass

Effect of Transient Heating on Vibration Frequencies of Some Simple Wing Structures . . . by Louis F. Vosteen, Robert R. McWithey, and Robert G. Thomson

Effects of Rapid Heating on Strength of Airframe Components . . . by Richard A. Pride, John B. Hall, Jr., and Melvin S. Anderson

The Combinations of Thermal and Load Stresses for the Onset of Permanent Buckling in Plates . . . by George W. Zender and Richard A. Pride

Some Experiments With Insulated Structures . . . by Richard J. Rosecrans, Aldie E. Johnson, Jr., and William M. Bland, Jr.

Some Research Results on Sandwich Structures . . . by Melvin S. Anderson and Richard G. Updegraff

Recent Research on the Creep of Airframe Components . . . by Eldon E. Mathauser, Avraham Berkovits, and Bland A. Stein

A Relation Between Stress, Strain Rate, Time, and Temperature for Metals at Elevated Temperatures . . . by Elbridge Z. Stowell and George J. Heimerl

Reactions of Materials in High-Temperature Air Flows . . . by Joseph G. Thibodaux, Jr., and Joseph N. Kotanchik

Fatigue

Fatigue-Crack Propagation and Residual Static Strength of Built-Up Structures . . . by Herbert F. Hardrath and Richard E. Whaley

Some Aspects of Fail-Safe Design of Pressurized Fuselages . . . by Paul Kuhn and Roger W. Peters

Results From Random-Loading Fatigue Tests of a Full-Scale Transport Wing . . . by John B. Garvin

Studies of Structural Failure Due to Acoustic Loading . . . by Robert W. Hess, Robert W. Fralich, and Harvey H. Hubbard

FLUTTER AND BUFFETING

Session Chairman: Arthur A. Regier

Buffeting

The Use of Wind Tunnels to Predict Flight Buffet Loads . . . by Don D. Davis, Jr., and Wilber B. Huston

Effects of Wing and Fuselage Modifications on Buffeting . . . by Fred B. Sutton and J. Walter Lautenberger, Jr.

Flutter

Theoretical and Experimental Investigations of Delta-Wing Vibrations . . . by Edwin T. Kruszewski, Eldon E. Kordes, and Deene J. Weidman

Oscillating Air Forces and a Presentation of Some Flutter Calculations . . . by Charles E. Watkins, Donald J. Woolston, and Herbert J. Cunningham

Flutter at Very High Speeds . . . by Harry L. Runyan and Homer G. Morgan

Flutter of Wings With and Without External Stores at Transonic and Supersonic Speeds . . . by Laurence K. Loftin, Jr., and William T. Lauten, Jr.

Aerodynamics of Oscillating Control Surfaces at Transonic Speeds . . . by Robert F. Thompson and Sherman A. Clevenson

Status of Flutter of Flat and Curved Panels . . . by Robert W. Leonard and John M. Hedgepeth

Flutter and Divergence of Rectangular Wings of Very Low Aspect Ratio . . . by Robert W. Fralich, John M. Hedgepeth, and W. J. Tuovila

Flutter Experiments With Various Control Configurations . . . by Robert W. Boswinkle, Jr., and Homer G. Morgan

[redacted]

INTRODUCTION

This document contains reproductions of technical papers on some of the most recent research results on aircraft loads, flutter, and structures from the NACA laboratories. These papers were presented by members of the staff of the NACA laboratories at the Conference held at the Langley Aeronautical Laboratory March 5, 6, and 7, 1957. The primary purpose of this Conference was to convey to contractors of the military services and others concerned with the design of aircraft these recent research results and to provide those attending an opportunity to discuss the results.

The papers in this document are in the same form in which they were presented at the Conference in order to facilitate their prompt distribution. The original presentation and this record are considered as complementary to, rather than as substitutes for, the Committee's more complete and formal reports. Accordingly, if information from this document is utilized it is requested that this document not be listed as a reference. Individual reports dealing with most of the information presented at the Conference will subsequently be published by NACA and will therefore be suitable as reference material.

A list of the conferees is included.

[redacted]

LIST OF CONFEREES

The following were registered at the NACA Conference on Aircraft Loads, Structures, and Flutter, Langley Aeronautical Laboratory, Langley Field, Va., March 5, 6, and 7, 1957:

ABBOTT, Ira H.	NACA Headquarters
ABRAHAM, Lewis	Subcommittee on Aircraft Structures
ADAMS, Fred T.	Naval Air Development Station
ADAMS, Laurence J.	Glenn L. Martin Company
ALBERI, Americo	Republic Aviation Corporation
ALEXANDER, Marvin M.	Convair
ALLEN, Robert	Civil Aeronautics Administration
ANBRO, Paul A.	Grumman Aircraft Engineering Corp.
ANDERSON, Enoch A.	Boeing Airplane Company
ANDERSON, Franklin C.	Bell Aircraft Corporation
ANDERSON, John W.	Convair
ANDERSON, Melvin S.	NACA - Langley Laboratory
ANTILL, Richard B.	Raytheon Manufacturing Company
ASHLEY, Holt	Subcommittee on Vibration and Flutter
BADGER, David M.	Northrop Aircraft
BAILEY, Robert A.	Lockheed Aircraft Corporation
BAILEY, Frederick J., Jr.	NACA - Langley Laboratory
BAIRD, Eugene F.	Subcommittee on Vibration and Flutter
BAKER, Wilfred E.	Ballistic Research Laboratory
BANAS, Conrad	United Aircraft Corporation
BANNER, Richard D.	NACA High-Speed Flight Station
BARCUS, Ronald	Bendix Aviation Research Labs.
BARD, Donald O.	Chrysler Corporation
BARKER, Lynn M.	Sandia Corporation
BARTER, John W.	Douglas Aircraft Company
BATTERSON, Sidney A.	NACA - Langley Laboratory
BAUM, C. Philemon	Bureau of Aeronautics
BECKER, John V.	NACA - Langley Laboratory
BEEBE, John	Subcommittee on Low-Speed Aerodynamics
BEELER, De Elroy	NACA High-Speed Flight Station
BERKOVITS, Avraham	NACA - Langley Laboratory
BERTRAM, Mitchel H.	NACA - Langley Laboratory
BEZBATCHENKO, John W.	Goodyear Aircraft Corporation
BIRNBAUM, Sidney	Glenn L. Martin Company
BITZ, Eugene A.	Naval Ordnance Laboratory
BLAND, William M., Jr.	NACA - Langley Laboratory
BOBBITT, Percy J.	NACA - Langley Laboratory
BOCK, Charles D.	Arma Div., American Bosch Arma Corp.
BOGEMA, Bernard L.	Glenn L. Martin Company

BOND, Aleck C.	NACA - Langley Laboratory
BOONE, Paul W.	Subcommittee on Aircraft Structural Materials
BOSWINKLE, Robert W., Jr.	NACA - Langley Laboratory
BOUTON, Innes	Northrop Aircraft
BOWMAN, John C.	Ryan Aeronautical Company
BRASSAW, Lloyd L., Jr.	Bell Aircraft Corporation
BREMER, Paul H.	Lockheed Aircraft Corporation
BRESSETTE, Walter E.	NACA - Langley Laboratory
BREUHAUSER, W. O.	Cornell Aeronautical Laboratory
BREWER, Jack D.	NACA Headquarters
BROOKS, Thurman P.	McDonnell Aircraft Corporation
BROOKS, William A., Jr.	NACA - Langley Laboratory
BROWN, Clinton E.	NACA - Langley Laboratory
BROWN, Harvey H.	NACA Headquarters
BUCKLEY, Edmond C.	NACA - Langley Laboratory
CAHEN, George L.	Glenn L. Martin Company
CARLSON, Harry W.	NACA - Langley Laboratory
CARLSON, Wendell C.	Raytheon Manufacturing Company
CASS, Lorne E.	Lockheed Aircraft Corporation
CATHAWAY, Russ G.	Lockheed Aircraft Corporation
CAYWOOD, William C.	Applied Physics Laboratory
CENTER, Kenneth W.	Grumman Aircraft Engineering Corp.
CHILTON, James P.	Douglas Aircraft Company
CLARK, Lt. John B.	Air Research and Development Command
CLARKE, Martyn V.	Civil Aeronautics Board
CLEVENSON, Sherman A.	NACA - Langley Laboratory
COLEMAN, Thomas L.	NACA - Langley Laboratory
COONEY, Thomas V.	NACA High-Speed Flight Station
COOPER, Ralph D.	David Taylor Model Basin
COWGILL, Lee C.	Lockheed Aircraft Corporation
COX, Joe F.	Cessna Aircraft Company
CRABILL, Norman L.	NACA - Langley Laboratory
CRAWFORD, Davis H.	NACA - Langley Laboratory
CREEL, Ralph	Bureau of Aeronautics
CROWLEY, John M.	Office of Naval Research
CROWLEY, John W.	NACA Headquarters
CULBERTSON, Philip E.	Convair
CUNNINGHAM, Herbert J.	NACA - Langley Laboratory
CYPHERS, Richard J., Jr.	Grumman Aircraft Engineering Corp.
CZARNECKI, K. R.	NACA - Langley Laboratory
DAUM, Fred L.	Subcommittee on Vibration and Flutter
DAVIS, Don D., Jr.	NACA - Langley Laboratory
DAWSON, John R.	NACA - Langley Laboratory
DEARING, David	Beech Aircraft Corporation
DEEP, Raymond A.	Redstone Arsenal

[redacted]

DeHART, Robert C.	Armed Forces Special Weapons Project
DeLANCEY, Lawrence M.	Naval Ordnance Test Station
DEPTULA, Capt. Alfred R.	Office Deputy Ch. of Staff, Development, USAF
DEUTSCHMAN, Jerome N.	Bell Aircraft Corporation
DIEHL, Capt. Walter S. USN (Ret.)	Committee on Aerodynamics
DOETSCH, H. K.	Wright Air Development Center
DOLEN, William K.	Sandia Corporation
DONELY, Philip	NACA - Langley Laboratory
DOTY, Ralph John	Boeing Airplane Company
DOUGHERTY, James E., Jr.	Subcommittee on Aircraft Structures
DOW, Norris	General Electric Company
DRALEY, Eugene C.	NACA - Langley Laboratory
DRYDEN, Dr. Hugh L.	NACA Headquarters
DUBERG, John E.	Aeronutronic Systems
DUKES, Wilfred H.	Bell Aircraft Corporation
DUNCAN, Lt. Cmdr. B. B.	Bureau of Aeronautics
DUNN, Maurice B.	Boeing Airplane Company
DUSSAULT, John	Cessna Aircraft Company
DYE, Lt. F. E., Jr.	Bureau of Aeronautics
EKREM, Clifford O.	Convair
ENTZ, Phillip H.	Boeing Airplane Company
EPSTEIN, Albert	Subcommittee on Aircraft Loads
ERICKSON, Albert L.	NACA - Ames Laboratory
ERTHAL, John F.	Naval Air Material Center
EVANS, Albert J.	NACA Headquarters
EVERETT, Maj. Phillip E.	AF Development Field Representative
FALABELLA, Gaetano, Jr.	Air Force Cambridge Research Center
FANTI, Roy	United Aircraft Corporation
FAVOR, Ronald J.	Battelle Memorial Institute
FEDZIUK, Henry A.	NACA - Langley Laboratory
FELLER, William V.	NACA - Langley Laboratory
FERNANDEZ, Jose	Convair
FETTIS, Henry E.	Wright Air Development Center
FINK, Martin	United Aircraft Corporation
FISCHLER, Jerome E.	Douglas Aircraft Company
FITZGERALD, Fred	Radioplane Company
FLYGARE, Richard W.	Sperry-Utah Engineering Lab.
FORMHALS, Edwin J.	Bureau of Aeronautics
FOSTER, Charles R.	Subcommittee on Aircraft Loads
FRALICH, Robert W.	NACA - Langley Laboratory
FRANCEY, Capt. R. G.	Air Force Special Weapons Center
FRICK, Charles W.	Convair
FROST, Richard C.	Convair
FURLONG, G. Chester	Arnold Engineering and Development Center

[redacted]

GARCIA, Manuel A.	Naval Air Missile Test Center
GARRICK, I. E.	NACA - Langley Laboratory
GARVIN, John B.	NACA - Langley Laboratory
GATES, Ordway B., Jr.	Glenn L. Martin Company
GAYMAN, William	Radioplane Company
GENIESSE, Major Eugene W., Jr.	Subcommittee on High-Speed Aerodynamics
GEUDTNER, Walter J., Jr.	Convair
GILLIG, Franklin J.	Cornell Aeronautical Laboratory
GILRUTH, Robert R.	NACA - Langley Laboratory
GIONFRIDDO, Maurice P.	Air Force Cambridge Research Center
GLASSMEYER, Clifford E., Jr.	Battelle Memorial Institute
GLOVER, Louis S.	Applied Physics Laboratory
GOLDIN, Robert	Subcommittee on Aircraft Loads
GOMZA, Alexander	Grumman Aircraft Engineering Corporation
GORANSON, R. Fabian	NACA Headquarters
GRANT, Frederick C.	NACA - Langley Laboratory
GREER, Major Edwin H.	Arnold Engineering Development Center
GRIFFIN, Edward J.	Bureau of Aeronautics
GRIFFITH, George E.	NACA - Langley Laboratory
GRIFFITH, Max O.	Bureau of Aeronautics
GRINSTED, Frank	British Ministry of Supply
HALL, Bertrand M.	Douglas Aircraft Company
HALL, John B., Jr.	NACA - Langley Laboratory
HALSEY, Robert M.	Bell Aircraft Corporation
HAMILTON, William T.	Subcommittee on Aerodynamic Stability and Control
HAMMERBERG, Fritchiof	Civil Aeronautics Administration
HAMMIL, John P.	Douglas Aircraft Company
HARDRATH, Herbert F.	NACA - Langley Laboratory
HARRINGTON, Joseph H.	Subcommittee on Aircraft Loads
HARRIS, Thomas A.	NACA - Langley Laboratory
HARTLEY, Richard M.	David Taylor Model Basin
HAVILAND, John K.	Chance Vought Aircraft
HAYDEN, Harold J.	Boeing Airplane Company
HEDGEPETH, John M.	NACA - Langley Laboratory
HEIMERL, George J.	NACA - Langley Laboratory
HEITHECKER, Heinrich A.	Holloman Air Development Center
HELDENFELS, Richard R.	NACA - Langley Laboratory
HELLEBRAND, Emil A. H.	Subcommittee on Aircraft Structures
HENDERSON, Arthur, Jr.	NACA - Langley Laboratory
HENDERSON, Campbell	North American Aviation
HEPPER, Richard H.	McDonnell Aircraft Corporation
HESS, Robert W.	NACA - Langley Laboratory
HOFF, Dr. Nicholas J.	Subcommittee on Aircraft Structures
HOFFMAN, Niles R.	Wright Air Development Center
HOGE, H. J.	Subcommittee on Aircraft Loads
HOLTZ, John R.	David Taylor Model Basin

HOOD, Manley J.	NACA - Ames Laboratory
HOOVER, Isaac H.	Civil Aeronautics Administration
HUBBARD, Harvey H.	NACA - Langley Laboratory
HUNT, Melvin W.	North American Aviation
HUNTLEY, H. W., Jr.	Subcommittee on Aircraft Loads
HUSIC, William J.	Civil Aeronautics Administration
HUSTON, Wilber B.	NACA - Langley Laboratory
ISRAELSEN, Lt. Col. Orson A.	Armed Forces Special Weapons Project
JACKSON, David W.	Wright Air Development Center
JENKINS, David R.	Batelle Memorial Institute
JOHNSON, Aldie E., Jr.	Avco Manufacturing Corporation
JOHNSON, H. Clay	Subcommittee on Vibration and Flutter
JOHNSON, Harry W.	Ramo-Wooldridge Corporation
JOHNSON, J. Aldridge	Lockheed Aircraft Corporation
JOHNSON, J. B.	Subcommittee on Aircraft Structural Materials
JOHNSTON, William M.	Lockheed Aircraft Corporation
JORDAN, Gareth H.	NACA High-Speed Flight Station
JORDAN, Peter F.	Glenn L. Martin Company
KAECHELE, Lloyd E.	Rand Corporation
KAMBACK, Elmer L.	Glenn L. Martin Company
KAPLAN, Abner	Ramo-Wooldridge Corporation
KASTEN, Herman G.	Ramo-Wooldridge Corporation
KEARNS, John P.	Applied Physics Laboratory
KEENER, Earl R.	NACA High-Speed Flight Station
KEIRSEY, Robert L.	Douglas Aircraft Company
KEITH, Bobbie C.	Wright Air Development Center
KERR, T. H.	British Ministry of Supply
KINNAMAN, Edward B.	Boeing Airplane Company
KINTAS, John	Beech Aircraft Corporation
KLEISS, Cmdr. N. J.	Naval Air Material Center
KORDES, Eldon E.	NACA - Langley Laboratory
KOTANCHIK, Joseph N.	NACA - Langley Laboratory
KRAMER, Edward H.	Fairchild Aircraft Division
KRICKENBERGER, Lt. Cmdr. Custer F., Jr.	Armed Forces Special Weapons Project
KROLL, Wilhelmina D.	National Bureau of Standards
KRUSZEWSKI, Edwin T.	NACA - Langley Laboratory
KUGEL, H. E.	Wright Air Development Center
KUHN, Paul	NACA - Langley Laboratory
KULLAS, Albert J.	Glenn L. Martin Company
KUNZE, Frank C.	Chrysler Corporation
LaFRANCE, Jeremie U., Jr.	Glenn L. Martin Company
LAIDLAW, William R.	Subcommittee on Vibration and Flutter

LAMPROS, Alexander F.	Naval Air Missile Test Center
LANDERS, C. B.	Lockheed Aircraft Corporation
LANDES, Paul E.	McDonnell Aircraft Corporation
LANDON, John M.	Chrysler Corporation
LAUTEN, William T., Jr.	NACA - Langley Laboratory
LAUVER, Dean C.	Bureau of Aeronautics
LECAT, Robert	Fairchild Guided Missile Division
LEISS, Abraham	NACA - Langley Laboratory
LEONARD, Robert W.	NACA - Langley Laboratory
LEVY, Samuel	General Electric Company
LI, Ta Chung-Heng	Convair
LIEBOWITZ, Harold	Office of Naval Research
LOCKE, Frederick W. S., Jr.	Bureau of Aeronautics
LOFTIN, Laurence K., Jr.	NACA - Langley Laboratory
LOMAX, Ted L.	Boeing Airplane Company
LoPRESTI, Antonio	Subcommittee on Aircraft Structures
LU, Hoshen	Republic Aviation Corporation
LUCAS, John W.	Jet Propulsion Laboratory, C.I.T.
MAGRATH, H. A.	Wright Air Development Center
MALVESTUTO, Frank S.	NACA High-Speed Flight Station
MARCOPULOS, George	North American Aviation
MARTIN, James E.	Chance Vought Aircraft
MARTIN, John W., Jr.	Glenn L. Martin Company
MARTZ, Ronald B.	Wright Air Development Center
MATHAUSER, Eldon E.	NACA - Langley Laboratory
MAY, Ralph W., Jr.	NACA Headquarters
MAYER, Frank S., Jr.	Douglas Aircraft Company
MAZELSKY, Bernard	Lockheed Aircraft Corporation
McCASKILL, Allan M.	Douglas Aircraft Company
McCLELLAND, Clyde M.	Douglas Aircraft Company
McFARLAND, Donald R.	NACA - Langley Laboratory
McGINNESS, Capt. W. T.	Subcommittee on Aircraft Structures
McGOWAN, W. A.	Bureau of Aeronautics
McHUGH, James G.	Subcommittee on Aerodynamic Stability and Control
McLEMORE, H. Clyde	NACA - Langley Laboratory
McWITHEY, Robert R.	NACA - Langley Laboratory
MELLQUIST, Victor G.	Aircraft Industries Association of America
MEREDITH, Lt. Oliver D.	Air Research and Development Command
MERZ, Ernest J.	Glenn L. Martin Company
METTLER, Stephen	Convair
MICHEL, Douglas	Subcommittee on Vibration and Flutter
MILLER, Chester W.	McDonnell Aircraft Corporation
MILLER, Lt. Cmdr. Jack N.	Bureau of Aeronautics
MILWITZKY, Benjamin	NACA - Langley Laboratory
MIROWITZ, L. I.	Subcommittee on Vibration and Flutter
MISKAM, Frederick C.	Douglas Aircraft Company

[redacted]

MITCHAM, Grady L.	U. S. Naval Ordnance Experimental Unit
MOLELLA, Roslo J.	Naval Air Material Center
MOORE, Lt. Col. John T., Jr.	Air University
MORAN, Herbert D.	Aircraft Industries Association of America
MORDFIN, Leonard	National Bureau of Standards
MORGAN, Homer G.	NACA - Langley Laboratory
MUGLER, John P., Jr.	NACA - Langley Laboratory
MULHERN, John J.	Naval Air Development Station
MULTHOPP, Hans	Glenn L. Martin Company
MUNDO, Charles J.	Arma Div., American Bosch Arma Corp.
MUNTER, Paul L.	Republic Aviation Corporation
MURRAY, James J.	Office of Ordnance Research, U. S. Army
MYERS, Boyd C., II	NACA Headquarters
MYKYTOW, Walter J.	Subcommittee on Vibration and Flutter
NAUGHTON, S. K.	Wright Air Development Center
NEELY, Robert H.	Fairchild Aircraft Division
NELSON, Lloyd W.	Lockheed Aircraft Corporation
NEWBERGER, Eli S.	Civil Aeronautics Administration
NEWBY, Clinton T.	Subcommittee on Aircraft Loads
NEWELL, Joseph S.	North American Aviation
NOREM, Allan G.	Aerophysics Development Corporation
NORTON, David A.	Boeing Airplane Company
O'BRIEN, R. J.	Wright Air Development Center
OFFTERMATT, Lt. Cmdr. Wilbur F.	Bureau of Aeronautics
OGNESS, Arthur M.	Northrop Aircraft
O'MALLEY, James A., Jr.	Subcommittee on Low-Speed Aerodynamics
OSBORN, Earl P.	Grumman Aircraft Engineering Corp.
PALMER, Carl B.	NACA Headquarters
PAYSON, Peter	Subcommittee on Aircraft Structural Materials
PEARSON, Albin O.	NACA - Langley Laboratory
PELOUBET, Raymond P.	Convair
PERSH, Jerome	Naval Ordnance Laboratory
PETERS, Roger W.	NACA - Langley Laboratory
PETERSON, James P.	NACA - Langley Laboratory
PFAFF, George C., Jr.	Glenn L. Martin Company
PHILLIPS, Franklyn W.	NACA Headquarters
PHILLIPS, William H.	NACA - Langley Laboratory
PIERCE, Harold B.	NACA - Langley Laboratory
PIERPONT, William G.	Beech Aircraft Corporation
PINES, Samuel	Republic Aviation Corporation
POLHAMUS, Edward C.	NACA - Langley Laboratory

[redacted]

[redacted]

PRESS, Harry	NACA - Langley Laboratory
PRIDE, Richard A.	NACA - Langley Laboratory
RACISZ, Stanley F.	Bell Aircraft Corporation
RAPHAEL, Coleman	Republic Aviation Corporation
RARING, Richard H.	NACA Headquarters
RAY, George D.	Committee on Aircraft Construction
RAYBURN, Leo	Raytheon Manufacturing Company
REEVES, Walter R.	Convair
REGIER, Arthur A.	Subcommittee on Vibration and Flutter
REID, Dr. Henry J. E.	NACA - Langley Laboratory
RELLER, John O., Jr.	NACA - Ames Laboratory
RHODE, Richard V.	NACA Headquarters
RICHARDSON, William B.	Naval Ordnance Laboratory
ROBERTS, William M.	Arnold Engineering Development Center
ROBERTSON, Donald K.	Glenn L. Martin Company
ROCHÉ, Jean A.	AF Development Field Office, NACA Langley Aeronautical Laboratory
RODDEN, William P.	North American Aviation
ROLFE, Rial E., Jr.	McDonnell Aircraft Corporation
ROSCHE, Melvin G.	NACA Headquarters
ROSECRANS, Richard J.	NACA - Langley Laboratory
ROSEN, B. Walter	Avco Manufacturing Corporation
ROSENBAUM, Robert	Subcommittee on Vibration and Flutter
ROTH, A. L.	Douglas Aircraft Company
ROTTMAYER, Earl	Goodyear Aircraft Corporation
ROZELLE, Harold L.	Ryan Aeronautical Company
RUMSEY, Charles B.	NACA - Langley Laboratory
RUNSTAD, Harold J.	Boeing Airplane Company
RUNYAN, Harry L., Jr.	NACA - Langley Laboratory
SALZBERG, Leo F.	Wright Air Development Center
SAUNDERS, John J.	Glenn L. Martin Company
SCHNEIDER, William C.	Bureau of Aeronautics
SCHNITT, Arthur	Bell Aircraft Corporation
SCHREIBER, Ralph	Radioplane Company
SCHUMACHER, Ernest A.	Glenn L. Martin Company
SCHUMACHER, John G.	Convair
SCROOC, D. J.	Ramo-Wooldridge Corporation
SECKLER, Sam	Bureau of Aeronautics
SEIDE, Paul	Ramo-Wooldridge Corporation
SENTKER, Lawrence C.	Civil Aeronautics Administration
SHARPE, Lawrence W.	Air Force Cambridge Research Center
SHATUNOFF, Stanley	Arma Division, American Bosch Arma Corporation
SHAW, S. L.	Douglas Aircraft Company
SHORTAL, Joseph A.	NACA - Langley Laboratory
SHOWERS, Nathan	Wright Air Development Center

[redacted]

E

[redacted]

SHUFFLEBARGER, C. C.	NACA - Langley Laboratory
SILSBY, Norman S.	NACA - Langley Laboratory
SKIMMIN, Kenneth D.	Wright Air Development Center
SMITH, Randall C.	Fairchild Aircraft Division
SMITH, Turner L.	Ballistic Research Laboratory
SOCKS, Glenn A.	Chrysler Corporation
SOULÉ, Hartley A.	NACA - Langley Laboratory
SPAHR, J. Richard	NACA - Ames Laboratory
SPAULDING, E. H.	Subcommittee on Aircraft Structures
SPEAKER, Robert F.	Bureau of Aeronautics
STACK, John	NACA - Langley Laboratory
STAHL, Harold F.	Chance Vought Aircraft
STAUFFER, Warren A.	Lockheed Aircraft Corporation
STEIGER, Arthur R.	Air Force Special Weapons Center
STEIN, Bland A.	NACA - Langley Laboratory
STEVENS, Clifton D.	Goodyear Aircraft Corporation
STEVENS, John E.	Subcommittee on Aircraft Structures
STEVENSON, C. H.	Committee on Aircraft Structures
STONE, Ralph W., Jr.	NACA - Langley Laboratory
STONEY, William E., Jr.	NACA - Langley Laboratory
STOWELL, Elbridge Z.	NACA - Langley Laboratory
STRASS, H. Kurt	NACA - Langley Laboratory
STRINGHAM, R. H.	Douglas Aircraft Company
SUTHERLAND, Rodney D.	Convair
SUTLIFF, John D.	Ryan Aeronautical Company
SUTTON, Fred B.	NACA - Ames Laboratory
SWANSON, Lt. Col. Arthur R.	Office of the Assistant Secretary of Defense
SWANSON, Theodore B.	Aero-General Corporation
SWIHART, John M.	NACA - Langley Laboratory
TARGOFF, Walter	Cornell Aeronautical Laboratory
TARNOWER, Gerald	Chance Vought Aircraft
TETENS, Robert C.	Temco Aircraft Corporation
THEODORSEN, Dr. Theodore	Republic Aviation Corporation
THIBODAUX, Joseph G., Jr.	NACA - Langley Laboratory
THOMPSON, Floyd L.	NACA - Langley Laboratory
THOMPSON, Robert F.	NACA - Langley Laboratory
THOMSON, Robert G.	NACA - Langley Laboratory
THORNE, Charles J.	U. S. Naval Ordnance Test Station
THORSON, Kenneth R.	Boeing Airplane Company
TOPP, LeRoy J.	Boeing Airplane Company
TRACY, Alfred C.	Douglas Aircraft Company
TROHA, Charles C.	Bureau of Aeronautics
TUOVILA, W. J.	NACA - Langley Laboratory
UJIHARA, Ben H.	North American Aviation
UNDERWOOD, William J.	NACA Liaison Officer, Wright-Patterson AFB

[redacted]

UPDEGRAFF, Richard G.	NACA - Langley Laboratory
UTTER, Emmet	Beech Aircraft Corporation
VANDREY, Dr. Friedrich	Glenn L. Martin Company
VETERITO, A. Michael	Fairchild Guided Missile Division
VOLLMECKE, Albert A.	Committee on Aircraft Construction
VOLLO, Samuel D.	Bell Aircraft Corporation
VOSTEEN, Louis F.	NACA - Langley Laboratory
WALLS, James H.	Bureau of Aeronautics
WATKINS, Charles E.	NACA - Langley Laboratory
WATSON, Robert E.	Boeing Airplane Company
WEBB, Everette L.	Boeing Airplane Company
WEIDMAN, Deene J.	NACA - Langley Laboratory
WEINBERGER, Robert A.	Bureau of Aeronautics
WEISMAN, Yale	Subcommittee on Aircraft Loads
WEST, F. E., Jr.	NACA - Langley Laboratory
WESTRUP, Robert W.	North American Aviation
WESTVIG, Roger	North American Aviation
WHALEY, Richard E.	NACA - Langley Laboratory
WHELDON, Wilbert G.	Northrop Aircraft
WHITE, Richard P., Jr.	Cornell Aeronautical Laboratory
WILLIAMS, Walter C.	NACA High-Speed Flight Station
WILLIAMSON, Leonard H.	Civil Aeronautics Administration
WILSON, Herbert A., Jr.	NACA - Langley Laboratory
WILSON, James N.	Jet Propulsion Laboratory, C.I.T.
WOLCOTT, Verne V.	Convair
WOOLSTON, Donald J.	NACA - Langley Laboratory
YATES, William B.	Glenn L. Martin Company
YORK, Joseph E.	Lockheed Aircraft Corporation
YOUNG, George E.	Northrop Aircraft
YOUNG, Willis H.	Bureau of Aeronautics
ZENDER, George W.	NACA - Langley Laboratory
ZISFEIN, Melvin B.	Bell Aircraft Corporation
ZLOTNICK, Martin	Avco Manufacturing Corporation

AIRCRAFT LOADS

HENDERSON & BERTRAM

N71-75383

FACTORS AFFECTING LOADS AT HYPERSONIC SPEEDS

By Arthur Henderson, Jr., and Mitchel H. Bertram

Langley Aeronautical Laboratory

SUMMARY

This paper gives a brief summary of current loads information at hypersonic speeds. Several methods which the designer can employ in estimating the loads on various aircraft components are discussed. The paper deals with the characteristics of both slender and blunt configurations and touches upon the effects of boundary-layer and aerodynamic interference.

INTRODUCTION

The calculation of loads at hypersonic speeds requires the use of techniques with which many designers are not very familiar. The methods based on linear or second-order theory, which were widely used at supersonic speeds, are inadequate for slender configurations at hypersonic speeds and, of course, are completely inapplicable to configurations with blunt noses or leading edges.

In this paper it is shown that certain simplifying features which allow good design approximations of loads to be made with a minimum of effort exist at hypersonic speeds. In addition, some of the unsolved problems associated with hypersonic phenomena are pointed out.

SYMBOLS

a	speed of sound
A	constant
c	local chord length
$\bar{c}$	mean aerodynamic chord
c_n	section normal-force coefficient

C_p	local surface pressure coefficient
d	maximum body diameter
h	height of wedge
K	hypersonic similarity parameter, $M \frac{d}{l}$
l	length of nose or wedge
M	Mach number
p	pressure
r	radius
R	Reynolds number
s	arc length
t	thickness
V	velocity
x	distance from nose or leading edge in body-axis system
α	angle of attack
γ	ratio of specific heats
δ	flap deflection angle
Δ	incremental value
ϵ	distance between adjacent streamlines
θ	cone shock angle
Λ	sweepback angle
σ	cone semiapex angle
τ	time
φ	meridian angle

Subscripts:

∞	free-stream conditions
B(W)	body in presence of wing
MAX	maximum
s	shoulder
t	based on thickness
d	based on diameter

DISCUSSION

There are several methods which the designer can employ in arriving at an estimate of the loads on the various aircraft components. Before discussing them, however, it is instructive to consider, qualitatively, how hypersonic phenomena differ from supersonic.

Although hypersonic flow introduces many problems which were not encountered at supersonic speeds, it also introduces certain simplifying features; and aerodynamicists have not been long in taking advantage of them. For example, one source of simplification at hypersonic speeds is the fact that, in the exact shock equations, the Mach number term is usually squared and often appears in the denominator. Thus, as the Mach number increases, these terms become insignificant; thus relatively simple expressions often yield accurate approximations for certain flow properties at hypersonic speeds.

Slender Configurations

Characteristics of hypersonic flow.- Some simplifying features of hypersonic flow are illustrated in figures 1 and 2. One of the characteristics of hypersonic flow is its tendency toward two-dimensionality when in contact with slender bodies or surfaces. (See fig. 1.) The upper half of figure 1 depicts a sharp-leading-edge sweptback wing in a low and in a high Mach number flow field. There are two streamlines the same distance ϵ apart. As shown by the dashed lines, the fields of influence from each disturbance point along the leading edge spread across the wing in supersonic flow, whereas they are confined to a relatively narrow region in hypersonic flow. In addition, the right streamline of each pair will strike the leading edge later than the left one, the time lag being $\Delta\tau = \frac{\epsilon \tan \Lambda}{Ma}$. Obviously, as the Mach number increases, the time

lag decreases; thus at high Mach numbers the right streamline strikes the leading edge at almost the same time as the left one. Consequently, as far as the fluid itself is concerned, it feels as though it is practically two dimensional.

The bottom half of figure 1 depicts the fundamental basis of the generalized shock-expansion method as applied to slender three-dimensional bodies. As Eggers and Savin (ref. 1) have shown, so long as the divergence of streamlines along the body is negligible, the flow on the body surface and the associated flow field will be essentially two-dimensional in nature; consequently, two-dimensional shock-expansion theory can be used to analyze the flow about slender bodies of revolution.

Hypersonic similarity law.- The designer has another powerful tool at his disposal in the form of the hypersonic similarity law (see, for example, refs 2 to 4), which states that the pressures at corresponding points on similarly shaped bodies are identical if, for the two bodies, the product of free-stream Mach number and thickness ratio is a constant.

The physical concept behind the hypersonic similarity law is illustrated qualitatively in figure 2. Two marbles are shown, each rolling toward its own wedge. The upper marble will rise a height h in the length l_1 with the velocity V_1, while the lower marble will rise the same height h in the longer length $l_2 = Al_1$ but with the higher velocity $V_2 = AV_1$. The ratio of lengths and velocities is such that both marbles rise the same height h in the same length of time; that is, they both experience the same change of velocity and, consequently, each marble will impart the same amount of momentum to its particular wedge. If the marbles are thought of as air molecules and the wedges as corresponding slopes on two similar bodies, a direct analogy with the hypersonic similarity law is immediately apparent.

The approximate region in which the hypersonic similarity law is applicable has been determined by Lees (ref. 5) to be about as shown in figure 3 for cones. This region is determined by the condition that the cone shock angle θ_s is less than 24°. Thus, the maximum cone angle for good correlation at hypersonic speeds will be about 20°. Bodies of revolution such as ogives are essentially conical at the nose and decrease in slopes thereafter. Therefore, if the nose of any pointed body is about 20° or less, it should correlate well with this law. For ogives, this means the fineness ratio should be about 3 or more.

Figure 4 presents the pressure-ratio distribution on ogives. The solid lines are the characteristic solutions of Rossow (ref. 4), each of which is for at least two different combinations of M_∞ and l/d within the range shown at the lower right. Although $M_\infty = 12$ was the

highest value of M_∞ used in the calculations, it should be pointed out that this value is not meant to be taken as an upper limit. Also shown are the tangent-cone approximations of Probstein and Bray (ref. 6). For $K \geq 1$, they applied the tangent-cone approximation to Lees' result which is for the case when the shock lies fairly close to the body; and for $K < 1$, that is, when the shock is well removed from the surface of the slender bodies, the tangent-cone approximation is applied to Kármán's result in linearized supersonic flow.

Van Dyke has pointed out in his work on the hypersonic small-disturbance theory (refs. 7 and 8) that the range of applicability of the hypersonic similarity law can be extended to the transonic range by replacing the Mach number term with the Prandtl-Glauert similarity factor $\sqrt{M_\infty^2 - 1}$. The degree to which this correlation is successful is illustrated in figure 5 for cones with semiapex angles of 5°, 10°, 15°, and 20°. In this figure $C_p/\tan^2 \sigma$ is plotted against $\sqrt{M_\infty^2 - 1} \tan \sigma$ for a Mach number range from 1.15 to hypersonic speeds. Each curve is ended when sonic velocity appears on the cone surfaces. The correlation is seen to be excellent.

The correlation for bluff cones as suggested by Newtonian theory is presented in figure 6, where $C_p/\sin^2 \sigma$ is plotted against σ. For the ranges of Mach number and σ shown, a good approximation to the pressure on the surface of a bluff cone is $\frac{C_p}{\sin^2 \sigma} \approx 2.2$.

Shock-expansion theory.- The use of two-dimensional shock-expansion theory to predict the pressures on slender bodies of revolution at zero angle of attack at hypersonic speeds is well known. Eggers and his associates (refs. 1 and 9) have shown that, provided conditions at the nose are known from either conical theory or experiment, the generalized shock-expansion method can be used for slender bodies of revolution at angle of attack.

Figure 7 shows a comparison of the shock-expansion theory with experiment for an ogival nose at an angle of attack of 15° and a free-stream Mach number of 5.05. The symbols show the experimental pressure coefficients along the top, side, and bottom meridians. The theoretical predictions begin with the assumption of conical flow at the nose. The solid curves use the theoretical cone approximation of Savin (ref. 10) as the starting point for the shock-expansion calculations, and the dashed curve uses experimentally determined conditions on the nose cone as the starting point for the calculations. Obviously, a reliable theoretical method is preferable for design work. It is seen that on the bottom meridian, which would be of most interest for loads considerations, the shock-expansion

calculations agree with experiment for both the theoretically and the experimentally determined starting conditions; that is, Savin's theoretical cone results combined with shock-expansion theory will give good design estimates of maximum loads on sharp noses at angle of attack.

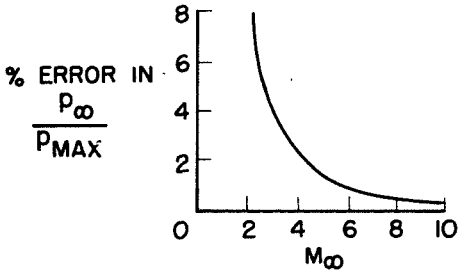
Effect of Blunting

In cases where high heat-transfer rates are expected, the use of blunt leading edges and noses is dictated. Figures 8 and 9 present results for both two-dimensional circular cylinders (refs. 11 and 12) and hemispherical-nose bodies of revolution (ref. 13). The results for circular cylinders (fig. 8) would be applicable both to bodies of revolution at high angles of attack and to the leading edges of blunt sweptback wings. Figure 8 is essentially a double correlation of pressure ratios. It shows the manner in which the pressure ratio varies with meridian angle, and it is good for a wide range of sweepback angles. Also note that, as the Mach number increases, the band of experimentally determined pressure ratios converges toward the theoretical curve of Goodwin (ref. 12) shown by the dashed line. Penland (ref. 11) has shown that p_{max} can be determined on yawed circular cylinders for sweepback angles from 0° to about 75° at $M_\infty = 6.9$ by using the normal component of M_∞. Thus, the absolute pressure distribution on the windward side of yawed circular cylinders can be obtained.

The results for hemispherical noses in figure 9 show excellent agreement with Newtonian theory. In this figure the pressure-coefficient ratio is plotted against s/r, which is the arc angle in radians. As can be seen, the pressure-coefficient ratio is independent of Mach number. The curve of $C_{p,MAX}$ against M_∞ in the upper right of the figure shows that, for values of M_∞ greater than about 4, $C_{p,MAX}$ is essentially a constant on the order of 1.8. Thus, with the aid of Newtonian theory, C_p can be closely estimated, and for values of M_∞ above about 4, the C_p distribution will be essentially invariant with M_∞.

As was mentioned previously, many of the exact flow parameters can be closely approximated with simple expressions in the hypersonic-flow regime. For example, for $\gamma = 1.4$ and $M_\infty \gg 1$, it can be shown that the ratio of free-stream static pressure to stagnation pressure on a blunt-nose body is approximately $0.777/M_\infty^2$. (This ratio is determined

in the appendix.) The percentage error in the true value of p_∞/p_{MAX} incurred by using the approximation is shown by the sketch. At $M_\infty = 3$, the error is only 4 percent and it decreases rapidly thereafter with increasing M_∞. It can also be shown that for $M_\infty \gg 1$, the ratio of local pressure to maximum pressure is approximately equal to the ratio of local pressure coefficient to maximum pressure coefficient. Consequently, the ratio of the local absolute pressure to the free-stream static pressure is given by $\frac{p}{p_\infty} \approx \frac{M_\infty^2}{0.777} \frac{C_p}{C_{p,MAX}}$; that is, at hypersonic speeds, the absolute pressure at any point on a blunt nose is directly proportional to the square of the Mach number. In particular, for any given altitude, the absolute pressure distribution on a hemispherical nose is given by $\frac{p}{p_\infty} = \frac{M_\infty^2}{0.777} \cos^2(s/r)$ for $0 \leqq s/r \lesssim 1.3$ radians.



The fact that the experimental pressures deviate from the theoretical pressures beyond about 1.3 radians is due to a combination of entropy, vorticity, and boundary-layer effects, which, of course, Newtonian theory does not include. For the Mach numbers considered herein, the effects are negligible as far as loads are concerned. As the Mach number is increased, however, these effects become increasingly important.

Figure 10 shows how, as a result of entropy gain, the surface pressure at the shoulder varies with Mach number. The model in figure 10 is a two-dimensional flat slab with a sonic-wedge leading edge. The pressures were calculated by simple inviscid shock-expansion theory. It can be seen that, as M_∞ increases, the shoulder pressure increases to very large values. The pressure on the shoulder of blunt-nose bodies and blunt-leading-edge wings would follow the same trend with Mach number.

Figure 11 presents theoretically and experimentally determined pressure distributions on a blunt-leading-edge flat plate for a free-stream Mach number of about 7. The theoretically determined pressure distributions were approximated by assuming sonic-wedge leading-edge conditions. Also indicated in the figure is the value of the pressure ratio for no entropy gain and zero vorticity. The assumption that free-stream static pressure exists on the flat plate was perfectly acceptable at lower supersonic speeds. At hypersonic speeds, however, the large entropy gain through the normal shock and the large entropy and vorticity gradients

induced in the flow field by the high shock curvature result in the type of pressure distribution shown by the solid curve. This curve was calculated for the inviscid flow at a Mach number of about 7 for the sonic-wedge leading-edge configuration shown at the upper left. The dashed curve is the experimental pressure distribution for the blunt-leading-edge plate shown on the right at one value of Reynolds number. The difference between these two curves is due to the presence of the boundary layer. If the Reynolds number had been lower, the boundary layer would have been thicker and the separation of these two curves would have been greater; the converse being true if the Reynolds number had been higher. It should also be pointed out that, as the Mach number increases, not only does the level of p/p_∞ at the shoulder increase but also the rate of decrease with distance becomes less, so that the entropy and vorticity effects are spread over a greater distance at higher Mach numbers.

Effect of Boundary-Layer Separation

When real fluid effects, including boundary layers, are brought into the picture, the consequences of boundary-layer separation must also be considered. At hypersonic speeds boundary-layer separation is often important, although it can sometimes be neglected.

Figures 12 and 13 illustrate examples of boundary-layer separation which must be considered and boundary-layer separation which may be neglected. Both the body with conical flare ("flared skirt") shown in figure 12 and the body with flapped wing shown in figure 13 were tested at $M_\infty \approx 7$. (See refs. 14 and 15, respectively.) The manner in which the separation point moves rearward along the flared-skirt body with increasing Reynolds number is indicated by the solid line in figure 12. The body-pressure-coefficient distributions for two extreme positions are shown above with corresponding symbols. The importance of knowing whether to design for separated or unseparated flows is obvious. For unseparated flow the skirt pressure is about what would be expected in the absence of viscosity, while the laminar separation region essentially protects the skirt from direct contact with the free stream.

On the other hand, a large portion of the upper surface of the wing with trailing-edge flap (fig. 13) is in a separated-flow region and there is essentially no effect on the upper surface pressure coefficient. Figure 13 shows the flap deflected 16°; however, the same effects would be true with a negative flap deflection. The loads on the upper surfaces of wings at angle of attack in hypersonic flow are essentially negligible whether separation exists or not; the difference between free-stream pressure and vacuum is so small in comparison with the pressures on the lower surface that, for all practical purposes, the upper surface can be neglected in loads calculations.

The separated flow on the lower surface is confined to a relatively small region. If this separation point were to move forward the lower surface loads would be affected more than shown in figure 13. The magnitude of the loads induced would also depend on the condition of the boundary layer, that is, whether it is laminar or turbulent.

There is as yet not enough knowledge about separation at hypersonic speeds to be able to predict when or where separation will occur for either laminar or turbulent flow.

Aerodynamic Interference

Another field which is relatively unexplored at hypersonic speeds is that of aerodynamic interference and the role that interference plays in altering the expected loads on any component.

One phase of the interference problem was investigated by building a scale model of a configuration which had previously been tested at $M_\infty = 3.36$. (See refs. 16 and 17.) This model was tested at $M_\infty = 6.85$ in the Langley 11-inch hypersonic tunnel. Some preliminary results are presented herein.

Figures 14 and 15 present the span-load distributions on the wing alone and on the wing in the presence of the body at an angle of attack of 15° for $M_\infty = 3.36$ and $M_\infty = 6.85$, respectively. The overall trends of the results at $M_\infty = 3.36$ are about what would be expected. The results at $M_\infty = 6.85$ show the large localized effect which the thick boundary layer plays in interference between adjacent components. The indicated position of the boundary layer was taken from schlieren pictures at $\alpha = 0^\circ$ on the sharp-nose body. The thickness and condition of the boundary layer at the wing-body juncture at $\alpha = 15^\circ$ is not known. Note also the effect of nose shape on the loadings. The blunt nose decreased the wing loadings. Although the decrement was not appreciable at this Mach number, it is to be expected that the greater losses incurred by a detached shock at higher Mach numbers will more seriously affect the loadings not only on the wing but also on all components within the region of influence of the highly rotational part of the flow field associated with blunt noses.

The shock-expansion theory predicts the loading on the wing alone at $M_\infty = 6.85$ fairly well. The results of the $M_\infty = 3.36$ tests are not a fair test of the adequacy of shock-expansion theory since at $\alpha = 15^\circ$ the leading-edge shock is detached at $M_\infty = 3.36$.

Figure 16 presents the interference loading on the body due to the presence of the wing at an angle of attack of 15° for $M_\infty = 3.36$ on the

sharp-nose body and $M_\infty = 6.85$ on the sharp- and blunt-nose bodies. The orientation of the wing and body with respect to the load-distribution curve is as indicated.

Mach number apparently does not play an important role in interference effects in this Mach number range, as evidenced by the fact that the general trends of the interference loading curves on the sharp-nose body at $M_\infty = 3.36$ and $M_\infty = 6.85$ do not differ widely. The effect of nose shape on body interference loadings is evidenced by the relative displacement of the curves with the square and diamond symbols, and, as already mentioned, the significance of this type of interference will probably increase with increasing M_∞. Also of interest is the fact that the maximum interference loading for each of the three curves was 50 to 60 percent of the corresponding body-alone loading.

CONCLUDING REMARKS

This paper has summarized briefly current loads information at hypersonic speeds. Several methods which the designer can employ in estimating the loads on various aircraft components have been discussed. The paper has considered the characteristics of both slender and blunt configurations and the effects of boundary-layer and aerodynamic interference. Many problems still confront the designer - the effect on tail loads of the wing flow field and its associated high-energy wake and the effect of the body flow field and its highly rotational flow for blunt-nose bodies. In addition, the effect on loads at hypersonic speeds of the inert degrees of freedom of the components of the air (molecular vibration, dissociation, and ionization) is essentially unknown.

APPENDIX

PRESSURE RELATION APPROXIMATIONS

The ratio of free-stream static pressure to stagnation pressure for a blunt-nose body can be calculated approximately from the following exact relation (see ref. 14, eq. (100)):

$$\frac{p_\infty}{p_{MAX}} = \frac{\left[\frac{2\gamma M_\infty^2 - (\gamma - 1)}{\gamma + 1}\right]^{\frac{1}{\gamma-1}}}{\left[\frac{(\gamma + 1)M_\infty^2}{2}\right]^{\frac{\gamma}{\gamma-1}}} \tag{1}$$

Since $\frac{\gamma}{\gamma - 1} = \frac{1}{\gamma - 1} + 1$, equation (1) can be written:

$$\frac{p_\infty}{p_{MAX}} = \frac{1}{M_\infty^2} \frac{\left[\frac{2\gamma}{\gamma + 1} - \frac{(\gamma - 1)}{(\gamma + 1)M_\infty^2}\right]^{\frac{1}{\gamma-1}}}{\left[\frac{\gamma + 1}{2}\right]^{\frac{\gamma}{\gamma-1}}} \tag{2}$$

As M_∞ becomes large, equation (2) is closely approximated by

$$\frac{p_\infty}{p_{MAX}} \approx \frac{1}{M_\infty^2} \frac{\left[\frac{2\gamma}{\gamma + 1}\right]^{\frac{1}{\gamma-1}}}{\left[\frac{\gamma + 1}{2}\right]^{\frac{\gamma}{\gamma-1}}} \tag{3}$$

For $\gamma = 1.4$, equation (3) becomes

$$\frac{p_\infty}{p_{MAX}} \approx \frac{0.777}{M_\infty^2} \tag{4}$$

In addition, since

$$C_p = \frac{2}{\gamma M_\infty^2}\left(\frac{p}{p_\infty} - 1\right)$$

and

$$C_{p,MAX} = \frac{2}{\gamma M_\infty^2}\left(\frac{p_{MAX}}{p_\infty} - 1\right)$$

the ratio of local surface pressure coefficient to maximum surface pressure coefficient becomes

$$\frac{C_p}{C_{p,MAX}} = \frac{p - p_\infty}{p_{MAX} - p_\infty} = \frac{\frac{p}{p_{MAX}} - \frac{p_\infty}{p_{MAX}}}{1 - \frac{p_\infty}{p_{MAX}}} \tag{5}$$

Rearranging the terms of equation (5) yields

$$\frac{p}{p_{MAX}} = \frac{C_p}{C_{p,MAX}} + \frac{p_\infty}{p_{MAX}}\left(1 - \frac{C_p}{C_{p,MAX}}\right) \tag{6}$$

which, with the aid of equation (4), yields for large M_∞

$$\frac{p}{p_{MAX}} \approx \frac{C_p}{C_{p,MAX}} \tag{7}$$

REFERENCES

1. Eggers, A. J., Jr., and Savin, Raymond C.: A Unified Two-Dimensional Approach to the Calculation of Three-Dimensional Hypersonic Flows, With Application to Bodies of Revolution. NACA Rep. 1249, 1955. (Supersedes NACA TN 2811.)

2. Tsien, Hsue-Shen: Similarity Laws of Hypersonic Flows. Jour. Math. and Phys., vol. XXV, no. 3, Oct. 1946, pp. 247-251.

3. Ehret, Dorris M., Rossow, Vernon J., and Stevens, Victor I.: An Analysis of the Applicability of the Hypersonic Similarity Law to the Study of Flow About Bodies of Revolution at Zero Angle of Attack. NACA TN 2250, 1950.

4. Rossow, Vernon J.: Applicability of the Hypersonic Similarity Rule to Pressure Distributions Which Include the Effects of Rotation for Bodies of Revolution at Zero Angle of Attack. NACA TN 2399, 1951.

5. Lees, Lester: Note on the Hypersonic Similarity Law for an Unyawed Cone. Jour. Aero. Sci. (Readers' Forum), vol. 18, no. 10, Oct. 1951, pp. 700-702.

6. Probstein, Ronald F., and Bray, Kenneth N. C.: Hypersonic Similarity and the Tangent-Cone Approximation for Unyawed Bodies of Revolution. Jour. Aero. Sci. (Readers' Forum), vol. 22, no. 1, Jan. 1955, pp. 66-68.

7. Van Dyke, Milton D.: Applications of Hypersonic Small-Disturbance Theory. Jour. Aero. Sci., vol. 21, no. 3, Mar. 1954, pp. 179-186.

8. Van Dyke, Milton D.: A Study of Hypersonic Small-Disturbance Theory. NACA Rep. 1194, 1954. (Supersedes NACA TN 3173.)

9. Eggers, A. J., Jr., Savin, Raymond C., and Syvertson, Clarence A.: The Generalized Shock-Expansion Method and Its Application to Bodies Traveling at High Supersonic Air Speeds. Jour. Aero. Sci., vol. 22, no. 4, Apr. 1955, pp. 231-238, 248.

10. Savin, Raymond C.: Application of the Generalized Shock-Expansion Method to Inclined Bodies of Revolution Traveling at High Supersonic Airspeeds. NACA TN 3349, 1955.

11. Penland, Jim A.: Aerodynamic Characteristics of a Circular Cylinder at Mach Number 6.86 and Angles of Attack Up to 90°. NACA TN 3861, 1957. (Supersedes NACA RM L54A14.)

12. Goodwin, Glen, Craeger, Marcus O., and Winkler, Ernest L.: Investigation of Local Heat-Transfer and Pressure Drag Characteristics of a Yawed Circular Cylinder at Supersonic Speeds. NACA RM A55H31, 1956.

13. Crawford, Davis H., and McCauley, William D.: Investigation of the Laminar Aerodynamic Heat-Transfer Characteristics of a Hemisphere-Cylinder in the Langley 11-Inch Hypersonic Tunnel at a Mach Number of 6.8. NACA TN 3706, 1956.

14. Becker, John V., and Korycinski, Peter F.: Heat Transfer and Pressure Distribution at a Mach Number of 6.8 on Bodies With Conical Flares and Extensive Flow Separation. NACA RM L56F22, 1956.

15. Ridyard, Herbert W., and Fetterman, David E., Jr.: Aerodynamic Characteristics of a 6-Percent-Thick Symmetrical Circular-Arc Airfoil Having a 30-Percent-Chord Trailing-Edge Flap at a Mach Number of 6.9. NACA RM L56B24, 1956.

16. Hill, William A., and Kaattari, George E.: Force and Pressure-Distribution Investigation to High Angles of Attack on All-Movable Triangular and Rectangular Wings in Combination With a Body at Supersonic Speeds. NACA RM A56C12, 1956.

17. Kaattari, G. E.: Pressure Distributions on Triangular and Rectangular Wings to High Angles of Attack - Mach Numbers 2.46 and 3.36. NACA RM A54J12, 1955.

18. Ames Research Staff: Equations, Tables, and Charts for Compressible Flow. NACA Rep. 1135, 1953. (Supersedes NACA TN 1428.)

TENDENCY TOWARD TWO-DIMENSIONALITY OF FLOW AT HYPERSONIC SPEEDS

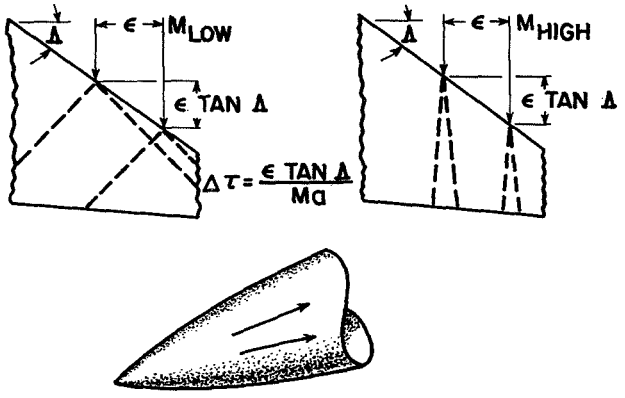
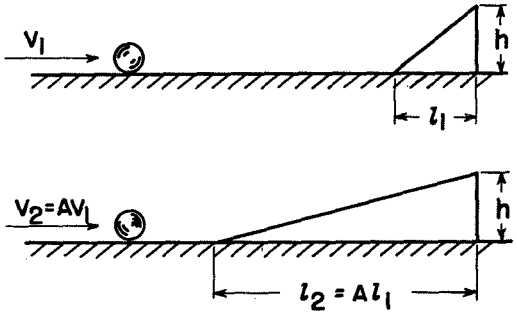


Figure 1

PHYSICAL CONCEPT FOR HYPERSONIC SIMILARITY LAW



$$V_2 \frac{h}{l_2} = V_1 \frac{h}{l_1} \propto M \frac{d}{l} = K$$

Figure 2

RANGE OF APPLICABILITY OF HYPERSONIC SIMILARITY LAW ($K=M_\infty \frac{d}{l}$) FOR CONES

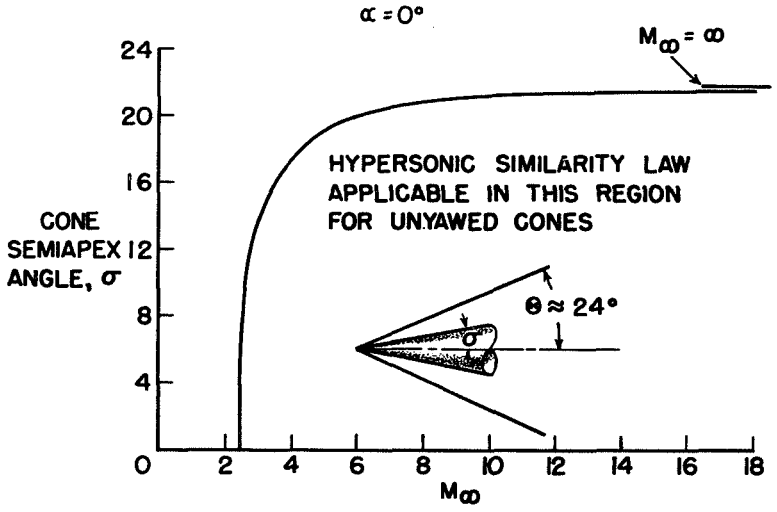


Figure 3

APPLICABILITY OF HYPERSONIC SIMILARITY LAW TO SLENDER BODIES

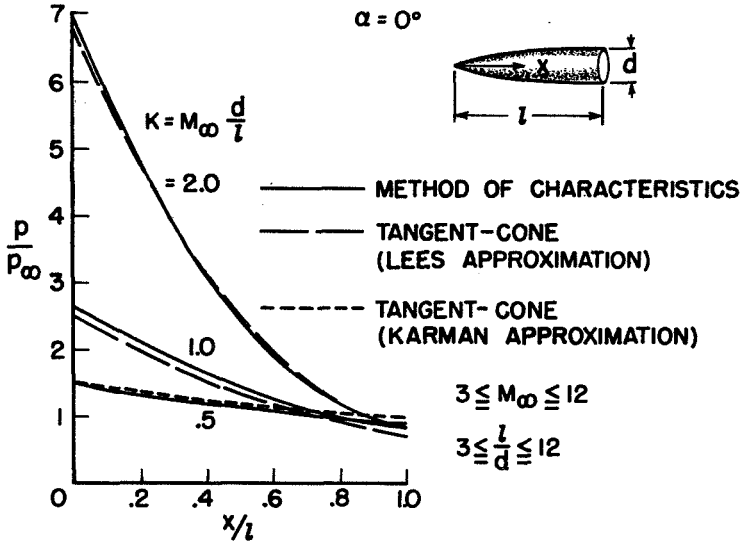


Figure 4

CORRELATION OF THEORETICAL PRESSURE COEFFICIENTS
ON SLENDER UNYAWED CONES

COMBINED SUPERSONIC-HYPERSONIC SIMILARITY RULE

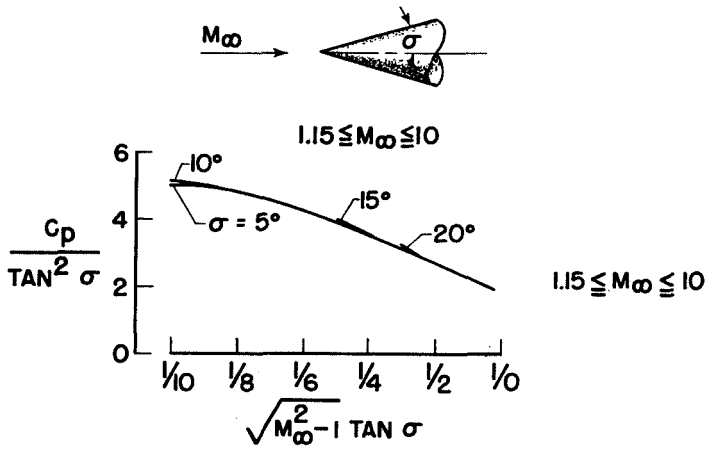


Figure 5

CORRELATION OF THEORETICAL PRESSURE COEFFICIENTS
ON BLUFF UNYAWED CONES

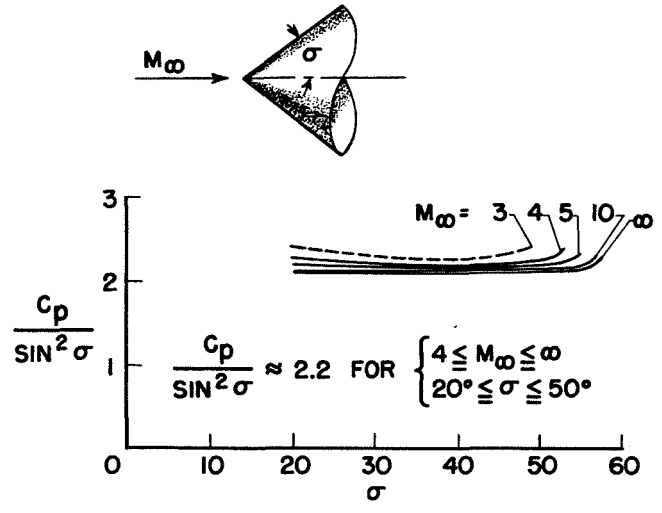


Figure 6

PREDICTION OF PRESSURE DISTRIBUTION ON OGIVE AT ANGLE OF ATTACK

GENERALIZED SHOCK-EXPANSION METHOD; $M_\infty = 5.05$

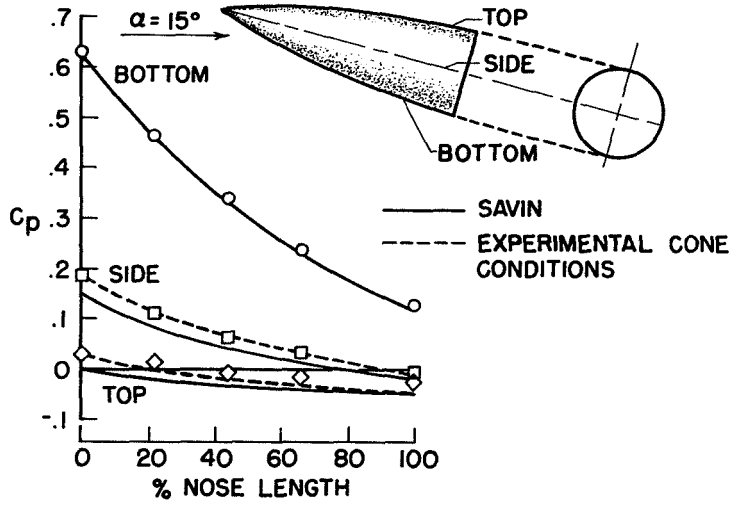


Figure 7

INVARIANCE OF CYLINDER PRESSURE RATIO WITH MACH NUMBER AND SWEEP ANGLE

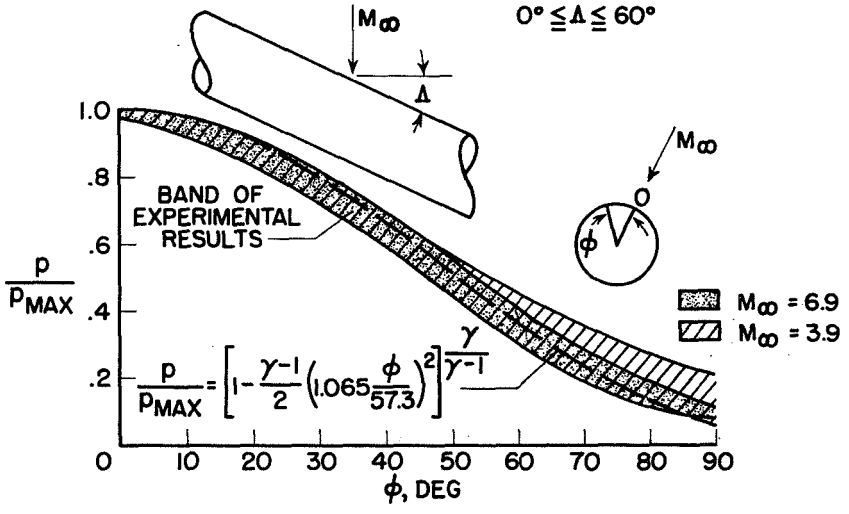


Figure 8

INVARIANCE OF PRESSURE-COEFFICIENT RATIO WITH MACH NUMBER FOR HEMISPHERICAL NOSES

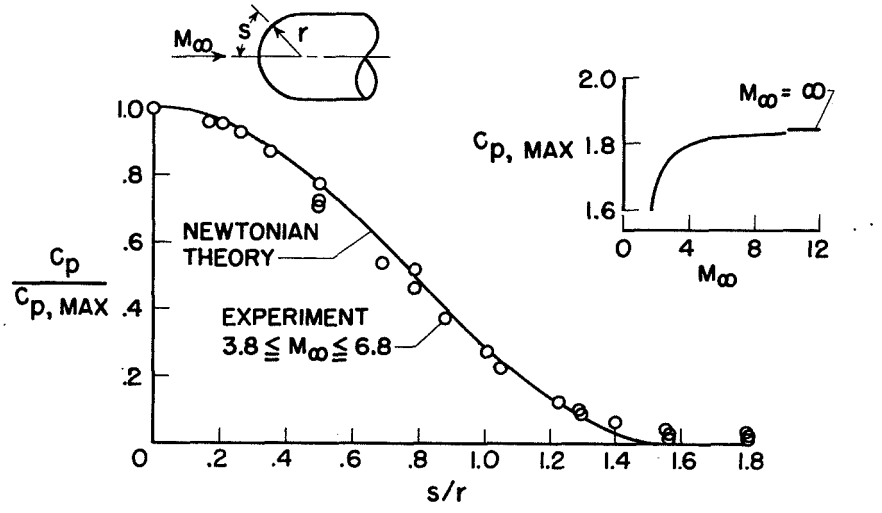


Figure 9

EFFECT OF ENTROPY ON SHOULDER PRESSURE OF SONIC-WEDGE FLAT PLATE

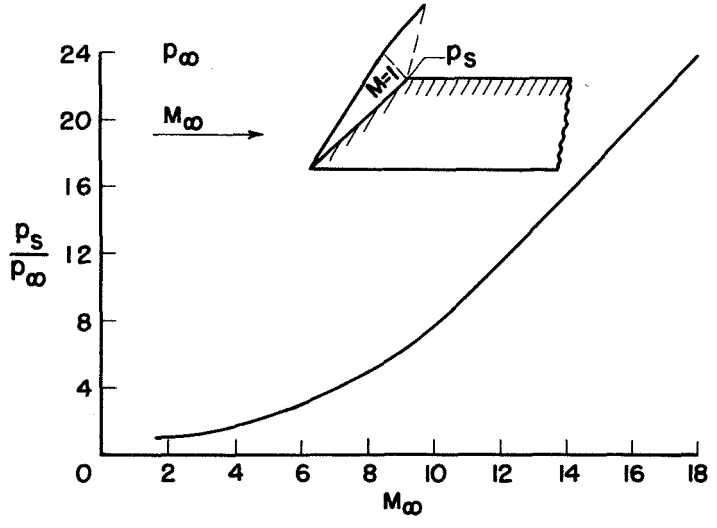


Figure 10

EFFECT OF BOUNDARY LAYER AND ENTROPY ON FLAT-PLATE PRESSURES

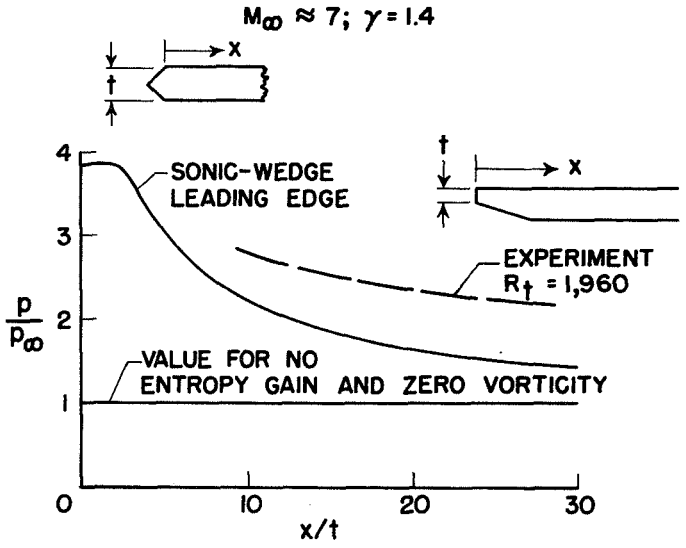
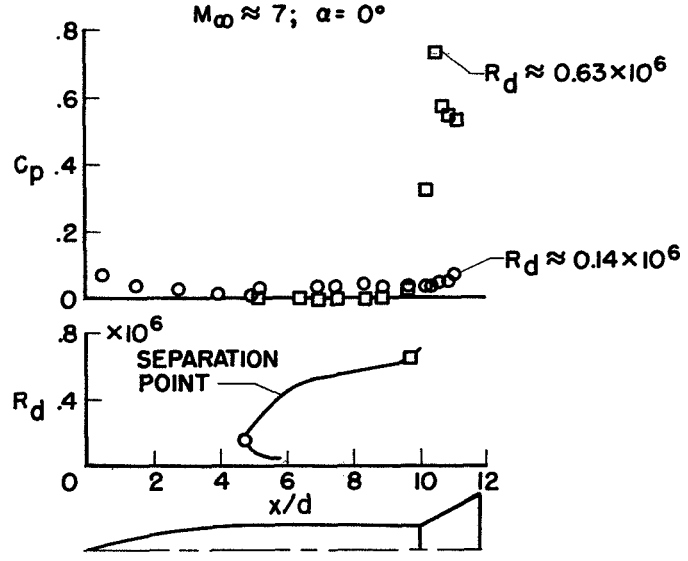


Figure 11

EFFECT OF SEPARATION ON PRESSURE DISTRIBUTION ON BODY OF REVOLUTION



37

Figure 12

EFFECT OF SEPARATION ON PRESSURES ON TWO-DIMENSIONAL WING FLAP

$\alpha = 16°$; $\delta = 16°$; $M_\infty \approx 7$; $R = 1.65 \times 10^6$

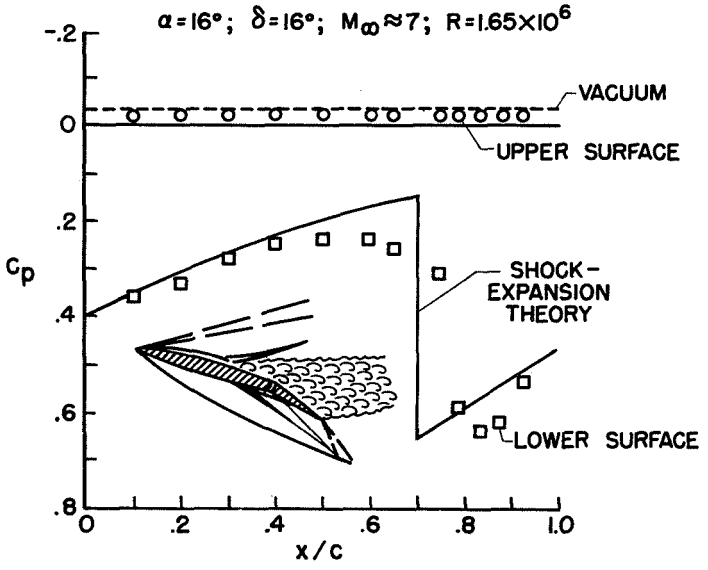


Figure 13

INTERFERENCE ON WING LOAD DISTRIBUTION AT $\alpha = 15°$

$M_\infty = 3.36$

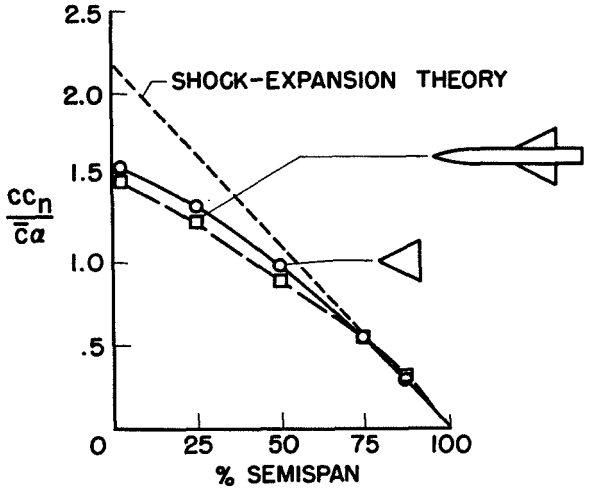


Figure 14

INTERFERENCE ON WING LOAD DISTRIBUTION AT $\alpha = 15°$
$M_\infty = 6.85$

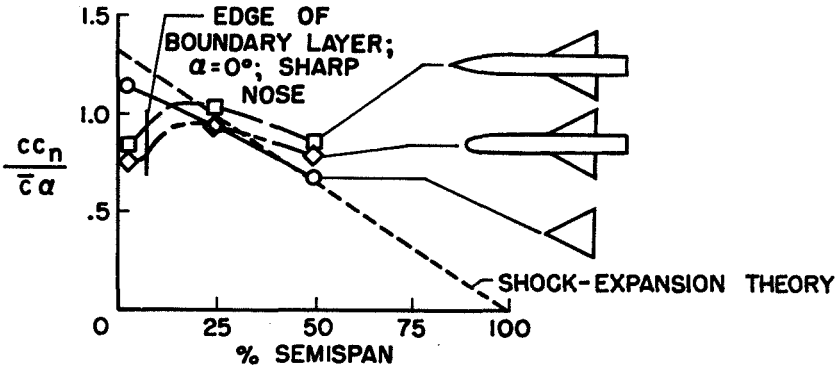


Figure 15

INTERFERENCE ON BODY LOAD DISTRIBUTION DUE TO WING
$\alpha = 15°$

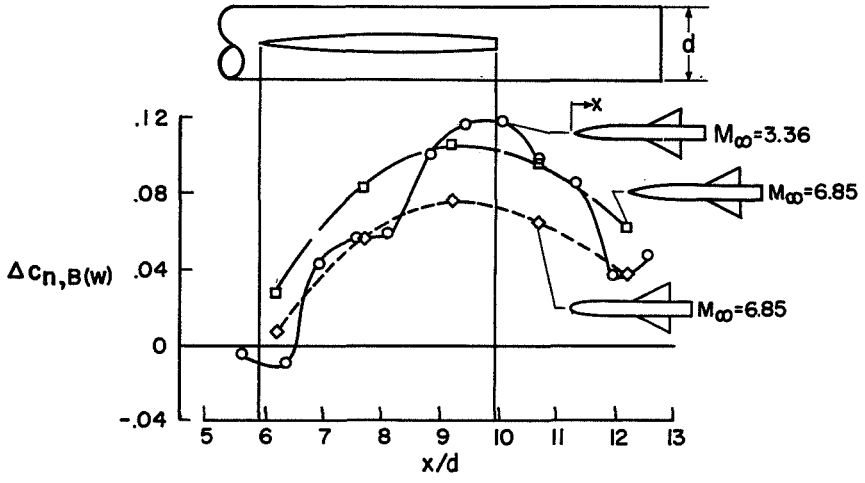


Figure 16

N71-75984

SPAN LOADINGS DUE TO WING TWIST AT TRANSONIC AND SUPERSONIC SPEEDS

By Frederick C. Grant and John P. Mugler, Jr.

Langley Aeronautical Laboratory

SUMMARY

Two similar tapered sweptback plan forms with the same two spanwise variations of twist have been tested in the Mach number range from 0.8 to 2.0. The test results showed, in general, rather good agreement with theoretical predictions of the incremental span loadings due to twist for zero angle of attack. The measured incremental span loadings due to twist generally diminished with increasing angle of attack through the Mach number range. At a Mach number of 0.9, the incremental loadings progressively vanished from the tip inboard with increasing angle of attack. For the highest angles of attack (about 20°) at Mach number 0.9, there was no difference in the span loadings of the flat and twisted wings. At the higher supersonic speeds, a similar vanishing at the tips of the incremental loading due to twist was starting at the highest angles of attack (near 20°).

For angles of attack lower than about 20° at supersonic speeds, no important change in the shape of the incremental loadings occurred, although the strength of the loading diminished with increasing angle of attack.

INTRODUCTION

The thin wings of modern high-speed airplanes deform appreciably in flight. The changes in air loading due to these deformations have not been extensively investigated. An aerodynamically important form of deformation is twist, or change in angle of attack at a given spanwise station on a wing. As part of a research program on the loads due to wing twist, two simple spanwise twist distributions have been tested at the Langley Aeronautical Laboratory in the Mach number range from 0.8 to 2.0. For a complete airplane with stores and nacelles acting on the wing, the twist distribution along the span may be rather complicated. It is hoped that the loadings due to simple twist distributions will, by superposition, give the loadings due to complicated distributions.

SYMBOLS

A	aspect ratio
b	span
c	chord
c_{AV}	average chord
c_n	section normal-force coefficient
M	Mach number
q	dynamic pressure
t	thickness
x	chordwise distance
y	spanwise distance
α	angle of attack
Δc_n	incremental normal-force coefficient
Δp	incremental lifting pressure
$\Lambda_{c/4}$	sweepback at quarter chord
λ	taper ratio

MODELS

The wings tested and the twist variations which were built in are shown in figure 1. The wings tested at transonic speeds had an aspect ratio of 4, 45° of sweepback at the quarter chord, and a taper ratio of 0.15. The semispan wing tested at supersonic speeds had an aspect ratio of 3.5, 50° of sweepback at the quarter chord, and a taper ratio of 0.20. The thickness of the transonic wings varied from 6 percent at the body center line to 3 percent at and beyond halfway to the tip. The thickness of the supersonic wings was a constant 5 percent. A small camber was built into the transonic wings. All the wings tested had the

same 65A-series thickness distribution and the same spanwise variations of built-in twist. The twist angle at the tip was 6°, in every case, which is attained by a linear and quadratic variation with spanwise position. The tips are at a lower angle of attack than the root, or washed out, for the positive direction assumed in this paper. Flat wings were tested in each speed range to provide a reference to which the twisted wings might be compared.

INCREMENTAL LOADING

Figure 2 shows the span loadings on the flat wing and the linearly twisted wing at $M = 1.6$ and at $\alpha = 12^\circ$. The difference in these span loadings, or incremental span loading, is also shown. Incremental span loadings formed in the same manner will be the basis of comparison between linear theory and the test results at the other Mach numbers and angles of attack.

The incremental loading shown in figure 2 is the isolated effect of spanwise wing twist with, of course, the nonlinear influence of angle of attack and thickness neglected. If real wings behave as do the wings of linear theory, the incremental loading for a given spanwise twist distribution will not change with angle of attack. For this case the increment in normal force produced by 6° of twist is 13 percent of the flat-plate normal-force coefficient. This illustrates the fact that, for a given overall accuracy in predicting the loading on a twisted wing, the accuracy of prediction of the incremental loading can diminish as the angle of attack increases.

PREDICTIONS AT ZERO ANGLE OF ATTACK

In order to eliminate, as far as possible, the influence of angle of attack, the root angle of attack may be set to zero. The predicted and measured incremental span loadings due to twist with the root angle of attack set to zero are shown in figures 3 and 4.

Wings With Linear Twist

Transonic speeds.- Figure 3 shows the comparative theoretical and experimental incremental span loadings for the transonic linearly twisted wing. The section loading parameter $\Delta c_n \, c/c_{AV}$ is plotted against the spanwise position $2y/b$, and the vertical dashed line indicates the spanwise position of the wing-body juncture.

At M = 0.90, the agreement between the data and theory is fairly good. The theory shown is a lifting-surface theory with a provision for approximating the presence of the body. (See ref. 1.) The prediction is better outboard than it is nearer the body.

At M = 1.20, there is close agreement between the data and theory, even though the validity of linear theory is becoming questionable as the Mach number approaches one. The theory used at supersonic speeds for subsonic leading edges is that given in references 2 and 3. In addition, the boundary conditions were only approximately satisfied in the theoretical computations for the transonic wings at M = 1.20. No attempt was made to account for the presence of the body. A feature of the results at M = 1.20 is the apparent absence of any marked influence of the body on the incremental span loadings.

Supersonic speeds.- Figure 4 shows the incremental span loadings with zero root angle of attack for the supersonic linearly twisted wings at M = 1.6 and 2.0.

Figure 4 shows that the data are about 20 percent lower than predicted values. As predicted, the loading is slightly weaker at the higher Mach number. The shock waves caused by the thickness seem to have no more effect on the span loadings at M = 2.0 than at M = 1.6, although the leading edge is supersonic at M = 2.0 and shock waves due to thickness must certainly be more severe. The theory used at M = 2.0 is given in reference 4.

Wings With Quadratic Twist

Transonic speeds.- Figure 5 shows the incremental span loadings on the wings with quadratic twist as measured and predicted at transonic speeds.

The agreement with theory is again rather good at M = 0.90. The agreement at M = 1.20 is about the same as it was in the case of the wings with linear twist. Again there is no apparent body effect at M = 1.20.

Supersonic speeds.- Figure 6 shows the predicted and measured incremental loadings for the wing with quadratic twist at M = 1.6. Data for M = 2.0 are not yet available.

The agreement is better in this case than it was for the linearly twisted wing at this Mach number. The values are only 7 percent lower as compared with about 20 percent for the wing with linear twist. This must be partly due to the fact that the average angle of twist over the plan form is lower than it was in the case of the linearly twisted wings.

LIFTING PRESSURE DISTRIBUTIONS

Figure 7 shows the chordwise lifting pressure distribution corresponding to two of the incremental span loadings previously shown. The lifting pressure coefficient $\Delta p/q$ is plotted against the chordwise position x/c; distributions are for Mach number 1.6, zero root angle of attack, and the spanwise station at which the data were taken is 0.7 of the semispan. Distributions for both linear and quadratic twist are shown. These distributions are typical of other spanwise stations at this Mach number. Linear-theory predictions of the lifting pressure are shown for both twist variations.

For the wing with linear twist, the agreement with theory is good. The level of agreement is comparable to that indicated by recent pressure measurements made on a zero-thickness delta wing. (See ref. 5.) Since a zero-thickness delta wing exactly satisfies the boundary conditions of linear theory, the agreement with theory obtained on such a wing typifies the best that can be expected. To have similar agreement on a wing with 5-percent thickness is surprising. The agreement for the wing with quadratic twist is even better than that for the wing with linear twist. The fine agreement shown here was reflected in the good agreement observed in the integrated loadings for the wing with quadratic twist.

PREDICTIONS AT ANGLE OF ATTACK

All the incremental loadings that have been shown thus far were for zero root angle of attack. According to the linear theory, the incremental loadings will not change with angle of attack, or, in other words, the twist will produce the same change in loading whether or not the wing is at an angle of attack. Of course, this simple prediction is not borne out by the data.

Transonic Speeds

Figure 8 shows the effect of angle of attack on the span loadings at $M = 0.90$. In this figure, instead of incremental loadings, the total span loadings are shown for the flat and linearly twisted wings. Data for angles of attack of 4°, 8°, and 12° are shown. For the transonic wings at angle of attack, incremental aeroelastic twists occurred which amounted to about 10 percent of the 6° of built-in twist at 12° angle of attack. Figure 8 shows that the shape of the incremental loadings (the vertical difference between curves) changes markedly with angle of attack while the strength of the incremental loading greatly diminishes.

At $\alpha = 4^\circ$, both wings show the same sort of span loading, the wing with linear twist carrying the lesser load. Between $\alpha = 4^\circ$ and $\alpha = 8^\circ$, the flow separates at the tip of the flat wing, and at $\alpha = 8^\circ$ the flow is separated outboard of about 60 percent of the semispan. The twisted wing at $\alpha = 8^\circ$, however, has much the same type of span loading as at $\alpha = 4^\circ$ and the flow appears unseparated. At $\alpha = 12^\circ$ both wings are separated outboard of about 40-percent semispan. The incremental loading, already small at $\alpha = 12^\circ$, effectively vanishes at the higher angles of attack. At the higher angles, then, there is no difference between the flat and twisted wings. Similar results have been obtained on the wing with quadratic twist. At Mach number 1.2 the results are consistent with those to be shown for the supersonic wings, but values will not be presented.

Supersonic Speeds

In figure 9, the percent of the theoretical loading which must be used to obtain a good fairing through the data in the outboard regions (beyond semispan), where most of the incremental lift is located, is plotted against the root angle of attack. The most striking feature of this plot is the rapid decrease of the effective linear twist with angle of attack. There is no marked effect of the Mach number, although the $M = 2.0$ data are for a supersonic leading edge and the $M = 1.6$ data are for a subsonic leading edge. As was mentioned previously, a less accurate prediction of the incremental loading is acceptable at the higher angles of attack. Even if 100 percent of the theoretical loading for the linear twist were used to predict the loading at 12° angle of attack, the 45-percent difference indicated by figure 9 would come to an error of about 12 percent in predicting the total loading. A better estimate of the incremental loading, such as the fractions of the theoretical loading indicated by the curves, could lead to a negligible error in the total loading.

For the wing with quadratic twist, only the $M = 1.6$ data, or subsonic-leading-edge data, are available. However, there is no reason to expect that the Mach number effects will be any stronger than they were for the linearly twisted wing. For the wing with quadratic twist, figure 9 shows that the good prediction of the incremental loading at zero angle of attack is coupled with a slow drop in effective twist as the angle of attack increases. This contrast with the relatively poorer prediction at zero angle of attack and more rapid drop with angle of attack observed on the linearly twisted wing.

There is little change in the shape of the incremental loadings from 12° angle of attack to about 20°. In the neighborhood of 20°, incremental loadings vanish on the outboard regions of the wing in a manner similar to that observed at $M = 0.90$.

CONCLUDING REMARKS

At higher subsonic speeds the theoretical predictions at zero angle of attack of incremental span loads due to twist were fairly good. Because of separation effects, these predictions failed as the angle of attack increased. At the highest angles, there was no difference in the loadings of the flat and twisted wings. At low supersonic speeds, the predictions at zero angle of attack were better although the validity of the linear theory is becoming questionable. At the higher supersonic speeds, the predictions at zero angle of attack were generally larger than the actual loadings. The prediction was better for the wings with lower average twist. At angles of attack up to 12°, factors were applied to the theoretical incremental loading which give good agreement with the data. Through the Mach number range of 0.9 to 2.0 the incremental loading steadily diminished with angle of attack.

REFERENCES

1. Crigler, John L.: Comparison of Calculated and Experimental Load Distributions on Thin Wings at High Subsonic and Sonic Speeds. NACA TN 3941, 1957.

2. Heaslet, Max. A., and Lomax, Harvard: Supersonic and Transonic Small Perturbation Theory. General Theory of High Speed Aerodynamics. Vol. VI of High Speed Aerodynamics and Jet Propulsion, sec. D, ch. 3, W. R. Sears, ed., Princeton Univ. Press, 1954, pp. 186-206.

3. Lomax, Harvard, Heaslet, Max. A., and Fuller, Franklyn B.: Integrals and Integral Equations in Linearized Wing Theory. NACA [illegible] p. 1054, 1951. (Supersedes NACA TN 2252.)

4. Kainer, Julian H.: Equations for the Loading on Triangular Wings Having Supersonic Leading and Trailing Edges Due to Various Basic Twist Distributions. Jour. Aero. Sci., vol. 20, no. 7, July 1953, pp. 469-476.

5. Boatright, William B.: Experimental Study and Analysis of Loading and Pressure Distributions on Delta Wings Due to Thickness and to Angle of Attack at Supersonic Speeds. NACA RM L56I14, 1956.

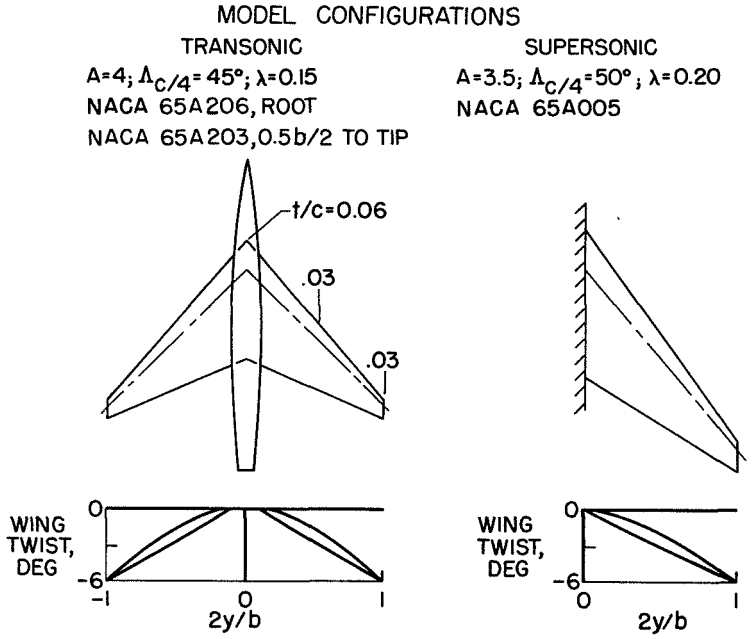
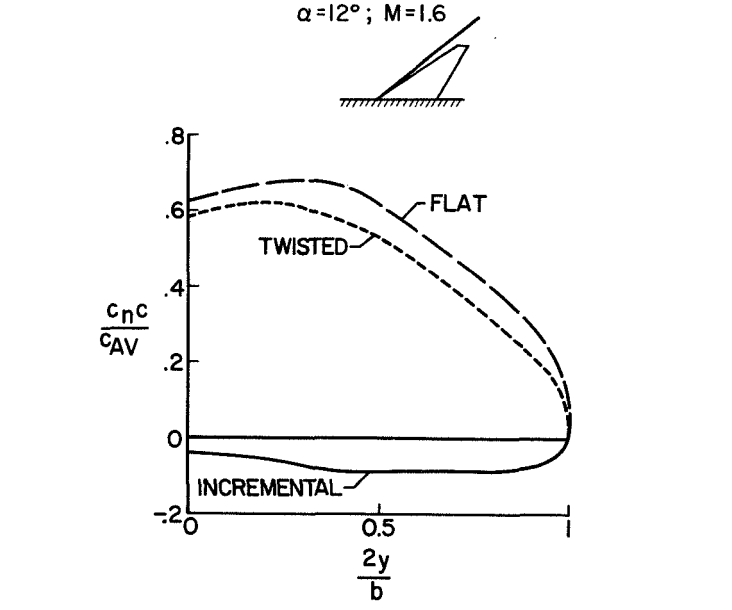


Figure 1



47

Figure 2

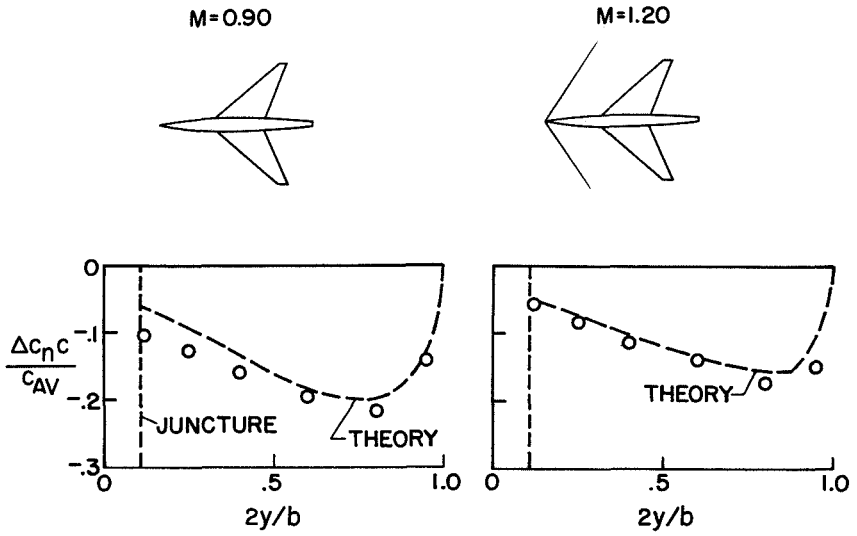


Figure 3

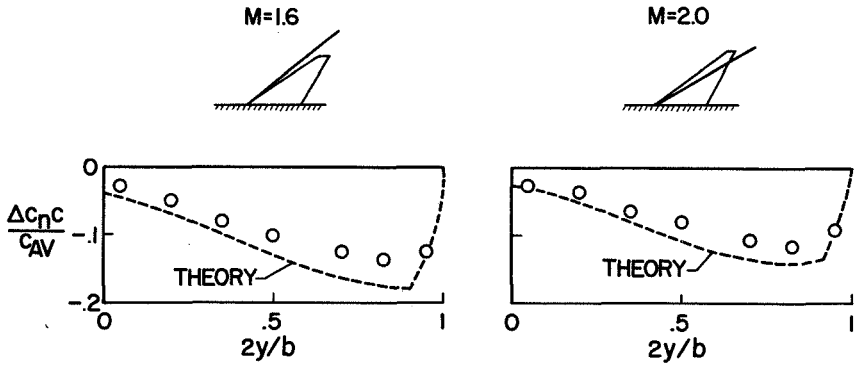


Figure 4

INCREMENTAL SPAN LOADINGS ON WING WITH QUADRATIC TWIST
$\alpha = 0°$

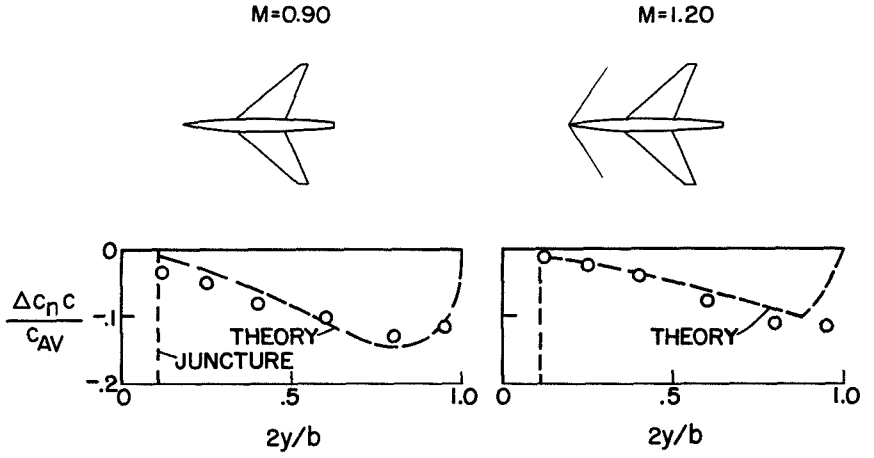


Figure 5

INCREMENTAL SPAN LOADINGS ON WING WITH QUADRATIC TWIST
$\alpha = 0°$; M=1.6

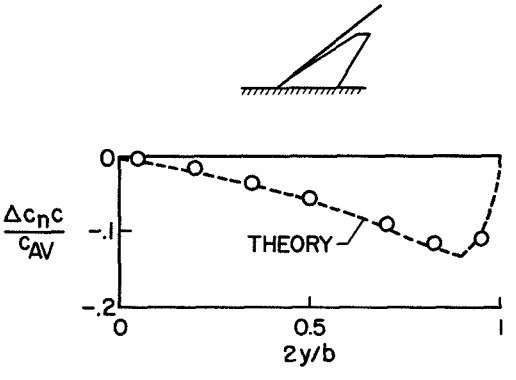


Figure 6

INCREMENTAL LIFTING PRESSURES ON TWISTED WINGS
M=1.6 ; α=0° ; 2y/b=0.7

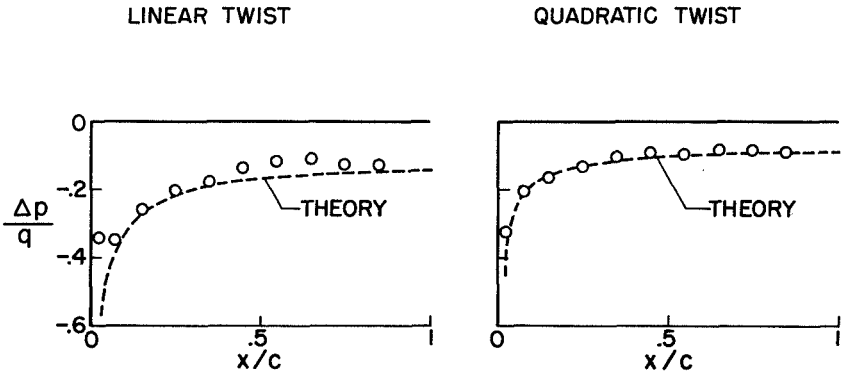


Figure 7

EFFECT OF ANGLE OF ATTACK ON SPAN LOADING
M=0.90

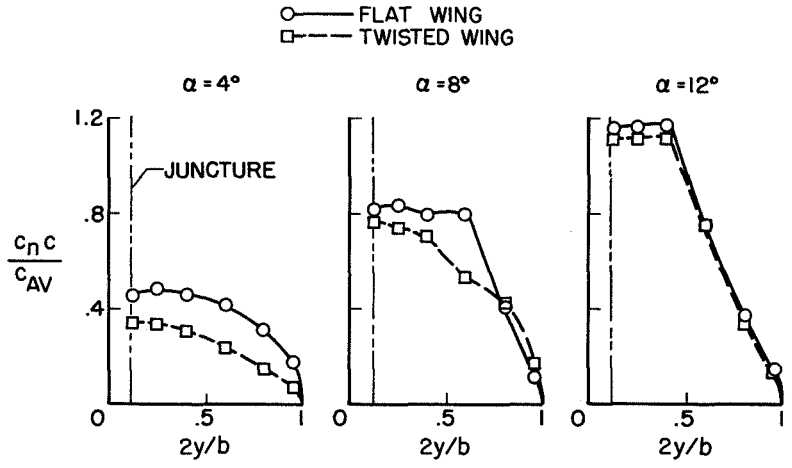


Figure 8

30

EFFECT OF ANGLE OF ATTACK ON INCREMENTAL LOADING

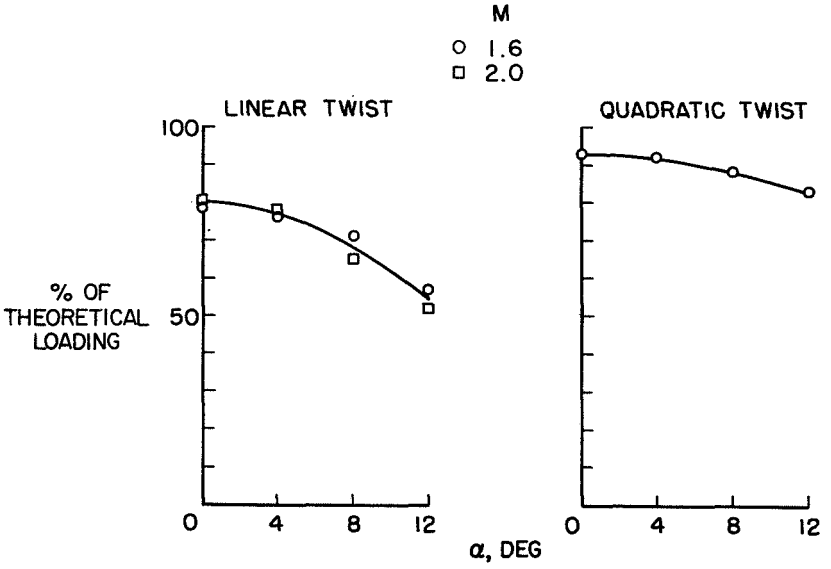


Figure 9

N71-75385

FLIGHT MEASUREMENTS AND CALCULATIONS OF WING LOADS AND LOAD DISTRIBUTIONS AT SUBSONIC, TRANSONIC, AND SUPERSONIC SPEEDS

By Frank S. Malvestuto, Thomas V. Cooney, and Earl R. Keener

NACA High-Speed Flight Station

SUMMARY

Presented in this report is a summary of local and net angle-of-attack wing-panel loads measured in flight on six airplanes. In addition, a comparison of these loads measured in flight with calculations based on simple theory is presented.

INTRODUCTION

At the High-Speed Flight Station of the National Advisory Committee for Aeronautics, full-scale research in the fields of stability, performance, and loads is conducted with a variety of completely instrumented research and military-type airplanes.

In the present paper, the aerodynamic loads aspect of this flight research is considered. The presentation will involve a summary of local and net angle-of-attack wing-panel loads measured in flight on a variety of airplanes flown during the past 5 or 6 years. In addition, a preliminary comparison of these loads measured in flight and the corresponding loads calculated by simple theory is presented. The object of this comparison is to assess the ability of simple theoretical techniques to predict the flight-measured loads for a variety of configurations. Only a cursory comparison of the flight measurements with comparable wind-tunnel results has been made. In a general sense, the flight results verify the tunnel findings. For the convenience of the reader, a bibliography has been added.

Figure 1 depicts with plan-view outlines the airplanes to be discussed in this report. The wing panels are darkened to emphasize the fact that only the wing loads will be considered. An inspection of the individual sketches and geometric data shows that there is a good coverage of wing sweep, plan form, aspect ratio, and thickness. In addition, the X-1E wing has 2° positive incidence and the D-558-II wing has 3° of positive incidence. The free-stream Reynolds number for the flights of these airplanes varied from 1×10^6 to 6×10^6 per foot. The altitude varied from 25,000 feet to 65,000 feet.

SYMBOLS

A	aspect ratio
b'	wing-panel span
b_f	flap span
c	chord
c_{av}	average chord
c_f	flap chord
c_n	section normal-force coefficient
C_N	net normal-force coefficient
C_{N_α}	slope of wing-panel normal-force coefficient
C_p	pressure coefficient
ΔC_p	pressure coefficient differential between upper and lower surfaces
H	altitude
M	Mach number
R_∞	free-stream Reynolds number
t	thickness
x	distance along x-axis
y	distance along y-axis
α	angle of attack
δ_e	elevon deflection
Λ_{LE}	leading-edge sweep

THEORIES CONSIDERED

A few preliminary remarks regarding the theories used for the wing-panel load calculations will be made. The wings are assumed to be rigid flat plates and of negligible thickness. In addition, the effect of the fuselage interference on the wing loads was approximated by assuming the fuselage to act as a perfect reflection plane located at the wing-fuselage juncture. On this basis, the wing load is predicted as the load on one panel of a symmetrical wing with its root chord coincident with the wing-fuselage juncture. It is realized that this approximation to the fuselage interference is subject to improvement; however, it is felt to be sufficient for the present study. With these assumptions in mind, the wing theories used for load predictions are given in the following table:

Theories used for calculation of wing loads -		
Subsonic ($0.5 < M < 0.85$)	Transonic ($M = 1.0$)	Supersonic ($M \geqq 1.2$)
All wings: linear lifting surface (refs. 1 to 4)	Swept wing: linear lifting surface (refs. 5 and 6) Unswept wing: two-dimensional flat plate; two-dimensional double wedge (refs. 7 and 8)	All wings: linear lifting surface (refs. 9 to 16)

In the subsonic range, for all wings, linear theory was applied. (See refs. 1 to 4.) These subsonic calculations were made up to a Mach number of 0.85, although in the neighborhood of this Mach number, transonic mixed-flow conditions no doubt exist. In the transonic range, calculations were made only for a free-stream Mach number of 1.0. In this range, for the swept wings, the linear theory presented by Mangler (ref. 5) which is in essence Jones' slender-wing theory (ref. 17) modified for linearized sonic-flow conditions was applied. For the unswept wing, at a Mach number of 1.0, use was made of the results of Guderley and Yoshihara (ref. 8) for a double-wedge section and the results of Guderley (ref. 7) for a flat plate of negligible thickness. For the supersonic Mach number range, the well-known lifting-surface theories were applied.

LOADING DISTRIBUTION

In the discussion of flight results, the chordwise and spanwise loadings for the unswept-wing X-1E airplane, the swept-wing D-558-II airplane, and the delta-wing JF-102A airplane are considered and then a force summary for all six airplanes is given.

Some idea of the flight Reynolds number, altitude, and angle-of-attack excursions for these airplanes can be determined from figure 2. The Reynolds number is given on a per-foot basis and for free-stream conditions. The open circular symbol represents the maximum Reynolds number obtained. It is noted that this flight Reynolds number varies from approximately 1×10^6 to 4×10^6. The altitude covers a range from approximately 25,000 to 65,000 feet. On the right-hand side of figure 2 the hatched boundary is indicative of the maximum angle-of-attack excursions obtained in flight. The discussion of the angle-of-attack wing loads will be within the region shown by the dashed boundary.

In figures 3 to 6 are presented the chord loadings and span loadings for the X-1E wing panel. The solid line represents the theory; the open symbol, the flight data. The dashed line through the open circles represents "faired" flight data. The sketches on the left-hand side of figure 4 indicate the panel normal-force coefficient C_N for the angles of attack at which the chord and span loadings are shown. Consider first the chord loadings of figure 3, that is, the variation of ΔC_p, the lifting pressure, with x/c, the normalized distance from the leading edge. These results are for a span station $\frac{y}{b'/2} = 0.46$. The symbol b' denotes the external panel span. The chord loadings are shown for Mach numbers of 0.8, 1.0, and 1.9. For each Mach number the chord loadings are shown for two angles of attack, a low angle and a high angle. The magnitude of the high angle of attack is limited by the availability of the data. The angle of attack is always the angle of attack of the wing panel. At $M = 0.8$, the calculated level and variation of the chord loading compares favorably with the flight data. For a Mach number of 1.0, there is no available finite-span unswept-wing theory. The theoretical variation shown here is the flat-plate two-dimensional theory of Guderley. Although the level of the lifting pressure is not predicted herein, the variation is similar to the flight-measured variation for both angles of attack.

At supersonic speed and low angle of attack, the comparison of flight and theory is acceptable. At the higher angle of attack, the loading distribution is not predicted by theory although the level of the local load can be calculated. The midspan chord loadings and the chord loadings at two additional spanwise stations, one near the root and one near the tip, are shown in figures 5 and 6.

If the span-load distributions (fig. 4) are considered, it is noted that, at $M = 0.8$ and $M = 1.9$, the calculated span loading compares favorably with the flight-measured loading. For $M = 1.0$, the span loading was not calculated, since, as mentioned previously, the two-dimensional results of Guderley were used; however, the flight data have been faired. The shapes of the span-loading curves strongly resemble each other for the three Mach numbers shown.

For the swept-wing D-558-II airplane the chordwise and span-load distributions for the wing panel are shown in figures 7 to 10. The solid line represents the calculations and the open circular symbol, the flight measurements. The panel normal-force coefficients corresponding to the angles of attack considered are indicated in the sketches on the left-hand side of figure 8. The chord loadings presented in figure 7 are for a spanwise station close to the midsemispan location. For the subsonic and supersonic speeds, the theory allows the calculation of the level and variation of the chord loading except at the high angle of attack for the supersonic Mach number. At $M = 1.0$, the measured distribution of the lifting pressure ΔC_p is not calculated by the linear theory. Theory gives a zero loading behind the linearized sonic shock that starts from the leading edge of the streamwise tip of the wing panel. It is possible to obtain a nonzero loading by minor alterations of the wing-tip geometry so that, for the portion of the wing behind the linearized shock, the local span increases with increasing longitudinal position; and hence lift is produced. (See ref. 17.) A discussion of this artifice is given in the report by Mangler (ref. 5) mentioned earlier. The midspan chord loadings and the chord loadings near the root and tip are shown in figures 9 and 10.

The span loading for the swept-wing D-558-II is presented in figure 8. At subsonic and supersonic speeds the calculated distribution compares favorably with the flight measurements. For $M = 1.0$, the calculated loading, especially at the high angle of attack (11°), does not represent the experiment because of the inability of the theory to predict the level of the loads in the vicinity of the root and tip regions. At an angle of attack of 11°, the C_N of the panel is approximately 0.8. It is possible that separation effects at the root and tip are important for this configuration. In addition, the simple end-plate correction used herein for fuselage interferences may be approximate. In this regard the application of an analysis such as that reported by Crigler (ref. 6) for wing-body interference at sonic speeds would improve the prediction of the loading in the vicinity of the root.

The flight-measured loads for the wing panel of the 60° delta-wing JF-102A airplane are considered next. In figure 11 is shown an exploded view of the wing. Note the two fences located in the forward portion of

the wing and the elevon surface which is operative during flight. This wing has conical camber and a reflexed tip. For the calculation of the wing-panel loads, the effect of the fences and the effects of the conical camber and the reflexed tip are neglected; however, the effect of the elevon has been considered.

In figures 12 and 13 are shown the chord loading and the span loading for this airplane. For the lower angle-of-attack range (angles of attack from 3° to 5°) the calculations of the chord loadings compare favorably with the measurements. Up-elevon deflection is negative. The fact that the loading at the leading edge is not predicted is partly due to the omission of camber effect in the calculations. Although the effect of elevon at $M = 1.0$ was not calculated, an inspection of the low-angle-of-attack results indicates that the elevon load calculations at low supersonic speeds such as those obtained at $M = 1.2$ are reasonable approximations to the elevon load at $M = 1.0$. At the high angles of attack the remarks made for the low angles of attack for the sonic and supersonic Mach numbers are still reasonably valid. For the subsonic Mach number, the angle of attack is 20° and the calculations do not predict the flight measurement primarily because of leading-edge separation. For the case of leading-edge separation, calculations of the loading should be made within the framework of the approximate separation flow theories such as reported by Brown and Michael (ref. 18). The panel span loadings for the JF-102A are shown in figure 13. The inability of the calculations to produce the flight trends at $M = 0.8$ and $\alpha = 20^\circ$ is clear from the remarks relating to the chord loading at this Mach number and angle of attack. At $M = 1.0$, since the elevon load was neglected, the calculations overestimate slightly the level of the distribution. The effect of the fences on the span loading distribution can clearly be seen at $M = 1.0$ and $\alpha = 10^\circ$.

In general, the overall impression from this preliminary comparison is what would be expected from similar comparisons with wind-tunnel results. Briefly, a reasonable approximation of the span loadings can be determined for the low and moderate angle-of-attack range. The estimation of the chord loadings is less satisfactory, particularly in the neighborhood of a Mach number of 1.0.

NORMAL FORCES

In figure 14 is shown the variation of the panel normal-force coefficient with panel angle of attack. Note in this illustration that the open circular symbol represents the flight measurements for Mach numbers of 0.8 and 1.0. The solid symbol represents the flight measurements for supersonic Mach numbers. The calculations are again represented by the

solid lines. For the unswept wing at a Mach number of 1, the calculated variation is simply the result of Guderley and Yoshihara (ref. 8) for a two-dimensional wing with a 4-percent-thick double-wedge section. The theory here does not predict the magnitudes or the variation for the range of angle of attack where flight measurements are available. Tunnel results, however, for a similar wing indicate that the C_N variation with α is not linear and in the lower angle-of-attack range (below 4° angle of attack), theory more nearly agrees with the experimental variation.

In figure 15 an attempt has been made to show the effect of Mach number on the normal-force derivative C_{N_α} for all six airplanes that were sketched in figure 1. The theory is again represented by the solid line and, in addition, the inverted "V" symbol has been used to indicate the magnitude of C_{N_α} at $M = 1.0$. The flight data are represented by a square symbol. The solid symbol represents a low C_N range; the open symbol, a moderate C_N range; and the half-solid, a high C_N range. In most cases, flight data were available for only one of these ranges. For the X-1E at sonic speed, the difference in the calculated and flight values results from lack of flight data in the low C_N range as pointed out in the discussion of figure 14.

In general the calculated normal-force-curve slopes compare favorably with those obtained from the flight data.

CONCLUDING REMARKS

In general, the overall impression from this preliminary comparison is what would be expected from similar comparisons with wind-tunnel results. Briefly, a reasonable approximation of the span loadings can be determined for the low and moderate angle-of-attack range. The estimation of the chord loadings is less satisfactory, particularly in the neighborhood of a Mach number of 1.0. In general, the calculated normal-force curve slopes compare favorably with those obtained from the flight data.

REFERENCES

1. DeYoung, John, and Harper, Charles W.: Theoretical Symmetric Span Loading at Subsonic Speeds for Wings Having Arbitrary Plan Form. NACA Rep. 921, 1948.

2. DeYoung, John: Theoretical Symmetric Span Loading Due to Flap Deflection for Wings of Arbitrary Plan Form at Subsonic Speeds. NACA Rep. 1071, 1952. (Supersedes NACA TN 2278.)

3. Glauert, H.: The Elements of Aerofoil and Airscrew Theory. Second ed., Cambridge Univ. Press, 1947. (Reprinted 1948.)

4. Allen, H. Julian: Calculation of the Chordwise Load Distribution Over Airfoil Sections With Plain, Split, or Serially Hinged Trailing-Edge Flaps. NACA Rep. 634, 1938.

5. Mangler, K. W.: Calculation of the Pressure Distribution Over a Wing at Sonic Speeds. R. & M. No. 2888, British A.R.C., Sept. 1951.

6. Crigler, John L.: Comparison of Calculated and Experimental Load Distributions on Thin Wings at High Subsonic and Sonic Speeds. NACA TN 3941, 1957.

7. Guderley, Gottfried: The Flow Over a Flat Plate With a Small Angle of Attack at Mach Number 1. Jour. Aero. Sci., vol. 21, no. 4, Apr. 1954, pp. 261-274.

8. Guderley, Gottfried, and Yoshihara, Hideo: Two-Dimensional Unsymmetric Flow Patterns at Mach Number 1. Jour. Aero. Sci., vol. 20, no. 11, Nov. 1953, pp. 757-768.

9. Piland, Robert O.: Summary of the Theoretical Lift, Damping-in-Roll, and Center-of-Pressure Characteristics of Various Wing Plan Forms at Supersonic Speeds. NACA TN 1977, 1949.

10. Harmon, Sidney M., and Jeffreys, Isabella: Theoretical Lift and Damping in Roll of Thin Wings With Arbitrary Sweep and Taper at Supersonic Speeds - Supersonic Leading and Trailing Edges. NACA TN 2114, 1950.

11. Malvestuto, Frank S., Jr., Margolis, Kenneth, and Ribner, Herbert S.: Theoretical Lift and Damping in Roll at Supersonic Speeds of Thin Sweptback Tapered Wings With Streamwise Tips, Subsonic Leading Edges, and Supersonic Trailing Edges. NACA Rep. 970, 1950. (Supersedes NACA TN 1860.)

12. Tucker, Warren A., and Nelson, Robert L.: Theoretical Characteristics in Supersonic Flow of Two Types of Control Surfaces on Triangular Wings. NACA Rep. 939, 1949. (Supersedes NACA TN's 1600 and 1601 by Tucker and TN 1660 by Tucker and Nelson.)

13. Malvestuto, Frank S., Jr., and Hoover, Dorothy M.: Lift and Pitching Derivatives of Thin Sweptback Tapered Wings With Streamwise Tips and Subsonic Leading Edges at Supersonic Speeds. NACA TN 2294, 1951.

14. Hannah, Margery E., and Margolis, Kenneth: Span Load Distributions Resulting From Constant Angle of Attack, Steady Rolling Velocity, Steady Pitching Velocity, and Constant Vertical Acceleration for Tapered Sweptback Wings With Streamwise Tips - Subsonic Leading Edges and Supersonic Trailing Edges. NACA TN 2831, 1952.

15. Martin, John C., and Jeffreys, Isabella: Span Load Distributions Resulting From Angle of Attack, Rolling, and Pitching for Tapered Sweptback Wings With Streamwise Tips - Supersonic Leading and Trailing Edges. NACA TN 2643, 1952.

16. Martin, John C., Margolis, Kenneth, and Jeffreys, Isabella: Calculation of Lift and Pitching Moments Due to Angle of Attack and Steady Pitching Velocity at Supersonic Speeds for Thin Sweptback Tapered Wings With Streamwise Tips and Supersonic Leading and Trailing Edges. NACA TN 2699, 1952.

17. Jones, Robert T.: Properties of Low-Aspect-Ratio Pointed Wings at Speeds Below and Above the Speed of Sound. NACA Rep. 835, 1946. (Supersedes NACA TN 1032.)

18. Brown, Clinton E., and Michael, William H., Jr.: On Slender Delta Wings With Leading-Edge Separation. NACA TN 3430, 1955.

[redacted]

BIBLIOGRAPHY

Banner, Richard D., Reed, Robert D., and Marcy, William L.: Wing-Load Measurements of the Bell X-5 Research Airplane at a Sweep Angle of 58.7°. NACA RM H55A11, 1955.

Cole, J. D., Solomon, G. E., and Willmarth, W. W.: Transonic Flow Past Simple Bodies. (Contract AF 18(600)383; NAw-6154), GALCIT, 1953.

Few, Albert G., Jr., and Fournier, Paul G.: Wind-Tunnel Investigation of the Aerodynamic Characteristics of a Series of Swept, Highly Tapered, Thin Wings at Transonic Speeds - Transonic-Bump Method. NACA RM L56I24, 1956.

Heaslet, Max. A., and Fuller, Franklyn B.: Particular Solutions for Flows at Mach Number 1. NACA TN 3868, 1956.

Heaslet, Max. A., and Spreiter, John R.: Three-Dimensional Transonic Flow Theory Applied to Slender Wings and Bodies. NACA TN 3717, 1956.

Henderson, Arthur, Jr.: Wind-Tunnel Investigation of the Static Longitudinal and Lateral Stability of a 1/62-Scale Model of the X-1E at Supersonic Speeds. NACA RM L56C23b, 1956.

Henderson, Arthur, Jr.: Wind-Tunnel Investigation of the Static Longitudinal and Lateral Stability of the Bell X-1A at Supersonic Speeds. NACA RM L55I23, 1955.

Holder, D. W.: Note on the Flow Near the Tail of a Two-Dimensional Aerofoil Moving at a Free-Stream Mach Number Close to Unity. C.P. No. 188, British A.R.C., June 30, 1954.

Keener, Earl R., and Jordan, Gareth H.: Wing Loads and Load Distributions Throughout the Lift Range of the Douglas X-3 Research Airplane at Transonic Speeds. NACA RM H56G13, 1956.

Keener, Earl R., and Jordan, Gareth H.: Wing Pressure Distributions Over the Lift Range of the Convair XF-92A Delta-Wing Airplane at Subsonic and Transonic Speeds. NACA RM H55G07, 1955.

Kuhl, Albert E., and Johnson, Clinton T.: Flight Measurements of Wing Loads on the Convair XF-92A Delta-Wing Airplane. NACA RM H55D12, 1955.

Kuhn, Richard E., Hallissy, Joseph M., Jr., and Stone, Ralph W., Jr.: A Discussion of Recent Wind-Tunnel Studies Relating to the Problem of Estimating Vertical- and Horizontal-Tail Loads. NACA RM L55E16a, 1955.

 [redacted]

Lindsey, Walter F., and Johnston, Patrick J.: Some Observations on Maximum Pressure Rise Across Shocks Without Boundary-Layer Separation on Airfoils at Transonic Speeds. NACA TN 3820, 1956.

Mayer, John P., and Hamer, Harold A.: A Study of Means for Rationalizing Airplane Design Loads. NACA RM L55E13a, 1955.

Moseley, William C., Jr.: Investigation at Transonic Speeds of the Hinge-Moment Characteristics of a 1/8-Scale Model of the X-1E Aileron. NACA RM L55F06a, 1955.

Neumark, S.: Critical Mach Numbers for Thin Untapered Swept Wings at Zero Incidence. R. & M. No. 2821, British A.R.C., Nov. 1949.

Neumark, S., and Collingbourne, J.: Velocity Distribution on Thin Tapered Wings With Fore-and-Aft Symmetry and Spanwise Constant Thickness Ratio at Zero Incidence. R. & M. No. 2858, British A.R.C., June 1951.

Nielsen, Jack N., Kaattari, George E., and Anastasio, Robert F.: A Method for Calculating the Lift and Center of Pressure of Wing-Body-Tail Combinations at Subsonic, Transonic, and Supersonic Speeds. NACA RM A53G08, 1953.

Nielsen, Jack N., Spahr, J. Richard, and Centolanzi, Frank: Aerodynamics of Bodies, Wings, and Wing-Body Combinations at High Angles of Attack and Supersonic Speeds. NACA RM A55L13c, 1956.

Polhamus, Edward C.: A Simple Method of Estimating the Subsonic Lift and Damping in Roll of Sweptback Wings. NACA TN 1862, 1949.

Polhamus, Edward C.: Summary of Results Obtained by Transonic-Bump Method on Effects of Plan Form and Thickness on Lift and Drag Characteristics of Wings at Transonic Speeds. NACA TN 3469, 1955. (Supersedes NACA RM L51H30.)

Robinson, Glenn H., Cothren, George E., Jr., and Pembo, Chris: Wing-Load Measurements at Supersonic Speeds of the Douglas D-558-II Research Airplane. NACA RM H54L27, 1955.

Runckel, Jack F., and Gray, W. H.: An Investigation of Loads on Ailerons at Transonic Speeds. NACA RM L55E13, 1955.

Shapiro, Ascher H.: The Dynamics and Thermodynamics of Compressible Fluid Flow. Vol. II. The Ronald Press Co., 1954.

Spreiter, John R.: On the Application of Transonic Similarity Rules to Wings of Finite Span. NACA Rep. 1153, 1953. (Supersedes NACA TN 2726.)

Spreiter, John R., and Alksne, Alberta: Theoretical Prediction of Pressure Distributions on Nonlifting Airfoils at High Subsonic Speeds. NACA Rep. 1217, 1955. (Supersedes NACA TN 3096.)

Van Dyke, Milton D.: The Similarity Rules for Second-Order Subsonic and Supersonic Flow. NACA TN 3875, 1957.

Vincenti, Walter G.: Measurements of the Effects of Finite Span on the Pressure Distribution Over Double-Wedge Wings at Mach Numbers Near Shock Attachment. NACA TN 3522, 1955.

Vincenti, Walter G., Dugan, Duane W., and Phelps, E. Ray: An Experimental Study of the Lift and Pressure Distribution on a Double-Wedge Profile at Mach Numbers Near Shock Attachment. NACA TN 3225, 1954.

Vincenti, Walter G., Wagoner, Cleo B., and Fisher, Newman H., Jr.: Calculations of the Flow Over an Inclined Flat Plate at Free-Stream Mach Number 1. NACA TN 3723, 1956.

Vincenti, Walter G., and Fisher, Newman H., Jr.: Calculation of the Supersonic Pressure Distribution on a Single-Curved Tapered Wing in Regions Not Influenced by the Root or Tip. NACA TN 3499, 1955.

Vincenti, Walter G., and Wagoner, Cleo B.: Theoretical Study of the Transonic Lift of a Double-Wedge Profile With Detached Bow Wave. NACA Rep. 1180, 1954. (Supersedes NACA TN 2832.)

Vincenti, Walter G., and Wagoner, Cleo B.: Transonic Flow Past a Wedge Profile With Detached Bow Wave. NACA Rep. 1095, 1952. (Supersedes NACA TN's 2339 and 2588.)

Willmarth, William W.: The Lift of Thin Airfoils at High Subsonic Speeds. OSR TN S4-168 (Contract AF-18(600)-383) GALCIT, June 1954.

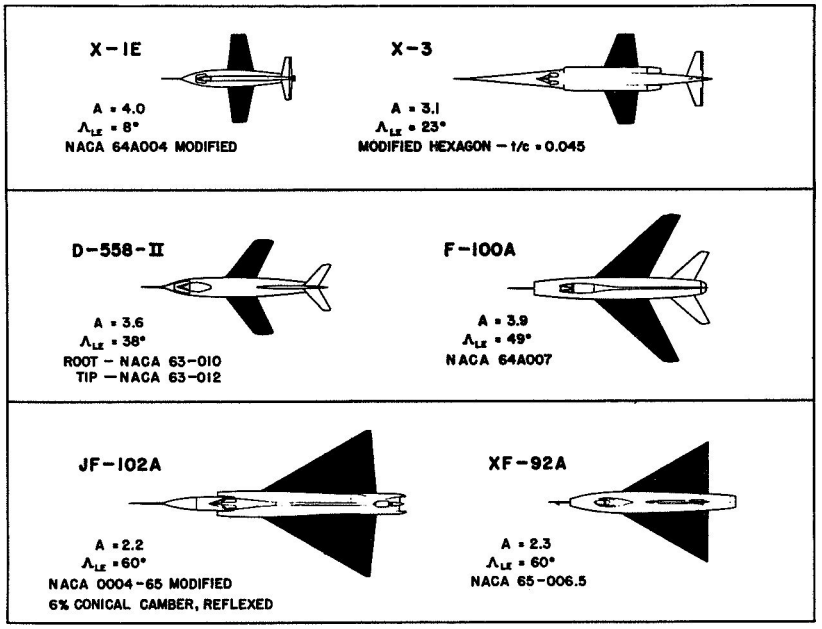


Figure 1

FLIGHT REYNOLDS NUMBER AND ANGLE OF ATTACK

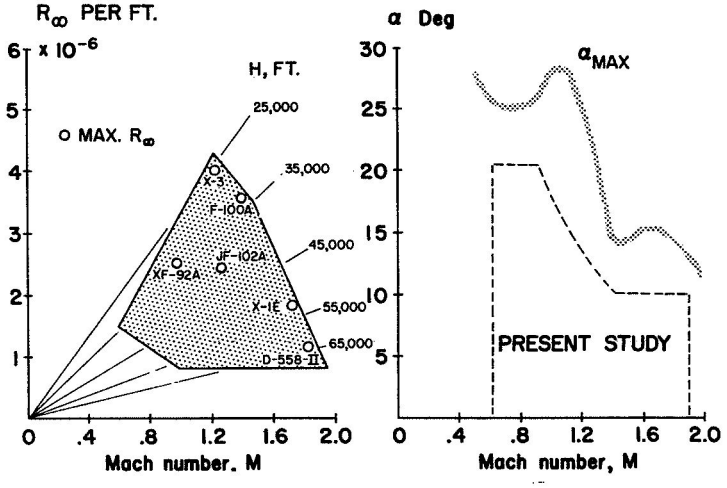


Figure 2

64

X-IE UNSWEPT WING. (t/c = 0.04) – CHORD LOADING
AT $y/b'/2 = 0.46$

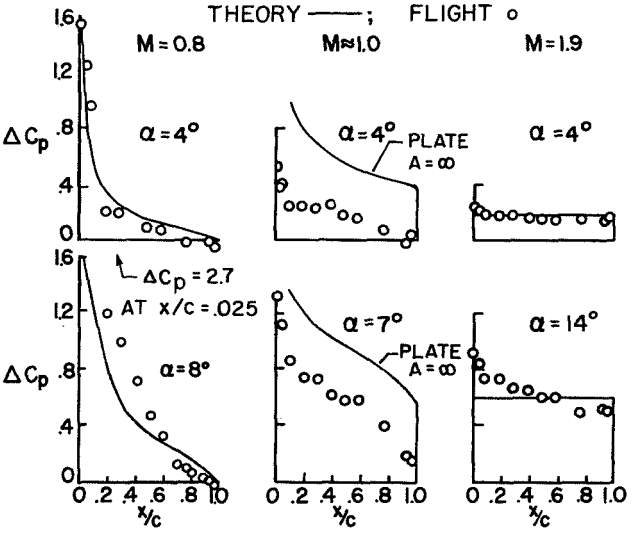


Figure 3

X-IE- UNSWEPT WING (t/c=0.04) SPAN LOADINGS
THEORY——; FLIGHT o, --o--

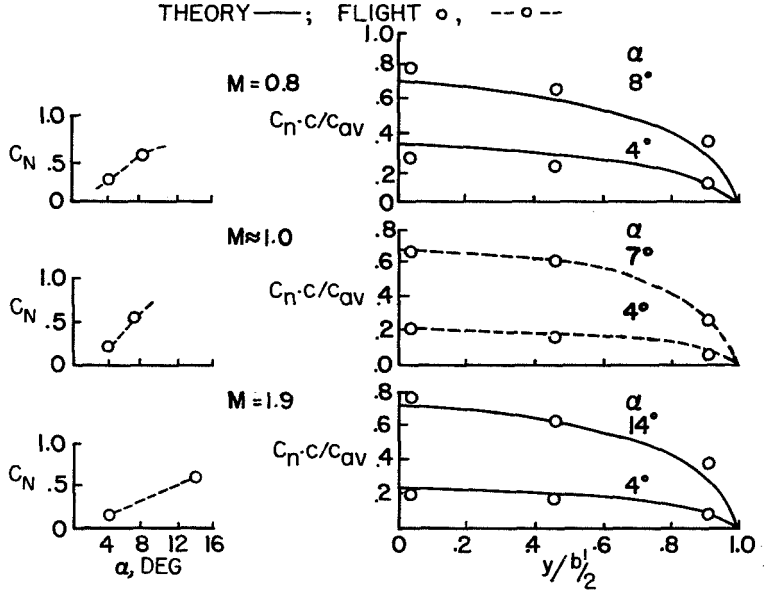


Figure 4

X-IE-UNSWEPT WING-CHORD LOAD DISTRIBUTIONS
THEORY—, FLIGHT o

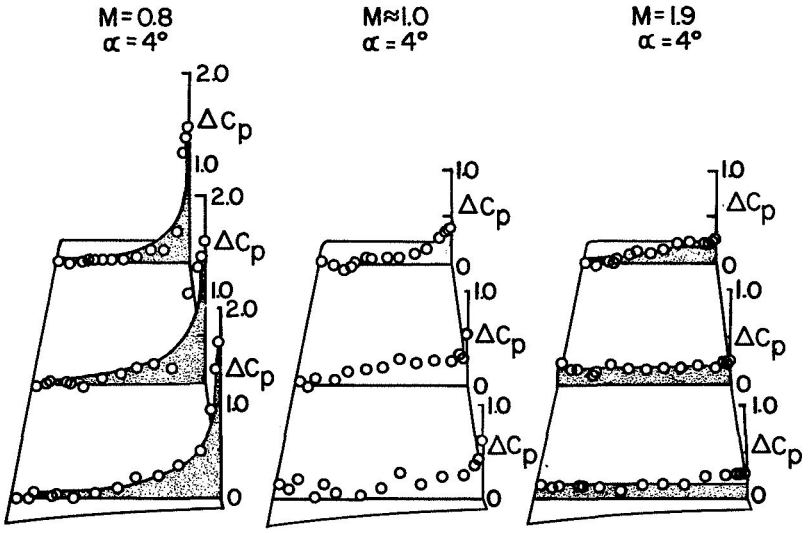


Figure 5

X-IE UNSWEPT WING-CHORD LOAD DISTRIBUTIONS
THEORY ——, FLIGHT o

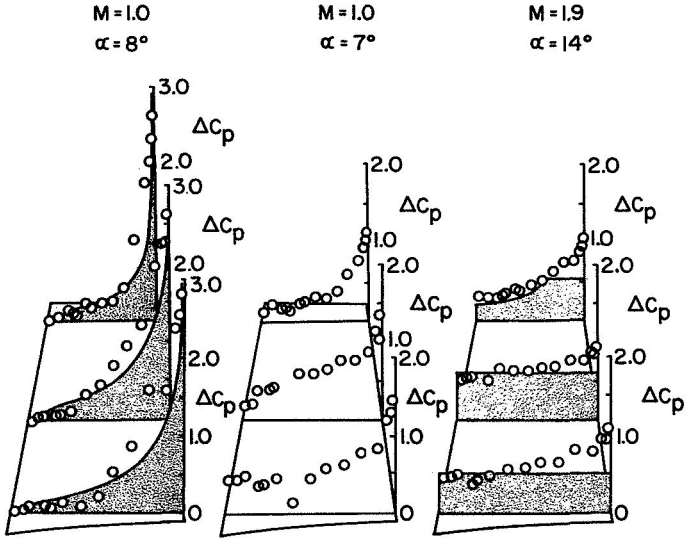


Figure 6

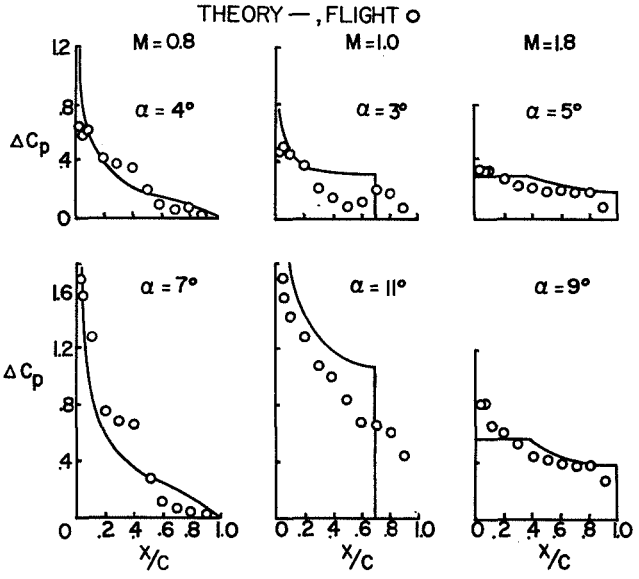


Figure 7

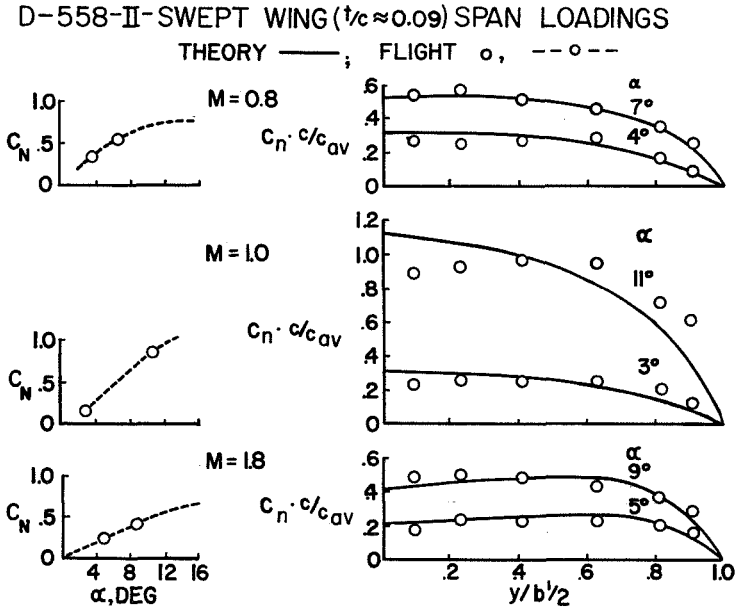


Figure 8

D-558-II-SWEPT WING-CHORD LOAD DISTRIBUTIONS
THEORY——, FLIGHT o

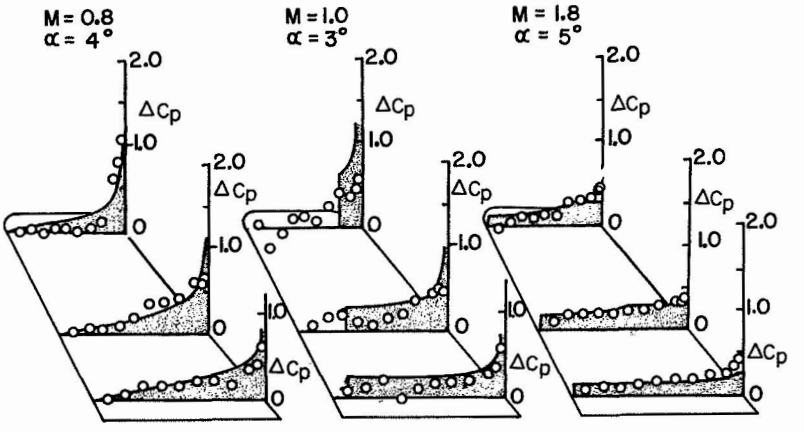


Figure 9

D-558II- SWEPT WING-CHORD LOAD DISTRIBUTION
THEORY——, FLIGHT o

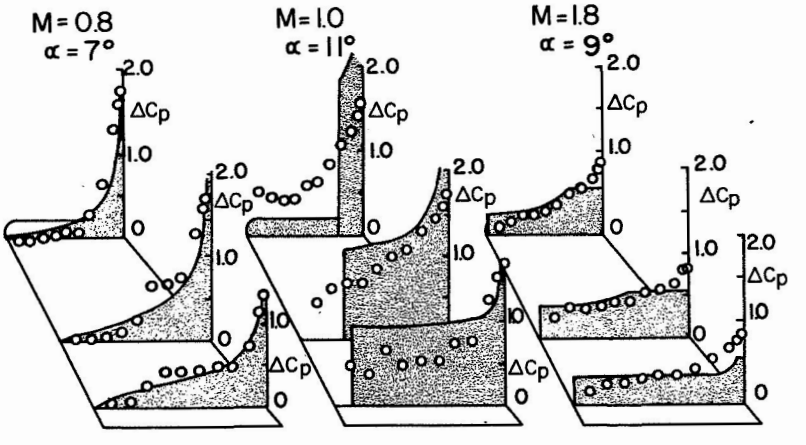
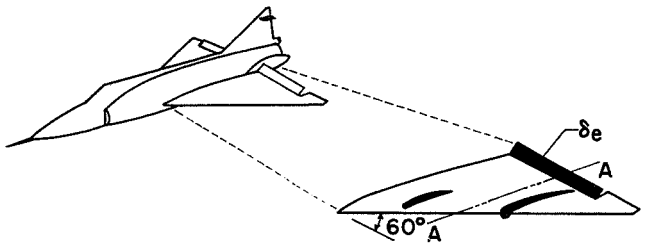


Figure 10

JF-102A AIRPLANE—SCHEMATIC OF WING



AT A-A, c_f/c = 0.17

$b_f/b' = \frac{12.9'}{16.2'} = .795$

Figure 11

JF-102A - DELTA WING (t/c=0.04) - CHORD LOADING AT $y/b_{/2}$ = 0.34

THEORY— (NO CAMBER), FLIGHT ○

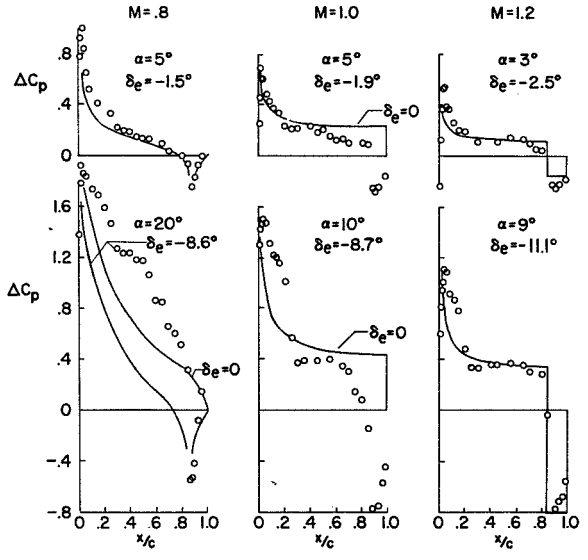


Figure 12

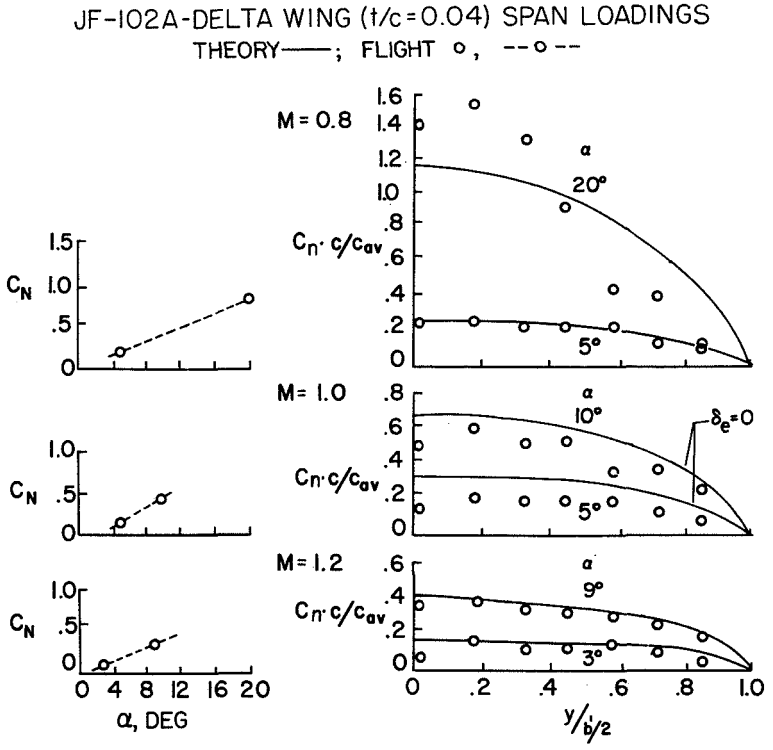


Figure 13

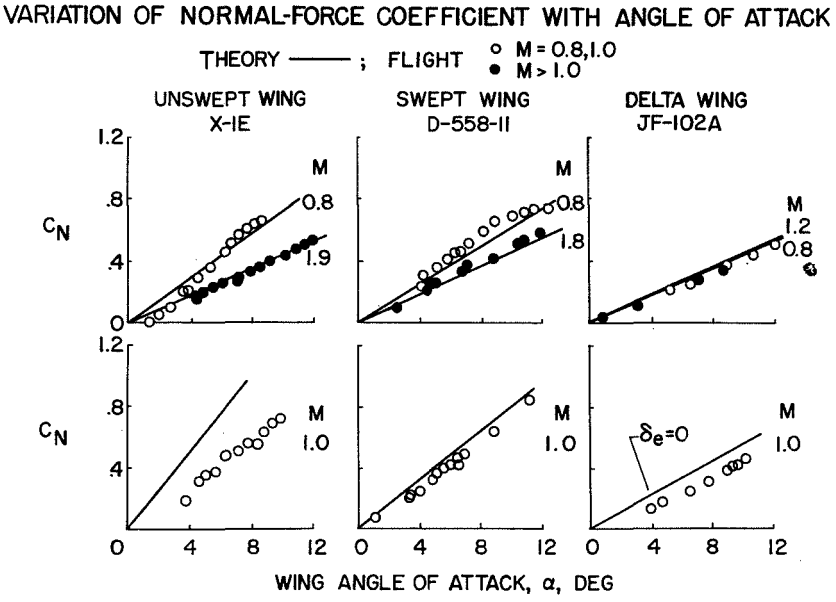


Figure 14

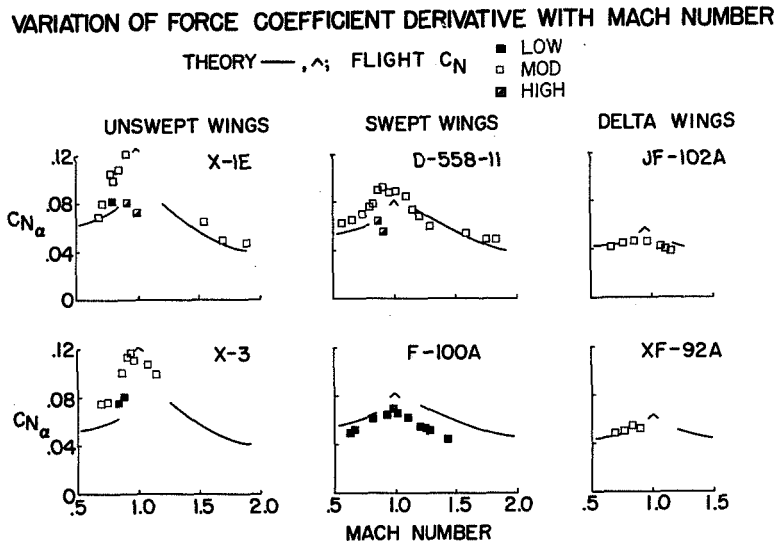

VARIATION OF FORCE COEFFICIENT DERIVATIVE WITH MACH NUMBER
THEORY —— , ^; FLIGHT C_N
LOW
MOD
HIGH
UNSWEPT WINGS
SWEPT WINGS
DELTA WINGS
X-1E
D-558-II
JF-102A
X-3
F-100A
XF-92A
C_{N_α}
.12
.08
.04
0
.5
1.0
1.5
2.0
MACH NUMBER

Figure 15

N71-75386

AIR LOAD DISTRIBUTIONS ON A FLAPPED WING RESULTING FROM LEADING-EDGE AND TRAILING-EDGE BLOWING

By H. Clyde McLemore

Langley Aeronautical Laboratory

SUMMARY

Results of recent wind-tunnel pressure-distribution tests on a large-scale boundary-layer-control model with a 49° sweptback wing have indicated that blowing air at low blowing rates over highly deflected trailing-edge flaps does not produce any unusual flap-load or wing-load problems at low speed. Blowing at very high momentum rates, however, produces large increases in flap loads and extremely high local negative pressures over the flap leading edge.

INTRODUCTION

The current and proposed fighter airplanes having thin highly loaded wings of low aspect ratio place imposing demands on suitable high-lift devices for acceptable low-speed performance. Conventional leading-edge- and trailing-edge-flap combinations have proved in wind-tunnel and flight tests (refs. 1 to 3) to be inadequate in this respect in many cases. Serious consideration has been given to methods for achieving additional lift augmentation by boundary-layer control or even to concepts of utilizing a large portion of the powerplant thrust for developing additional lift at low flight speeds.

The boundary-layer-control method, which utilizes only sufficient blowing energy to prevent flow separation, can be expected to achieve, as a maximum, the ideal fluid loading of a given wing configuration with flaps. The concept of utilizing a large amount of engine thrust for lift augmentation, however, introduces the design concepts for short take-off and landing and vertical take-off and landing.

This paper presents an initial wind-tunnel pressure-distribution exploration of lift augmentation by blowing and primarily covers a boundary-layer-control system for a fighter-type airplane. Some of the problems associated with heavily loaded flaps, however, are discussed with a view toward determining the effects of very high momentum blowing rates on the flap loads.

The model used in this investigation was a large-scale wing-body-tail configuration. The wing was swept back 49° at the leading edge and had an aspect ratio of 3.5, a taper ratio of 0.3, and NACA 65A006 airfoil sections streamwise.

Chordwise pressure distributions were obtained at spanwise stations of 0.31b/2, 0.56b/2, 0.76b/2, and 0.90b/2; however, only the data obtained at the 0.56b/2 station are presented herein. Tests of this investigation were conducted at a Reynolds number of 5.2×10^6 which corresponds to a Mach number of 0.08.

SYMBOLS

C_L	lift coefficient
c	wing chord
c_f	flap chord
$c_{n,f}$	flap section normal-force coefficient
$C_{\mu,f}$	flap blowing momentum coefficient, $wV_j/gq_\infty S$
$x_{cp,f}$	flap chordwise center of pressure, percent flap chord
c_p	section pressure coefficient
x	distance along wing chord, measured from leading edge
w	weight flow of slot ejected air, lb/sec
V_j	velocity of slot ejected air
g	acceleration due to gravity
q_∞	free-stream dynamic pressure
A	aspect ratio
b	wing span
λ	taper ratio
S	wing area
B.L.C.	boundary-layer control

Subscript:

MAX maximum

DISCUSSION

The geometric characteristics of the large-scale pressure-distribution model and a general description of the wing configurations to be discussed are presented in figure 1. The 24-percent-chord flap extends over 50 percent of the semispan. The leading-edge flow-control devices were a 15-percent-chord slat and a 17-percent-chord droop. The drooped-nose configuration incorporated a blowing slot at the "knee" of the droop, formed by the transition curvature between the drooped nose and the wing upper surface.

The three wing configurations of figure 1 were selected because they represent three relatively good landing configurations from the viewpoint of having the largest possible values of lift coefficient commensurate with acceptable longitudinal stability characteristics up to the stall. For configuration I, a 60-percent-span slat was the largest spanwise extent that would produce longitudinal stability at maximum lift. With flap blowing applied, a full-span leading-edge device is required to maintain the lift effectiveness to high angles of attack; therefore, configuration II incorporated a full-span slat. Configuration III is an alternate method of maintaining the lift effectiveness to high angles of attack.

For the nonblowing configuration (configuration I) the trailing-edge flap was deflected 40°. With flap blowing applied, however, the flap was deflected 60°. The leading-edge slat and the leading-edge droop were deflected 33° and 45°, respectively, measured normal to the wing leading edge.

The chordwise pressure distributions at station 2 (0.56b/2) for configurations I and II at a constant value of lift coefficient of 1.27 are shown in figure 2. The flap blowing rate used for configuration II was only sufficient to prevent flow separation over the flap through the lift range. The blowing flap of configuration II experienced a significant increase in load as compared with the nonblowing case, and the blowing also induced some additional load over the rear portion of the wing chord. It should be noted that the most significant loading phenomenon is the large local surface load over the flap, especially in the region of the flap leading edge.

The load on configuration I is concentrated near the wing leading edge in a normal manner. With flap blowing applied, however, the center of load is seen to be concentrated more toward the rear portion of the wing chord.

The chordwise pressure distribution of configuration II of figure 2 is compared in figure 3 with the chordwise pressure distribution of configuration III at the same lift coefficient of 1.27. Configuration III has drooped-nose-knee and trailing-edge-flap blowing in an amount only sufficient to control flow separation through the lift range. Mainly because of the absence of a flow-control device located ahead of the wing leading edge, configuration III has the center of load concentrated still farther rearward.

Although one effect of flap blowing is to move the wing chordwise center of pressure rearward, which would require somewhat larger tail balancing loads, experiments have shown that a tail of normal tail-volume coefficient suitably located with respect to the wing downwash field and operating within its low-speed lift capabilities could supply these additional balancing loads.

The spanwise center-of-pressure characteristics of configurations I, II, and III are not presented in this paper. It has been determined, however, that the maximum spanwise center-of-pressure movement caused by flap blowing was a maximum outboard movement at $C_L = 1.27$ of about 3 percent of the semispan. This outboard movement was no greater than that experienced by the nonblowing configuration at lift coefficients of the order of 0.8. Flap blowing, therefore, should not introduce additional low-speed wing-root bending moments.

Probably the most significant information is presented in figures 4 to 6. The chordwise pressure distribution (station 2) of configuration III at an angle of attack of 12.5° for a wide range of flap blowing rates is shown in figure 4. The blowing momentum coefficient $C_{\mu,f}$ of 0.031 is representative of the boundary-layer-control case; whereas, the value of $C_{\mu,f}$ of 0.187 represents mass-flow rates of the order of 40 to 50 pounds of air per second. If the loading over the flap is observed, it is noted that the flap loads and their contribution to the moment on the rear spar are a function of the blowing momentum. For the boundary-layer-control case $\left(C_{\mu,f} = 0.031\right)$ the conventional methods of potential-flow calculations are applicable for calculating the section loading characteristics (ref. 4). The other cases shown in figure 4 (the higher blowing rates) have not been examined extensively from the viewpoint of calculating the section loads. The form of these pressure distributions (their smoothness and uniform buildup with increasing blowing rate) suggests, however, that a method can be determined to calculate the section loadings at these high blowing rates.

It should be noted that not only does the load build up over the rear portion of the flap and over the main wing but also an appreciable load buildup occurs over the flap leading edge. The maximum negative pressure

coefficients over the flap leading edge were too large for the higher blowing rates to plot in figure 4; however, the maximum values are listed. For the curve of $C_{\mu,f} = 0.187$, the peak negative pressure coefficient over the flap leading edge was -26.48.

In order to show the overall perspective of the wing and flap loads for a high flap blowing rate, the curve for $C_{\mu,f} = 0.187$ of figure 4 is shown plotted to a greatly compressed scale in figure 5. The load over the flap is seen to be a large portion of the total load, and the peak negative pressures existing over the flap leading edge are extremely high as compared with the peak pressures existing at the wing leading edge.

In order to obtain a more general, and perhaps more informative, outlook on the significance of these large indicated flap loads with increasing blowing rate, the flap section normal-force coefficients together with the flap centers of pressure for configuration III for a wide range of flap blowing rates are shown as functions of lift coefficient in figure 6.

The flap section normal-force coefficients are seen to increase greatly with increased blowing rate but, as in the case of a normal unseparated flap, increasing lift coefficient has no significant effect on the flap normal-force coefficients. It should be noted here that the large values of $c_{n,f}$ are associated with the large flap blowing rates $C_{\mu,f}$ which are, in turn, inversely proportional to the square of the flight speed, if the momentum of the blowing jet is assumed constant. At relatively high flight speeds the momentum coefficients are small. These high values of $c_{n,f}$ at the high $C_{\mu,f}$ rates are, therefore, necessarily restricted to low to moderate flight speeds in the latter phase of the landing approach and flare.

The flap center of pressure is seen to move toward the flap leading edge with increasing blowing rate because of the high loading over the flap leading edge, and this movement produces some compensating relief of the flap moments. Increasing lift coefficient also has no significant effect on the location of the flap center of pressure.

CONCLUDING REMARKS

The results of wind-tunnel pressure-distribution tests of a large-scale boundary-layer-control model with a 49° sweptback wing indicate that, for the relatively small amount of blowing necessary to prevent flow separation over the flap, no unusual flap-load or wing-load problems are anticipated. When a considerable amount of additional blowing energy

is used, however, large increases in flap loads can be expected; particularly, the loads are extremely high near the flap leading edge and may be the critical design flap load in the landing maneuver.

REFERENCES

1. McLemore, H. Clyde, and Fink, Marvin P.: Blowing Over the Flaps and Wing Leading Edge of a Thin 49° Swept Wing-Body-Tail Configuration in Combination With Leading-Edge Devices. NACA RM L56E16, 1956.

2. Kelly, Mark W., and Tolhurst, William H., Jr.: Full-Scale Wind-Tunnel Tests of a 35° Sweptback Wing Airplane With High-Velocity Blowing Over the Trailing-Edge Flaps. NACA RM A55I09, 1955.

3. Anderson, Seth B., Quigley, Hervey C., and Innis, Robert C.: Flight Measurements of the Low-Speed Characteristics of a 35° Swept-Wing Airplane With Blowing-Type Boundary-Layer Control on the Trailing-Edge Flaps. NACA RM A56G30, 1956.

4. Allen, H. Julian: Calculation of the Chordwise Load Distribution Over Airfoil Sections With Plain, Split, or Serially Hinged Trailing-Edge Flaps. NACA Rep. 634, 1938.

GEOMETRIC CHARACTERISTICS OF LARGE-SCALE
PRESSURE-DISTRIBUTION MODEL

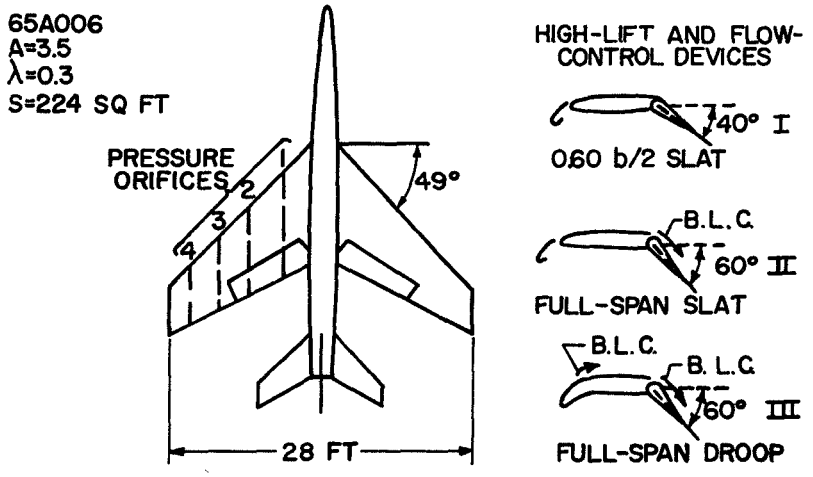


Figure 1

CHORDWISE PRESSURE DISTRIBUTIONS
FOR CONSTANT C_L=1.27
EFFECT OF FLAP BLOWING

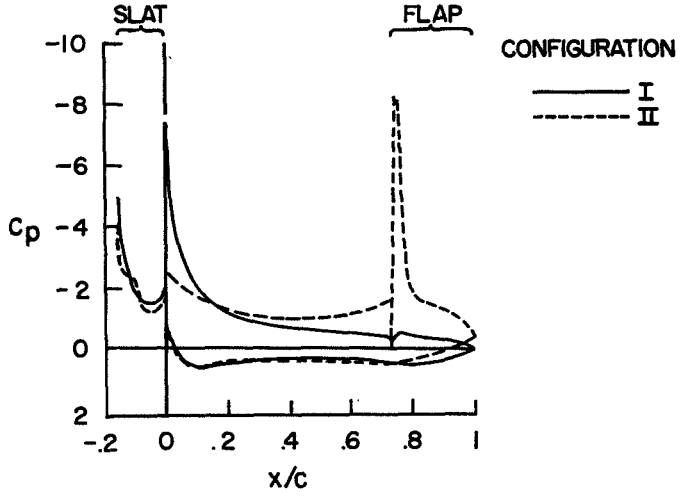


Figure 2

CHORDWISE PRESSURE DISTRIBUTIONS
FOR CONSTANT C_L=1.27
EFFECT OF NOSE DROOP

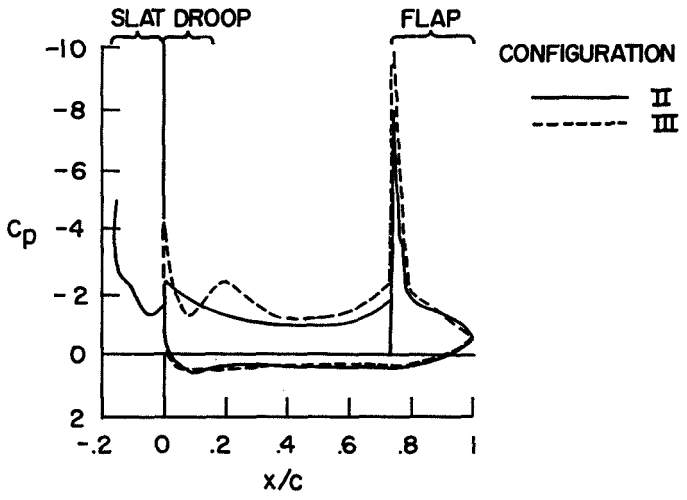
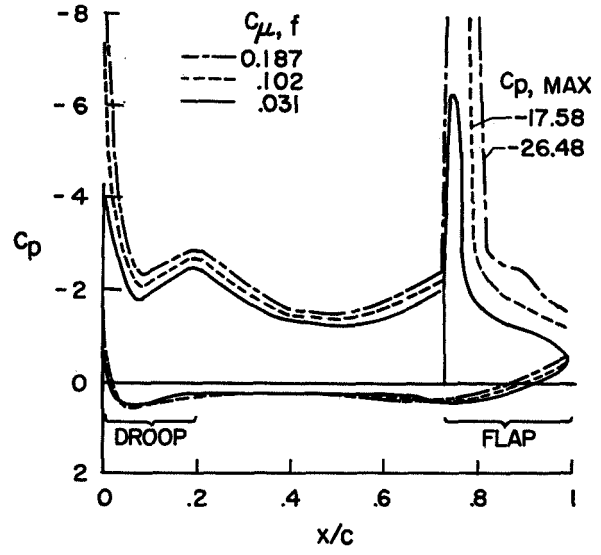


Figure 3

VARIATION OF CHORDWISE PRESSURE DISTRIBUTION WITH INCREASING FLAP BLOWING
CONFIGURATION III; α=12.5



79

Figure 4

VARIATION OF CHORDWISE PRESSURE DISTRIBUTION
FOR HIGH MOMENTUM RATE
CONFIGURATION III; $\alpha = 12.5°$

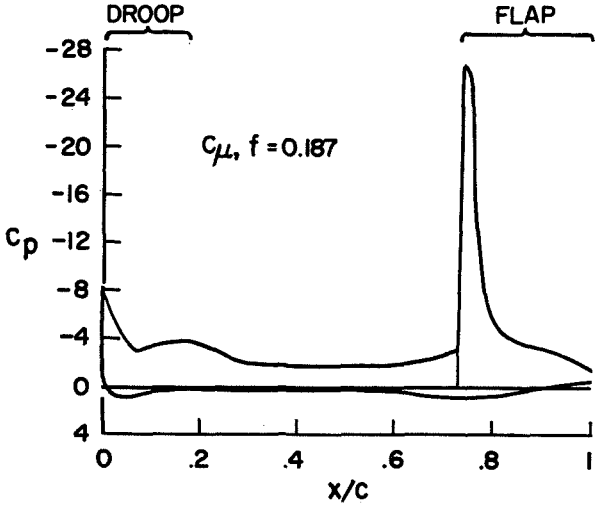


Figure 5

VARIATION OF FLAP NORMAL-FORCE COEFFICIENT AND FLAP
CENTER OF PRESSURE
CONFIGURATION III

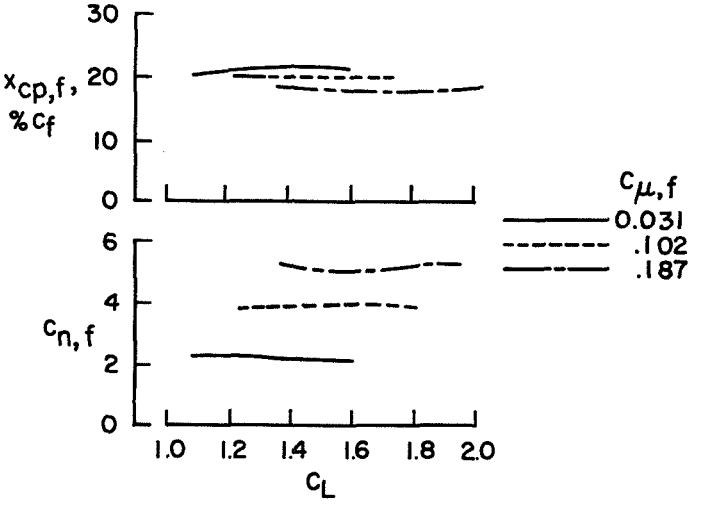


Figure 6

N71-75387

BOBBITT, CARLSON & PEARSON

CALCULATION OF EXTERNAL-STORE LOADS AND CORRELATION WITH EXPERIMENT

By Percy J. Bobbitt, Harry W. Carlson, and Albin O. Pearson

Langley Aeronautical Laboratory

SUMMARY

A theory for evaluating the mutual interference between a wing and tip tank has been extended to apply to store-pylon configurations. By use of this analysis and the flow-field formulas of NACA Research Memorandum L55L30b and NACA Technical Note 3938, theoretical store-pylon side-force estimates have been made for a number of store-pylon configurations. Considered in this paper are the separate effects of spanwise store position, chordwise store position, angle of sideslip, store fins, store-store interference, and fuselage indentation. The experimental data and theory indicate that the pylon and pylon-induced side forces are the largest contributors to the total store-pylon side force. A short bibliography of recent NACA publications dealing with store and missile loads is included.

INTRODUCTION

In reference 1, the results were presented of a study made to determine the ability of linearized theory to predict the side force acting on wing stores at supersonic speeds. Though the theoretical and experimental correlations of this study were made for only a limited number of configurations and one Mach number, indications were that linear theory might be capable of doing a satisfactory job. It was apparent also from this study that additional calculations and correlations were needed to refine the theoretical approach and at the same time further define its limitations or capabilities.

The purpose of the present paper is to present the results of some recent calculations and correlations made to partially fulfill this need and at the same time indicate the type of data now being obtained at the National Advisory Committee of Aeronautics which are pertinent to the store-loads problem. Of particular interest are the data presented herein on pylon loads and pylon-induced store loads.

A short bibliography of recent NACA publications dealing with store and missile loads is included.

SYMBOLS

M Mach number, $\frac{\text{Free-stream velocity}}{\text{Velocity of sound in free stream}}$

α angle of attack

b wing span

S_s maximum store cross-sectional area

q free-stream dynamic pressure

A_p aspect ratio of pylon

b_p span of pylon

S_p pylon area

$\left(C_{Y_\beta}\right)_p = \frac{\text{Side force on pylon}}{qS_p\beta}$

$\left(C_{Y_\beta}\right)_s = \frac{\text{Side force on store}}{qS_p\beta}$

$C_{Y,s} = \frac{\text{Side force on store}}{qS_s}$

$C_{Y,sp} = \frac{\text{Side force of store and pylon}}{qS_s}$

DISCUSSION

In order to gain some insight into the mutual interference effects between a store and pylon and thus into the division of loads, both a theoretical analysis and experimental program have been carried out. In this section, a short description of the theoretical analysis just referred to is presented followed by a discussion of the ability of this theory, when used in conjunction with the flow-field formulas of references 1 and 2, to predict a number of experimentally measured effects. Several points of interest discussed at the end of this section is illustrated by data obtained for stores situated below the wing but not connected with a pylon. Through the use of theory, an estimation of what

the order of magnitude of these data would be if the store were connected with a pylon is made.

Theory For Store-Pylon Side Force

The complex, three-dimensional, nonplanar problem of determining rigorously the side load on a store and pylon attached to a finite wing is one of insurmountable difficulty. Obviously, some simplifying assumptions must be made and some rigor sacrificed if the problem is to be treated by analytical means. One of the most profitable simplifications which can be affected when evaluating the interference effects between the store, pylon, and wing is the replacement of the wing by an infinite reflection plane. Inherent in this simplification is that the magnitude of the lateral-flow velocity beneath the wing be determined separately and by other methods. (See refs. 1 and 2.)

The problem of determining the loads on a pylon-store reflection-plane configuration subjected to a uniform lateral flow can be analyzed in the same manner as a wing tip-tank configuration at an angle of attack since the insertion of an infinite plane, perpendicular to the wing and in the plane of symmetry, does not alter the flow pattern. When the configuration of wing, tip tank, and vertical reflection plane is rotated through 90°, the wing semispan becomes the pylon, the vertical reflection plane becomes the wing, and the tip-tank becomes the store. Also, the uniform vertical velocity to which the wing and tip-tank are subjected and which is equivalent to $V\alpha$ becomes the lateral-flow velocity and is given the value $-V\beta$. The wing tip-tank problem has been treated in reference 3; however, the ratios of tank diameter to wing semispan of the configurations for which numerical results were obtained were not high enough to be of use in evaluating pylon or store loads. Consequently the analytical procedure given in reference 3 has been utilized to extend the numerical results from values of D/b_p up to 0.3 to values of D/b_p up to 1.6.

Shown in figure 1 are the variations of the pylon and pylon-induced store forces in coefficient form with the ratio of the store diameter to pylon span. The nondimensionalizing area for these coefficients is the pylon area. Note that when the store diameter is 1.6 times the pylon span, the pylon-induced side force on the store and the side force on the pylon are almost equal. It is conceivable that in this situation the pylon could contribute on the order of 20 to 25 percent to the total root-bending moment.

Scope of Test Configurations

The curves given in figure 1 and the flow-field formulas of references 1 and 2 have been utilized to make side-force calculations for a number of configurations recently tested at the Langley Aeronautical Laboratory. Before making comparisons of the calculated and experimental

results, it would seem appropriate to present a few details of the tests and test configurations.

Some idea of the scope of tests can be obtained from the two wing-body models and associated store and store-pylon configurations shown in figure 2. The wing-body and store-pylon configurations on the left of figure 2 were tested at a Mach number of 1.6 in the Langley 4- by 4-foot supersonic pressure tunnel; those on the right, at Mach numbers from 0.8 to 1.43 in the Langley 8-foot transonic pressure tunnel. In the 4-foot-tunnel tests, store and store-pylon loads have been obtained for a variety of store-pylon configurations and a number of spanwise and chordwise locations as indicated by the circles showing store midpoint locations. Five-component store forces and moments were measured in this investigation with the store in presence of the pylon, three components were measured for the store-pylon combination and the full six components for the wing body. The models were tested through an angle-of-attack range extending from -2° to 12° and an angle-of-sideslip range from -12° to 12°.

The wing-fuselage model and the two store shapes pictured on the right of figure 2 represent two separate investigations conducted in the Langley 8-foot transonic pressure tunnel. For the store without a pylon systematic investigations have been conducted using both the basic and contoured fuselages shown. The circles on the wing body at the right indicate the positions at which store forces and moments were obtained. In addition to being tested singly, several of the stores were tested in combination, that is, two stores on a panel. Forces and moments for the finned store were measured only on the contoured fuselage airplane configuration at two positions. These positions are indicated by the squares. In each of the investigations, five-component store forces and moments and three-component wing-fuselage forces and moments were obtained through an angle-of-attack range extending from -2° to 8°.

There is, evidently, a large amount of recent experimental data which can be utilized to test the worth of the theoretical methods. In subsequent figures showing experimental results and calculations for a variety of effects only a representative cross section of this data will be utilized.

CONTRIBUTION OF STORE AND PYLON TO COMBINED LOAD

Given in figure 3 are the separate contributions of the store and pylon to the combined store-pylon side-force coefficient at a Mach number of 1.6. The angle of sideslip is zero as it is for all other figures unless otherwise noted. Data and curves shown are for a sweptforward pylon and store combination located at the 0.55-wing-semispan station. The vertical scale of figure 3, which is labeled side-force coefficient, is simply the particular side force being considered nondimensionalized

by q and the maximum cross-sectional area of the store. Negative side-force coefficient indicates that the side force acting on the store or store-pylon located below the left-hand half-wing is directed toward the wing tip.

In the calculation of the total store-pylon load, the loads on the store and pylon are determined separately and added. The load acting on the store is itself further broken down into two separate components. One is the load on the store determined as if the pylon were not present and the other is the load induced on the store by the pylon. It should be noted that the latter of these two loads is determined by the use of figure 1. Fortunately for the stores used in the investigation in the Langley 4- by 4-foot supersonic pressure tunnel, experimental data is available for each of the store-load components in addition to the total store-pylon load. Consider first the side force acting on the store when no pylon is present. It is evident that for this condition the rate of change of the side force with angle of attack is underestimated by the theory. This is not surprising since a calculation of the lift-curve slope for the store alone in a uniform flow field underestimates experiment by about 50 percent. The use of static experimental force data for the isolated store to form a correction factor for the theoretical computations would lead to a more accurate estimate of this component if desired.

The total side force acting on the store when the pylon is added (see fig. 3), agrees rather well with the calculated curve. Evidently this agreement is fortuitous since the increment in the store side force caused by the insertion of the pylon is overpredicted; that is, the difference between the squares and circles is overpredicted. Perhaps the fact that the theoretical curves used to estimate this increment were meant primarily for an unswept pylon and also that the theoretical sidewash acted only over the rear portion of the pylon are partly responsible for the overprediction.

The total force acting on the store and pylon combination as determined by experiment and given by the diamonds agrees satisfactorily with theory which is the solid line. Contributing to this agreement is the overprediction of the slope and the underprediction of the zero angle of attack or thickness effects. It is interesting to note that the pylon, carrying about the same amount of side load as the store, contributes about 25 percent of the total root-bending moment.

Before leaving figure 3, it is of interest to translate the combined store-pylon side-force coefficient into terms of a load in pounds for a practical situation. For example, if an airplane of this configuration having a 40-foot wing span and operating at 40,000 feet and a Mach number of 1.6 were to experience the largest store-pylon force indicated, it would amount to 6,600 pounds.

EFFECT OF STORE SPANWISE LOCATION ON THE STORE-PYLON SIDE-FORCE COEFFICIENT

There are other limitations and inadequacies of the theoretical methods used which have not yet been mentioned that will be pointed out at the appropriate places subsequently. An excellent opportunity to illustrate one of these shortcomings is afforded by figure 4.

Figure 4 shows the effect of store spanwise location on the angle-of-attack variation of the store-pylon side-force coefficient. The relative position of the store-pylon configuration with respect to the wing leading edge remains the same for all three spanwise locations as indicated by the sketches. Looking first at the experimental points, it can be seen that as you go from the inboard to the outboard position there is an increase in the slope. Theoretical predictions using the supersonic leading-edge sidewash calculated for the free-stream Mach number of 1.6 (the solid-line curves) also show an increase in slope as the store moves outboard, but the rate at which the slope increases is overpredicted.

Schlieren photographs taken of these models, one of which is shown in figure 5, revealed that the wing leading edge, instead of being slightly supersonic as predicted by the theory, was actually subsonic. In an attempt to obtain better agreement between the theoretical and experimental slopes, the wing angle-of-attack flow field was recalculated for the Mach number giving the same location of the Mach cone emanating from the wing root as indicated in the schlieren photograph. Use of this flow field in determining the store-pylon side forces resulted in the dashed-line curves. For the inboard location, calculations using the subsonic edge flow field did not yield a noticeable change; whereas, for the mid-span and tip locations, better agreement resulted. The agreement in magnitudes might be further improved if the side forces induced by the wing-thickness flow field were also reevaluated. Because of the time required, only a very rough estimation of the wing thickness effect was made. This is true of most of the curves shown in subsequent figures.

EFFECT OF PYLON SWEEP AND STORE CHORDWISE LOCATION

Having examined the effect of spanwise location on a particular store-pylon configuration, the next logical effect to discuss is that of store chordwise location and accompanying pylon sweep. The spanwise position for which data will be presented is at the 0.55-wing-semispan station. The store-pylon configurations at the different chordwise locations are shown by the sketches in figure 6. Actually since the pylon carries or

induces the major portion of the total load, this figure might be more properly titled the effect of pylon sweep and location. The experimental data and theoretical curve for the most forward position are repeated from the previous figures. When the store is moved to the rear from the most forward position and the pylon becomes unswept, there is an increase in the slope and a slight decrease in the thickness effects. In this position, the pylon is almost completely immersed in the wing flow field and feels the maximum effect of the high flow angularities in the region just to the rear of the wing leading edge. The agreement between theory and experiment for this position is good. For the store in the rear position, a considerable change in the side-force coefficient angle-of-attack variation from those of the more forward positions is noted. This can be attributed to the fact that the sweptback pylon is situated in a region of much lower wing angle-of-attack sidewash and also that it is subjected to the inflow in the region of the trailing edge due to wing thickness. The theoretical slope, though somewhat less than it was for the other two locations, still overpredicts the experimental slope. The change in thickness effects, estimated, as mentioned before, in a rather rough manner, were also overpredicted. Generally speaking, the agreement for the three positions is satisfactory.

Effect of Sideslip on the Store-Pylon Side-Force Coefficient

Another factor which has a major influence on the magnitude of the side force a store-pylon will be required to carry is the angle of sideslip. Plotted in figure 7 is the variation of the store-pylon side-force coefficient with angle of sideslip for the sweptforward pylon and store combination located at the 0.55-semispan station. The angle of attack chosen to illustrate this effect is 8°. Note the large magnitude of the side-force coefficients at the highest angles of sideslip and also the steepness of the slope. A comparison of experimental curves indicates that more side force results from 1° of sideslip than from 1° of angle of attack but perhaps not as much more as might be expected. The theory used to obtain the solid-line curve assumes that the store and pylon are side slipped in the presence of an infinite flat plate hence the effect of the changing leading-edge sweep relative to the free-stream direction and the effect of the fuselage are neglected. It is evident that the simplified theory overpredicts the incremental load due to sideslip by about 50 percent. A rough calculation taking into account the changing leading-edge sweep yielded considerably better agreement. It should be pointed out here that the rate of change of the side-force coefficient with angle of sideslip varied little from one position to another in this investigation.

[redacted]

Effect of Fins on Store Side-Force Coefficient

There are many stores in use today which employ fins. An indication of how important the fin loads are relative to the pylon and pylon-induced store loads may be obtained from figure 8. In this figure is plotted the variation of the store side-force coefficient with angle of attack. The vertical scale has been reduced by a factor of one-half from the previous figures so that the changes caused by the addition of the fins can be more easily seen. The store pylon and wing body on the left are the same as that used for a number of the previous figures and, it may be remembered, was tested in the Langley 4- by 4-foot supersonic pressure tunnel at a Mach number of 1.6. The configuration on the right is completely different in all respects and was tested in the Langley 8-foot transonic pressure tunnel at a variety of Mach numbers in addition to the Mach number for which data is given in this figure. For the store on the left, the addition of fins causes an increase in the slope and only negligible displacement in the zero angle-of-attack value. Theory adequately predicts the slope change but overestimates the displacement. For the store on the right, the addition of the fins causes a displacement in the curves though little change in slope. Theory for the fins-off situation accurately predicts the magnitude and rate of change with angle of attack of the store side-force coefficient. For the fins-on situation only the increment at zero angle of attack is predicted. This estimate is indicated by the tick mark. Because the fin closest to the wing is affected by the wing vortex wake, no attempt has been made to calculate the angle-of-attack variation with the fins on. For the store on the left, the effect of the fins is small when compared to the total side-force acting on the store and pylon. For the store on the right where the store-pylon side forces are much smaller, the effect of the fins assumes a more important role.

Interference Effects Between Inboard and Outboard Stores

Another source of store side forces is the flow field created by another store, particularly when this other store is located on the same half-wing as in a four-store or four-nacelle configuration. To give some idea of the magnitude of these effects and to indicate whether the store flow fields can be accurately predicted, figure 9 has been prepared. Shown on the left of figure 9 is the effect of the outboard store on the side force acting on the inboard store and on the right, the effect of the inboard store on the outboard-store side force. These stores were not connected to the wing with a pylon. The dashed lines and the circles are the theory and experiment for the side force on the store alone and the solid line and the squares for the side force on the store in the presence of the other store.

The points to be made relative to the inboard-store curves on the left are the large effect of the outboard store on the inboard and the

[redacted]

accuracy with which this effect is predicted. The displacement of the two curves is primarily due to the radial flow away from the outboard store caused by the outboard-store thickness and is, therefore, almost independent of angle of attack. If the inboard store were connected to the wing by a pylon, the increment in store side-force coefficient instead of being of the order of 0.08 might be as large as 0.6 or 0.7 depending on the geometric characteristics of the pylon. An effect of this magnitude would most certainly have to be accounted for to obtain reliable values of the store-pylon side force. The calculated curves shown are based on linear theory corrected by use of experimental force data for the isolated store. An examination of the right-hand plot shows that the change in the slope of the side-force-coefficient curve for the outboard store when the inboard store is added is fairly well predicted by theory. The magnitude agreement between theory and experiment for the outboard-store side-force coefficients is evidently not so good as for the inboard store. The reason for this is thought to be a local Mach number loss similar to that illustrated by the schlieren photograph of figure 5. In terms of store-store interference, this means that one store will affect the other further forward than it would if the local Mach numbers were the same as the free-stream Mach numbers. Experimental data is available which indicates the effect on the store-store interference of these Mach numbers losses. Some of these data are presented in figure 10.

Shown in this figure are the side forces and yawing moments on an inboard store, alone and in the presence of the outboard store, for Mach numbers of 1.43, 1.2, and 0.8. The stores for the test results pictured were located at the 0.28- and 0.70-wing-semispan stations. The dashed lines are for the inboard store alone and the solid lines are for the inboard in the presence of the outboard store. At a Mach number of 1.43, note that the outboard store has a negligible effect on the inboard store, whereas at a Mach number of 1.2 there is a large effect. If the local Mach number were supersonic, it would be impossible for the outboard store to effect the inboard store at a Mach number of 1.2. The fact that the induced moment on the inboard store at zero angle of attack is positive, or nose in, and the fact that the angle-of-attack variations at this Mach number are almost identical to those at subsonic speeds, typified by the $M = 0.8$ curves, indicates that the local flow is actually subsonic.

Effect of Fuselage Contouring

It is well known that contoured fuselages are in use on many of todays production and design stage airplanes. While effecting a change in the pressure field to yield a lower drag than the basic fuselage configuration, these indented fuselages also have an appreciable effect on the lateral flow field and hence on the loads induced on stores attached to the wing. An indication of the difference between the loads on a store located beneath wing-fuselage models with and without a fuselage indentation can be obtained from figure 11. The Mach number of

experimental results plotted in this figure is 1.2. Data for two spanwise store positions, 0.28- and 0.5-wing-semispan stations, is depicted. Judging from the difference between the curves for the basic and indented fuselages the effect of fuselage indentation is to cause an increase in the outward flow in the vicinity of the leading edge, giving rise to a negative increment in the side force and negative and positive increments to the yawing moments for the inboard and outboard stores, respectively. If the stores were connected to the wing with a pylon the largest increment shown instead of being approximately 0.05 would be of the order of 0.3 or 0.4.

The effect of fuselage indentation on the surface pressures and flow fields of configurations at an angle of attack has not yet been analyzed theoretically. At zero angle of attack the area-rule papers of Lomax and Heaslet (ref. 4) and Nielsen and Pitts (ref. 5) permit an evaluation of these effects though the procedure is rather involved.

CONCLUDING REMARKS

It can be said that theoretical methods are capable of predicting satisfactorily a variety of effects. More detail in the calculations of some of these effects than used in the present paper seems desirable. The experimental data and theory indicate that the pylon and pylon-induced side forces are the largest contributors to the total store-pylon side force. The separate effects of spanwise store position, chordwise store position, angle of sideslip, store fins, store-store interference, and fuselage indentation all play a part in determining the store-pylon side loads.

REFERENCES

1. Bobbitt, Percy J., Malvestuto, Frank S., Jr., and Margolis, Kenneth: Theoretical Prediction of the Side Force on Stores Attached to Configurations Traveling at Supersonic Speeds. NACA RM L55L30b, 1956.

2. Bobbitt, Percy J., and Maxie, Peter J., Jr.: Sidewash in the Vicinity of Lifting Swept Wings at Supersonic Speeds. NACA TN 3938, 1957.

3. Hartley, D. E.: Theoretical Load Distributions on Wings With Cylindrical Bodies at the Tips. C.P. No. 147, British A.R.C., 1954.

4. Lomax, Harvard, and Heaslet, Max. A.: A Special Method for Finding Body Distortions That Reduce the Wave Drag of Wing and Body Combinations at Supersonic Speeds. NACA RM A55B16, 1955.

5. Nielsen, Jack N., and Pitts, William C.: General Theory of Wave-Drag Reduction for Combinations Employing Quasi-Cylindrical Bodies With an Application to Swept-Wing and Body Combinations. NACA TN 3722, 1956. (Supersedes NACA RM A55B07.)

[redacted]

BIBLIOGRAPHY

Silvers, H. Norman, and King, Thomas J., Jr.: Investigation at High Subsonic Speeds of Bodies Mounted From the Wing of an Unswept-Wing—Fuselage Model, Including Measurements of Body Loads. NACA RM L52J08, 1952.

Robinson, Samuel W., Jr., and Zlotnick, Martin: A Method for Calculating the Aerodynamic Loading on Wing—Tip-Tank Combinations in Subsonic Flow. NACA RM L53B18, 1953.

Silvers, H. Norman, and O'Bryan, Thomas C.: Some Notes on the Aerodynamic Loads Associated With External-Store Installations. NACA RM L53E06a, 1953.

O'Bryan, Thomas C.: Flight Measurements of Aerodynamic Loads and Moments on an External Store Mounted Under the Wing of a Swept-Wing Fighter-Type Airplane. NACA RM L53G22, 1953.

Alford, William J., Jr., and Silvers, H. Norman: Investigation at High Subsonic Speeds of Finned and Unfinned Bodies Mounted at Various Locations From the Wings of Unswept- and Swept-Wing—Fuselage Models, Including Measurements of Body Loads. NACA RM L54B18, 1954.

Alford, William J., Jr., Silvers, H. Norman, and King, Thomas J., Jr.: Preliminary Low-Speed Wing-Tunnel Investigation of Some Aspects of the Aerodynamic Problems Associated With Missiles Carried Externally in Positions Near Airplane Wings. NACA RM L54J20, 1954.

Alford, William J., Jr., Silvers, H. Norman, and King, Thomas J., Jr.: Experimental Aerodynamic Forces and Moments at Low Speed of a Missile Model During Simulated Launching From the Midsemispan Location of a 45° Sweptback Wing-Fuselage Combination. NACA RM L54K11a, 1955.

Alford, William J., Jr.: Experimental Static Aerodynamic Forces and Moments at Low Speed on a Canard Missile During Simulated Launching From the Midsemispan and Wing-Tip Locations of a 45° Sweptback Wing-Fuselage Combination. NACA RM L55A12, 1955.

Alford, William J., Jr., Silvers, H. Norman, and King, Thomas J., Jr.: Experimental Static Aerodynamic Forces and Moments at Low Speed on a Missile Model During Simulated Launching From the 25-Percent-Semispan and Wing-Tip Locations of a 45° Sweptback Wing-Fuselage Combination. NACA RM L55D20, 1955.

Smith, Norman F., and Carlson, Harry W.: Some Effects of Configuration Variables on Store Loads at Supersonic Speeds. NACA RM L55E05, 1955.

[redacted]

Alford, William J., Jr.: Effects of Wing-Fuselage Flow Fields on Missile Loads at Subsonic Speeds. NACA RM L55E10a, 1955.

Guy, Lawrence D.: Loads on External Stores at Transonic and Supersonic Speeds. NACA RM L55E13b, 1955.

Smith, Norman F., and Carlson, Harry W.: The Origin and Distribution of Supersonic Store Interference From Measurement of Individual Forces on Several Wing-Fuselage-Store Configurations. II.- Swept-Wing Heavy-Bomber Configuration With Large Store (Nacelle). Lateral Forces and Pitching Moments; Mach Number, 1.61. NACA RM L55E26a, 1955.

Hamer, Harold A., and O'Bryan, Thomas C.: Flight Measurements of the Loads and Moments on an External Store Mounted Under the Wing of a Swept-Wing Fighter-Type Airplane During Yawing and Rolling Maneuvers. NACA RM L55G22, 1955.

Smith, Norman F., and Carlson, Harry W.: The Origin and Distribution of Supersonic Store Interference From Measurement of Individual Forces on Several Wing-Fuselage-Store Configurations. III.- Swept-Wing Fighter-Bomber Configuration With Large and Small Stores. Mach Number, 1.61. NACA RM L55H01, 1955.

Guy, Lawrence D., and Hadaway, William M.: Aerodynamic Loads on an External Store Adjacent to a 45° Sweptback Wing at Mach Numbers From 0.70 to 1.96, Including an Evaluation of Techniques Used. NACA RM L55H12, 1955.

Morris, Odell A.: The Origin and Distribution of Supersonic Store Interference From Measurement of Individual Forces on Several Wing-Fuselage-Store Configurations. IV.- Delta-wing Heavy-Bomber Configuration with Large Store. Mach Number, 1.61. NACA RM L55I27a, 1955.

Carlson, Harry W., and Geier, Douglas J.: The Origin and Distribution of Supersonic Store Interference From Measurement of Individual Forces on Several Wing-Fuselage-Store Configurations. V.- Swept-Wing Heavy-Bomber Configuration With Large Store (Nacelle). Mach Number, 2.01. NACA RM L55K15, 1956.

Hadaway, William M.: Aerodynamic Loads on an External Store Adjacent to an Unswept Wing at Mach Numbers Between 0.75 and 1.96. NACA RM L55L07, 1956.

Smith, Norman F.: The Origin and Distribution of Supersonic Store Interference From Measurement of Individual Forces on Several Wing-Fuselage-Store Configurations. VI.- Swept-Wing Heavy-Bomber Configuration With Stores of Different Sizes and Shapes. NACA RM L55L08, 1956.

Hallissy, Joseph M., Jr., and Kudlacik, Louis: A Transonic Wind-Tunnel Investigation of Store and Horizontal-Tail Loads and Some Effects of Fuselage-Afterbody Modifications on a Swept-Wing Fighter Airplane. NACA RM L56A26, 1956.

Hadaway, William M.: Aerodynamic Loads on an External Store Adjacent to a 60° Delta Wing at Mach Numbers From 0.75 to 1.96. NACA RM L56B02a, 1956.

Alford, William J., Jr., and King, Thomas J., Jr.: Experimental Static Aerodynamic Forces and Moments at High Subsonic Speeds on a Missile Model During Simulated Launching From the Midsemispan Location of a 45° Sweptback Wing-Fuselage-Pylon Combination. NACA RM L56J05, 1957.

Alford, William J., Jr., and King, Thomas J., Jr.: Experimental Static Aerodynamic Forces and Moments at High Subsonic Speeds on a Canard Missile During Simulated Launching From the Midsemispan Location of a 45° Sweptback Wing-Fuselage-Pylon Combination at Zero Sideslip. NACA RM L56J15a, 1957.

Alford, William J., Jr., and King, Thomas J., Jr.: Experimental Investigation of Flow Fields at Zero Sideslip Near Swept- and Unswept-Wing—Fuselage Combinations at Low Speed. NACA RM L56J19, 1957.

Alford, William J., Jr.: Theoretical and Experimental Investigation of the Subsonic-Flow Fields Beneath Swept and Unswept Wings With Tables of Vortex-Induced Velocities. NACA TN 3738, 1956.

VARIATION OF STORE AND PYLON FORCES
WITH RATIO OF STORE DIAMETER TO PYLON SPAN

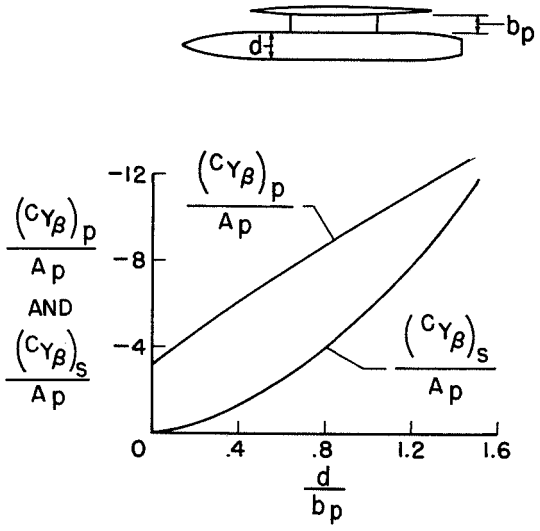


Figure 1

SCOPE OF TEST CONFIGURATIONS

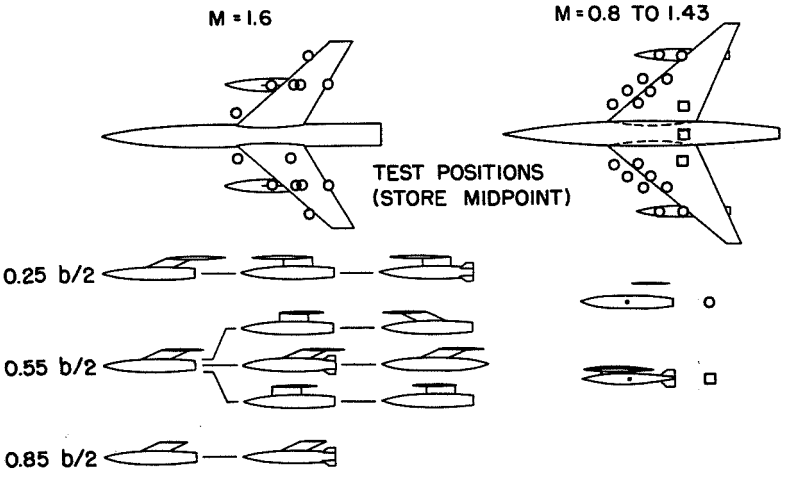


Figure 2

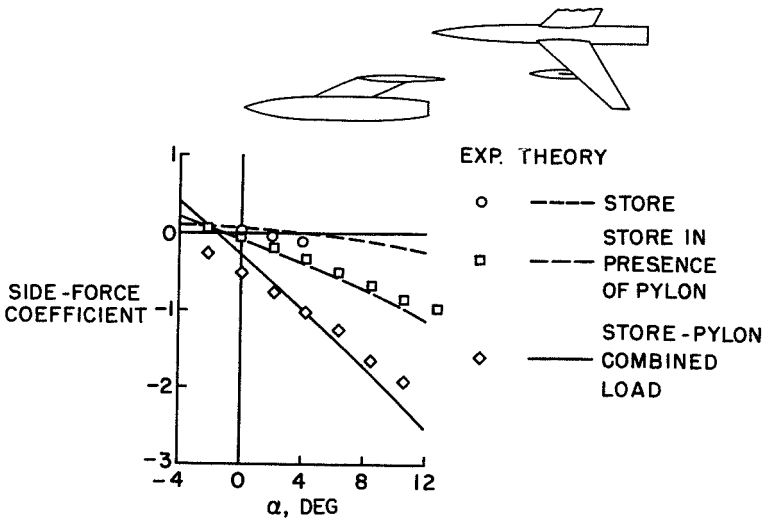


Figure 3

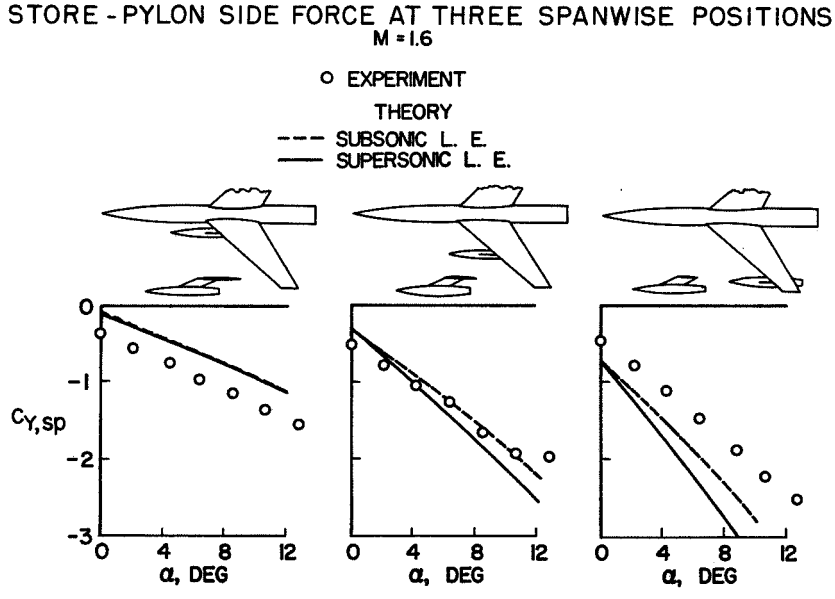


Figure 4

SCHLIEREN PHOTOGRAPH OF TEST CONFIGURATION
M=1.6 ; α=0°

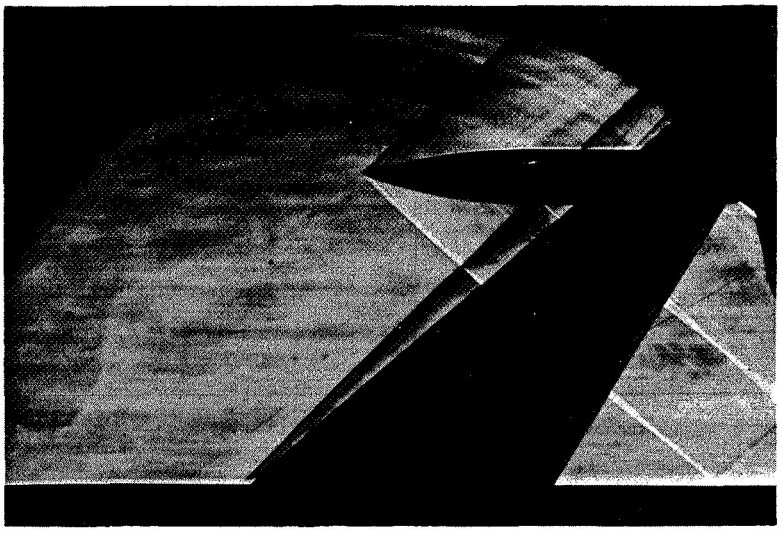


Figure 5 L-57-179

EFFECT OF PYLON SWEEP AND STORE CHORDWISE LOCATION
M=1.6

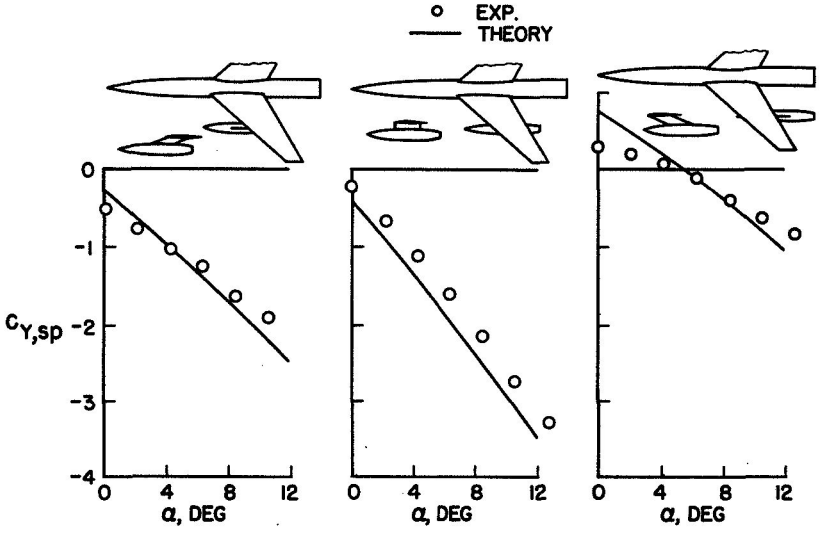


Figure 6

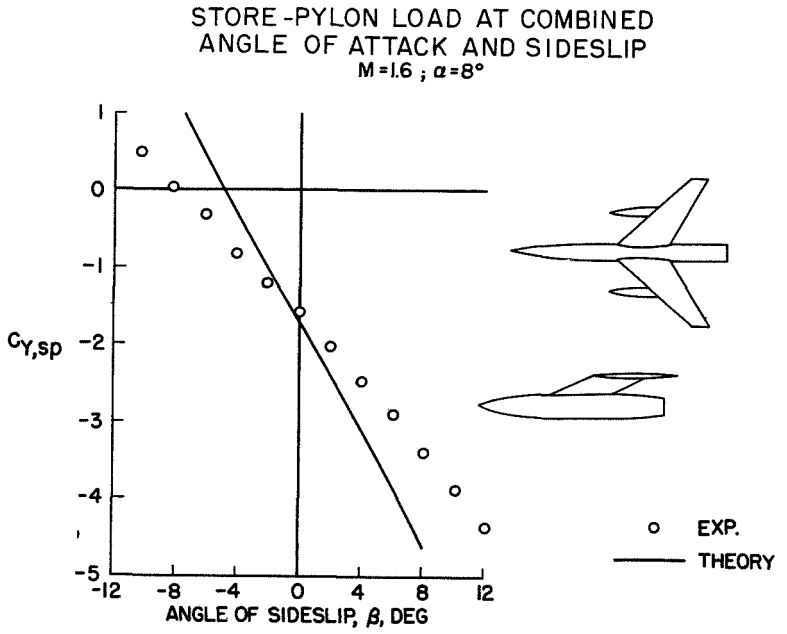


Figure 7

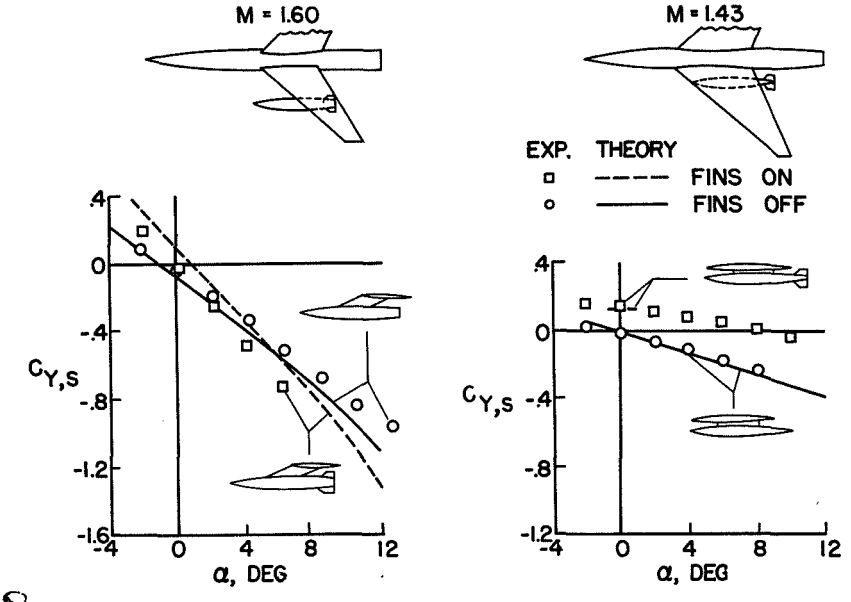


Figure 8

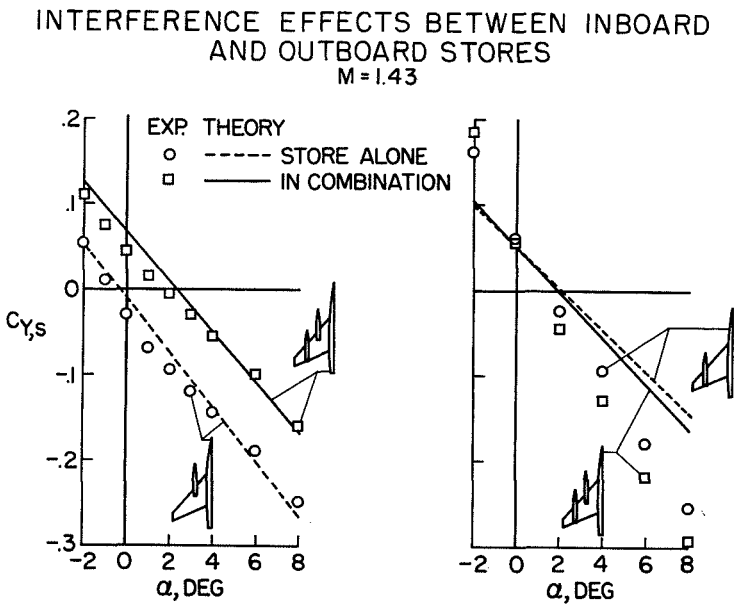


Figure 9

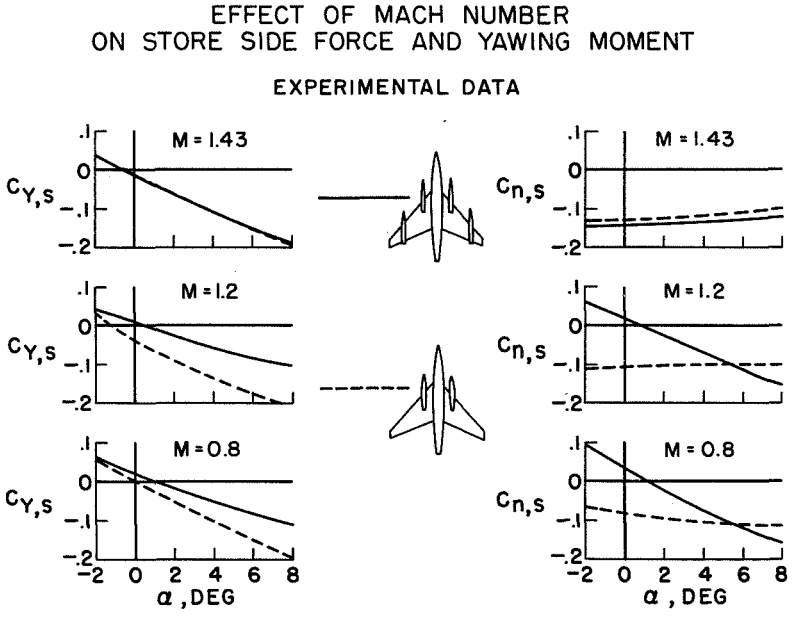


Figure 10

EFFECT OF FUSELAGE INDENTATION ON STORE
SIDE FORCE AND YAWING MOMENT
M=1.2

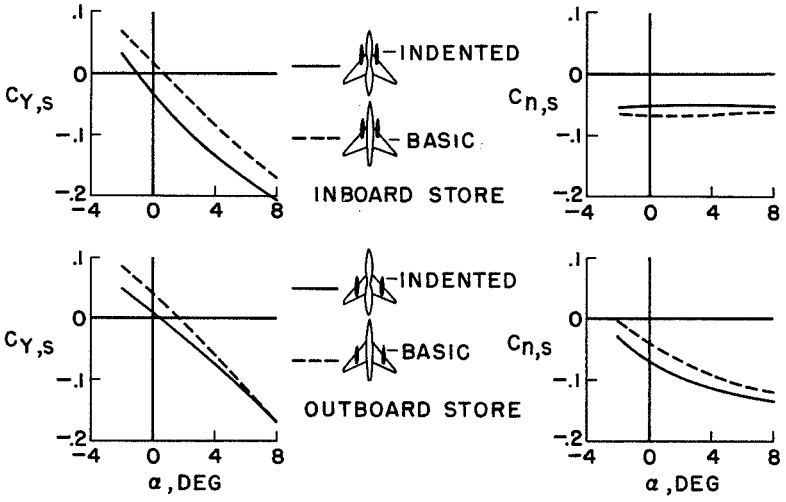


Figure 11

N71-75388

STEADY LOADS DUE TO JET INTERFERENCE ON WINGS, TAILS, AND FUSELAGES AT TRANSONIC SPEEDS

By John M. Swihart and Norman L. Crabill

Langley Aeronautical Laboratory

SUMMARY

This paper gives the results of some recent investigations of jet-interference effects on actual airplane configurations at transonic speeds. Data presented herein were obtained with hot jets on both wind-tunnel and flight models. Results indicate that jet-induced effects are small at subsonic speeds; however, at low supersonic Mach numbers, these effects are comparable to those obtained at substantially higher Mach numbers.

INTRODUCTION

In recent years there have been several investigations of turbojet-exhaust interference effects at supersonic speeds (refs. 1 and 2); however, only a limited amount of data has been obtained at transonic speeds. It is the purpose of this paper to show the results of some recent investigations of the jet interference on actual airplane configurations at transonic speeds. This discussion will be limited to steady loads induced by simulated jets on nearby wings, tails, and overhanging fuselages. Data presented in this paper cover the Mach number range of 0.85 to 1.20 and were obtained with hot jets at total pressure ratios corresponding to current turbojet-engine pressure ratios.

SYMBOLS

b	span
c	local chord
$\bar{c}$	mean aerodynamic chord
c_n	section normal-force coefficient
C_N	normal-force coefficient

ΔC_N incremental normal-force coefficient, $C_{N,\text{jet on}} - C_{N,\text{jet off}}$

C_p pressure coefficient, $\frac{p_{local} - p_\infty}{q}$

ΔC_p incremental pressure coefficient, $C_{p,\text{jet on}} - C_{p,\text{jet off}}$

d_j primary jet diameter

p pressure

q dynamic pressure

y spanwise distance

z distance below wing chord plane

Subscripts:

AV average

j jet

R resultant, Lower surface - Upper surface

t total

T tail

∞ free stream

APPARATUS

The models used in these investigations are shown in figure 1. The sting-mounted 60° delta-wing model was tested in the Langley 16-foot transonic tunnel with one jet nacelle located at 41 and 69 percent of the semispan on one wing panel only. At the inboard station, the jet exit was located at 38 and 69 percent of the local chord and at 1, 2, and 4 jet diameters below the wing. At the outboard location, the nacelle was tested only at 4 jet diameters below the wing, and the exit was at 63 percent of the local chord. Simulation of the exhaust of a non-afterburning turbojet engine was achieved through the use of a hydrogen peroxide gas generator exhausting through a sonic exit. The jet total pressure ratio was varied from 1 (power off) to about 7 with a jet stagnation temperature of about 1,400° F at each test Mach number. At six spanwise stations, pressures were measured at static orifices located at about every 5 percent of the chord on the upper and lower surfaces.

The twin-engine model with part of the fuselage overhanging the jet exhaust was also a 16-foot-transonic-tunnel model and was supported at the wing tips by a bifurcate sting-support system. Two hydrogen peroxide turbojet simulators were mounted in arm-pit nacelles; their exhausts were partially separated by a short keel. Static pressures were measured along this keel and the shoulder of the overhanging fuselage. The horizontal tail was mounted in both a high position (on the vertical tail) and a relatively low position (on the boom). Pressure distributions were obtained on both tails directly above the jet center line extended.

The single-engine model with the fuselage overhang was flight tested with the horizontal tail located ahead of the jet exit and at two positions downstream of the jet exit. An afterburning turbojet engine was simulated by using a solid-propellant rocket motor exhausting through a sonic exit at a total pressure ratio of 6.0 and a stagnation temperature of 3,200° F. Pressures were measured on the top and bottom of the fuselage overhang and at two spanwise stations on the tails at a Mach number of 1.2.

An investigation was conducted in the Langley 16-foot transonic tunnel of a target-type thrust reverser mounted on a single-engine fighter model to evaluate the thrust reverser as a speed brake. The design of the reverser was taken from reference 3, and the jet exhaust was simulated by a hydrogen peroxide simulator operating at a jet total pressure ratio of 5. During the course of this investigation, static pressures were measured around half of the fuselage at 6 meridians and for about 3 jet diameters ahead of the base. Flow visualization was achieved by tufts on the other half of the fuselage.

Data are presented for the wind-tunnel models from $M = 0.85$ to 1.05; data are presented for the flight model at $M = 1.20$.

RESULTS AND DISCUSSION

Effects of Isolated Jets

Before discussing the results of these tests, a review will be given of the phenomena pertinent to the exhaust of an isolated overpressure sonic jet into subsonic and supersonic external streams. At current jet total pressure ratios, the jet bulges outward immediately downstream of the jet exit at both Mach numbers (fig. 2). At subsonic speeds, since the internal structure of shocks and expansions cannot penetrate the subsonic mixing boundary (see ref. 4), the only significant effects in the external flow are some compression due to the bulge near the exit and a subsequent expansion downstream due to entrainment of the external stream by the jet (fig. 2). Contrariwise, for supersonic speeds, Leiss

and Bressette (ref. 1), Love and Grigsby (ref. 4), and others have shown that the external flow is marked by a shock at the initial bulge (exit shock), an expansion over the curved jet boundary, and a shock (jet shock) which occurs where the shock internal to the jet penetrates the supersonic mixing boundary (fig. 2). Even though the initial deflection angle of the bulge is only about half that for subsonic speeds (ref. 4), the presence of shocks in the external flow indicates that the effects on the external stream may be considerably larger than in subsonic flow and probably extend to greater distances from the jet boundary.

Jet Effects on Wings

Figure 3 shows the jet-induced resultant pressures on the 60° delta-wing model at $M = 0.90$ and 1.05 for $\alpha = 5^\circ$ for one nacelle located 1 jet diameter below the right wing and with the jet exit at 69 percent of the local chord. Qualitatively, the results are about what might be expected from the discussion given for isolated jets (fig. 2). At $M = 0.90$, the effects of flow inclination near the jet exit and the subsequent expansion due to entrainment produce $\Delta C_{p,R}$ peaks of no more than 0.09 and -0.05, respectively. At $M = 1.05$, the effect of the exit shock is to give a positive peak of $\Delta C_{p,R} = 0.27$; the negative peak is slightly less than 0.10. The effects diminish rapidly with increasing spanwise distance from the jet at $M = 0.90$ and only moderately at $M = 1.05$.

Figure 4 presents jet-induced resultant pressures for the same test conditions as those for figure 3 except the whole nacelle has been moved forward so that the exit is now at 38 percent of the local chord. In general, the jet effects are shifted correspondingly forward and, at $M = 0.90$, the effects are somewhat diminished. At $M = 1.05$, however, the maximums and minimums are comparable with those obtained when the nacelle was located only 1 jet diameter below the wing (fig. 3) as far as the exit shock intersects the wing. The data indicate that the exit shock has passed off the leading edge of the wing slightly outboard of $\frac{y}{b/2} = 65$ percent and that the jet effect shown for $\frac{y}{b/2} = 74$ percent comes entirely from the influence of the jet on the wing upper-surface pressures. Evidently, this effect results from some interaction of the jet-exit shock and the wing leading edge.

The chordwise pressure distributions obtained at $\alpha = 5^\circ$ and $M = 0.90$ and 1.05 for the two nacelle positions shown in figures 3 and 4 have been integrated to obtain the spanwise loading curves shown in figure 5. Additional data obtained for the nacelle located at 69 percent of the wing semispan with the jet exit at 63 percent of the local chord and 4 jet diameters below the wing are given in figure 6. Spanwise loadings for the basic wing (no nacelle or pylon) are also given in

figures 5 and 6 for comparison. It is seen that the largest effects occur at $M = 1.05$ in all three cases, and that, at this Mach number, the effect is smallest for the case where the exit-shock intercept passes off the wing before reaching the tip. Although the $\Delta C_N = 0.010$ measured for the nacelle positioned at the inboard location and 1 jet diameter below the wing is only about 5 percent of the wing normal force, it is actually about 1.5 times the thrust of the jet causing this effect. This is comparable in magnitude to the effects shown in reference 1 at a Mach number of 1.8.

The wing chordwise and spanwise center-of-pressure locations for the nacelle located at the inboard position and for $z/d_j = 1$ and 4 are shown in figure 7. Jet operation has a very small effect on the chordwise center of pressure and practically no effect on the spanwise center of pressure at subsonic speeds. In general, the data indicate that the slight forward and inboard movement of the center of pressure is more pronounced for $z/d_j = 1$.

Jet Effects on Fuselage Overhangs and Horizontal-Tail Surfaces

The data shown in figure 8 give the effect of Mach number on jet-induced pressures measured along the overhanging portions of two different exit configurations. Although these data were obtained on two different configurations at different jet total pressure ratios, these differences are unimportant in showing the effects that are discussed here. For the data at $M = 0.85$ (the twin-engine fighter), the increment of $\Delta C_p = 0.25$ at the center line indicates that the jet is probably in contact with the center-line row of orifices over the entire length of the short keel; however, very little jet effects were measured at the orifice row around the shoulder. Extensive pressure surveys of this kind have been shown in reference 5.

At $M = 1.20$, the data (the single-engine type) indicate that the orifices on the bottom of the boom were probably in contact with the jet at least near the exit. The pressure measurements made along the top of the boom when the horizontal tail was located ahead of the exit indicate that moderate positive pressure increments are experienced even though this position is "blanketed" by the boom. Additional data, not shown here, indicate that the leading edge of this upper-surface jet-effect zone moves aft with increasing Mach number.

Thus, at subsonic speeds, the region of fuselage overhangs subject to significant jet effects is nearly confined to that in contact with the jet. At supersonic speeds, the region of significant jet effects extends much further away from the jet boundary and can even affect blanketed areas.

The effect of tail position on the jet-induced tail chordwise pressure distributions measured at $M = 1.20$ on the single-engine model is shown in figure 9. The data indicate that the loading over the forward third of the tail is greatest for the forward tail position and that the loading is greater outboard. The lower loading at the inboard location may be due to the effects of a subsonic jet mixing boundary in the region immediately under the boom and this subsonic mixing boundary may give way to a supersonic mixing boundary outboard, with consequent increase in jet effects.

Figure 10 shows the effect of tail position and free-stream Mach number on jet-induced tail and tail-plus-afterbody normal-force coefficients. Pressure distributions obtained for the high and low horizontal tails at $M = 0.85$ on the twin-engine model were integrated to obtain the jet-induced effect on section normal-force coefficient as a function of angle of attack. The data indicate that for the high tail there is no jet effect on c_n at any angle of attack, whereas, in the low tail position, a constant reduction of 0.07 in c_n was obtained at all angles of attack. This result indicates that the flow entrainment effect of a jet in subsonic flow diminishes rapidly with distance from the jet boundary.

Accelerometer data taken at $M = 1.20$ for the three longitudinal positions of the horizontal tail on the single-engine models were reduced to show ΔC_N induced by the jet on the afterbody and afterbody plus tail. The data, based on the plan-form area downstream of the jet, indicate that ΔC_N probably goes through a maximum as the position of the exposed tail centroid is varied between 0 and 2.3 jet diameters downstream of the jet exit. If the reduction in tail-section normal-force coefficient obtained at $M = 0.85$ be taken as representative of the effect over the entire tail, then the total jet-induced tail loads are seen to change sign as the free-stream Mach number is increased from $M = 0.85$ to 1.20.

Jet Effects Due to Thrust Reverser

The effect of thrust-reverser operation on afterbody pressures on a single-engine blunt-based fighter-type configuration flying at $M = 1.05$ is given in figure 11. The curves shown represent averages of the six pressures measured around the periphery of the left side of the afterbody at each fuselage station. When no reverser is present, the pressures ahead of the base are negative and decrease to -0.27 at the base. When the target-type reverser was extended, the pressures were increased to positive values for about 3 jet diameters ahead of the base. The tuft studies indicated that separation occurred on the fuselage forward of 3 jet diameters and this separation was very unstable. The resulting large lateral oscillations of the model on the relatively rigid support system used in the wind-tunnel test indicate that the operation of this

device on an airplane in free flight might render the airplane unflyable. Although it is now known that this reverser is not a good design, it is believed that the magnitude of these local pressure changes is typical of what should be expected with most thrust reversers.

CONCLUSIONS

Examination of the data from recent investigations of jet-interference effects on actual airplane configurations at transonic speeds has led to the following tentative conclusions:

1. At subsonic speeds, jet-induced effects on wings, tails, and fuselages are small and decrease rapidly with distance from the jet boundary.

2. At low supersonic Mach numbers, jet-induced effects comparable to those obtained previously at substantially higher Mach numbers can be realized. Generally, these effects do not diminish as rapidly with distance from the jet boundary as those induced in subsonic flow.

REFERENCES

1. Leiss, Abraham, and Bresette, Walter E.: Pressure Distribution Induced on a Flat Plate by a Supersonic and Sonic Jet Exhaust at a Free-Stream Mach Number of 1.80. NACA RM L56I06, 1957.

2. Rainey, Robert W.: The Effects Upon Body Drag of Jets Exhausting From Wing-Mounted Nacelles. NACA RM L56A09, 1956.

3. Povolny, John H., Steffen, Fred W., and McArdle, Jack G.: Summary of Scale-Model Thrust-Reverser Investigation. NACA TN 3664, 1956.

4. Love, Eugene S., and Grigsby, Carl E.: Some Studies of Axisymmetric Free Jets Exhausting From Sonic and Supersonic Nozzles Into Still Air and Into Supersonic Streams. NACA RM L54L31, 1955.

5. Cornette, Elden S., and Ward, Donald H.: Transonic Wind-Tunnel Investigation of the Effects of a Heated Propulsive Jet on the Pressure Distribution Along a Fuselage Overhang. NACA RM L56A27, 1956.

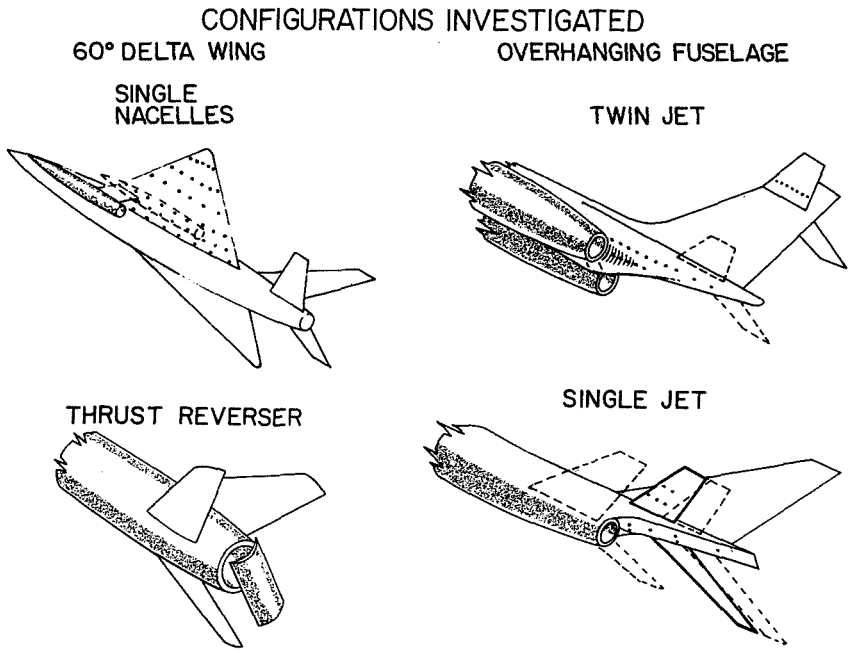


Figure 1

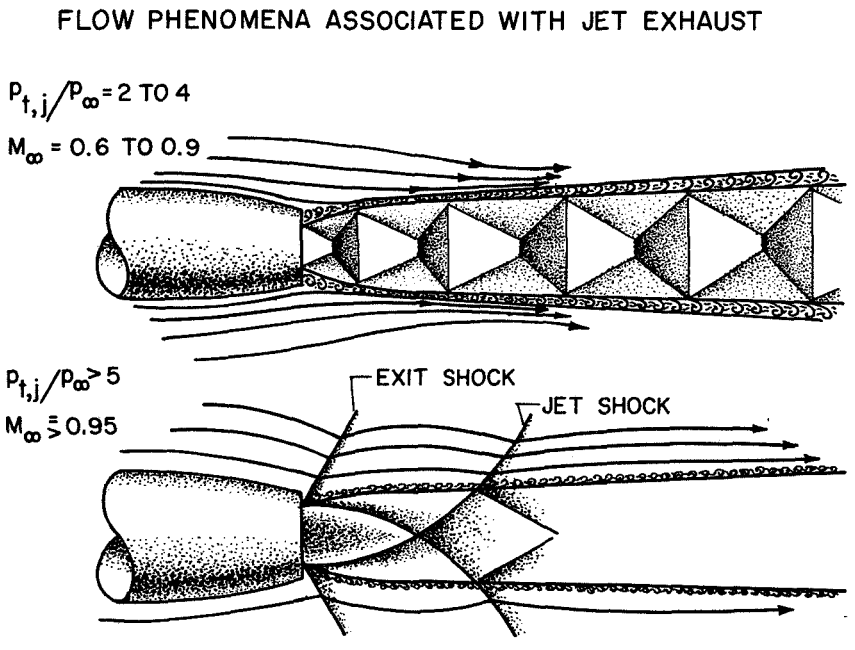


Figure 2

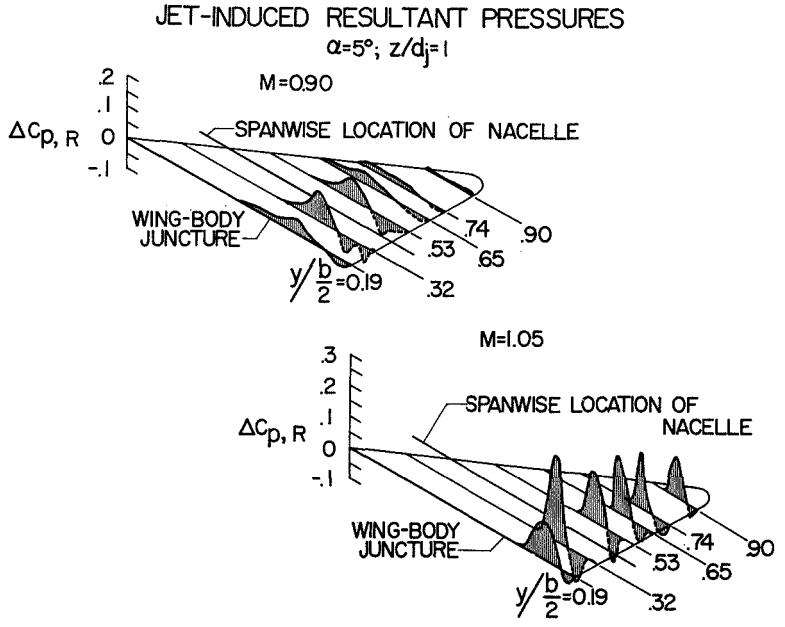


Figure 3

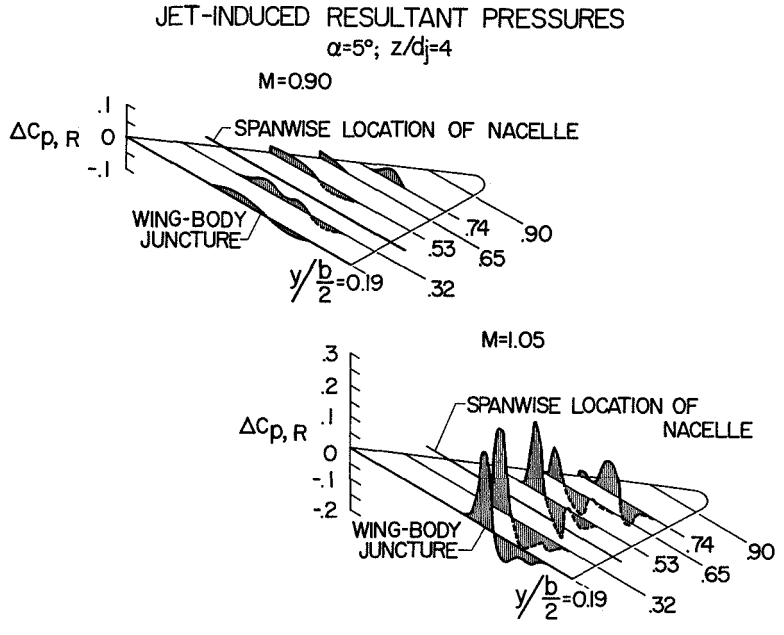


Figure 4

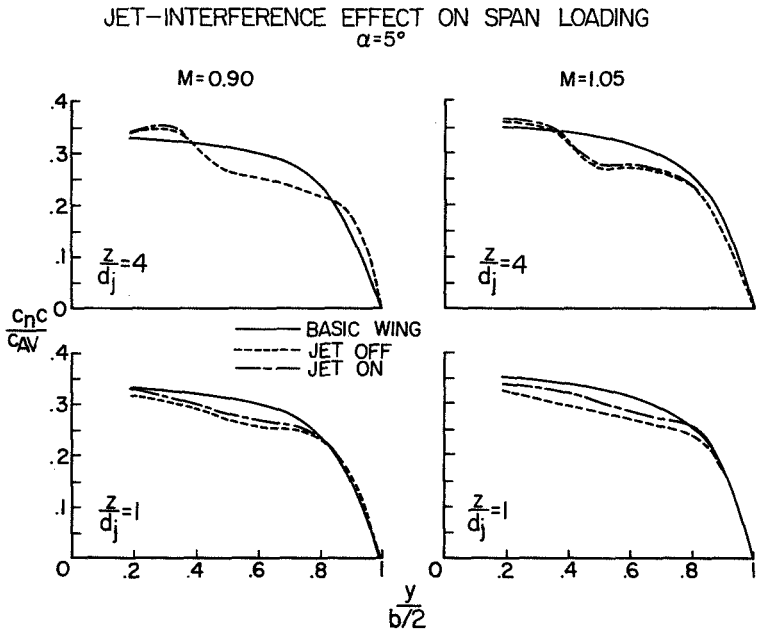


Figure 5

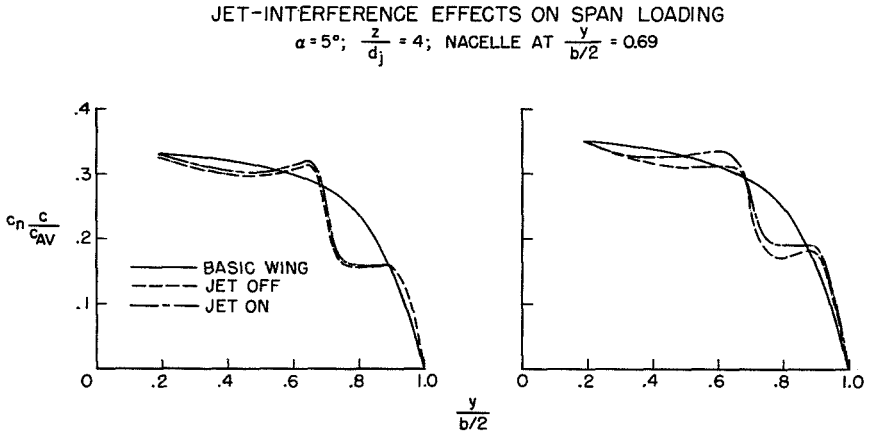


Figure 6

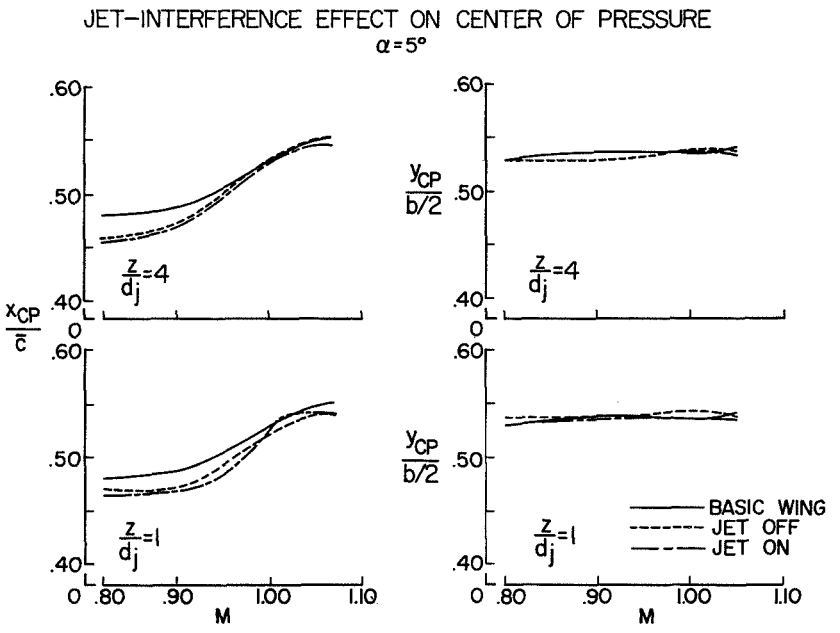


Figure 7

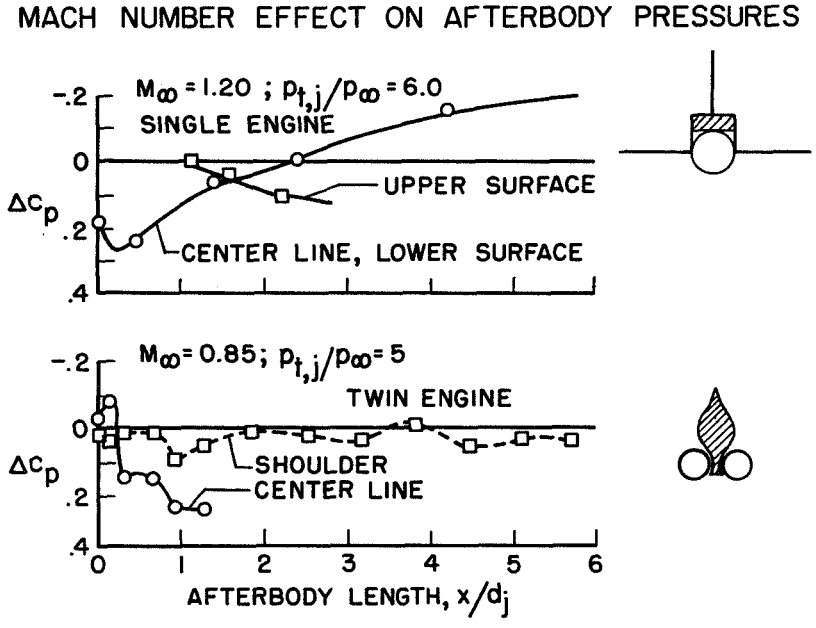


Figure 8

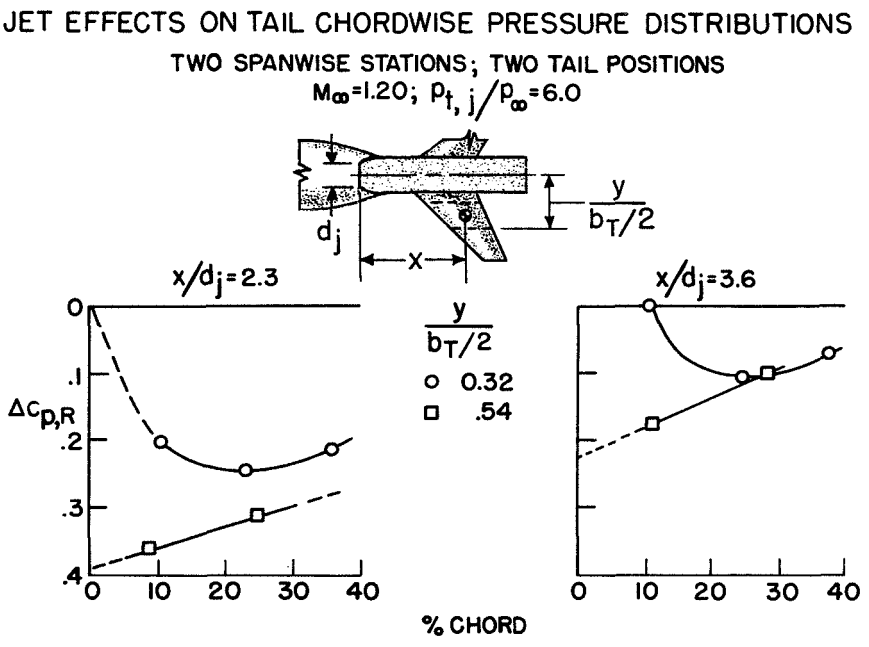


Figure 9

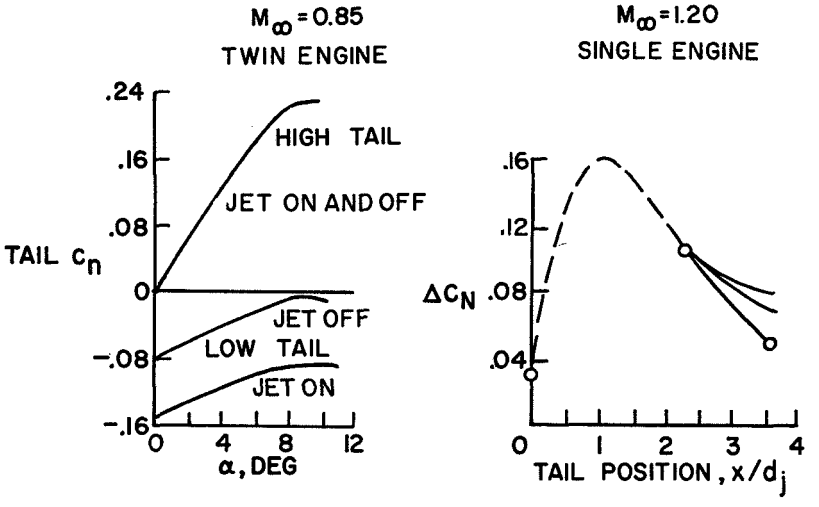


Figure 10

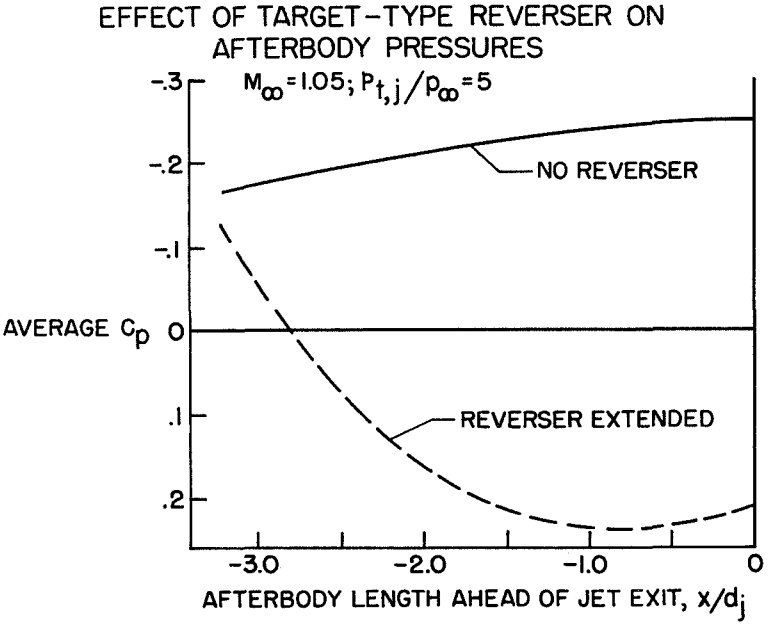

EFFECT OF TARGET-TYPE REVERSER ON
AFTERBODY PRESSURES
M_∞=1.05; $P_{t,j}/P_\infty$=5
NO REVERSER
REVERSER EXTENDED
AVERAGE C_p
-.3
-.2
-.1
0
.1
.2
-3.0
-2.0
-1.0
0
AFTERBODY LENGTH AHEAD OF JET EXIT, x/d_j

Figure 11

N71-75389

EFFECTS ON ADJACENT SURFACES FROM THE FIRING OF ROCKET JETS

By Walter E. Bressette and Abraham Leiss

Langley Aeronautical Laboratory

SUMMARY

This paper is a preliminary and brief account of some research currently being conducted to determine the jet effects on adjacent surfaces from the firing of rocket jets. Measurements of jet-effect pressures on a flat plate as well as shadowgraphs are presented that were obtained when a rocket jet at a Mach number of 3 was exhausted downstream and upstream into free-stream flow at a Mach number of 2 located from 2 to 4.7 rocket-jet-exit diameters from the plate. The jet effects on the flat plate with the rocket jet exhausting downstream are of the same order of magnitude as those previously obtained from sonic exits with a total pressure 10 times lower. A maximum pressure coefficient on the plate of 1.35 was obtained when the rocket jet was exhausted upstream at 2 rocket-jet-exit diameters below the plate, and an integration of the measured jet-effect pressures at this position resulted in a normal force on the plate equal to 2.3 times the thrust output of the rocket jet.

INTRODUCTION

During the past few years the use of air-to-air rocket-propelled missiles for supersonic aircraft has become prominent. Also, it is reasonable to expect that, in the future, large-sized aircraft will be used as platforms for the launching of large-sized guided rocket-propelled missiles. These missiles might be fired not only forward but also rearward and sideways. It is important, then, to know the short-duration loads on adjacent wings and body surfaces of the aircraft from the rocket jet of the missile. Therefore, in the Langley preflight jet of the Pilotless Aircraft Research Station at Wallops Island, Va., a testing program has been initiated to determine the jet effects on adjacent surfaces from high-pressure short-duration rocket jets exhausting downstream, upstream, and normal to the free-stream flow. Up to the present time only preliminary tests from rocket jets firing downstream and upstream at a Mach number of 2 have been completed. The results from some of these tests are discussed in this paper.

SYMBOLS

C_p	pressure coefficient, $\frac{p_w - p_\infty}{q_\infty}$
d_j	diameter of rocket-jet exit
F_N	normal force
M_j	Mach number at exit of rocket jet
M_∞	free-stream Mach number
p_j	static pressure at exit of rocket jet
$p_{t,j}$	total pressure at exit of rocket jet
p_w	measured static pressure on plate
p_∞	free-stream static pressure
q_∞	free-stream dynamic pressure, $\frac{\gamma}{2} p_\infty M_\infty^2$
x	chordwise distance on plate
y	spanwise distance on plate
γ	ratio of specific heats (1.4 for air)

APPARATUS

Presented in figure 1 is a sketch of the test setup showing the location of a rocket-jet exit having a Mach number 3 nozzle below a flat plate at the exit of the blowdown tunnel having a Mach number 2 nozzle. Also shown in the figure is the relation of the rocket-jet exit relative to the flat plate for the four test positions that are discussed in this paper. These positions are for one rocket jet exhausting downstream that is located at $3.4d_j$ below the plate and $6.5d_j$ from the end of the plate and for three rocket jets exhausting upstream at 2, 3.4, and $4.7d_j$ below the plate, all of which were located at $0.74d_j$ upstream from the end of the plate. These upstream firing positions are henceforth referred to

as positions A, B, and C, respectively. The rocket-jet variation of total pressure with time was similar during each of the tests. The actual total firing time of the rocket jet was approximately 0.6 second with the rocket jets exhausting at a total pressure of approximately 1,000 pounds per square inch during the first 0.3 second and then reducing to zero pressure during the remaining 0.3 second. The data as presented in this paper were taken with the rocket jet exhausting at a total pressure of approximately 1,000 pounds per square inch.

INSTRUMENTATION

The location on the flat plate of 47 static-pressure orifices relative to the rocket-jet exits is shown in figure 2 as well as the area on the plate integrated to obtain the jet-effect normal load. As can be seen in this figure, the plate was pressure surveyed on only one side of the rocket-jet center line.

RESULTS AND DISCUSSION

Presented in figure 3 is the rocket-jet-off and rocket-jet-on centerline pressure distribution on the flat plate plotted over the jet-effect shock pattern that was obtained from shadowgraphs with the rocket jet exhausting downstream at $p_{t,j}/p_\infty = 68$ and $p_j/p_\infty = 2.1$. The shadowgraphs revealed the now-familiar two-shock jet-effect pattern that is obtained with a sonic turbojet exit. These two shocks are commonly called the exit shock and the jet shock. The maximum pressure coefficient of approximately 0.1 that was obtained directly behind the intersection on the plate of the exit shock is about the same that would be obtained from a sonic turbojet exit at $p_j/p_\infty = 3$ and $p_{t,j}/p_\infty = 6$.

Figure 4, which presents a typical shadowgraph with the rocket jet exhausting upstream at position A, shows a bow shock, upstream from the rocket-jet exit, standing in front of the maximum penetration of the rocket-jet exhaust which is burning. This bow shock is strong enough at the intersection with the plate to cause separation of the plate boundary layer. Figure 5, which presents a typical shadowgraph at position C, shows a bow shock, upstream from the rocket-jet exit, standing in front of the maximum penetration of the rocket-jet exhaust. This bow shock at position C is farther upstream from the rocket-jet exit than the one obtained at position A; also, it has a greater curvature from its normal position at the center, and at the intersection point on the plate it is reflected.

Presented in figure 6 is the rocket-jet-off center-line pressure distribution as well as the rocket-jet-on center-line pressure distribution on the plate, and presented in figure 7 is the rocket-jet-on spanwise pressure distribution obtained at position A. When the rocket jet was fired at this position, figure 6 shows that the bow shock in front of the rocket-jet exit with the rocket jet off moved from a position approximately $0.7d_j$ to a position $2d_j$ to $3d_j$ upstream from the exit. This bow shock stands in front of the most forward pentration of the rocket-jet fuel-rich exhaust which is mixing with the incoming free-stream air and is burning in the zone designated as the mixing zone. At the same time, this bow shock induced separation of the plate boundary layer upstream of its intersection on the plate. The resulting initial rise in the rocket-jet-on center-line pressure distribution on the plate is similar to that obtained in references 1 and 2 from the separation of a turbulent boundary layer by the step technique; the first peak value of 0.35 as obtained in this test agrees very favorably with the step-technique value obtained in reference 1 on a flat plate at $M_\infty = 2$. Also, as illustrated in reference 2, the overall pressure rise for incipient separation can be considerably greater than the first peak pressure rise. In this test the overall pressure rise resulted in a maximum pressure coefficient of 1.35, which is 85 percent of the pressure coefficient that might be obtained directly behind a normal shock. This maximum pressure coefficient is reduced rapidly as the spanwise distance is increased in figure 7 as would be expected from the intersection of a bow shock and a flat plate, whereas the first peak value is essentially constant with the same increase in spanwise distance. A normal force on the plate of 2.3 times the rocket-jet thrust output was obtained at this position of $2d_j$ below the plate by integrating the pressure field that was measured on one side of the rocket-jet center line and multiplying the result by 2 on the assumption that the pressure distribution on the opposite side of the rocket-jet center line was the same.

In figures 8 and 9 is shown the center-line and spanwise pressure distribution on the plate with the rocket jet exhausting upstream at position C. When the rocket jet was fired at this position, the bow shock in front of the rocket-jet exit with the rocket jet off did not intersect the plate at this position and moved from approximately $0.7d_j$ to approximately $9d_j$ upstream from the exit. This large upstream movement of the bow shock resulted in the bow shock intersecting the plate upstream of the pressure-orifice field. A pressure coefficient of approximately 0.2 was obtained at the most forward orifice location, and this value gradually reduced on the plate in the downstream direction as well as in the spanwise direction.

CONCLUSIONS

An investigation is being made to determine the effects on adjacent surfaces from the firing of rocket jets. The following conclusions were obtained from observations of jet-effect pressures measured on a flat plate in conjunction with shadowgraphs when a rocket jet at a Mach number of 3 was exhausted downstream and upstream into free-stream flow at a Mach number of 2:

1. The jet effects on the flat plate with the rocket jet exhausting downstream are of the same order of magnitude as those previously obtained from sonic exits with a total pressure 10 times lower.

2. A maximum pressure coefficient on the plate of 1.35 was obtained when the rocket jet was exhausted upstream at two rocket-jet-exit diameters below the plate.

3. An integration of the measured jet-effect pressures on the plate with the rocket jet located at 2 rocket-jet-exit diameters below the plate resulted in a normal force on the plate equal to 2.3 times the thrust output of the rocket jet.

REFERENCES

1. Lange, Roy H.: Present Status of Information Relative to the Prediction of Shock-Induced Boundary-Layer Separation. NACA TN 3065, 1954.

2. Chapman, Dean R., Kuehn, Donald M., and Larson, Howard K.: Preliminary Report on a Study of Separated Flows in Supersonic and Subsonic Streams. NACA RM A55L14, 1956.

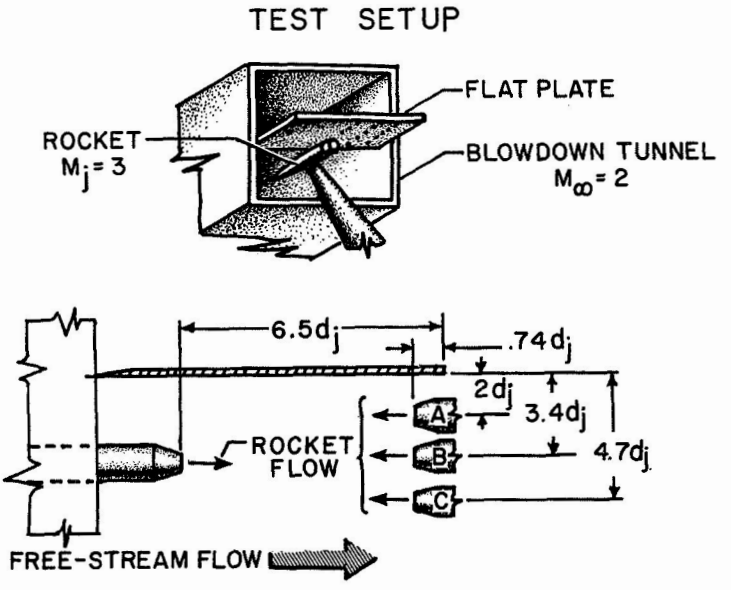


Figure 1

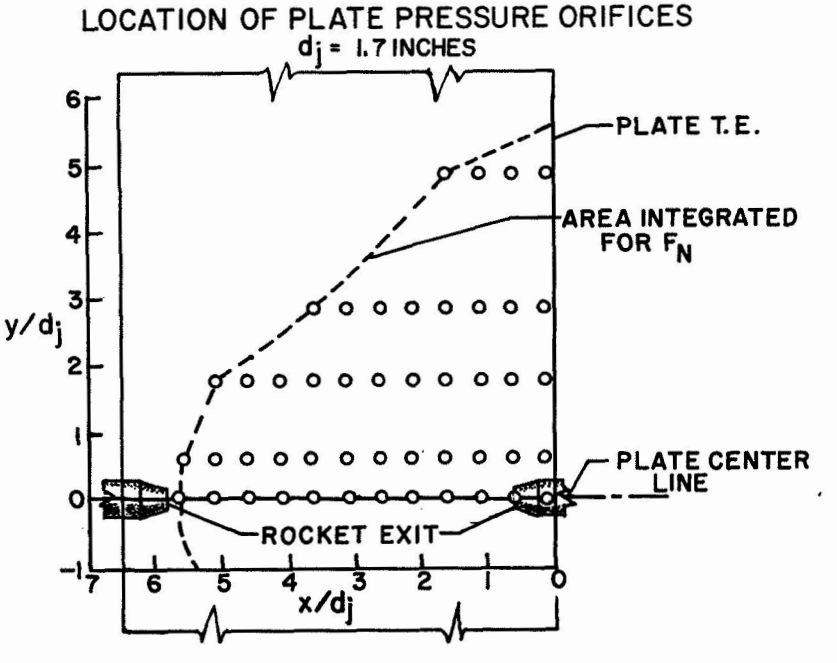


Figure 2

CENTER-LINE PRESSURE DISTRIBUTION
ROCKET EXHAUSTING DOWNSTREAM; $M_j=3$; $p_{t,j}/p_\infty=68$; $p_j/p_\infty=2.1$

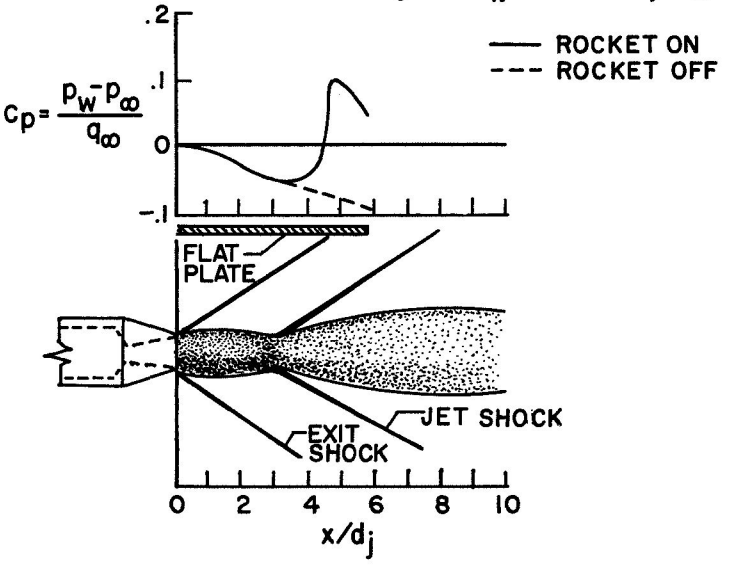


Figure 3

TYPICAL SHADOWGRAPH FOR POSITION A
ROCKET EXHAUSTING UPSTREAM

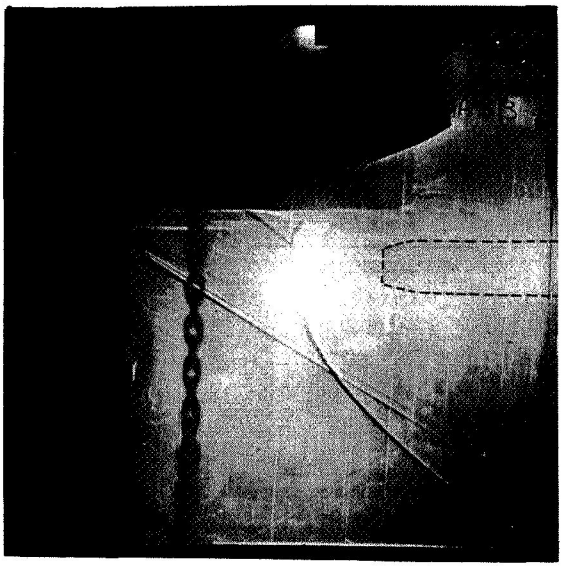
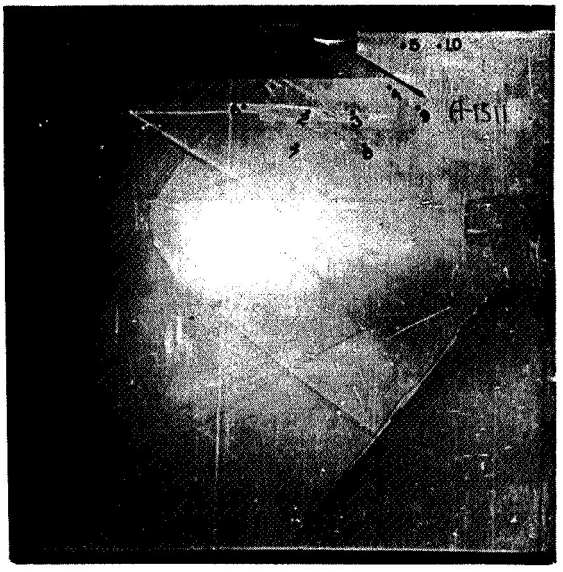


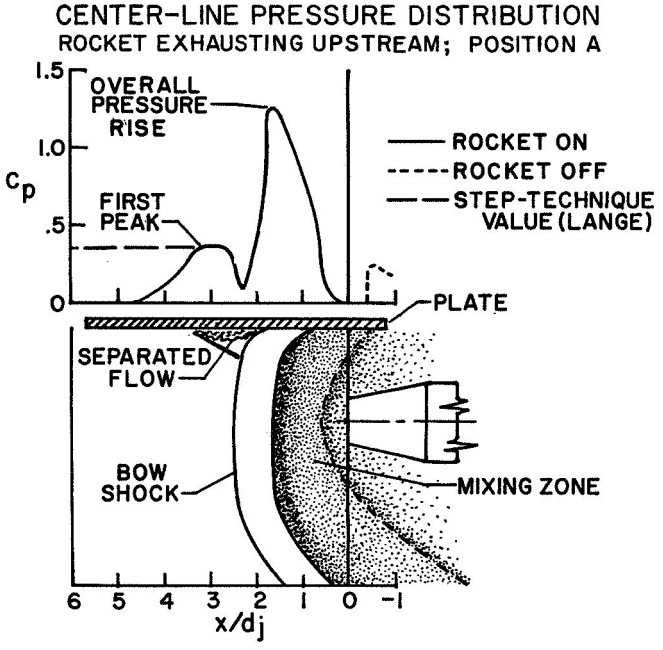
Figure 4 L-57-161

TYPICAL SHADOWGRAPH FOR POSITION C
ROCKET EXHAUSTING UPSTREAM



L-57-160

Figure 5



121

Figure 6

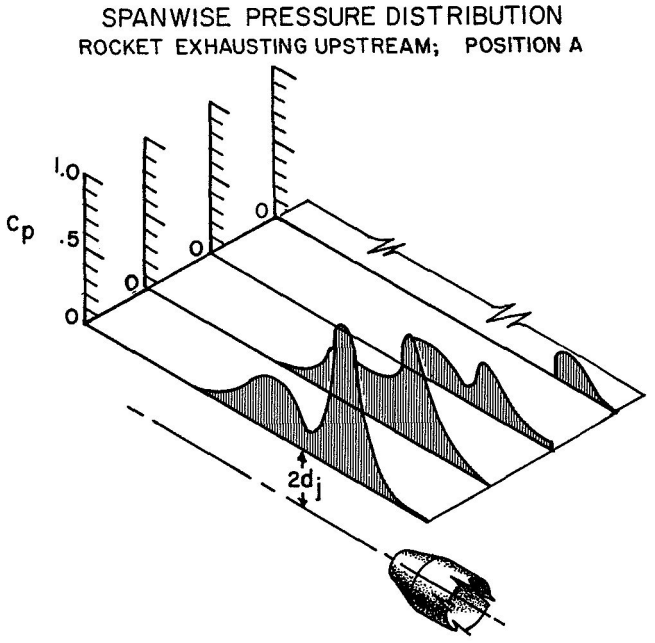
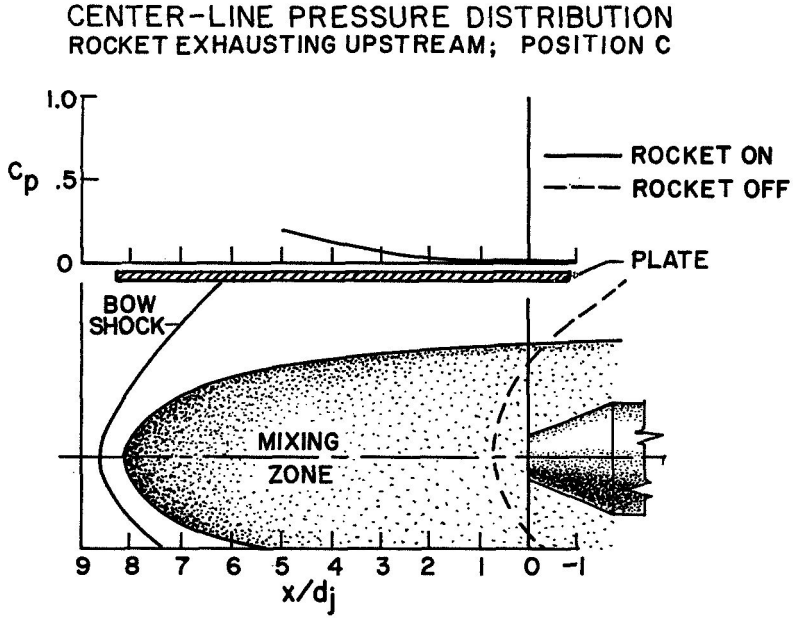


Figure 7



122

Figure 8

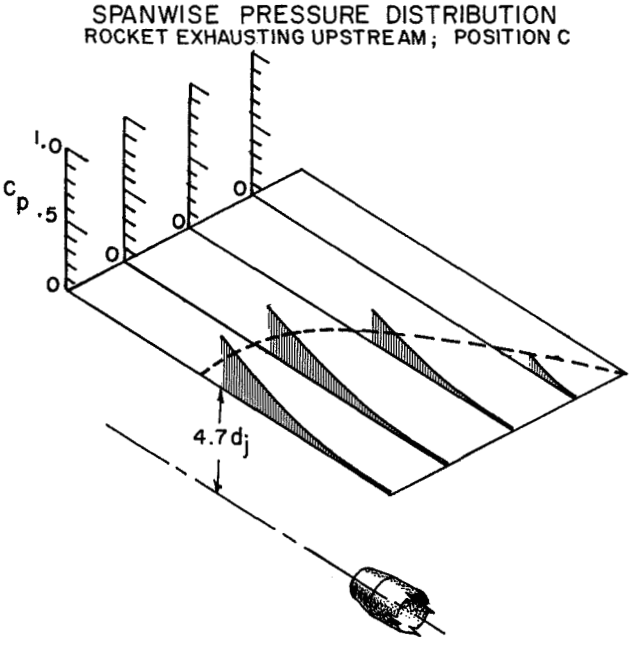

SPANWISE PRESSURE DISTRIBUTION
ROCKET EXHAUSTING UPSTREAM; POSITION C
1.0
C_p .5
0
0
0
0
$4.7d_j$

Figure 9

7E

N71-75390

INFLUENCE OF AUTOMATIC CONTROL OF ROLL COUPLING AND PITCH-UP ON TAIL LOADS

By Ralph W. Stone, Jr.

Langley Aeronautical Laboratory

SUMMARY

An analytical study has been made of the effects of automatic augmentation or controlling systems on the tail loads experienced in rolling maneuvers and in pitch-up. The results were calculated on an analog computer and the equations of five degrees of freedom were used for the rolling maneuvers and three degrees of freedom for pitch-up. The results of this report are not intended to be of general application, but rather to point out some of the problems that may be encountered on any specific design and to indicate some probable trends.

The results indicate that, for the rolling cases calculated, most automatic systems tend to reduce not only the violence of the maneuver but also the tail load encountered. The results show, however, that if automatic systems are to be used, they must be considered in the initial design to obtain acceptable motions in rolls and to evaluate properly the tail loads.

For the pitch-up problem, the maximum tail loads are predominantly the result of control deflection, and systems which essentially reduce the input or pull-up deflections will generally improve the acceleration overshoots and reduce the horizontal-tail loads. In general, systems used for pitch-up may be compatible with problems of roll coupling. On the other hand, of the systems studied for roll coupling, only the pitch damper would be helpful for pitch-up.

INTRODUCTION

Trends in performance and design of airplanes have brought about some very serious stability deficiencies in recent years. In problems involving such deficiencies, aerodynamic changes, of course, should first be considered. There is a major trend, however, toward the use of automatic augmentation systems or controllers in meeting these deficiencies. This paper is concerned with the effects of such systems on the aerodynamic-loading conditions for two of the more critical deficiencies, these being

divergencies in rolls and pitch-up. The fundamentals of these problems have been discussed in numerous publications (refs. 1 to 10 and 11 to 21, respectively). This report, therefore, is confined primarily to the horizontal- and vertical-tail loads encountered when automatic systems are used. The results presented herein are indicative of only some of the problems and trends that may be expected and are not necessarily of general application.

SYMBOLS

C_L	lift coefficient
C_D	drag coefficient
C_Y	side-force coefficient
C_l	rolling-moment coefficient
C_m	pitching-moment coefficient
C_n	yawing-moment coefficient
I_X, I_Y, I_Z	moments of inertia about the X, Y, and Z body axes, respectively, slug-ft^2
I_{XZ}	product of inertia (positive when principal axis is inclined below X body axis), slug-ft^2
$I_{X_e}\omega_e$	angular momentum of engine rotating parts, ft-lb-sec
W	weight, lb
m	mass, W/g, slugs
g	acceleration of gravity, 32.2 ft/sec^2
S	wing area, sq ft
b	wing span, ft

$\bar{c}$	mean aerodynamic chord, ft
X_{HT}	longitudinal distance from center of gravity to $\bar{c}/4$ of horizontal tail, ft
X_{VT}	longitudinal distance from center of gravity to $\bar{c}/4$ of vertical tail, ft
Z_{VT}	vertical distance from center of gravity to $\bar{c}/4$ of vertical tail, ft
ρ	air density, slugs/cu ft
V	velocity, ft/sec
M	Mach number
h_p	pressure altitude, ft
δ_a	aileron deflection, deg
i_T	stabilizer deflection, positive when trailing edge is down, deg
δ_r	rudder deflection, positive when trailing edge is to the left, deg
α	angle of attack, deg
β	angle of sideslip, deg
ϵ	downwash angle, deg
p	rolling angular velocity, radians/sec
q	pitching angular velocity, radians/sec
r	yawing angular velocity, radians/sec
t	time, sec
L_{HT}	horizontal-tail load, lb
L_{VT}	vertical-tail load, lb
n_Z	normal acceleration, g units

n_Y	lateral acceleration, g units
ζ	damping ratio
$\frac{d\zeta}{d\alpha}$	rate of change of damping ratio with angle of attack
Δ	increment

$$C_{L_\alpha} = \frac{\partial C_L}{\partial \alpha} \qquad C_{l_\beta} = \frac{\partial C_l}{\partial \beta}$$

$$C_{m_\alpha} = \frac{\partial C_m}{\partial \alpha} \qquad C_{n_\beta} = \frac{\partial C_n}{\partial \beta}$$

$$C_{m_q} = \frac{\partial C_m}{\partial \frac{q\bar{c}}{2V}} \qquad C_{Y_\beta} = \frac{\partial C_Y}{\partial \beta}$$

$$C_{l_p} = \frac{\partial C_l}{\partial \frac{pb}{\partial V}} \qquad C_{n_p} = \frac{\partial C_n}{\partial \frac{pb}{\partial V}}$$

$$C_{l_r} = \frac{\partial C_l}{\partial \frac{rb}{\partial V}} \qquad C_{n_r} = \frac{\partial C_n}{\partial \frac{rb}{\partial V}}$$

$$C_{Y_{\delta_r}} = \frac{\partial C_Y}{\partial \delta_r}$$

Subscripts:

0	initial value
max	maximum
HT	horizontal tail
VT	vertical tail

Dot over a symbol indicates derivative.

METHODS

The results discussed herein are based primarily on calculations for hypothetical airplanes typical of contemporary fighters. Table I lists the characteristics of the airplane used for the roll cases. Table II lists those of the airplane used for the pitch-up cases. In the calculations, five degrees of freedom were used for the roll cases and three degrees of freedom for the pitch-up cases. The equations for five degrees and three degrees of freedom appear in many references, for example, references 11 and 22, respectively. In the three-degree-of-freedom calculations, however, C_L, C_D, and C_m were introduced as functions of angle of attack and Mach number, these functions being nonlinear with angle of attack. For some rolling maneuvers, calculations were made of the loads from motions obtained in actual flights. The equations used for calculating the horizontal- and vertical-tail loads are:

$$L_{HT} = \frac{\rho V^2 S}{2} C_{L_{\alpha,HT}} \left[\alpha \left(1 - \frac{d\epsilon}{d\alpha} \right) + \frac{X_{HT}}{V} q + i_T \right]$$

and

$$L_{VT} = \frac{\rho V^2 S}{2} \left[C_{Y_{\beta,VT}} \left(\beta - \frac{X_{VT}}{V} r + \frac{Z_{VT}}{V} p \right) + C_{Y_{\delta_r,VT}} \delta_r \right]$$

DISCUSSION

Roll Coupling

Divergences in rolls are caused generally by rolling too rapidly for the directional stability that exists (ref. 1). Thus, rolling velocity and vertical-tail size are dominant factors in rolling divergences. The effects of these factors are shown in figure 1. Here, the maximum maneuvering horizontal-tail loads and the maximum vertical-tail loads encountered in rolls at different rolling velocities are plotted against the average rolling velocity of each maneuver.

Results are shown for an original tail size and for a tail size optimum for roll coupling. Also shown is the critical rolling velocity, which, as defined by Phillips in reference 1, is that rolling frequency which equals the lower of the pitching or yawing (in this case the yawing) natural frequency.

128

The results show a very large increase in the tail loads encountered as the rolling velocity approaches critical and then a drop-off in the loads beyond this value. Limiting the rolling velocity to some value less than critical would clearly solve the problem. How fast an airplane must roll, however, is a controversial subject and is not one for present discussion. It is sufficient to say herein only that pilots generally insist and (because of this insistence) the services require that airplanes roll at velocities larger than critical for many current and planned configurations.

Changing the tail size is the second direct approach to the problem. There is, however, an optimum tail size; smaller or larger tails lead to more violent motions and larger loads. (See ref. 3.) For the case in this paper the optimum tail is somewhat larger than the original tail. The optimum tail size is that for which the pitching and yawing natural frequencies are the same. For this situation no roll divergence, as such, is possible. A resonance condition exists, however, when the rolling frequency is about equal to the natural frequencies in pitch and yaw, and the loads increase near this rolling velocity with the optimum tail; thus, relatively large loads also exist and the motions still may be rather violent.

Because of the wide variety of flight conditions, speeds, and altitudes now possible, a solution such as an optimum tail size may not be sufficient or feasible for any specific design. (This is true for normal stability as well as for rolling divergencies.) Thus, the trend towards the extensive use of automatic systems prevails. For the problem of roll coupling, several systems are possible. This report treats briefly five types of systems which are shown in table III.

The first system is a perfect controller which maintains zero sideslip and zero changes in angle of attack (ref. 10). This is a rather complex system requiring the sensing of attitude angles. The next system is a more practical representation of this system (ref. 10). The third system is called a coupling-moment canceler (ref. 5). This canceler in effect balances or cancels the inertia coupling parts of the pitching and yawing moments, which, as indicated in reference 5, are the primary cause for rolling divergences. The last two systems are dampers, a pitch damper and a yaw damper.

The choice of systems presented does not imply that they are the most promising controlling or augmentation systems but is intended only to show the influence of some typical systems on the loads encountered. For the calculations shown, the automatic systems are assumed to have no lags and all proper gains. For any specific design the influence of these factors must, of course, be obtained.

Some typical results of two of these systems (the pitch damper and the perfect controller) are shown. In many investigations of roll coupling, the predominant influence of pitching velocity has been evident (refs. 1, 3, 4, and 9, for example) and the pitch damper has been indicated as a simple and direct way to influence the motions encountered.

Figure 2 shows the effect of a pitch damper on the tail loads. Here are plotted the maximum maneuvering horizontal-tail loads and the maximum vertical-tail loads encountered as functions of average rolling velocity with and without the pitch damper operating. The damping ratio of the airplane with the damper operating was 0.5, and the maximum stabilizer deflection allowed for the damper (the control authority) was 1.8°. These results were obtained from flight tests of a contemporary fighter which except for a larger vertical tail is similar to the hypothetical airplane used in the other rolling calculations. As noted before, these are not measured loads but they have been calculated from motions encountered in actual rolls and aerodynamic loading coefficients measured during other flights.

A considerable improvement in the loads encountered with the damper operating is shown. Rolling velocities much in excess of critical were not obtained, however, and the effects of larger roll rates with the damper operating have not been established in flight. Some calculations of this nature have been made, however, and a summary of such results in comparison with the results for other automatic systems are discussed in this section.

The pitch damper is more effective in reducing the vertical-tail loads than the horizontal-tail loads; this indicates the dominant influence of pitching velocity through inertia coupling. The results shown here for the pitch damper are typical of those obtained for most of the other systems except, of course, the magnitude of reductions varies for each system. These differences are discussed subsequently.

Some results for the most complex of the various systems in table III, the perfect controller, are shown in figure 3. For this controller no variations in normal acceleration or lateral acceleration exist. Plotted are the maximum maneuvering horizontal-tail load and the vertical-tail load as functions of average rolling velocity. The controlled and uncontrolled cases are compared and the results are shown for two initial normal accelerations, 1 g and 2g flights.

These results show that the controller not only eliminates the violence of the maneuver but reduces the tail loads encountered, except at the largest rolling velocities when the controller tends to cause the horizontal-tail loads to be larger than are otherwise encountered. The uncontrolled loads occur primarily from angle of attack and sideslip, whereas the controlled loads occur primarily from control deflections.

These control deflections (ref. 10) are a direct function of the rolling velocity, its square, and its derivative; therefore, increasing rolling velocity requires larger deflections and, as a consequence, larger tail loads. For the uncontrolled case the loads drop off beyond the critical rolling velocity in that the motions eventually become stable again (ref. 1). Thus, loads with the controller tend to become larger than those without at rolling velocities beyond critical.

Another pertinent point regarding the perfect controller is shown in figure 3, that is, the increase in loads both with and without the controller at the higher initial acceleration. The loads are, thus, a function of the initial angle of attack, and even larger initial accelerations will lead to larger loads.

Before the results of all the calculations are summarized, a point of significant interest which exists, particularly with the perfect controller, merits some attention here. Because the automatic systems (particularly the perfect controller) reduce the excursions in angle of attack and sideslip, the airplane with the systems operating tends to roll faster at any aileron deflection than without the system operating. In figure 4 are shown the maximum maneuvering horizontal-tail loads plotted against average rolling velocity and aileron input for 2g flight with and without the perfect controller operating.

For 1 g flight (not shown here) the loads are smaller with the controller operating than without at any aileron deflection as well as any rolling velocity except for the largest rolling velocity as shown in figure 3. For 2g flight, however, the loads, although smaller at a given rolling velocity with the controller, are always larger for any given pilot or aileron input. Thus, there is a tendency in rolls from greater than 1 g flight for the horizontal-tail loads with this type of controller to be larger than without the controller for any amount of applied aileron.

In figure 5 is shown a summary of the maximum maneuvering horizontal-tail loads and the maximum vertical-tail loads calculated in 360° rolls at all average rolling velocities up to about 2.2 radians per second. Each bar represents the magnitude of the maximum load for each of several conditions:

The original tail
The optimum-sized tail
The perfect controller (A)
The coupling-moment canceler (C)
The pitch damper (0.7 critically damped) (D)
The yaw damper (1.246 critically damped) (E).

The practical controller is omitted here because it resulted in loads and motions quite similar to those of the perfect controller.

For 1 g flight, these results show the least horizontal-tail load for the coupling-moment canceler; the pitch damper shows similar results. The yaw damper showed little improvement over the original unaugmented case. For the vertical tail, the perfect controller has the least load with reductions shown for the coupling-moment canceler and the pitch damper, but again little improvement is shown for the yaw damper. The optimum tail shows the improvements previously discussed (fig. 1).

For 2g flight, the horizontal-tail load for the perfect controller has the increase in load that was discussed previously (fig. 4). Sizable reductions in tail load with the coupling-moment canceler and the pitch damper exist, however.

For the vertical-tail load, the least load is encountered with the perfect controller as for the 1 g case, only fair reductions in loads are obtained with the coupling-moment canceler, and a somewhat larger reduction with the pitch damper. No data are available for the optimum tail and the yaw damper for this flight condition.

It is clear, however, that for all systems the loads increase markedly with the initial normal acceleration of the flight.

The tail loads without an automatic system are, of course, caused primarily by the angles of attack and sideslip. With an automatic system, however, the loads are caused by the stabilizer and rudder deflections as well. The amount of control deflection required by any system is therefore of extreme significance.

Figure 6 shows the maximum control deflections required for each of the various systems. Each bar represents the magnitude of the maximum deflection required in rolls of various average rolling velocities up to about 2.2 radians per second. The basic airplanes with the original and optimum tails of course use no controls as noted by the zeros. No data are available for the optimum tail or the yaw damper in 2g flight. The deflections used in 2g flight are appreciably larger than those used in 1 g flight. The largest stabilizer deflection is used by the perfect controller and the least, by the pitch damper. The largest rudder deflection is used by the coupling-moment canceler and the least, by the yaw damper.

Stabilizer deflections of the order of 11°, used by the perfect controller, may be a larger portion of the total available deflection than it is desirable to use. The rudder deflections used by the perfect controller and the coupling-moment canceler are extremely excessive and certainly could not be used. They are larger than the total available deflection of 40°. For specific cases, therefore, the effects of limiting the amount of control deflection used must certainly be investigated.

It is not sufficient to evaluate an automatic system on the basis of the tail loads encountered or the control deflections required alone because, except for the perfect controller, variations in the normal and lateral accelerations also exist. With some automatic systems operating, these accelerations still may be intolerable to the pilot.

In figure 7 are shown the maximum normal and lateral accelerations calculated in 360° rolls at all average rolling velocities up to about 2.2 radians per second. Each bar represents the magnitude of the maximum accelerations calculated for each of the various systems previously discussed. The accelerations shown occurred during rolling maneuvers which were initiated from 1 g and 2g flight.

The results (for both 1 g and 2g flight) show that the variations in normal acceleration below the initial values of 1 g or 2g are only slightly improved by any of the systems except, of course, the perfect controller for which no changes occur. Negative accelerations are experienced for all other systems. The positive variations in normal acceleration are, however, appreciably reduced by all systems but the yaw damper. For the lateral accelerations, improvement is obtained by all systems, although accelerations of $\frac{1}{2}$ g for 1 g flight and 1g for 2g flight still are experienced.

There is a sizable increase in the accelerations encountered in rolls from 2g flight over those from 1 g flight.

It appears that, in coping with the roll-coupling problem, a considerable compromise must be made between the motions or accelerations that the pilot must tolerate, the tail-loads encountered, and the control deflections required by a system.

Pitch-Up

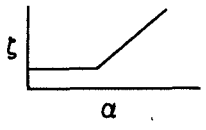
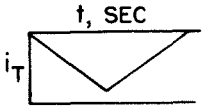
The other dominant stability deficiency is the problem of pitch-up. Pitch-up occurs, of course, from nonlinearities in the pitching-moment characteristics of an airplane.

The pitching-moment characteristics for the hypothetical airplane used for the calculations of this paper are typical of those of airplanes with swept wings and high horizontal tails having moderate nonlinearities with angle of attack and are shown in figure 8. The calculations were made from a Mach number of 1, and changes in aerodynamic-center position (fig. 8) with Mach number as well as pitching-moment nonlinearities with angle of attack influence the results.

It is important to realize that the dangers from pitch-up are not only those occurring in the pitch plane, but also those which may occur

in the lateral modes of motion when the large angles of attack resulting from pitch-up may cause instabilities in sideslip, violent wing dropping, and spinning. Aerodynamic cures are most desirable, of course, but if not possible, automatic augmentation of some sort appears necessary. For the cases shown herein, the nonlinearities occur in the range of angles of attack and normal acceleration for which it is desirable to operate the airplane. Thus, automatic systems which abort a maneuver rather than allow it to progress reasonably are not desirable.

For the results presented herein, only two automatic systems are treated. These systems are shown in the following table:

SYSTEM	SENSING REQUIRED	DESCRIPTION
VARIABLE-PITCH DAMPER	q AND α OR n_Z	ζ=DAMPING RATIO 
STICK PUSHER	n_Z	

The first system is a rather complex pitch damper, a variable pitch damper. It is representative, however, of systems which do not abort maneuvers. The variable damping system is one which becomes operative beyond some predetermined angle of attack so that the motion is not sluggish in the normal operating range of angles of attack, but also so that the damping increases rapidly as the angle of attack of pitch-up is approached, as shown by the small sketch of the variation in damping ratio.

The second system is a stick pusher which does abort the maneuver. The pusher used, however, is one which senses only angle of attack or normal acceleration and becomes operative only after the desired normal acceleration is reached. For the results considered herein the pusher returned the stabilizer only to the original trim position as shown by the small sketch.

In figure 9 are shown the results for the variable pitch damper. The maximum normal acceleration, the maximum horizontal-tail load (which is negative and increases in magnitude downward on the figure), and the maximum stabilizer deflection required are shown as functions of rate of change of damping ratio with angle of attack. For these cases, the augmenter became active when the angle of attack exceeded the initial trim

angle of attack for 1 g. Also shown are the values of the loads for the airplane with a linear pitching-moment curve. The results show an appreciable reduction in the normal-acceleration overshoot (accelerations greater than 4g) with increasing rate of change of damping ratio, the large values leading to less acceleration overshoot than even the linear case. The tail loads are similarly reduced in magnitude and again, at the larger damping ratios, smaller loads are obtained than for the linear case. Rather sizable stabilizer deflections are required by this system; however, values of as much as 5° are required and this is somewhat greater than that used by a moderate authority system. This may be considered an excessive amount of control.

Some results for the stick pusher are shown in figure 10. Here are shown the maximum normal acceleration and the maximum horizontal-tail load as functions of push rate, that is, the rate of change of stabilizer deflection with time. The results are shown for three different stabilizer input rates, or rates of pull-up. The results show little improvement for a stick pusher of this type. The normal acceleration overshoot is reduced only slightly and the tail loads are essentially unchanged. Both the loads and accelerations are appreciably larger than the values for the linear pitching-moment case.

It appears that a pusher of this type, which allows the maneuver to reach its desired acceleration before operating, not only aborts the maneuver but does little good for the maximum loads encountered. A pusher which operates earlier would, of course, produce less loads but would also stop the maneuver much sooner. A pusher with anticipation based on pitching velocity or acceleration in conjunction with a pitch damper undoubtedly would prove useful on all counts.

Compatibility of Systems for Rolling Maneuvers and Pitch-Up

Inasmuch as airplanes may be afflicted by both pitch-up and rolling divergences, the compatibility of an automatic system for one deficiency with the needs of the other deficiency is important. Because of the nature of pitch-up, all systems, used as a cure, require nose-down pitching moments. In addition, all roll-coupling systems require nose-down pitching moments at the onset of the rolling motion, primarily because of the initial positive pitching velocity that exists. As a matter of fact, all systems but the pitch damper require only nose-down moments. Thus, systems for pitch-up would generally not have detrimental effects in rolls and may be helpful. Systems used for roll-coupling which require a sensing of rolling velocity would not operate in a pitching maneuver and thus would have no effect on pitch-up.

It must be pointed out that in rolling maneuvers for which the principal axis is below the flight path, in front of the center of gravity, initial negative pitching velocities are developed rather than positive

values which occur for the cases discussed herein. Thus, for such cases nose-up rather than nose-down pitching moments would be required by an automatic system at the onset of a roll. An automatic system for pitch-up such as a pusher might thus be detrimental, whereas a pitch-damper would still be effective for rolling maneuvers.

CONCLUDING REMARKS

In summary, a cursory study has been made of the effects of automatic augmentation and controlling systems on the tail loads and accelerations in rolls and pitch-up. The results of this study are not necessarily of general application but primarily show some of the problems and trends that may be expected. Calculations similar to those presented herein must, of course, be made for any specific design.

The results for rolls indicate the existence of an optimum tail size from the standpoint of the loads encountered, this size being most naturally that which is least likely to cause divergences. Automatic systems ranging from a simple pitch damper to a perfect controller show reductions in the violence of the motions and, in general, a reduction in the tail loads. At average rolling velocities somewhat larger than critical, the horizontal-tail loads obtained with controllers which sense rolling velocity may be larger than are obtained with no controller. In any event, if automatic systems are to be used, they must be considered in the initial design to obtain acceptable motions in rolls and to evaluate properly the loads encountered.

For the pitch-up problem the maximum tail loads are primarily the result of control deflection and thus systems which essentially reduce the input or pull-up deflections will generally improve the acceleration overshoots and reduce the horizontal-tail loads encountered.

Finally, in general, systems used for pitch-up may be compatible with the problems of roll coupling and generally should not be detrimental. On the other hand, of the systems studied for roll coupling, only the pitch damper would be helpful for pitch-up.

REFERENCES

1. Phillips, William H.: Effect of Steady Rolling on Longitudinal and Directional Stability. NACA TN 1627, 1948.

2. White, R. J., Uddenberg, R. C., Murray, D., and Graham, F. D.: The Dynamic Stability and Control Equations of a Pivoted-Wing Supersonic Pilotless Aircraft, With Downwash, Wake and Interference Effects Included. Doc. No. D-8510, Boeing Aircraft Co., Jan. 9, 1948.

3. Weil, Joseph, and Day, Richard E.: An Analog Study of the Relative Importance of Various Factors Affecting Roll Coupling. NACA RM H56A06, 1956.

4. Gates, Ordway B., Jr., Weil, Joseph, and Woodling, C. H.: Effect of Automatic Stabilization on the Sideslip and Angle-of-Attack Disturbances in Rolling Maneuvers. NACA RM L55E25b, 1955.

5. Phillips, William H.: Analysis of an Automatic Control To Prevent Rolling Divergence. NACA RM L56A04, 1956.

6. Gates, Ordway B., Jr., and Woodling, C. H.: A Theoretical Analysis of the Effect of Engine Angular Momentum on Longitudinal and Directional Stability in Steady Rolling Maneuvers. NACA RM L55G05, 1955.

7. Finch, Thomas W., Peele, James R., and Day, Richard E.: Flight Investigation of the Effect of Vertical-Tail Size on the Rolling Behavior of a Swept-Wing Airplane Having Lateral-Longitudinal Coupling. NACA RM H55L28a, 1956.

8. Sisk, Thomas R., and Andrews, William H.: Flight Experience With a Delta-Wing Airplane Having Violent Lateral-Longitudinal Coupling in Aileron Rolls. NACA RM H55H03, 1955.

9. Stone, Ralph W., Jr.: Some Notes on the Violent Lateral-Longitudinal Coupling Motions of the Douglas X-3 Airplane in Aileron Rolls. NACA RM L56C15, 1956.

10. Woodling, C. H.: Theoretical Investigation of the Effect of Rudder and Stabilizer Deflections on the Angles of Attack and Sideslip in Rapid Rolls. NACA RM L57A30a, 1957.

11. Shortal, Joseph A., and Maggin, Bernard: Effect of Sweepback and Aspect Ratio on Longitudinal Stability Characteristics of Wings at Low Speeds. NACA TN 1093, 1946.

12. Donlan, Charles J., and Weil, Joseph: Characteristics of Swept Wings at High Speeds. NACA RM L52A15, 1952.

13. Weil, Joseph, and Gray, W. H.: Recent Design Studies Directed Toward Elimination of Pitch-Up. NACA RM L53I23c, 1953.

14. Toll, Thomas A.: Longitudinal Characteristics of Wings. NACA RM L53I21b, 1953.

15. Polhamus, Edward C., and Hallissy, Joseph M., Jr.: Effect of Airplane Configuration on Static Stability at Subsonic and Transonic Speeds. NACA RM L56A09a, 1956.

16. Curfman, Howard J., Jr.: Theoretical and Analog Studies of the Effects of Nonlinear Stability Derivatives on the Longitudinal Motions of an Aircraft in Response to Step Control Deflections and to the Influence of Proportional Automatic Control. NACA Rep. 1241, 1955. (Supersedes NACA RM L50L11.)

17. Oswald, Telford W.: The Effect of Nonlinear Aerodynamic Characteristics on the Dynamic Response to a Sudden Change in Angle of Attack. Jour. Aero. Sci., vol. 19, no. 5, May 1952, pp. 302-316.

18. Bielat, Ralph P., and Campbell, George S.: A Transonic Wind-Tunnel Investigation of the Longitudinal Stability and Control Characteristics of a 0.09-Scale Model of the Bell X-5 Research Airplane and Comparison With Flight. NACA RM L53H18, 1953.

19. Campbell, George S., and Weil, Joseph: The Interpretation of Nonlinear Pitching Moments in Relation to the Pitch-Up Problem. NACA RM L53I02, 1953.

20. Sadoff, Melvin, Matteson, Frederick H., and Havill, C. Dewey: A Method for Evaluating the Loads and Controllability Aspects of the Pitch-Up Problem. NACA RM A55D06, 1955.

21. Sadoff, Melvin, Stewart, John D., and Cooper, George E.: A Method for Predicting Relative Severity of Pitch-Up Based on A Correlation of the Computed Dynamic Behavior of Several Airplane Configurations With Pilot Opinion. Prospective NACA paper.

22. Bihrle, William, Jr., and Stone, Ralph W., Jr.: Analytical Studies of the Response to Longitudinal Control of Three Airplane Configurations in Landing Approaches. NACA RM L53B10, 1953.

[redacted]

TABLE I

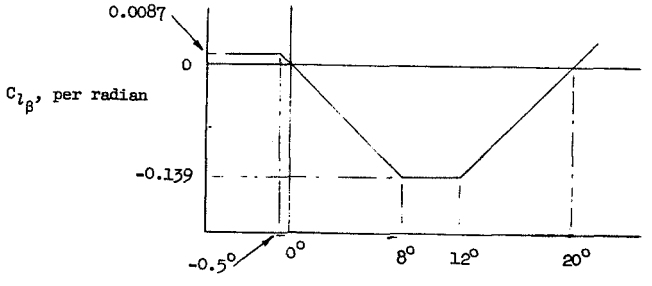
MASS CHARACTERISTICS, STABILITY DERIVATIVES, AND OTHER FACTORS

USED IN THE CALCULATIONS OF ROLLING MANEUVERS

[All coefficients and derivatives are based on wing area]

I_X, slug-ft^2	10,976
I_Y, slug-ft^2	57,100
I_Z, slug-ft^2	64,975
I_{XZ}, slug-ft^2	942
q, lb/sq ft	197
S, sq ft	376
b, ft	36.6
$\bar{c}$, ft	11.32
W, lb	23,900
m, slugs	742
V, ft/sec	691
h_p, ft	32,000
ρ, slugs/cu ft	0.000826
M	0.7
$I_{X_e}\omega_e$, ft-lb-sec	17,554
$C_{l_{\delta_a}}$, per radian	-0.0528
C_{l_p}, per radian	-0.255
C_{l_r}, per radian	0.042
$C_{m_{i_T}}$, per radian	-1.0
C_{m_q}, per radian	-3.5
$C_{m_{\dot{\alpha}}}$, per radian	-1.5
C_{m_α}, per radian	-0.36
$C_{n_{\delta_a}}$, per radian	0
$C_{n_{\delta_r}}$, per radian	-0.03
C_{n_r}, per radian	-0.095
C_{n_p}, per radian	0
C_{n_β}, per radian (original tail)	0.057
C_{n_β}, per radian (optimum tail)	0.114
C_{y_β}, per radian	-0.50
C_{L_α}, per radian	3.85
$C_{l_{\alpha,HT}}$, per radian	0.755
$\frac{d\epsilon}{d\alpha}$	0.43
$C_{Y_{\beta,VT}}$, per radian	-0.23
$C_{y_{\delta_r,VT}}$, per radian	0.074

$C_{l_\beta}(\alpha)$, per radian (shown in following plot):



139

[redacted]

TABLE II

MASS CHARACTERISTICS, STABILITY DERIVATIVES, AND OTHER FACTORS USED IN THE CALCULATIONS OF PITCH-UP

I_y, slug-ft^2	109,172
$\frac{1}{2}\rho V^2 S$, lb/sq ft	348
S, sq ft	530
$\bar{c}$, ft	16
W, lb	34,450
m, slugs	1,070
V, ft/sec	971
h_p, ft	35,000
ρ, slugs/cu ft	0.000737
Mach number	1.00
$C_{m_{i_T}}$, per radian	-0.773
C_{m_q}, per radian	-2.27
C_{m_α}, per radian	0.867
C_{L_α}, per radian	4.41

TABLE III

SOME TYPES OF ROLL-COUPLING CONTROLLERS AND AUGMENTERS

System		Sensing required	Controls used
A	Perfect controller	α_0, p, $\dot{p}$, and attitude	i_T and δ_r
B	Practical controller	α_0, $\dot{p}$, and p	i_T and δ_r
C	Coupling-moment canceler	p, q, and r or pq and pr	i_T and δ_r
D	Pitch damper	q	i_T
E	Yaw damper	r	δ_r

EFFECT OF ROLLING VELOCITY ON MAXIMUM TAIL LOADS
360° LEFT ROLLS FROM 1 g FLIGHT

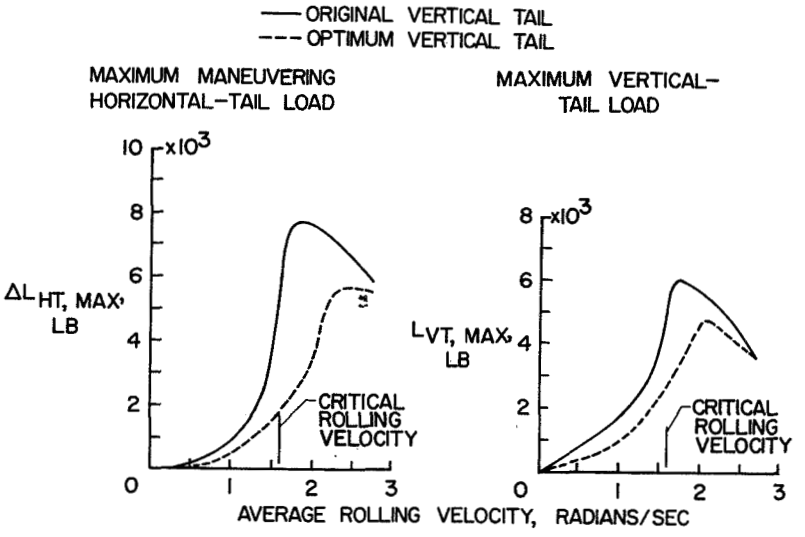
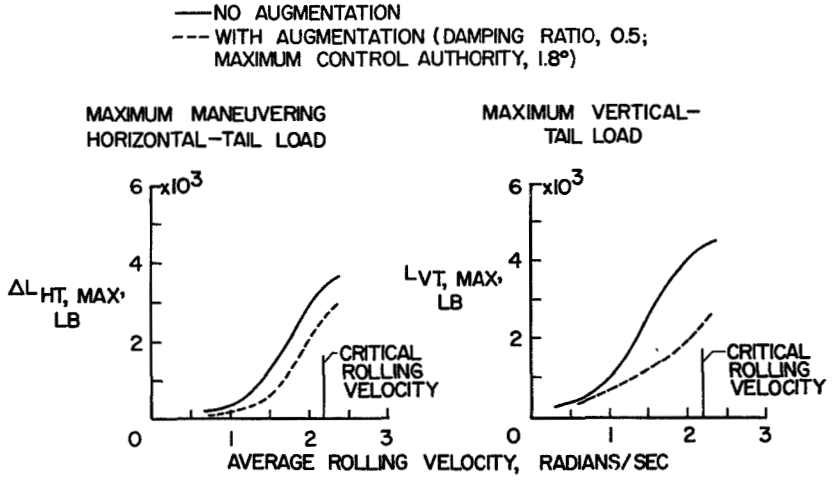


Figure 1

EFFECT OF A PITCH DAMPER IN ROLLING MANEUVERS FROM FLIGHT TESTS
360° LEFT ROLLS FROM 1 g FLIGHT



111

Figure 2

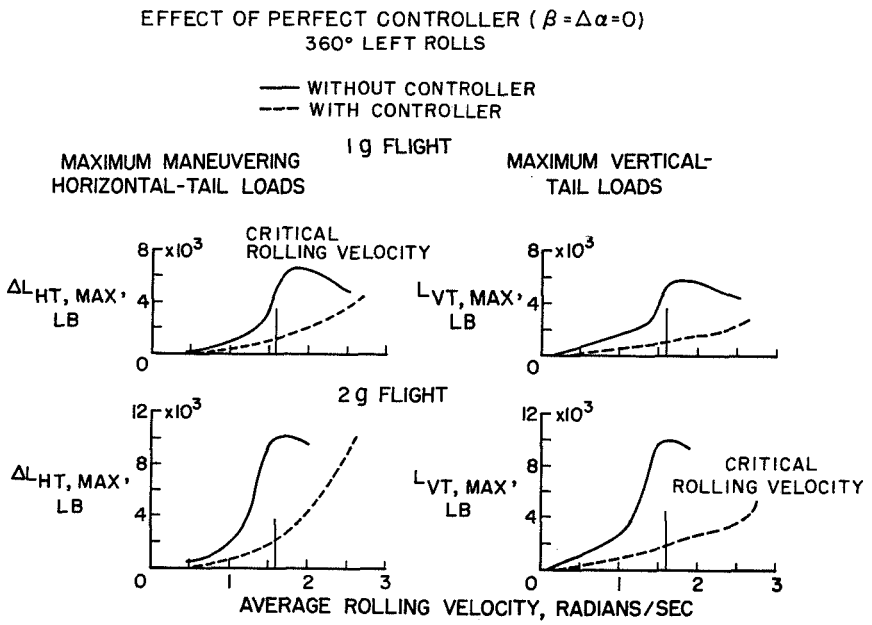


Figure 3

MAXIMUM MANEUVERING HORIZONTAL-TAIL LOADS WITH PERFECT CONTROLLER

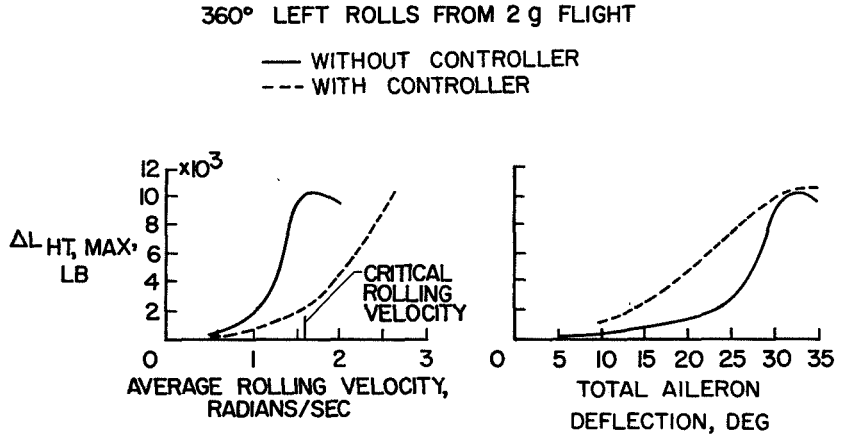


Figure 4

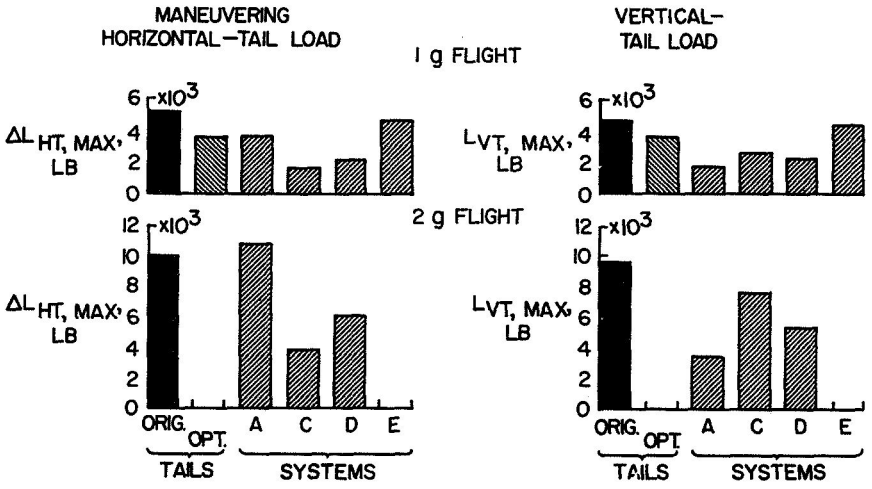


Figure 5

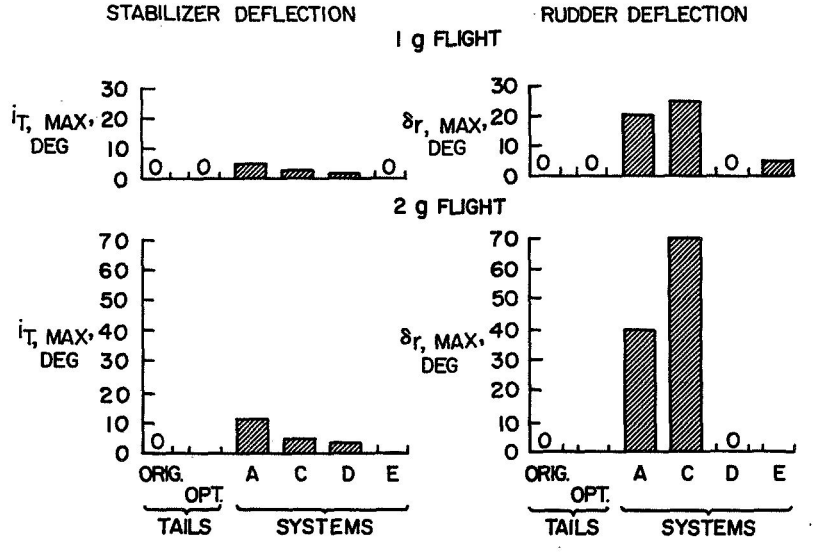


Figure 6

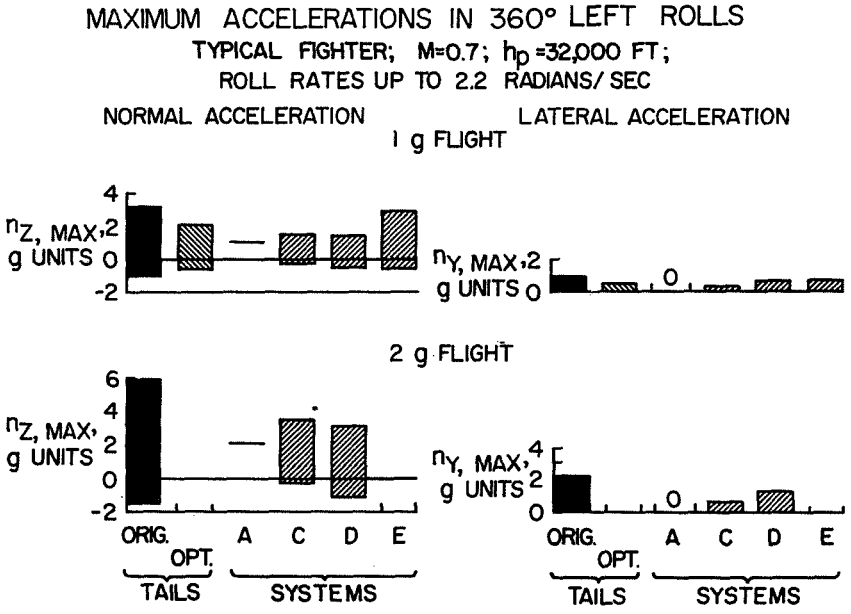


Figure 7

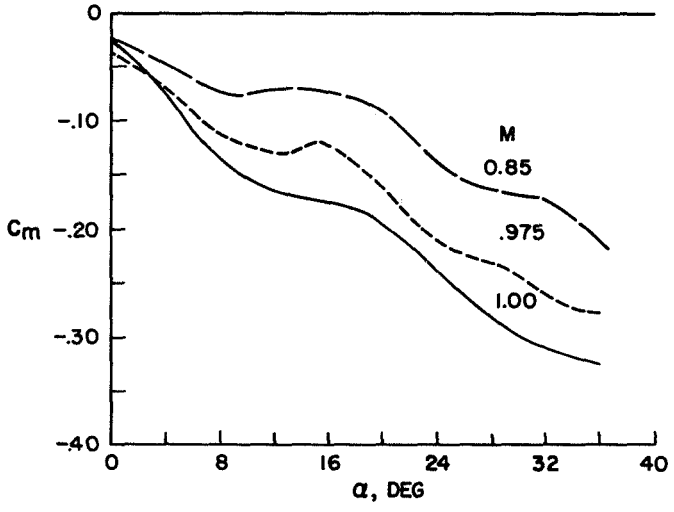


Figure 8

414

EFFECT OF MAGNITUDE OF VARIABLE PITCH DAMPING ON LOADS IN PITCH-UP

M=1.0; h_p=35,000 FT; PULL-UP TO 4 g; INPUT RATE, 2.5°/SEC

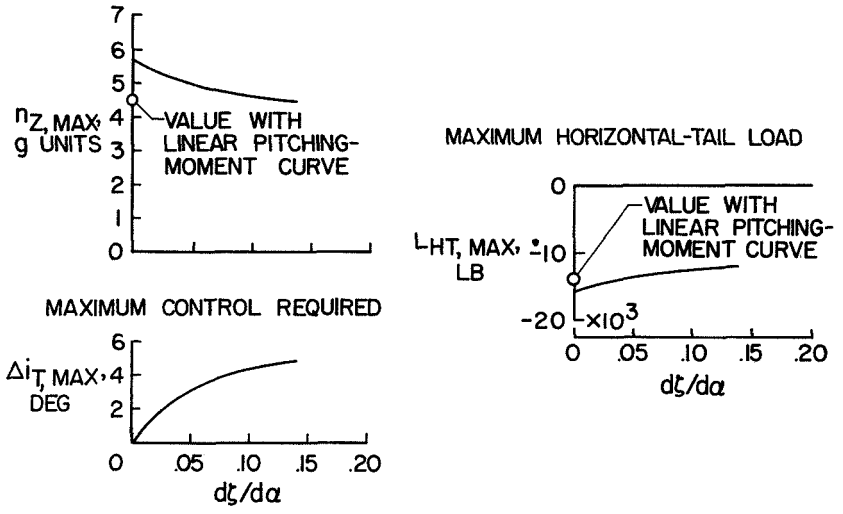
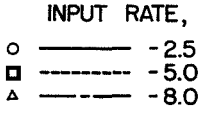
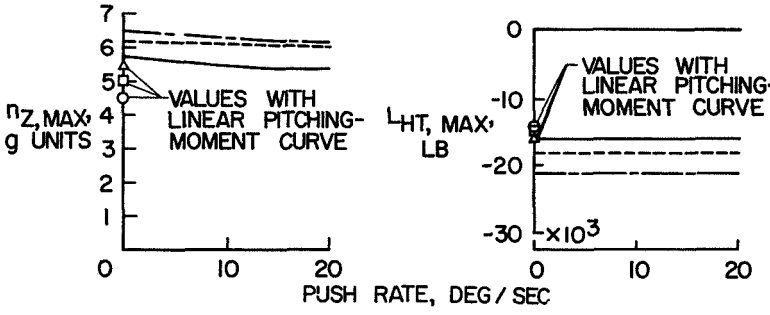


Figure 9

EFFECT OF STICK PUSHER ON LOADS IN PITCH-UP

M=1.0; h_p=35,000 FT; PULL-UP TO 4 g; INPUT RATE, 2.5°/SEC





145

Figure 10

N71-75391

SPAHR & POLHAMUS

AERODYNAMIC LOADS ON TAILS AT HIGH ANGLES OF ATTACK AND SIDESLIP

By J. Richard Spahr
Ames Aeronautical Laboratory

and Edward C. Polhamus
Langley Aeronautical Laboratory

SUMMARY

Results are presented for the loads and moments acting on the individual tail surfaces of a body-tail combination over a wide range of angles of attack and sideslip. The effects of forebody length and panel-panel interference on the characteristics are included. It is shown that large nonlinear variations in these loads and moments occur at some combinations of angle of attack and sideslip which cannot be predicted by low-angle theory. A relatively simple, but general, theoretical method for calculating these load and moment characteristics is described, and the results from this method are found to be in good agreement with experiment provided the initial positions of the forebody vortices are known.

It is shown that a simple application of slender-body theory can be used to predict the side loads due to sideslip that are contributed by a vertical tail on a wide variety of wing-body-tail combinations at low angles of attack. Several configuration changes are indicated which reduced the vertical-tail loads per unit yawing moment of the configuration at large angles of attack.

Some results are presented on the effect of high angle of attack on the induced-flow field and tail loads due to a wing at supersonic speed.

INTRODUCTION

Airplanes and missiles are frequently required to operate over a wide range of angles of attack and sideslip. The aerodynamic loading on most aircraft configurations at small angles of attack and sideslip can be adequately predicted by linearized theories. However, at combined angles where either the angle of attack or sideslip is large, serious nonlinearities in the load characteristics occur for which no general theoretical method has heretofore been developed. The results of

reference 1 have shown that, at subsonic Mach numbers, such nonlinearities in the tail loads are caused by the effects of the body and wing vortices and that these effects can be estimated if the strength and positions of the vortices are known.

The purpose of this paper is threefold: (1) to summarize the results at supersonic Mach numbers of recent fundamental and systematic measurements of the loads and moments on the exposed panels of body-panel combinations through a wide range of angles of attack and sideslip; (2) to present a general theoretical method for calculating these load characteristics at any Mach number, which requires only a knowledge of the initial positions of the forebody vortices; and (3) to show the influence of several configuration changes in reducing the vertical-tail loads required for a given yawing moment of the configuration.

SYMBOLS

a maximum body radius

b wing span

c local chord

$\bar{c}$ mean aerodynamic chord

c_n section normal-force coefficient

C_b bending-moment coefficient, $\dfrac{\text{Bending moment about root of exposed panel}}{2qSs_v}$

C_h hinge-moment coefficient, $\dfrac{\text{Hinge moment about centroid of exposed panel}}{2qS\bar{c}}$

C_n yawing-moment coefficient of configuration

$C_{N,t}$ normal-force coefficient on exposed vertical tail, $\dfrac{\text{Normal force}}{qS}$

C_N normal-force coefficient on tail in presence of wing

C_{N_∞} normal-force coefficient on tail alone

C_Y	side-force coefficient, $\frac{\text{Side force on vertical panel}}{2qS}$
ΔC_Y	change in side-force coefficient of configuration due to vertical tail
Δi_t	total differential horizontal-tail incidence
M	free-stream Mach number
q	free-stream dynamic pressure
s	spanwise distance from body center to panel tip
s_v	span of one exposed panel
S	area of one exposed panel
V	free-stream velocity
Z	vertical coordinate with origin at tail-body juncture
α	angle of attack, radians unless otherwise specified
β	angle of sideslip
ϵ	semiapex angle of plan form
ϵ'	angle of average downwash acting over span of tail

Subscripts:

U	upper panel
L	lower panel
V	due to body vortices
W	wing alone

DISCUSSION

Basic Panel-Load Characteristics

The loads and moments acting on the individual lifting surfaces of a cruciform combination are considered first. These surfaces can

be considered wing panels of a body-wing-tail combination or the tail surfaces of a wingless configuration. Systematic wind-tunnel tests of the configuration shown in figure 1 have been made at the Ames Aeronautical Laboratory to measure the forces and moments acting on the four individual panels over a wide range of combined angles of attack and sideslip. Representative results of these tests are presented in figure 2 in which the loads and moments acting on the upper and lower vertical panels are given for combined angles of attack and sideslip. The coefficients of side force C_Y on each panel and hinge moment about the panel centroid C_h are shown as functions of sideslip angle β for angles of attack of 0° and 20°. It is seen that the effect of angle of attack on the lower panel is to increase progressively the force while the hinge moment remains unchanged. In contrast, the load and hinge moment on the upper panel are both decreased by angle of attack. The important characteristic to note here is that this decrease is not proportional to angle of sideslip but reaches a maximum at low values of sideslip and results in a large rearward shift in the panel center of pressure and a highly nonlinear variation of the loads and moments on this panel with angle of sideslip. It is this loss in load on the upper vertical panel when serving as a tail fin which is one of the causes of the serious decay in directional stability of most airplanes at large angles of attack. It is apparent that this undesirable characteristic can be alleviated by the use of a lower vertical (ventral) fin, because such a surface does not lose effectiveness with angle of attack but actually gains effectiveness. Results for the panel root bending moment are presented in figure 3. The bending-moment results in conjunction with the side-force results show that the lateral center of pressure of the lower panel remains fixed with changes in angle of attack, whereas that of the upper panel moves outboard with an increase in angle of attack. It is apparent from symmetry that the results of figures 2 and 3 apply directly to horizontal panels if the angles of attack and sideslip are interchanged. The left-hand curves apply to the left horizontal panel and the right-hand curves apply to the right panel.

Consider now the basic cause of these effects of cross coupling between angle of attack and sideslip. The loading due to sideslip on a vertical panel in the presence of a body varies with angle of attack because of two different effects: (1) the change in effective sweepback of the panel and, (2) the change in the influence of the forebody vortices on the panel loading.

Consider, first, the sweepback effect. It can be shown by use of slender-body theory that the lift effectiveness of a wing panel in the presence of a body decreases with increasing sweepback as in the case of a wing alone. This effect is illustrated in figure 4 which shows the side view of the vertical panels in combination with the body at an arbitrary angle of attack and sideslip. The effect of angle of attack

is to increase the leading-edge sweepback of the upper panel and to decrease the sweepback of the lower panel. The resulting changes in the loading due to sideslip over each wing panel is indicated in the right-hand sketch of figure 4. Here, it is shown that the symmetrical spanwise load distribution at zero angle of attack is changed to an asymmetrical distribution at positive angle of attack. The loading on the lower panel is increased and that on the upper panel is decreased.

Consider next the second factor influencing the panel loads at combined angles of attack and sideslip, that is, the influence of the forebody vortices. At moderate and large angles of attack or sideslip, the flow over a body is characterized by a pair of symmetrically disposed vortices on the leeward side caused by crossflow separation. The presence of a vortex in the vicinity of a wing or tail surface changes the loading on the surface by virtue of the induced flow field created by the vortex. Two critical conditions are indicated in figure 5 for which a vortex passes close to one panel and thus has the greatest effect on the loading: first, the combination of high angle of attack and low sideslip in which the upper panel is primarily affected by the vortex and, second, high sideslip and low angle of attack in which the left panel is most affected. It will be recalled from a previously given figure that these were the two conditions for which the largest nonlinear changes in panel loading occurred. The effect of a vortex on the panel loads is illustrated by sketches which show the changes in the spanwise load distribution, from strip theory, due to a vortex passing near the tip of each panel. It is observed that, above the vortex on the upper panel, a loading to the left occurs and below the vortex a loading to the right occurs. This loading corresponds to the distribution of sidewash induced by the vortex along the span of the panels. The magnitude of the loading increases with the strength of the vortex and decreases with the distance of the vortex from the panel. With the vortex located near the tip of the panel, the net force due to the vortex is to the right and reduces the load and bending moment existing on the panel without the vortex present. If the vortex is moved toward the body, its effect on the net panel load would diminish, because the two regions of opposite loading would become more nearly compensating.

Expressions based on simple theoretical concepts have been derived for the prediction of the forces and moments acting on a panel at arbitrary angles of attack and sideslip in which the effects of both sweepback and body vortices have been taken into account. These expressions are illustrated in figure 6 which gives the equations for the side force acting on the two vertical panels at a given sideslip angle. The first term in each of these expressions represents the side force at zero angle of attack; the second term represents the effect of sweepback due to angle of attack; and the last term represents the contribution of the forebody separation vortices. The factor C_{Y_W} is the side force of

the panel alone at zero angle of attack and is evaluated from experiment, where available, or from a suitable wing theory. The factors K_W and K_ϕ are both computed by slender-body theory and, for a circular body, depend only on the ratio of the body radius a to the panel semispan s as shown by the curves in figure 6. It is observed that K_W increases from 1 to 2 as the configuration changes from an all-wing configuration to a body with no wings. The factor K_ϕ, on the other hand, increases to a maximum for combinations with relatively small bodies and then decreases to zero as the wings vanish. It is also noted that, because of panel-panel interference, K_ϕ is larger for the planar configuration than for the cruciform arrangement, but that this effect becomes smaller as a/s increases. Although the factors K_W and K_ϕ have been computed from slender-body theory, these equations are not necessarily restricted to combinations having slender panels because K_W and K_ϕ are simply load ratios which modify the load on a vertical-tail panel alone to take into account the presence of the body and of the angle of attack. The theoretical and experimental comparisons of Nielsen and Kaattari (ref. 2) have established the validity of the factor K_W for essentially any plan form or aspect ratio.

The importance of the panel leading-edge sweepback on the side force is seen from the equations where $\tan \epsilon$, which is proportional to the aspect ratio for a triangular plan form, appears in the denominator. Thus, the lower the aspect ratio the larger the effect of angle of attack on the vertical panel loads due to sideslip.

The evaluation of the last terms in these equations requires the computation of the effect of each of the forebody vortices and their images on the wing-panel loading. The strength and paths of these vortices have been calculated by means of a stepwise procedure based on incompressible vortex theory. Such calculations, however, require a knowledge of the normal-force distribution along the forebody and the initial vortex position. The work of Jorgensen and Perkins (ref. 3) has demonstrated the validity of this method for bodies of circular cross section, and subsequent work has indicated its applicability to bodies of arbitrary cross section. The calculation of the effect of a vortex of known strength and position on the loading of a wing panel in the presence of a body is most simply made by means of strip theory. In the application of the strip theory, it is assumed that the strength and path of each vortex remain unchanged by the addition of the wing panel to the body. The downwash for an ideal vortex is then calculated and the additional spanwise load distribution due to the vortex flow field is computed. The lifting effectiveness of each longitudinal strip is taken as the two-dimensional value for a wing having the same leading-edge sweepback. An alternate method, based on slender-body theory, is

currently being investigated at the Ames Aeronautical Laboratory for the calculation of the effects of a vortex on a wing panel in the presence of a body. In this method the influence of the wing-panel flow field on the vortex paths is taken into account and, thus, one of the assumptions of the strip-theory method is avoided. Preliminary results of this study indicate that the effects of such changes in the vortex path on the wing load may be important for plan forms of low aspect ratio.

Calculations have been made by means of these theoretical methods to predict the experimental panel-load characteristics discussed earlier. Figure 7 shows a comparison between experiment and theory at an angle of attack of 20° for the variation of side force and hinge moment with sideslip angle for the two vertical panels.

In addition to the experimental values shown by the symbols three theoretical curves are shown in each case to illustrate the importance of the two aerodynamic effects just discussed: first, a low-angle theory, given by the first term in the equations of figure 6; second, the theory including the sweepback effect, given by the first two terms; and, third, the theory including both the sweepback and vortex effects (based on the experimental initial vortex positions) as given by the complete equations. It is seen from these comparisons that the load characteristics of either panel can be predicted adequately by the complete theory. However, it is noted that for the lower panel the vortex effect is negligible, a result of the body vortices being a relatively large distance from this panel.

The effects of forebody length on the vertical-panel loads are indicated in figure 8. In this figure is presented a comparison of the load characteristics of the original combination with a combination having one-half the original forebody length. The importance of forebody length is evident from this comparison which shows that this change in the forebody virtually eliminates the nonlinearities due to the body vortices. This result is caused by the reduction in the vortex strength and by the inboard movement of the vortices, both of which tend to reduce the effect of the vortices as pointed out earlier. These experimental results are in good agreement with those predicted by the theoretical method described earlier.

The effects of the presence of adjacent surfaces on the loads acting on a wing or tail surface are illustrated in figure 9. In this figure is shown the variation of the side force and hinge moment of each vertical panel with angle of sideslip at a high angle of attack in the presence of each of the other panels of a cruciform arrangement. These curves show that the addition of the opposite vertical or the left horizontal panel has no effect on the loads of either vertical panel, but the addition of the right horizontal panel increases the load on the lower panel and decreases the load on the upper panel. These panel-panel

interference effects are associated partly with the cross coupling of the sidewash velocities in potential flow and partly with interference effects of the forebody vortex flow.

The loads on the tail surfaces of complete configurations at zero or small angles of attack are next considered. Under these conditions, the side load contributed by a wing or tail surface to an arbitrary configuration at any sideslip angle or Mach number can be computed by means of a simple theoretical method. In this method the side-force contribution of a vertical-tail surface is given by the product of the side force acting on the surface alone and an interference factor which is a function only of the cross-sectional shape of the combination at the tail location. Slender-body theory in conjunction with apparent-mass relationships are used to evaluate this interference factor for a given configuration. This theoretical method has been used to predict the side-force characteristics of a number of current aircraft configurations shown in figure 10, for which such experimental information was available. Most of these configurations represent recent fighter airplanes and include a wide variety of wing-body-tail arrangements. In addition, a research model from the National Advisory Committee for Aeronautics is included. The cross-sectional arrangements used in the theoretical calculations to approximate the actual configurations are shown in figure 11. The correlation between experiment and theory is given in terms of the change in side force due to the addition of the surface designated by the solid line in each of the sketches. The results for subsonic speeds are indicated by the flagged symbols and those for supersonic speeds by the plain symbols. Although the change in side force ΔC_Y shown in this figure includes the load induced on the body by the surface, the load on the surface itself can also be calculated by the theoretical method. The good agreement shown here between experiment and theory for such a wide variety of configurations at both subsonic and supersonic speeds shows the general usefulness of the theoretical method in the prediction of side loads and vertical-tail loads due to sideslip at small angles of attack where in some cases these loads are maximum.

The effects of angle of attack on the tail loads of wing-body-tail combinations are now considered. Figure 12 shows some results obtained at the Langley Aeronautical Laboratory which show the effect of angle of attack on the spanwise load distribution due to sideslip on the vertical tail of an airplane configuration having a low, midposition, or high wing at a Mach number of 0.8. It is observed that in all cases an increase in angle of attack causes an increase in the loading along the outer portion of the span and a decrease near the root. From the previous discussions it can be recognized that this effect is associated with the forebody crossflow separation vortices. It can also be noted by comparing the low- and high-wing results that the effect of wing

height is considerably greater at an angle of attack of 16° than at an angle of attack of 0°; thus, the probability of a rather strong effect of the wing on the forebody vortices is indicated. Figure 13 shows similar results for a Mach number of 1.4 but, in this case, the effects of angle of attack and wing height are somewhat less.

Effect of Directional Stability

This paper so far has dealt with methods of estimating wing or tail loads and comparisons of the vertical-tail loads encountered by various configurations for a given sideslip angle where it has been shown that for conventional configurations the vertical-tail load generally decreases with angle of attack. This reduction in tail load is, however, usually accompanied by a loss in directional stability which results in larger sideslip angles being encountered before the restoring moment necessary to counteract a given disturbance is developed. If, as in the usual case, the wing-fuselage combination is directionally unstable, then the increased sideslip angle would require more tail load to counteract the instability of the wing-fuselage combination and the total tail load would increase with angle of attack despite the fact that the tail load per unit sideslip decreased with angle of attack. However, if the wing-fuselage combination has neutral directional stability throughout the angle-of-attack range, the vertical-tail load would (if any variation of carryover with angle of attack is neglected) be independent of overall directional stability. Unfortunately, the instability of the wing-fuselage combination often increases with angle of attack (see ref. 4) and results in an increase in the vertical-tail loads encountered.

In view of the importance of the wing-fuselage directional stability characteristics, it is the purpose of this portion of the paper to illustrate the effect, on the vertical-tail load per unit restoring moment, of several wing-fuselage-configuration changes which appear attractive from stability considerations. Figures 14 to 16 illustrate the effect of stability by presenting, as a function of angle of attack, the vertical-tail-load coefficient for a unit yawing-moment coefficient of the complete configuration. Inasmuch as the only purpose of these figures is to indicate the effect of angle of attack and compare changes to a given configuration, and since the wing areas and spans and moment reference points are involved when making comparison between different configurations, the scales have been omitted. One such change is the use of narrow horizontal strips, or strakes, on the fuselage forebody to alleviate the loss in directional stability with angle of attack. (See ref. 5.) The effect that these strakes have on the measured load of the exposed vertical tail per unit yawing moment of the complete configuration are shown in figure 14 for a Mach number of 0.6. The strakes had spans equal to 10 percent of the maximum fuselage diameter and extended over the front 27 percent of the fuselage. The wing, which

was an aspect-ratio-4 delta wing that was clipped to an aspect-ratio-3 delta wing, differed from that in reference 5 and was selected because, for this wing, the strakes also provide a beneficial effect on the longitudinal stability characteristics. The strake-off condition is represented by the circular symbols and it can be observed that the tail load per unit yawing moment increases rapidly. With the strakes on (denoted by square symbols), however, the vertical-tail load decreases with angle of attack and is considerably less than that for the basic configuration. This rather large improvement is associated with a rather large reduction in the wing-fuselage instability at the higher angles of attack.

The effect of a change in fuselage-afterbody shape on the vertical-tail loads, as indicated by the tail contribution to side force, is presented in figure 15 for a Mach number of 2.0. Two configurations were investigated, one having a cylindrical afterbody and the other having an elliptical afterbody. Both fuselages had the same volume and the same longitudinal distribution of cross-sectional area. The elliptical afterbody is used as an attempt to reduce the fuselage instability over the entire angle-of-attack range while maintaining the necessary fuselage volume. The desired stability results were obtained and were accompanied by large reductions in the vertical-tail load for a given yawing moment. This is illustrated by the two variations with angle of attack. The solid curve represents the tail load for the configuration with the cylindrical afterbody, and the dashed curve represents the tail load for the elliptical afterbody configuration. The results indicate a large reduction in the tail load over the entire angle-of-attack range. This reduction in vertical-tail load results from the decrease in fuselage instability and a transfer of load from the tail to the fuselage afterbody which may, in many cases, be a desirable trade.

The effect of wing height on the vertical-tail loads at a Mach number of 2.9 is shown in figure 16. In this figure are shown the tail-load results (as indicated by the tail contribution to side force) for a configuration having a triangular wing of aspect ratio 4 in a low and high position as indicated in the upper left-hand sketch. From a comparison of these curves, it is observed that raising the wing from the low to high position effects a significant reduction in the tail loads, especially at large angles of attack. This reduction is caused by the influence of the wing pressure field acting on the body as indicated in the sketches on the right. As pointed out earlier, the normal force on the right panel is greater than that on the left panel, and thus a lateral pressure difference across the body is created by the wing. It is apparent that the difference in the positive pressures from the high wing causes an increase in the body side force and, hence, a stabilizing moment, but that the low wing produces a decrease in side force. The yawing moment induced by the low wing is small because of the short moment arm. Thus, the favorable effect of a high wing on the tail loads is the result of the improvement in the tail-off directional stability.

In the estimation of tail bending moments, however, the adverse effect of a high wing on the span loading, as previously pointed out, must be considered.

Effect of Lateral Control

One lateral-control device which has been found to induce rather large loads on the vertical tail is the differentially deflected horizontal tail. This device is illustrated in figure 17 where the measured normal force induced on the exposed portion of the vertical tail by a differentially deflected horizontal tail is presented (denoted by the square symbols) as a function of Mach number. The vertical-tail loads presented for the differentially deflected horizontal tail were obtained at zero sideslip with a total differential deflection of 30° (right down 15°, left up 15°). These deflections produce a positive roll and a wing-tip helix of approximately 0.07 throughout the Mach number range investigated. The vertical-tail load, which, of course, occurs only instantaneously as the roll control is applied, increases rather rapidly with Mach number and approximately doubles between a Mach number of 0.6 and 0.9. Although experimental results are not available for supersonic speeds, theoretical considerations of the effect of Mach number on the effectiveness of the horizontal and vertical tails and the amount of vertical-tail area within the Mach cone from the horizontal tail indicate that a rather rapid reduction in the vertical-tail load might be expected at supersonic speeds. It would appear, therefore, that the maximum loads induced on the vertical tail probably occur at high subsonic speeds. In order to give a better indication of the magnitude of the normal force induced on the vertical tail, the normal force encountered at an angle of sideslip of 6° with no differential deflection of the horizontal tail is presented by the circular symbols as a function of Mach number for comparison. This comparison indicates that at high subsonic speeds vertical-tail normal forces corresponding to an angle of sideslip of approximately 7° are induced by a total differential deflection of 30° of the horizontal tail.

Effects of Wing on Horizontal-Tail Loads

The influence of a wing on the horizontal-tail-load characteristics at two angles of attack is indicated in figures 18 and 19. In these figures are shown some recent wind-tunnel results for the induced flow field behind a rectangular wing at zero sideslip and the influence of this flow field on the load acting on a rectangular horizontal-tail surface. The local downwash and sidewash angles, dynamic pressure, and Mach number were surveyed in a vertical plane at the tail location. In these figures the variations in downwash and in the tail load are shown as functions of the tail height in wing chords. The tail normal force



C_N is computed from the average downwash, dynamic pressure, and Mach number existing at the tail plane. The results for an angle of attack of 6° (fig. 18) show that, when the tail is located between the two trailing-edge waves, the average downwash is small, that is, $1 - \frac{\epsilon'}{\alpha}$ is nearly 1, and the loss in tail load is small, that is, the lift ratio is close to 1. The effect of the viscous wake from the blunt trailing edge of the wing is evidenced by the variations in this region directly behind the trailing edge. If the tail surface passes through either of the trailing-edge waves, a sudden downwash occurs which actually reverses the load on the tail, a situation obviously to be avoided. As the tail is raised farther above the wing plane, the downwash diminishes to zero and the tail load returns to its free-stream value at the point for which the tail is located at the shock wave from the wing leading edge. Similarly, the curves for negative values of tail height would be expected to return to free-stream conditions when the tail passes below the lower shock wave from the wing leading edge. The close agreement of the downwash and tail-load curves is an indication of the small deviations in the average dynamic pressure and Mach number in the wake from their free-stream values at this angle of attack. The results for an angle of attack of 20° (fig. 19) also show a sudden downwash and loss in tail load as the tail moves through the upper wave from the wing trailing edge. However, it is noted that, in contrast to the results for an angle of attack of 6°, the tail-load curves do not follow the downwash curves in the rest of the wake, and despite the increase in downwash below the wing, the tail load is preserved. This effect results from changes in dynamic pressure and Mach number in the wing wake at this angle of attack and demonstrates the necessity of accounting for these changes in the prediction of loads on both horizontal- and vertical-tail surfaces behind a wing at large angles of attack.

CONCLUDING REMARKS

The results of wind-tunnel tests have shown that variations in the loads and moments on a lifting surface in the presence of a body can exhibit large nonlinearities at combined angles of attack and sideslip which cannot be predicted by low-angle theory. A relatively simple, but general, theoretical method for calculating these loads under such conditions has been described in which both the effects of leading-edge sweepback and of the forebody vortex flow are taken into account. This calculative method, however, requires a knowledge of the initial positions of the forebody vortices. It was found that the results of this theoretical method were in good agreement with experiment. Results have been presented which show the effects of forebody length and panel-panel interference on the load characteristics.



It was demonstrated that a simple application of slender-body theory could be used successfully to predict the side loads contributed by a vertical tail on a wide variety of wing-body-tail combinations at small angles of attack and at both subsonic and supersonic Mach numbers.

The three configuration changes described which reduced the vertical-tail loads required for a given yawing moment of the configuration at large angles of attack were the addition of horizontal strakes along the forebody, the change in the afterbody cross-sectional shape from circular to elliptical in which the major axis is vertical, and the movement of the wing from a low to a high position.

[redacted]

REFERENCES

1. Kuhn, Richard E., Hallissy, Joseph M., Jr., and Stone, Ralph W., Jr.: A Discussion of Recent Wind-Tunnel Studies Related to the Problem of Estimating Vertical- and Horizontal-Tail Loads. NACA RM L55E16a, 1955.

2. Nielsen, Jack N., and Kaattari, George E.: Method for Estimating Lift Interference of Wing-Body Combination at Supersonic Speeds. NACA RM A51J04, 1951.

3. Jorgensen, Leland H., and Perkins, Edward W.: Investigation of Some Wake Vortex Characteristics of an Inclined Ogive-Cylinder Body at Mach Number 1.98. NACA RM A55E31, 1955.

4. Polhamus, Edward C., and Hallissy, Joseph M., Jr.: Effect of Airplane Configuration on Static Stability at Subsonic and Transonic Speeds. NACA RM L56A09a, 1956.

5. Sleeman, William C., Jr.: Investigation at High Subsonic Speeds of the Effects of Various Horizontal Fuselage Forebody Fins on the Directional and Longitudinal Stability of a Complete Model Having a 45° Sweptback Wing. NACA RM L56J25, 1957.

[redacted]

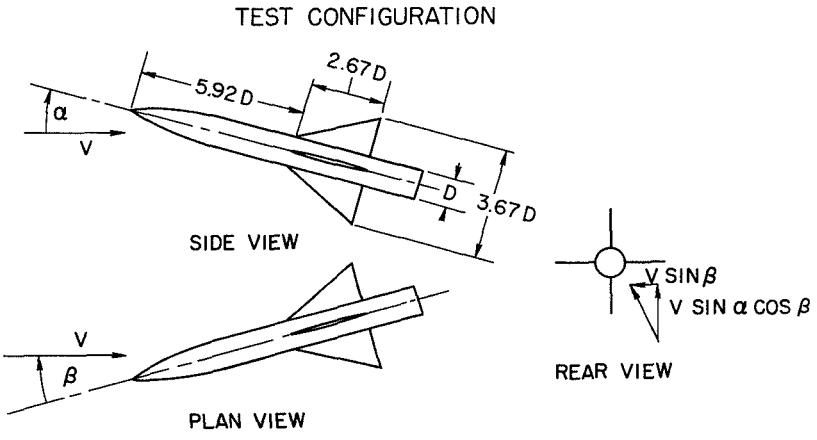


Figure 1

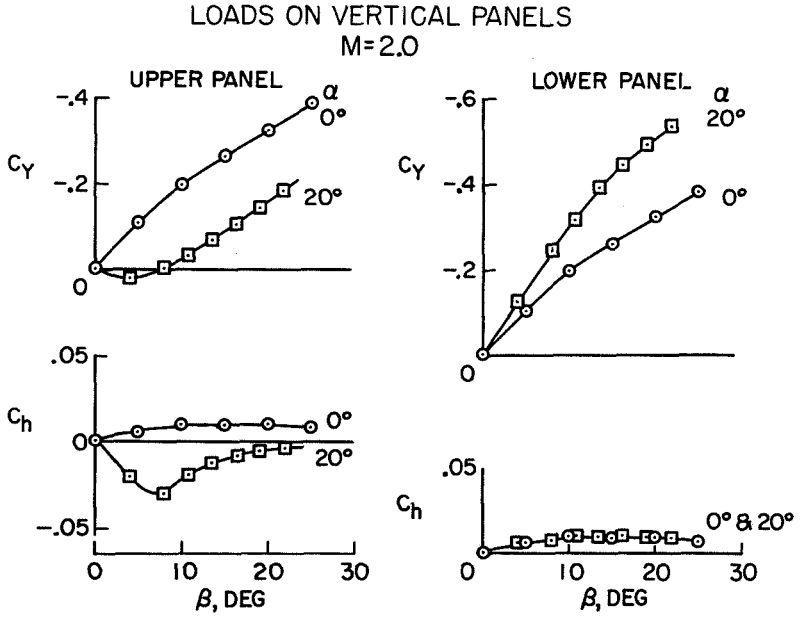


Figure 2

BENDING MOMENTS ON VERTICAL-TAIL PANELS
M = 2.0

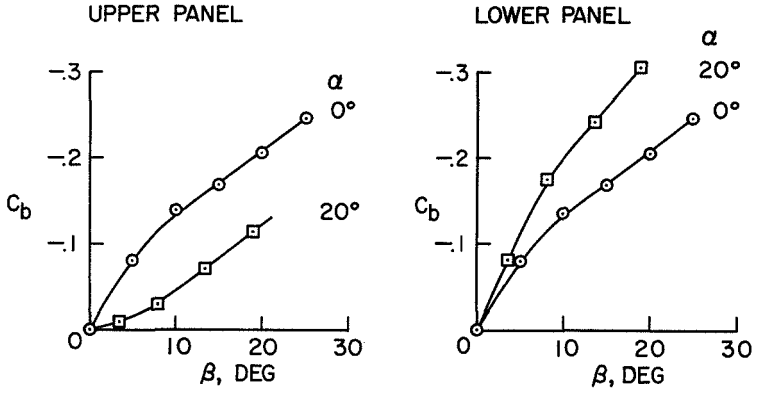


Figure 3

EFFECT OF ANGLE OF ATTACK ON LOADING
DUE TO SIDESLIP

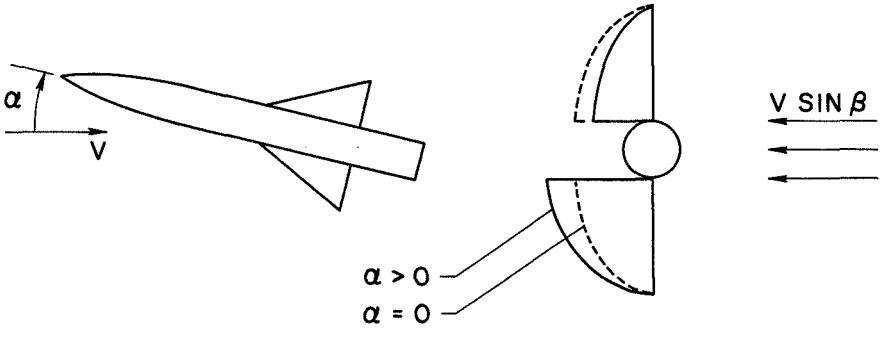


Figure 4

EFFECT OF FOREBODY VORTICES

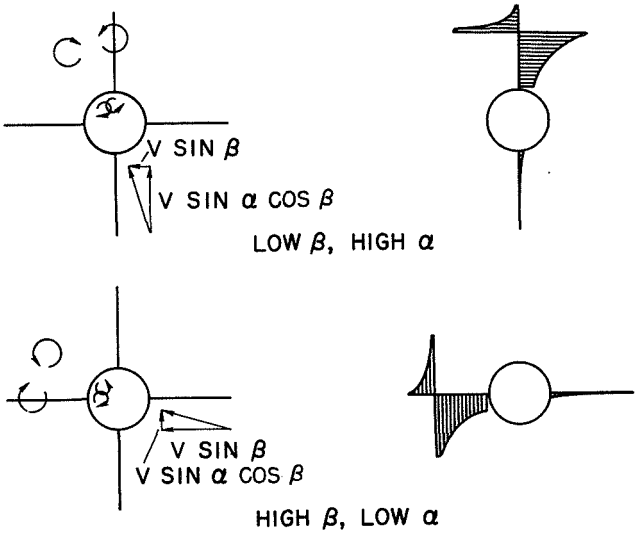
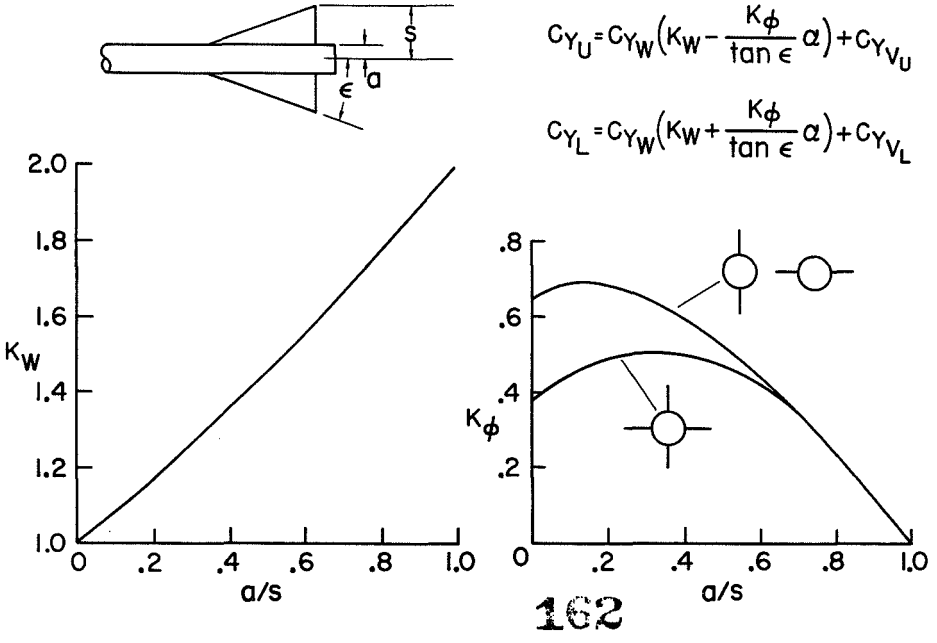


Figure 5

PANEL FORCES FOR COMBINED α AND β



162

Figure 6

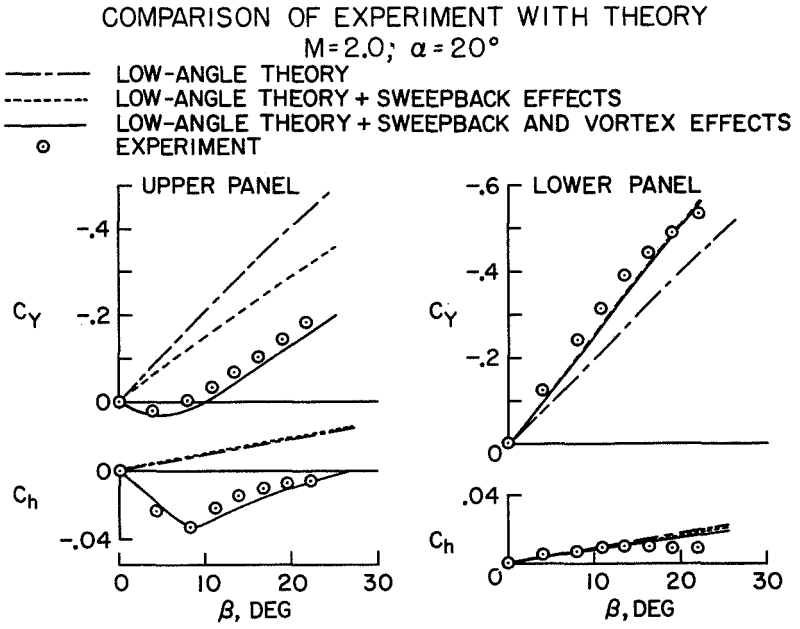
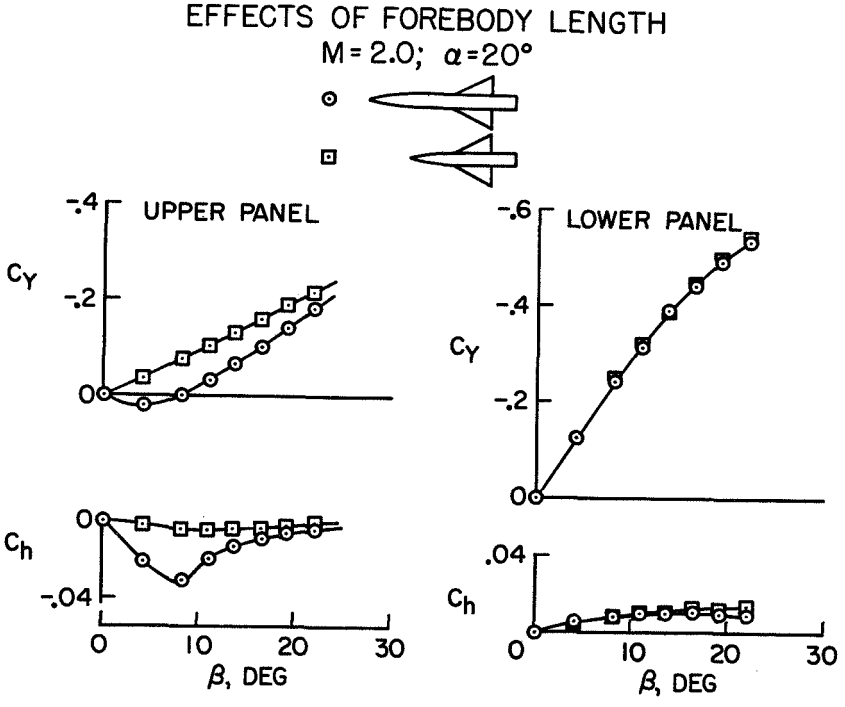


Figure 7



163

Figure 8

EFFECTS OF PANEL-PANEL INTERFERENCE
M=2.0; α=20°

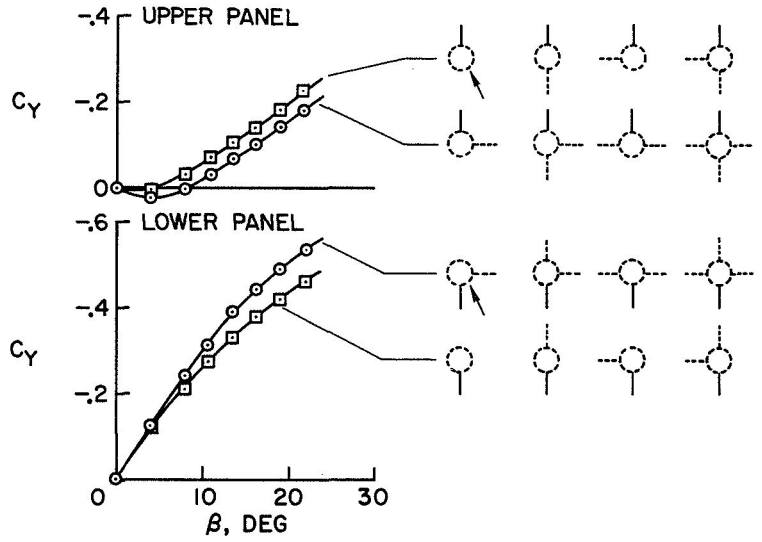


Figure 9

CONFIGURATIONS STUDIED

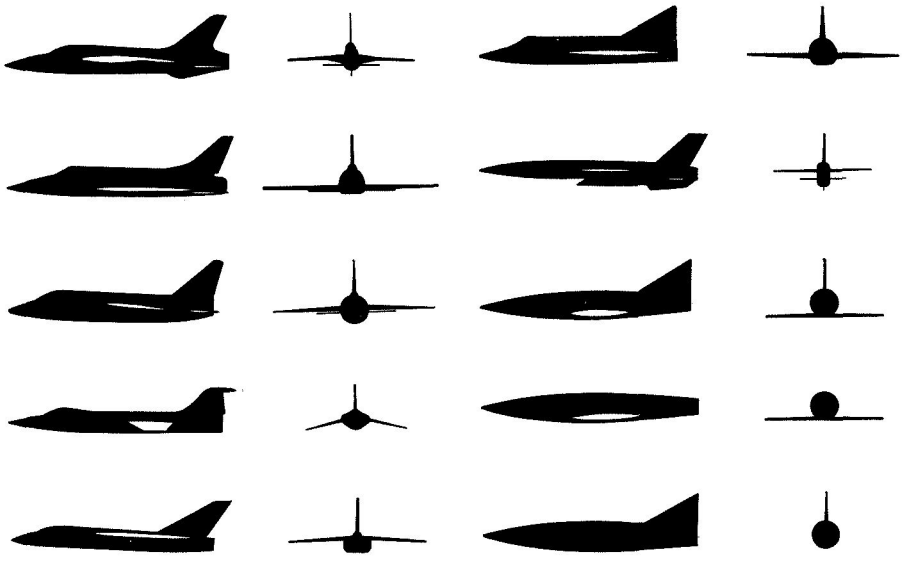


Figure 10

SIDE-LOAD CORRELATION FOR SMALL ANGLE OF ATTACK

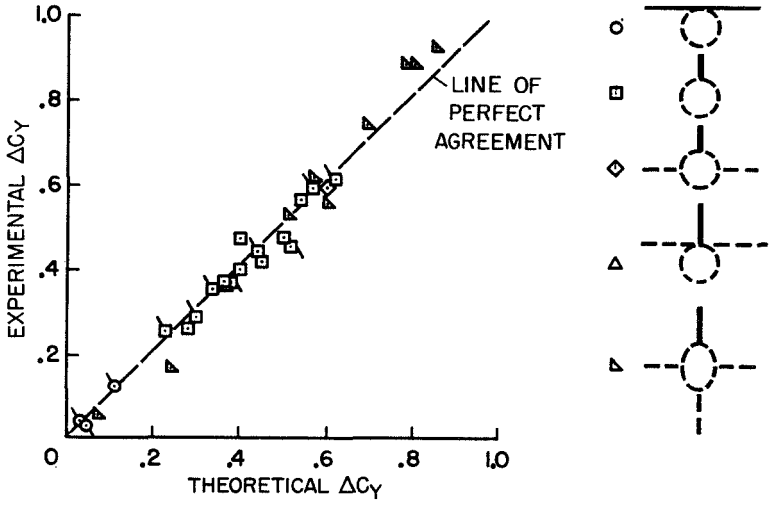
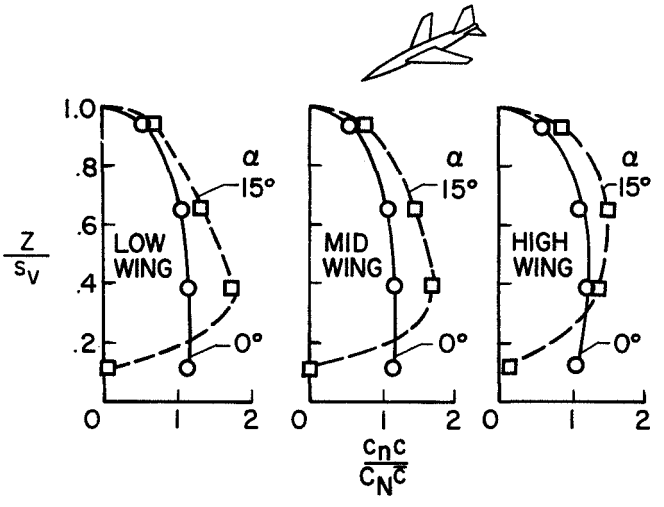


Figure 11

EFFECT OF WING HEIGHT ON VERTICAL-TAIL LOADING

M= 0.8 ; β =5°



165

Figure 12

EFFECT OF WING HEIGHT ON VERTICAL-TAIL LOADING

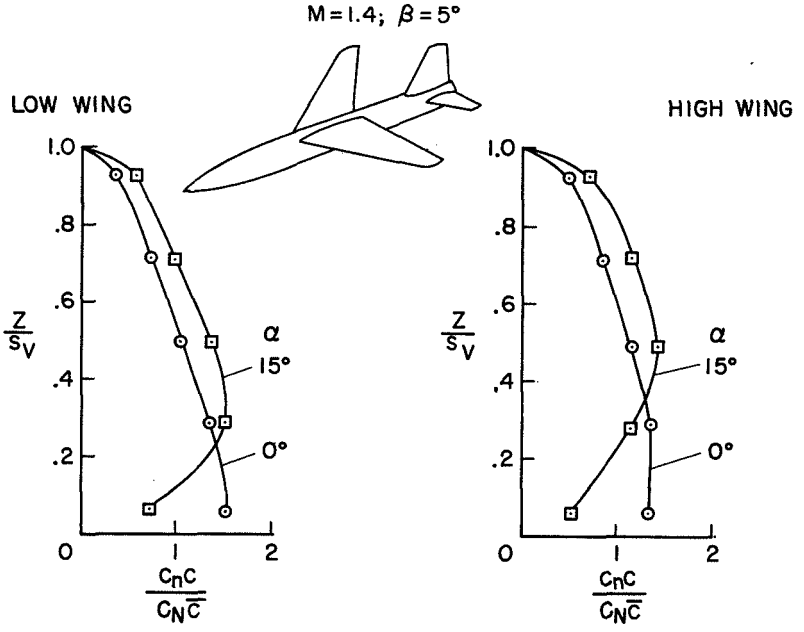
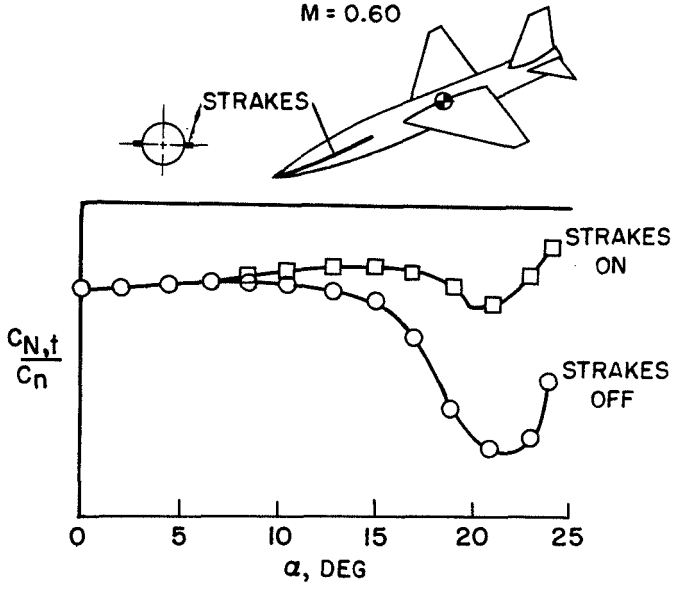


Figure 13

EFFECT OF FUSELAGE STRAKES ON VERTICAL-TAIL LOAD



166

Figure 14

EFFECT OF AFTERBODY SHAPE ON VERTICAL-TAIL LOAD
M=2.0

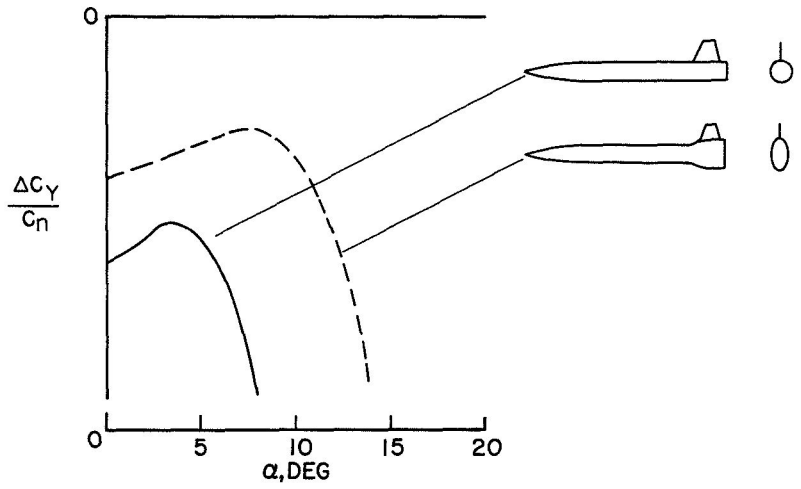


Figure 15

EFFECT OF WING HEIGHT ON SIDE FORCE DUE TO VERTICAL TAIL M=2.9

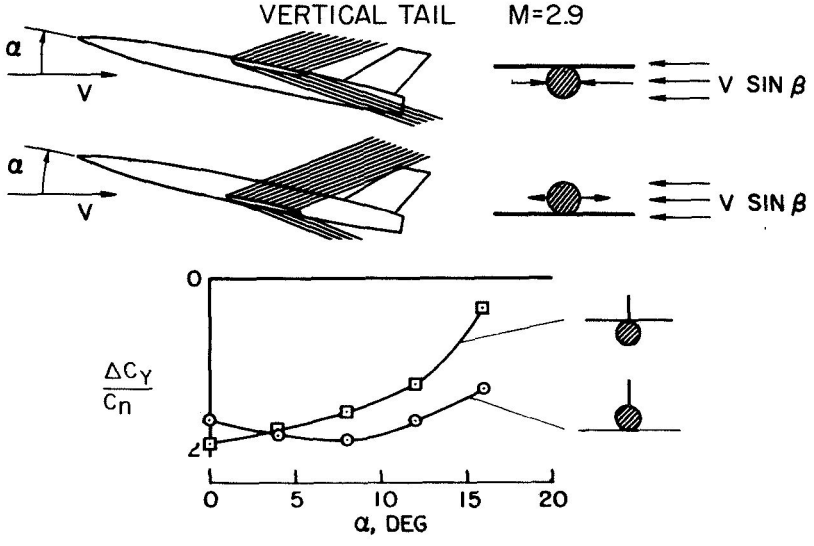


Figure 16

EFFECT OF TAIL ROLL CONTROL
ON VERTICAL-TAIL LOAD

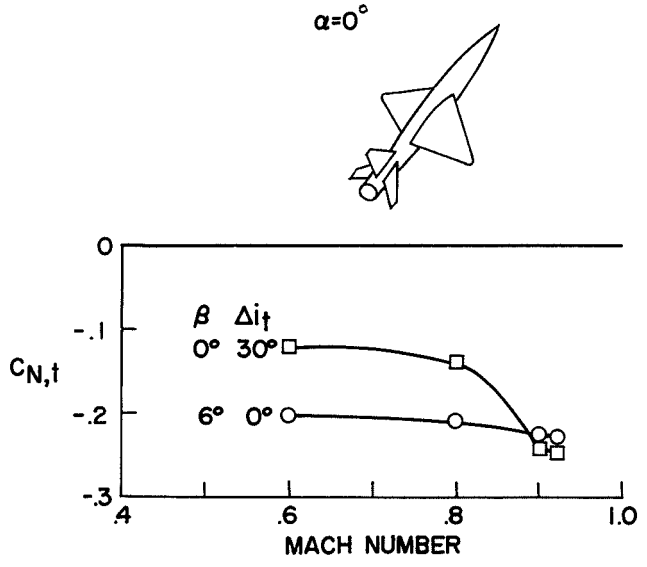
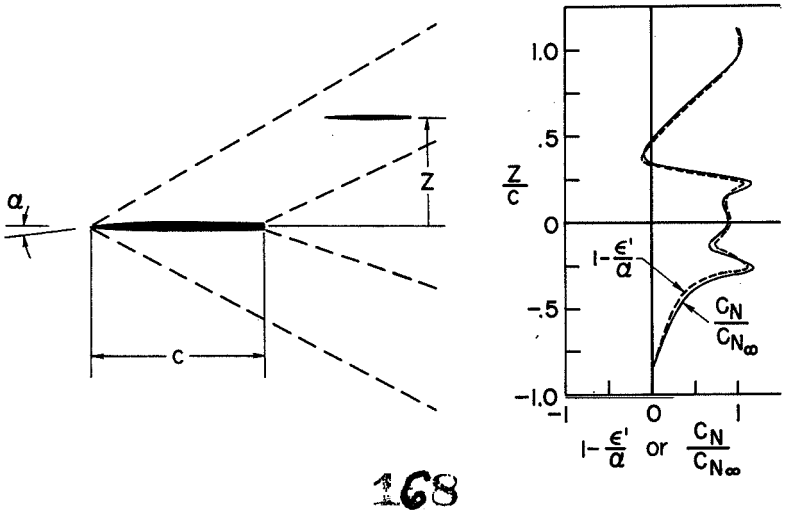


Figure 17

EFFECT OF WING ON TAIL LOADS
M=2.46; β=0°; α=6°



168

Figure 18

EFFECT OF WING ON TAIL LOADS
M=2.46; β=0°; α=20°

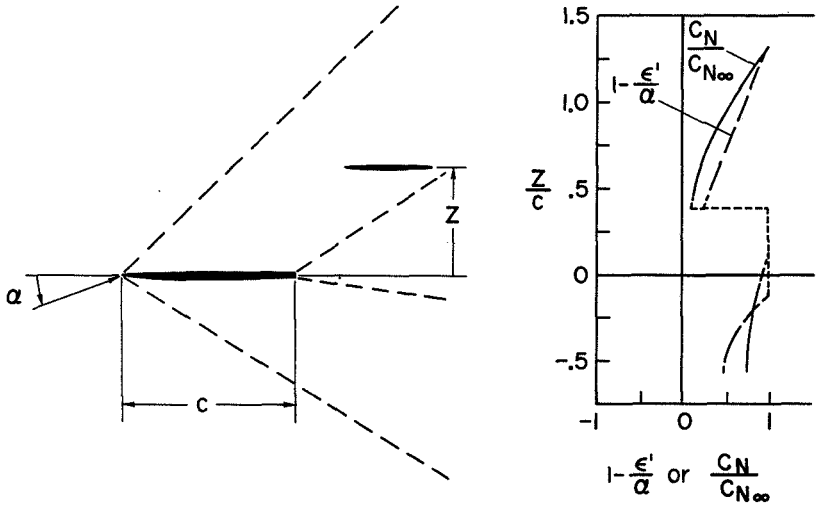


Figure 19

N71-75392

LOADS DUE TO CONTROLS AT TRANSONIC AND LOW SUPERSONIC SPEEDS

By F. E. West, Jr., and K. R. Czarnecki

Langley Aeronautical Laboratory

SUMMARY

Some results of recent experimental investigations at supersonic and transonic speeds are presented to show the present status in the estimation of load distributions on controls and adjacent wing surfaces resulting from the deflection of flap controls and spoiler controls. The results indicate that the development of methods for predicting loads associated with controls has not kept pace with the acquisition of experimental data. At low supersonic speeds sweeping the hinge line induces strong three-dimensional-flow characteristics which cannot be treated by the simplified methods previously developed for controls without sweep. At transonic speeds the estimation of loads associated with controls must usually be dependent upon experimental information inasmuch as the latest attempts to predict chordwise and spanwise loadings have met with only limited success.

INTRODUCTION

Two problems must be considered in the estimation of loads associated with controls: the direct loads on the controls themselves, and those loads induced on adjacent surfaces. In the last few years a fairly large amount of experimental information has been obtained on these types of loads. Some success in the prediction of these loads has also been realized at supersonic speeds, but at transonic speeds success in the prediction of these loads has been much more limited.

In this paper some results of the most recent investigations at supersonic speeds pertaining to flaps with a swept hinge line and to spoilers are discussed. However, most of the paper pertains to transonic results, since the transonic range is where the loads problems of most concern still appear to exist. An attempt is made to indicate the present status of knowledge in the estimation of loads due to controls for this speed range. The results at supersonic speeds were obtained in the Langley 4- by 4-foot supersonic pressure tunnel, and the results at transonic speeds were obtained in the Langley 16-foot transonic tunnel. In the tests at

supersonic speeds transition was fixed near the leading edge by strips of carborundum grains, while in the tests at transonic speeds the Reynolds numbers were always sufficiently high to insure a turbulent boundary layer over most of the wing chord.

SYMBOLS

ΔC_p	increment in pressure coefficient due to control deflection or projection
$\Delta C_{p,R}$	resultant difference in pressure coefficients between upper and lower surfaces due to control deflection
$\frac{\Delta c_n c}{\Delta C_N c_{AV}}$	normalized section normal-force loading parameter due to control deflection
Δc_n	section normal-force coefficient due to control deflection
ΔC_N	wing panel normal-force coefficient due to control deflection (based on semispan wing area extended to fuselage center line)
A	aspect ratio
HL	flap hinge line
b	span
c	local chord
c_{AV}	average chord
M_∞	Mach number
x	chordwise distance
y	spanwise distance
α	angle of attack
δ_a	angle of aileron deflection
δ_d	deflector projection
δ_s	spoiler projection

$\Lambda_{c/4}$ sweep angle at quarter-chord line

Λ_{HL} sweep angle of flap hinge line

Subscripts:

s spoiler

d deflector

RESULTS AND DISCUSSION

Supersonic Speeds

At the supersonic speeds simple configurations were initially studied, such as unswept-wing and delta-wing configurations, and considerable success was attained in predicting the loadings, except possibly for the high-angle-of-attack, high-control-deflection case. (See ref. 1.) Now configurations are being investigated for which more difficulty is expected in the prediction of loads; for example, a sweptback-wing model with a swept-hinge-line flap was recently investigated, and some of the results are presented in figure 1.

Effects of hinge-line sweep.- Figure 1 shows the effect of flap hinge-line sweep and wing sweep at a Mach number of 1.61 on the chordwise loading due to flap deflection. On the vertical scale of the plots in this figure are shown the changes in pressure coefficient on the upper and lower surfaces that are due to flap deflection. These values are plotted against fraction of the local wing chord. The curves in these plots represent loadings at the various spanwise stations indicated on the model sketches. The plot on the left represents the unswept-hinge-line configuration for which it was previously shown (ref. 1) that the flap load as shown behind the hinge line is about 0.7 of the value predicted by linear theory if the carryover on the wing ahead of the hinge line is not too large. It was also previously indicated in reference 1 that the results for this unswept-hinge-line case can be used for prediction of control loadings at higher Mach numbers, perhaps up to Mach numbers of 3.5 or 4.0. For this case there was very little effect of spanwise location on the flap loading or on the wing carryover load as shown ahead of the hinge line. There was no carryover load on the wing upper surface.

In figure 1 in the pressure plot for the swept-hinge-line model it can be seen that spanwise location had a considerable effect on the loading, particularly on the carryover load ahead of the hinge line.

Both angle of attack and control deflection are more important factors for this configuration than for the unswept-hinge-line configuration. For the swept case the complexities of three-dimensional flow are of great concern. Also the effect of sweep may have reduced the local Mach numbers normal to the flap hinge line sufficiently to cause complications of mixed subsonic and supersonic flows such as are typical in the transonic range. At present no reliable general procedure for estimating flap or carryover loads for the swept-hinge-line case is available. There are indications that a solution at higher Mach numbers will be simpler. For example, it was shown in a paper on loads at hypersonic speeds (ref. 2) that the flow over configurations of this sweep may generally be regarded as two-dimensional.

Prediction of spoiler loads on three-dimensional wings.- In addition to the theoretical approach to the problem of loads due to controls, another approach which is sometimes useful is to apply data for simple configurations to more complex configurations. For supersonic speeds pressure data are available on a flat plate with an unswept spoiler (ref. 3) and also on a three-dimensional wing with a similar unswept spoiler (ref. 4). A preliminary evaluation of this approach was made, and the results are shown in figure 2.

The top part of figure 2 shows the wing and its spoiler, which had a height of 5 percent of the mean aerodynamic chord. The lower part of figure 2 shows ΔC_p, which represents the change in loading on the upper surface due to a spoiler deflection, plotted against chordwise distance from the spoiler in terms of spoiler height. The lower-surface pressures were not affected by spoiler deflection. The symbols represent the wing data for angles of attack of 0° and 12° which were obtained at the spanwise station indicated in the sketch of the wing. Spanwise location had no effects on these data, except near the wing tip. The solid lines represent the flat-plate data which, in this case, are two-dimensional and which were obtained at the same Mach number as the wing data. For the 12° angle-of-attack case, however, it was necessary to adjust the flat-plate data by a method developed by Lord and Czarnecki in reference 4. In simple terms, this method adjusts the data by taking into consideration the changes in Mach number on the basic wing which are due to angle of attack.

The agreement between the wing data and the adjusted flat-plate data is generally very good. In other words, it appears that results for a flat plate can be used to predict the load, including the effects of angle of attack, on a wing where the flow is approximately two-dimensional. It is also believed that there may be a possibility of obtaining agreement in cases where the flow over the wing tends to be more three-dimensional, although sufficient data to test this belief are lacking. For any case, however, the flow over the wing must not be stalled, and there must be no sharp changes in the pressure distribution on the wing without the spoiler.

Transonic Speeds

Estimation of chordwise loadings.- For transonic speeds the problems of predicting loads associated with controls are generally more difficult than for supersonic speeds. One of the most difficult problems is the prediction of the chordwise loads due to control deflection. Some idea of the present status of this problem for a typical swept-wing configuration is shown in figure 3.

In the top part of figure 3 is shown a swept-wing configuration which has an inboard flap. In the plots at the bottom of the figure, $\Delta C_{p,R}$ represents the total change in wing and flap loading due to flap deflection and is shown on the vertical scales. These coefficients are plotted against fraction of the local wing chord as the abscissa. The solid lines in these plots represent experimental pressure data which were obtained at a Mach number of 0.98 for an angle of attack of 0° and a flap deflection of -15°. The dashed line represents calculations from a lifting-surface theory for a Mach number of 1.0. The theory was very recently developed for the flap-deflected case by Keith C. Harder and E. B. Klunker of the Langley Theoretical Mechanics Division, and these unpublished results are based on the slender-wing theory by Jones (ref. 5) as extended to the case with trailing-edge sweep by Mirels (ref. 6).

This theory predicts the chordwise loading fairly well at the inboard station; however, at the outboard station the theoretically determined loading is located forward of most of the experimentally determined loading. Perhaps the main reason for this difference in load distribution is that in the theoretical case the shocks and Mach lines extend normal to the free stream, whereas in the experimental case it is known that the shocks and Mach lines are swept. Better agreement could probably be obtained for a configuration having a lower aspect ratio; however, since the theory is very new, no attempt has been made to define its range of application.

Other theoretical approaches to the problem of chordwise loading at transonic speeds such as the use of the hodograph technique are also being considered. In the meantime, some experimental loads data also have been obtained for a fairly large range of thin-wing (thickness-to-chord ratios of 0.03 to 0.06) configurations. These configurations are indicated in figure 4.

New experimental loads data.- The upper part of figure 4 shows configurations having flap controls. The configurations shown in the bottom part of the figure have spoiler controls. The sketch on the lower right shows an enlarged cross section of the spoiler-slot-deflector control. For some of these configurations only force data were obtained, including the forces and moments on the controls; however, for most of the configurations pressures were obtained over both the wings and controls. All of

these configurations were investigated at angles of attack up to about 23° with generally a fairly large range of control deflection. The maximum Mach number was usually 1.03. The results for the configuration at the upper left are the only results that have so far been reported (see ref. 7).

An attempt has been made to use the data for these various configurations to develop empirical methods for estimating chordwise load distribution due to control deflection; however, little success was realized in deriving any simple correlations for even the loading over flaps. Thus, for the chordwise pressures or loadings, experience indicates that, in general, recourse must be made to data for configurations that approximate the configuration being designed.

Fortunately, for transonic speeds the prediction of spanwise load distributions due to control deflection is not always as difficult as the prediction of chordwise loadings. Studies indicate that the shape of these span-load distributions is essentially unaffected by Mach number in the transonic range for some configurations. This lack of Mach number effect suggests the possibility of using subsonic theory for prediction. Figures 5 to 7 show results of a study made of this possibility and also of the effects of Mach number for some of the configurations shown in figure 4. Most of these results are for spoiler controls since such controls are of considerable interest, and fewer loads data exist for spoiler controls than for flap controls.

Flap and spoiler at wing trailing edge.- Figure 5 which pertains to spanwise load distribution indicates the span loadings for an inboard flap configuration and an inboard spoiler configuration. The load distributions shown in the top part of the figure are due to the deflection of the inboard flap, and the load distributions shown in the bottom part of the figure are due to the deflection of the inboard trailing-edge spoiler. Both of these controls were tested on the same swept-wing—body combination. On the vertical scale is shown the weighted section normal-force coefficient due to control deflection divided by the wing-panel normal-force coefficient due to control deflection. The coefficients are plotted against fraction of wing semispan. The curves show the incremental load distribution over the wing and control, but because the curves have been normalized the actual magnitude of the load, of course, is not indicated. The experimentally determined data are indicated by the symbols and are presented for an angle of attack of 4°.

For both configurations these symbols show that increasing the Mach number from 0.80 to 0.98 had very little effect on the incremental load distribution. These results are representative of those found to exist for angles of attack from about 0° to 6°. Because the inboard end of the flap was actually slightly outboard of the fuselage, the loadings for the flap configurations show a large decrease in this region.

The solid lines in figure 5 represent calculations for a Mach number of 0.80 which are based on a subsonic theory as presented by DeYoung (ref. 8) in which the inboard flap and the inboard trailing-edge spoiler were differentially deflected. This theory was devised to apply to flap configurations as long as flow separation does not occur on the wing. Since no theory is available for the spoiler case, calculations for a flap at an arbitrary deflection and with the same span as the trailing-edge spoiler are compared with the spoiler results. For the flap configuration the calculations show very good agreement with the experimental data; however, for the spoiler configuration the agreement, as would be expected, is not as good.

For outboard controls larger effects than those shown in figure 5 can probably be expected. It has been previously shown (ref. 9) that Mach number has fairly large effects on the lateral position of the center of load due to the deflection of outboard flaps; thus, it appears that subsonic theory cannot generally be extrapolated to as high Mach numbers for the outboard-control case as for the inboard-control case.

Spoiler controls ahead of wing trailing edge.- Figure 6 shows spanwise load distribution for a wing with spoiler controls located ahead of the trailing edge. These controls were more highly swept than the spoiler control shown in figure 5 and extend over more of the wing semispan. The distributions shown in the top portion of figure 6 are due to the deflection of a flap spoiler. The distributions shown in the lower part of figure 6 are due to the deflection of a spoiler-slot-deflector on the same model. This type of control has been of particular interest because of its good effectiveness at high angles of attack.

The results of experimental investigations represented by the symbols in figure 6 show a somewhat larger effect of Mach number than is shown in figure 5. An increase in Mach number from 0.80 to 1.00 caused an outboard shift in the center of additional load for both configurations. These results are typical of results found to exist over a range of angle of attack from about 0° to 6°. The experimental span-load distributions for the spoiler-slot-deflector configuration are considerably different from those for the spoiler configuration. These differences are mainly due to the influence of the deflector on the flow. The solid lines shown here represent subsonic calculations similar to those shown in figure 5 except these calculations are the average of curves from references 8 and 10 since the controls were restricted to one wing panel. It is seen that the agreement between the calculations and experiment in figure 6 is about the same as that shown for the spoiler configuration in figure 5.

Loads at a high angle of attack.- Thus far in the discussion of spanwise load distributions at transonic speeds, the high-angle-of-attack case has not been considered. In figure 7, therefore, are shown distributions at a high angle of attack for the spoiler-slot-deflector

configuration shown in figure 6. Subsonic calculations for a Mach number of 0.60 are indicated by the solid line. The experimental data are indicated by the dashed lines.

The results for this particular configuration indicate that Mach number has a large effect and that theory no longer predicts the shape of the loadings. These effects are mainly the result of flow separation in the region of the wing tip; therefore, as is well known, when separated flow has a large effect on loading then recourse must be made to experimental data for loads information.

Loads on control surfaces.- Now that the discussion in this paper on the recent overall wing-loads information has been concluded, the control loads on the flap spoiler and the spoiler-slot-deflector are considered. Some of these control loads are shown in figure 8.

In the lower part of figure 8 is presented a comparison of the spanwise load distribution for the spoiler and deflector components of these controls. On the vertical scale is plotted the weighted control section normal-force coefficient divided by the total control normal-force coefficient. These coefficients are plotted against fraction of the wing semispan. The span-load distributions are for an angle of attack of 0° and a Mach number of 1.00. Other unpublished data for the same configurations show very little effect of Mach number for Mach numbers from 0.60 to 1.03. The results show that the type of control component has very little effect on the distributions; therefore, these distributions appear to be primarily affected by the wing geometry and the control location.

In the upper right part of figure 8 is shown the variation of total control normal-force coefficient with angle of attack for the spoiler and deflector components of the spoiler-slot-deflector. The solid and dashed lines indicate the effect of increasing Mach number from 0.60 to 1.00. For both the spoiler and deflector components this Mach number effect is not very large over the range of angle of attack. The normal-force coefficients for the spoiler portion of the control decrease in magnitude with increasing angle of attack, whereas those for the deflector are not affected. The data in the present case and other available data (ref. 11) indicate that for large control deflections tests need be made only at low angles of attack in order to establish the maximum control loads.

CONCLUDING REMARKS

The results of this study show that success in predicting loads associated with controls has not kept pace with the acquisition of

experimental data. At supersonic speeds data for loads are now available for swept-flap configurations, but methods of prediction for these cases must still be developed. At transonic speeds more experimental data are available, but only limited success in correlating experimental data with theory has been realized.

[redacted]

REFERENCES

1. Czarnecki, K. R., and Lord, Douglas R.: Simplified Procedures for Estimating Flap-Control Loads at Supersonic Speeds. NACA RM L55E12, 1955.

2. Henderson, Arthur, Jr., and Bertram, Mitchel H.: Factors Affecting Loads at Hypersonic Speeds. (Prospective NACA paper.)

3. Lord, Douglas R., and Czarnecki, K. R.: Aerodynamic Loadings Associated With Swept and Unswept Spoilers on a Flat Plate at Mach Numbers of 1.61 and 2.01. NACA RM L55L12, 1956.

4. Lord, Douglas R., and Czarnecki, K. R.: Pressure Distributions and Aerodynamic Characteristics of Several Spoiler-Type Controls on a Trapezoidal Wing at Mach Numbers of 1.61 and 2.01. NACA RM L56E22, 1956.

5. Jones, Robert T.: Properties of Low-Aspect-Ratio Pointed Wings at Speeds Below and Above the Speed of Sound. NACA Rep. 835, 1946. (Supersedes NACA TN 1032.)

6. Mirels, Harold: Aerodynamics of Slender Wings and Wing-Body Combinations Having Swept Trailing Edges. NACA TN 3105, 1954.

7. Hieser, Gerald: Transonic Investigation of the Effectiveness and Loading Characteristics of a Flap-Type Aileron With and Without Paddle Balances on an Unswept-Wing—Fuselage Model. NACA RM L56B02, 1956.

8. DeYoung, John: Theoretical Antisymmetric Span Loading for Wings of Arbitrary Plan Form at Subsonic Speeds. NACA Rep. 1056, 1951. (Supersedes NACA TN 2140.)

9. Hammond, Alexander D., and West, F. E., Jr.: Loads Due to Flaps and Spoilers on Sweptback Wings at Subsonic and Transonic Speeds. NACA RM L53D29a, 1953.

10. DeYoung, John: Theoretical Symmetric Span Loading Due to Flap Deflection for Wings of Arbitrary Plan Form at Subsonic Speeds. NACA Rep. 1071, 1952. (Supersedes NACA TN 2278.)

11. Hammond, Alexander D.: Low-Speed Pressure Distribution Investigation of a Spoiler and a Spoiler-Slot-Deflector on a 30° Sweptback Wing-Fuselage Model Having an Aspect Ratio of 3, a Taper Ratio of 0.5, and NACA 65A004 Airfoil Section. NACA RM L55I29, 1956.

[redacted]

EFFECT OF HINGE-LINE SWEEP AT $M_\infty = 1.61$

$\alpha = 6°$; $\delta_a = 20°$; $A = 3.1$

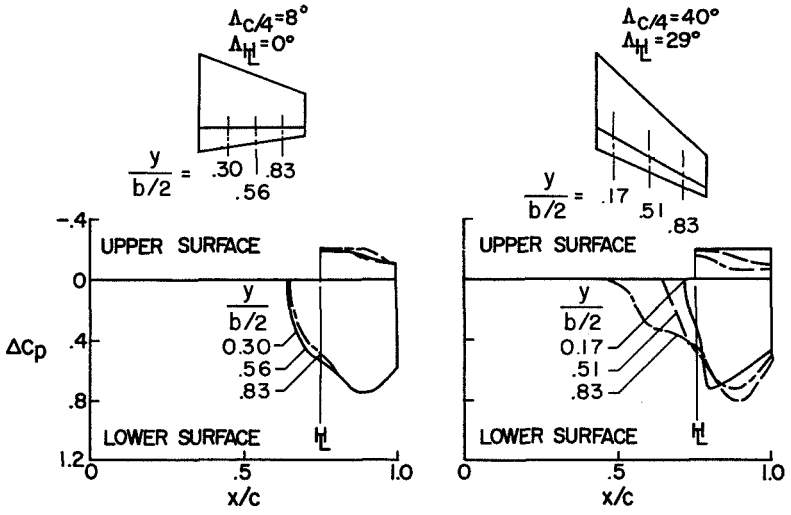


Figure 1

CHORDWISE LOADING DUE TO SPOILER AT $M_\infty = 1.61$

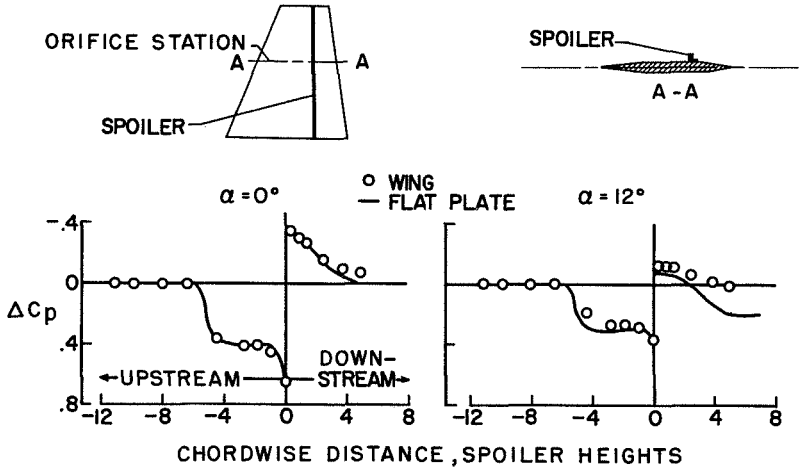


Figure 2

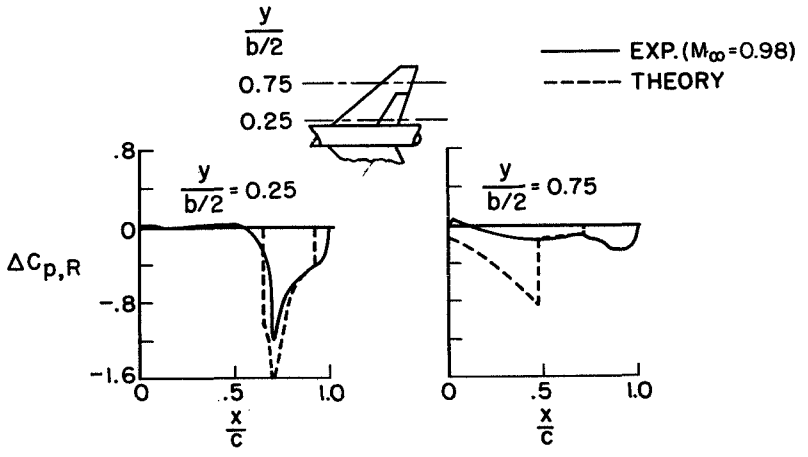


Figure 3

RECENT TRANSONIC LOAD STUDIES

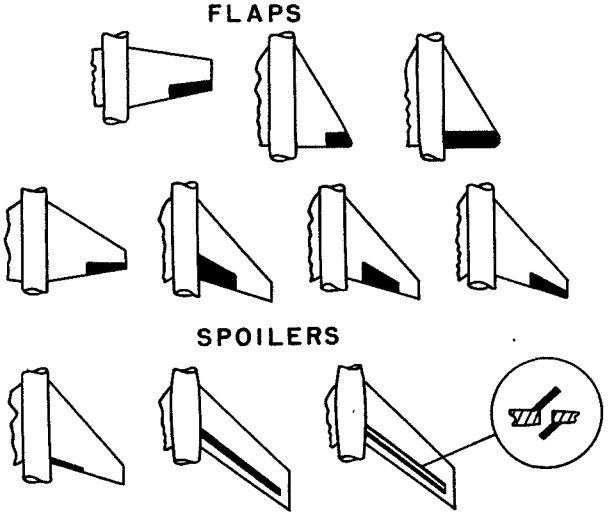


Figure 4

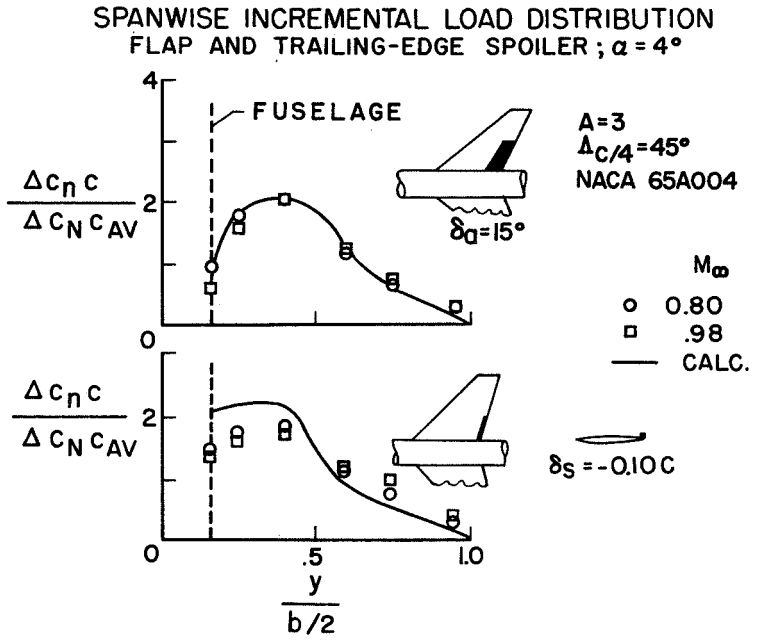
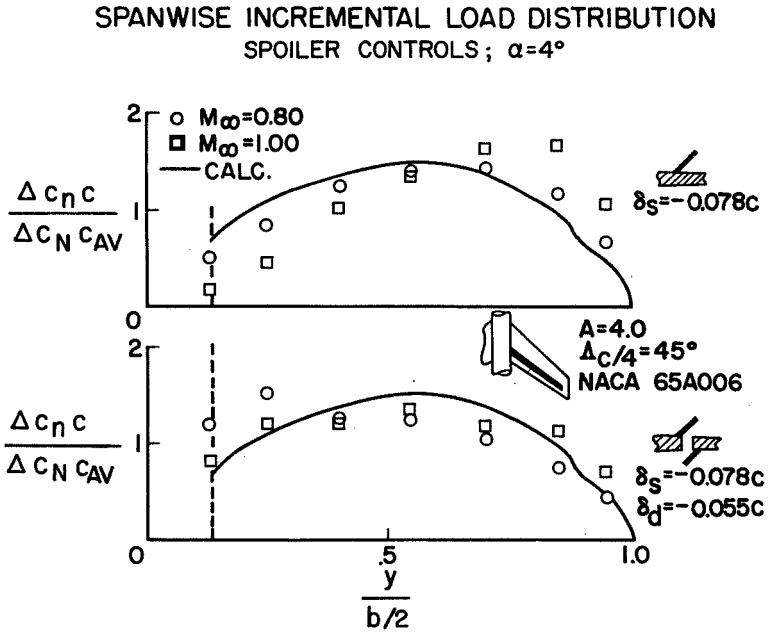


Figure 5



182

Figure 6

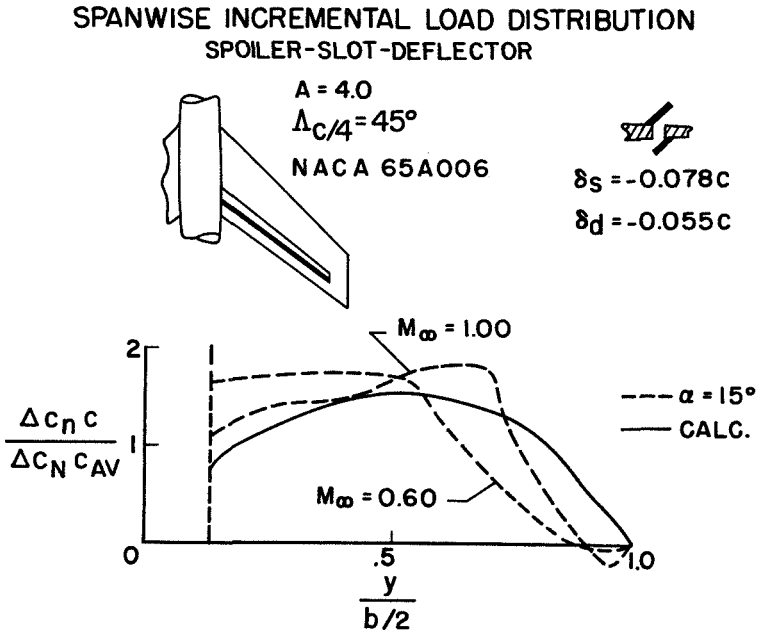
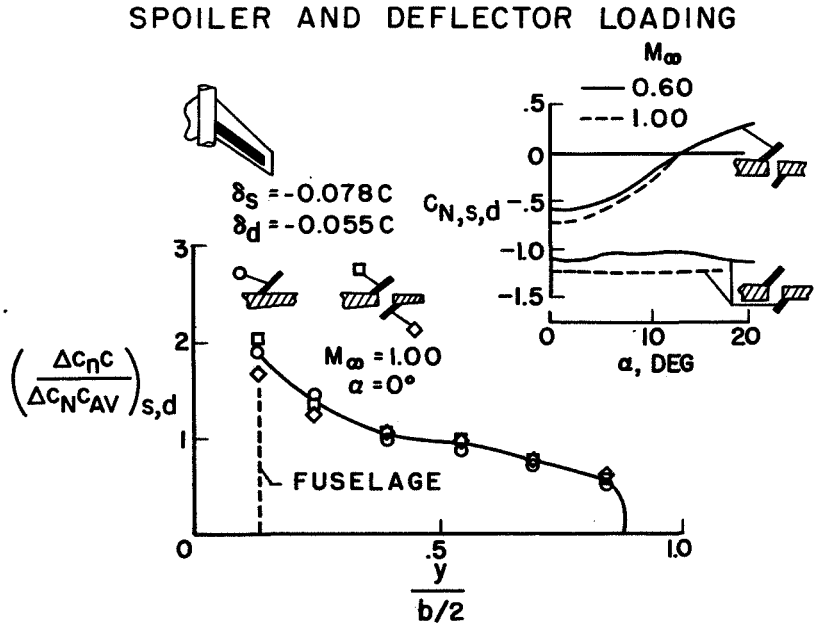


Figure 7



183

Figure 8

[redacted] N71-75393

EXPERIMENTAL RESULTS ON WING LOADS DUE TO BLASTS

By Harold B. Pierce and Donald R. McFarland

Langley Aeronautical Laboratory

SUMMARY

Recent data obtained in the investigation of the loads caused by blast-induced gusts are presented. These data indicate that, when the gusts cause angle-of-attack changes to a point well beyond the stall angle, a load peak travels along the chord which is caused by a vortex formed by the diffraction of the blast wave around the airfoil. When the angle caused by the gust is below the stall angle of the airfoil, it appears that the loading may be calculated by existing unsteady-lift theory for a wide range of the blast position with respect to the wing.

INTRODUCTION

This paper is concerned primarily with some recent information on the traveling-load peak which was found to occur when an intense blast-induced gust increases the angle of attack of the wing to a point well above the steady-flow stall angle (refs. 1 and 2). In addition, some data will be presented for the conditions where weak blast waves strike from directions normal to the wing surface and nearly parallel to the wing span, producing angle-of-attack changes to angles less than the stall angle.

SYMBOLS

Δp_R	resultant pressure, measured from conditions existing prior to blast-wave arrival, lb/sq in.
q	dynamic pressure, lb/sq in.
τ	airstream movement, or aerodynamic time, chords
α	angle of attack, deg

[redacted]

DISCUSSION

Figure 1 is presented as a review of the information previously available on the traveling-load peak. Shown are three sets of load distributions plotted as load coefficient $\Delta p_R/q$ against percent wing chord. These distributions are for three successive times after blast-wave arrival as represented by the values of 0.53, 1.24, and 2.31 chords of travel of the model. The dashed lines with the points represent the model flight data, whereas the solid lines were calculated by simple potential-flow theory ignoring stall and unsteady-lift effects. Two unusual features are apparent in the model flight data. The first is that a loading peak was found that traveled rearward as time passed, and the second is that this peak showed a larger load than the potential-flow calculations which would normally be considered an upper limit to the loading.

The traveling-load peak was believed to result from a vortex that had been formed when the blast wave diffracted around the leading edge of the airfoil and subsequently had been pushed rearward over the upper surface by the steady airflow over the wing. However, no direct evidence was available to substantiate this premise. Accordingly, an experimental investigation was undertaken in the laboratory to visualize the traveling vortices by means of schlieren techniques and to determine how the vortices would move along the chord. The manner in which this was accomplished is shown schematically in figure 2. At the right, an airfoil having one-twentieth the chord of the wing of the model used in the free-flight tests was placed in the airstream issuing from the slot in the flat surface. The airfoil was struck by the blast wave from the actual explosion at the left. The airstream velocity and the gust velocity induced by the blast wave were set at the values obtained for the free-flying model, but the duration of the blast wave was one-twentieth of that to which the free-flying model was subjected in order to account for the reduction in the chord length of the airfoil.

A series of tests was made with the schlieren apparatus adjusted to take photographs of the airfoil and flow at various time intervals after the blast wave struck. A sequence of three photographs, with the airfoil oriented the same as shown in figure 2, is given in figure 3. The picture at the left, which was taken shortly after the blast-wave front passed, shows that vortices have actually been formed by the diffraction of the blast wave around the airfoil and that the one formed at the leading edge has moved slightly back along the chord. The second and third pictures, taken at later times, show that this vortex has moved still farther back along the chord and successively become less distinct and more spread out. The reduction in distinctness is an indication of loss of intensity and conforms to the results from the flight tests shown in figure 1 where the loading peak reduces and spreads out as it moves along the chord.

In reference 1, it was found that the load peak traveled along the chord at a velocity slower than that of the airstream. This is illustrated in figure 1 by the fact that the load peak is still on the airfoil in the third load distribution shown although the airstream has moved more than two chords since the blast wave struck. The schlieren photographs of figure 3 also show the same thing for the vortex. For example, in the middle photograph in figure 3, the vortex which was formed at the leading edge is seen to be only about a third of the way along the chord although the airstream has moved more than 0.9 of a chord. Note that the vortex formed at the trailing edge appears to move at airstream velocity, for it is nearly 1 chord away from the airfoil. The movement of the load peak and the vortex are compared in figure 4. The positions of each along their respective airfoils are shown in terms of percent chord plotted against the chord-length movement of the airstream across the two airfoils. The circles represent the load peak and the squares, the vortex. It is obvious that, despite the twenty-to-one difference in scale, the movement of the load peak and the vortex is the same function of chord-length travel of the airstream. The average velocity of travel of the load peak and vortex appears to be about one-third stream velocity since, in the time they take to pass over the airfoil, the airstream has moved nearly 3 chords.

Recent experimental results are now considered from another phase of the investigation, that of determining the loadings when a weak blast-induced gust strikes a wing and causes an angle change less than the stall angle. Earlier unpublished results have indicated that when a weak blast wave strikes normal to the wing, the loading can be calculated by using existing unsteady-lift theory. Questions have arisen as to whether this procedure would apply if the blast wave struck from a direction well to the side, say at an angle of 20° to 30° to the wing surface. Figure 5 presents the load distribution along the wing chord from one test for such a blast direction together with the results previously mentioned for the blast wave striking normal to the wing. Both represent the load distribution existing at the same very short time after the blast waves struck. Again, the data are plotted as load coefficient $\Delta p_R/q$ as a function of percent of wing chord. The circles are the experimental points associated with the orientation at the right where the blast wave strikes normal to the wing, and the squares are the results obtained when the model rolled as shown so that the blast wave struck at an angle of about 28° to the wing surface. The blast wave and the induced gust velocities were the same for each condition. In making the unsteady-lift calculations, the full gust velocity imposed by the blast wave was used in determining the distribution shown by the solid line for the condition where the blast wave struck normal to the wing. For the rolled condition, however, a simple resolution of vectors was used to determine the component of the gust velocity which acted normal to the wing, and the result of that unsteady-lift calculation is plotted as the dashed line. Both load-distribution calculations are seen to agree well with

the experimental data along most of the chord. Near the leading edge, the circle representing the flight result for the blast normal to the wing is somewhat lower than the potential-flow calculation, as often happens, but the square representing the rolled condition is well above its corresponding calculated value. The flow phenomena which caused this are not understood, and, unfortunately, the pressure cell at the 12-percent-chord station did not operate on this flight so it could not be determined if the effect was confined only to the leading edge. The square at the 28-percent-chord station is also high, and again it is not known whether it represents some carryover from the condition found at the leading edge or if its position reflects instrument malfunction. It appears, however, that by a simple resolution of the gust velocity vectors, the loading over the major portion of the chord can be calculated over a wide range of blast incidence angles.

SUMMARY OF RESULTS

Recent data obtained in the investigation of the loads produced by blast-induced gusts have shown that:

1. When the angle-of-attack change caused by the gust is much greater than the stall angle of the airfoil, the load peak traveling along the chord is caused by a vortex formed by the diffraction of the blast wave around the leading edge and its movement is a function of aerodynamic time or chord-length travel.

2. For weak blast waves causing small angle-of-attack changes, it appears that the chord loading may be calculated by existing unsteady-lift theory for a wide range of the blast position with respect to the wing by making a simple resolution of the gust velocity vector to a plane normal to the wing.

REFERENCES

1. Pierce, Harold B., and Reisert, Thomas D.: Initial Experimental Investigation of the Aerodynamic Load on the Wing of a Model Caused by a Blast-Induced Gust That Increases the Angle of Attack Into the Stall Region. NACA RM L55H22b, 1955.

2. Pierce, Harold B., and Spahl, Raymond J.: Experimental Investigation To Determine the Loads on a Horizontal Tail of a Model Caused by a Blast-Induced Gust. NACA RM L57A28a, 1957.

EXPERIMENTAL AND CALCULATED LOAD DISTRIBUTIONS

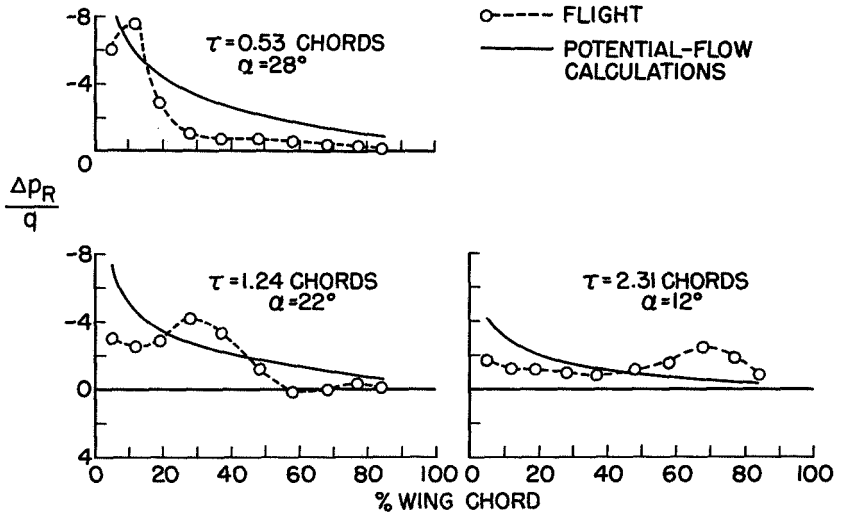
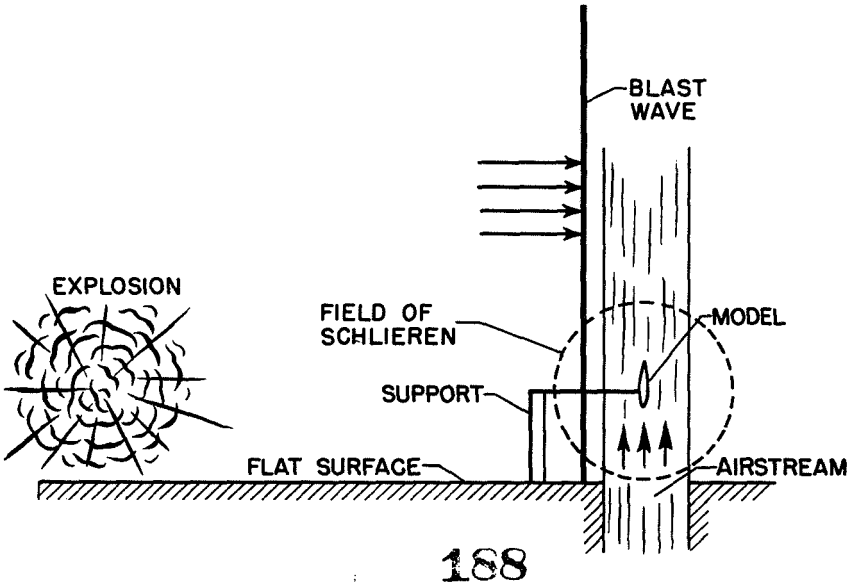


Figure 1

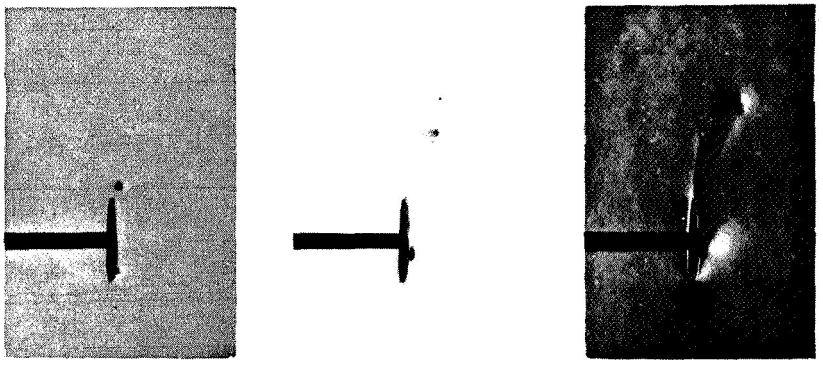
ARRANGEMENT FOR VORTEX-FLOW STUDY



188

Figure 2

VORTICES FROM BLAST-WAVE DIFFRACTION



τ=0.28 CHORDS τ=0.93 CHORDS τ=1.31 CHORDS

L-57-178

Figure 3

LOAD-PEAK AND VORTEX TRAVEL ALONG CHORD

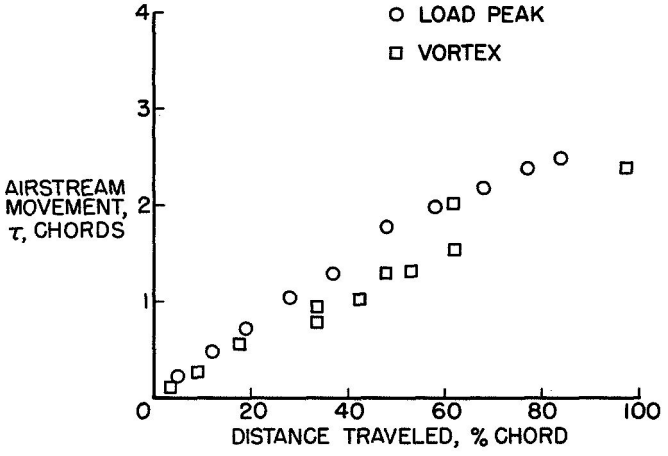


Figure 4

EFFECT OF BLAST-GUST DIRECTION ON LOAD DISTRIBUTION

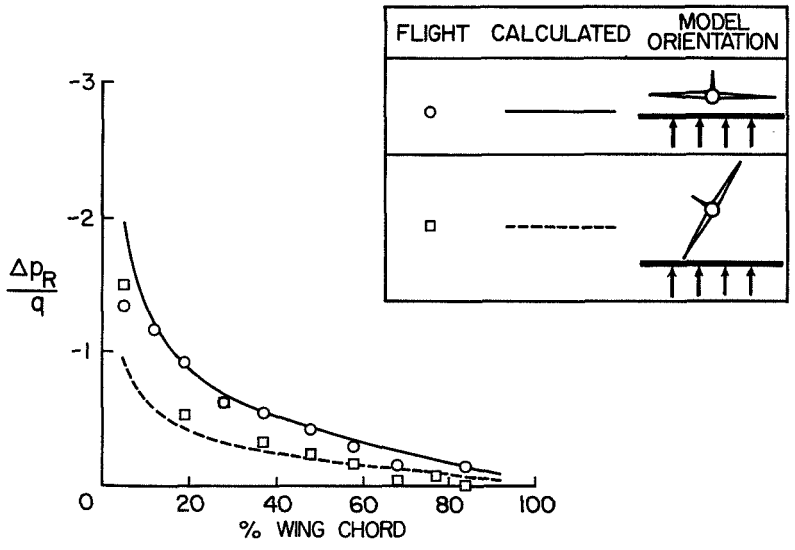


Figure 5

N71-75394

AIRPLANE MOTIONS AND LOADS INDUCED BY FLYING THROUGH THE FLOW FIELD GENERATED BY AN AIRPLANE AT LOW SUPERSONIC SPEEDS

By Gareth H. Jordan, Earl R. Keener,
and Stanley P. Butchart

NACA High-Speed Flight Station

SUMMARY

An exploratory flight investigation was conducted to determine the disturbances to an airplane while flying in formation with another airplane at low supersonic speeds. The most significant motions were encountered as a result of flying through the flow field of the lead airplane. Several of these supersonic passes were made using two swept-wing fighter-type airplanes in order to evaluate the gross effects of time to pass through the flow field, lateral distance, and altitude within a Mach number range from 1.2 to 1.3.

Significant airplane motions and vertical-tail loads can be experienced as a result of close-proximity side-by-side passes at supersonic speed. The most severe motions and vertical-tail loads were experienced during passes made at separation distances less than 100 feet and at a time to pass near and slightly greater than the airplane natural period in yaw. The passing airplane experienced maximum sideslip angles of about 5.4° and maximum vertical-tail loads of approximately 50 percent of design limit in shear, bending moment, and torsion. Maximum vertical-tail loads can be determined essentially from the maximum airplane sideslip angle and the vertical-tail lift-curve slope. Increasing the lateral separation distance was shown to decrease the maximum sideslip angle and, thus, to reduce the maximum vertical-tail load.

INTRODUCTION

Military pilots have reported that severe disturbances are encountered while flying in formation at supersonic speed. The implication of these reports was that severe loading conditions might be imposed on an airplane by flying in the flow field generated by another airplane at supersonic speed. As a result of these reports, the NACA High-Speed Flight Station has conducted an exploratory flight investigation to determine the nature and severity of the disturbances that might be encountered. During the

investigation, it was found that the most significant airplane motions and loads were imposed on the airplane as a result of flying through the flow field in a passing maneuver.

The purpose of this paper is to summarize the results of this investigation and to point out some of the factors believed to be important in an assessment of the overall problem of supersonic passes. The experimental data were obtained at Mach numbers from 1.1 to 1.3 at altitudes from 20,000 to 40,000 feet.

SYMBOLS

c	chord, ft (fig. 1)
F_a	aileron stick force, lb
F_r	rudder pedal force, lb
F_s	stabilizer stick force, lb
$F_{Y,v}$	vertical-tail structural load, lb
g	acceleration due to gravity, ft/sec^2
h_p	pressure altitude, ft
I_X	moment of inertia about X-axis, slug-ft^2
I_Y	moment of inertia about Y-axis, slug-ft^2
I_Z	moment of inertia about Z-axis, slug-ft^2
I_{XZ}	product of inertia, slug-ft^2
i_t	incidence angle of all-movable stabilizer, positive when leading edge up, deg
M	Mach number as measured by airspeed head mounted on nose boom
$M_{b,v}$	vertical-tail structural bending moment, in-lb
n_Y	transverse-load factor, g units

n_Z normal-load factor, g units

P_n period of natural frequency of airplane in yaw, sec

p static pressure as measured by airspeed head mounted on nose boom, lb/sq ft, or rolling angular velocity, radians/sec

Δp approximate variation of static pressure in flow field from free stream

$\dot{p}$ rolling angular acceleration, radians/sec^2

q free-stream dynamic pressure, lb/sq ft, or pitching angular velocity, radians/sec

$\dot{q}$ pitching angular acceleration, radians/sec^2

r yawing angular velocity, radians/sec

$\dot{r}$ yawing angular acceleration, radians/sec^2

T_V vertical-tail structural torque, in-lb

t time, sec

y lateral separation distance between flight paths of airplanes, ft

α airplane angle of attack as measured at nose boom, deg

β airplane angle of sideslip as measured at nose boom, deg

δ_a total aileron deflection, deg

δ_r rudder deflection, deg

ζ damping ratio

Subscript:

max maximum

DESCRIPTION OF AIRPLANE AND INSTRUMENTATION

The test airplane used for this investigation was a swept-wing fighter-type airplane capable of supersonic speed in level flight. A three-view drawing of the airplane giving overall dimensions is presented in figure 1. The physical characteristics are given in table I.

The test airplane used for these studies was instrumented to measure quantities pertinent to these investigations. Structural loads on the test airplane were measured by strain gages located at the root of each surface. The strain-gage station and torque axis for the vertical-tail loads are shown in figure 1.

The airspeed head from which static-pressure measurements were obtained and the angle-of-sideslip vane were mounted on the nose boom of the test airplane. Pertinent dimensions of this installation are shown in figure 2.

The lead airplane for these formation flights was furnished by the Air Force Flight Test Center and was an uninstrumented airplane of the same type as the test airplane.

TESTS

The motions and loads associated with supersonic passes were investigated by the test procedure shown in figure 3. The instrumented test airplane was flown through the flow field generated by the lead airplane in a side-by-side passing maneuver. These supersonic passes were made at various lateral separation distances and at various passing rates within a Mach number range of 1.1 to 1.3 and at altitudes from 20,000 to 40,000 feet. The speed differentials for the passing rates investigated varied from about 5 feet per second to 50 feet per second or incremental Mach numbers less than 0.05.

RESULTS AND DISCUSSION

Factors Involved

Some of the factors that should be considered in a general assessment of the supersonic pass problem are as follows:

Mach number
altitude

rate of passing
separation distance

relative flight paths

relative size
initial conditions
stability
configuration

The dynamic pressure, which has a direct bearing on the loads, is determined by Mach number and altitude. Mach number and altitude also determine the physical characteristics of the flow field and the strength of the shocks in the flow field for a given configuration. The effect of rate of passing and lateral separation distance on the response of the airplane to the flow-field disturbance is discussed in the presentation of the experimental results to follow. Only the side-by-side pass has been investigated; however, many variations in relative flight paths are possible, such as overhead passes, head-on passes, and curved flight paths. No experimental results are available to indicate the effect of relative size of the lead and passing airplanes, initial conditions before passing, stability, or configuration; however, these factors must be considered before a complete assessment of the problem can be made. It should be pointed out that, although this investigation concerns the motions and loads experienced by the passing airplane, a similar disturbance was felt by the other airplane as the flow field of the passing airplane swept over it.

Time History of a Supersonic Pass

In order to have a more complete understanding of the supersonic pass problem and of the resulting airplane motions and loads, a more detailed sketch of the flow field and a time history of a supersonic pass are shown in figures 4 and 5. The flight conditions for this supersonic pass are $M \approx 1.3$, $h_p \approx 32{,}400$ feet, $y \approx 100$ feet, and a speed differential of about 12 feet per second. In figure 4, the lead airplane and a portion of the shocks generated by this airplane are shown. For simplicity, the shocks are represented by parallel lines at the Mach angle for $M = 1.3$. The flow field is further assumed to be one fuselage length in a direction parallel to the flight path. The incremental pressure changes within the flow field were obtained from the airspeed record during this supersonic pass and are shown in the lower part of the figure. The three stronger shocks resulted in abrupt pressure jumps of 15 to 17 pounds per square foot. In addition, the approximate path of a streamline (somewhat exaggerated) through this flow field is indicated in figure 4 and the test airplane is shown just entering the flow field. From a consideration of the flow direction, it may be seen that the test airplane experiences a local lateral velocity over its fuselage and then over its tail as the flow field is traversed; hence, the test airplane experiences a yawing-moment input.

From the time histories of the measured quantities in figure 5, it is seen that the test airplane experienced an excursion in sideslip in which a maximum sideslip angle of 4.7° was measured. The maximum lateral acceleration associated with this airplane motion was $\pm 0.7g$. The vertical-tail loads in figure 5(c) are mainly a function of the airplane

sideslip angle; and the maximum vertical-tail shear, bending moment, and torque measured during this pass were about 50 percent of design limit.

Maximum Sideslip Angle

A summary of the supersonic passes performed within a Mach number range of 1.1 to 1.3 at altitudes from 20,000 feet to 40,000 feet is shown in figure 6. The maximum sideslip angles measured during these passes are shown as a function of time to pass. Time to pass is defined as the time in seconds required for any part of the test airplane to traverse the distance from the trailing shock to the bow wave of the generating airplane and was determined for these tests from the airspeed-head static-pressure record. The time-to-pass values in figure 6 represent speed differentials from about 50 feet per second at the fast rate of passing to about 5 feet per second at the slow rate of passing. Also shown in this figure is the natural period of the airplane in yaw for the range of Mach number and altitude of these passes.

The solid symbols in figure 6 represent the maximum sideslip response measured during passes made at separation distances less than 100 feet, the half-solid symbols represent passes at distances from 100 feet to 300 feet, and the open symbols represent passes made at distances greater than 400 feet. The effect of distance may be seen by comparing the response of the airplane at various distances. As would be expected, the largest response was obtained at distances less than 100 feet and the response is seen to decrease as the separation distance is increased.

A noticeable effect of rate of passing may be seen by comparing the response of the airplane at distances less than 100 feet. For a time to pass considerably less than the natural period of the airplane in yaw, very little airplane motion was encountered. At times to pass near and greater than the natural period, significant airplane sideslip angles were obtained. In addition, a small reduction in sideslip response is evident at the higher time-to-pass values.

The effect of Mach number on the airplane motions could not be determined because of the limited range of Mach number investigated. No effect of altitude on the airplane motion was found within the range investigated (20,000 to 40,000 feet).

It is apparent from these data that there is some dynamic response to the flow-field disturbance. Some preliminary calculations were made in an effort to predict the maximum airplane motions. These calculations were based on the simple dynamic response of a linear single-degree-of-freedom system to a yawing-moment input. (See, for example, ref. 1.) The results of these calculations are compared with the flight results in figure 7. The data in this figure have been corrected to a lateral

separation distance of 100 feet by the expression $\beta_{max}\sqrt{y/100}$. This correction is based on some theoretical work by G. B. Whitham (ref. 2) in which it is shown that the lateral velocity in the flow field of a body at supersonic speed varies inversely with the square root of the lateral separation distance. The curve of the calculated response is based on a damping ratio of 0.07 which corresponds to the flight-determined damping ratio of the airplane at low supersonic Mach numbers (ref. 3). These calculations predict extremely large sideslip angles near the airplane natural period that have not been realized in flight. It is evident that more refined calculations are necessary before reliable estimates of the maximum airplane motions can be predicted. Additional calculations employing an analysis based on the recent traveling-gust concept are presently under way.

Maximum Vertical-Tail Loads

A summary of the maximum vertical-tail loads (measured during these supersonic passes) is shown in figure 8. The maximum vertical-tail loads have been corrected to an altitude of 30,000 feet by a dynamic-pressure correction. On the left-hand side of the figure, the maximum vertical-tail loads measured during passes at distances less than 100 feet are shown as a function of time to pass. The vertical-tail loads vary in a manner similar to that previously shown for maximum sideslip angle, and vertical-tail loads of 50 percent of design limit were experienced at a time-to-pass slightly greater than the natural period of the airplane in yaw.

As a matter of interest, the fast rate of passing resulted in negligible airplane motion and, thus, in relatively small vertical-tail loads. Some evidence of structural excitation was visible, however, in the flight records for this pass. This excitation is a result of an impact type of loading imposed on the vertical tail during high passing rates.

On the right-hand side of figure 8 the maximum vertical-tail loads from all of the supersonic passes are shown as a function of the maximum sideslip angle. Also included is the variation of the vertical-tail load based on the experimental lift-curve slope of the vertical tail from other experimental results. A comparison of the vertical-tail loads experienced during these passes with the experimental lift-curve slope indicates that the maximum vertical-tail loads can be determined from the maximum airplane sideslip angle and the vertical-tail lift-curve slope.

As previously mentioned the magnitude of the airplane motions was found to be relatively unaffected by altitude within the range of this investigation. It might be expected that loads in excess of design

limit would be experienced as a result of close-proximity passes at an altitude lower than the range investigated because of the increase in dynamic pressure.

Pilot's Comments

Formation flying at supersonic speeds does not differ from subsonic formation work as long as the wingman remains in a position behind the flow field of the lead airplane. If the wingman gets out of position, either by overshooting during join up or by drawing abreast of the lead plane as a result of a turn-in maneuver of the lead plane, control of the airplane can become quite difficult.

If the wingman moves ahead slowly, the first encounter with the flow field of the lead airplane causes an abrupt yaw toward the lead plane. (The first impression is that you will fly right through the middle of the lead airplane.) A little difficulty is experienced in holding vertical position at this point also, not unlike flying in the wing wake of another airplane at slower speeds. It is possible to retrim and to hold formation position after the airplane has penetrated some distance into the flow field. Moving ahead a little farther releases the yaw toward the lead plane and sets up a slight yaw in the opposite direction. It is possible to move out from the lead airplane for a distance of 500 to 600 feet or more and still remain in this yawed position.

The most startling experience occurs when the wingman slides up past the lead aircraft at a speed where the yaw toward the lead plane and then away from the lead plane comes in phase with the natural frequency of the airplane in yaw. Under this condition the airplane ends up in a yawing oscillation that can be four or five times greater than that attainable when rudder alone is used at that same speed. The airplane controls are not effective in preventing the oscillation and the airplane feels out of control for a few seconds.

CONCLUDING REMARKS

Results of an investigation of airplane motions and loads induced by flying through the flow field of an airplane at low supersonic speeds have indicated that significant airplane motions and vertical-tail loads can be experienced as a result of close-proximity side-by-side passes at supersonic speed. The most severe motions and vertical-tail loads were experienced during passes made at separation distances less than 100 feet

and at a time to pass near and slightly greater than the airplane natural period in yaw. The passing airplane experienced maximum sideslip angles of about 5.4° and maximum vertical-tail loads of approximately 50 percent of design limit in shear, bending moment, and torsion. Maximum vertical-tail loads can be determined essentially from the maximum airplane sideslip angle and the vertical-tail lift-curve slope. Increasing the lateral separation distance was shown to decrease the maximum sideslip angle and, thus, to reduce the maximum vertical-tail load.

A general assessment of the problem of supersonic passes requires that several additional factors be considered - namely, effects of Mach number, stability, configuration, relative size, and relative flight path on the airplane motions and loads.

REFERENCES

1. Triplett, William C., Brown, Stuart C., and Smith, G. Allan: The Dynamic-Response Characteristics of a 35° Swept-Wing Airplane As Determined From Flight Measurements. NACA Rep. 1250, 1955. (Supersedes NACA RM A51G27 by Triplett and Smith and RM A52I17 by Triplett and Brown.)

2. Whitham, G. B.: The Flow Pattern of a Supersonic Projectile. Communications on Pure and Appl. Math., vol. V, no. 3, Aug. 1952, pp. 301-348.

3. Wolowicz, Chester H.: Time-Vector Determined Lateral Derivatives of a Swept-Wing Fighter-Type Airplane With Three Different Vertical Tails at Mach Numbers Between 0.70 and 1.48. NACA RM H56C20, 1956.

[redacted]

TABLE I

PHYSICAL CHARACTERISTICS OF THE TEST AIRPLANE

Wing:	
Airfoil section	NACA $64_{(06)}$A007
Total area (including aileron and 83.84 sq ft covered by fuselage), sq ft	385.21
Span, ft	38.58
Mean aerodynamic chord, ft	11.16
Root chord, ft	15.86
Tip chord, ft	4.15
Taper ratio	0.262
Aspect ratio	3.86
Sweep at 25-percent-chord line, deg	45
Incidence, deg	0
Dihedral, deg	0
Geometric twist, deg	0
Aileron:	
Area rearward of hinge line (each), sq ft	19.32
Span at hinge line (each), ft	7.81
Chord rearward of hinge line, percent wing chord	25
Travel (each), deg	±15
Leading-edge slat:	
Span, equivalent, ft	12.71
Segments	5
Spanwise location, inboard end, percent wing semispan	23.3
Spanwise location, outboard end, percent wing semispan	89.2
Ratio of slat chord to wing chord (parallel to fuselage reference line), percent	20
Rotation, maximum, deg	15
Horizontal tail:	
Airfoil section	NACA 65A003.5
Total area (including 31.65 sq ft covered by fuselage), sq ft	98.86
Span, ft	18.72
Mean aerodynamic chord, ft	5.83
Root chord, ft	8.14
Tip chord, ft	2.46
Taper ratio	0.30
Aspect ratio	3.54
Sweep at 25-percent-chord line, deg	45
Dihedral, deg	0
Travel, leading edge up, deg	5
Travel, leading edge down, deg	25

[redacted]

TABLE I.- Continued

PHYSICAL CHARACTERISTICS OF THE TEST AIRPLANE

Vertical tail:	
Airfoil section	NACA 65A003.5
Area (excluding dorsal fin and area blanketed by fuselage), sq ft	42.7
Area blanketed by fuselage (area between fuselage contour line and line parallel to fuselage reference line through intersections of leading edge of vertical tail and fuselage contour line)	2.45
Span (unblanketed), ft	7.93
Mean aerodynamic chord, ft	5.90
Root chord, ft	8.28
Tip chord, ft	2.49
Taper ratio	0.301
Aspect ratio	1.49
Sweep at 25-percent-chord line, deg	45
Rudder:	
Area, rearward of hinge line, sq ft	6.3
Span at hinge line, ft	3.33
Root chord, ft	2.27
Tip chord, ft	1.50
Travel, deg	±20
Spanwise location, inboard end, percent vertical-tail span	3.1
Spanwise location, outboard end, percent vertical-tail span	44.8
Chord, percent vertical-tail chord	28.4
Aerodynamic balance	Overhanging, unsealed
Fuselage:	
Length (afterburner nozzle closed), ft	45.64
Maximum width, ft	5.58
Maximum depth over canopy, ft	6.37
Side area (total), sq ft	230.92
Fineness ratio (afterburner nozzle closed)	7.86
Speed brake:	
Surface area, sq ft	14.14
Maximum deflection, deg	50
Powerplant:	
Turbojet engine	One Pratt & Whitney J57-P7 with afterburner
Thrust (guarantee sea level), afterburner, lb	15,000
Military, lb	9,220
Normal, lb	8,000

TABLE I.- Concluded

PHYSICAL CHARACTERISTICS OF THE TEST AIRPLANE

Airplane weight, lb:	
Basic (without fuel, oil, water, pilot)	19,662
Total (full fuel, oil, water, pilot)	24,800
Center-of-gravity location, percent mean aerodynamic chord:	
Total weight - gear down	31.80
Total weight - gear up	31.80
Moments of inertia (estimated total weight):	
I_X, slug-ft^2	11,103
I_Y, slug-ft^2	59,248
I_Z, slug-ft^2	67,279
I_{XZ}, slug-ft^2	941
Inclination of principal axis (estimated total weight):	
Below reference axis at nose, deg	0.8

203

TEST AIRPLANE

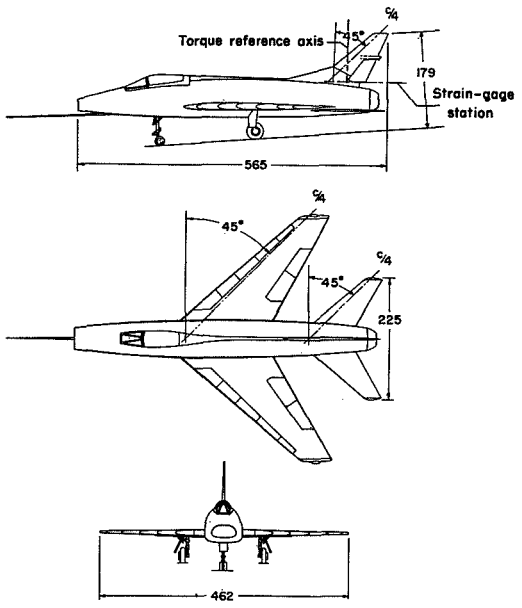


Figure 1

INSTRUMENTATION ON NOSE BOOM OF TEST AIRPLANE

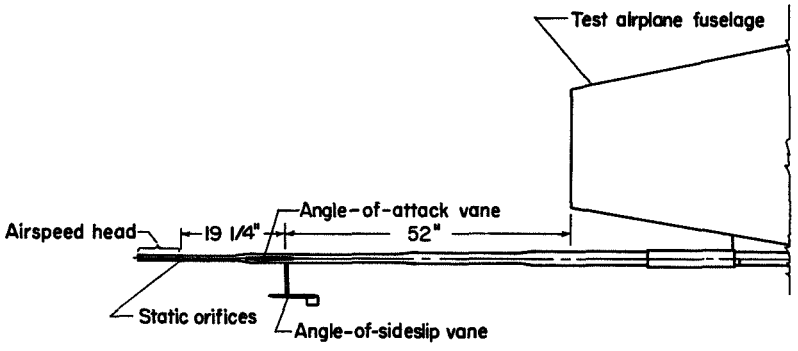


Figure 2

DESCRIPTION OF TESTS

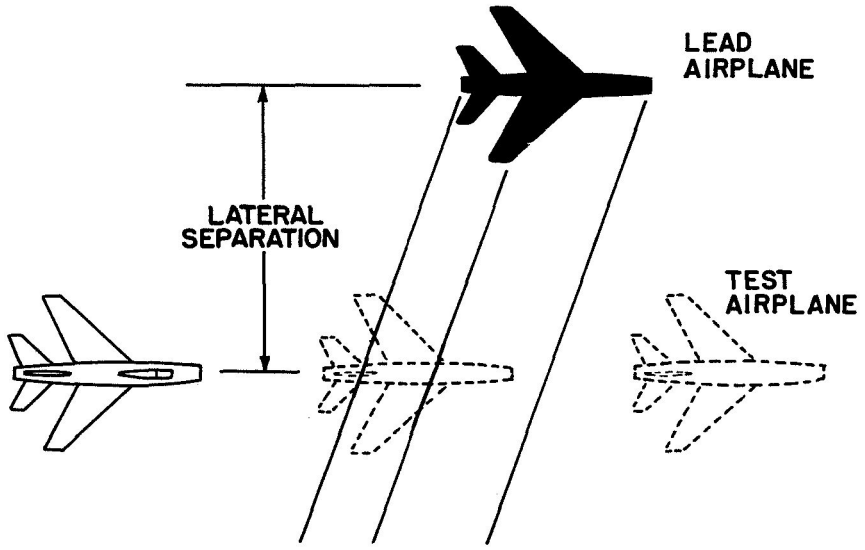


Figure 3

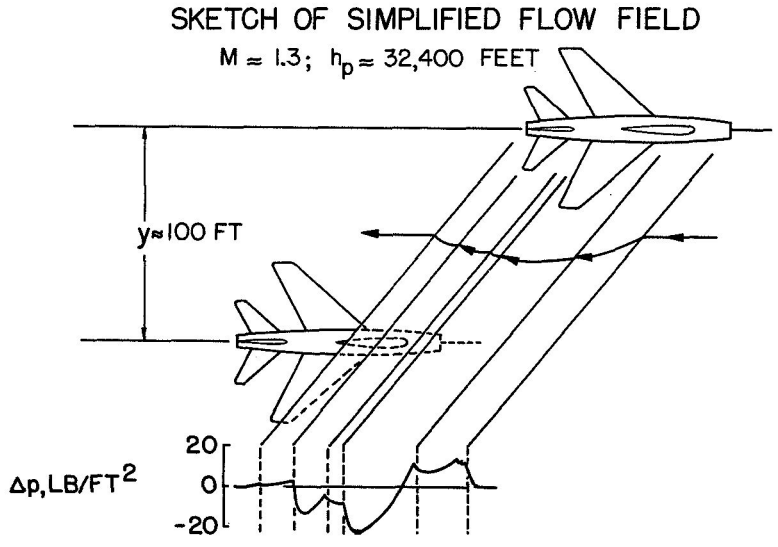


Figure 4

204

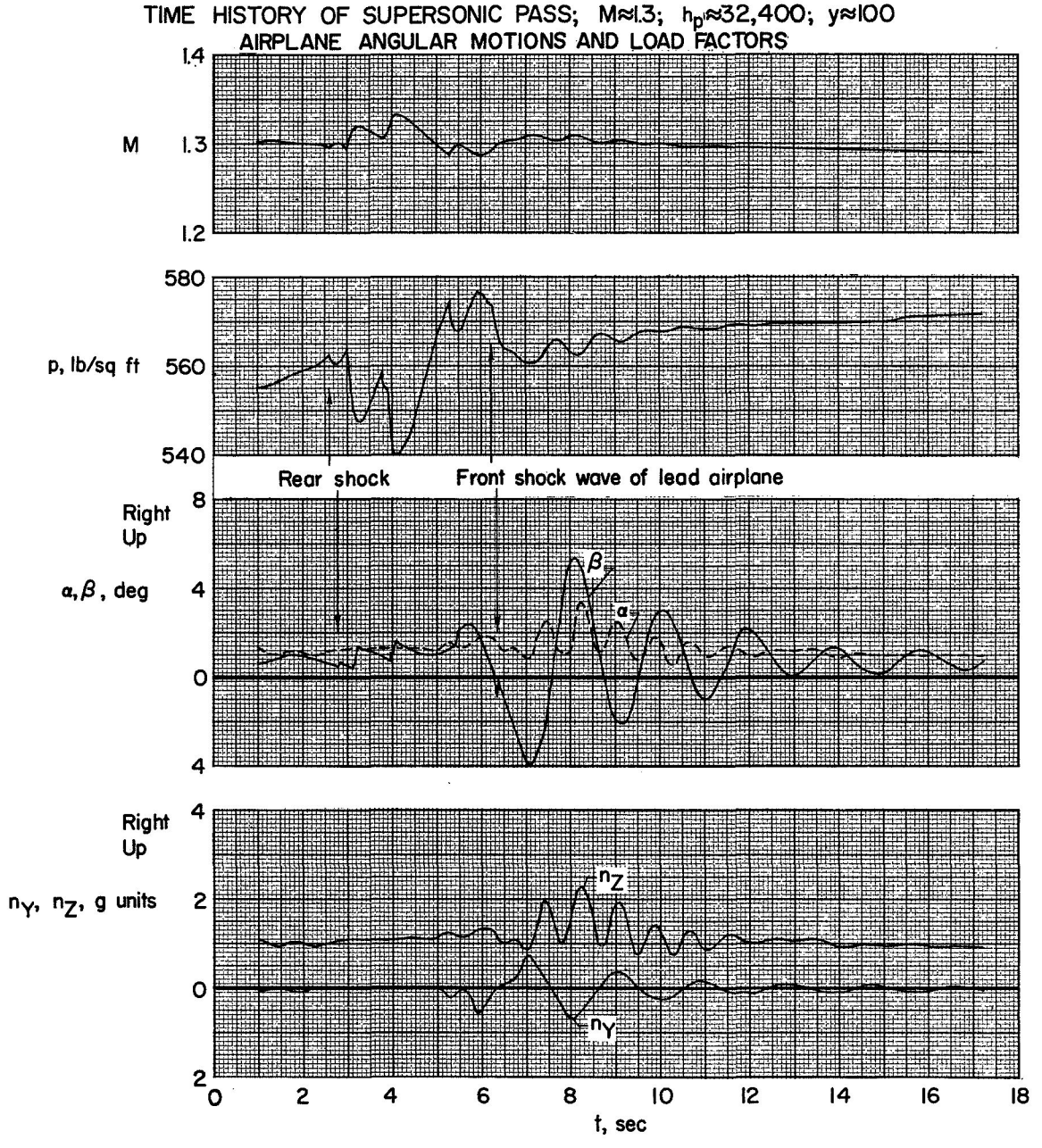

TIME HISTORY OF SUPERSONIC PASS; M≈1.3; h_p≈32,400; y≈100
AIRPLANE ANGULAR MOTIONS AND LOAD FACTORS
M
1.4
1.3
1.2
p, lb/sq ft
580
560
540
Rear shock
Front shock wave of lead airplane
Right
Up
α, β, deg
8
4
0
4
β
α
Right
Up
n_Y, n_Z, g units
4
2
0
2
n_Z
n_Y
0
2
4
6
8
10
12
14
16
18
t, sec

Figure 5(a)

[redacted]

TIME HISTORY OF SUPERSONIC PASS; M≈1.3; h_p≈32,400; γ≈100
CONTROL POSITIONS AND FORCES; ANGULAR VELOCITIES AND ACCELERATIONS

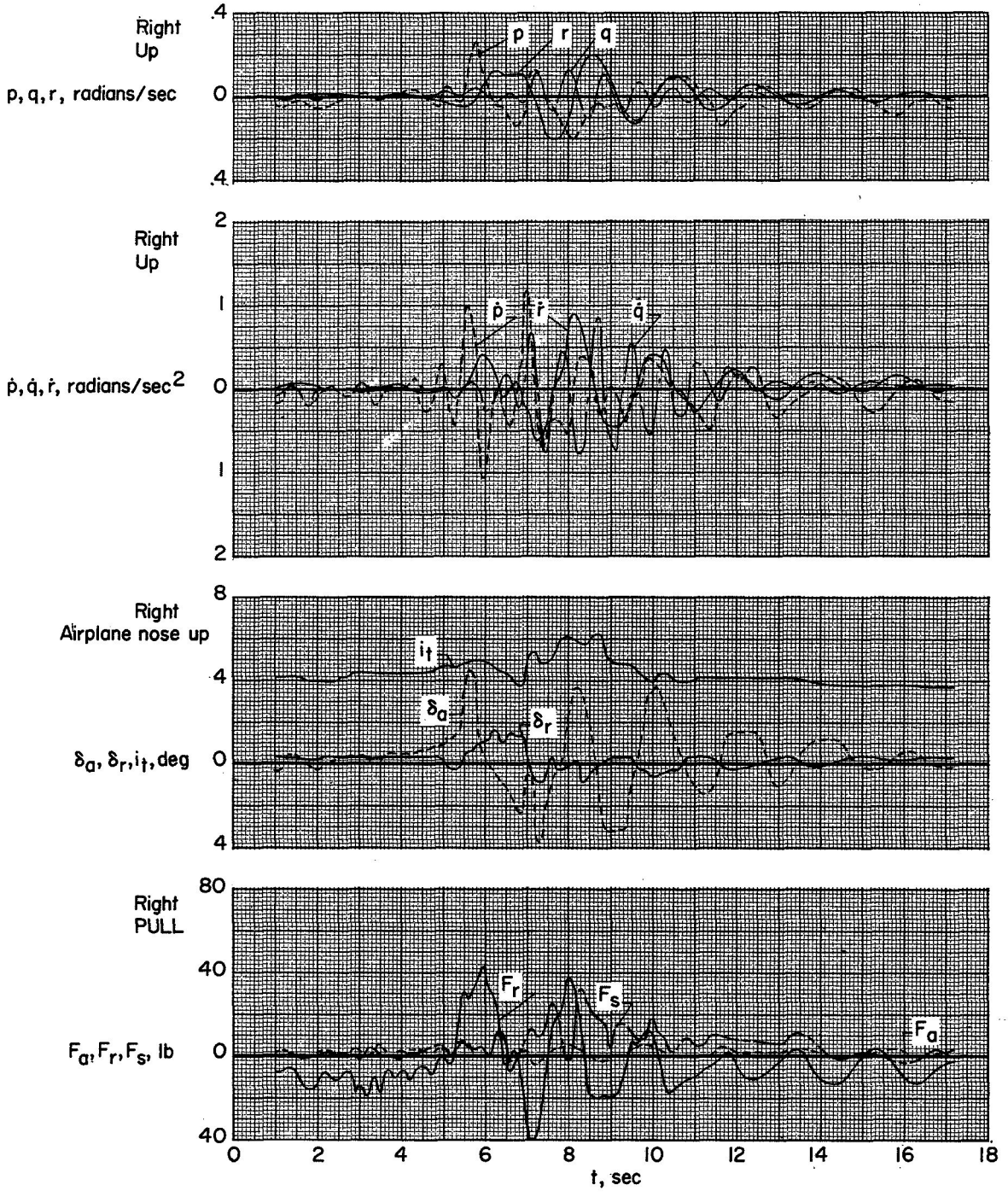


Figure 5(b)

[redacted]

TIME HISTORY OF SUPERSONIC PASS; M≈1.3; h_p≈32,400; y≈100

VERTICAL-TAIL STRUCTURAL LOADS

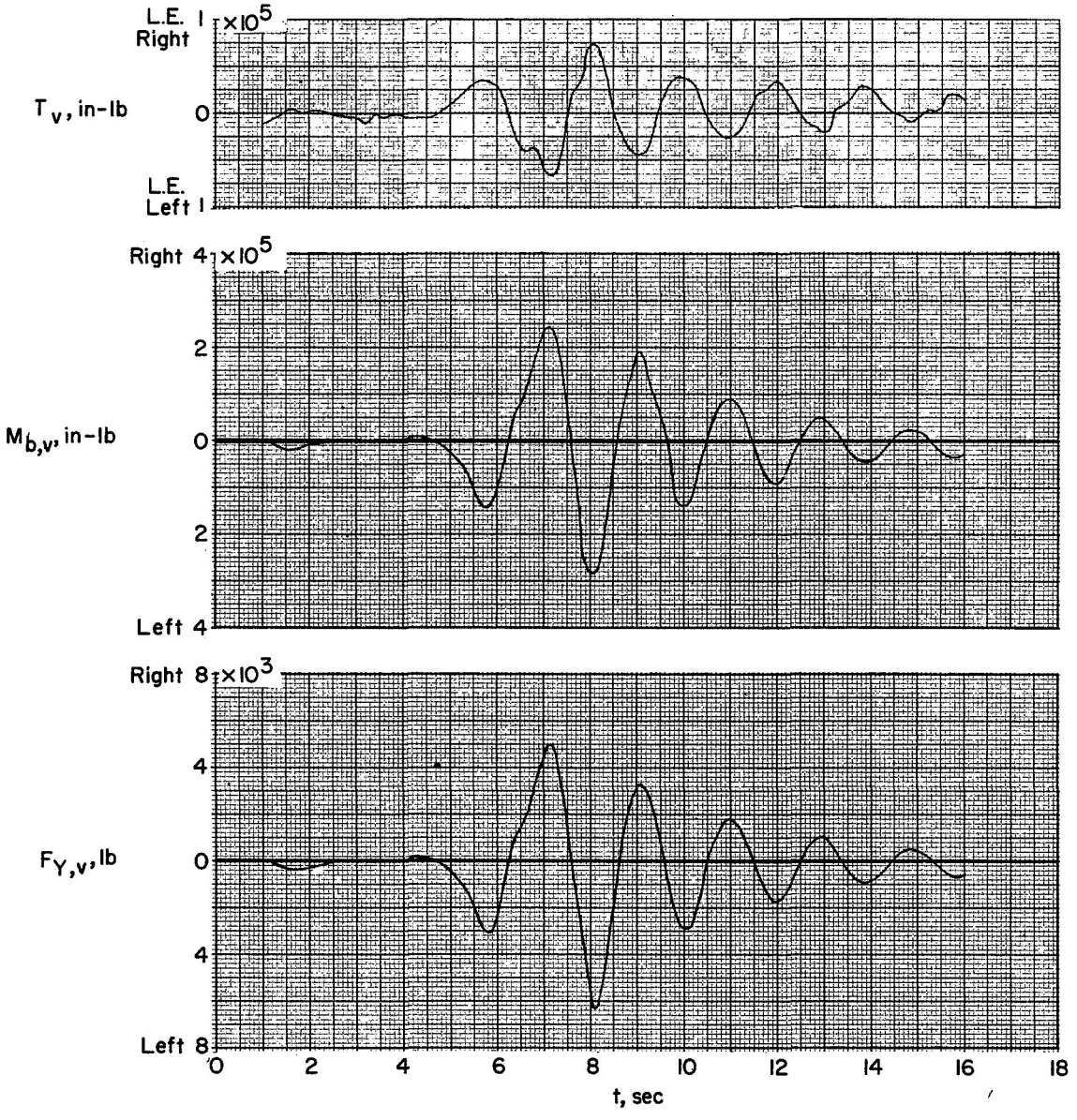


Figure 5 (c)

SUMMARY OF SUPERSONIC PASSES

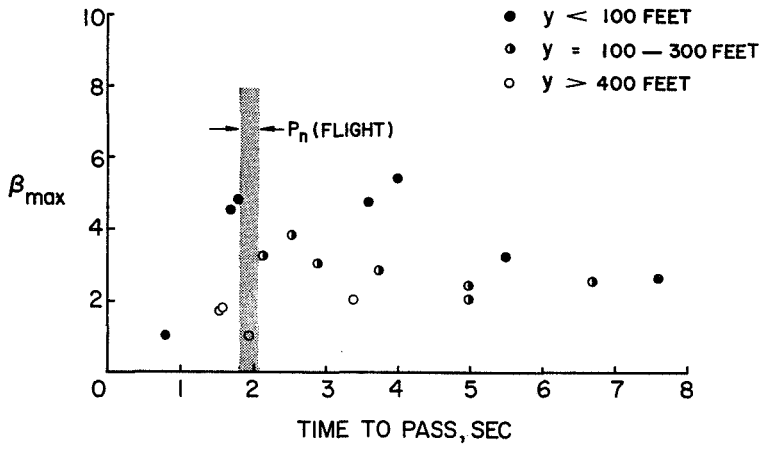
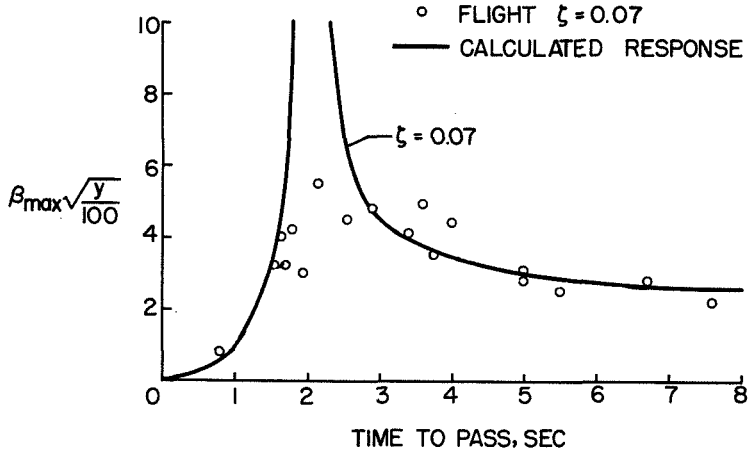


Figure 6

COMPARISON OF CALCULATED AND EXPERIMENTAL MAXIMUM SIDESLIP ANGLES



208

Figure 7

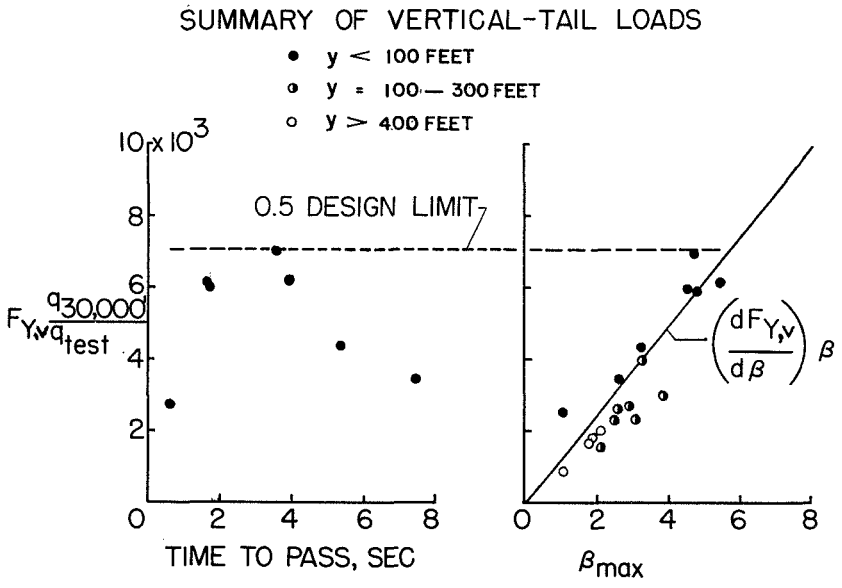

SUMMARY OF VERTICAL-TAIL LOADS
y < 100 FEET
y = 100 — 300 FEET
y > 400 FEET
10 x 10^3
8
6
4
2
0
0.5 DESIGN LIMIT
F_Y,v q_30,000 / q_test
0 2 4 6 8
TIME TO PASS, SEC
(dF_Y,v / dβ) β
β_max

Figure 8

N71-75395

COLEMAN, PRESS, & SHUFFLEBARGER

EFFECTS OF AIRPLANE FLEXIBILITY ON WING BENDING STRAINS IN ROUGH AIR

By Thomas L. Coleman, Harry Press, and C. C. Shufflebarger

Langley Aeronautical Laboratory

INTRODUCTION

Previous investigations (refs. 1 to 3) have indicated that wing flexibility could cause substantial amplification in the wing strains in rough air for such straight-wing airplanes as the Douglas DC-3, Martin 2-0-2, and the Boeing B-29. Also, by application of power-spectral methods of analysis, good correlation has been obtained between the measured root bending strains and calculated results for these three airplanes (ref. 3). As a continuation of the work in this area, the B-29 investigation has been extended to cover the bending-strain amplifications at several other wing stations. In addition, a flight investigation involving the swept-wing Boeing B-47A airplane has been undertaken in order to assess the significance of the wing sweep on the elastic response in rough air.

In the present paper, an effort is made to summarize some of the more important results obtained in recent studies. The material to be covered includes experimental results on the bending-strain responses at various stations for both the Boeing B-29 and the Boeing B-47A airplanes. For the B-29 airplane investigation, comparisons are made between the experimental results and calculations. Unfortunately, similar results are not yet available for the B-47A investigation. Finally, some indirect evidence obtained in the B-47A investigation on the effects of spanwise variations in turbulence on the strain and acceleration responses is described.

AIRPLANES, INSTRUMENTATION, AND TEST CONDITIONS

Figure 1 shows plan-form views of the two test airplanes and the locations of some of the primary instrumentation. The basic instrumentation of the two airplanes included strain gages (denoted by the small + signs) to measure bending- and shear-strain indications on the front and rear spars at 5 spanwise stations. Accelerometers were installed at a number of locations on the airplanes. The accelerometer measurements

pertinent to the present paper are shown by the shaded circles on the figures and were at the nodal points of the fundamental wing bending mode of the B-29 airplane and at the center of gravity of the B-47A airplane. In addition to the accelerometers and strain gages, the instrumentation included control position recorders and attitude and rate gyros. One significant addition to the B-47A instrumentation was a flow-direction vane from which a time history of the vertical gust velocity could be derived by correcting for airplane motions.

Relative to the present investigations, these two airplanes differed in a number of respects. The airplane weights were about the same with the test weight of the B-29 airplane at 105,900 pounds and the weight of the B-47A airplane at 113,200 pounds. However, the B-29 airplane had a far greater proportion of its total weight (about 80 percent) in the wings since almost all the fuel was in wing tanks. The B-47A carries all its fuel in the fuselage, and the ratio of the wing weight to total weight for this airplane was 36 percent. In addition to the differences in the proportion of weight in the wing, it should be mentioned that the weight distribution of the B-29 wing was relatively uniformly distributed over the span, whereas that for the B-47A wing was typified by large concentrated masses due to engine nacelles. The airplanes also differed significantly in stiffness distribution with the wing of the B-29 airplane being about twice as stiff as that of the B-47A airplane. A further difference, which will be of some consequence in the results to be presented, arises from the swept wing of the B-47A. Because of the swept wing, the lower stiffness, and the concentrated masses, the B-47A airplane has rather large static aeroelastic effects in contrast to the absence of significant aeroelastic effects on the B-29 airplane and on the other airplanes studied.

The flight tests for both airplanes were in clear air turbulence at an altitude of about 2,000 feet above terrain. The flight test speeds were 250 miles per hour for the B-29 airplane and 478 miles per hour for the B-47A airplane. The basic test results were obtained in flight test runs of several minutes duration in continuous rough air for each of these test airplanes. In addition to the rough-air tests, slow maneuver pull-ups were also made in smooth air at various test conditions in order to determine quasi-static reference strains.

METHODS FOR DETERMINATION OF FREQUENCY RESPONSE

In discussing the results of these investigations, the basic quantity that will be used is the frequency-response functions of the wing strains or accelerations to gust disturbances. This function describes the airplane response in strain or in normal acceleration, as the case may be, to unit sinusoidal gusts of various frequencies. The airplane response

to continuous rough air depends essentially on the product of the amplitude squared of the frequency-response function and the power spectrum of the gust velocity. Two basic approaches may be used for the experimental determination of the frequency-response functions to gust inputs, and these are given as follows: The first method, called the spectrum method, is based upon the relation between the power spectrum of a random disturbance and the power spectrum of the response of a linear system to the disturbance. From this relation, the amplitude squared of the frequency-response function is given by

$$\left|H(f)\right|^2 = \frac{\Phi_o(f)}{\Phi_i(f)}$$

where

$\left\|H(f)\right\|^2$	amplitude squared of frequency-response function
$\Phi_o(f)$	power spectrum of airplane response
$\Phi_i(f)$	power spectrum of disturbance or gust input

The application of this method simply requires the measurement of the response power spectrum Φ_o and the power spectrum of the gust input Φ_i.

The second method designated as the cross-spectrum method is based upon the relationship for linear systems between a random input disturbance and the cross spectrum between the input disturbance and the system response to the disturbance. From this relationship, the frequency-response function is given by the following expression:

$$H(f) = \frac{\Phi_{i,o}(f)}{\Phi_i(f)}$$

where $\Phi_{i,o}(f)$ is the cross spectrum between the disturbance input and the airplane response. Note in this second method that both the amplitude and phase of the frequency-response function $H(f)$ are obtained since $\Phi_{i,o}(f)$ is, in general, complex.

In the material to be presented, both of these methods will be applied. It should be noted that if the measurements of turbulence such as that obtained from the angle-of-attack vane adequately represent the gust input, then the two methods should yield identical results for the amplitude of the frequency-response function. If, however, complicating factors are present, such as significant variations in turbulence across the

airplane span, the results obtained by the two methods will differ (see appendix). In the following material, this property will be used in assessing the significance of spanwise variations in the turbulence on the test results.

RESULTS FOR THE B-29 AIRPLANE

The measurements obtained in the course of the B-29 flight investigation have been used to estimate the frequency-response function for the bending strains at the various stations by application of the spectrum method described in the preceding section. In estimating the frequency-response function, it was necessary to assume a shape for the gust spectrum since the gust spectrum was not measured in the B-29 investigation. The gust spectrum used for this purpose is given by the following expression:

$$\Phi(\Omega) = \sigma^2 \frac{L}{\pi} \frac{1 + 3\Omega^2 L^2}{\left(1 + \Omega^2 L^2\right)^2}$$

where $\Omega = 2\pi f/V$ and V is the airplane speed. This spectrum has been found to approximate the atmospheric conditions covered by flight measurements of gust spectra when a value of about 1,000 is used for the scale of the turbulence L. The intensity of the turbulence which is described by the root-mean-square gust velocity σ is, however, not known for the B-29 measurements.

In order to permit direct comparisons of the frequency-response functions at the various wing stations, the results were converted to "equivalent accelerations" by dividing the strains at each station by the strain per g measured at the station during slow pull-ups. The results obtained for the amplitude of the frequency-response function on this basis are shown in figure 2. The ordinate represents the amplitude of the bending-strain response for a unit sinusoidal gust velocity at the various frequencies. The four solid-line curves shown in the figure are the results for the four spanwise stations whose locations are designated in terms of the fraction of the semispan $\frac{y}{b/2}$. Also shown in figure 2, by the dashed-line curve, is the frequency-response function obtained from the measured nodal accelerations and which can be considered as a reference for static loading. Thus, the difference between this reference and the other curves gives an indication of the effects of wing flexibility. (Flexibility also has an effect on the nodal accelerations, but this effect is small.)

Comparison of the solid curves of figure 2 with the reference curve of nodal acceleration shows that the principal effects of flexibility

are associated with a large peak at the first bending mode, which is at 2.7 cps. The amplification is highest for the 15-percent-semispan station and progressively decreases with outboard wing span station. Above about 4 cps, the curves are somewhat disorderly, probably because of the effects of higher structural modes.

In order to see how well the frequency-response functions could be determined analytically, calculations were also made. The calculated strain frequency-response functions were converted to equivalent accelerations for direct comparison with the results of figure 2 and are shown in figure 3. These results are for three modes or degrees of freedom, that is, airplane vertical motion and the first and second symmetrical bending modes. Comparison of the results in figures 2 and 3 shows that, in general, the character and trends of the experimental and calculated frequency-response functions are in fairly good agreement in regard to flexibility effects. Both figures indicate that the principal effects of flexibility are associated with the first bending mode and that the amplification is largest at the root station and progressively decreases with outboard wing span station.

It is of interest to note that the calculated and measured frequency-response functions (figs. 3 and 4) differ below about 1 cps. This difference is due principally to the omission of the pitching motion in the calculations. Because of the high gust input power at these low frequencies, it would thus appear that the inclusion of the pitching mode is quite important in determining the actual output response.

The effect which the frequency-response functions have on the overall bending-strain amplification is shown in figure 4. In the upper part of the figure, the ordinate is the ratio of the root-mean-square strain for the flexible airplane $\sigma_{\epsilon,FLEX}$ to the root-mean-square strain for the reference condition $\sigma_{\epsilon,REF}$. The reference strains were based on the nodal-point accelerations measured in rough air and the strain per g as measured at the various spanwise stations in slow pull-ups. This reference condition represents the strains for the static application of loads, and thus this ratio provides a measure of dynamic-strain amplification. The circles represent the measured amplification factors, and the curves represent calculated results. The dashed curve was obtained by considering two modes: airplane vertical motion and the first symmetrical mode in bending. The solid curve was obtained by using three modes: airplane vertical motion and the first two symmetrical bending modes. The measured results show that the overall strain amplification is approximately 10 percent at the root station and is somewhat lower at the outboard wing stations. Both the two-mode and three-mode calculations are in rather good agreement with the measured results except at the farthest outboard station.

A second set of strain-amplification factors is shown in the lower part of figure 4. This ordinate is the ratio of the strains that would occur with equal frequency for the flexible airplane ϵ_{FLEX} and for the reference airplane condition ϵ_{REF}. The frequency level at which this strain ratio was taken corresponds to a value of strain equal to about twice the root-mean-square strain. These experimental amplifications are about twice as large as those shown in the top figure based on root-mean-square strains. This is a consequence of flexibility having a greater effect on the number of peak strains than on the root-mean-square values. The calculations which use only two modes underestimate the strain amplifications at the outboard stations, whereas the analysis using three modes gives a good approximation to the measured results.

The foregoing results imply that, for this straight-wing airplane, calculations using only vertical motion and the fundamental bending mode are adequate for determining the effects of flexibility on the root-mean-square strain values but that the second bending mode must also be included when considering peak strains.

RESULTS FOR THE B-47A AIRPLANE

Frequency-Response Functions

The rest of this paper will cover test results obtained from the B-47A airplane investigations. Figure 5 shows the measured frequency-response functions for the rear-spar bending strains for various wing stations. Similar results were also obtained for the strains on the front spar but are not included. The results shown are for both the amplitude and the phases and were obtained by the cross-spectrum method. The gust input spectrum was obtained from the vane angle-of-attack measurements corrected for airplane motions according to the method given in reference 4. For present comparisons, the measured strains at the various stations were converted to equivalent accelerations by dividing by the strains per g in pull-ups at the same test conditions. The reference curve shown in the figure was based on the center-of-gravity accelerations which appear to be relatively uninfluenced by the fundamental airplane vibration mode and provides a measure of the strains for static loading. (The use of the center-of-gravity accelerations for the reference loading is discussed in more detail later.) The differences between the reference curve and the other curves thus provide a direct measure of the effects of the dynamic flexibility on the local strains. As in the case of the B-29, the effects of flexibility show up principally as a large peak at the first bending mode frequency which is around $1\frac{1}{2}$ cps. In contrast to the B-29, however, the magnitude of the peak is now smallest at the root station and progressively increases for the outboard stations. Another

significant difference between the frequency-response functions for the B-47A and the B-29 airplanes is the closer proximity of the first bending mode to the short-period mode which is at about 0.6 cps. As a consequence, the gust input, which decreases rapidly with frequency, will be relatively much higher at the first bending mode in this case, and larger overall amplification effects may be expected.

The phases shown in figure 5(b) indicate a linear increase in phase lag with increasing frequency, as is the case for a simple system with a moderate amount of damping. Above 2 cps, the curves appear to be erratic. The results above 2 cps are not, however, considered to be reliable.

Strain-Amplification Factors

Figure 6 shows the variations in the bending-strain-amplification factors with spanwise positions. Again, the results are shown based on both root-mean-square values and strains having an equal frequency of occurrence. Note that the ordinate scale is compressed and covers a wider range of amplification values than the scale used earlier for the corresponding B-29 results.

For the swept-wing airplane, the effects of flexibility are complicated by large static aeroelastic or twist effects which act to reduce the gust loading and the strain response. Thus, the derivation of amplification factors for this case is not straightforward, and several procedures might be used. For present purposes, three strain responses are considered. These are the actual measured strains, the numerator of the ordinate, and two reference strain conditions. These reference strains are

(1) The strains obtained by the static application of the same loads to the airplane.
(2) The strains obtained by the static application of the loads to an essentially "rigid" airplane, that is, an airplane embodying no static aeroelastic effects.

The ratio of the measured strains to the strains in the statically elastic airplane yields the solid-line curves and provides a measure of the purely dynamic strain amplification. (See fig. 6.) The ratio of the measured strains to the strains for the airplane without static aeroelastic effects yields the dashed-line curves and provides a measure of the combined effects of the static alleviation and the dynamic amplification.

The procedure used in the determination of the reference strains was based upon the use of the actual measured center-of-gravity accelerations as a measure of the airplane loading in rough air. Examination of the power spectra of the normal accelerations had indicated that the

first mode had only a minor effect on the center-of-gravity accelerations. As a further check, the average airplane acceleration was determined for a short section of the test run by using the accelerometer measurements from 22 locations along the wing and fuselage of the test airplane along with their associated masses. The results obtained indicated that, except for the presence of high-frequency fluctuations associated with the higher structural modes, the center-of-gravity acceleration provided a good measure of the airplane acceleration. On this basis, the center-of-gravity acceleration measurements were faired to remove the effects of the higher structural modes and used as a measure of the airplane loading. The loads obtained on this basis were then converted to strains for the various stations on a static basis by using the strains per g as measured in slow pull-up maneuvers at the test dynamic pressure. The strains obtained on this basis provide a measure of the strains for a statically elastic airplane and were used in obtaining the solid-line curves of figure 6.

In order to provide a measure of the static-aeroelastic effects on the strains, the strains per g in pull-ups were also determined for the condition of low or zero dynamic pressure. At low dynamic pressure, the static aeroelastic effects tend to be minimized, and thus the strains per g obtained at low dynamic pressure provide a basic "rigid" airplane reference condition. Figure 7 illustrates the values of bending strain per g obtained at one station $\left(\frac{y}{b/2} = 0.60\right)$ for various values of dynamic pressure. The variation of the strain per g appears linear over the wide range of dynamic pressure represented. A linear extrapolation to a value of dynamic pressure of 0 was therefore used. The difference between the strain per g (0.65) for a dynamic pressure of 0 and the value (0.51) for the test dynamic pressure provides a measure of the static aeroelastic strain alleviation for this station. The amount of this alleviation is about 22 percent for this station and varied somewhat for the other stations.

The strains per g for the condition at a dynamic pressure of 0 were used with the airplane center-of-gravity acceleration to obtain the second set of reference strains. These reference strains constitute strains for an airplane embodying no dynamic flexibility or static aeroelastic effects and were used to obtain the dashed curves of figure 6.

In the upper part of figure 6, the dynamic amplification, shown by the solid curve, is about 10 percent at the root but increases rapidly along the span and reaches a value of about 2 at the 60-percent-semispan station. The amplification factors obtained by considering both the static alleviation and dynamic effects, shown by the dashed line, are below 1 at the inboard stations but reach values of about 1.5 at the 60-percent-semispan station.

The amplification factors based on the ratios of strains for equal frequency of occurrence, shown in the lower part of figure 6, follow the same pattern as those based on the root-mean-square values but are everywhere higher. It thus appears that, for the swept-wing B-47A airplane, the effects of dynamic flexibility are quite large, particularly at the mid-span stations, but that favorable static aeroelastic alleviation moderates the large dynamic amplifications. In addition, it is evident that several values for the amplification factor may be obtained depending upon the particular definition or reference used. The particular amplification factor of significance depends upon the specific application.

EFFECTS OF SPANWISE VARIATIONS IN TURBULENCE

As a final point, some indirect evidence of the effects of spanwise variations in turbulence on airplane gust response will be presented. As mentioned previously, two methods could be used in determining the frequency-response functions for the B-47A: the spectrum and the cross-spectrum methods. As indicated, if no spanwise variations in turbulence existed, then the gust input would be adequately reflected by the point measurements of the angle-of-attack vane. For this case, both methods should yield identical results for the frequency-response function. Figure 8 shows the frequency-response functions obtained by the two methods for the airplane center-of-gravity normal acceleration. It is quite clear that the cross-spectrum results are consistently lower than those obtained by the spectrum method. Similar differences also have been found between strain frequency-response functions obtained by the two methods. The differences between these two results are suggestive of the effects of spanwise variations in gusts which have received considerable attention recently in analytical studies by Diederich, Drischler, and Liepmann. (See refs. 5, 6, and 7.)

By making use of some results obtained by Diederich (ref. 5), first-order adjustments for the effects of spanwise variations of turbulence for the condition of isotropic turbulence were made to these two results in accordance with the analysis given in the appendix. The adjusted frequency-response functions obtained are shown in figure 9. Two effects may be noticed from this adjustment. First, the two frequency-response functions are now in much better agreement, and second, the adjustment has raised the two curves by from 10 to 20 percent over most of the frequency range in accordance with the span averaging functions of figure 10. The basis for the underestimation and distortion in the apparent frequency-response function of figure 8 stems from the fact that the point gust input used is too high. The effective gust input is the average gust velocity across the span which, as indicated in reference 5, tends to fall below the point input at all frequencies. As a consequence, the airplane acceleration response is lower than what would be expected for uniform

turbulence across the span in accordance with the point measurements. These results thus suggest that the effects of spanwise variations in turbulence are significant for such airplanes as the B-47A. In addition, since analytic results indicate that the effects of spanwise variations in turbulence are primarily a function of span, these effects may be even more important for airplanes with larger span than the present airplane.

CONCLUDING REMARKS

It has been indicated that, for the B-29 airplane, the effects of the first and second symmetrical bending modes yield moderate strain amplifications in rough air all along the airplane span. Calculations involving one or preferably two structural modes appear to yield reliable estimates of flexibility on the strains.

For swept-wing airplanes, the effects of flexibility are complicated by the importance of static aeroelasticity effects in addition to the dynamic response. In the case of the B-47A airplane, the dynamic amplifications appear to be quite large, particularly in the midspan region. These amplifications are at least partially balanced by large and favorable static aeroelastic effects associated with sweep. Finally, some indirect results suggest that spanwise variations in turbulence have a significant effect on the responses of the B-47A airplane.

APPENDIX

EFFECTS OF SPANWISE VARIATIONS IN TURBULENCE ON MEASURED FREQUENCY-RESPONSE FUNCTIONS

In the main body of this paper, it was indicated that, for uniform turbulence across the airplane span, the amplitude of the frequency-response function for gust disturbances $|H(f)|$ can be obtained experimentally by two methods; the spectral method which is based on the relation

$$|H_s(f)|^2 = \frac{\Phi_o(f)}{\Phi_i(f)} \tag{A1}$$

and the cross-spectral method which is based on the relation

$$H_c(f) = \frac{\Phi_{i,o}(f)}{\Phi_i(f)} \tag{A2}$$

The subscripts s and c are used to differentiate between the estimates obtained by the two methods. In this appendix, the effects on these estimates of spanwise variations of turbulence will be outlined. The material to be presented is based on the analysis of the effects of spanwise gust variations given in reference 5.

The response of an airplane $z(t)$ to two-dimensional turbulence, that is, turbulence varying along the flight path and along the spanwise direction, may be expressed as

$$z(t) = \int_{-b/2}^{b/2} \int_{-\infty}^{\infty} x(t - t_1, y)\, h(t_1, y)\, dt_1\, dy \tag{A3}$$

where

b wing span

$x(t,y)$ vertical gust velocity impinging at wing leading edge at time t and span location y

$h(t,y)$ response at time t due to unit impulse gust impinging at wing between station y and $y + dy$ at time zero

The power spectrum of $z(t)$ as derived in reference 5 is given by

$$\Phi_z(f) = \int_{-b/2}^{b/2}\int_{-b/2}^{b/2} \Phi_x\left(f,\ y_2-y_1\right)H\left(f,y_1\right)H^*\left(f,y_2\right)dy_1\ dy_2 \qquad (A4)$$

where

$\Phi_z(f)$ power spectrum of response $z(t)$

$\Phi_x\left(f,\ y_2-y_1\right)$ cross-spectrum between gust velocities impinging at wing leading edge at stations y_2 and y_1

$H(f,y)$ influence function describing response of airplane to unit sinusoidal gusts impinging at wing leading edge at station y and is given by

$$H(f,y) = \int_0^\infty h(t,y)e^{-ift}dt$$

The asterisk designates the complex conjugate.

In these terms, the frequency-response function obtained by the spectral method can be expressed as

$$\left|H_s(f)\right|^2 = \frac{\int_{-b/2}^{b/2}\int_{-b/2}^{b/2} \Phi_x\left(f,\ y_2-y_1\right)H\left(f,y_1\right)H^*\left(f,y_2\right)dy_1\ dy_2}{\Phi(f,0)} \qquad (A5)$$

where $\Phi(f,0)$ is the power spectrum of the gust input at span station 0 (such as measured with the vane).

The expression for $\left|H_s(f)\right|^2$ given by equation (A5) may be viewed as an average frequency-response function. Further insight into this result can be obtained by considering the special case

$$H(f,y) = H(f)\gamma(y) \qquad (A6)$$

where

$$\int_{-b/2}^{b/2} \gamma(y)dy = 1$$

For this case

$$\left|H_s(f)\right|^2 = \left|H(f)\right|^2 \left[\frac{\int_{-b/2}^{b/2}\int_{-b/2}^{b/2} \Phi_x(f,\, y_2-y_1)\gamma(y_1)\gamma(y_2)\,dy_1\,dy_2}{\Phi(f,0)}\right]$$

$$= \left|H(f)\right|^2 \bar{\gamma}_1^2(f) \qquad \text{(A7)}$$

Equation (A7) indicates that the quantity $\left|H_s(f)\right|^2$ determined from measurements represents the "frequency part" of the frequency-response function and is multiplied by the term in brackets, which might be considered a span averaging function. For the case of uniform turbulence across the span, equation (A7) reduces to

$$\left|H_s(f)\right|^2 = \left|H(f)\right|^2$$

If the turbulence is isotropic with a known spectrum, the averaging function given by the term in brackets in equation (A7) can be evaluated. Evaluations of the numerator of the term in brackets are given in references 5 and 6 for several assumed power spectra of turbulence and for several assumed span distributions y. By using these results, the function $\bar{\gamma}_1(f)$ was evaluated for a particular case and the results obtained are shown in figure 10. The result shown in figure 10 is for the case of a uniform span distribution ($\gamma(y) = 1/b$) and a spectrum of vertical gust velocity given by

$$\Phi(\Omega) = \sigma_w^2 \frac{L}{\pi} \frac{1 + 3\Omega^2L^2}{\left(1 + \Omega^2L^2\right)^2} \qquad \text{(A8)}$$

where $\Omega = \frac{2\pi f}{V}$ and V is the airplane forward speed. In equation (A8), σ_w is the root-mean-square gust velocity and L is the scale of turbulence. A value of L = 1,000 feet appears to be representative of conditions for atmospheric turbulence. For present purposes, a value of b/L = 0.1 was assumed.

A similar analysis may be applied to the cross-spectrum case and yields the following results:

[redacted]

$$H_c(f) = H(f)\left[\frac{\int_{-b/2}^{b/2} \Phi_x(f,y)\gamma(y)dy}{\Phi(f,0)}\right]$$

$$= H(f)\bar{\gamma}_2(f) \qquad \text{(A9)}$$

where the weighting function given by the term in brackets may also be viewed as an average span weighting function $\bar{\gamma}_2(f)$. The function $\bar{\gamma}_2(f)$ can also be evaluated from figure 4 of reference 5 for the case of uniform span loading and the gust spectrum of equation (A8). This function $\bar{\gamma}_2(f)$ is also shown in figure 10.

If the weighting functions $\bar{\gamma}_1(f)$ and $\bar{\gamma}_2(f)$ given in equations (A7) and (A9) are divided into the measured values of $|H_s(f)|$ and $|H_c(f)|$, respectively, of figure 8, estimates of $|H(f)|$ may be obtained which are compatible. The results obtained in this manner are shown in figure 9.

[redacted]

[redacted]

REFERENCES

1. Mickleboro, Harry C., and Shufflebarger, C. C.: Flight Investigation of the Effects of Transient Wing Response on Wing Strains of a Twin-Engine Transport Airplane in Rough Air. NACA TN 2424, 1951.

2. Murrow, Harold N., and Payne, Chester B.: Flight Investigation of the Effect of Transient Wing Response on Wing Strains of a Four-Engine Bomber Airplane in Rough Air. NACA TN 2951, 1953.

3. Houbolt, John C., and Kordes, Eldon E.: Structural Response to Discrete and Continuous Gusts of an Airplane Having Wing-Bending Flexibility and a Correlation of Calculated and Flight Results. NACA Rep. 1181, 1954. (Supersedes NACA TN 3006; also contains essential material from TN 2763 and TN 2897.)

4. Crane, Harold L., and Chilton, Robert G.: Measurements of Atmospheric Turbulence Over a Wide Range of Wavelength for One Meteorological Condition. NACA TN 3702, 1956.

5. Diederich, Franklin W.: The Response of an Airplane to Random Atmospheric Turbulence. NACA TN 3910, 1957.

6. Diederich, Franklin W., and Drischler, Joseph A.: Effect of Spanwise Variations in Gust Intensity on the Lift Due to Atmospheric Turbulence. NACA TN 3920, 1957.

7. Liepmann, H. W.: Extension of the Statistical Approach to Buffeting and Gust Response of Wings of Finite Span. Jour. Aero. Sci., vol. 22, no. 3, Mar. 1955, pp. 197-200.

[redacted]

[redacted]

TEST AIRPLANES

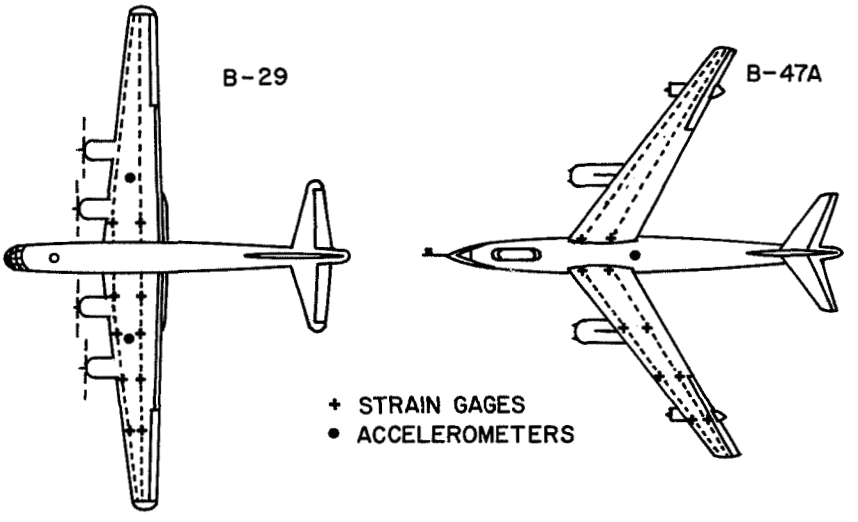


Figure 1

MEASURED B-29 STRAIN
FREQUENCY RESPONSE FUNCTION

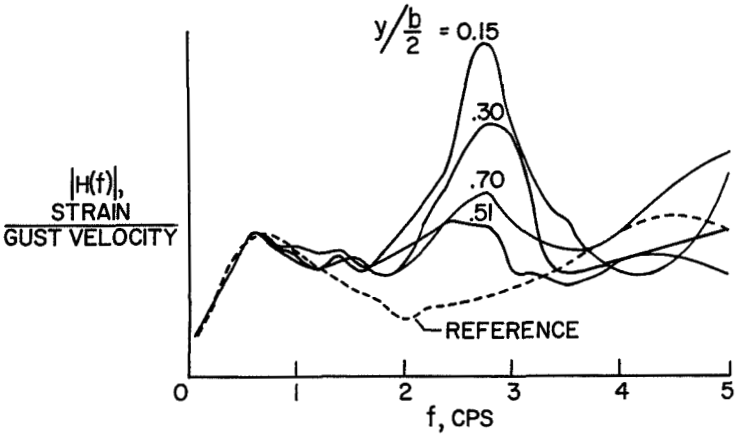


Figure 2

CALCULATED B-29 STRAIN
FREQUENCY RESPONSE FUNCTION

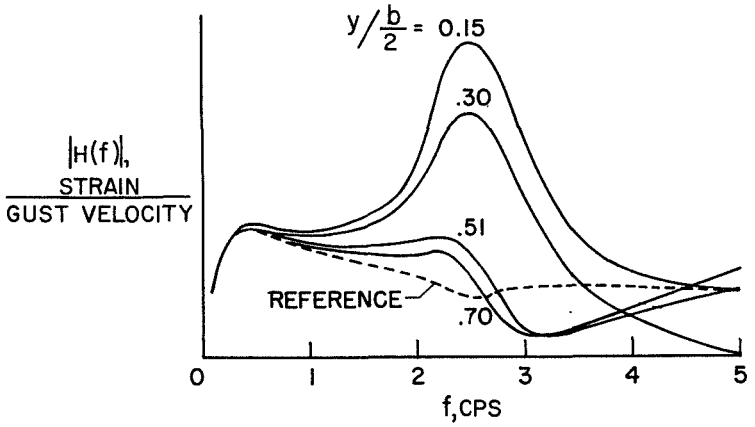


Figure 3

B-29 STRAIN AMPLIFICATION

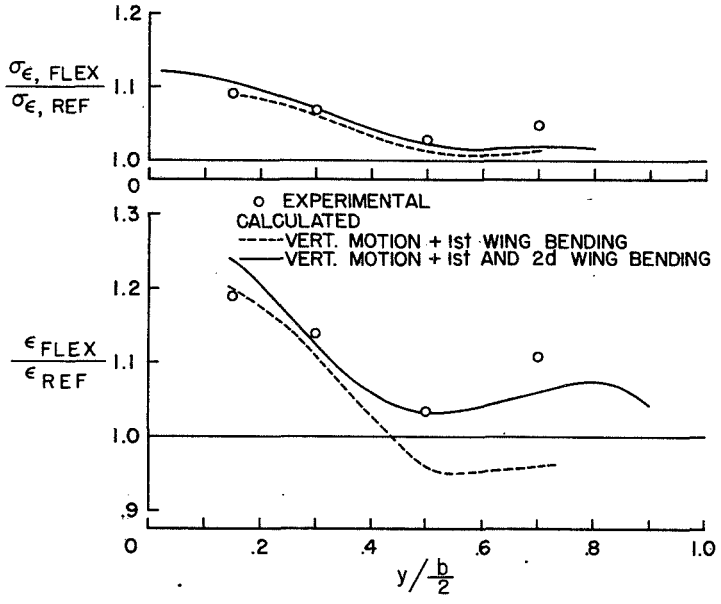


Figure 4

MEASURED B-47A STRAIN FREQUENCY-RESPONSE FUNCTION

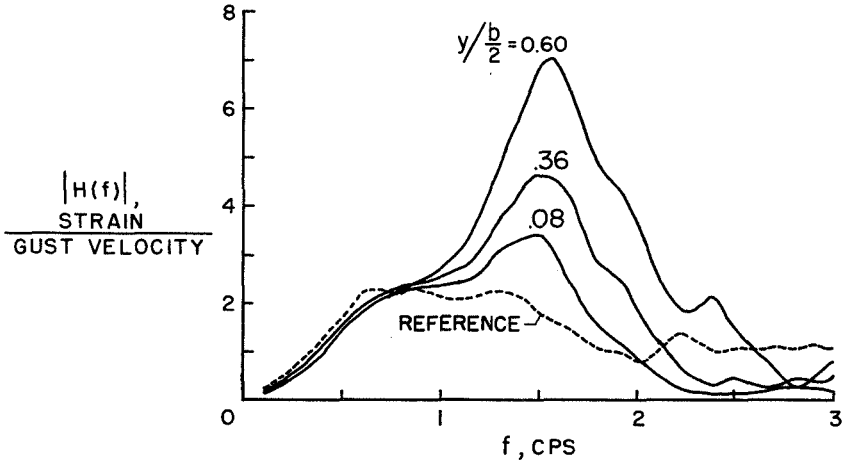
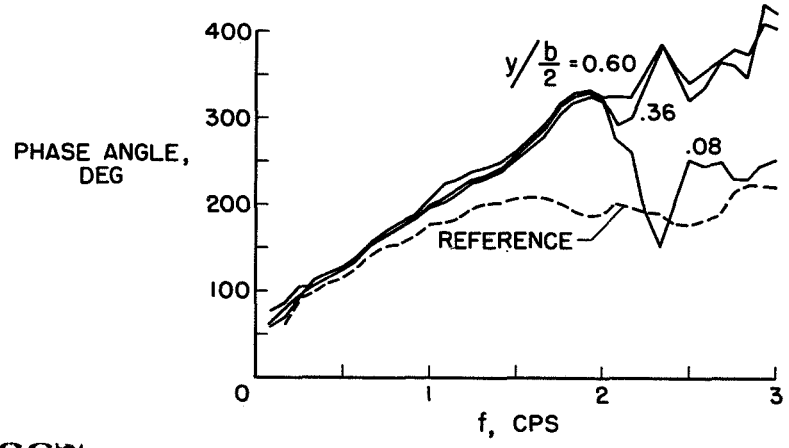


Figure 5(a)

MEASURED B-47A STRAIN FREQUENCY-RESPONSE FUNCTION
PHASE ANGLE



227

Figure 5(b)

B-47A STRAIN AMPLIFICATION

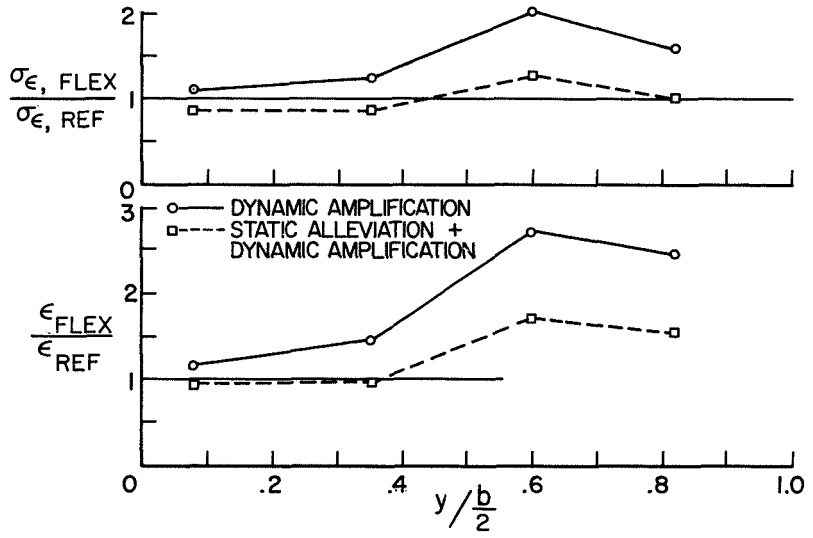
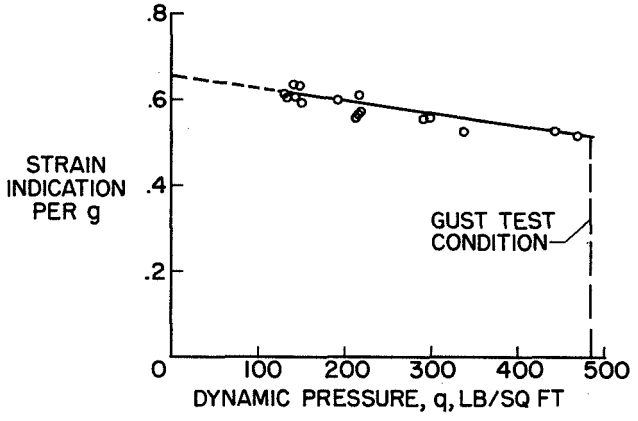


Figure 6

VARIATION OF STRAIN PER g IN PULL-UP WITH DYNAMIC PRESSURE



228

Figure 7

[redacted]

B-47A NORMAL—ACCELERATION FREQUENCY-RESPONSE FUNCTION

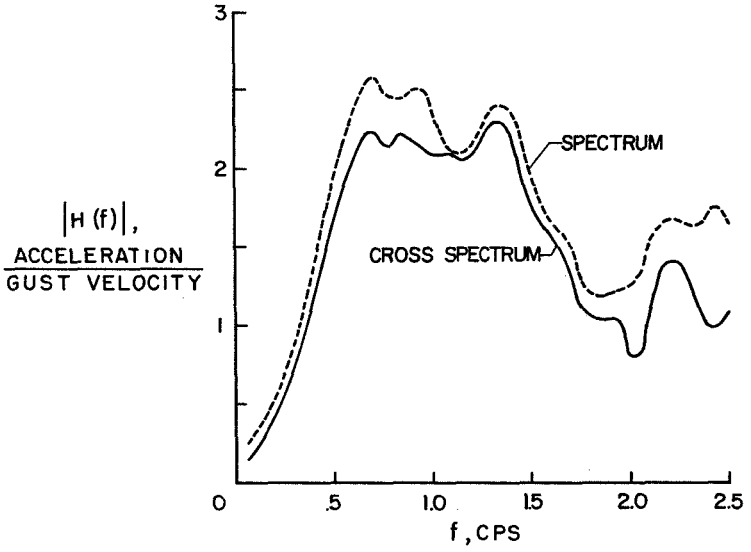


Figure 8

B-47A NORMAL—ACCELERATION FREQUENCY-RESPONSE FUNCTION
ADJUSTED FOR SPANWISE GUST VARIATIONS

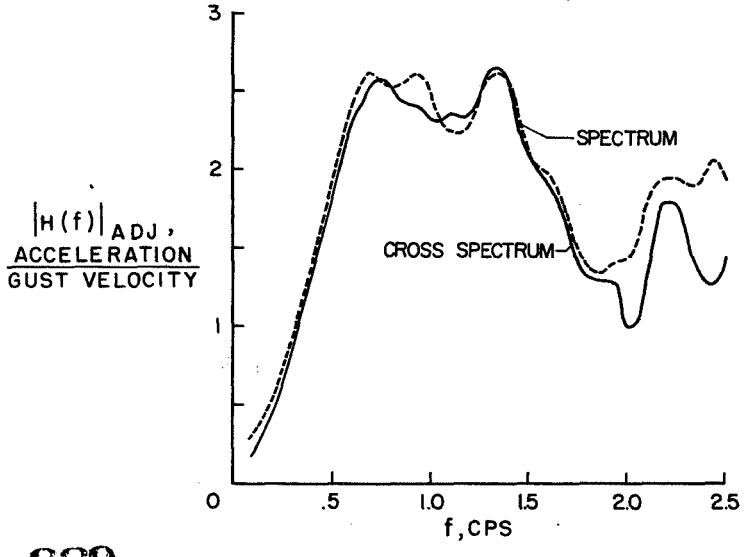


Figure 9

[redacted]

SPAN AVERAGING FUNCTIONS $\overline{\gamma}_1(f)$ AND $\overline{\gamma}_2(f)$ FOR b/L = 0.1

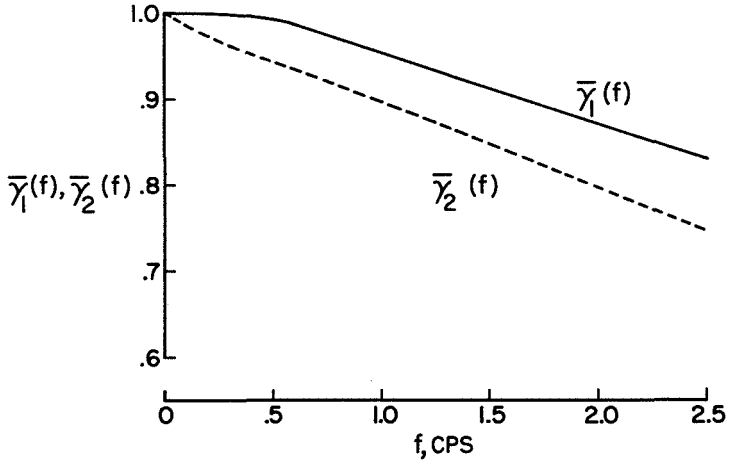


Figure 10

N71-75396

LOADS IMPLICATIONS OF GUST-ALLEVIATION SYSTEMS

By William H. Phillips

Langley Aeronautical Laboratory

SUMMARY

A review is presented of the factors affecting gust loads and the methods or devices which reduce these loads. Aerodynamic devices which reduce the lift-curve slope include spoiler-deflector controls, for which some data are presented in the Mach number range from 0.4 to 1.1. Systems are also considered in which a sensing device is used to operate gust-alleviation controls. Two basically different types of sensing devices are possible, the load-sensing type and the angle-of-attack-sensing type. These devices are compared and their limitations discussed. Some preliminary flight measurements of wing-root bending moment due to turbulence are presented for a gust-alleviation system installed in a small twin-engine transport airplane. This system increased the wing-root bending moments as compared with those of the basic airplane. This increase resulted from the fact that the system as tested was adjusted to reduce acceleration and, as a result, overcompensated for the wing-root bending moments due to gusts. Some flight measurements of the effects of a yaw damper on the tail loads of a bomber airplane are also presented.

INTRODUCTION

Gust alleviation has been of continued interest to almost every group in aviation since its inception, but it has not been incorporated in production airplanes. Apparently the reason for the lack of use of gust alleviation is that detailed analyses of promising devices either pose problems insoluble at a given stage in aircraft development or result in practical disadvantages that seem to outweigh the potential benefits. Systems have been studied by various organizations with the objectives of providing improved riding comfort, increased safety due to load reductions, reduced structural weight, and more stable gun platforms.

Inasmuch as the various systems are perennially proposed as means of improving aircraft, a need for a summary of the methods available for gust alleviation and the problems associated with these methods is apparent. The present report considers the loads implications of gust-alleviating methods.

[redacted]

SYMBOLS

c	wing chord
C_{L_α}	lift-curve slope
q	dynamic pressure
U	gust velocity
V	true airspeed
ΔC_D	drag-coefficient increment
M	Mach number
α	angle of attack
V_S	velocity at stall
V_C	cruising speed
V_{MAX}	maximum speed

DISCUSSION

The factors affecting gust loads are shown in table 1. The first factor is the direct load due to the gust. As indicated by the formula, this load is proportional to the lift-curve slope C_{L_α}, the dynamic pressure q, and the change in angle of attack due to the gust, U/V, where U is the gust velocity and V is the true airspeed. This load may therefore be reduced by reducing C_{L_α} or by reducing q. The second factor is the airplane motion due to gusts or due to controls. The airplane motion is dependent on the basic airplane stability, and may also be influenced by the operation of controls manually or by an autopilot. The third factor to be considered is the action of special controls to offset the gust load directly. This category would include the relieving effects due to wing bending, the use of hinged surfaces or wings, and finally the use of special gust-alleviating controls, such as wing flaps, operated by a servomechanism.

[redacted]

Effect of Spoiler-Deflector Control

Aerodynamic devices which reduce the lift-curve slope include the use of sweep or reduced aspect ratio, the effects of which are well known, and the use of chordwise slots which, in effect, reduce the aspect ratio. Another device for reducing the lift-curve slope is the spoiler-deflector control (ref. 1). The effects of this device as a function of Mach number on a swept wing are shown in figure 1. This figure shows the percent of the basic wing load produced by the wing with a spoiler-deflector control covering 18 percent of the span. The increment in drag coefficient is also shown. These data are taken from reference 2. The spoiler height above the wing was 0.025c and the deflector projection below the wing was 0.15c. In this case, the reason for the short span of the spoiler-deflector control was to locate it inboard of the aileron and outboard of the horizontal tail. This device provides a large increase in drag as well as a reduction in lift-curve slope. For this reason, this control might be useful for slowing an airplane down when rough air is encountered but it would not be desirable for continuous use in high-speed flight. Tests on specific configurations have shown that this control may be located so as to minimize longitudinal trim changes. Location of the spoiler-deflector control ahead of an aileron, however, has been found to reduce greatly the aileron effectiveness, as might be expected. Possibly, the spoiler-deflector control could be operated in conjunction with the aileron to overcome this difficulty.

Effect of Sensor and Servo System Operating Special Controls

In systems which use a sensing device to detect the gusts and to operate gust-alleviation controls, two basically different types of sensing devices are possible: one, the load-sensing type such as strain gages or an accelerometer, and the other, the angle-of-attack-sensing type. The effects of these devices differ in several important respects. First, as shown in figure 2, these sensing devices exhibit different trends of effectiveness as a function of airspeed. The gust envelope for a typical transport airplane is also shown in this figure. With the load-sensing type of gust alleviation the percent alleviation increases with increasing speed, whereas with the angle-of-attack-sensing type the percent alleviation tends to remain constant. Thus, if the two systems are designed to have the same effectiveness at a given speed, the load-sensing type will show greater effectiveness at higher speeds. These results apply only if the system gain is held constant as might occur with the use of some simple types of aerodynamically operated gust alleviators. If a servo system is used, of course, it is possible to vary the gain of the system as a function of speed and thereby change the effects of speed from those shown.



The second difference between the two systems is concerned with the different nature of the effects which limit the maximum alleviation obtainable. The usual limitation in the case of the load-sensing system is the occurrence of a high-frequency instability. Figure 3 shows the percent load experienced with a load-sensing system as a function of the relative gain. A relative gain of 1 on this scale represents a condition in which, for example, a load increment corresponding to 1 g on the sensor will operate the controls to produce a load increment of -1 g on the airplane. Very high gains are required to obtain a large percent of alleviation. A load-sensing system, however, is a typical closed-loop system, for which high gains are likely to result in instability. Analog-computer studies for certain typical cases have shown that reduction in load below 50 percent of the unalleviated case resulted in an oscillatory response and that these oscillations became unstable at a higher gain as shown.

With the angle-of-attack-sensing system, this type of instability is much less likely to be encountered because this arrangement is much more nearly an open-loop system, that is, operation of the angle-of-attack sensor causes deflection of the alleviation controls but operation of the alleviation controls has only a minor effect on the indications of the angle-of-attack sensor. For this reason, the limitation is less on the amount of gain which may be employed, and systems are designed usually so that the effect of a uniform gust is completely counteracted by the alleviation controls. With this type of system the limits on the load reductions obtainable result primarily from the fact that sensing the gust at one point does not give a representative indication of the average angle of attack across the wing span. Unpublished theoretical studies have shown that the effect of nonuniform gust velocity across the span for the angle-of-attack-sensing system is a function of the ratio of the wing span to the scale of turbulence. Because of the large scale of atmospheric turbulence, values of alleviation as high as 80 percent may be obtained with a single sensor located ahead of the nose which operates the controls with no lag. The addition of a suitable filter to the output of the sensor which reduces the response to high-frequency gusts further improves the alleviation theoretically attainable. Such a filter may also be desirable in order to reduce the effects of structural feedback, which might cause the system to reinforce structural modes of oscillation if the system response were not attenuated at high frequencies.

Flight Tests of Gust-Alleviation System Installed in Airplane

A flight investigation has been made of a gust-alleviation system installed in a small twin-engine transport airplane. Some preliminary results of this study have been reported previously (refs. 3 and 4). This system was designed p[redacted] improvement of passenger

comfort. The system uses an angle-of-attack vane to operate wing flaps through a servo system. The reduction in acceleration obtained with this system is shown in figure 4. The relative values of normal acceleration as a function of frequency, obtained with the basic airplane and the gust-alleviated airplane for comparable conditions of turbulence, and the effect of the system on pitching velocity are shown. The relative values plotted in this figure are proportional to the square root of the power spectral density of the response and show the correct relative values as well as the variation of the response with frequency. The normal acceleration for the alleviated airplane was reduced to 30 or 40 percent of that for the basic airplane in the frequency range from 0 to 2 cyles per second. The pitching velocity, which was small for the basic airplane, was further reduced for the alleviated case.

Extensive strain-gage measurements have been made to determine the effect of this system on the structural loads. These data have not been completely evaluated at this time. The effect of the system on wing-root bending moment is shown in figure 5. The wing-root bending moment is actually increased by the gust-alleviation system. The explanation of this increase is indicated by the insert on the figure which shows the change in span load distribution for basic and alleviated airplanes due to a small positive increment of angle of attack. In the alleviated case, the flaps on the wing are deflected up on the outboard sections and down near the root. This arrangement provides downwash conditions at the tail which minimize pitching moments due to the gusts. The resultant lift due to this combination is about zero, but because the tip sections are much more effective in producing bending moment, the result is a negative bending moment due to an up gust. The magnitude of this negative bending moment is actually greater for a given gust than the positive bending moment on the basic airplane.

These results apply only so long as the system is operating in its linear range. At a gust velocity of about 10 feet per second, the flaps reach their stops. For greater up-gust velocities, the bending moments would increase in the positive direction as on the basic airplane. Thus, for a gust velocity of 20 feet per second, the bending moment would be expected to come back to about zero, and for higher gust velocities would again become positive. This sytem is therefore one which serves to improve passenger comfort in the frequently encountered small gust velocities, but which reduces the structural loads due to severe gusts. No flight data are available, however, to show the characteristics of the system in severe turbulence. The system increased the magnitude and frequency of tail loads as well as the stresses in minor structural components such as the rear spar, the wing flaps, and so forth. This result indicates that fatigue loads would be a more serious problem for the gust-alleviated airplane.

[redacted]

Effect of Yaw Damper on Vertical-Tail Loads

Some measurements have been made to determine the effect of a yaw damper on the vertical-tail loads experienced by a bomber airplane in rough air at various altitudes. These results are shown in figure 6, which presents the probability of exceeding a given value of vertical-tail spar strain with the yaw damper on and off at two altitudes, 35,000 feet and 5,000 feet. The yaw damper reduces the magnitude of loads considerably in the high-altitude case. The damping of the Dutch roll motion of the airplane under these conditions is low so that a large resonance at the Dutch roll frequency is obtained. The effect of the yaw damper is primarily to reduce this amplification of load due to the Dutch roll motion. At low altitude where the damping of the airplane is better, the gains due to the yaw damper are small.

Some studies have been made to determine the feasibility of reducing the loads on the wings by use of the normal elevator control. The results are similar to those obtained in the lateral case; that is, if the airplane has very low damping in pitch the loads may be reduced through elimination of the resonant peak of the short-period mode (ref. 5). However, any attempt to reduce the direct effect of the gust on the lift of the surfaces by heading the airplane into the gusts requires large pitching motions of the airplane.

CONCLUDING REMARKS

A brief review has been given of the basic methods of gust alleviation, and some results obtained in flight tests of a gust-alleviation system have been presented. A system designed for improvement of passenger comfort did not reduce structural stresses while operating in its linear range. The system would be expected to reduce the wing loads due to severe gusts, but loads in the tail and other structural components were increased.

[redacted]

[redacted]

REFERENCES

1. Croom, Delwin R., Shufflebarger, C. C., and Huffman, Jarrett K.: An Investigation of Forward-Located Fixed Spoilers and Deflectors as Gust Alleviators on an Unswept-Wing Model. NACA TN 3705, 1956.

2. Croom, Delwin R., and Huffman, Jarrett K.: Investigation at Transonic Speeds of Deflectors and Spoilers as Gust Alleviators on a 35° Swept Wing - Transonic-Bump Method. (Prospective NACA paper.)

3. Kraft, Christopher C., Jr.: Initial Results of a Flight Investigation of a Gust-Alleviation System. NACA TN 3612, 1956.

4. Cooney, T. V., and Schott, Russell L.: Initial Results of a Flight Investigation of the Wing and Tail Loads on an Airplane Equipped With a Vane-Controlled Gust-Alleviation System. NACA TN 3746, 1956.

5. Vitale, A. James, Press, H., and Shufflebarger, C. C.: An Investigation of the Use of Rocket-Powered Models for Gust-Load Studies With an Application to a Tailless Swept-Wing Model at Transonic Speeds. NACA TN 3161, 1954.

[redacted]

[redacted]

[redacted]

TABLE I

FACTORS AFFECTING GUST LOADS

Δ LOAD = SUM OF

1- DIRECT LOAD DUE TO GUST- $\left(C_{L_\alpha} q \frac{U}{V}\right)$

(A) C_{L_α}

(B) q

2- AIRPLANE MOTION DUE TO GUST OR CONTROLS

(A) BASIC AIRPLANE STABILITY

(B) OPERATION OF CONTROLS MANUALLY OR BY AUTOPILOT

3- ACTION OF SPECIAL CONTROL TO OFFSET LOAD

(A) WING FLEXIBILITY

(B) HINGED SURFACES

(C) SENSOR AND SERVO SYSTEM OPERATING SPECIAL CONTROLS

[redacted]

LOAD ALLEVIATION AND DRAG OF A SPOILER-DEFLECTOR

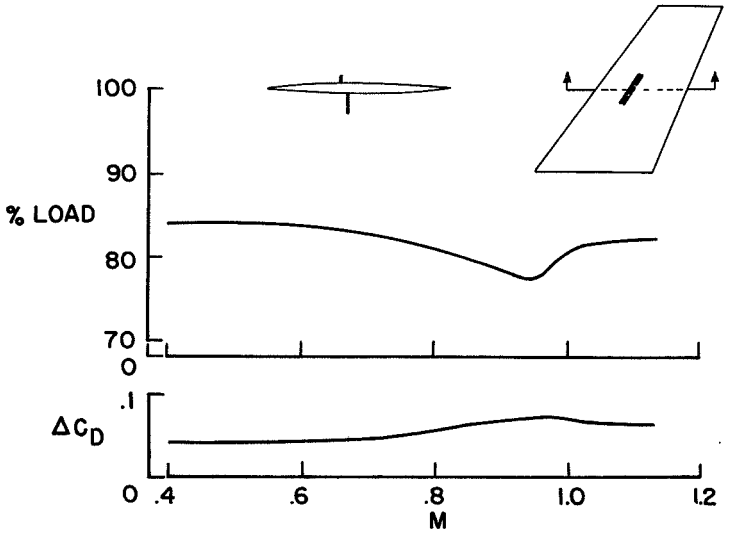


Figure 1

EFFECT OF SENSING SYSTEM ON
VARIATION OF LOAD WITH AIRSPEED

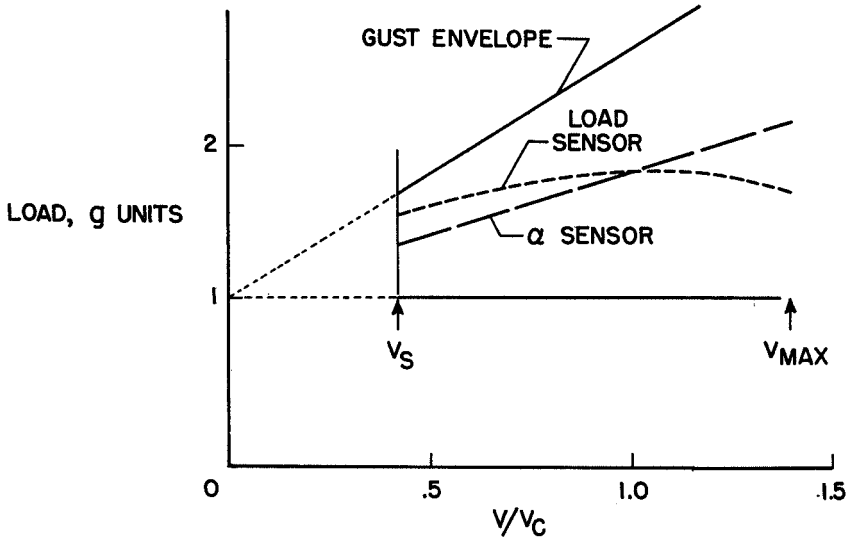


Figure 2

LOAD REDUCTION WITH LOAD-SENSING SYSTEM

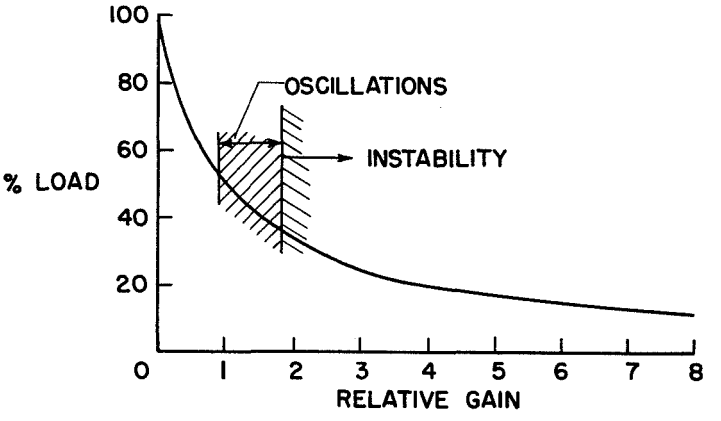


Figure 3

EFFECT OF GUST-ALLEVIATION SYSTEM ON AIRPLANE MOTIONS

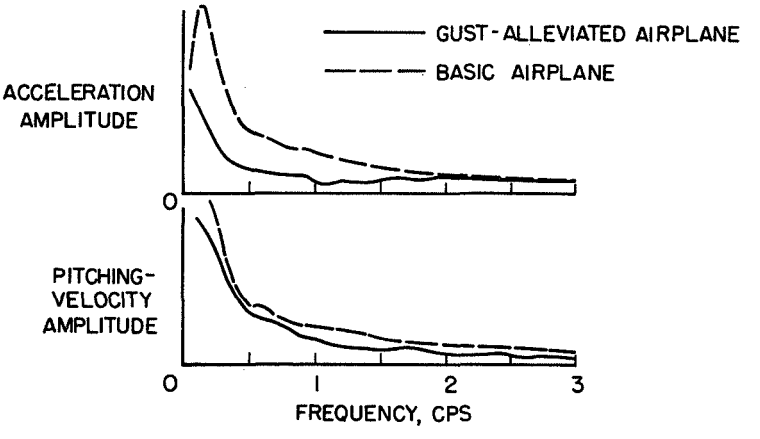


Figure 4

EFFECT OF GUST-ALLEVIATION SYSTEM
ON ROOT BENDING MOMENTS

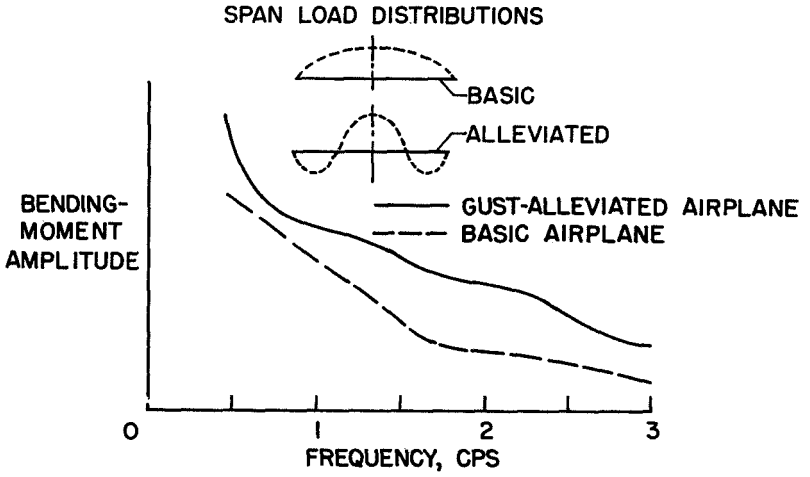


Figure 5

EFFECT OF YAW DAMPER ON VERTICAL-TAIL LOADS

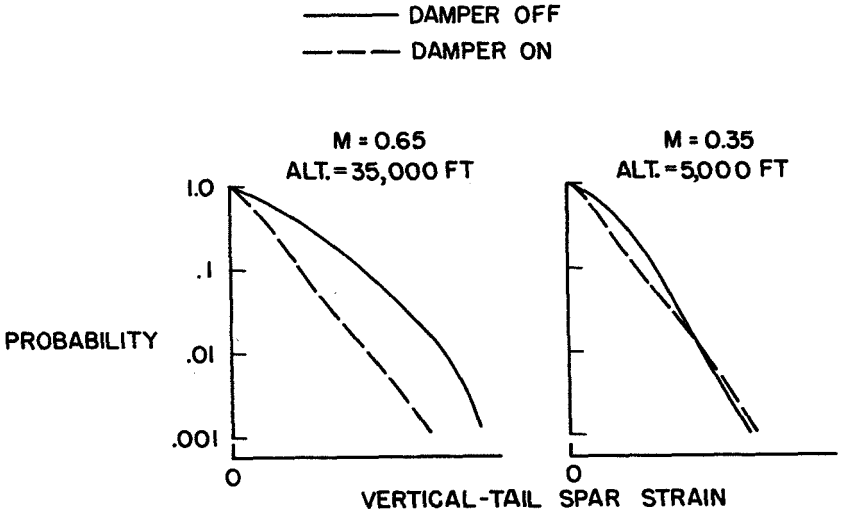


Figure 6

N71-75397

RECENT DATA ON TIRE FRICTION DURING LANDING

By Sidney A. Batterson

Langley Aeronautical Laboratory

SUMMARY

An investigation was made at the Langley landing-loads track to obtain data on the coefficient of friction during wheel spin-up. A landing gear was tested at horizontal velocities ranging from 0 to 180 feet per second together with vertical velocities of 7.0 and 9.3 feet per second. The results indicate the effect of forward speed and tire inflation pressure on the coefficient of friction.

INTRODUCTION

The National Advisory Committee for Aeronautics has been engaged for some time in an experimental study of the wheel spin-up phenomenon during landing. As a result of these investigations, it has been possible to separate the effects of a number of parameters on the coefficient of friction. Until recently, however, data could not be obtained under controlled conditions for either the large landing gears or the high forward speeds which are required for modern airplanes. In order to obtain such data the NACA has put into operation a new research facility called the landing-loads track. This paper presents the first data obtained at the track and indicates the effect of forward speed and tire inflation pressure on the coefficient of friction. Although the trends are clear it is not yet possible to define the variations accurately because of the limited number of available test results.

TEST CONDITIONS

The total dropping weight was 20,000 pounds. The test covered a horizontal velocity range from 0 to 180 feet per second and vertical velocities of 7 and 9.3 feet per second. The landing gear was equipped with a 44 × 13, type VII, 26-ply-rating tire. The normal inflation pressure for the 20,000-pound weight is 140 pounds per square inch; however, the tire pressure was varied in one series of tests. All tests were made with the strut inclined at an angle of 15°. A lift force of 20,000 pounds was applied to the dropping mass throughout the impact,

[redacted]

but the airplane flexibility characteristics were not simulated. Comparisons made of the landing surface at the landing-loads track and an active runway at Langley Field, Va., showed the roughness of both surfaces to be about the same.

RESULTS AND DISCUSSION

Effect of Horizontal Velocity

Figure 1 shows the effect of forward speed on the vertical and drag reactions at the ground and on the coefficient of friction. Time histories are shown of three tests made at horizontal velocities V_h of 110, 130, and 160 feet per second. The sinking speed V_v was 9.3 feet per second for all three tests. In reference 1 it was shown that the coefficient of friction is affected by the vertical load. However, during the three tests shown in figure 1, the maximum coefficient of friction occurred at approximately the same value of vertical load. This is apparent from the upper set of curves where the circles appearing on the curves indicate the value of the vertical load at the instant of maximum coefficient of friction for each test. These data, therefore, isolate the effect of forward speed on the maximum coefficient of friction, and show that increases in forward speed reduce the maximum coefficient of friction. At the present time insufficient data are available at constant vertical load to define this variation accurately.

In figure 1 it can be seen that the maximum drag reaction as well as the maximum coefficient of friction changes over a limited range of forward speed. Figure 2 shows the variation of maximum drag reaction over a much larger range of horizontal velocities. The vertical velocity is 9.3 feet per second. This vertical velocity is the same as for the data in figure 1. Each point represents a separate test, and the maximum drag reaction is plotted against the horizontal velocity of the test. The curve reaches a maximum at a forward speed of about 110 feet per second. It can be seen in figure 1 that this is the forward speed where wheel spin-up occurs just as the vertical load roughly levels off. At forward speeds less than 110 feet per second spin-up occurs sooner and at a lower value of vertical load and results in smaller drag loads. At the higher forward speeds, although the vertical loads remain approximately constant, the decrease in maximum coefficients of friction causes smaller drag loads.

Effect of Tire Pressure

Figure 3 shows the effect of variation in tire pressure on the coefficient of friction. Four tests were made at a horizontal velocity of

[redacted]

160 feet per second and a vertical velocity of 7 feet per second. The tire inflation pressures p covered a range from 35 to 210 pounds per square inch. In figure 3 the coefficient of friction is plotted against the instantaneous skidding velocity. Skidding velocity is defined as the difference in velocity between the peripheral speed of the tire and the runway. Since the skidding velocity is maximum at the instant of touchdown, spin-up occurs from right to left in figure 3. In the region where the skidding velocity is large, the curves form two groups. Although the difference between the two curves which form each group is small, the difference between the two groups is large. Furthermore, the curves obtained at the higher tire pressures exhibit lower coefficients of friction. It is believed that this is caused primarily by differences in temperature in the tire footprint region. Since as the tire inflation pressure is increased the tire footprint areas decrease, the heat generated during skidding is distributed over a small area, and the rubber is hot and primarily molten and exhibits a low coefficient of friction. However, at the low inflation pressures, where the tire footprint areas are larger, the heat is distributed over a greater area; the rubber is cooler and primarily in the solid state and exhibits a higher friction coefficient. Evidently, the transition region from solid to molten rubber occurs somewhere in the region of tire pressures between 70 and 140 pounds per square inch. All the curves reach approximately the same maximum value at the low skidding velocities. This indicates that the tire has turned sufficiently so that cool rubber predominates in the footprint region when spin-up occurs.

Figure 3 shows that the maximum coefficient of friction obtained at a tire inflation pressure of 35 pounds per square inch occurs at an appreciably higher skidding velocity than those obtained at the higher tire pressures. This is attributed primarily to the method used in measuring the skidding velocity. In order to obtain the peripheral speed of the tire, measurements are made of the rotational velocity of the wheel, and the rotational motion of the tire with respect to the wheel is neglected. As the tire pressure is decreased the response of the wheel to the motion of the tire is lowered. This is not too critical in the early stages of the impact where the increase of the drag load is relatively slow. However, appreciable errors are introduced as spin-up is approached since the wheel is unable to follow the rapid changes of the tire motion caused by the rapidly changing drag load.

Effect of Braking and Wet Landing Surface

Figure 4 shows time histories of drag reactions obtained for tests made at a horizontal velocity of 160 feet per second and a vertical velocity of 7 feet per second. Wheel spin-up in all cases occurred subsequent to the leveling off of the vertical-load curve. The curve indicated as "braked" was obtained during a landing made with partial brake pressure



applied to the wheel. The curve labeled "free" was obtained during a normal landing with the wheel free to rotate. Braking caused reduced spin-up accelerations and, to a certain degree, simulated the effect of increasing the moment of inertia of the wheel. It can be seen that, even though the braked wheel skidded for a longer time, the maximum drag load in both cases was the same.

The curve labeled "wet" in figure 4 was obtained from a landing made on a wet runway with the wheel free to turn. The other curve was obtained from a landing made with the wheel locked, and the rubber in the footprint area was undoubtedly molten. For both curves the skidding velocities are high, up to 0.10 second after impact, and it can be seen that the drag loads are approximately the same during this time. This indicates that the lubricating effects of water and molten rubber are about the same.

In the case of the landings on wet concrete where the lubricant is spread along the runway, an appreciable reduction is seen in the maximum drag load when compared with the maximum drag loads occurring in either the free or the braked landing. This indicates that runway lubrication, in addition to reducing the coefficient of friction at high skidding velocities, also results in a reduction in the coefficient of friction at the very low skidding velocities where the friction is of the static or interlocking type.

SUMMARY OF RESULTS

The principal results indicated by these tests are as follows:

1. The maximum coefficient of friction developed during wheel spin-up appeared to decrease as the horizontal velocity was increased.

2. Landings made with varying tire inflation pressures indicated that at the high skidding velocities the coefficient of friction was lower for the higher tire inflation pressures. However, at the low skidding velocities, the value of the maximum coefficient of friction appeared to be substantially independent of the tire inflation pressure.

3. The maximum drag load obtained during a landing made with partial brake application was the same as that obtained during a landing with the same initial conditions and with the wheel free to rotate.

4. At high skidding velocities the lubricating effect of water on the runway is approximately the same as that of molten rubber.



[redacted]

REFERENCE

1. Milwitzky, Benjamin, Lindquist, Dean C., and Potter, Dexter M.: An Experimental Study of Applied Ground Loads in Landing. NACA Rep. 1248, 1955. (Supersedes NACA TN 3246.)

[redacted]

[redacted]

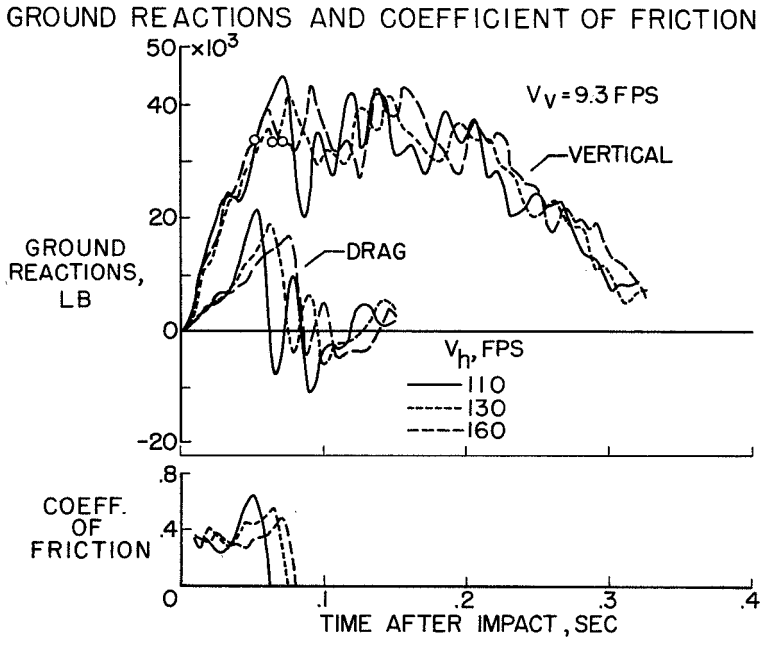
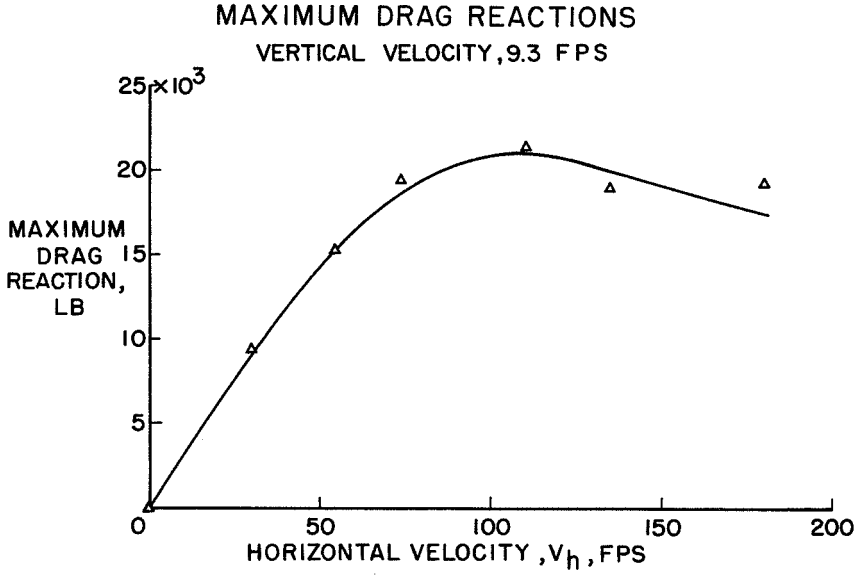


Figure 1



217

Figure 2

[redacted]

[redacted]

EFFECT OF TIRE PRESSURE ON COEFFICIENT OF FRICTION
HORIZONTAL VELOCITY, 160 FPS; VERTICAL VELOCITY, 7 FPS

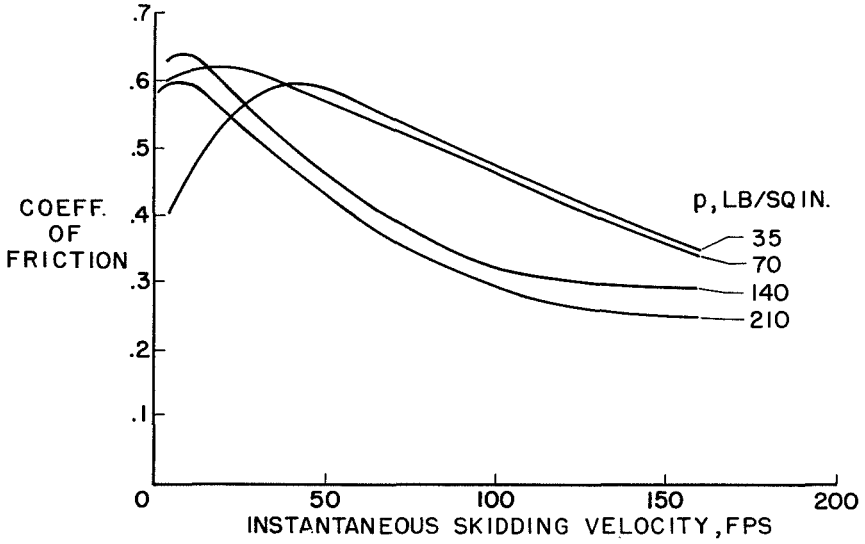


Figure 3

DRAG REACTIONS
HORIZONTAL VELOCITY, 160 FPS; VERTICAL VELOCITY, 7 FPS

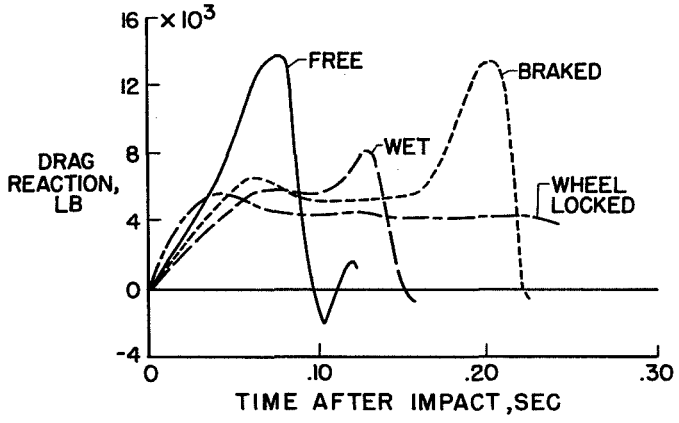


Figure 4

N71-75398

A SUMMARY OF GROUND-LOADS STATISTICS

By John R. Westfall, Benjamin Milwitzky,
Norman S. Silsby, and Robert C. Dreher

Langley Aeronautical Laboratory

SUMMARY

This paper briefly summarizes the more important statistical data obtained by the NACA on the subject of ground loads. The information presented relates primarily to landing-impact and taxiing loads; however, some limited data are also presented on one phase of ground-handling loads, namely, braking friction. A number of experimental and theoretical papers dealing with various aspects of the subject are listed in the bibliography.

INTRODUCTION

The NACA has for some time been concerned with the study of ground loads on aircraft; these include landing-impact loads, taxiing loads, and loads due to ground handling. A number of experimental and theoretical reports that have been published on various aspects of the subject are listed in the bibliography. The present paper summarizes the more important statistical data on ground loads obtained by the NACA, which may serve as a basis for predicting the ground-loads experience of aircraft.

The two major phases of the ground-loads problem considered herein are landing impact and taxiing loads; however, some limited data are also presented on one phase of ground-handling loads, namely, braking friction.

The section on landing impact considers first the initial contact conditions, then landing-gear reactions and airplane response. The contact conditions are in the form of statistical data on five parameters: vertical velocity, horizontal velocity, bank angle, rolling velocity, and wing lift. Although there are other parameters, the ones considered appear to be the most important. The discussion of ground reactions and airplane response is primarily concerned with the analytical prediction of vertical and drag loads from the known initial conditions.

On the subject of taxiing loads, data are available in the form of runway profiles and acceleration measurements from VGH records in taxiing; the latter are presented in statistical form. Some considerations on airplane structural response in taxiing are also given.

With regard to ground handling, some limited data are presented on the coefficient of friction as measured in braking tests with an airplane and with a specially designed tow cart.

SYMBOLS

F_V	vertical ground force, lb
f	frequency, cps
g	acceleration due to gravity, ft/sec^2
Δn	incremental center-of-gravity acceleration, g units
p_{tire}	tire pressure, lb/sq in.
V_V	vertical velocity at contact, fps
W	airplane weight, lb
μ	coefficient of friction

Subscript:

max	maximum

RESULTS AND DISCUSSION

Landing Impact

Statistics.- The available statistics on the initial contact conditions are summarized in figures 1 to 4. Figure 1 shows probability curves for the vertical velocity at contact. The ordinate is the probability of equaling or exceeding a given value of vertical velocity; the abscissa is the vertical velocity. Because there appeared to be definite differences in the statistics for civil and military (land-based) airplanes, the probability curves for these two categories are shown separately. Although the reasons for the differences between the two categories are not completely understood, it is probably significant that, on the whole, two different generations of airplanes are involved - the civil airplanes were all piston powered, whereas the military airplanes were mostly jets. Furthermore, some of the military landings were transitional-training flights. The more severe character of the military landings is indicated

by the generally higher values of vertical velocity at a given probability level. For example, 1 in 10,000 landings of military airplanes would be expected to equal or exceed a vertical velocity of about $8\frac{1}{2}$ feet per second; the corresponding value for the civil airplanes is about 5 feet per second.

Figure 2 shows similar probability curves for the airspeed at contact. The ordinate is the probability of equaling or exceeding a given value of airspeed; the abscissa is the airspeed at contact, expressed as percent above the stalling speed. Again, the military operations appear to give higher velocities at a given probability level.

With regard to bank angle and rolling velocity at contact, which are of concern for unsymmetrical landings, wing span appeared to be a better criterion for separating the data than types of operations. Accordingly, with the number of engines taken as a crude measure of wing span, the airplanes with four and more engines were put into one category and the single- and twin-engine airplanes into another. Figure 3 presents the probability curves for bank angle. As might be expected from geometric considerations, the larger span airplanes have somewhat smaller angles of bank. The probability curves for rolling velocity are shown in figure 4; here the differences are more pronounced than for bank angle. It may be that these differences reflect not only the geometrical span effect, but also the greater moments of inertia and damping in roll of the larger airplanes.

A study was made to determine whether there was any statistical correlation between bank angle and rolling velocity, on the one hand, and vertical velocity or horizontal velocity, on the other hand. It was found that no such correlation existed. There was also no correlation between bank angle and rolling velocity. It therefore appears that all of these parameters may be treated as independent quantities in calculating unsymmetrical landing loads.

With regard to the wing lift at contact, both past and more recent studies have shown that, for civil transport airplanes, the most probable value of wing lift at contact is 1 g and that in 95 percent of the landings the wing lift was between 0.9g and 1.1g.

The statistical analysis indicated no significant correlations between wing lift and vertical velocity.

Although a fairly substantial amount of statistical data has been obtained on these initial contact conditions, the sizes of the samples are still insufficient to permit the final resolution of the effects of such variables as airplane type, size, wing loading, and so forth.

[redacted]

Reactions and response.- On the subject of landing-gear reactions and airplane response, the first problem to be discussed is the determination of the vertical loads when the initial contact conditions are given.

In recent years analytical methods have been developed for predicting the behavior of the landing gear during impact and the loads applied to the airplane. Good agreement has been obtained between the theoretical results and data from landing-gear drop tests. The analytical method also appears to be reasonably satisfactory when compared with flight-test data.

Figure 5 shows a comparison of the maximum vertical loads obtained from flight tests of the SNJ airplane and calculated maximum loads based on the assumption that the airplane is a rigid body. The ordinate is the maximum center-of-gravity acceleration obtained for each impact, and the abscissa is the vertical velocity at contact. There is considerable scatter in the flight data, about 30 percent above 4 feet per second, reflecting the effects of such factors as shock-strut binding due to drag loads, unsymmetrical landings, side force due to yawed landings, and so forth, all of which can modify the vertical loads developed. At the lower values of vertical velocity the experimental data are somewhat higher than the calculated curve, largely because of the effects of shock-strut preloading and breakout friction which were not considered in these calculations. Above a vertical velocity of about 4 feet per second, the calculated curve seems to lie fairly close to the mean of the experimental data.

Figure 6 shows a similar comparison of measured and calculated maximum vertical loads for the larger and more flexible B-29 airplane. The ordinate is the maximum landing-gear vertical-load factor and the abscissa is the vertical velocity. The dashed line represents the calculated values. The break in the curve results from the effects of shock-strut breakout, which were included in these calculations. Although there is a scarcity of test points at the higher values of vertical velocity, it does appear that the calculated results are in fairly good agreement with the flight-test data.

With regard to the prediction of spin-up drag loads, the most important unknowns have been the magnitude and variation of the coefficient of friction between the tire and runway during the impact. Figure 7 summarizes the available experimental information on the variation of coefficient of friction during the wheel spin-up process. The ordinate is the coefficient of friction, and the abscissa is the skidding velocity, which is defined as the instantaneous difference between the forward speed of the airplane and the peripheral speed of the tire. The shaded bands are envelopes of the data obtained in several different test programs. The two relatively narrow bands represent tests with an SNJ landing gear in the Langley impact basin. The shorter of these two bands is for true forward-speed impacts; the longer one represents impacts with forward

 [redacted]

speed in combination with reverse wheel prerotation (to simulate higher horizontal velocities beyond the range of the impact-basin equipment). The wider dotted band shows results obtained with the B-29 airplane in flight tests. The lowest band represents data recently obtained with a B-57 landing gear at the new landing loads track.

All these bands illustrate the fairly well-known fact that the coefficient of friction decreases with increasing skidding velocity. The width of the bands represents the effects of other factors which influence the coefficient of friction, such as the slip ratio, the vertical load, variable-heating and contamination effects, and variations in the runway surface conditions, plus, of course, experimental errors. It will be noted that the SNJ and B-29 data, which are for relatively low tire pressures, are generally in good agreement with one another, whereas the results for the B-57 landing gear, which has a much higher tire pressure, indicate appreciably lower coefficients of friction. These results appear to verify a previously suspected trend, namely, that the coefficient of friction decreases at higher tire pressures.

Although the shapes of the bands are fairly consistent for the various tests, it is not as yet possible to take into account quantitatively all the factors that contribute to the spread of the values of the coefficient of friction. Therefore, it seems that the most practical approach at present is to select a shape for the curve, and then normalize it on the basis of the maximum value. From inspection of the data it appears that a reasonable range of the maximums might be from about 0.4 to 0.9, the value to be used depending on the conditions involved.

Taxiing Loads

On the subject of taxiing loads, essentially two types of data are available at present; that is, measurements of runway profiles and center-of-gravity acceleration data from the impact portion of VGH records.

Two possible ways of utilizing runway profile data are: (1) as specific displacement inputs in analog computations, or (2) as statistical power spectra in generalized harmonic analysis. Both of these approaches present certain practical difficulties. In the case of the analog method, one of the major problems is to define a representative runway. As to the use of generalized harmonic analysis, the main stumbling blocks are as yet unsolved problems of nonlinear landing-gear response and the determination of a unique transfer function.

With regard to the VGH acceleration data, several general relationships have been found which appear to be applicable to a number of

different types of airplanes and which provide a common basis for estimating the loads experience in taxiing. These are shown in the following table:

		AIRPLANE TYPES
TAXIING TIME	APPROX. 5 MIN	3
C.G. RESPONSE	1 TO 2 CPS	5
SPEED AT Δn_{MAX}	< 20 MPH	4
SCATTER AT CUM. FREQ. = 10^4	1.5 : 1	4

First, an analysis of the time spent in taxiing, for three transport airplane types, showed that this time was remarkably constant, averaging within a few seconds of 5 minutes.

Second, it was found that the predominant frequency in the center-of-gravity accelerations - that is, the frequency at which the airplanes respond most to the runway roughness inputs - is also remarkably constant for five different types of airplanes ranging from the B-36 bomber to a small jet fighter. This predominant frequency varied only from about 1 to 2 cps, with an average value of about 1.75 cps, despite a very wide range of wing bending frequencies for the airplanes involved. This frequency of about 1.75 cps appears to be associated with the natural vibration of the airplane on its tires.

Third, it was found that, for four transport types in several hundred taxi runs, the maximum taxiing loads occurred at speeds usually below 20 mph.

Fourth, detailed analysis of all the loads experienced in taxiing for four airplane types showed that the probability distributions were very similar, and the scatter in the load level at a given probability was small, being about 1.5 to 1, or less than the scatter for such parameters as vertical velocity or horizontal velocity. Consequently, it may be assumed that a combined distribution of taxiing loads can be used to represent all taxiing operations.

Figure 8 shows distributions of center-of-gravity accelerations in taxiing, per 1,000 flights. The ordinate is the number of times a given value of center-of-gravity acceleration is equaled or exceeded in 1,000 flights; the abscissa is the center-of-gravity incremental acceleration. The ordinate scale can be ratioed in direct proportion to the

number of flights considered. In calculating these curves, the approach used was first to construct a cumulative frequency distribution of all the individual incremental load peaks, both positive and negative, based on a very detailed analysis of a relatively few VGH records; these results were ratioed up to represent 1,000 flights, and are shown by the upper curve. Then, on the basis of data for 7,000 flights, a cumulative frequency distribution was obtained for the maximum taxiing load in each flight. This distribution of maximum loads was also ratioed to represent 1,000 flights and is shown by the lower curve. In the limit, the two curves should coincide at a cumulative frequency of 1. In view of the nature of the assumptions involved and the fact that the two distributions were obtained independently, the convergence appears to be quite good.

If the predominant frequency of the input to the airplane is assumed to be 1.75 cps, one can make a straightforward response calculation for steady-state forced vibration and, thus, determine the variation of the acceleration along the span, which can then be compared with the acceleration at the center of gravity. The ratios resulting from such a comparison would permit converting the abscissa scale in figure 8 from center-of-gravity acceleration to acceleration at any point along the span.

As an example, such a response calculation has been made for the B-29 airplane; two flexible symmetrical bending modes were considered and a steady-state sinusoidal input force at 1.75 cps was assumed to act at the landing-gear attachment point. Figure 9 shows a plot of the acceleration response of the B-29 as a function of position along the span. The dashed line is the rigid-body response; the solid line is the total dynamic response. For the input frequency of 1.75 cps, the ratio of incremental wing-tip acceleration to incremental center-of-gravity acceleration is about 7.9. It is of interest to note that data obtained in taxiing tests of a B-29 at the Wright Air Development Center showed acceleration ratios of the same order. However, there are still some aspects of the problem which are not fully understood; for example, even though the B-29 records showed frequencies of about 1.5 to 2.0 cps at the center of gravity, the frequencies at the wing tip were, in some cases, considerably higher.

Braking Loads

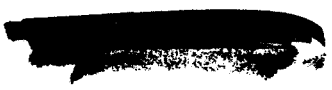
The last topic to be discussed is the subject of braking friction. Recent NACA tests with a special tow cart and with a C-123B airplane have provided the data shown in figure 10. Here the maximum coefficient of friction in braking on dry concrete is plotted against the horizontal velocity. The circles are data obtained with the C-123B airplane; the squares are results obtained with the tow cart at lower speeds. Although this type of information can be useful in the calculation of maximum



braking loads, no statistical data are as yet available regarding pilot operating practice in applying the brakes, that is, the magnitude and frequency distributions of braking loads.

CONCLUDING REMARKS

The foregoing material summarizes the more important NACA data applicable to the calculation of repeated ground loads. Additional work will be necessary to extend the size and scope of the statistical samples and to fill in the several analytical gaps which still exist.



BIBLIOGRAPHY

Statistical Data

Silsby, Norman S., Rind, Emanuel, and Morris, Garland J.: Some Measurements of Landing Contact Conditions of Transport Airplanes in Routine Operations. NACA RM L53E05a, 1953.

Silsby, Norman S.: Statistical Measurements of Contact Conditions of 478 Transport-Airplane Landings During Routine Daytime Operations. NACA Rep. 1214, 1955. (Supersedes NACA TN 3194.)

Silsby, Norman S., and Harrin, Eziaslav N.: Statistical Measurements of Landing-Contact Conditions of a Heavy Bomber. NACA RM L55E03, 1955.

Silsby, Norman S., and Harrin, Eziaslav N.: Landing Conditions for Large Airplanes in Routine Operations. NACA RM L55E18c, 1955.

Kolnick, Joseph J., and Morris, Garland J.: Statistical Measurements of Landing Contact Conditions of the Boeing B-47 Airplane. NACA RM L55H24, 1955.

Lindquist, Dean C.: A Statistical Study of Wing Lift at Ground Contact for Four Transport Airplanes. NACA TN 3435, 1955.

Silsby, Norman S.: Statistical Measurements of Landing Contact Conditions of Five Military Airplanes During Routine Daytime Operations. NACA RM L56F21a, 1956.

Harrin, Eziaslav N.: Comparison of Landing-Impact Velocities of First and Second Wheel To Contact From Statistical Measurements of Transport Airplane Landings. NACA TN 3610, 1956.

Dreher, Robert: A Method for Obtaining Statistical Data on Airplane Vertical Velocity at Ground Contact From Measurements of Center-of-Gravity Accelerations. NACA TN 3541, 1956.

Loads and Response

Milwitzky, Benjamin, and Cook, Francis E.: Analysis of Landing-Gear Behavior. NACA Rep. 1154, 1953. (Supersedes NACA TN 2755.)

Cook, Francis E., and Milwitzky, Benjamin: Effect of Interaction on Landing-Gear Behavior and Dynamic Loads in a Flexible Airplane Structure. NACA Rep. 1278, 1956. (Supersedes NACA TN 3467.)

Milwitzky, Benjamin, Lindquist, Dean C., and Potter, Dexter M.: An Experimental Study of Applied Ground Loads in Landing. NACA Rep. 1248, 1955. (Supersedes NACA TN 3246.)

Sawyer, Richard H., Hall, Albert W., and McKay, James M.: Vertical and Drag Ground-Reaction Forces Developed in Landing Impacts of a Large Airplane. NACA RM L55E12c, 1955.

Milwitzky, Benjamin, and Lindquist, Dean C.: Evaluation of the Reduced-Mass Method of Representing Wing-Lift Effects in Free-Fall Drop Tests of Landing Gears. NACA TN 2400, 1951.

Yntema, Robert T., and Milwitzky, Benjamin: An Impulse-Momentum Method for Calculating Landing-Gear Contact Conditions in Eccentric Landings. NACA TN 2596, 1952.

Walls, James H., Houbolt, John C., and Press, Harry: Some Measurements and Power Spectra of Runway Roughness. NACA TN 3305, 1954.

Houbolt, John C., Walls, James H., and Smiley, Robert F.: On Spectral Analysis of Runway Roughness and Loads Developed During Taxiing. NACA TN 3484, 1955.

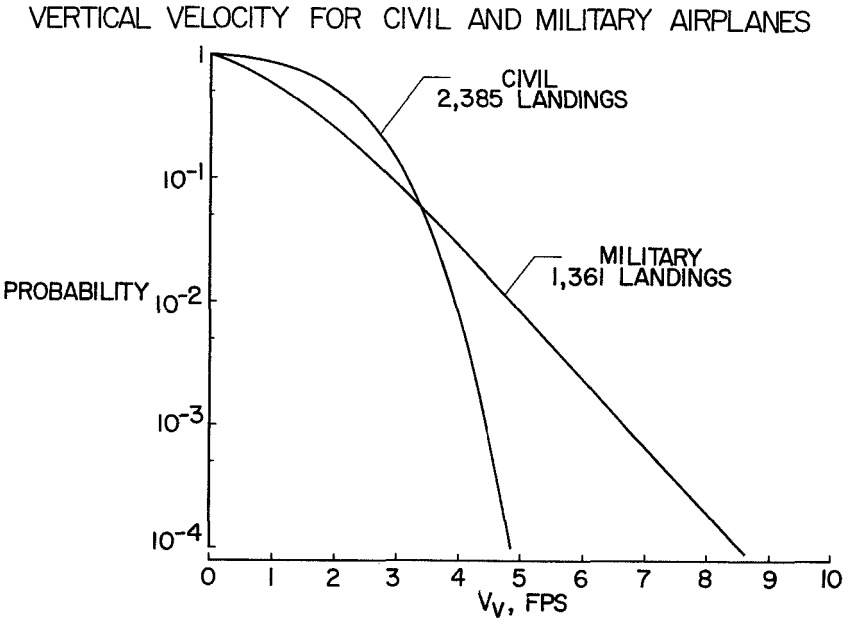


Figure 1

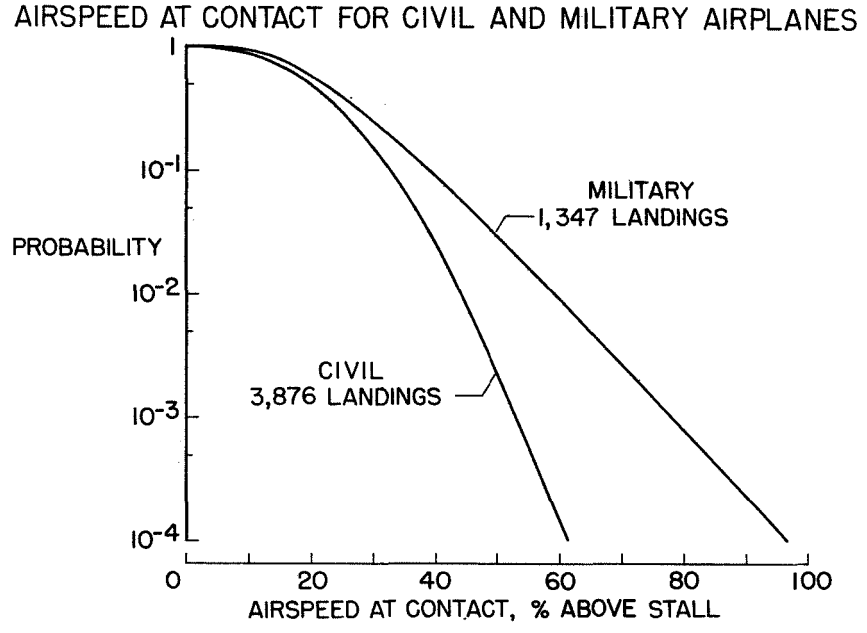


Figure 2

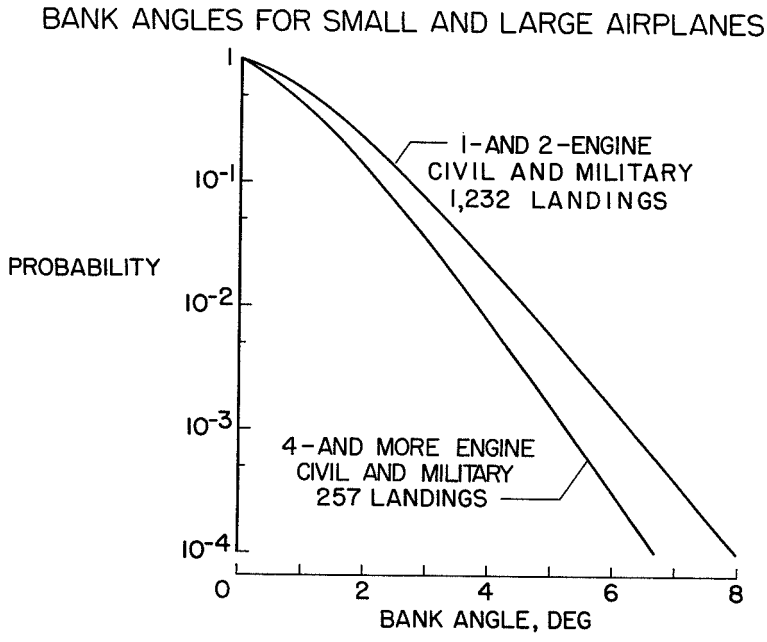


Figure 3

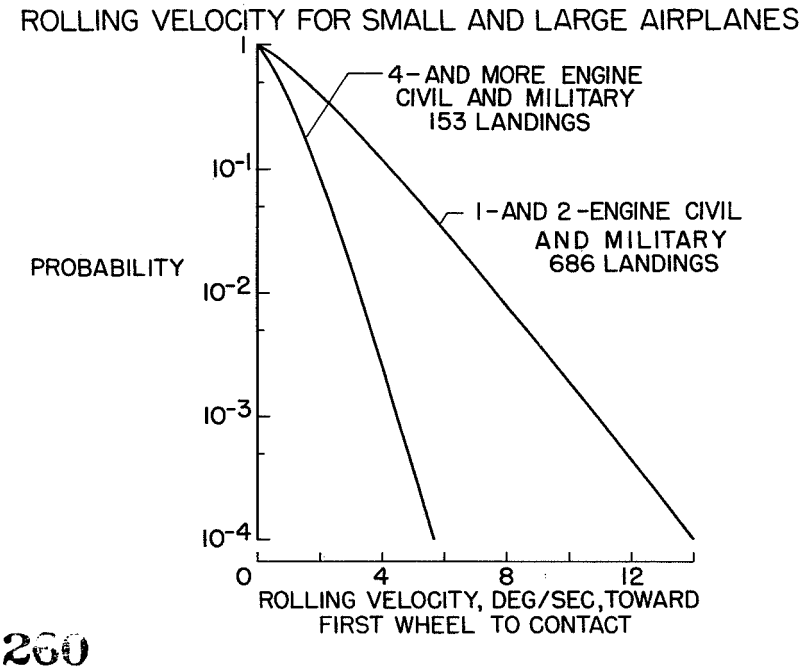


Figure 4

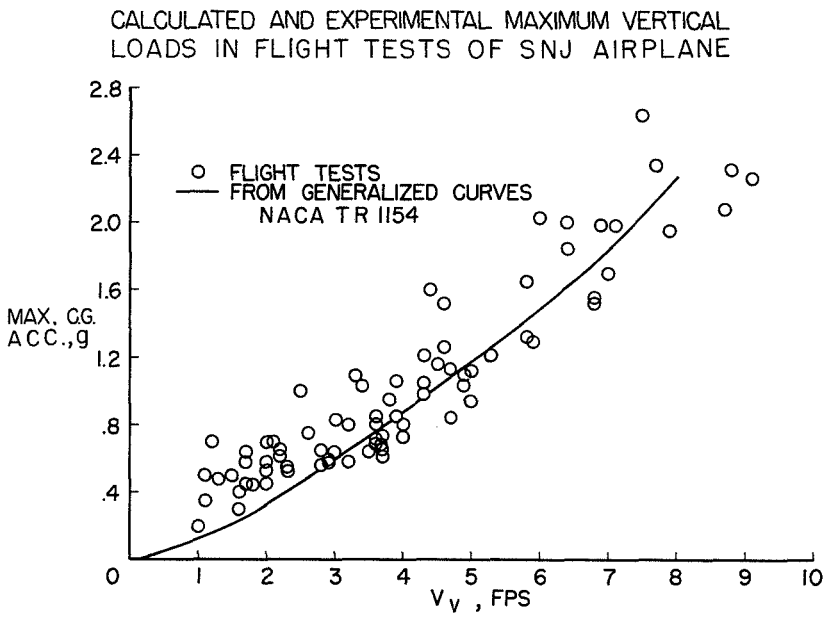
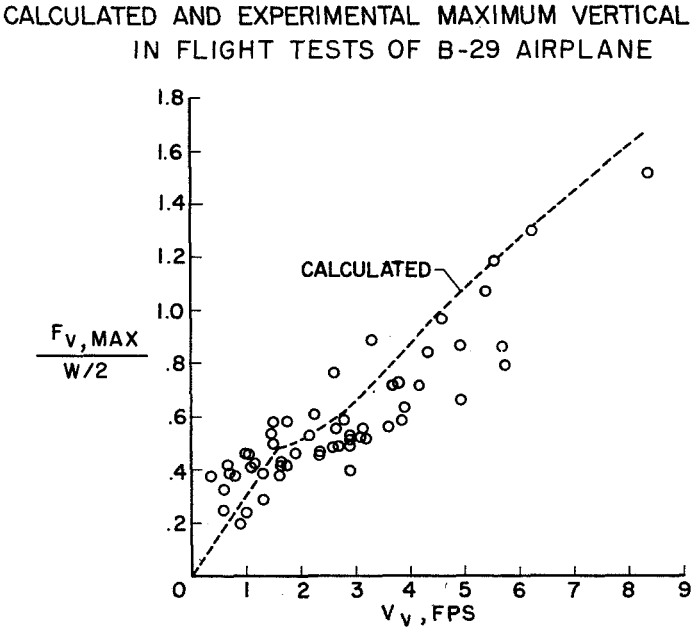


Figure 5



261

Figure 6

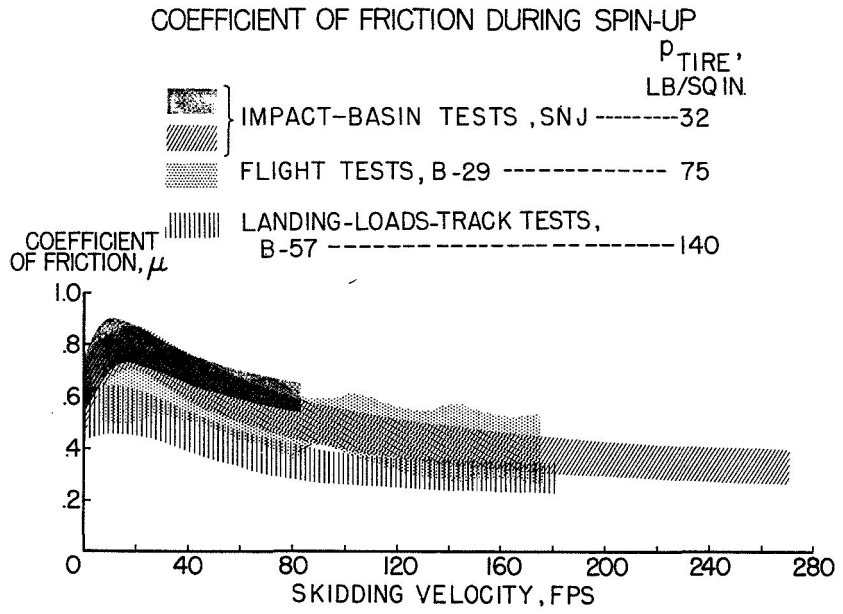
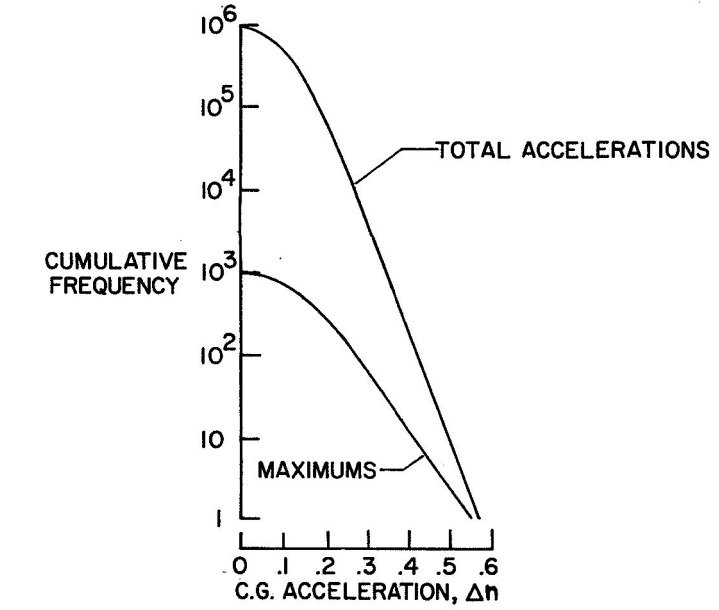


Figure 7



262

Figure 8

RESPONSE OF B-29 AIRPLANE
f = 1.75 CPS

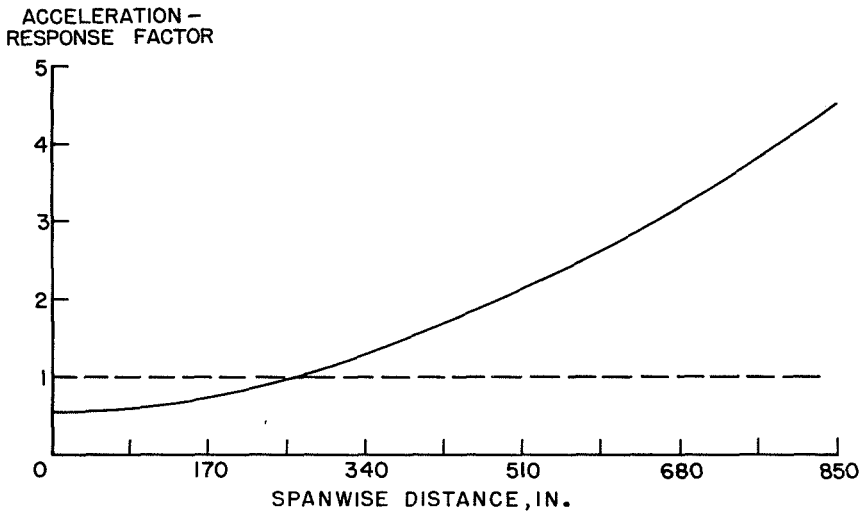


Figure 9

BRAKING TESTS ON DRY CONCRETE

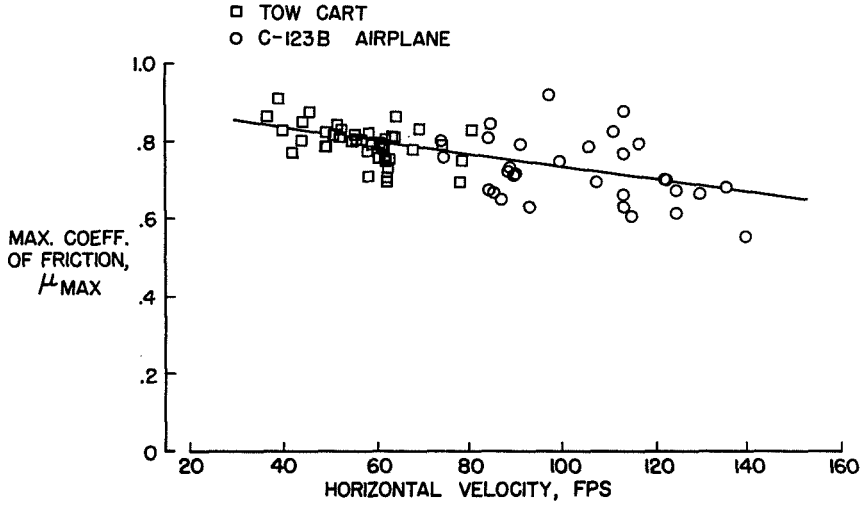


Figure 10

STRUCTURES

N71-75399

BOND, FELLER, & BLAND

AERODYNAMIC HEAT TRANSFER TO WING SURFACES AND WING LEADING EDGES

By Aleck C. Bond, William V. Feller,
and William M. Bland, Jr.

Langley Aeronautical Laboratory

SUMMARY

A compilation is presented of some recent results obtained at various facilities of the Langley Aeronautical Laboratory on the heat transfer to wing surfaces and wing leading edges. Data obtained from hypersonic tunnel tests, rocket-powered-model flight tests, and high-stagnation-temperature jet tests are included and compared with applicable theories. Measured heat transfer to wing surfaces exposed to high-heat fluxes, in general, showed good agreement with theory. Theory was also shown to be adequate in predicting the heat transfer to wing surfaces over a range of local Reynolds numbers from 1×10^6 to 20×10^6. Heat-transfer measurements on a blunted slab wing at a Mach number of 6.86 showed that surface heating at zero angle of attack was essentially the same for sweep angles of 0°, 40°, and 60°; also, increasing the angle of attack of the slab wing increased the heating of the windward surface and decreased the heating of the leeward wing surface. Measurements at high Reynolds numbers showed that rates of heat transfer that are much higher than laminar rates can be experienced on leading edges in the region of the wing-body juncture. Transpiration-cooling tests on a wedge surface showed that theoretical predictions on the effectiveness of nitrogen as a transpiration coolant apply equally as well for conditions of either high or low heating potentials. Further cooling tests showed that helium is about five times more effective as a transpiration coolant than nitrogen.

INTRODUCTION

Considerable emphasis has recently been placed on the experimental study of the aerodynamic heat transfer to wing surfaces and wing leading edges. The wing leading edge has received a large amount of consideration and has been treated both theoretically and experimentally in references 1 to 4. A qualitative type of investigation on wing leading edges at conditions of high stagnation temperature has been reported in reference 5. Investigations are reported in references 6 to 8 of the

aerodynamic heating of wing surfaces at angles of attack at low supersonic speeds; however, data on the effects of leading-edge bluntness, sweep, and angle of attack, particularly at hypersonic speeds, as well as the effects of high heating potentials and high Reynolds numbers on wing-surface heating are indeed lacking in the current literature.

Results of experiments conducted at various facilities of the Langley Aeronautical Laboratory have recently become available which provide some extension of the state of the art regarding the heat transfer to wing leading edges and wing surfaces. Rocket-powered-model flight tests have provided some large-scale measurements of the heat transfer to wing surfaces as well as of the heating of blunt leading edges in the vicinity of the wing-body juncture. Hypersonic wind-tunnel tests have provided information on both the effects of sweep and angle of attack on the heat transfer to a wing having large leading-edge bluntness. Tests in a jet having a high stagnation temperature have also provided results on the heating of wings under conditions of high rates of heat transfer. Furthermore, data on the effectiveness of transpiration cooling of flat surfaces, under conditions of high stagnation temperature, have also recently become available from tests in a hot-jet facility. It is, therefore, the purpose of this paper to present a compilation of these recent results which are applicable to the high-speed wing-heating problem.

SYMBOLS

F	injection parameter, $\frac{\rho_c V_c}{\rho_l V_l}$
M	Mach number
N_{St}	Stanton number based on local conditions, $\frac{h}{C_{p_l}\rho_l V_l}$
$N_{St,\infty}$	Stanton number based on free-stream conditions, $\frac{h}{C_{p_\infty}\rho_\infty V_\infty}$
R	Reynolds number, $\frac{\rho V s}{\mu}$
R_d	Reynolds number based on diameter, $\frac{\rho_\infty V_\infty d}{\mu_\infty}$
T	temperature, $^\circ F$ or $^\circ R$

V	velocity, ft/sec
C_p	specific heat of air at constant pressure, $\frac{\text{Btu/slug}}{^{\circ}\text{F}}$
d	diameter of cylindrical leading edge, ft
h	local aerodynamic heat-transfer coefficient, $\frac{\text{Btu}}{(\text{sq ft})(\text{sec})(^{\circ}\text{F})}$
q	dynamic pressure, lb/sq ft
s	length from stagnation point to measurement station, as indicated when used, ft
Λ	sweep angle, deg
α	angle of attack, deg
μ	viscosity of air, lb-sec/sq ft
ρ	density, slugs/cu ft

Subscripts:

AW	adiabatic wall
c	coolant
EXP	experimental
l	conditions outside boundary layer
0	zero coolant flow rate
TH	theoretical
t	total conditions
W	conditions pertaining to skin of model
∞	free-stream conditions

RESULTS AND DISCUSSION

Heat Transfer at High Stagnation Temperature

In order to study heating problems associated with high-heat fluxes, one of the free jets of the Langley preflight jet of the Pilotless Aircraft Research Station at Wallops Island, Va., has been modified to allow testing of relatively large test specimens at stagnation temperatures up to about 3,500° R which corresponds to a Mach number of about 6.5 at altitude. The test Mach number is maintained the same (M = 2.0); however, the stream temperature is increased by burning ethylene gas upstream of the exit nozzle. This mode of testing provides heating rates corresponding to Mach numbers much higher than the stream Mach number in a test medium not much different from air. Recent tests with wings subjected to high heating rates have yielded heat-transfer data which show good agreement with theory. Results for a wing tested at a stagnation temperature of 3,476° R, a stream Mach number of 2.0, and a stream Reynolds number of 2.4×10^6 per foot are shown in figures 1 and 2. The wing was a tapered unswept wing of hexagonal cross section, was constructed of magnesium, and had a span of 11 inches. The leading edge which was blunted to a 1/16-inch radius was covered with a 1/32-inch Inconel cap to increase its endurance at the test temperature. Sweep of the leading edge was 17°. At the 63-percent spanwise station (coinciding with the center line of the jet), temperature measurements were made at four chordwise locations: the stagnation-point and the 1-, 2-, and 3.77-inch stations. Temperature time histories measured on the wing are shown in figure 1. The temperature at the stagnation point rises rapidly and in approximately 2.1 seconds (time of failure of the leading-edge cap) has reached 2,731° R, just about 229° R below the melting temperature of Inconel. The temperatures at the three rearward stations show a maximum rise of about one-half the stagnation-point value. It should be noted, however, that the temperature of the 2-inch station, which is immediately behind the end of the leading-edge cap, is generally about 200° higher than the temperatures of the other two stations during most of the test.

In figure 2 these wing heating data are reduced to the nondimensional Stanton number evaluated at local conditions and are also plotted as a function of time. In the plot at the upper left, the stagnation-point data are compared with the average laminar stagnation-point theory of Goodwin, Creager, and Winkler (ref. 4). Comparison with the average theoretical stagnation-point values rather than with local values is made since it was felt that, because of the small physical size of the leading edge, the measurements at this point more nearly represented average values rather than local point values. The first data point shows good agreement with the theory; however, with increasing time, the data show increasing deviation from the theory. This disagreement is believed to be due mainly to large lateral conduction losses from the stagnation

point as the leading edge increases in temperature, since it is known that the temperature gradient across the jet is not uniform but tends to peak in the vicinity of the jet center line. The data for the other three stations are compared with the flat-plate theories of Van Driest (refs. 9, 10, and 11) and, in general, show good agreement. The theoretical curves were determined by using calculated local conditions and a Reynolds number length equal to the streamwise distance from the stagnation point to the measurement station. These data show that the flow was initially laminar at the 1-inch station and that transition took place between the 1- and 2-inch stations and then gradually moved forward with time. Initially, transition could have been caused by the abrupt discontinuity at the end of the leading-edge cap, and the forward movement with time may have been due to the increased temperature (i.e., temperature ratio) of the surfaces with time. It is obvious that, had the transition point not moved forward, a serious hot spot would have developed at or near the 2-inch measurement station. The comparison of the data for the three downstream stations with those of the stagnation point show that the turbulent level of heating of the downstream stations was of the order of one-half that of the stagnation point.

It might be mentioned at this time that, in the reduction of the heating data for the 1-inch station to local Stanton number, the local conditions were determined by considering the losses through the normal shock caused by the blunted leading edge. This procedure gave much better agreement with the theory than was obtained when the losses were neglected. For the two stations downstream, the agreement between theory and experiment was not enhanced when taking these losses into account; thus, the effects of this small amount of bluntness did not propagate very far downstream in this case.

Large-Scale Heat-Transfer Measurements

In recent rocket-powered-model flight tests, some relatively large-scale heat-transfer measurements have been obtained on two different wing configurations at free-stream Reynolds numbers up to approximately 27×10^6 based on the wing chord. This Reynolds number is equivalent to that of a wing of 120-inch chord flying at an altitude of 50,000 feet and a Mach number of 2.5. In order to show the general agreement which was obtained with theory over this large Reynolds number range, representative data from these tests are shown in figure 3 as the ratio of experimental to theoretical Stanton number as a function of the local Reynolds number. It might be mentioned at this time that there was no indication of laminar heating on either of the wings throughout the usable portion of the flight tests; however, at the beginning of the tests there was some indication of transitional flow at the most forward measurement stations. The theoretical Stanton numbers were, therefore, evaluated from the turbulent flat-plate theory of Van Driest (refs. 10

[redacted]

and 11) by using calculated local conditions and a value of 0.6 for the ratio of Stanton number to skin-friction coefficient.

One of the test wings was unswept, untapered, of approximately 20-inch chord and span, employed a 5-percent circular airfoil section, and had for all practical purposes a sharp leading edge. The other wing, the heating data of which are reported in reference 12, had a leading-edge sweep of 30°, a span of 25 inches, and employed a hexagonal airfoil section with a leading-edge radius of approximately 1/8 inch. The data for the unswept wing are shown by the circular symbols and represent measurements at seven chordwise stations (35.7-percent span) and a free-stream Mach number range from 1.75 to 2.66. The data for the swept wing, indicated by the square symbols, were obtained at five chordwise stations (42-percent span) and are for a free-stream Mach number range from 2.0 to 3.64. Local Reynolds numbers up to about 20×10^6 were obtained on the unswept wing; however, on the swept wing the maximum local Reynolds number is only of the order of 10×10^6. Even though the stream Reynolds numbers of the two wings were of the same order of magnitude, the local Reynolds numbers for the swept wing were lower as a result of its blunted leading edge.

In the lower Reynolds number range the agreement with theory is generally within ±15 percent, with the majority of the points showing agreement within ±10 percent. At the higher Reynolds numbers the data show agreement within about 20 percent of the theory. The decreasing trend with increasing Reynolds number which is exhibited by the data may be due to the reduction in the ratio of Stanton number to skin-friction coefficient with increasing Reynolds number which was observed by Seiff in reference 13. Since the present data were obtained in the presence of temperature, pressure, and Mach number variations, it is felt that no definite conclusions can be drawn on this point. The important feature of these data is that reasonable agreement with theory is shown for two totally different wing configurations over a rather wide variation of Reynolds number.

Heat Transfer at Angle of Attack and Sweep

Theory and experiment have shown that both leading-edge sweep and bluntness have the general effect of reducing the local rates of heat transfer to the leading edge. In order to study the effects of sweep as well as the effects of angle of attack on the heating of the surfaces of a wing with a blunt leading edge, tests have been conducted in the Langley 11-inch hypersonic tunnel at a Mach number of 6.86 on a slab wing with a semicircular leading edge. In figure 4 are presented some of the results of these tests which show the effect of sweep on the wing-surface heat transfer at zero angle of attack. The data are for a stream Reynolds

 [redacted]

number of 0.151×10^6 based on the 3/4-inch diameter of the leading edge and correspond to an actual flight altitude of about 76,000 feet at the test Mach number. The data are plotted as Stanton number based on free-stream conditions as a function of s/d, where s is the surface length, measured in a streamwise plane, from the stagnation point to the measurement station, and d is the leading-edge diameter. Data are presented for sweep angles of 0°, 40°, and 60°. In order to show the relative magnitude between the leading edge and surface heating, theory curves for the cylinder are presented for each of the sweep angles; however, since heat transfer to swept cylinders has been presented in the past (refs. 3 and 4), attention is called to the flat-plate portion of the wing. The measured data for all sweep angles lie essentially on one line and show no effect of sweep angle on the surface heating. The theory curve included in figure 4 was computed by using the Van Driest theory for laminar boundary layer (ref. 9) with local conditions determined by taking into account the losses through the normal shock and by assuming the local static pressure on the surface equal to stream static pressure. In the vicinity of the leading edge ($s/d = 1$ to 2) the data are considerably higher than this theoretical calculation, mainly as a result of the higher-than-stream pressures which are known to exist there; but as the pressure falls off with distance downstream, the data show better agreement with the theory. Measured pressure distributions on the wing showed that, just behind the leading edge, the surface pressures were several times higher than stream static pressure and dropped off to about twice the stream static pressure at values of s/d of about 7.5. The theory curve shown in the figure was actually computed for zero sweep, but it is interesting to note that calculations for the 40° and 60° sweep angles showed only small variation from the 0° sweep condition.

Measured surface heat transfer at angle of attack for the 40° swept slab wing is presented in figure 5 as being generally typical of the effect of angle of attack on the wing surface heating for all the sweep angles. Here, again the data are plotted as Stanton number based on free-stream conditions as a function of streamwise s/d. Measurements are presented of surface heating of the lower or windward surface with the wing at angles of attack of 5° and 7.5° and of the upper or leeward surface with the wing at angles of attack of 5° and 10°. The curve of zero-angle-of-attack data, of course, applies to both upper and lower surfaces of the wing. Increasing the angle of attack increases the heating of the lower surface and decreases the heating of the upper surface. The variation of heating with angle of attack is essentially linear for both the upper and lower surfaces; however, the rate of increase of heating on the lower surface is about twice the rate of decrease of heating on the upper surface.

[redacted]

Heating of Wing Leading Edge in Vicinity

of Wing-Body Juncture

The heat transfer to swept cylinders in an undisturbed flow field has been studied over a wide range of conditions and, in general, the experimental data agree well with existing theories. A rocket-powered-model flight test was recently conducted for the purpose of measuring the heat transfer to leading edges in the vicinity of the wing-body juncture at relatively high Reynolds numbers. A sketch is shown in figure 6 of the rocket-powered model which carried small stubs representing only the leading-edge portions of 0° and 75° swept wings. The stubs had cylindrical leading edges of 3/4-inch diameter which became tangent to flat surfaces inclined at 4.3° to the chord plane. Thermocouple measurements were made in a direction perpendicular to the leading edge of each stub at locations shown in the cross-section sketch. Four measurement points were obtained on the 0° swept stub; however, on the 75° swept stub, the most rearward thermocouple failed to operate properly and, hence, measurements at only the three forward locations were obtained.

Measured heating data for the two leading edges at a stream Mach number of 3.12 and a stream Reynolds number of 18.7×10^6 per foot are presented in figure 7 along with appropriate theoretical curves for comparison. The data are presented as the nondimensional Stanton number evaluated at free-stream conditions as a function of s/d where s is the surface length, measured in a plane normal to the leading edge, from the stagnation point to the measurement station and d is the leading-edge diameter. The measured data on the cylindrical portion of the leading edge for both the 0° and 75° swept stubs are considerably higher than that predicted by the laminar leading-edge theory in reference 4. On the 0° swept leading edge, the heating at the stagnation point is of the order of 2 times that which is predicted by laminar theory, and on the 75° swept leading edge, the heating is of the order of 4.5 times as great. Since there is such a large difference between the measured values and the laminar theory for the cylindrical portion of the leading edges, it was felt that the flow over this portion must be turbulent. This was verified for the 0° swept leading edge by integrating the measured values over the cylindrical portion to obtain the average heat transfer. This average value $\left(N_{St,\infty} = 34.96 \times 10^{-4}\right)$ was found to agree very well with the theoretical average $\left(N_{St,\infty} = 34.85 \times 10^{-4}\right)$ computed from the turbulent theory in reference 3. Comparison of the measured data on the flat portion following the cylinder with the Van Driest turbulent flat-plate theory (refs. 10 and 11) also shows good agreement and tends to establish further that the flow on the 0° swept leading edge was turbulent. The analysis for turbulent heating on the 75° swept leading edge was not carried out because of the absence of information on the local flow conditions at this sweep angle and Mach number.

[redacted]

The reason for turbulent flow over the 0° swept leading edge cannot be deduced from the measurements made on the model. Since the measurements were made at a distance of only $1\frac{1}{4}$ inches from the body, the heating to the leading edge could have been influenced by conditions existing in the body boundary layer. The Reynolds number for the body at the leading-edge body juncture was approximately 66×10^6 and the body boundary-layer thickness was estimated to be of the order of 1/2 inch. With these conditions prevailing, it is possible that interaction between the bow shock ahead of the leading edge and the thick turbulent boundary layer of the body could have increased the heating of the leading edge to the turbulent level. Although exact simulation of the flow field at the wing-body juncture may not have been provided by the short leading-edge stubs, these data indicate that rates of heat transfer much higher than laminar rates can be experienced on leading edges in the region of the wing-body juncture, and that, further, more complete investigations are needed to understand this phenomenon.

Transpiration Cooling at High Stagnation Temperatures

At lower flight speeds the problem of convective heating of an aircraft surface can generally be handled by designing the surface as a heat sink and allowing the skin to attain some allowable equilibrium temperature. As flight speeds increase, the idea of some type of cooling for the hotter surfaces appears more attractive. One type of cooling which shows promise is transpiration cooling, in which the coolant passes from the interior of the aircraft through a porous skin into the hot boundary layer. Experimental data on transpiration cooling at relatively low heating potentials have been reported in references 14, 15, and 16, and have shown appreciable reduction in the convective heating with transpiration cooling. In order to investigate the effectiveness of transpiration cooling at higher heating potentials, exploratory tests have been conducted at high stagnation temperatures in the Langley preflight jet of the Pilotless Aircraft Research Station at Wallops Island, Va. The model employed for the tests was a blunted wedge of 20° half-angle which had a porous stainless-steel segment inserted in one surface through which coolant was ejected. Tests were conducted at a nominal free-stream dynamic pressure of 5,000 pounds per square foot and a free-stream Mach number of 2.0; however, the local-surface Mach number on the wedge was of the order of 1.2. Results of these tests showing the effect of transpiration cooling on the wedge-surface temperature for both nitrogen and helium coolants are presented in figure 8. The ordinate is the non-dimensional wall-temperature parameter $\frac{T_W - T_c}{T_{AW,0} - T_c}$ where T_W is the porous-wall temperature, T_c is the coolant temperature, and $T_{AW,0}$ is the boundary-layer recovery temperature for zero coolant flow rate. The

abscissa is the coolant flow rate in pounds per square foot per minute. Such a presentation of cooling data shows directly the reduction in wall temperature which can be achieved for a given coolant flow rate. Data are presented for stagnation temperatures in the range from 2,355° R to 3,370° R for nitrogen coolant and from 1,755° R to 3,195° R for helium coolant. For the various tests, ratios of wall temperature to local temperature ranged from 0.2 to 0.5 and the local Reynolds numbers ranged from 0.6×10^6 to 8.2×10^6. It might also be mentioned that the present data were obtained for average operating temperatures of the porous wall in the range from about 200° F to 1,300° F. Comparison of the nitrogen and helium data in figure 8 shows that the helium performs as a much more effective coolant than nitrogen, as would be expected because of the higher specific heat of the helium. For example, in order to maintain the skin at a temperature of about 0.3 of the uncooled value, approximately 10 pounds of nitrogen per square foot per minute would be required as compared with 2 pounds per square foot per minute for helium. It might be added that this ratio of 5 to 1 in required coolant flow rates is roughly the same as the ratio of the specific heat of helium to that of nitrogen.

In order to show how these high-temperature data compare with theory and other low-temperature data, as well as to show the effect of cooling on the heat transfer, the data were reduced to heat-transfer coefficients and are presented in dimensionless form in figure 9. The ordinate is the ratio of the Stanton number with cooling to the Stanton number for zero cooling, and the abscissa is the injection parameter F (the ratio of coolant weight flow to local stream weight flow) divided by the Stanton number for zero cooling. In the reduction of the measured data to Stanton number, the recovery temperature with coolant flow was evaluated by using recovery-factor values computed from the theory of reference 17, which gives the variation of recovery factor with Mach number, coolant flow rate, and Reynolds number. Included for comparison are the theoretical curve applicable to nitrogen from the theory in reference 18 for $M = 1.0$ and a ratio of wall temperature to local temperature of 0.2, and the experimental data in reference 14 for the transpiration cooling of an 8° cone with both nitrogen and helium coolants at a stagnation temperature of 1,060° R. The experimental wedge data for nitrogen coolant form a band which has the same trend as the theory and shows slightly greater cooling effectiveness. The present data for the nitrogen also show good agreement with the trend established by the 8° cone data. The present helium data do not show as good agreement with the prior cone data with helium coolant as is observed in the case with nitrogen. Since both sets of data for the helium coolant are for small flow rates, the discrepancy between the two sets of data may be due to the lesser accuracy in determining the flow rates in the lower range of flow rates.

With this type of correlation, the comparison of the effectiveness of helium with nitrogen as transpiration coolants is about in the same

relation as noted in figure 8. The theory which is strictly derived for transpiration of air to air but is applicable also to nitrogen because of the similarity of the physical characteristics may be said to apply equally as well for either high or low heating potentials.

CONCLUSIONS

The pertinent conclusions which may be drawn from the foregoing compilation of wing-heating data may be summarized briefly as follows:

1. Measured heat transfer tc wing surfaces exposed to high-heat fluxes have, in general, shown good agreement with theory. Theory has also been shown to be adequate in predicting the heat transfer to wing surfaces over a wide range of Reynolds number.

2. Heat-transfer measurements on a blunted slab wing at a Mach number of 6.86 showed that the surface heating at zero angle of attack was essentially the same for sweep angles of 0°, 40°, and 60°. Increasing the angle of attack of the slab wing increased the heating of the windward surface and decreased the heating of the leeward surface.

3. Measurements at high stream Reynolds numbers have shown that rates of heat transfer much higher than laminar rates can be experienced on leading edges in the region of the wing-body juncture.

4. Theoretical predictions of the effectiveness of nitrogen as a transpiration coolant have been shown to apply equally as well for conditions of either high or low heating potentials. Measurements have shown that helium is about five times more effective as a transpiration coolant than nitrogen.

[redacted]

REFERENCES

1. Reshotko, Eli, and Cohen, Clarence B.: Heat Transfer at the Forward Stagnation Point of Blunt Bodies. NACA TN 3513, 1955.

2. Beckwith, Ivan E.: Theoretical Investigation of Laminar Heat Transfer on Yawed Infinite Cylinders in Supersonic Flow and a Comparison With Experimental Data. NACA RM L55F09, 1955.

3. Beckwith, Ivan E., and Gallagher, James J.: Experimental Investigation of the Effect of Boundary-Layer Transition on the Average Heat Transfer to a Yawed Cylinder in Supersonic Flow. NACA RM L56E09, 1956.

4. Goodwin, Glen, Creager, Marcus O., and Winkler, Ernest L.: Investigation of Local Heat-Transfer and Pressure Drag Characteristics of a Yawed Circular Cylinder at Supersonic Speeds. NACA RM A55H31, 1956.

5. Bland, William M., Jr., and Bressette, Walter E.: Some Effects of Heat Transfer at Mach Number 2.0 at Stagnation Temperatures Between 2,310° and 3,500° R on a Magnesium Fin With Several Leading-Edge Modifications. NACA RM L57C14, 1957. (Prospective NACA Paper.)

6. Carter, Howard S.: Heat Transfer on the Lifting Surfaces of a 60° Delta Wing at Angle of Attack for Mach Number 1.98. NACA RM L56C23, 1956.

7. Bartlett, G. E., Hilton, J. H., Vidal, R. J., and Woolard H. W.: Experimental Investigations of Heat Transfer on a 10-Percent Double-Wedge Airfoil at Mach No. 2.0. Rep. No. CAL/CM-832 (Contract NOrd-14523), Cornell Aero. Lab., Inc., Jan. 1955.

8. Sterbutzel, Gerald A., and Kajencki, Stephen S.: Experimental Investigation of Heat Transfer From Aerodynamic Bodies in Supersonic Flow. Rep. No. AF-473-A-9 (Contract W33-038-ac-16701), Cornell Aero. Lab., Inc., Apr. 1950.

9. Van Driest, E. R.: Investigation of Laminar Boundary Layer in Compressible Fluids Using the Crocco Method. NACA TN 2597, 1952.

10. Van Driest, E. R.: The Turbulent Boundary Layer for Compressible Fluids on a Flat Plate With Heat Transfer. Rep. No. AL-997, North American Aviation, Inc., Jan. 27, 1950.

11. Van Driest, E. R.: The Turbulent Boundary Layer With Variable Prandtl Number. Rep. No. AL-1914, North American Aviation, Inc., Apr. 2, 1954.

[redacted]

12. Swanson, Andrew G., and Rumsey, Charles B.: Aerodynamic Heating of a Wing As Determined From a Free-Flight Rocket-Model Test to Mach Number 3.64. NACA RM L56F11a, 1956.

13. Seiff, Alvin: Examination of the Existing Data on the Heat Transfer of Turbulent Boundary Layers at Supersonic Speeds From the Point of View of Reynolds Analogy. NACA TN 3284, 1954.

14. Chauvin, Leo T., and Carter, Howard S.: Exploratory Tests of Transpiration Cooling on a Porous 8° Cone at M = 2.05 Using Nitrogen Gas, Helium Gas, and Water as the Coolants. NACA RM L55C29, 1955.

15. Leadon, B. M., and Scott, C. J.: Measurement of Recovery Factors and Heat Transfer Coefficients With Transpiration Cooling in a Turbulent Boundary Layer at M = 3 Using Air and Helium as Coolants. Res. Rep. No. 126, Univ. of Minnesota Inst. Tech., Dept. Aero. Eng. (Contract AF 18(600)-1226), Feb. 1956.

16. Rubesin, Morris W., Pappas, Constantine C., and Okuno, Arthur F.: The Effect of Fluid Injection on the Compressible Turbulent Boundary Layer - Preliminary Tests on Transpiration Cooling of a Flat Plate at M = 2.7 With Air as the Injected Gas. NACA RM A55I19, 1955.

17. Rubesin, Morris W.: An Analytical Estimation of the Effect of Transpiration Cooling on the Heat-Transfer and Skin-Friction Characteristics of a Compressible, Turbulent Boundary Layer. NACA TN 3341, 1954.

18. Dorrance, William H., and Dore, Frank J.: The Effect of Mass Transfer on the Compressible Turbulent Boundary Layer Skin Friction and Heat Transfer. Rep. ZA-7-013, Convair, Aug. 5, 1954.

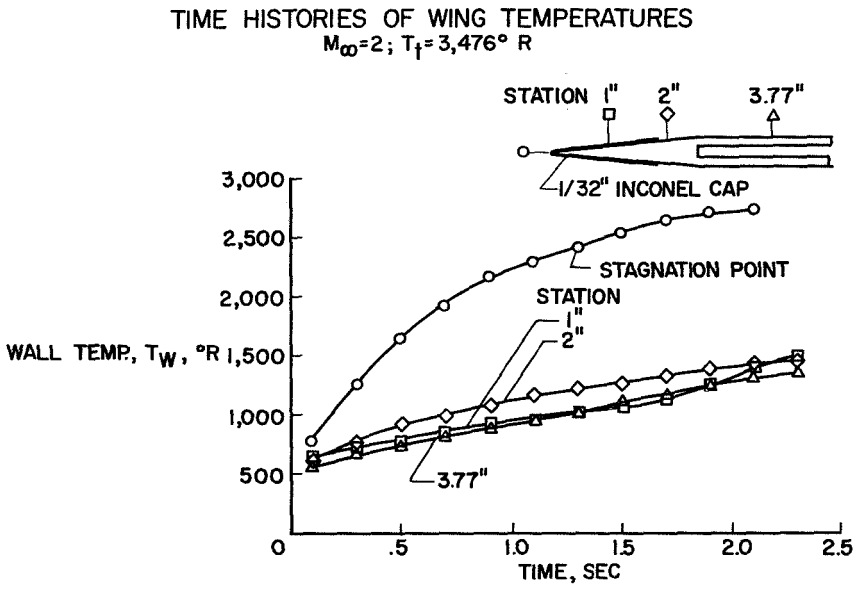


Figure 1

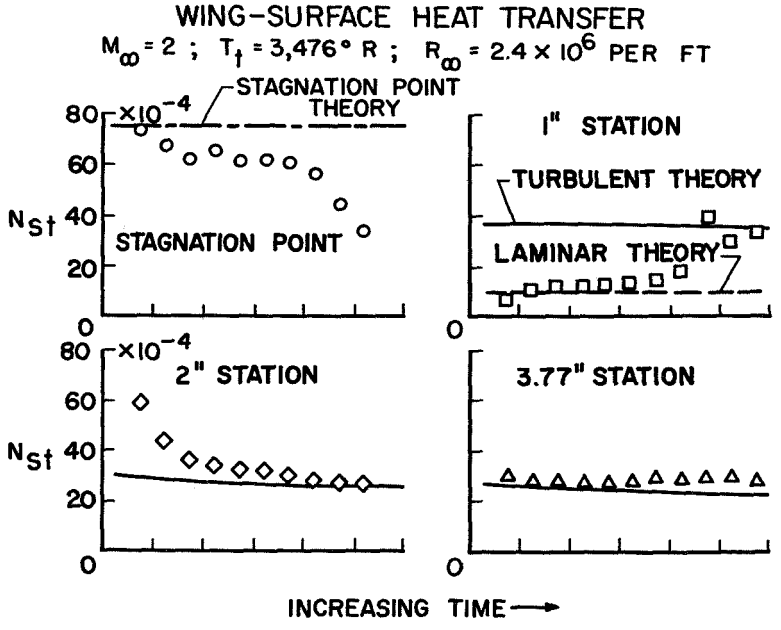


Figure 2

COMPARISON OF EXPERIMENT AND THEORY FOR LARGE-SCALE HEAT-TRANSFER TESTS

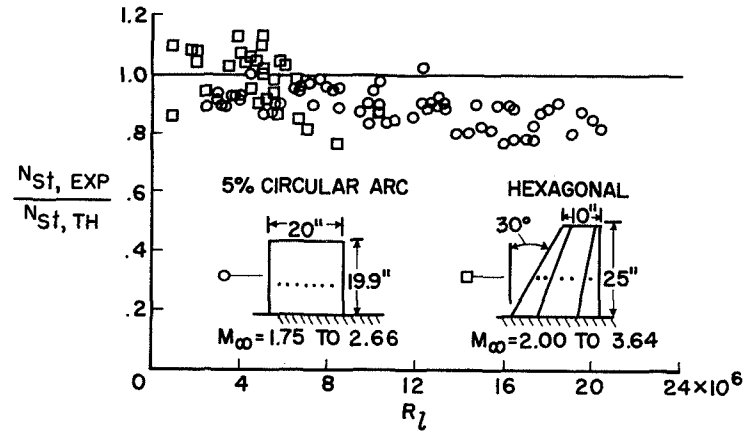


Figure 3

EFFECT OF SWEEP ON HEAT TRANSFER TO A BLUNT L.E. WING

α=0°; M=6.86; R_d=0.151×10^6

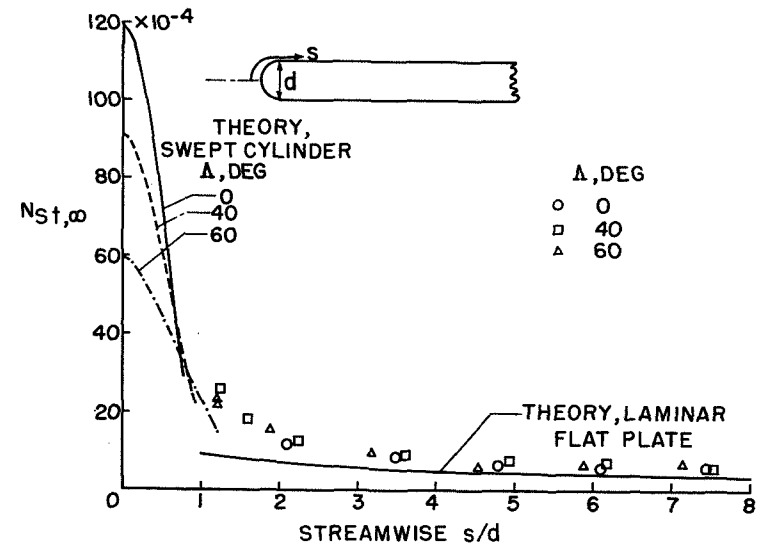


Figure 4

EFFECT OF ANGLE OF ATTACK ON HEAT TRANSFER TO A BLUNT L.E. WING

$\Lambda = 40°$; $M = 6.86$; $R_d = 0.151 \times 10^6$

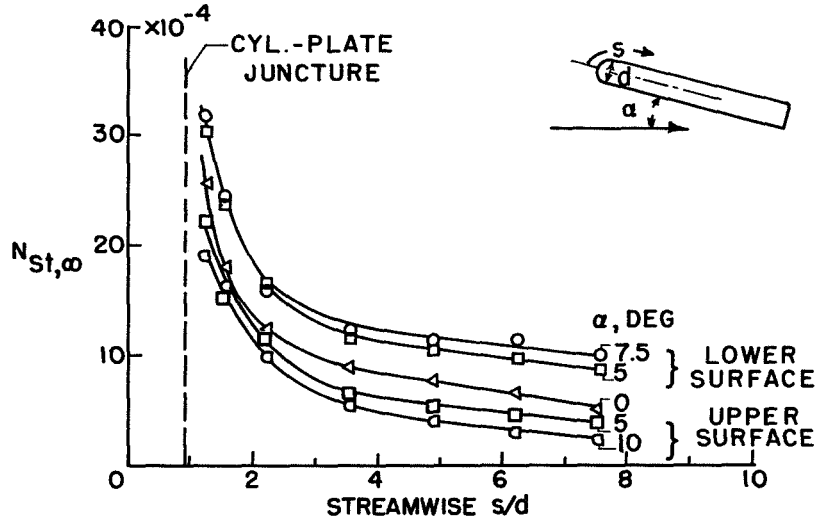
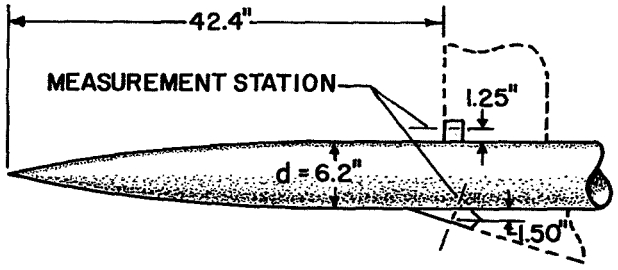


Figure 5

LEADING-EDGE HEAT-TRANSFER MODEL



LEADING-EDGE CROSS SECTION



Figure 6

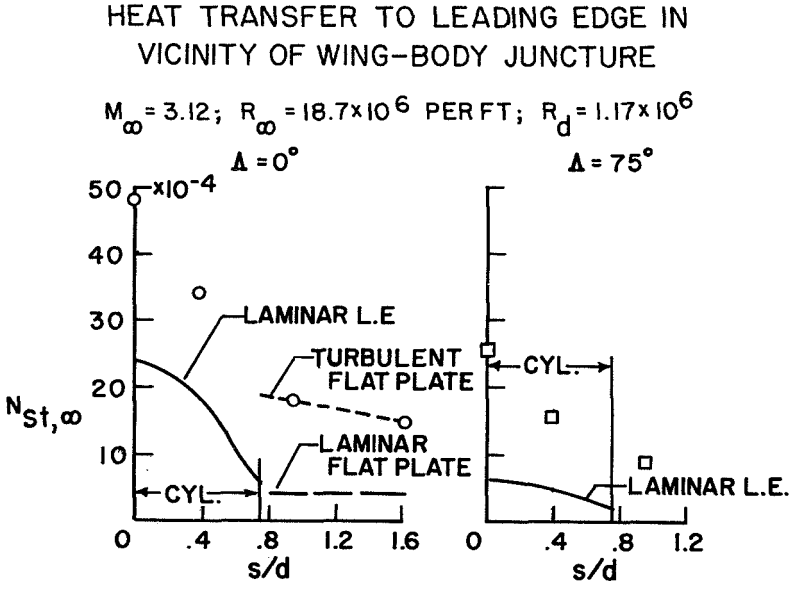


Figure 7

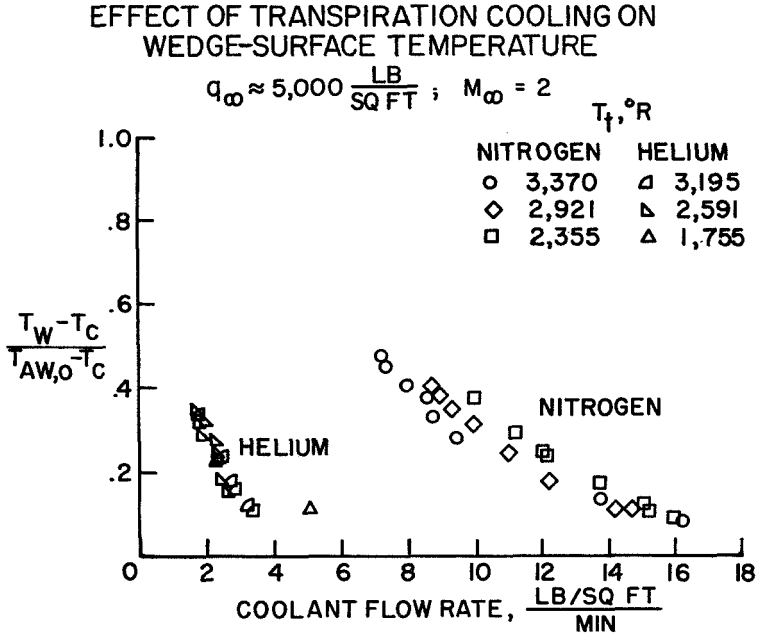


Figure 8

EFFECT OF TRANSPIRATION COOLING ON HEAT TRANSFER

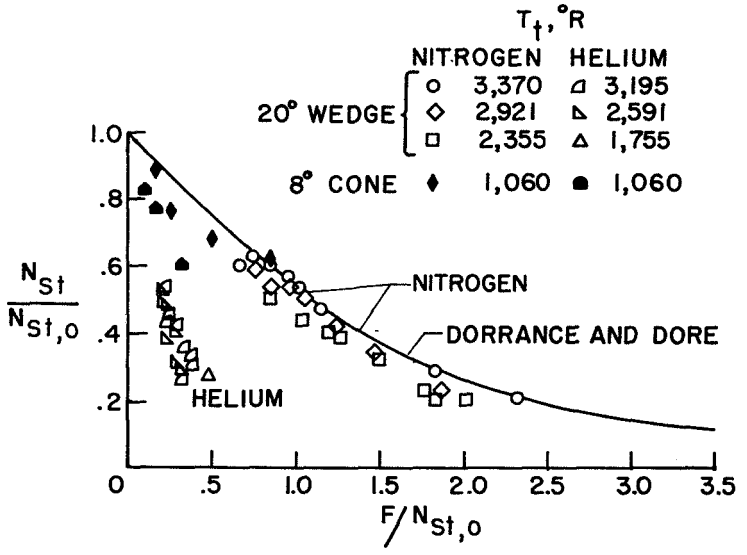


Figure 9

N71-75400

TOTAL HEAT TRANSFER TO BLUNT-NOSE SHAPES WITH LAMINAR BOUNDARY LAYERS AT HIGH SUPERSONIC SPEEDS

By John O. Reller, Jr.

Ames Aeronautical Laboratory

SUMMARY

A method of designing blunt shapes has been devised which proposes to reduce the heat transfer to a body by virtue of low-velocity flow over the nose and low-density flow over the afterbody. A typical body consists of a flat nose and a highly curved afterbody surface defined by a modified Newtonian theory.

Tests were conducted in the Ames 10- by 14-inch supersonic wind tunnel at Mach numbers from 3.0 to 6.3 and it was found that total heat-transfer rates for these flat-nose shapes is less than that of a cone of about the same drag. Comparison of experimental results with theory indicates higher than average heat-transfer rates near the shoulder of a typical shape and relatively low values over most of the afterbody.

INTRODUCTION

It is a well-known fact that blunting can reduce the rate of heat transfer to the nose of a body in supersonic flow. The problem is, however, to determine a type of blunting which tends to minimize the heat-transfer rate. The purpose of this paper is to describe an investigation of this problem in which it was undertaken first to devise a method of designing blunt shapes and then to check by experiment the effectiveness of these shapes in reducing heat transfer.

BLUNT-NOSE BODIES

The basic heat-transfer equation, in the form of Reynolds analogy, is shown at the top of figure 1. Although this analogy is not strictly applicable for blunt shapes, in general the convective heat-transfer coefficient is proportional to the product of the local density, local velocity, specific heat, and local skin-friction coefficient. The specific heat is a factor over which relatively little control can be exerted. Likewise, control over the skin-friction coefficient is limited

primarily by the extent to which laminar boundary-layer flow can be preserved. Attention is therefore focused on the product of the local density and the local velocity. This product, and hence the local heat-transfer coefficient, may be kept low over a shape designed to have low velocities at the nose and low densities over the afterbody. Such a shape would, in its simplest form, be a truncated cone, inasmuch as the flat nose minimizes local velocities, while the highly inclined sides minimize local pressures and hence densities. The fact is, however, that the sharp corner at the intersection of the face and afterbody of a truncated cone tends to cause local separation and reattachment of the flow with an attendant shock wave and unfavorable pressure gradient. These conditions tend to promote transition to a turbulent boundary layer, which increases the local heating rate. Therefore, the surface in this shoulder region should be curved to avoid local separation and possible tripping of the boundary layer. In order to promote laminar flow over the entire afterbody it is desirable to have a contour which generates a continuously favorable pressure gradient. Such a contour is easily determined with the modified Newtonian theory of Eggers, Resnikoff, and Dennis (ref. 1), providing the square of hypersonic similarity parameter $M/\frac{L}{D}$ is large compared with unity. This condition is satisfied by blunt bodies at the high supersonic Mach numbers of this investigation. The resultant expression defining the shape of the afterbody surface is shown as the second equation in figure 1. Note that the coordinates $\bar{x}$ and $\bar{y}$ are the local x and y dimensions, respectively, divided by the radius of the flat nose. The parameter K in this expression fixes the level and gradient of pressure on the afterbody.

Two families of blunt-nose bodies of revolution were designed according to this equation. The first family is shown at the left in figure 1 and consisted of eight bodies of the same fineness ratio, but of varying diameters of the flat nose. For the second family of bodies, shown at the right in figure 1, the nose and base diameters were held constant and the fineness ratio was varied from about 0.3 to 1.6. The corresponding values of K are shown on the superimposed sketches of these bodies. The bodies of this second family have approximately the same pressure drag and for this reason two reference bodies of similar pressure drag were included in the test program. These were the sharp-pointed and hemispherical-tipped 60° cones shown in figure 1. A full hemisphere of the same base diameter was also tested.

EXPERIMENTAL APPARATUS

Tests were conducted in the Ames 10- by 14-inch supersonic wind tunnel at Mach numbers from 3 to 6.3. As shown in figure 2, models were sting supported from the rear and were in effect insulated to prevent

heat loss to the support system by a guard heater which was used to equalize the temperature in the support shell. Heat input was through a resistance heater of Inconel wire wound on a copper spool. From the known resistance and measured voltage the overall heat-transfer rate could be determined for equilibrium conditions. This apparatus did not permit the measurement of local heat-transfer rates. Models were made of aluminum and provided essentially constant-temperature heat-transfer surfaces because of their high conductivity. Thermocouples were installed within the models to measure temperatures near the outer surface. No correction was made to the measured data to account for the heat flow through the exposed portion of the model bases. This heat flow was estimated to be a small fraction of the total and hence has been neglected since the primary interest of this investigation is the relative effects of shape on heat transfer.

EFFECT OF BLUNTNESS ON HEAT TRANSFER

The effect on heat transfer of varying nose diameter while holding fineness ratio constant is shown in figure 3. Representative data at zero angle of attack and free-stream Mach number M of 4.24 are presented in the form of nondimensional heat-transfer coefficients, that is, Stanton numbers, based on free-stream properties. At the top of the figure, Stanton numbers are referenced to model base area and as such are a direct comparison of the total heat-transfer rates. As nose diameter is increased from zero, Stanton number first decreases slightly, then remains nearly constant up to a diameter ratio of one-half, and thereafter increases substantially up to a diameter ratio of 1. The Stanton numbers presented in the lower part of figure 3 are referenced to wetted surface area, exclusive of the base, and hence are indicative of the average heating rate per unit surface area. They decrease significantly with increasing diameter ratio up to about one-half and then remain essentially constant. These results suggest that a body with a nose-to-base diameter ratio of about one-half is a good compromise for low values of both total and average heat transfer. Furthermore, this amount of bluntness yields drags which are in the range of practical interest for ballistic missile shapes. It was for this reason that a diameter ratio of 0.52 was used in designing the second family of bodies.

EFFECT OF FINENESS RATIO ON HEAT TRANSFER TO BLUNT BODIES

Total heat transfer to the bodies of different fineness ratio at zero angle of attack is shown in figure 4 as a function of free-stream

Mach number. Comparative data for a hemisphere are also presented. Stanton numbers are referenced to model base area. The upsweep of the data with increasing Mach number results from the decrease of free-stream Reynolds number R typical of a wind tunnel operating with a fixed supply pressure. As determined from shadowgraph pictures the boundary layer was laminar over the flat-nose bodies at all test conditions. This is in contrast to the reference cones on which transition occurred at low Mach numbers and is an illustration of the effect of blunting on the length of laminar run. In fact, at $M = 3$, the length of laminar run was increased by as much as a factor of 4. Total Stanton numbers for the flat-nose shapes were less than corresponding cone values at all Mach numbers. Thus, by blunting it was possible to increase surface area and volume by a factor of 3 with no heat-transfer penalty.

When the Stanton numbers are referenced to wetted surface area, a pronounced effect of fineness ratio is apparent as shown in figure 5. Note, for example, that values of average Stanton number for the $K = 6$ shape are 35 percent lower than those for the cone with all-laminar boundary layer ($M > 4$). The maximum reduction in average Stanton number with all-laminar flow is 70 percent for the $K = 9$ shape at $M = 4.24$. These data are, as are all the data discussed previously in this report, for zero angle of attack. It should be pointed out, however, that no measurable change in Stanton numbers has been observed for the flat-nose shapes at angles of attack up to 3°.

The fact should not be overlooked that the rate of aerodynamic heating is actually proportional to the product of Stanton number and temperature recovery factor. Thus, it is a tacit assumption of the discussion in previous sections that recovery factor is essentially constant. The validity of this assumption is illustrated in figure 6 where average temperature recovery factors based on free-stream conditions are shown as a function of free-stream Mach number. It is apparent that shape has little effect on recovery factor; hence, this factor plays no significant role in this discussion of the effect of shape on heating.

DISTRIBUTION OF LOCAL HEAT-TRANSFER COEFFICIENTS

The measurement of overall rates of heat transfer described in this paper can, at best, give only a qualitative idea of local heating rates. It was undertaken to determine a theoretical distribution of heat-transfer coefficients around one typical shape and to make a limited experimental comparison. The method of Stine and Wanlass (ref. 2) was used to calculate heat-transfer coefficients. This calculation requires a knowledge of the local flow properties just outside the boundary layer. These properties were derived from experimental pressure distributions such as those shown in figure 7. Also shown in figure 7 are the predicted pressures

of the modified Newtonian theory which was used to design the blunt-nose bodies. These predicted pressures are in good agreement with experiment, the differences being most pronounced in the region of the shoulder of the body. The calculated variation of local heat-transfer coefficient with distance along the body surface is shown in figure 8 where the results of the Stine-Wanlass method, which includes the effect of pressure gradient, are compared at free-stream Mach numbers 3 and 5 with flat-plate values taken from the laminar boundary-layer theory of Van Driest (ref. 3). All heat-transfer coefficients are based on local flow properties just outside the boundary layer. Reference values near the stagnation point were computed by the method of Sibulkin (ref. 4). Predicted heat-transfer coefficients remain essentially constant over the first half of the nose flat but then increase to 2 to 3 times this value near the shoulder. (A portion of the curve in this region has been shown as a dashed line because spacing of the pressure taps did not permit an accurate determination of the maximum.) Subsequently, local coefficients decrease sharply to less than one-half the initial value and continue in a gradual decline to the base. The notable feature of this prediction is the pronounced increase of heat-transfer coefficients over the forepart of the body as a result of three-dimensional and pressure-gradient effects. These relatively large local heating rates indicate that perhaps the design of these bodies has been somewhat oversimplified. Very qualitatively, it appears that a slightly convex nose would tend to reduce the heat-transfer peak at the shoulder by reducing the local density, although at the expense of a slight increase in heat transfer to the nose.

COMPARISON OF THEORY WITH EXPERIMENT

Integrated values of the theoretical heat-transfer coefficients for portions of the body surface are compared with experimental measurements in figure 9. The flat-nose and nose-shoulder data were obtained with composite models that isolated the heat-transfer surfaces from the rest of the body. Agreement is reasonably good except for the flat nose at free-stream Mach numbers above 3. Both computed and measured Stanton numbers show that roughly 55 percent of the total heat transfer was concentrated in the nose-shoulder region which has less than 20 percent of the surface area. Thus, on an average basis, heat-transfer rates in this region are greater by a factor of 5 than those for the rest of the body.

These results apply only when boundary-layer flow is entirely laminar. A qualitative indication of the effect of transition on total heat transfer was obtained, in one case, by artificially tripping the boundary layer in the shoulder region. The resultant Stanton number is shown as the solid point in figure 9. It is indicated that the overall

heating rate is not substantially increased by the presence of a turbulent boundary layer in this region of relatively low density flow.

CONCLUDING REMARKS

The results of this investigation can be summarized as follows:

1. A method of designing blunt shapes has been devised which reduces the heat transfer to a body by virtue of low-velocity flow over the nose and low-density flow over the afterbody.

2. An afterbody curvature has been found which augments the favorable effect of a flat nose in promoting long runs of laminar boundary layer.

3. Total heat transfer to these shapes is the same or less than to a cone of about the same drag, although heat-transfer rates per unit of surface area are considerably lower.

4. Comparison of theory and experiment indicates higher than average heat-transfer rates near the shoulder of a typical flat-nose shape and relatively low values over most of the afterbody.

REFERENCES

1. Eggers, A. J., Jr., Resnikoff, Meyer M., and Dennis, David H.: Bodies of Revolution Having Minimum Drag at High Supersonic Airspeeds. NACA TN 3666, 1956. (Supersedes NACA RM's A51K27 by Eggers, Dennis, and Resnikoff and A52D24 by Resnikoff.)

2. Stine, Howard A., and Wanlass, Kent: Theoretical and Experimental Investigation of Aerodynamic-Heating and Isothermal Heat-Transfer Parameters on a Hemispherical Nose With Laminar Boundary Layer at Supersonic Mach Numbers. NACA TN 3344, 1954.

3. Van Driest, E. R.: The Laminar Boundary Layer With Variable Fluid Properties. Rep. No. AL-1866, North American Aviation, Inc., Jan. 19, 1954.

4. Sibulkin, M.: Heat Transfer Near the Forward Stagnation Point of a Body of Revolution. Jour. Aero. Sci. (Readers' Forum), vol. 19, no. 8, Aug. 1952, pp. 570-571.

BODY SHAPES USED IN HEAT-TRANSFER INVESTIGATION

REYNOLDS ANALOGY $h \propto \rho U C_p C_f$

EQUATION OF BODY SHAPE $\bar{X} = \int_1^{\bar{y}_{MAX}} \sqrt{\bar{y}^{K-1}}\, d\bar{y}$ WHERE $\bar{X} = \frac{x}{y_{NOSE}}$, $\bar{y} = \frac{y}{y_{NOSE}}$

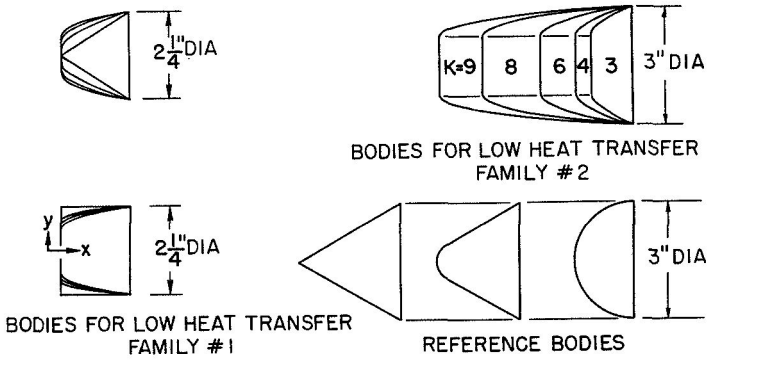


Figure 1

HEAT TRANSFER APPARATUS

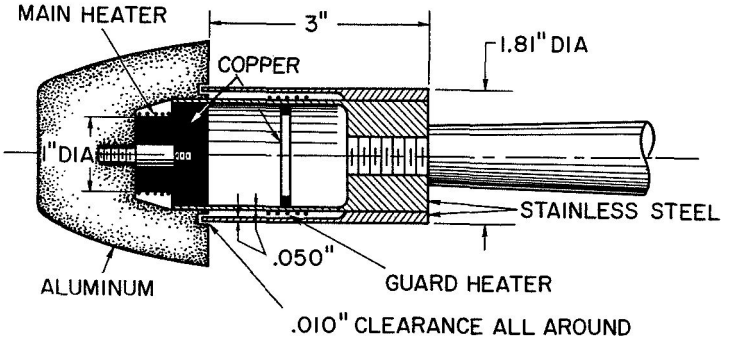


Figure 2

EFFECT OF BLUNTNESS ON HEAT TRANSFER AT M=4.24

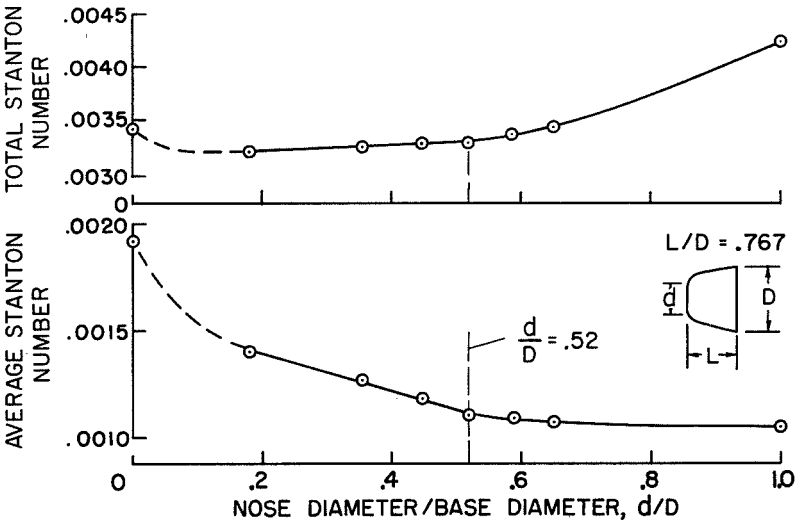
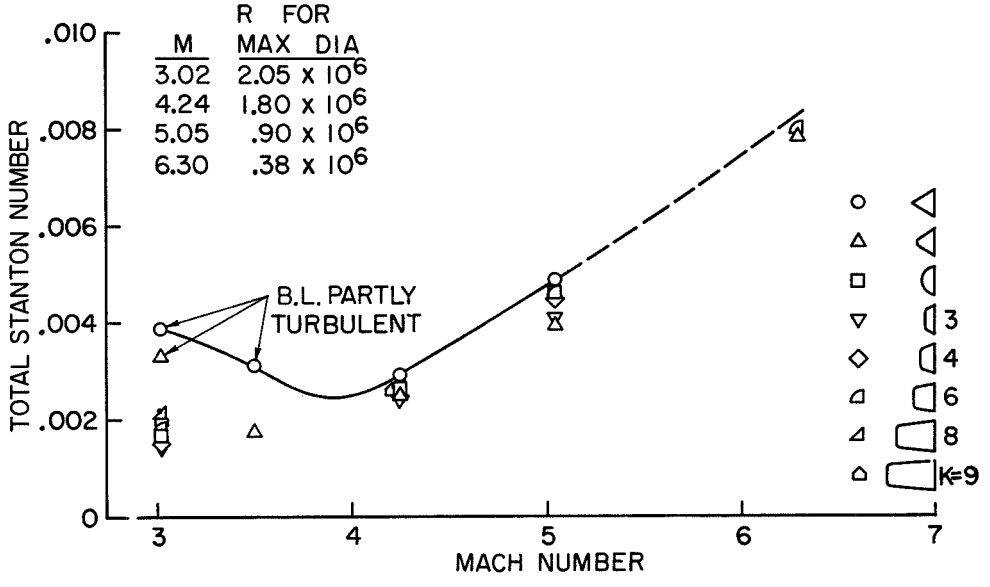


Figure 3

TOTAL HEAT TRANSFER TO BODIES



290

Figure 4

AVERAGE HEAT TRANSFER TO BODIES

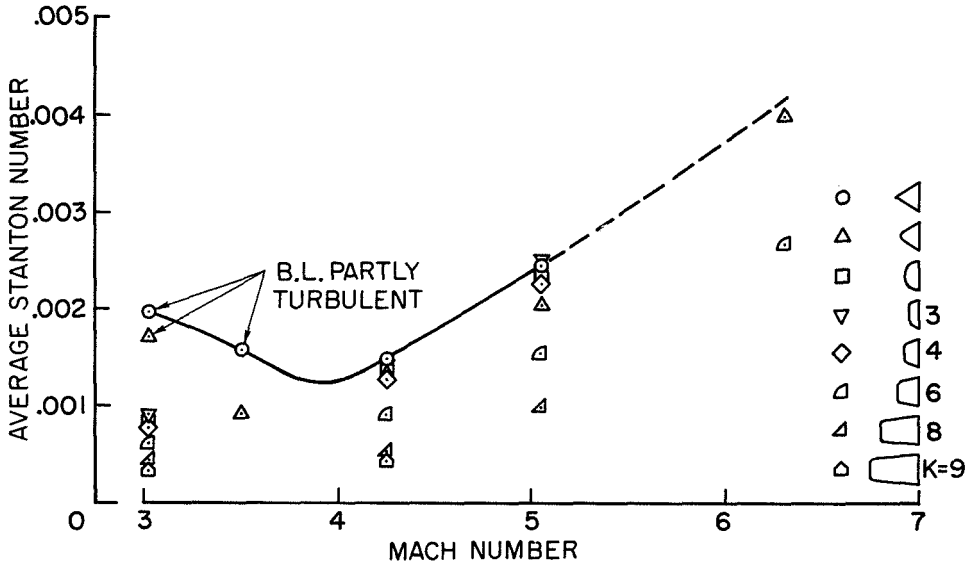


Figure 5

AVERAGE TEMPERATURE-RECOVERY FACTORS OF BODIES

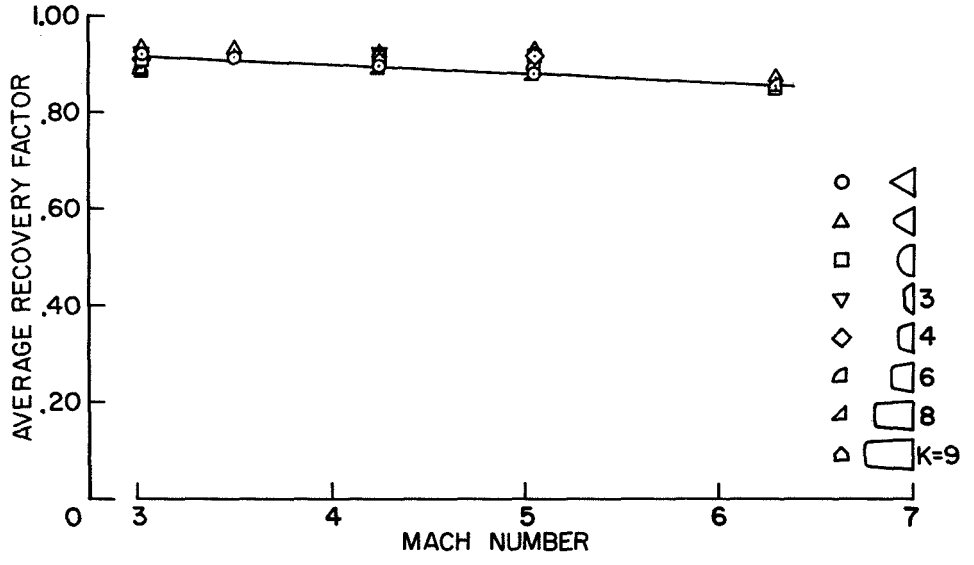


Figure 6

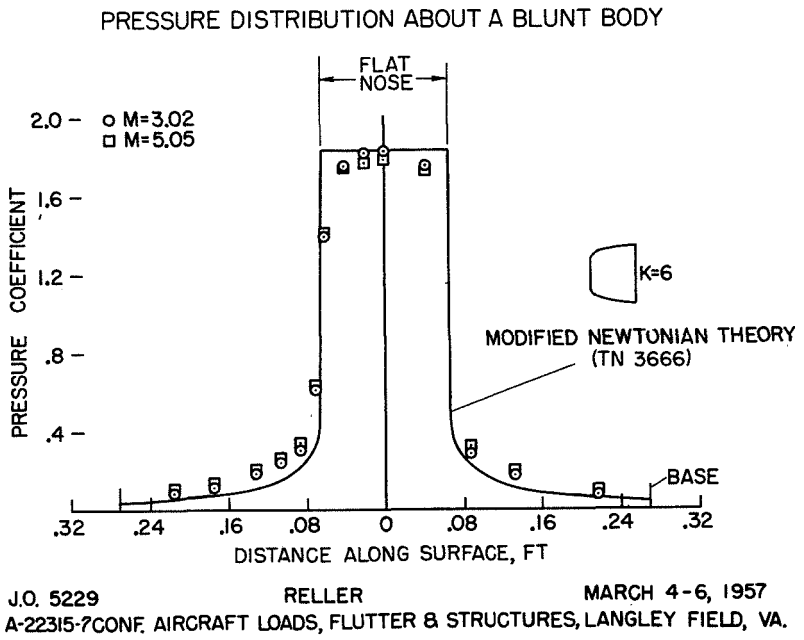


Figure 7

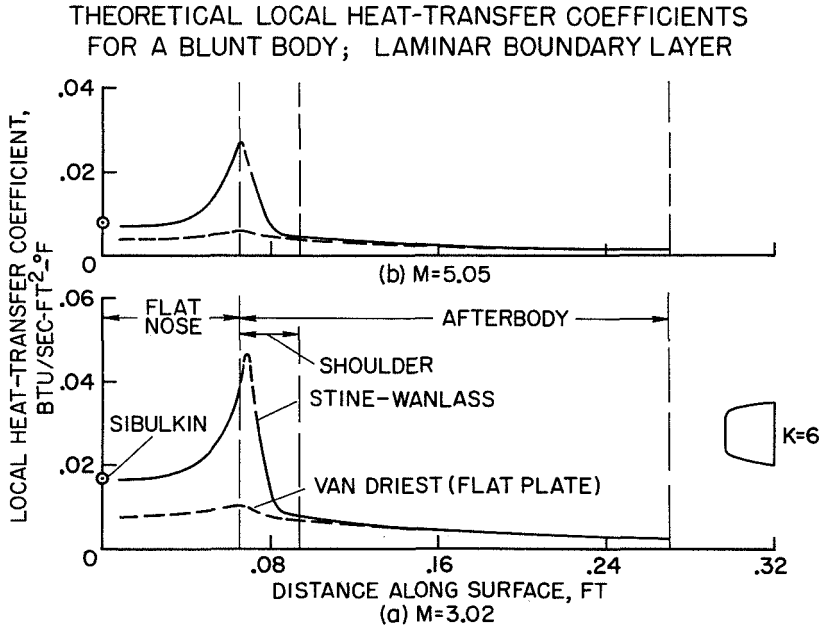


Figure 8

HEAT TRANSFER TO A BLUNT BODY

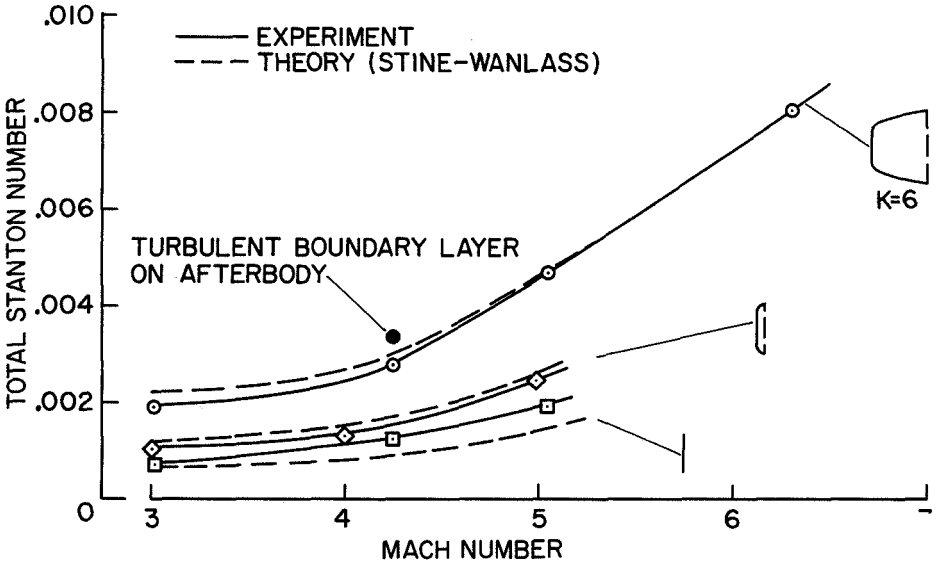


Figure 9

N71-75401

LOCAL HEAT TRANSFER TO BLUNT NOSES AT HIGH SUPERSONIC SPEEDS

By William E. Stoney, Jr.

Langley Aeronautical Laboratory

SUMMARY

A brief summary is presented of the recent theoretical and experimental work on local heat-transfer rates on blunt-nose bodies. Comparisons of theoretical and measured heating rates indicate the following conclusions: The calculation of local conditions over noses of high radius of curvature needs more study and testing at the present time. If local flow conditions are known, the laminar heating rates over the whole nose shape can be calculated within most engineering accuracy requirements for the whole range of Mach numbers up to 13.8. For the case of turbulent flow, turbulent flat-plate theory based on local flow properties can provide good estimates of the heating rates possible. The prediction of transition remains at present the biggest unknown.

INTRODUCTION

The importance of blunt-nose shapes has increased in recent years because such shapes have many advantages in comparison with the more common sharp-nose shapes for missiles having high heating rates. High drag is sometimes desirable for ballistic missiles and does not penalize the total efficiency of these missiles since they operate at essentially drag-free altitudes for the major part of their flight. As shown in reference 1, extremely blunt noses develop lower total heating rates than do sharp noses of about the same size and drag. Finally, and perhaps most importantly, there are many indications that extremely blunt shapes foster longer runs of laminar flow than do sharp shapes.

For these reasons the calculation of the local heating rates on such shapes has become extremely important. The present paper gives a brief summary of present-day techniques and their effectiveness. This summary together with the attached list of references should be helpful to those orienting themselves in this fast-changing field.

[redacted]

SYMBOLS

C_p	pressure coefficient
l	surface distance measured from stagnation point
M	Mach number
p	pressure
q	heating rate, Btu/(sec)(sq ft)
$R_{\infty,d}$	free-stream Reynolds number based on body diameter
r_b	base radius
r_h	nose radius or radius of curvature
s	surface distance from stagnation point to junction of hemisphere and cylinder; on flat face, distance from stagnation point to edge, that is, cylinder radius
T	temperature, ^{o}F
x	distance along center line measured from apex of nose
θ	angle between free stream and normal to surface of nose
μ	viscosity of air
ρ	density of air

Subscripts:

HEMIS	hemispherical nose
l	local
w	based on temperature of wall surface
0	at stagnation point
∞	free stream

[redacted]

DISCUSSION

Calculation of Local Flow Conditions

Before any attempt can be made to calculate heat-transfer rates, the local flow conditions must be calculated. Blunt noses can be classified roughly into two groups: those for which the Newtonian flow concept $\left(C_{p,l}/C_{p,0} = \cos^2\theta\right)$ is applicable and thus for which the local conditions can be easily calculated, and those for which the Newtonian flow concept is not applicable and for which no simple solutions exist.

A rough boundary can be fixed between these two groups of nose shapes by consideration of a series of noses having constant radii of curvature. Such a series is illustrated in figure 1; this series progresses from the hemispherical nose on the left to the flat nose (infinite radius) on the right. The intermediate case for this series would be the nose shown in the center - the nose for which, according to Newtonian theory, the flow just before the corner is at a Mach number of 1. Until stricter criteria are provided, Newtonian calculations should be checked with experiment or with a more comprehensive theory for noses having a radius of curvature at the stagnation point greater than $\sqrt{2}r_b$. Recently, several theoretical approaches have been presented to the blunt-nose problem. (See refs. 2 to 5; theories presented in refs. 4 and 5 may also be found in appendix D of ref. 6.) Some of these appear to be promising, but more experience with them is needed before their general usefulness can be determined.

This paper considers only shapes whose local conditions are known. Experimental data and theoretical results are applied to the hemispherical and the flat noses to bring out the following points:

(1) If the rate of change of velocity at the stagnation point is known, the heat-transfer rate at this point can be calculated accurately enough for most engineering purposes.

(2) With the proper pressure distribution the laminar heating rates over the entire nose can be calculated satisfactorily, and reasonably good estimates of the possible turbulent heating rates can be made.

Prediction of Stagnation-Point Heating Rates

The prediction of stagnation-point heating rates is well proved for the lower Mach number range and needs demonstration only at the higher Mach numbers where real gas effects come into play.

In figure 2 the ratios of measured stagnation-point heating rates to theoretical calculations are presented as functions of free-stream Mach number. The test results were obtained from a flight of the Lockheed X-17 rocket having a nose defined by the equation $r/r_b = (x/2r_b)^{1/3}$ (ref. 6), a flat-face cylinder in free flight (ref. 7), and shock-tube experiments performed by Alexander P. Sabol of the Langley Aero-Physics Section for 1-inch-diameter spheres. The line for the Lockheed data represents the Mach number time history for the flight, the lower portion being that for the accelerating part of the flight and the upper portion representing the decelerating Mach numbers. The difference between accelerating and decelerating values at any given Mach number is probably a measure of the test accuracy rather than a real effect due to the higher Reynolds numbers of the deceleration portion of the flight path. The NACA rocket data should be considered as preliminary data.

The theoretical heating rates for both rockets were calculated by the stagnation-point theory of Fay and Riddell, cited in appendix B of reference 6, for the equilibrium boundary layer with a Prandtl number of 0.71 and a Lewis number of 1.4. The stagnation-point theory of Lees (ref. 8) was compared with the shock-tube experiments. The theories are different because Lees assumes $\rho\mu = \rho_w\mu_w = \text{Constant}$ through the boundary layer while Fay and Riddell use an approximately correct variation. Probstein (ref. 9) notes that, for hypersonic flight conditions, the heat-transfer rate for a realistic variation of $\rho\mu$ across the boundary layer is significantly lower than that calculated from the approximation $\rho\mu = \rho_w\mu_w$. If Probstein's conclusions are assumed to apply directly to Lees' calculations, the level of the ratio of the shock-tube experimental values to Lees' calculated values shown in figure 1 would be raised to somewhere between 1.1 and 1.4. This would not change the general conclusion derived from this figure that, although the scatter shown indicates that many details of the heat-transfer processes under these high-temperature conditions are still unknown, the agreement of these data is close enough so that it can be felt that their general nature is understood.

Calculation of Heating Rates Over Entire Nose

In the calculation of heating rates over the entire nose, the stagnation-point heat-transfer rates of the hemispherical noses are used as datum points, and all the data and calculations are presented as ratios of these values.

Figure 3 presents the ratios of local laminar heating rates on a hemispherical nose to stagnation heating rates plotted as functions of position along the surface of the hemisphere. The test points are for

a variety of conditions from $M_\infty = 2$ to 6.8 and free-stream Reynolds numbers based on diameter of 1.0×10^6 to 14.3×10^6. (Data for $M = 2$ and $M = 3.9$ are presented in ref. 10 and data for $M = 6.8$ in ref. 11. The data for $M = 2.5$ were obtained from a free-flight investigation conducted by James J. Buglia at the Langley Pilotless Aircraft Research Station at Wallops Island, Va.) Good agreement with the theoretical distributions, which were calculated by the method of Lees (ref. 8), can be seen immediately. Corrections by the Probstein theory to Lees' stagnation-point theory mentioned previously would probably not affect the ratios presented in figure 3. It is also important to notice that the distribution of heating rates does not vary markedly with Mach number.

Another interesting condition indicated by the data in figure 3 is the extremely high Reynolds number (14.3×10^6) for which laminar flow was obtained in one flight test. This model, however, was a special case for which extreme pains were taken to obtain a mirror finish on the nose of the order of 2 microinches - not an ideal process for assembly-line fabrication.

Similar agreement with test results can be shown for the other extreme in the series of nose shapes - the perfectly flat face. In figure 4 the local heating rates were not divided by the flat-face stagnation heating rates but by the appropriate hemispherical stagnation heating rates. This allows a direct comparison of the flat and hemispherical values. The solid line gives the theoretical laminar results for the flat face by the method of Lees (ref. 8); and the dashed line above it, the same ratio calculated by the method of Stine and Wanlass (ref. 12). The latter calculations differ from Lees' because they include a correction for the effect of pressure gradient. (For the relatively low pressure gradients of the hemisphere, the two methods agree closely.) As can be seen from the figure the agreement with either theory is reasonably good and the uncertainties in the measurements do not permit a choice between them.

Since the flat nose is a shape for which Newtonian flow concepts do not work at all, a pressure-ratio distribution p_l/p_0 obtained experimentally at a Mach number of 2 (see ref. 13 and theoretical work of ref. 14) was assumed to be constant for all higher Mach numbers and was used in the theoretical calculations. The agreement of the data, which cover Mach numbers from 2 to 13.8, indicates that this approximation was adequate for this case. (Data for $M = 2$ are presented in ref. 13; data for $M = 13.8$ are presented in ref. 7; and data for $M = 5$ were determined in an investigation of 2-inch flat-face cylinders conducted by Morton Cooper in the Mach number 5 axisymmetric blowdown jet at the Langley Gas Dynamics Branch.)

What is gained by the flat face in lower local heating rates in the center is lost at its edge. However, it must be remembered that high local heating rates are not necessarily the critical points in a particular design, as can be shown by the time history of temperature profiles on the front and side of the flat-face rocket model on which the heating rates at a Mach number of 13.8 were obtained. These temperature profiles and a sketch of the nose are presented in figure 5. The nose was made of copper and was three-sixteenths of an inch thick on the front and one-eighth of an inch thick at the sides. The datum points represent the temperatures as measured along the front surface and down the side for three different times during the high Mach number part of the flight. At the earliest time not much heating has occurred and the temperature profile is relatively flat. At peak Mach number the effects of conduction in the skin can be seen since the highest temperature is reached at 0.8ℓ/s in spite of the peak heating which occurs at the corner. The reason that the sides are able to act as good heat sinks lies in their extremely low heating rates. Measurements of these rates for the first two side thermocouples are shown in figure 4. Seven seconds later, the model has slowed down to a Mach number of 7, and the lateral flow of heat in the skin was so large that the maximum temperature of the flight occurred in the center of the model - not at the corners. This is, of course, only an example but it does show that a fairly detailed study of the particular nose must be made if its effectiveness is to be evaluated correctly.

There are some indications (for example, ref. 1) that flat noses or closely allied shapes may have some advantages in retaining laminar flow, and, as is shown, on a hemispherical nose this retention can be very important since turbulent heating rates can be very high. In figure 6 the ratios of local heating rates to stagnation heating rates are presented as functions of surface location. The test points were determined from an investigation conducted by Ivan E. Beckwith and James J. Gallagher in a blowdown jet at the Langley Gas Dynamics Branch. For this investigation a Mach number of 2 and free-stream Reynolds numbers (based on body diameter) of 2.7×10^6 and 3.4×10^6 were used. Transition obviously took place forward on the hemisphere for both tests and heating rates nearly $2\frac{1}{2}$ times the stagnation rate were reached. The solid line represents flat-plate turbulent values based on the local Reynolds numbers around the body. This comparison and similar comparisons from other tests indicates that even this relatively crude theoretical approach may have considerable value in estimating the turbulent heating rates. (See also refs. 15 and 16. The theoretical approach of ref. 16 may also be found in appendix C of ref. 6.)

CONCLUDING REMARKS

The calculation of the local heating conditions over noses of high radius of curvature needs more investigation at the present time, although data obtained in low Mach number tests may be adequate at much higher Mach numbers for use in these calculations. However, if the local conditions are known, the laminar heating rates over the whole nose shape can be calculated within most engineering accuracy requirements for the whole range of Mach numbers up to at least 13.8.

For turbulent flow, flat-plate theory may provide good estimates of the heating rates possible. Of course, the prediction of transition still remains and is the biggest unknown at the present time.

[redacted]

REFERENCES

1. Reller, John O., Jr.: Total Heat Transfer to Blunt-Nose Shapes With Laminar Boundary Layers at High Supersonic Speeds. (Prospective NACA paper.)

2. Maslen, Stephen H., and Moeckel, W. E.: Inviscid Hypersonic Flow Past Blunt Bodies. Preprint No. 665, S.M.F. Fund Preprint, Inst. Aero. Sci., Jan. 1957.

3. Probstein, Ronald F.: Inviscid Flow in the Stagnation Point Region of Very Blunt-Nosed Bodies at Hypersonic Flight Speeds. WADC TN 56-395 (Contract No. AF 33(616)-2798), Wright Air Dev. Center, U. S. Air Force, Sept. 1956. (Also available from ASTIA as Doc. No. AD97273.)

4. Hayes, Wallace D.: Some Aspects of Hypersonic Flow. The Ramo-Wooldridge Corp., Jan. 4, 1955.

5. Hayes, Wallace D.: Hypersonic Flow Fields at Small Density Ratio. Doc. No. 34, The Ramo-Wooldridge Corp., May 12, 1955.

6. Anon.: X-17 Re-Entry Test Vehicle - R-3 Final Flight Report. Rep. No. MSD-3013 (Contract No. AF 04 (645)-7), Lockheed Aircraft Corp., Oct. 31, 1956.

7. Stoney, William E., Jr., and Swanson, Andrew G.: Heat Transfer on a Flat-Face Cylinder Measured in Free Flight at Mach Numbers Up to 13.8. (Prospective NACA paper.)

8. Lees, Lester: Laminar Heat Transfer Over Blunt-Nosed Bodies at Hypersonic Flight Speeds. Jet Propulsion, vol. 26, no. 4, Apr. 1956, pp. 259-269.

9. Probstein, Ronald F.: The Effect of Variable Fluid Properties on the Equilibrium Laminar Boundary Layer Surface Heat Transfer Rate at Hypersonic Flight Speeds. WADC TN 56-2 (Contract No. AF 33(616)-2798), Wright Air Dev. Center, U. S. Air Force, Dec. 1955.

10. Garland, Benjamine J., and Chauvin, Leo T.: Measurements of Heat Transfer and Boundary-Layer Transition on an 8-Inch-Diameter Hemisphere Cylinder in Free Flight for a Mach Number Range of 2.0 to 3.88. (Prospective NACA paper.)

11. Crawford, Davis H., and McCauley, William D.: Investigation of the Laminar Aerodynamic Heat-Transfer Characteristics of a Hemisphere-Cylinder in the Langley 11-Inch Hypersonic Tunnel at a Mach Number of 6.8. NACA TN 3706, 1956.

[redacted]

12. Stine, Howard A., and Wanlass, Kent: Theoretical and Experimental Investigation of Aerodynamic-Heating and Isothermal Heat-Transfer Parameters on a Hemispherical Nose With Laminar Boundary Layer at Supersonic Mach Numbers. NACA TN 3344, 1954.

13. Markley, J. T., and Stoney, William E., Jr.: Heat-Transfer and Pressure Measurements on a Flat-Face Cylinder at a Mach Number of 2. (Prospective NACA paper.)

14. Maccoll, J. W., and Codd, J.: Theoretical Investigations of the Flow Around Various Bodies in the Sonic Region of Velocities. British Theoretical Res. Rep. No. 17/45, B.A.R.C. 45/19, Ministry of Supply, Armament Res. Dept., 1945.

15. Van Driest, E. R.: The Problem of Aerodynamic Heating. Aero. Eng. Rev., vol. 15, no. 10, Oct. 1956, pp. 26-41.

16. Denison, M. Richard: Turbulent Boundary Layer on Blunt Bodies of Revolution at Hypersonic Speeds. Res. Memo., Lockheed Aircraft Corp., Missiles Systems Div., Apr. 13, 1956.

BLUNT-NOSE FLOW FIELDS

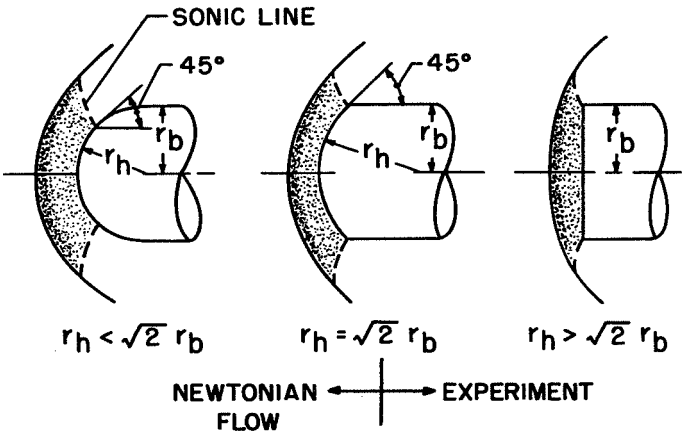


Figure 1

COMPARISON OF MEASURED AND CALCULATED STAGNATION HEAT-TRANSFER RATES

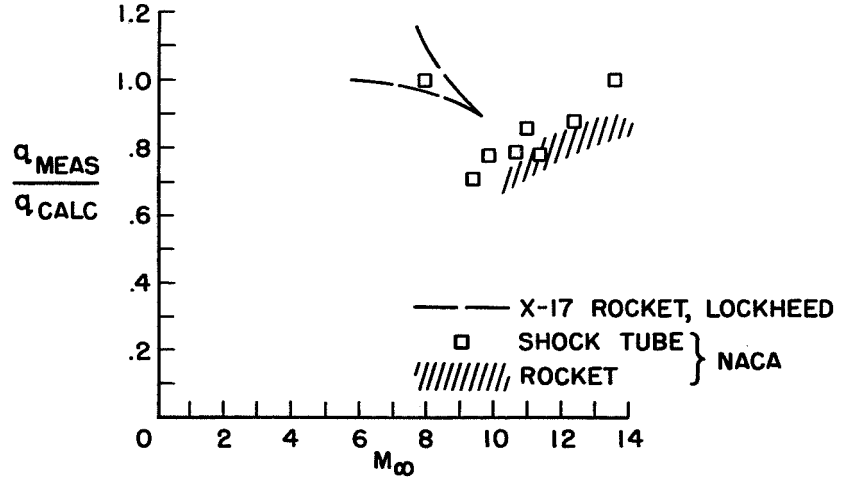


Figure 2

LAMINAR HEATING RATES ON HEMISPHERICAL NOSES

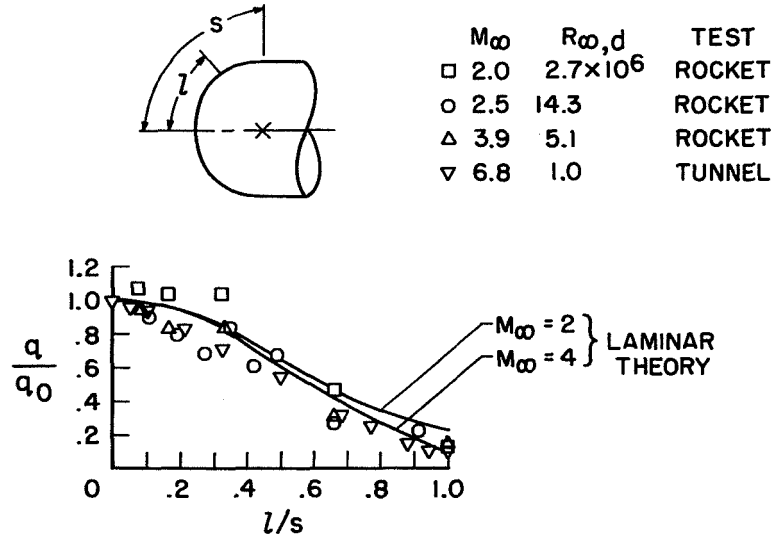


Figure 3

LAMINAR HEATING RATES ON A FLAT-FACE CYLINDER

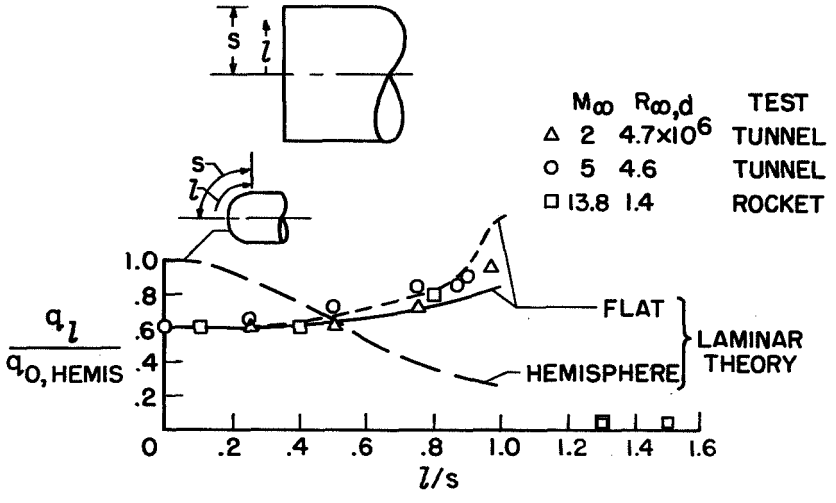


Figure 4

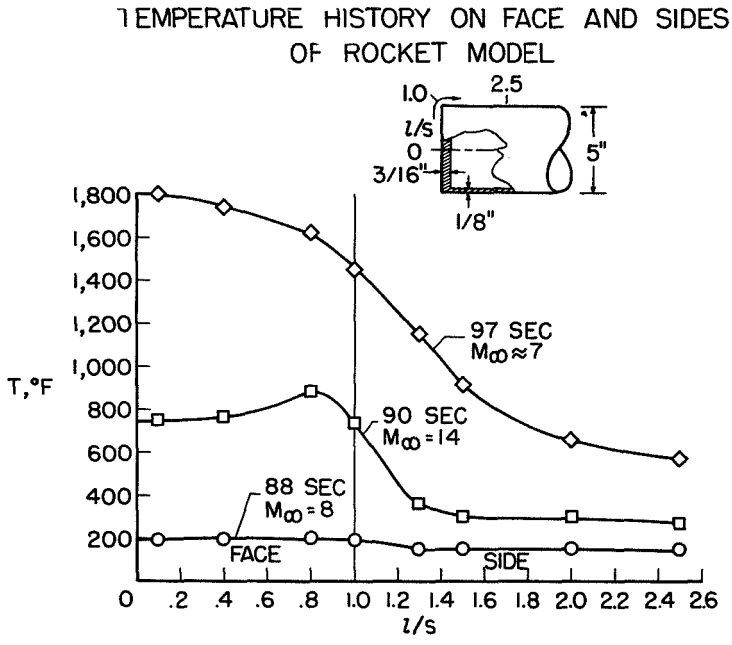


Figure 5

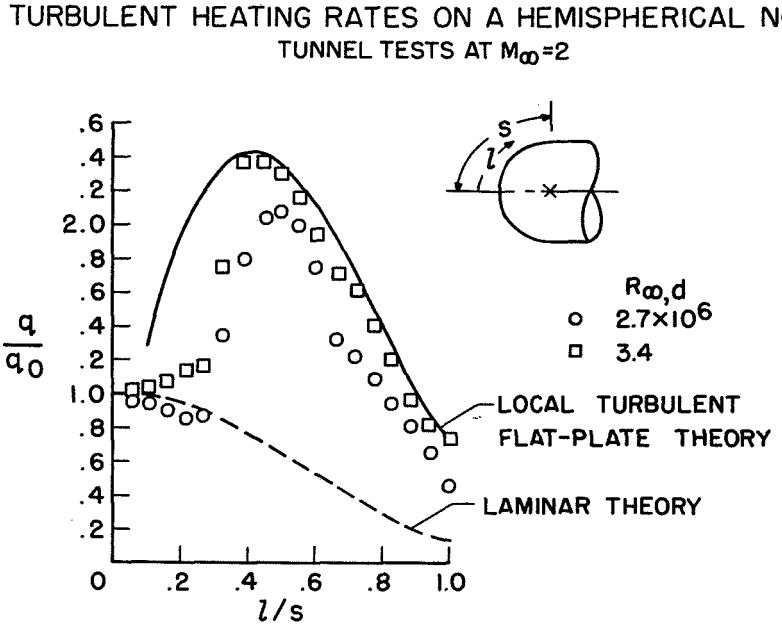


Figure 6

[redacted] N71-75402

HEAT TRANSFER TO BODIES AT ANGLES OF ATTACK

By William V. Feller

Langley Aeronautical Laboratory

SUMMARY

Heat-transfer rates were measured on a modified Karman nose shape at an angle of attack of 0° at Mach numbers of 6.86 and 3.69, and at angles of attack up to 25° at a Mach number of 3.69. Data are presented for a smooth model, which showed natural transition, and for the model with roughness strips, which caused fully turbulent flow.

INTRODUCTION

The heat transfer to bodies of revolution at zero angle of attack with laminar flow has been extensively studied, both theoretically and experimentally, so that in general calculations can be made for a given configuration with confidence. For turbulent boundary layers at zero angle of attack, the solutions for cones and flat plates have been used with the local flow conditions along the body to obtain good approximations. Very little study has been made of the heat transfer to bodies at angles of attack. At very large angles of attack, it might be expected that the results found for swept infinite cylinders would be applicable, but there is a decided lack of information on heat transfer at intermediate angles of attack.

This paper presents some of the results from an experimental study of the heat-transfer rates to a particular body of revolution at angles of attack up to 25°, in order to give some idea of the distribution of heat-transfer rates that can be expected at supersonic speeds on an airplane fuselage.

SYMBOLS

N_{St} Stanton number based on free-stream air properties

R_D Reynolds number based on body maximum diameter and free-stream air properties

[redacted]

X	axial distance measured from nose
D	body maximum diameter
Λ	sweep angle, deg
α	angle of attack, deg
M	Mach number

APPARATUS

The body tested is shown at the top of figure 1. It is a Karman nose shape of fineness ratio 5, modified by the addition of a tangent 10° half-angle cone in front, and a length of cylindrical section behind. Tests were made at zero angle of attack in the Langley 11-inch hypersonic tunnel at a Mach number of 6.86, and at angles of attack from 0° to 25° in the Langley Unitary Plan wind tunnel at a Mach number of 3.69.

RESULTS

In figure 1 are shown the results of the tests at the two Mach numbers at zero angle of attack for laminar flow. The laminar correlating parameter $N_{St}\sqrt{R_D}$ is plotted on a logarithmic scale against the axial station along the model in diameters, X/D. The circles are the data from the tests at $M = 6.86$ and the squares at $M = 3.69$. The dashed curves, calculated by the theory of Stine and Wanlass (ref. 1) for the two Mach numbers, fit the data well over the body, except that, at axial stations behind $X/D = 4.2$ at $M = 3.69$, the rise in the data indicates transition to turbulent flow. Also shown in figure 1 are curves calculated for $M = 6.86$, by the flat-plate theory of Van Driest (ref. 2) for the cone and flat plate. The calculated curves for the cone and flat plate agree fairly well with the experimental data on the parts of the body that are nearly conical and cylindrical, respectively.

In figure 2 are shown data for the same model at $M = 3.69$ and zero angle of attack but with turbulent flow tripped by roughness applied in a ring near the nose as indicated in the sketch at the top of the figure. The same parameter $N_{St}\sqrt{R_D}$ is presented in order to facilitate comparison with the laminar values in figure 1. The data near the nose are not quite up to the values calculated in turbulent cone theory (ref. 3) but show the same trend along the length as did the laminar data, and agree well with the turbulent flat-plate theory (ref. 4) toward the rear of the body.

 [redacted]

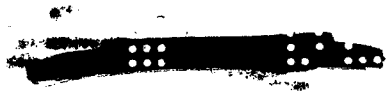


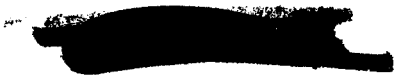
Figure 3 shows the variation of the Stanton number based on the free-stream conditions along the lower or windward meridian line of the body at several angles of attack. On the left are shown the data for the smooth model. The curve at zero angle of attack is the same as was shown in figure 1, with transition starting at X/D = 4.2. As the angle of attack increases, the heat-transfer rates increase, as would be expected, and the point of transition moves forward, up to 14° angle of attack. The curves at angles of attack of 21° and 25° show a somewhat different trend.

In order to obtain turbulent heat-transfer data, a strip of roughness was applied in a band along the lower meridian line as well as in a ring near the nose. The results are shown on the right in figure 3. As in the case of laminar flow, the Stanton numbers increase with angle of attack from 0° to 14°. The curve for $\alpha = 21°$ does not follow the trend with angle of attack, and is in fact lower than that for $\alpha = 14°$. The curve for $\alpha = 25°$ is very irregular and will be discussed later. The behavior of the Stanton number distribution curves suggests that the flow around the body changes to a mainly crosswise flow at some angle between 14° and 21°.

In figure 4 the distribution of Stanton number along three meridian lines is shown for two angles of attack, 7° on the left, and 25° on the right. Again, roughness was applied to produce turbulant flow. At an angle of attack of 7° the Stanton number drops from its value at the windward meridian to about half at 90°, and about 1/3 on the leeward side (180°). On the leeward side, behind X/D = 3, the Stanton number is independent of X/D, so that separated flow is indicated.

At an angle of attack of 25°, the values on the windward meridian are very erratic, ranging from values near those found for laminar flow up to values in good agreement with the turbulent swept-cylinder theory. This behavior is due to the fact that the local Reynolds numbers over the roughness strip are very low, so that transition is not fully completed at all stations. The range of values of the data represents various stages in the transition to fully turbulent flows. The curves at meridian stations 90° and 180° are smooth. Values of Stanton number at the 90° station for $\alpha = 25°$ are not very different from those found for $\alpha = 7°$, but at the 180° station are somewhat lower than at $\alpha = 7°$.

Figure 5 shows a polar plot of Stanton number around the circumference of the body at X/D = 5.12, where the body is cylindrical, for several angles of attack. On the right side are the distributions for fully turbulent flows, produced by a roughness strip along the windward meridian. On the left side of this figure are values obtained on the smooth model. As the angle of attack increases, the fully turbulent Stanton numbers increase on the windward side and decrease on the leeward side up to 14°. The curve for $\alpha = 21°$ nearly coincides with that





for $\alpha = 14^\circ$, and the curve for $\alpha = 25^\circ$ shows a further increase. The long-short-dash curve for $\alpha = 25^\circ$ is calculated by a semiempirical method developed for swept cylinders. The basis of the calculation is the theory for the average heat-transfer coefficients over the front half of swept circular cylinders with fully turbulent boundary layers presented by Beckwith and Gallagher in reference 5. This theory was combined with an unpublished experimentally measured distribution of local heat-transfer coefficients around a swept cylinder obtained at the Langley Laboratory by Beckwith and Gallagher, on the assumption that the distribution curve is independent of sweep angle and Mach number (as has been shown for laminar flow). The agreement with experiment is very good.

On the left side of the figure are shown the distributions of Stanton number obtained on the smooth model at $\alpha = 0^\circ$, 7°, and 25°. The values at $\alpha = 0^\circ$, with natural transition, are in fair agreement with the artificial transition values on the right. At an angle of attack of 7°, the boundary layer is laminar near the windward meridian and low heat-transfer values are obtained. Transition starts at a meridian angle about 45°. At $\alpha = 25^\circ$, transition starts earlier, about 20° from the lower meridian line, after which the Stanton numbers increase and fair into this curve for fully turbulent flow at $\alpha = 25^\circ$ which was transposed from the data on the right.

In figure 5 the data at $\alpha = 25^\circ$ agree well with crossflow theory. The behavior of the curves at $\alpha = 14^\circ$ and 21° indicates that the type of flow may be changing in the interval between. To show the trend more clearly, the Stanton numbers on the windward meridian are plotted in figure 6 against angle of attack for two stations on the model; $X/D = 2.8$ and 5.1. The curve labeled "longitudinal-flow theory" was calculated by flat-plate theory, by use of the local flow conditions outside the boundary layer for the equivalent free stream. The curve labeled "crossflow theory" was calculated by use of the semiempirical method described earlier for swept cylinders, the body being considered to be made up of a series of cylinders of varying diameter and sweep angle. The experimental values increase uniformly from $\alpha = 0^\circ$ to 14° but the trend does not agree with that predicted by the modified flat-plate (longitudinal-flow) theory. At $\alpha = 21^\circ$ and 25°, the data agree well with the crossflow theory curve.

CONCLUDING REMARKS

The experimental results presented in this paper have shown that at zero angle of attack, the available theoretical methods give a good estimate of the heat-transfer coefficients on a body of revolution. At large angles of attack, the methods based on the cross flow over swept



cylinders are applicable. For intermediate angles of attack, however, there is as yet no theoretical approach, and reliance will have to be placed on extrapolation from experimental studies. It is believed that the results presented in this paper can be considered typical of simple fuselages of moderate fineness ratio at supersonic Mach numbers for which the air may still be considered an ideal gas.

REFERENCES

1. Stine, Howard A., and Wanlass, Kent.: Theoretical and Experimental Investigation of Aerodynamic-Heating and Isothermal Heat-Transfer Parameters on a Hemispherical Nose With Laminar Boundary Layer at Supersonic Mach Numbers. NACA TN 3344, 1954.

2. Van Driest, E. R.: The Laminar Boundary Layer With Variable Fluid Properties. Rep. No. AL-1866, North American Avaiation, Inc., Jan. 19, 1954.

3. Van Driest, E. R.: Turbulent Boundary Layer on a Cone in a Supersonic Flow at Zero Angle of Attack. Jour. Aero. Sci., vol. 19, no. 1, Jan. 1952, pp. 55-57, 72.

4. Van Driest, E. R.: Turbulent Boundary Layer in Compressible Fluids. Jour. Aero. Sci., vol. 18, no. 3, Mar. 1951, pp. 145-160, 216.

5. Beckwith, Ivan E., and Gallagher, James J.: Experimental Investigation of the Effect of Boundary-Layer Transition on the Average Heat Transfer to a Yawed Cylinder in Supersonic Flow. NACA RM L56E09, 1956.



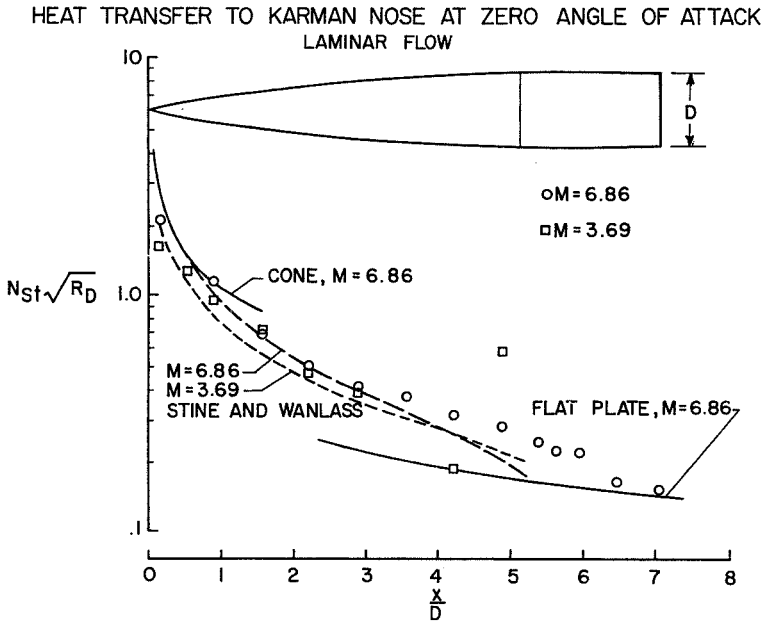


Figure 1

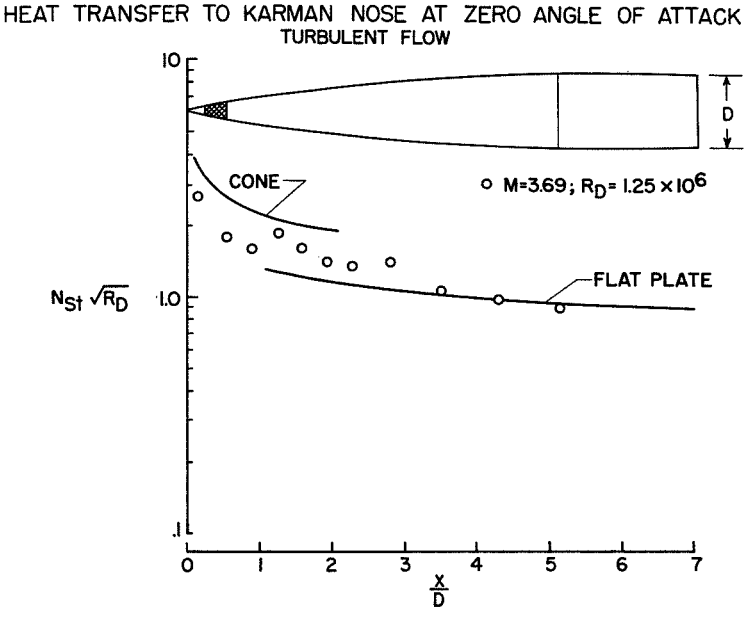
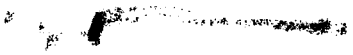
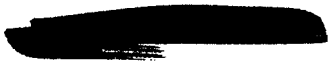


Figure 2





HEAT TRANSFER TO LOWER MERIDIAN

KARMAN NOSE ; M = 3.69 ; $R_D = 1.2 \times 10^6$

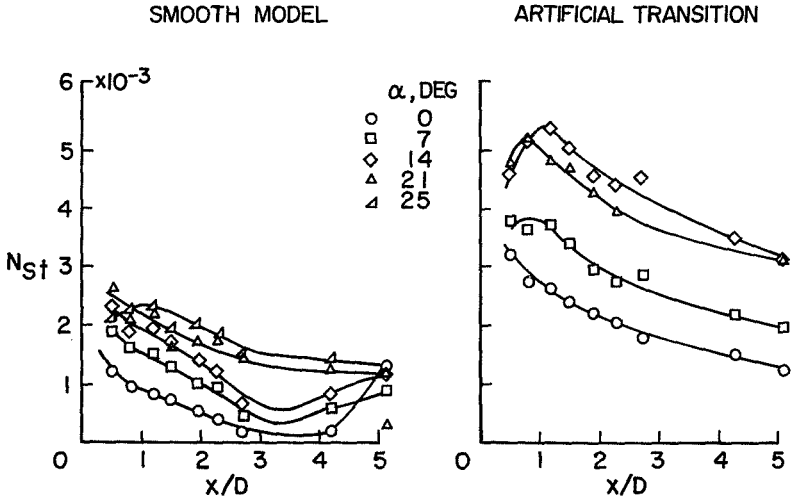


Figure 3

HEAT TRANSFER TO KARMAN NOSE

M = 3.69 ; $R_D = 1.2 \times 10^6$; ARTIFICIAL TRANSITION

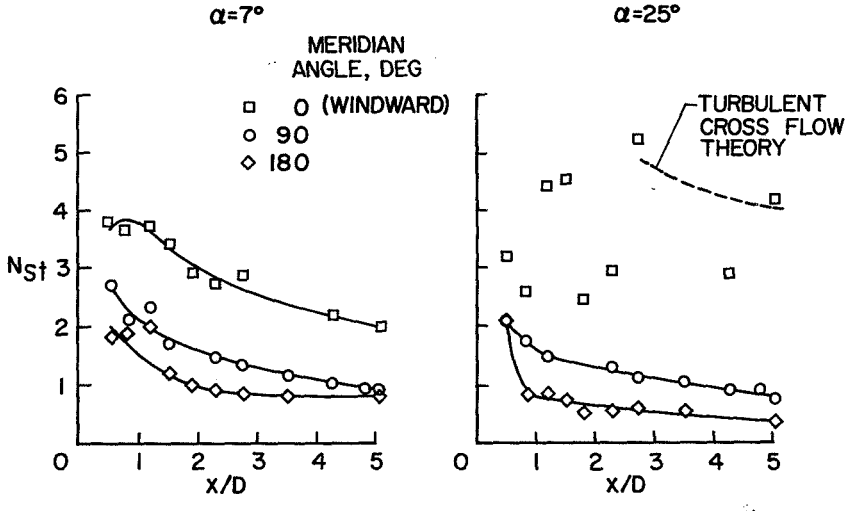


Figure 4

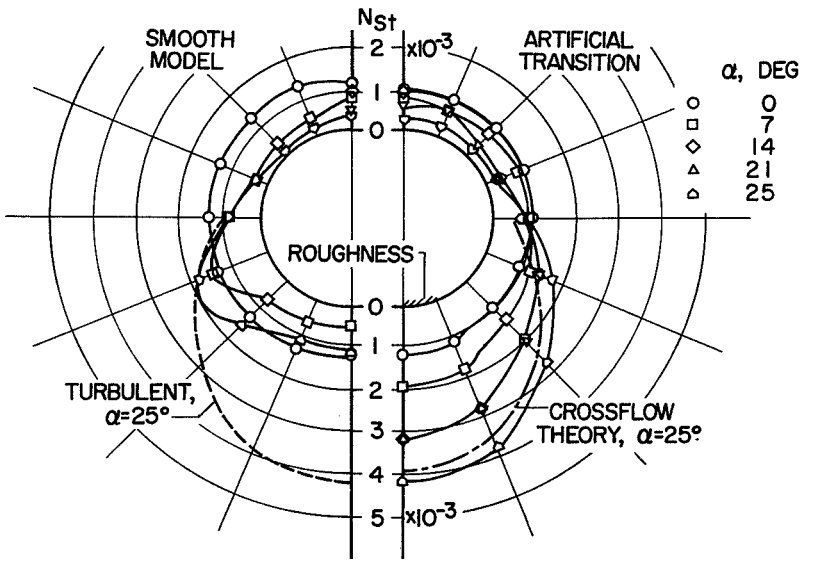


Figure 5

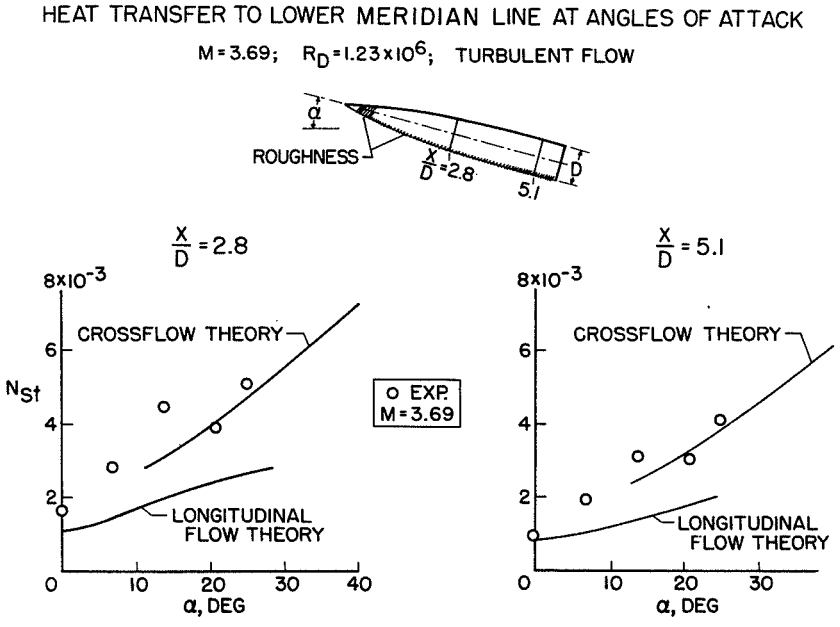


Figure 6

313

CRAWFORD & RUMSEY

N71-75403

HEAT TRANSFER IN REGIONS OF SEPARATED AND REATTACHED FLOWS

By Davis H. Crawford and Charles B. Rumsey

Langley Aeronautical Laboratory

SUMMARY

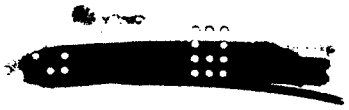
Past experimental work has indicated that separated flow can greatly increase the heat transfer to a surface; whereas, some theoretical studies have indicated a possible decrease. Recent investigations have helped to clarify the effects of separation on heat transfer and have indicated a method of reducing separation. This paper considers the results of some of these investigations and shows the heat transfer in regions of separation and reattachment for a few specific shapes. These results have shown that the heat transfer in a separated region is strongly affected by the extent of separation, the location of the reattachment point, and the location of transition along the separated boundary.

INTRODUCTION

Recent experimental and theoretical investigations have shown that the separation of the boundary layer from a surface can have a great effect on the heat flow to the surface. At high altitudes and high Mach numbers, the presence of separation is more likely, and the regions of separation are more extensive because of the thicker boundary layers characteristic of this type of flight. Past experimental work has indicated that separated flow can greatly increase the heat transfer to a surface (ref. 1), whereas some theoretical studies have indicated a possible decrease (ref. 2). Recent investigations have helped to clarify the effects of separation on heat transfer and have indicated a method of reducing separation. This paper considers the results of some of these investigations and shows the heat transfer in regions of separation and reattachment for a few specific shapes. For one of these shapes, boundary-layer bleed was used to delay separation and to alter the heat transfer in the region of possible separation.

SYMBOLS

b distance along surface from zero station to sphere-cylinder juncture



C_D	drag coefficient
d	diameter of vehicle at characteristic station, as indicated in figures
l	length
M	Mach number
N_{St}	Stanton number
q	heat transfer per unit area per unit time
$q_{0,ns}$	heat transfer per unit area per unit time at zero station with no spike
R	Reynolds number based on characteristic length along surface
R_d	Reynolds number based on d
s	distance along surface from zero station
x	distance along axis of test vehicle, as indicated in figures

DISCUSSION

Flare Skirt

One interesting case of separation is the flow about an ogive-cylinder body with a 30° tail flare (ref. 3). The tail flare is a possible stabilizing device as well as a drag brake for many missile shapes. The lower curve of figure 1 shows the position of the start of separation as a function of Reynolds number. Figure 2 shows the approximate shape of the flow pattern for three Reynolds numbers. At low Reynolds numbers the start of separation moves forward slightly with increasing Reynolds number as is expected from laminar theory (ref. 4). The shape of the flow pattern when the separation is a maximum is shown in the top diagram of figure 2. As the Reynolds number increases, the boundary layer near the start of separation tends to become transitional which delays the separation. Then the position of the start of separation moves back along the model until at a Reynolds number of 0.5×10^6 the flow pattern appears as is shown in the center diagram of figure 2. At high Reynolds numbers, the boundary layer is fully turbulent ahead of the separation, as is shown in the lower diagram of figure 2, and this causes the flow to



EFFECT OF WING ON TAIL LOADS
M=2.46; β=0°; α=20°

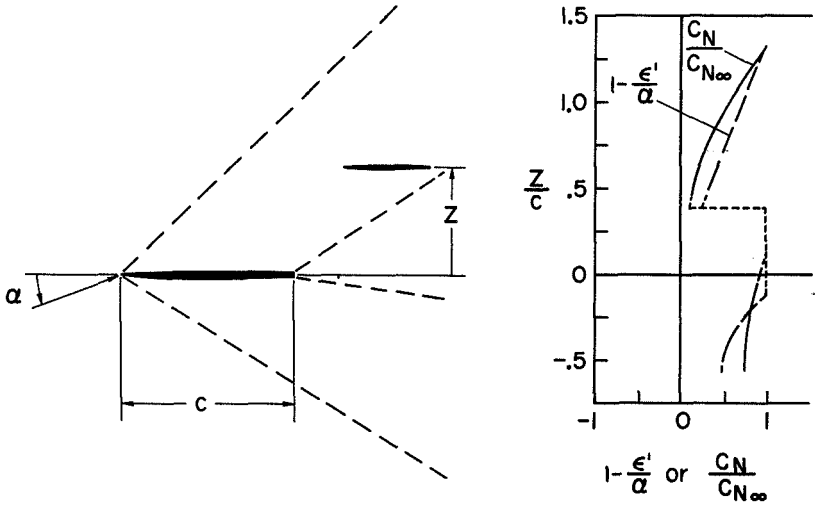


Figure 19

EFFECT OF TAIL ROLL CONTROL
ON VERTICAL-TAIL LOAD

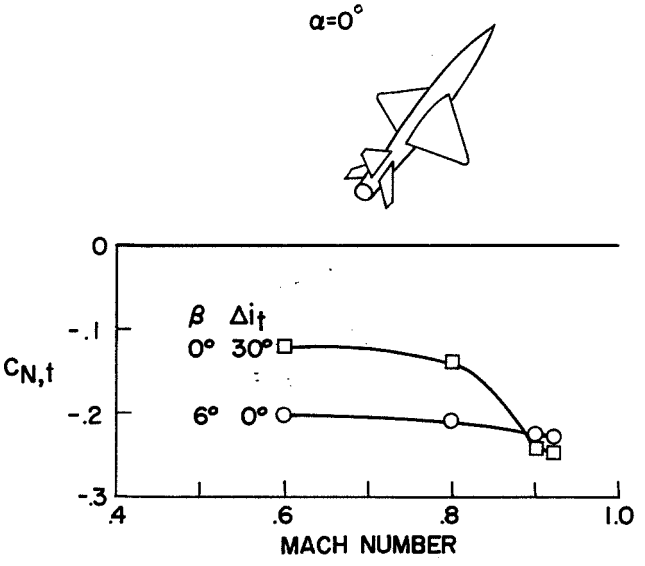
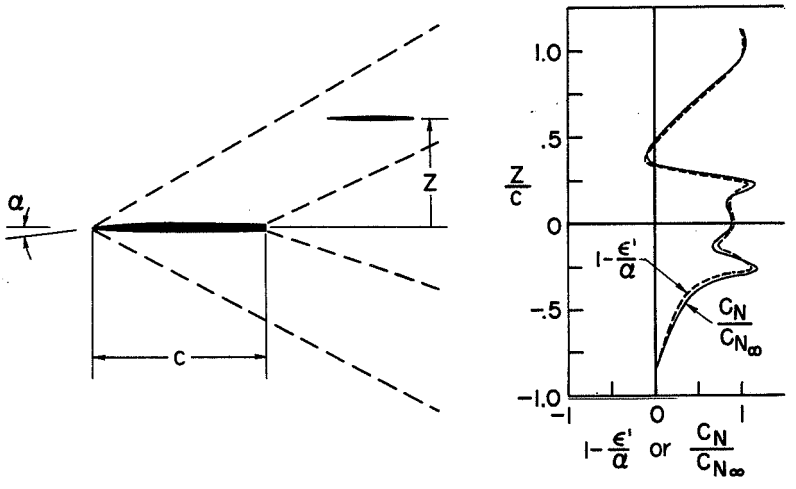


Figure 17

EFFECT OF WING ON TAIL LOADS
M=2.46; β=0°; α=6°



317

Figure 18

N71-75404

FLIGHT MEASUREMENTS OF AIRPLANE STRUCTURAL TEMPERATURES AT SUPERSONIC SPEEDS

By Richard D. Banner

NACA High-Speed Flight Station

SUMMARY

Skin and structural temperatures have been obtained on the X-1B and X-1E research airplanes under transient aerodynamic heating conditions at speeds up to Mach numbers near 2.0. Extensive temperature measurements were obtained throughout the X-1B airplane, and temperature distributions are shown on the nose cone, the wing, and the vertical tail. Temperatures for the X-1E wing leading edge and internal wing structure were compared with similar data for the X-1B.

No critical skin and structural temperatures were obtained on the two airplanes over the range of these tests.

Simplified calculations of the skin temperatures in the laminar-flow regions of the nose cone and the leading edges agreed favorably with the general trends in the measured data. The flat-plate skin-temperature calculations in the turbulent-flow regions agreed favorably with the measured data on the nose cone and at the midsemispan station of the wing but overestimated the vertical-tail skin temperatures and also the upper wing skin temperature near the wing tip. The relatively low values of the upper skin temperatures that were measured at the wing tip were believed to be caused by separated-flow effects in this region.

INTRODUCTION

In the design of supersonic aircraft, aerodynamic heating is becoming increasingly important. Analytical studies and controlled testing represent the basic methods utilized in the design of complex structures to withstand the effects of aerodynamic heating.

Concurrent with the basic research studies, the National Advisory Committee for Aeronautics is conducting a program at the NACA High-Speed Flight Station at Edwards, Calif., to investigate the skin and structural temperatures actually experienced by airplanes during flight at supersonic speeds. The purpose of this paper is to summarize the results of

this program to the present time. The results of simplified calculations of the skin temperatures are compared with the measured data in the regions of the fuselage nose cone and the wing and vertical-tail skins and leading edges.

SYMBOLS

$b/2$	wing semispan
c	chord length
h_{av}	average heat-transfer coefficient, Btu/sq ft-hr-^{o}F
h_p	pressure altitude, ft
M	Mach number
P	local surface pressure, lb/sq ft
P_∞	free-stream static pressure, lb/sq ft
q_∞	free-stream dynamic pressure, lb/sq ft
r	recovery factor
T	skin temperature, ^{o}F
T_{aw}	adiabatic wall temperature, ^{o}F
T_T	free-stream stagnation temperature, $T_\infty(1 + 0.2M^2)$, ^{o}F
T_∞	free-stream ambient air temperature, ^{o}F
t	time, sec
α	angle of attack, deg
τ	thickness, in.

TESTS

Data have recently been obtained on the X-1E airplane at Mach numbers up to 2.10 and on the X-1B at Mach numbers up to 1.94. (See fig. 1.)

These speeds do not necessarily represent the maximum speed capabilities of the airplanes. Both airplanes are constructed primarily of aluminum. Temperature measurements were made at approximately 60 locations on the X-1E, and approximately 300 temperatures were measured on the X-1B.

Figure 2 shows the flight conditions for both airplanes under which the temperatures were obtained. The Mach number, pressure altitude, ambient air temperature, and angle of attack are shown as time histories. As can be seen, the two flights are generally similar.

Transient heating conditions were experienced by both airplanes during the flights. The maximum heating rate was experienced on the thinner skinned X-1B and was on the order of 3° per second. This heating rate is relatively low in comparison with the rates being obtained on missiles and rocket models and in controlled wind-tunnel tests; however, it is believed to be representative of the heating rates which are being experienced or which will be experienced in the near future by fighter and interceptor aircraft.

CALCULATIONS

For laminar flow in the stagnation regions, approximate heat-transfer coefficients were calculated from expressions relating the Nusselt number and the Reynolds number given by Stine and Wanlass. (See ref. 1.) In the regions of flat-plate turbulent flow, approximate heat-transfer coefficients were calculated by using Colburn's expression. These calculations were greatly simplified by the use of free-stream conditions. This procedure was considered justified in that only the overall effects were desired. A detailed theoretical analysis is not considered to be within the scope of this report.

The results of the calculations just described indicated relatively small variations in the heat-transfer coefficients with time; therefore, average values were determined and used in calculating the skin temperatures.

Newton's law of heat flow to the skin, which considers the heat capacity of the material and neglects the effects of conduction, was assumed.

RESULTS AND DISCUSSION

The X-1B installation provides a rather detailed case history of the temperatures that exist throughout an actual airplane; and, in view of this fact, more attention is given to the X-1B data in the present paper.

[redacted]

The X-1E data are used to point out any differences that exist in the measured temperatures due to either the configuration or the construction or both.

Some of the maximum temperatures that were measured on the X-1B and an indication of the higher temperature areas on the airplane are shown in figure 3. The nose of the airplane and the leading edges of the wing and tail surfaces are shaded in figure 3 to indicate the higher temperature areas. The approximate thermocouple locations are indicated by the dark points. The maximum stagnation temperature for the flight was 220° F.

A maximum skin temperature of 185° F was measured at the forward point of the nose cone. On the wing leading edge the maximum temperature was 168° F. A maximum temperature on this order was also measured on the leading edge of the vertical tail. The maximum temperatures in other general areas are also shown. Some of the temperatures shown at these locations are appreciably affected by internal heat sources and heat sinks; for instance, the fuselage skin temperatures adjacent to the liquid oxygen tank are relatively low (13° F); whereas, just ahead of that area on the fuselage skin a maximum of 122° F was measured. Other areas of interest are the windshield and canopy and the rearward part of the fuselage in the region of the rocket engine.

It should be pointed out that the maximum temperatures shown in figure 3 did not all occur at the same time. In areas where internal conduction is negligible, skin thickness, boundary-layer temperature, and the heat-transfer coefficient are the primary factors affecting the skin temperature rise.

Figure 3 gives an overall picture of the measured temperatures. In subsequent figures, the temperature distributions in the areas of the nose cone, the wing skins, the leading edges and the vertical tail are considered in greater detail; and comparisons are made with calculated results. Attention is given only to the supersonic portion of the flights, since at the subsonic speeds the combined effects of increasing Mach number and decreasing ambient air temperature produced only small changes in the skin temperatures.

Figure 4 shows the nose of the X-1B, where both skin-temperature and pressure measurements were made at intervals along the nose between station 0 and station 55.0. The pressure data are plotted as pressure coefficients at the bottom of the figure. The measured skin temperatures are shown in the upper part of the figure as the open symbols. The skin temperature decreases over the forward part of the nose cone, the laminar flow calculations showing fairly good agreement. This variation is followed by a region of no change in the skin temperature and then an increase toward the rear of the nose cone where the calculated turbulent flat-plate and cone temperatures are approached. It is about here that the nose-cone

[redacted]

shape asymptotically approaches the cylindrical shape of the fuselage, and the pressure drops to near the free-stream value. The overall temperature variations that are shown suggest that transition from laminar to turbulent flow takes place along the nose at about 25 to 30 percent of the nose-cone length, fully turbulent flow developing at the rear of the nose cone. A summary of various wind-tunnel data on cones and bodies of revolution indicated this general transitional area.

The skin here on the nose cone was relatively thin in comparison with that on other areas on the airplane. The effects of varying skin thickness on the skin temperatures can be seen in figure 5. Figure 5 shows the spanwise distributions of maximum temperatures on the upper wing skin at the 66-percent-chord line and at the leading edge. The spanwise variation in the skin thickness is shown below. The temperature variations indicate an inverse relationship between the skin temperature and the skin thickness at both chordwise positions. The trend which would give rise to thermoelastic considerations at higher temperature levels is clearly seen in the data here.

The calculated temperatures, shown by the dashed lines in figure 5, were based on a constant spanwise heating input, laminar for the leading edge and turbulent for the 66-percent-chord line; and the same variations due to thickness are seen in the calculated temperatures.

The data in figure 5 also illustrate the differences in the skin temperature with chordwise position. Both top and bottom skin temperatures were measured at several chordwise positions at about midsemispan and near the tip of the wing. These data are presented in figure 6. In this figure the calculated temperatures were estimated on the basis of zero angle of attack. No detailed consideration is given to the effects of angle of attack on the measured temperatures; however, from an overall standpoint it should be recalled from figure 2 that the angles of attack were positive during the flight and were on the order of 2° to 10°.

The data of figure 6 illustrate several interesting trends. First, notice the chordwise temperature gradients that are shown at the midsemispan station. The higher temperatures are experienced at the leading edge and the trailing edge (which at this location is the outboard tip of the flap), and the lower temperatures are experienced on the thicker skinned wing box section.

Secondly, note the differences in temperature between the top and bottom skins at the two span stations, the bottom skin temperature being higher in both cases. At the tip station, the fairly large differences seen between the top and bottom skin suggest that the flow might be partly separated in this area.



The approximate calculations, which were based on the assumption of laminar flow over the leading-edge section and turbulent flow over the remainder of the chord, give a fairly good overall estimate of the skin temperatures at the midsemispan stations. At the tip station the calculations agree fairly well with the bottom skin temperature; however, they indicate an overestimate of the top skin temperature, probably because of the flow effects previously mentioned.

An example of the internal temperatures that were measured through the wing is seen in figure 7. Shown in the figure are the front wing spars at about midsemispan on the X-1B and the X-1E. The temperatures were measured at the locations shown by the black dots on the structures, and the values are given on the right-hand side of the figure. The higher temperatures shown for the X-1B were measured on the skin a slight distance from the spar.

In order to give an indication of the temperature rise that has taken place in the internal structure, it is worthwhile to mention that the ambient air temperatures were between -70° F and -90° F and that the assumed turbulent adiabatic wall temperatures were on the order of 200° F for the highest Mach numbers shown here. The measured internal temperatures are relatively low and show only slight temperature gradients across the thickness of the X-1B wing, the lower temperature being obtained on the spar center line. Essentially no differences are seen on the thick spar construction of the X-1E wing, the heavier type of construction of the X-1E having a temperature-neutralizing tendency due to the higher heat capacity. The thermal lag effect is also seen in figure 6 by the increase in the measured temperatures as the Mach number decreases in the later portions of the flights.

Effects of material thickness differences are also seen in the measured leading-edge temperatures. These data are shown in figure 8 in time-history form together with time histories of the assumed laminar adiabatic wall temperatures. The locations at which the temperatures were measured are shown by the dark points on the leading-edge sketches, and the material thicknesses are given at these locations. Values of the average heat-transfer coefficients utilized for the calculated temperatures are shown below the sketches. The calculated temperatures are seen to agree very well with the measured data.

Maximum temperatures on the same order of magnitude were measured on the wing and vertical-tail leading edges of the X-1B. For comparison, the temperatures that were measured at the rear of the solid leading edge of the X-1E are seen in the middle of the figure. It will be noticed here that the maximum measured temperature was on the order of 20° F. The high heat capacity of the solid leading edge is the contributing factor to the small rise in the temperature measured at this location. The calculated skin temperature is shown to agree very well with the



measured data; however, this result is not considered significant because the measured temperatures are relatively low. (For example, a 50-percent reduction in the assumed heat-transfer coefficient at this point would produce a decrease in the calculated maximum temperature of 7° F.)

The chordwise variation in the vertical-tail temperatures is shown in figure 9 for a time near maximum Mach number at near midspan. The temperatures were measured on the skin and spar center lines at the locations shown by the black dots on the sketch. No appreciable gradients are seen in the chordwise variation of the measured skin temperature.

Transition from laminar to turbulent flow was assumed to take place at the point where the leading-edge section attaches to the front spar because inspection revealed a relatively large discontinuity in the skin at this point. Skin temperatures calculated from the average heat-transfer coefficients shown and based on these assumptions agree fairly well with the measured trends in the leading-edge region but deviate somewhat over the remainder of the chord and give a conservative overall estimate in this region.

CONCLUDING REMARKS

Skin and structural temperatures have been obtained on the X-1B and X-1E research airplanes under transient aerodynamic heating conditions at speeds up to Mach numbers near 2.0. Extensive temperature measurements were obtained throughout the X-1B airplane, and temperature distributions are shown on the nose cone, the wing, and the vertical tail. Temperatures for the X-1E wing leading edge and internal wing structure were compared with similar data for the X-1B.

No critical skin and structural temperatures were obtained on the two airplanes over the range of these tests.

Simplified calculations of the skin temperatures in the laminar-flow regions of the nose cone and the leading edges agreed favorably with the general trends in the measured data. The flat-plate skin-temperature calculations in the turbulent-flow regions agreed favorably with the measured data on the nose cone and at the midsemispan station of the wing but overestimated the vertical-tail skin temperatures and also the upper wing skin temperature near the wing tip. The relatively low values of the upper skin temperatures that were measured at the wing tip were believed to be caused by separated-flow effects in this region.

[redacted]

REFERENCE

1. Stine, Howard A., and Wanlass, Kent: Theoretical and Experimental Investigation of Aerodynamic-Heating and Isothermal Heat-Transfer Parameters on a Hemispherical Nose With Laminar Boundary Layer at Supersonic Mach Numbers. NACA TN 3344, 1954.

[redacted]

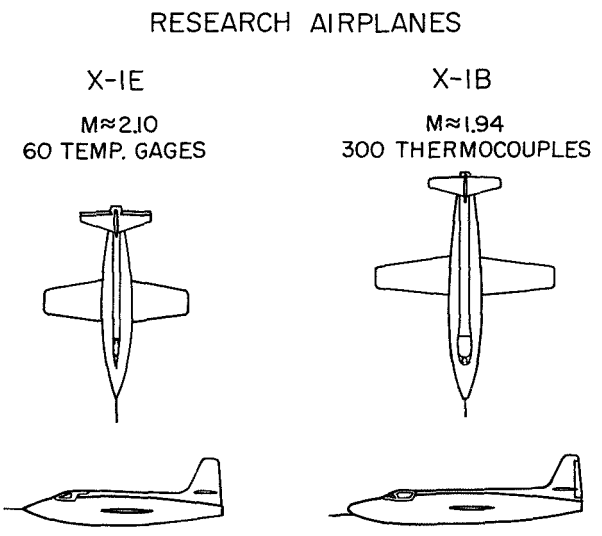


Figure 1

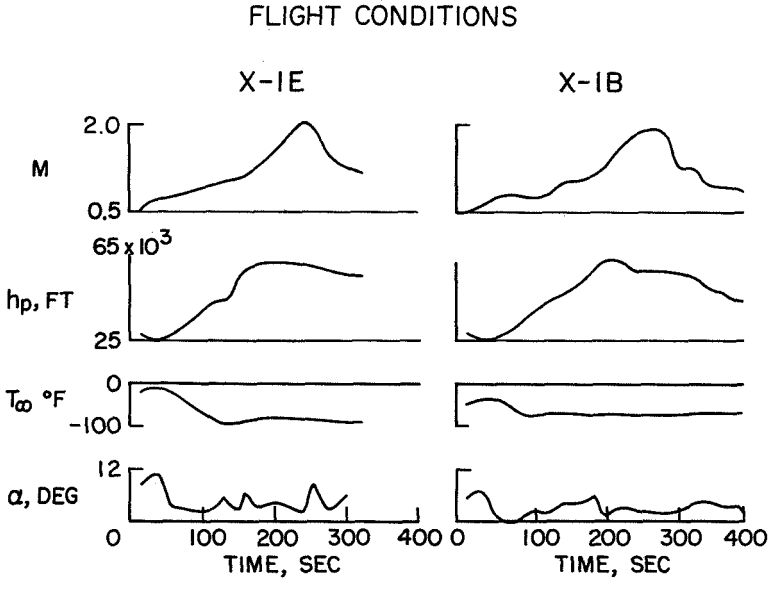


Figure 2

326

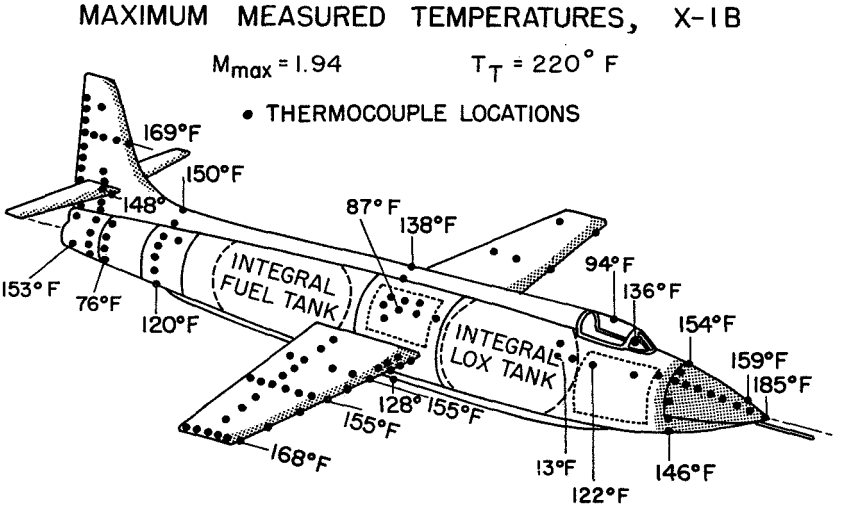


Figure 3

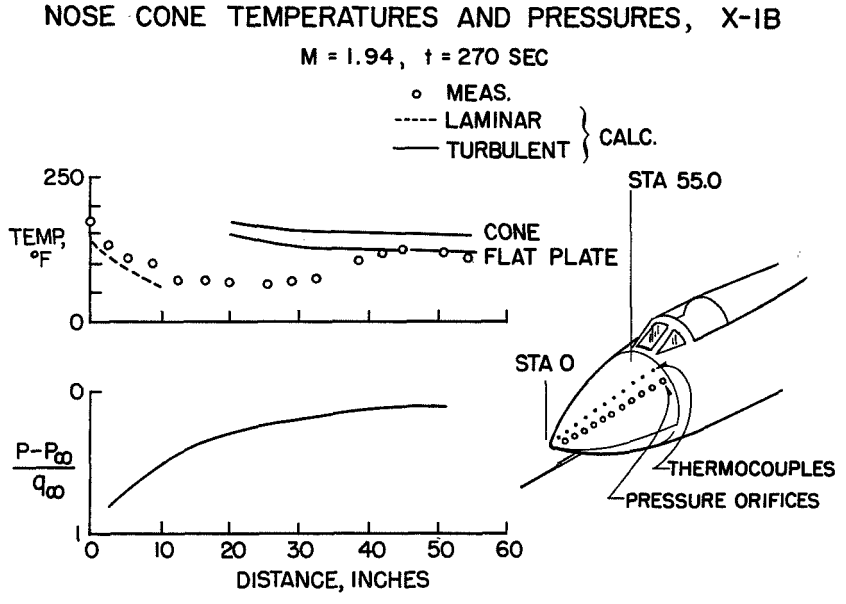


Figure 4

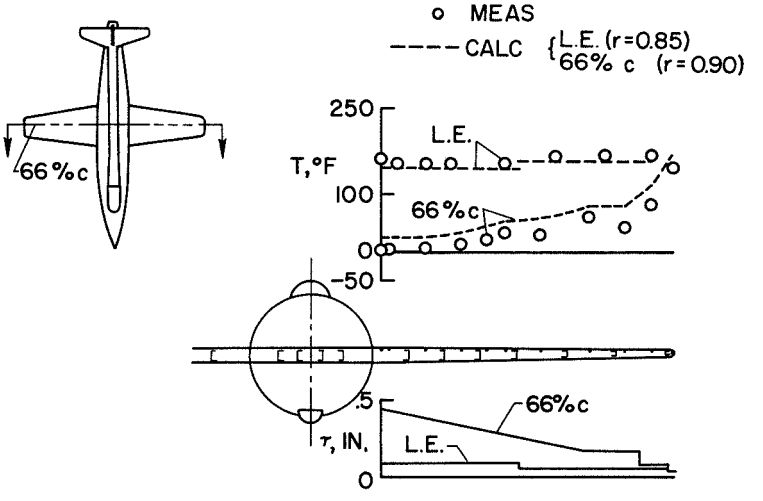


Figure 5

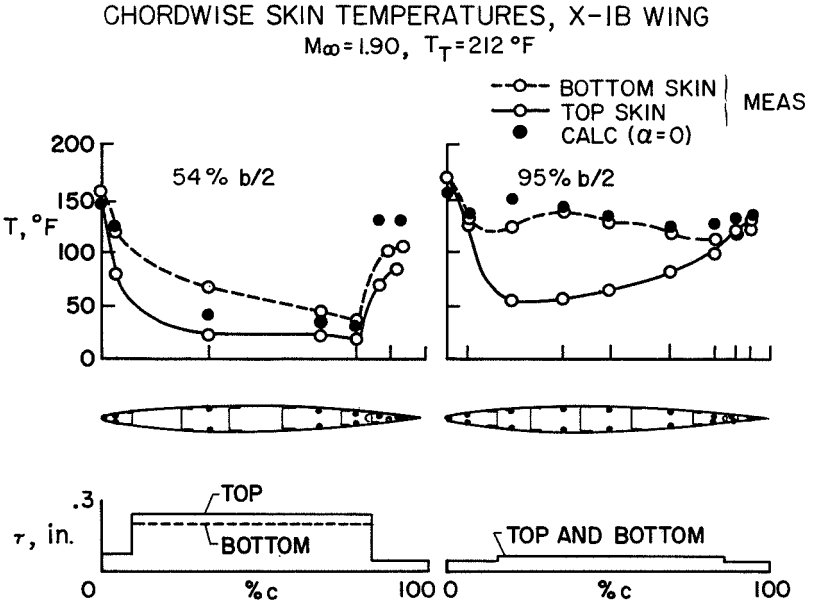


Figure 6

328



MEASURED INTERNAL WING TEMPERATURES

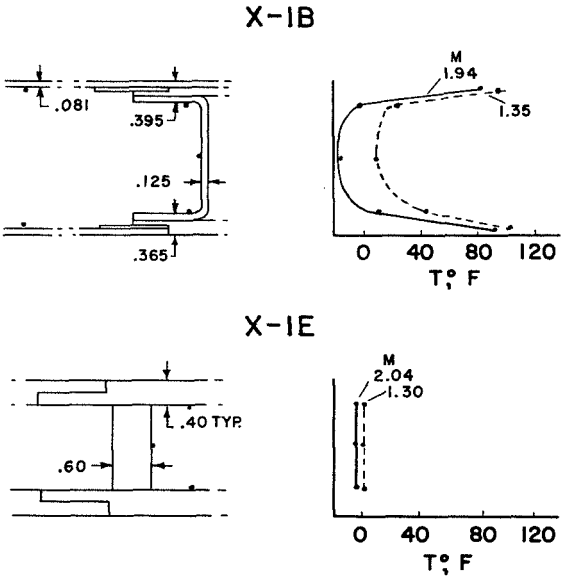


Figure 7

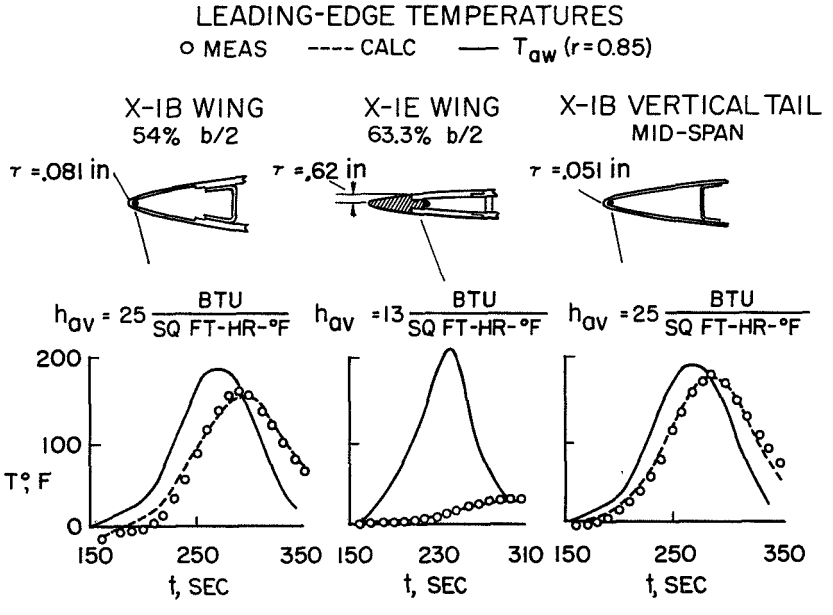


Figure 8



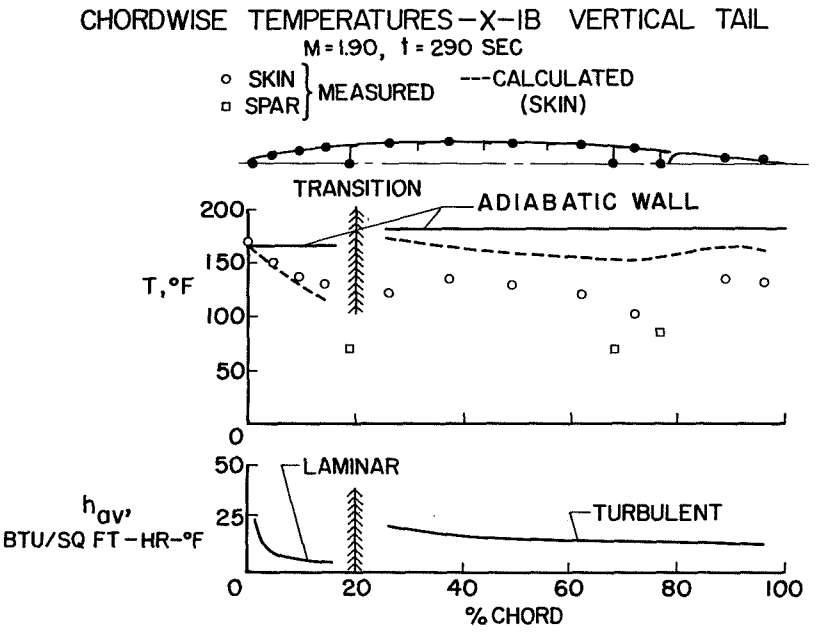

CHORDWISE TEMPERATURES – X-IB VERTICAL TAIL
M = 1.90, t = 290 SEC
SKIN
SPAR
MEASURED
---CALCULATED (SKIN)
TRANSITION
ADIABATIC WALL
T, °F
200
150
100
50
0
LAMINAR
TURBULENT
h_{av}, BTU/SQ FT – HR – °F
50
25
0
20
40
60
80
100
% CHORD

Figure 9

TWO FACTORS INFLUENCING TEMPERATURE DISTRIBUTIONS AND THERMAL STRESSES IN STRUCTURES

N71-75405

By William A. Brooks, Jr., George E. Griffith, and H. Kurt Strass

Langley Aeronautical Laboratory

SUMMARY

The influence of joint conductivity and internal radiation on temperature distribution and thermal stresses has been discussed. Joints of poor conductivity can occur in normal fabrication procedure and greatly alter temperature distributions and increase thermal stresses. On the other hand, internal radiation tends to make the temperature distributions more uniform and thereby relieves thermal stress.

INTRODUCTION

Thermal stresses are unquestionably an important consideration in the design of supersonic aircraft. Such stresses are usually produced by nonuniform temperature distributions - the greater the temperature variation within the structure, the larger the thermal stresses. The present paper deals briefly with two factors which may affect the temperature distribution, and thus the thermal stresses, within a structure; these two factors are joint conductivity and internal radiation. In order to indicate some of the effects of these two factors without unnecessary structural complications, the basic structure considered consists of a length of skin with an integral or an attached web. In addition to theoretical results, experimental data were obtained by heating the structure either aerodynamically or by laboratory radiant-heat sources.

SYMBOLS

α coefficient of thermal expansion

c specific heat

E modulus of elasticity

[redacted]

ϵ	emissivity
h	heat-transfer coefficient
h_j	joint conductivity coefficient
k	thermal conductivity
M	Mach number
q	heating rate
t	skin thickness
T	temperature
T_0	initial temperature
T_1	maximum skin temperature
T_2	minimum web temperature
T_{aw}	equilibrium temperature
τ	time
w	specific weight
σ	thermal stress

Subscripts:

RC	radiation and conduction
C	conduction
MAX	maximum

DISCUSSION

Simple Integral Structure

Consider first the simplest possible type of skin-web combination, one without joints and without internal radiation effects. Figure 1 shows such a structure, a symmetrical integral H-section with a flange (or skin) of thickness t symmetrically heated at a constant rate q;

[redacted]

within this structure heat transfer takes place by conduction only. The actual temperature T minus the initial temperature T_0, multiplied by the material thermal conductivity k and divided by the heating rate q and skin thickness t is plotted against a time parameter in which τ is the elapsed time, c the specific heat, and w the specific weight. The choice of these dimensionless parameters makes it possible to present on the same plot the results for a given cross section of different materials subjected to different heating rates. The calculated results, shown by the solid lines, are obtained by a simple analysis assuming constant material thermal properties and no heat losses. Point 1, which is farthest from the heat sink afforded by the web, will be the hottest point in the structure, whereas point 2, which is farthest from the heat source, will be the coolest. As a consequence of assuming no heat losses and a constant heat input, the average temperature of the structure is proportional to the mass of the section and varies linearly with time. In order to check the theory, three tests were made involving constant heating rates of 5, 16, and 41 Btu/ft^2-sec. Each test is represented by a different symbol, and the experimental temperatures are plotted for various times until the maximum skin temperature reached 450° F. The parameters are such that the data for the highest heating rate, shown by the diamonds, appear at the extreme lower end of the curves, whereas the data for the lowest heating rate extend the full length of the curves. The test results are in fairly good agreement with the theory; any discrepancy is due largely to the assumption of constant thermal properties used in the theory.

At any point in the structure, the thermal stress is proportional to the difference between the average temperature and the temperature of the point in question. When multiplied by the appropriate material properties, these differences can be converted into thermal stresses, such as shown in figure 2.

In this figure thermal-stress distributions are shown for both the low and high heating rates of 5 and 41 Btu/ft^2-sec for the times when the maximum skin temperature reached 450° F. The skin stresses appear in region A and the web stresses, in region B. The solid lines represent thermal stresses calculated from measured temperatures shown in figure 1, and the symbols represent experimental stresses obtained from strain-gage readings corrected for differential expansion between the gage and specimen. The agreement between theory and experiment is quite good. As would be expected, the higher heating rate allows less time for heat to be conducted into the web, thus provides larger temperature differences in the structure, and consequently yields larger thermal stresses. For the heating rate of 41 Btu/ft^2-sec the maximum skin stress, shown at the extreme right, and the maximum web stress, at the extreme left, are more than twice the values shown for the rate of 5 Btu/ft^2-sec, despite the fact that the skin temperature rise was the same.



Another significant point is that the maximum stresses are not related in the same proportion as the heating rates, which have an 8 to 1 ratio. The stresses shown here are those which existed when the skin temperature T_1 was 450° F. If, however, the skin temperature were not limited to 450° F and a comparison made at the same time, then, indeed, the stresses would be proportional to the heating rate.

It is also possible to present the stresses in a dimensionless form as was done for the temperatures. Figure 3 shows the dimensionless thermal stresses at various times during the progress of the three tests at heating rates of 5, 16, and 41 Btu/ft^2-sec. It is again evident that the high-heating-rate data are grouped at the lower end of the theoretical curves which are represented by the solid lines, whereas the data for the low heating rate extend the full length of the curves. The theoretical stresses are obtained by using the theoretical temperature of figure 1. The agreement between theory and experiment is about the same as that in figure 1, and any discrepancy is due to the same reason.

The results of these three figures indicate that fairly accurate temperatures and stresses can be predicted in a simple integral structure where only conductive heat transfer need be considered and, further, that strain-gage readings, if treated properly, can give reasonable stress results. However, if this structure had contained any joints, greater temperature differences would have resulted, and accurate calculations would have become somewhat more difficult.

Structure With Attached Webs

In order to show some of the effects of joints, the temperatures in one skin-web combination of a multiweb wing, a more realistic aircraft-type structure which contains riveted joints, will be examined. When six 20-inch-chord, multiweb wings identical in cross section - that is, with the same overall size, skin thickness, material, and so forth - were tested at sea-level conditions at a Mach number of 2 in a blowdown jet, the results were as shown in figure 4. This figure shows the temperature difference $T_1 - T_2$ between the maximum temperature in the skin (point 1) and the minimum web temperature (point 2) divided by the maximum possible skin temperature rise $T_{aw} - T_0$ plotted against time. The upper dot-dash curve gives the theoretical temperature-ratio drop if no heat is conducted into the stiffener, that is, if the joint conductivity h_j is equal to zero, and the lower dot-dash curve gives the theoretical results for perfect joint conductivity. The experimental data for five of the wings, indicated by the shaded area, lie close to the curve for perfect joint conductivity. On the other hand, the data for the sixth wing show that the increased temperature drop is somewhat closer to the curve for no joint conductivity. Since the temperature distribution depends mainly



upon heat conduction within the structure, this increased temperature difference can be attributed almost solely to a lower joint conductivity. The much poorer thermal conductivity of the joints of the one wing, compared with the other five wings, was not obtained by design but rather results from the small variations in otherwise identical structures expected from normal fabrication techniques. The 50-percent increase in temperature drop of the one wing over the average of the other five wings also resulted in a substantial increase in thermal stress. In fact, the wing with the largest temperature drop fluttered and then suffered a dynamic failure; whereas, the one wing among the other five, which was identical in every detail, survived its test without damage. Construction details, such as the inclusion of ribs, invalidate further comparison with the other models. However, it seems obvious that joint conductivity can have an important, and sometimes adverse, effect on the temperature variation in a structure and hence on the thermal stresses and, as a result, on the structural integrity.

In figure 5 the maximum nondimensional temperature drops have been plotted against a dimensionless joint conductivity parameter $h_j t/k$ where h_j is the thermal conductivity of the joint. Calculated results are shown by the solid lines. In the calculations the value of 0.013 for ht/k, the Biot number (an index of the rate of external to internal heat transfer), was determined by the experimental aerodynamic heat-transfer coefficient h. The symbols indicate data obtained from the tests and show a 6 to 1 variation in h_j which apparently can be expected even from good shop practice. Data obtained by Barzelay, Tong, and Holloway (refs. 1 and 2) cover an even wider range in h_j. Although a considerable scatter in h_j is shown by the five lowest test points, these points are in good agreement with the theory since they lie in a region where a fairly large change in joint conductivity has little effect on the temperature drop. Thus, the band for the five wings shown in figure 4 masks a considerable variation in h_j. The sixth point, which does not show such good agreement, is in a region where a small change in h_j can alter the temperature drop appreciably. The spread of h_j within the band shown in figure 4 is of the same order of magnitude as the variation from the top of the band to the curve for the one wing.

If the maximum skin or stiffener stress were plotted instead of the temperature drop, a similar variation with $h_j t/k$ could be observed - the lower the value of h_j, the higher the thermal stress, as evidenced by the failure of the one wing.

Actual flight-test results are shown in figure 6 for a duplicate of one of the five wings which had very good joint conductivity. The Mach number and altitude for the flight are shown at the top of the figure. The temperature difference $T_1 - T_2$ from the skin to the stiffener

[redacted]

center line is plotted against time. When this wing was attached to a rocket model, the results were as shown by the solid line, which lies much closer to the calculated curve for $h_j = 300$ Btu/ft^2-hr-$^\circ$F than to the curve for perfect joint conductivity. Since a value of $h_j = 300$ would lie slightly to the left of the test point for the one wing with the largest temperature difference shown in figure 5, the joints of this wing would be considered poor from the standpoint of thermal conductivity. In this case failure of the wing was prevented by the inclusion of a chordwise rib.

Internal Radiation in an Integral Structure

As was mentioned previously, the effect of joints is to increase the magnitude of the thermal stresses. However, if the temperatures involved are sufficiently high, it is possible that internal radiation in a structure may bring about some thermal-stress relief. The hotter parts of the structure transfer heat to the cooler parts by radiation and thereby lessen the temperature differences. Although there is an increased interest in this phenomenom, very little information can be found on this subject.

Therefore, in order to evaluate some of the effects of internal radiation on the temperature distribution within a multicell beam, such as shown in figure 7, an analog solution was made to determine the temperature distribution of an infinitely long box whose internal surfaces have an emissivity of 1. The procedure was to assume a constant rate of heat input until the maximum skin temperature reached a prescribed limit and then to maintain this skin temperature while the web temperature approached the skin temperature.

Heat was put into both skins at the rate of 5 Btu/ft^2-sec until the maximum skin temperature T_1 reached 1,200° F, at which time the skin temperature was kept constant. The maximum skin temperature T_1 and the minimum web temperature T_2 are plotted against time in seconds. The dashed lines are the solution when internal radiation is neglected; the solid lines represent the case when radiation is included. In this situation it can be seen that, when radiation is included, steady state is reached much more rapidly than when conduction only is considered. It can also readily be seen that the maximum temperature difference between the skin and the web, when conduction and radiation are considered, occurs at approximately 75 seconds and is about two-thirds of that when conduction only is considered.

In order to make a preliminary survey, other heating rates and skin-temperature levels were also investigated as shown in figure 8. Here,

[redacted]

in order to show one of the effects of internal radiation, the ratio of the maximum difference between skin temperature and web temperature for both radiation and conduction to the maximum difference for conduction only is plotted against the skin temperature T_1. For a given heating rate, the ratio of the temperature differences will approach a minimum value as the skin temperature increases. In the case of $q = 1$ Btu/ft^2-sec, the limit is nearly reached at a skin temperature of 1,200° F. The curve for the highest heating rate will eventually reach the lowest limit but at a temperature far in excess of 1,200° F. For the conditions in the figure, radiation effects are most significant when heating rates are low and temperatures are high.

Figure 9 shows some preliminary experimental results. The specimen was made of $\frac{1}{16}$-inch Inconel with the cross section as shown and was 12 inches long. The emissivity of the internal surfaces was about 0.8. The heating rates were approximately 5 and $2\frac{1}{2}$ Btu/ft^2-sec. Although there is a measurable reduction in the maximum temperature difference, the reduction is not as large as indicated by the idealized theoretical results.

CONCLUDING REMARKS

In summary, two factors, joint conductivity and internal radiation, which influence temperature distribution and therefore thermal stresses, have been discussed. Even normal fabrication techniques can produce joints of such poor conductivity as to cause the temperature differences to increase markedly over those of an integral structure. On the other hand, at the higher temperatures internal radiation has the effect of making the temperature differences less severe and the thermal stresses smaller. At the higher temperatures these two effects tend to cancel one another.

REFERENCES

1. Barzelay, Martin E., Tong, Kin Nee, and Holloway, George F.: Effect of Pressure on Thermal Conductance of Contact Joints. NACA TN 3295, 1955.

2. Barzelay, Martin E., Tong, Kin Nee, and Holloway, George F.: Thermal Conductance of Contacts in Aircraft Joints. NACA TN 3167, 1954.

TEMPERATURES IN RADIANTLY HEATED H-SECTION

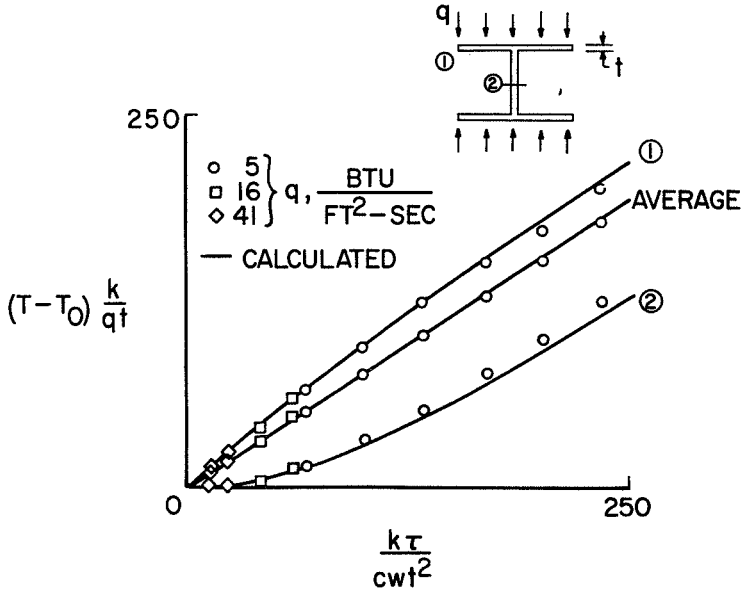


Figure 1

THERMAL STRESSES IN RADIANTLY HEATED H-SECTION

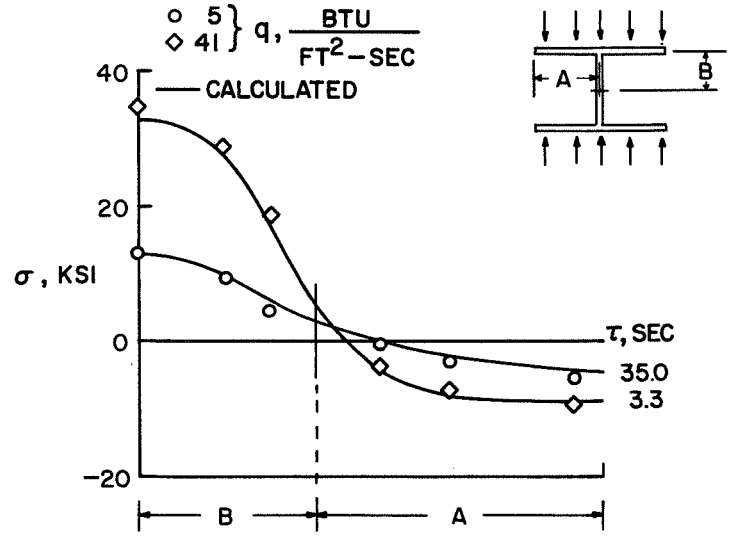


Figure 2

338

THERMAL STRESSES IN RADIANTLY HEATED H-SECTION

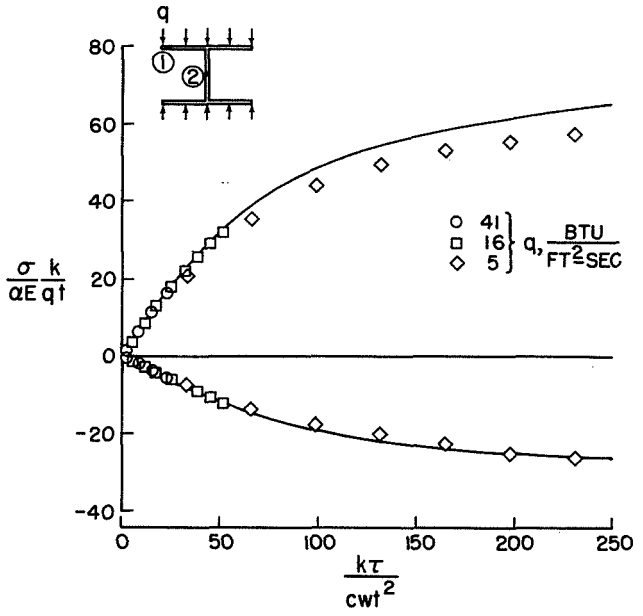


Figure 3

TEMPERATURE DIFFERENCES IN 6 MULTIWEB WINGS

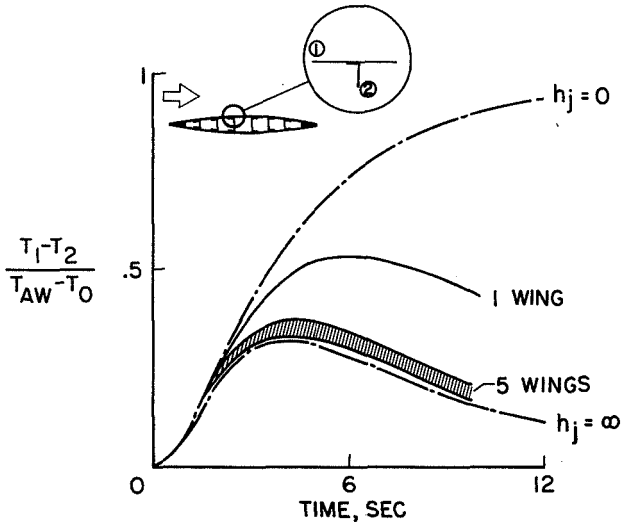


Figure 4

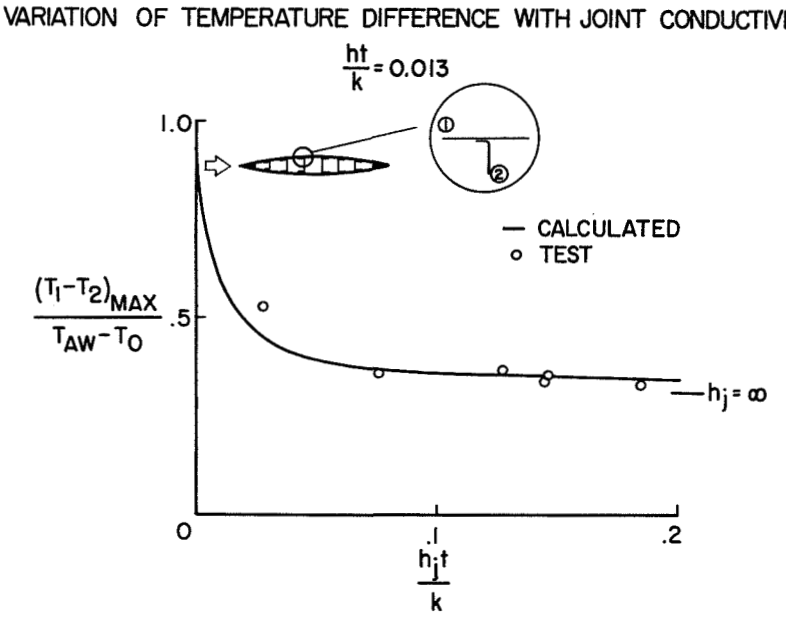


Figure 5

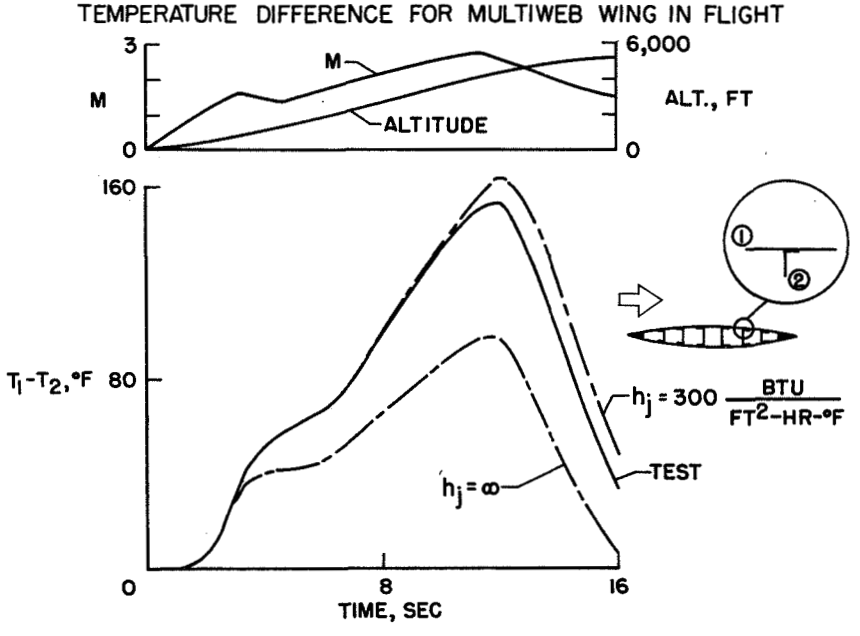


Figure 6

TEMPERATURE HISTORIES FOR BOX BEAM WITH INTERNAL RADIATION

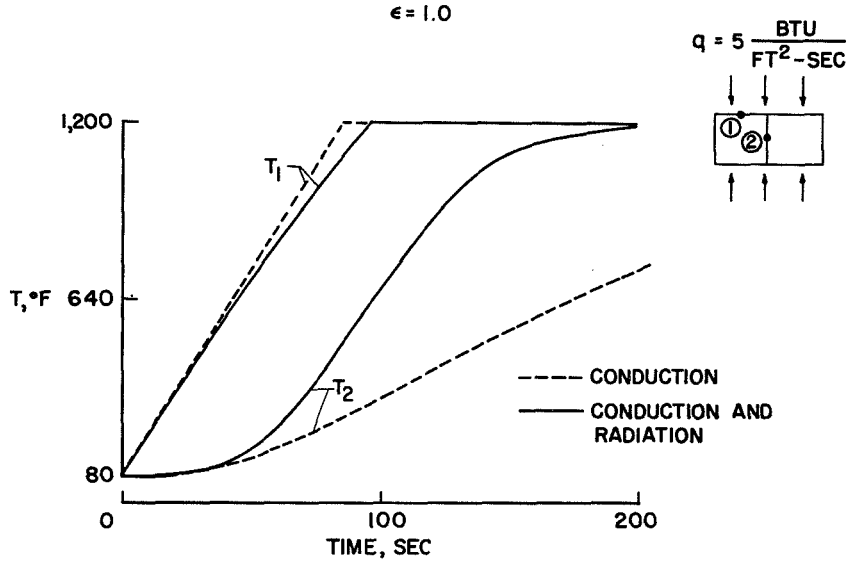


Figure 7

INTERNAL RADIATION EFFECTS FOR VARIOUS HEATING RATES

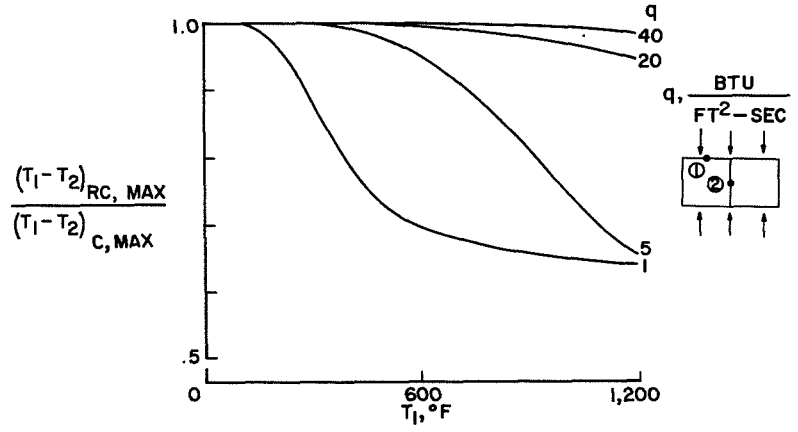


Figure 8

EXPERIMENTAL RESULTS FOR INTERNAL RADIATION

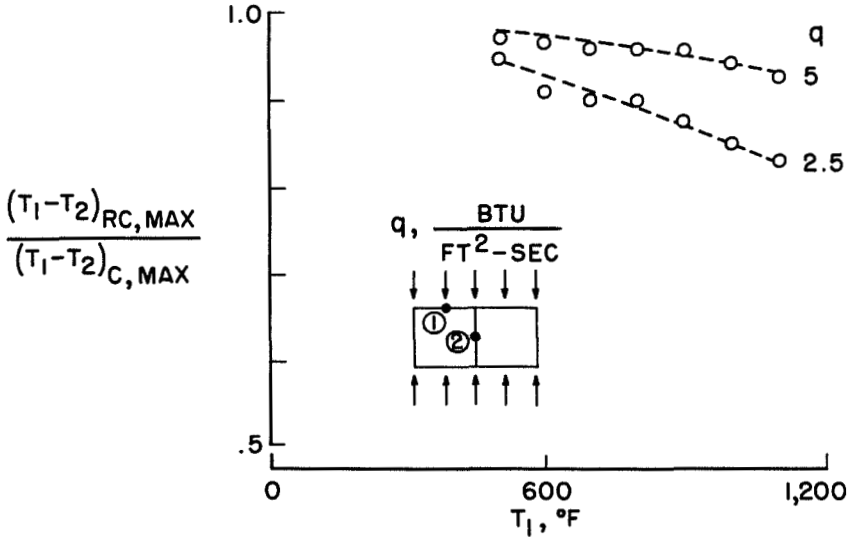


Figure 9

N71-75406

EFFECT OF TRANSIENT HEATING ON VIBRATION FREQUENCIES OF SOME SIMPLE WING STRUCTURES

By Louis F. Vosteen, Robert R. McWithey,
and Robert G. Thomson

Langley Aeronautical Laboratory

SUMMARY

Thermal stresses caused by nonuniform temperature distributions associated with transient heating can cause changes in the effective stiffness of wing structures. Some of the effects of this change in stiffness were investigated experimentally by testing three types of simple wing structures under various radiant-heating conditions. The structures tested were a uniform plate, a solid double-wedge section, and a circular-arc multiweb-wing section. Changes in stiffness were measured by measuring the changes in natural frequency of vibration during transient heating. In order to measure changes in frequency, a resonance-following system was developed which keeps the model vibrating at its natural frequency. Some of the data are compared with theoretical calculations and show that, at temperature differences near those required for thermal buckling, distortions have a marked effect on the frequency. The conclusion was made that, in order to predict the effects of aerodynamic heating on the stiffness of wing structures by means of laboratory radiant-heating tests, care must be taken to simulate closely the temperature distributions produced aerodynamically.

INTRODUCTION

One of the effects of the nonuniform temperature distributions produced by aerodynamic heating is a change in the effective structural stiffness caused by thermal stresses. Changes in stiffness have been observed in laboratory tests of several types of simple wing structures, and, in reference 1, thermal stresses were cited as the cause of failure of wing models subjected to aerodynamic heating. In order to obtain more information on this thermoelastic phenomenon, laboratory tests were conducted on several types of simplified wing structures for which changes in stiffness were measured during rapid heating. The results of these tests are presented and some comparisons with theoretical calculations are made.



The structures considered and the manner in which they were heated are shown in figure 1. The structures had a square plan form and were mounted as cantilevers. The first structure is a plate of uniform thickness which was heated radiantly along the longitudinal edges. The second is a solid double-wedge section which was subjected to a constant heat input over the top and bottom surfaces. The third is a symmetrical circular-arc multiweb airfoil. The heat input varied along the chord as indicated in the figure.

TEST PROCEDURE AND RESULTS

Resonance-Following System

Inasmuch as the natural frequency of vibration is a function of the model stiffness, changes in stiffness can be measured by measuring the changes in natural frequency during transient heating. The mechanism used to detect the changes in frequency is shown schematically in figure 2. The mechanism consists basically of a forcing system, the vibrating body, a vibration pickup, and the servo detecting system. The system is operated by setting the frequency of the signal generator so that the model is forced in one of its natural modes of vibration. The phase detector is then set to maintain the phase relation that exists between the applied force, as indicated by the signal generator, and the response of the model, as indicated by the vibration pickup. If the natural frequency of the model changes, the phase relation between the force and the response will change. The servo system detects this change, and, through a servomotor, mechanically drives the signal generator until the resonant phase relation is recovered. In this manner the model is continuously forced at its resonant frequency.

Uniform Plate

The plate tested was of aluminum alloy 20 inches square and 1/4 inch thick. As the plate was heated, the temperature at the edges rose rapidly, but the center section remained relatively cool. The thermal stresses which resulted caused a change in the natural frequencies of the plate. In reference 2 results were presented for changes in frequency of the first two modes. These tests were repeated by using the resonance-following system; in addition, the next three higher modes were investigated. The frequency histories which were obtained during transient heating are shown in figure 3.

The variation with time of the temperature difference ΔT, between the edge and the midchord in degrees Fahrenheit, is shown at the top of figure 3. Heat was applied to the plate for about 20 seconds at which



time the temperature difference between the edge and the midchord was about 190° F. In the lower portion of the figure the ratio of the frequency measured during heating f to that of the unheated plate f_o is plotted as a function of time in seconds for the first five natural modes. The mode shape and corresponding initial frequency are shown for each curve. Of these five modes, the first torsion mode underwent the largest change in frequency, a reduction of about 35 percent. The first chordwise bending mode was least affected by this type of heating. Since the plate was not initially flat, the heating also caused the plate to deform. These deformations were primarily torsional and, therefore, an analysis that considered only torsional deflections was made for the effect of heating on the torsional mode of vibration. Such an analysis is given in reference 3. Some results of this analysis are shown in figure 4.

In figure 4 the ratio of the frequency of a heated plate to that of a flat unheated plate is shown as a function of the ratio of the temperature difference between the edge and the midchord ΔT to the theoretical temperature difference required to produce thermal buckling of the flat plate ΔT_{cr}. Curves are shown for various values of initial distortion which have been expressed as a twist parameter θ_o. For the perfect plate, $\theta_o = 0$, the frequency ratio decreases until the buckling temperature of the plate is reached. At this time the plate buckles; and, since the stiffness of the buckled plate is greater than that of the flat plate, the torsional frequency begins to increase. For a plate which has an initial twist, the heating has two effects. The thermal stresses lower the frequency, but, since the plate is also deforming, its stiffness due to twist is increasing. The frequency therefore reaches a minimum below the buckling temperature and any further heating causes the frequency to increase. The plate tested had a value of θ_o of 0.06 which corresponded to a tip twist of about one-third degree. As the frequency history indicates, the stiffness actually began to increase while heat was still being applied.

Figure 5 shows a comparison between measured and calculated frequency histories. The ratio of the frequency during heating to the frequency of the unheated plate is shown as a function of time in seconds. A small-deflection theory which neglects the effects of distortion on the stiffness overestimates the frequency change. When a large-deflection theory which includes the effects of distortion is used, the agreement is substantially improved.

Double-Wedge Section

The double-wedge section tested was made of stainless steel 1 inch thick and 20 inches square. Both the upper and lower surfaces were

subjected to a constant heat input by means of radiant heating. The temperature distribution in the chordwise direction is then primarily a function of the mass distribution. Again the changes in stiffness were measured by measuring the changes in natural frequency. Some of the test results are shown in figure 6.

The variation of temperature rise T with time for an edge, the surface at the midchord, and a point at the centroid of the section is shown at the top of figure 6. The changes in frequency ratio with time are shown for the first five modes in the lower part of the figure. The mode shapes and their corresponding starting frequencies are shown for each curve.

The reductions in frequency which occurred during heating are surprisingly small in comparison with the reductions calculated by Budiansky and Mayers (ref. 4) for the aerodynamic heating of similar wings instantaneously accelerated to moderately high Mach numbers. The discrepancies arise because of the marked difference between aerodynamic heating and this type of radiant heating. In aerodynamic heating, the temperature at the leading and trailing edges is limited by the boundary-layer temperature. In the radiant heating, the temperature right at the leading and trailing edges becomes prohibitively high before a temperature distribution is obtained which results in large stiffness changes. A theoretical calculation was made for the first torsion mode by using the same method as that used by Budiansky and Mayers but based on the experimental temperature distribution obtained from the radiant-heating test. These calculations gave a frequency reduction about the same as that obtained in the test. Therefore, larger reductions in frequency probably would have been obtained if the test could have been continued for a longer time or if the temperature distribution had more closely simulated that generated aerodynamically.

Multiweb-Wing Section

The third section tested was a 5-percent-thick multiweb-wing section of aluminum-alloy construction with a 20-inch chord and span. This specimen is the same as one which was tested in the preflight jet of the Langley Pilotless Aircraft Research Station at Wallops Island, Va., at a Mach number of 2. A description of the test of this model, designated MW-2, is given in reference 1. The radiant-heating test did not simulate the aerodynamic heating correctly although an effort was made to reproduce the average heat input. The test results are shown in figure 7.

The temperature in degrees Fahrenheit is plotted as a function of time in seconds for a point on the skin and at the center of a spar at the top of figure 7. The changes in the frequency ratio with time have been shown for five modes of vibration at the bottom of the figure. The

largest reduction in frequency, as shown by the lowest curve, occurred for a mode which involved chordwise bending. The smallest reduction in frequency occurred for the first torsion mode.

The radiant heating has not simulated the aerodynamic heating very well; therefore, these results cannot be applied directly to aerodynamic tests. However, the type of frequency reductions obtained here are significant. The similar model (described in ref. 1) tested at a Mach number of 2 fluttered in a mode which involved a large amount of chordwise bending as did the one which had the largest frequency reduction.

At the present time, no theoretical method is available for predicting the effects of transient heating on the frequencies of the more complicated types of modes which are the important ones for this structure.

CONCLUDING REMARKS

Three types of simple wing structures have been tested under various radiant-heating conditions and changes in stiffness as indicated by changes in natural frequency of vibration were measured. In order to measure the changes in frequency during transient heating, a resonance-following system was developed which keeps the specimen vibrating at its natural frequency.

For temperature differences near those required for thermal buckling, initial distortions have a marked effect on the frequency. Calculations which include the effects of these distortions are found to be in good agreement with the measured frequency.

The results obtained from these tests indicate that the magnitude of the effects of thermal stress depends strongly on the manner in which the structure is heated. Therefore, in order to determine the effects of aerodynamic heating on the stiffness of wing structures by means of laboratory radiant-heating tests, care must be taken to simulate closely the temperature distributions produced aerodynamically.



REFERENCES

1. Heldenfels, Richard R., and Rosecrans, Richard: Preliminary Results of Supersonic-Jet Tests of Simplified Wing Structures. NACA RM L53E26a, 1953.

2. Vosteen, Louis F., and Fuller, Kenneth E.: Behavior of a Cantilever Plate Under Rapid-Heating Conditions. NACA RM L55E20c, 1955.

3. Heldenfels, Richard R., and Vosteen, Louis F.: An Approximate Analysis of the Effects of Large Deflections and Initial Twist on the Torsional Stiffness of a Cantilever Plate Subjected to Thermal Stress. (Prospective NACA paper.)

4. Budiansky, Bernard, and Mayers, J.: Influence of Aerodynamic Heating on the Effective Torsional Stiffness of Thin Wings. Jour. Aero. Sci., vol. 23, no. 12, Dec. 1956, pp. 1081-1093, 1108.



MODEL CONFIGURATIONS

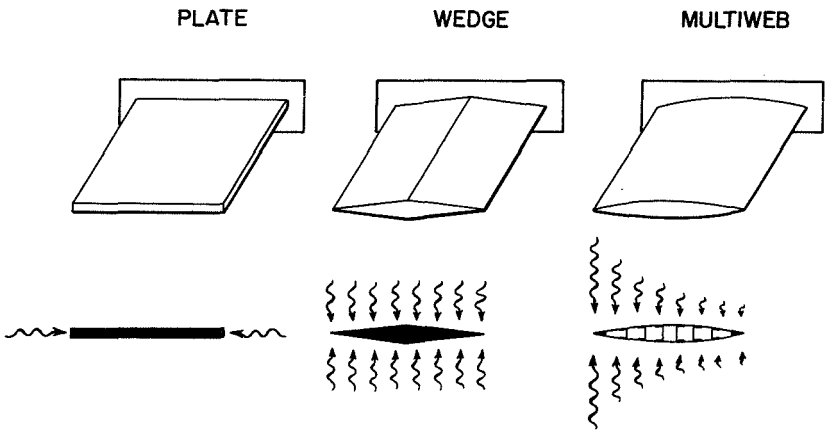


Figure 1

RESONANCE-FOLLOWING SYSTEM

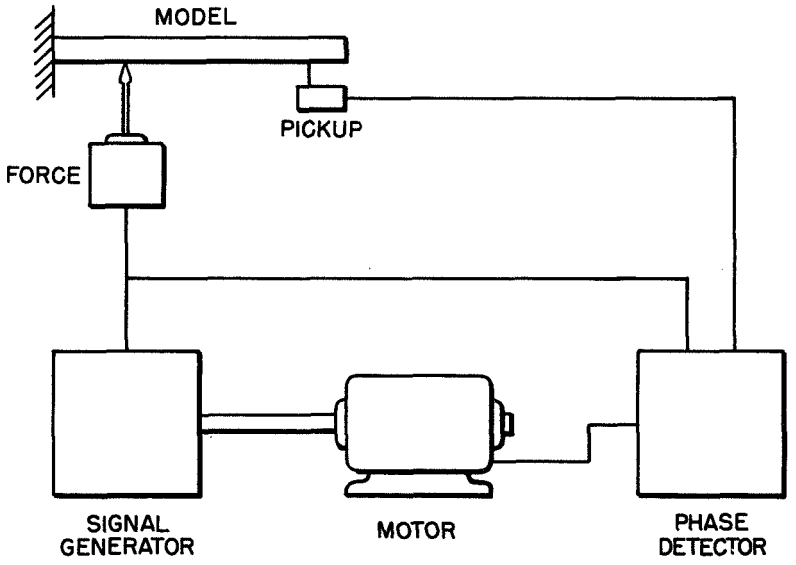


Figure 2



FREQUENCY HISTORIES
CANTILEVER PLATE

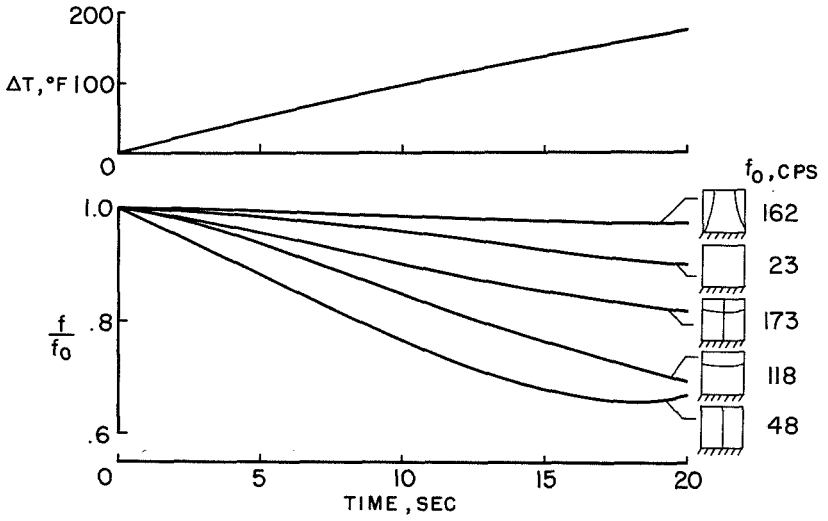


Figure 3

THEORETICAL FREQUENCY CHANGES
FIRST TORSION MODE

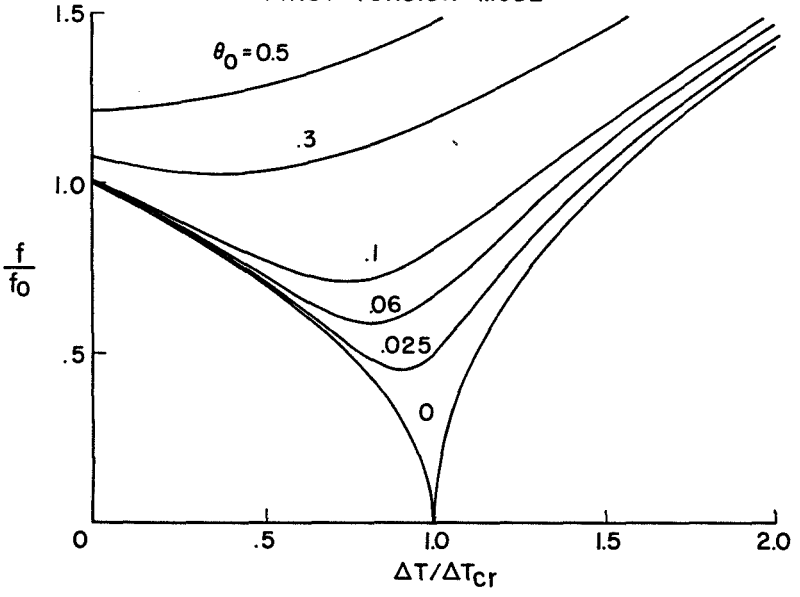
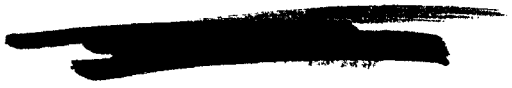


Figure 4



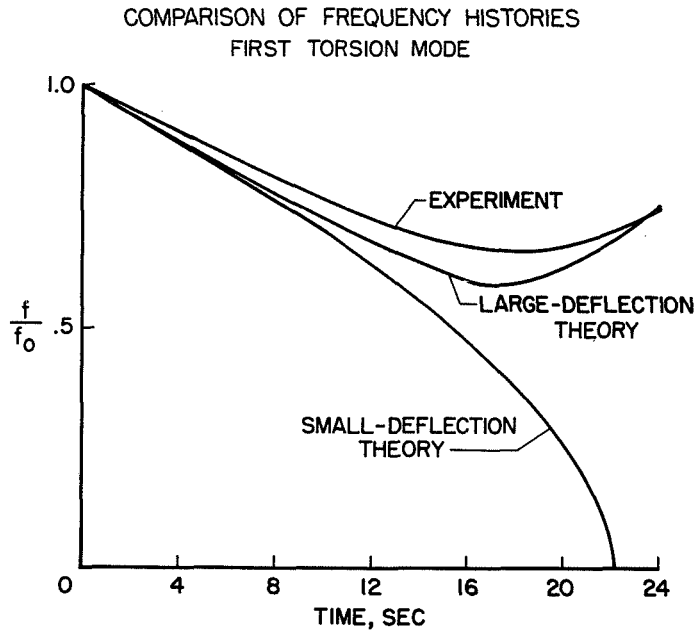


Figure 5

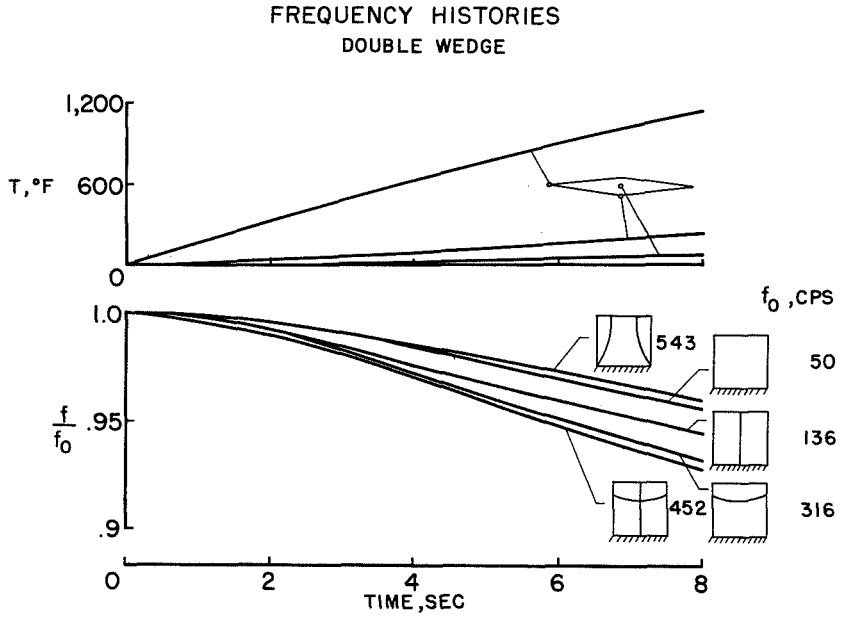


Figure 6

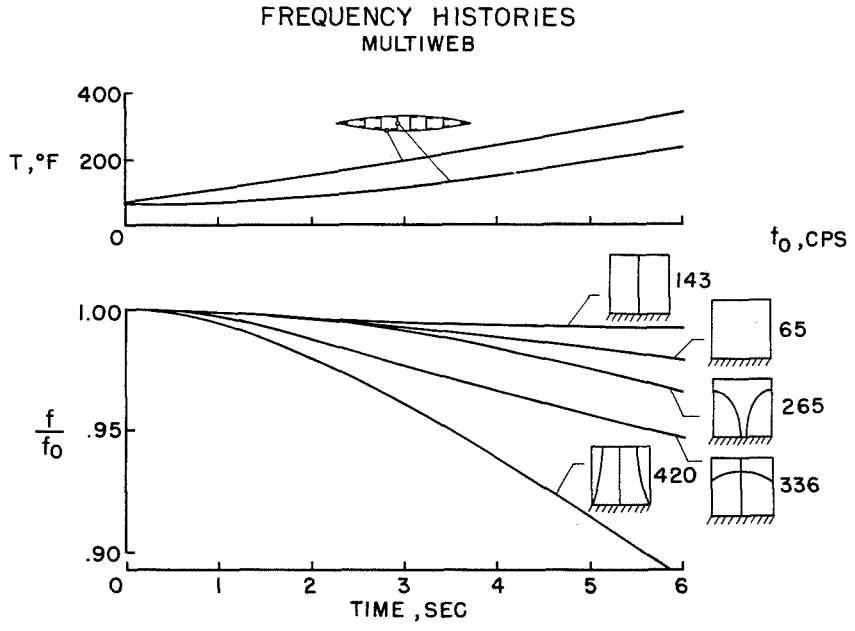

FREQUENCY HISTORIES
MULTIWEB
400
T, °F 200
0
f_0, CPS
143
65
265
420
336
1.00
$\frac{f}{f_0}$.95
.90
0
1
2
3
4
5
6
TIME, SEC

Figure 7

N71-75407

PRIDE, HALL, & ANDERSON

EFFECTS OF RAPID HEATING ON STRENGTH OF AIRFRAME COMPONENTS

By Richard A. Pride, John B. Hall, Jr., and Melvin S. Anderson

Langley Aeronautical Laboratory

SUMMARY

Results of several experimental investigations are presented which indicate the effects of rapid heating on the bending strength of multiweb beams and ring-stiffened cylinders. It is shown that thermal stresses reduce the bending load carried at buckling by both beams and cylinders. The influence of thermal stress on maximum load is found to depend largely on the mode of buckling. For beams that buckle locally, no apparent effect of thermal stress on the maximum load has been found. A reduction in maximum load has been observed for beams that buckle in the wrinkling mode and for cylinders.

INTRODUCTION

Aerodynamic heating rates currently contemplated in airplanes and missiles may impose severe thermal stresses on primary structures. This paper considers the influence of such thermal stresses on the bending strength of multiweb beams and ring-stiffened cylinders.

Observation of the behavior of various types of structures under combinations of loads and thermal stresses has indicated that the effect of thermal stress on buckling is to reduce the bending load which may be carried prior to buckling and that the effect of thermal stress on maximum load may be correlated with the type of stress-shortening diagram of the structure.

Some typical stress-shortening diagrams and associated buckling modes are presented in figure 1. Local buckling has a stress-shortening curve that permits considerable increase in both stress and shortening to occur after buckling and prior to failure. Within this region of increasing stress and shortening, it is possible that a redistribution of stress would alleviate the detrimental effect of thermal stress on maximum load.

In contrast, the stress-shortening curve for a structure such as a ring-stiffened cylinder usually drops abruptly after buckling (fig. 1). Hence, a reduction in buckling stress produced by thermal stress should be reflected as a corresponding loss in maximum strength. A stress-shortening diagram in which considerable shortening occurs for negligible increase in stress exists for structures such as multiweb beams with formed-channel webs which buckle in a mode known as wrinkling. This mode is characterized by buckles extending across the chord of the beam. The considerable shortening that can occur after buckling indicates that some influence of thermal stress on failure may be anticipated; however, this influence may not be as great as for the cylinder.

Tests to explore thermal-stress effects on the bending strength of these three types of structures have been made and some of the results are presented in preliminary form in this paper.

SYMBOLS

A	cross-sectional area, sq in.
b	plate width, in.
c	distance from neutral axis to center of skin, in.
E	Young's modulus, ksi
E_B	secant modulus for bending stress in skin, ksi
E_S	secant modulus for skin, ksi
E_W	secant modulus for web, ksi
I	moment of inertia, $in.^4$
k	plate buckling coefficient
l	cylinder ring spacing, in.
M	bending moment, in-kips
r	cylinder radius, in.
s	peripheral distance, in.

T	temperature, $^{\circ}F$
$\overline{T}$	average temperature, $^{\circ}F$
$\dot{T}$	temperature rate with respect to time, $^{\circ}F/sec$
t	plate thickness, in.
α	coefficient of thermal expansion, per $^{\circ}F$
η	plasticity reduction factor
σ	stress, ksi
$\bar{\sigma}$	average stress, ksi
μ	Poisson's ratio

Subscripts:

B	bending
cr	critical
cy	0.2-percent-offset compressive yield
f	failure
S	skin
W	web

BEAM STRENGTH

The test setup for applying both bending loads and rapid heating on beams is shown in figure 2. A one-cell beam is shown supported on columns about one-third the distance from each end and loaded in bending by the hydraulic jacks at the ends. Rapid heating is applied to the top and bottom skins of the beam by means of high-intensity quartz-tube lamp radiators located behind the reflectors. Strain gages and deflection pickups mounted on the cold webs give an indication of overall beam behavior during the test.

[redacted]

Failure Associated With Local Buckling

A large number of tests have been made on one-cell beams that buckle in the local mode. (Some of the results have been reported in ref. 1.) A representative temperature distribution around the cross section is shown in figure 3 for a beam 7.35 inches square with a wall thickness of 0.152 inch. The variation of temperature with peripheral distance for one quadrant of the beam is shown. For the maximum heating time in these tests, the temperature of the center of the skin rises to about 600° F, while the temperature of most of the webs rises to only about 100° F. Temperature distributions such as this will produce large thermal stresses in these beams.

For these aluminum-alloy beams, skin temperatures in the range from 400° to 600° F also produce deterioration in the material properties. In order to separate the loss in beam strength caused by deterioration of material properties from the loss in beam strength caused by thermal stress, a different type of test was made in which all sides of the beam were uniformly heated at a high rate. The test results for local buckling of these one-cell beams are shown in figure 4. The bending load stress in the skin of the beam is plotted against the average skin temperature. For the uniform heating case the skin temperature is the average temperature around the entire beam cross section; whereas, the average skin temperature is indicated for the nonuniform heating case in which the skins are heated at about 100° F/sec. For the nonuniform heating tests the existence of a difference in temperature between skins and webs is implied as was shown in figure 3.

Results are given in figure 4 for beams having two different values of width-thickness ratio for the skin; for one beam proportion buckling occurred in the elastic-stress range so that a large increase in stress after buckling was possible, and for the other beam proportion buckling occurred in the plastic range so that only a slight increase in stress beyond buckling was obtained. The upper curve for $b/t = 48$ gives the calculated buckling stress for uniformly heated beams and shows the effect of material deterioration on the elastic buckling stress. The buckling stress was determined from the following equation:

$$\sigma_{cr} = \frac{k\pi^2 \eta E}{12(1 - \mu^2)} \left(\frac{t_s}{b_s}\right)^2 \qquad (1)$$

The slight reduction in buckling stress shown is the result of changes in elastic modulus with temperature. The open square test points in figure 4 are the confirming tests for this curve.

 [redacted]

The lower curve for $b/t = 48$ determined from the following equation is the calculated amount of bending load stress required to produce buckling when thermal stress is present along with material deterioration:

$$\sigma_B = \sigma_{cr} - \frac{\alpha E_S(\bar{T}_S - \bar{T}_W)}{1 + \frac{E_S A_S}{E_W A_W}} \qquad (2)$$

Equation (2) follows directly from equations (1) and (2) of reference 2. The region between the two lower curves in figure 4 is a measure of the thermal stress as calculated by the last term in equation (2). The solid square test points indicate confirming tests for this elastic thermal-stress buckling condition.

For $b/t = 30$ the buckling stress is in the plastic range for this material. The upper curve in figure 4 gives the calculated effect of material deterioration on buckling stress for uniform heating. The buckling stress was again determined from equation (1) by using the plasticity reduction coefficient $\eta = E_S/E$. The lower curve gives the calculated amount of bending load stress required to produce buckling when both material deterioration and thermal stress are considered (eq. (2)). Again the region between these two curves represents the amount of thermal stress present at buckling. The tests are in agreement with the calculations. It should be noted that about one-half of the test results presented in figure 4 were obtained for beams that were loaded first and then heated, with the remaining beams heated first and then loaded. No discernable effects of sequence could be found.

Thus, it appears that local buckling of beams with integral webs can be predicted at elevated temperatures either with uniform heating or with temperature gradients, and in both the elastic and the plastic stress ranges.

The maximum strength of these same beams is given in figure 5. The curves show the maximum strength of the beams for uniform heating calculated from the following equation:

$$\bar{\sigma}_f = \frac{M_f c}{I} \qquad (3)$$

[redacted]

where

$$M_f = 1.847\sqrt{E_B\sigma_{cy}}\, t_s^2 b_w + 0.460\sigma_{cy} b_w^2 t_w \qquad (4)$$

Equation (4) is taken from reference 1 and is dependent only on beam dimensions and material properties at elevated temperature. The calculated curves of figure 5 correspond to the same uniform heating case as the upper buckling curves for each value of b/t in figure 4. A considerable difference exists between the buckling stress and failure for $b/t = 48$. At $b/t = 30$ this difference in stress is practically gone as a result of plastic buckling; however, a considerable amount of beam deflection occurred between buckling and failure, even though the stress increased only slightly. The open test points corresponding to uniform heating indicate that the failure calculation is valid for both types of beams. The solid points represent test conditions at maximum load for the beams which had developed large thermal stresses at buckling. As indicated by the intermingling of the open and solid test points, no effect of thermal stress is evident on the maximum load. This result is equally true for beams that buckled either elastically or plastically.

Failure Associated With Wrinkling

The preliminary results obtained for a series of multiweb beams designed to aircraft proportions and fabricated from 17-7 PH stainless steel are given in figure 6. The interior structure consists of thin formed-channel webs riveted to the skins. In this particular configuration, no post-buckling strength was found in the room-temperature test. Therefore, the upper curve calculated from equation (1) gives the buckling strength and failure strength for uniform heating based on material deterioration with temperature. The lower curve gives the calculated bending load stress that produces buckling under the nonuniform-heating test condition (eq. (2)). The region between the curves then represents the amount of thermal stress that was calculated to be present in the tests. The circles give the failure-test results obtained from three beams. The results from two of the tests for nonuniform heating indicate that thermal stress in the beam reduced the maximum load. The maximum possible reduction was not large in the particular beam proportions tested, and it remains to be determined whether or not corresponding results will be obtained in beam proportions where the induced thermal stresses are a larger percentage of the beam buckling stress.

358

[redacted]

CYLINDER STRENGTH

Tests have been completed on 2024-T3 aluminum-alloy ring-stiffened circular cylinders (table I), and a program has been started with 17-7 PH stainless steel cylinders. The test setup is shown in figure 7. The cylinder is loaded in bending by the large weight cage acting through a linkage system. A quartz-tube lamp radiator constructed around the outside of the cylinder test section permits rapid heating of the cylinder skin with heat flowing into the rings primarily by conduction from the skin.

The effect of heating at different temperature rates on cylinder strength is shown in figure 8. The solid curve is the calculated bending strength of the ring-stiffened cylinder for uniform heating of both skin and rings and is based on the room-temperature test results of reference 3 The decrease in strength shown by the curve is caused by the change in elastic modulus at high temperatures.

Three nominally identical cylinders were loaded with two-thirds of the room-temperature failing load in bending and then heated to failure at temperature rates of 1° F/sec, 20° F/sec, and 90° F/sec. With the slowest temperature rate which corresponded essentially to a uniform heating test, the ring temperature followed the skin temperature very closely. For this case it would be expected that the buckling failure would be influenced mainly by the change in elastic modulus with temperature. The close agreement of the test at 1° F/sec with the curve for uniform heating checks the validity of such a calculation. For the two higher heating rates, ring temperatures lagged the skin temperature by a large amount. The lower curve in figure 8 is faired for these rapid heating tests and the gap between the curves indicates the effect of restrained expansion. Variations in cylinder diameter caused by restraint of thermal expansion of the skin by the rings were observed in the tests. The bulging between rings and circumferential compression stress produced by this restraint are the most probable causes for the reduction of strength of the two cylinders subjected to the high heating rates. For these particular cylinder proportions, temperature rates substantially less than the 20° F/sec would be required to avoid this reduction in strength.

The effect of changing the ring spacing is shown in figure 9 for a constant temperature rate of 90° F/sec. At room temperature the same value of failure stress is obtained for l/r equal to 1/2 or greater. At a uniform elevated temperature a single calculated curve represents the strength of these cylinders. For l/r equal to 1/4, the small ring spacing results in an increased bending strength for uniform heating conditions as shown by the top solid curve. The dashed curves are drawn to their respective test points for nonuniform heating at the high rate. The gap between the dashed curves and the corresponding solid curves is

[redacted]

a measure of the loss in bending strength caused by the restrained skin expansion. As the ring spacing increases, the loss in bending strength also increases.

It is believed to be significant that the mode of failure of these tests was the usual diamond buckle pattern and not a circumferential bulge such as would correspond to the eccentricity of the restrained skin. This behavior and the greater reduction in failure strength with increasing ring spacing suggest that the circumferential compression due to restrained skin expansion interacts more with the bending stress than does the eccentricity. This interaction becomes more serious as ring spacing is increased, inasmuch as the ratio of the actual to the critical circumferential compression stress increases.

CONCLUDING REMARKS

It may be concluded from these tests that thermal stresses will interact with bending load stresses to reduce the buckling load carried by a structure. Depending upon the mode of buckling, the thermal stresses may or may not affect the magnitude of the maximum load. In tests of structures where increases in load are required to produce deformation in the post-buckling range, no apparent effect of thermal stress on the failure load has been found; in structures which tend to deform with loss of load beyond buckling, tests indicate that a loss of strength due to thermal stress can be expected.

REFERENCES

1. Pride, Richard A.: Transient Heating Effects on the Bending Strength of Box Beams. M. S. Thesis, Va. Polytechnic Inst., 1956.

2. Pride, Richard A.: An Investigation of the Effects of Rapid Skin Heating on Box Beams Loaded in Bending. NACA RM L55B03, 1955.

3. Peterson, James P.: Bending Tests of Ring-Stiffened Circular Cylinders. NACA TN 3735, 1956.

[redacted]

TABLE I

TEST RESULTS FOR 2024-T3 ALUMINUM-ALLOY RING-STIFFENED CYLINDERS

SUBJECTED TO RAPID HEATING AND BENDING LOADS

[Cylinder: diameter, 19.16 in.; skin thickness, 0.0318 in. ±1 percent.
Rings: $1\frac{1}{4}$ in. deep Z-section; 0.051 in. thick; area, 0.10 sq in.]

Cylinder	Ring spacing, in.	Failing stress at room temperature, psi (a)	Applied stress, psi (a)	Nominal-skin-temperature rise rate, °F/sec	Average skin temperature at failure, °F	Ratio of E at failing temperature to E at room temperature	Temperature in rings at failure, °F (b)	Increase in diameter of ring, in.	Increase in diameter of skin at midspan, in.
I	$4\frac{3}{4}$	[c]17,500	11,800	1	599	0.68	487 to 596	-----	-----
II	$4\frac{3}{4}$	[c]17,500	11,800	20	499	.80	144 to 297	0.032	0.131
III	$4\frac{3}{4}$	[c]17,500	11,800	90	489	.81	80 to 214	.007	.113
IV	$2\frac{3}{8}$	[d]20,700	14,300	90	550	.74	80 to 260	0	.124
V	$9\frac{1}{2}$	[c]17,500	11,800	90	410	.88	86 to 196	-----	-----

[a]Extreme fiber bending stress.

[b]Minimum and maximum temperatures measured over the ring cross sections.

[c]Stress obtained from test results for 7075-T6 cylinders of reference 3.

[d]Actual test.

STRESS-SHORTENING CURVES FOR VARIOUS STRUCTURAL COMPONENTS

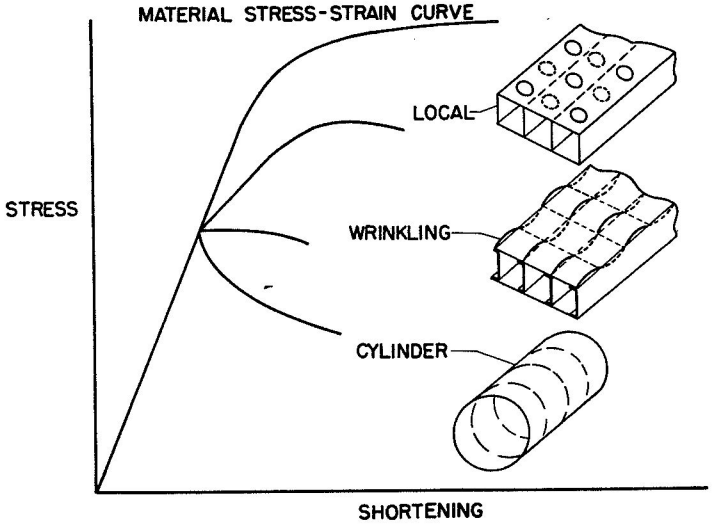
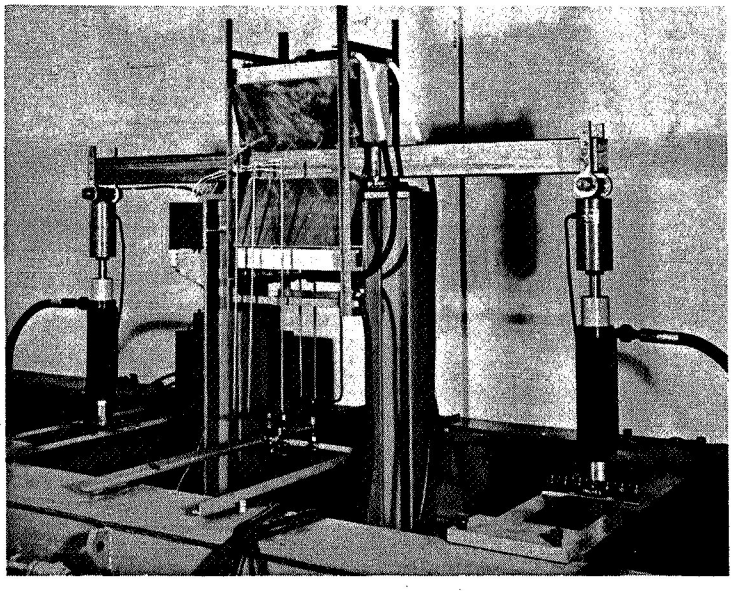


Figure 1

TEST SETUP FOR RAPID HEATING AND BENDING OF BEAMS



L-91930.1

Figure 2

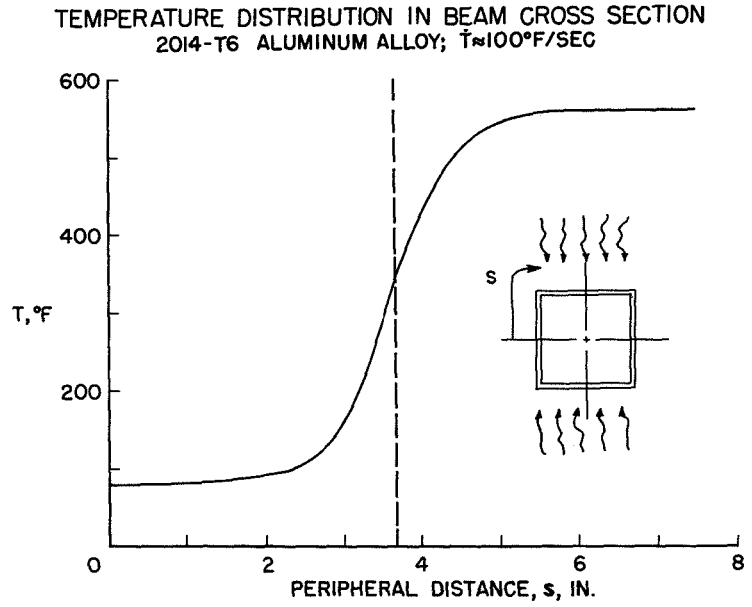


Figure 3

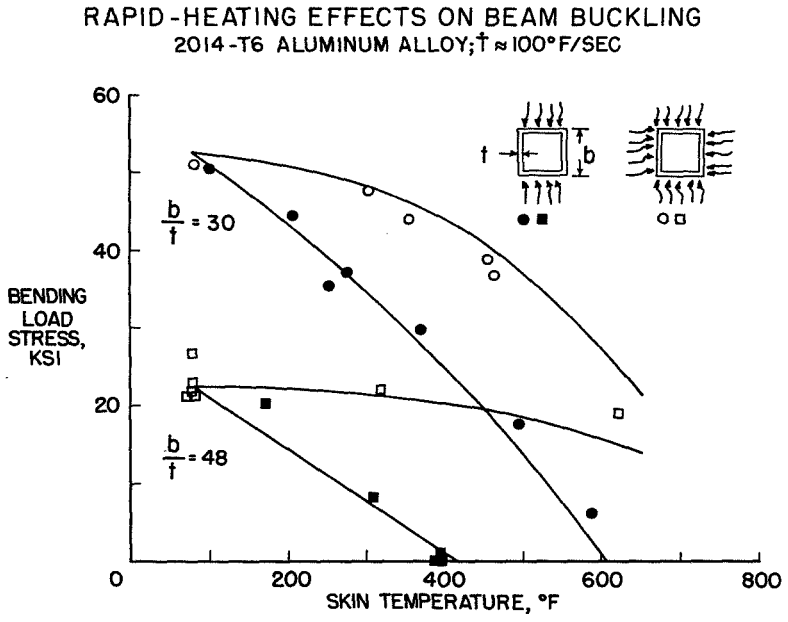


Figure 4

RAPID-HEATING EFFECTS ON BEAM FAILURE
2014-T6 ALUMINUM ALLOY; $\dot{T} \approx 100°$ F/SEC

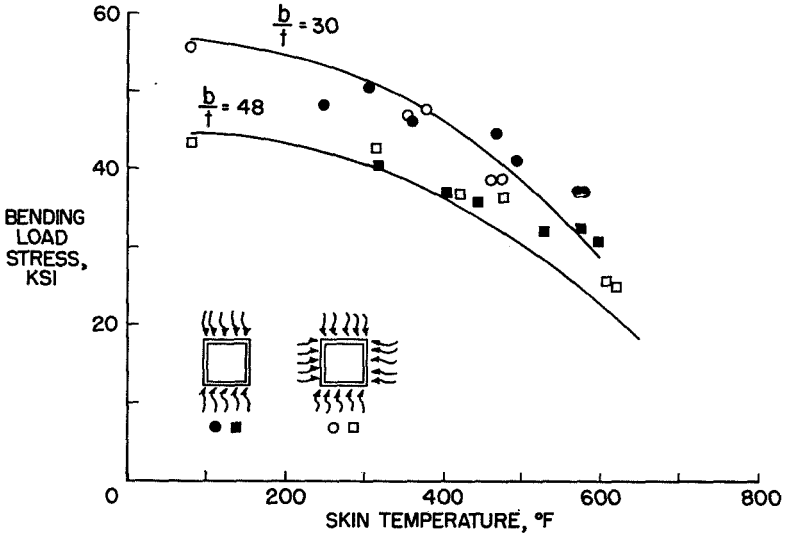


Figure 5

RAPID-HEATING EFFECTS ON BEAMS (WRINKLING MODE)
17-7 PH STAINLESS STEEL; $\dot{T} \approx 100°$F/SEC

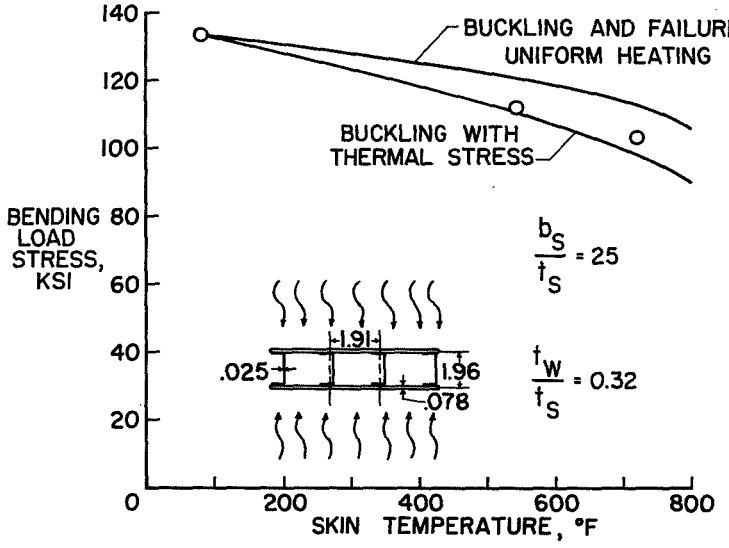


Figure 6

TEST SETUP FOR RAPID HEATING AND BENDING OF CYLINDERS

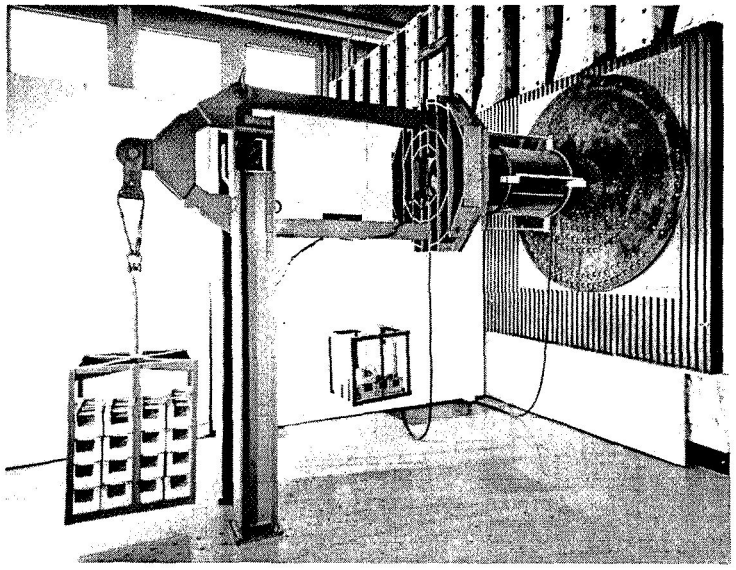


Figure 7 L-90701.1

RAPID-HEATING-RATE EFFECT ON RING-STIFFENED CYLINDER STRENGTH

2024-T3 ALUMINUM ALLOY; $\frac{l}{r}=\frac{1}{2}$; $\frac{r}{t}=300$

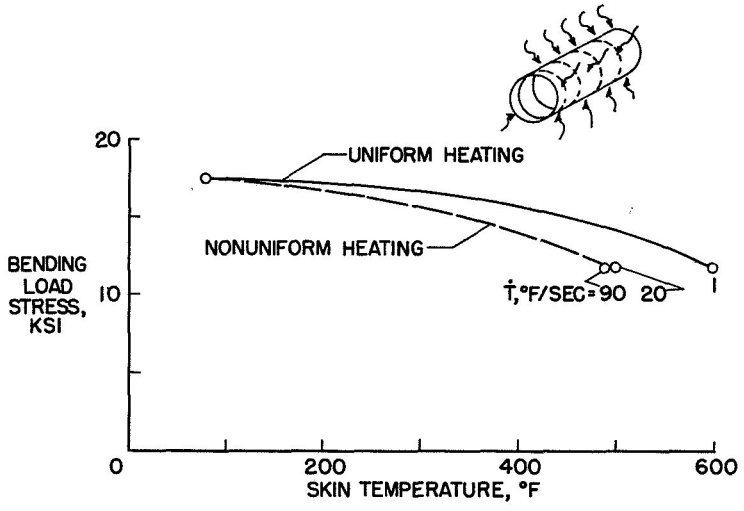


Figure 8

[redacted]

RING SPACING EFFECT ON STRENGTH OF RAPIDLY HEATED RING-STIFFENED CYLINDERS

2024-T3 ALUMINUM ALLOY; $\frac{r}{t} = 300$; $\dot{T} = 90\ ^\circ F/SEC$

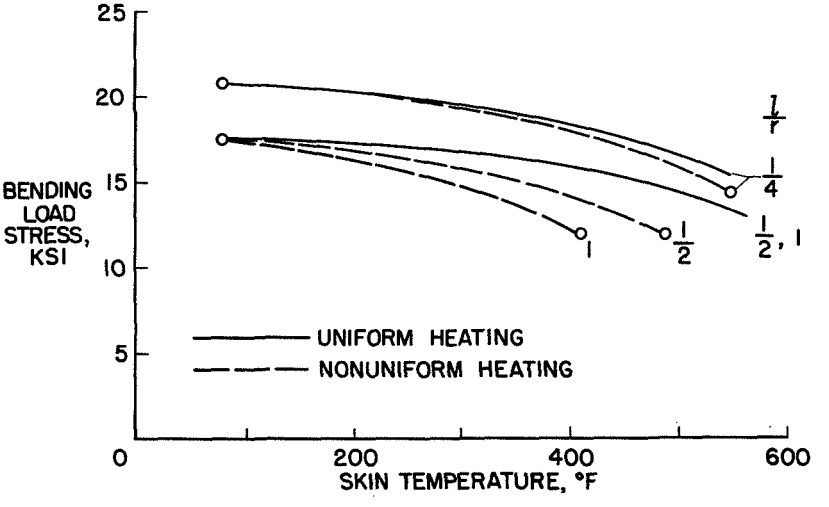


Figure 9

[redacted]

N71-75408

THE COMBINATIONS OF THERMAL AND LOAD STRESSES FOR THE ONSET OF PERMANENT BUCKLING IN PLATES

By George W. Zender and Richard A. Pride

Langley Aeronautical Laboratory

SUMMARY

A simple and practical method for evaluating the onset of permanent buckling in plates in the presence of combined thermal and load stresses is outlined. A particular application of the method shows reasonable agreement with tests of 17-7 PH stainless-steel square tubes. The results indicate that the load stress which the plate can support at the onset of permanent buckling is substantially reduced as the temperature difference of the plate and adjoining members increases.

INTRODUCTION

The use of high-density materials in supersonic aircraft causes concern with respect to buckling of the thin skin surfaces, particularly where permanent buckles may develop in the structure. Methods of analysis are needed which include the effects of thermal stresses in combination with the usual load stresses. In order to provide such methods, the behavior of plates due to combined thermal and load stresses is being studied; this paper presents initial results obtained for predicting the onset of permanent buckling and compares the results with experiment.

SYMBOLS

A_S	cross-sectional area of skin, sq in.
A_W	cross-sectional area of webs or stringers restraining thermal expansion of skin, sq in.
b	width of skin, in.
e	unit shortening of skin

E_S modulus of elasticity of skin material at average skin temperature, ksi

E_W modulus of elasticity of web material at average web temperature, ksi

t thickness of skin, in.

ΔT average temperature of skin minus average temperature of web, $^{\circ}F$

α linear coefficient of thermal expansion, per $^{\circ}F$

ϵ_{cr} strain at which buckling initiates

ϵ_{el} elastic limit strain

σ average stress over cross-sectional area of skin, ksi

σ_L average load stress over cross-sectional area of skin, ksi

σ_T average thermal stress over cross-sectional area of skin, ksi

METHOD OF ANALYSIS

A simple approximation for the beginning of permanent buckling in a plate subjected to compressive load is suggested by the experimental observation that permanent buckling begins when the unit shortening of the plate is about the same value as the elastic-limit strain of the material. This concept appears useful for approximating the compressive load required for the onset of permanent buckling in a plate in the presence of thermal stresses. Consider a plate which has been shortened beyond the value required for buckling. (See fig. 1.) In the usual sense, the shortening of the plate comes from compressive loads; however, in effect, shortening also occurs when the plate is heated but the thermal expansion is restrained, such as would occur if the edges of the plate were bounded by stringers or shear webs at a lower temperature. This effective shortening due to restrained thermal expansion is the difference in length between the restrained and the unrestrained plate when heated. The lower curve of figure 2 shows the manner in which the effective unit shortening due to restrained thermal expansion increases with the difference in average temperature of the plate and

the adjoining member. The dashed line in figure 2 indicates the critical strain or the unit shortening for buckling of the plate. The upper solid curve indicates the elastic-limit strain which decreases somewhat with increasing temperature. For a given temperature difference, then, the plate is in a state of shortening due to restrained thermal expansion; additional shortening by compressive loading causes the plate to buckle; and further compressive-load shortening causes the buckles to deepen but the buckles are not permanent until the limit given by the upper curve is exceeded. The region between the solid lines, then, defines the permissible amount of compressive-load shortening which may be applied in conjunction with the effective shortening from restrained thermal expansion without causing permanent buckling.

SPECIMENS AND METHOD OF TESTING

In order to test the validity of the foregoing approximate analysis, tests were performed on $\frac{1}{16}$-inch-thick 17-7 PH stainless-steel plates fabricated into square tubes by welding the corners. The tubes were 32 inches long and had b/t ratios of 40, 60, or 80. Two opposite walls of the tubes (skins) were exposed to heat supplied by two banks of quartz-tube radiators as shown in figure 3. The other two walls (webs) were shielded from the radiators by aluminum plates which ran lengthwise of the tube and projected diagonally outward from each corner of the tube. The shields have been removed in figure 3 in order to show the tube. Temperature distributions in the tubes were obtained with thermocouples, and records of the extension near the corners, along 15 inches of the length, were obtained with four differential transformers. Figure 3 shows the setup when the square tubes were subjected to heat without end load. The same test setup was placed in a testing machine and compressive loads were applied in combination with heat. In addition, compression tests of tubes at room temperature were performed. The square tubes were unloaded and/or cooled to room temperature after loading and/or heating, and profiles of the amplitude of the permanent buckles were obtained with a pantograph apparatus which multiplied the amplitude by a factor of 11. For each run, the average of the buckle depths (measured from crest to valley or twice maximum amplitude) in the skins was obtained. Figure 4 shows an example of the permanent-buckle information obtained for the square tubes subjected to heat. The particular data shown are for the square tube subjected to heat without compressive load and with $b/t = 60$. The ordinate shown in figure 4 is the difference of the average temperatures of the skin and web of the tube. Before the tube was subjected to heat, the average value of buckle depth was obtained from the pantograph measurements and is indicated in figure 4 (initial imperfection). After the tube had been subjected to an elevated temperature and cooled to room temperature, the permanent-buckle depth was slightly larger than the

initial imperfection. Subsequent tests on the same tube but with progressively higher values of temperature resulted in progressively larger values of permanent-buckle depth. The temperature difference when the permanent-buckle depth began to exceed the initial imperfection was defined as the start of permanent buckling, as is indicated in figure 4. Similar information was obtained for all tubes tested except that load stress was plotted in place of temperature difference for the square tubes subjected to compressive load but not to heat. The load stress in the skin at the start of permanent buckling for the square tubes subjected to both heat and compressive load was evaluated from the extension measurements and the total load on the tube since the compressive stress in the skin for this case differs considerably from that in the webs.

RESULTS AND DISCUSSION

Figure 5 presents a comparison of the experimental results with curves obtained from the approximate analysis previously given. The ordinate shown in figure 5 is the average compressive load stress for the onset of permanent buckling in the plate, and the abscissa is the difference in average temperatures of the skin and web. The details of evaluation of the curves are given in the appendix. It is apparent that the load stress which the plate can support at the onset of permanent buckling is substantially reduced as the temperature difference increases.

In general, reasonable agreement of the approximate analysis and the experiment exists. Somewhat better agreement exists when load stress only is applied than when large thermal stresses are present. The poorer agreement is largely attributed to the assumption that the properties of the heated skin are represented by properties for the average value of skin temperature. This representation is somewhat inaccurate at high values of temperature difference when rather large-temperature gradients exist.

CONCLUDING REMARKS

A simple and practical method for evaluating the onset of permanent buckling in plates in the presence of thermal stresses is given. A particular application of the method shows reasonable agreement with tests of 17-7 PH stainless-steel square tubes. The results indicate that the load stress which the plate can support at the onset of permanent buckling is substantially reduced as the temperature difference of the plate and adjoining members increases.

APPENDIX

EVALUATION OF LOAD STRESS

Compressive stress-strain curves of 17-7 PH stainless-steel material for a wide range of temperatures are presented in reference 1 and are assumed to represent the material of the square tubes. Beyond buckling, the average stress in the buckled skin is approximated by the expression (ref. 2):

$$\sigma = E_S\sqrt{e\epsilon_{cr}} \qquad \left(\epsilon_{cr} \leqq e \leqq \epsilon_{el}\right) \tag{1}$$

which is in substantial agreement with the experimental measurements obtained on the square tubes subjected to compressive loads without thermal stresses (room-temperature tests). The combined thermal and load stress for the onset of permanent buckling is then

$$\sigma_T + \sigma_L = E_S\sqrt{\epsilon_{el}\epsilon_{cr}} \tag{2}$$

The thermal stress as given by equation (2) of reference 3 is

$$\sigma_T = \frac{\alpha E_S \Delta T}{1 + \dfrac{E_S A_S}{E_W A_W}} \tag{3}$$

Equation (3) was modified for thermal stresses exceeding the buckling stress by employing assumptions consistant with equation (1), in order to allow for the effect of the reduced longitudinal stiffness of the buckled skin. After evaluating the thermal stress, the load stress σ_L was obtained from equation (2) and the results are shown by the curves of figure 5.

[redacted]

REFERENCES

1. Stein, Bland A.: Compressive Stress-Strain Properties of 17-7 PH and AM 350 Stainless Steel Sheet at Elevated Temperatures. (Prospective NACA paper.)

2. Von Kármán, Theodor, Sechler, Ernest E., and Donnell, L. H.: The Strength of Thin Plates in Compression. A.S.M.E. Trans., APM-54-5, vol. 54, no. 2, Jan. 30, 1932, pp. 53-57.

3. Pride, Richard A.: An Investigation of the Effects of Rapid Skin Heating on Box Beams Loaded in Bending. NACA RM L55B03, 1955.

[redacted]

BUCKLED PLATE

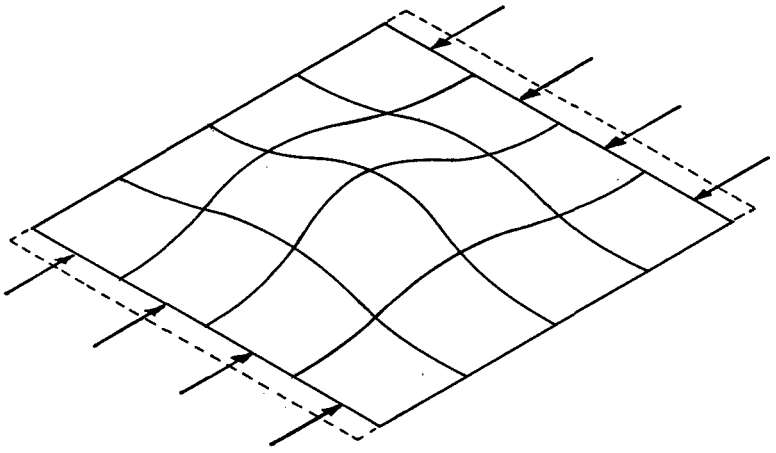


Figure 1

METHOD OF ANALYSIS

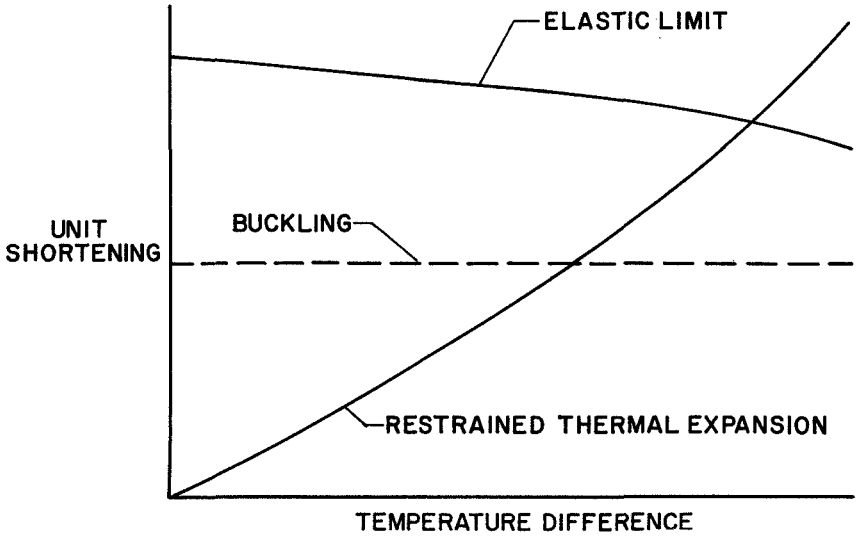


Figure 2

TEST SETUP FOR THERMAL PERMANENT BUCKLING
OF SQUARE TUBE

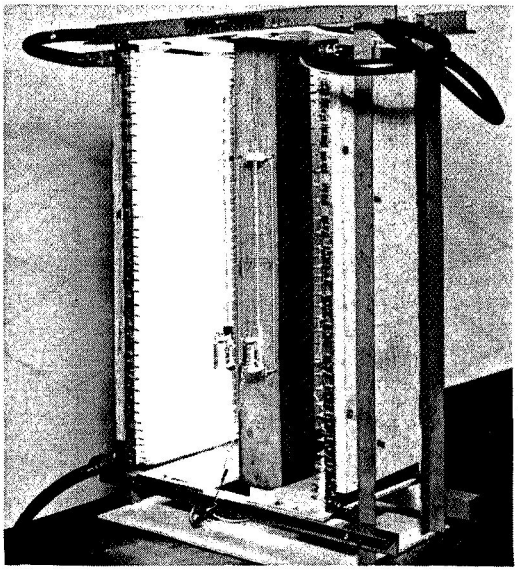
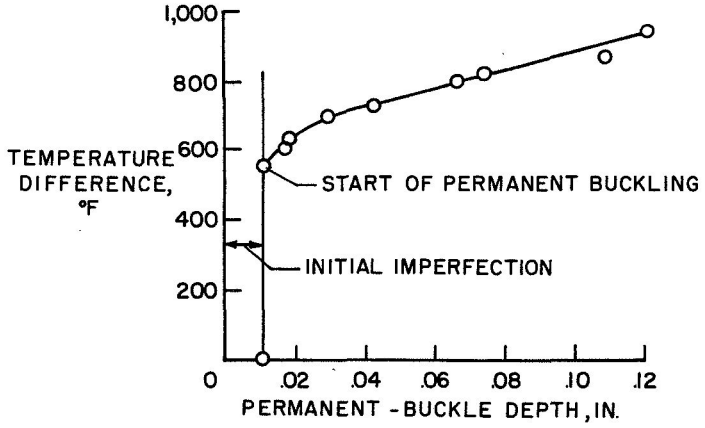


Figure 3 L-57-64.1

EXPERIMENTAL MEASUREMENTS OF PERMANENT-BUCKLE DEPTH
17-7 PH STAINLESS STEEL, b/t = 60



374

Figure 4

COMBINATIONS OF LOAD STRESS AND TEMPERATURE DIFFERENCE FOR THE START OF PERMANENT BUCKLING

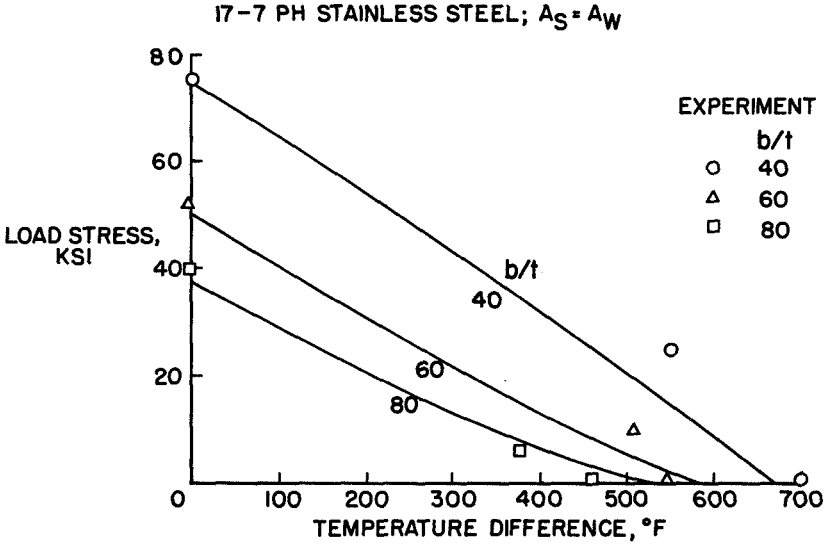


Figure 5

N71-75409

SOME EXPERIMENTS WITH INSULATED STRUCTURES

By Richard Rosecrans, Aldie E. Johnson, Jr.,
and William M. Bland, Jr.

Langley Aeronautical Laboratory

SUMMARY

Two methods of insulating structures, one for short-time use and the other for somewhat longer protection, were studied by radiant-heating tests and supersonic-wind-tunnel tests. Results of these tests indicated that effective temporary protection can be obtained with fairly light-weight structures; however, it is emphasized that care should be given to design details to prevent flutter of the insulation cover in some cases.

INTRODUCTION

One proposed method of coping with the problem of aerodynamic heating is to provide an insulating cover or radiation shield to reduce the amount of heat entering the structural airframe. In order to be most effective, such a covering must have high insulating value and as little weight and thickness as possible. If it is necessary to protect the basic structure for only a short time, a simple, thin, lightweight system can be employed. For longer protection, a more elaborate method is necessary. Even the more extensive insulating systems permit heat to get through eventually; therefore, for very long time exposure to high temperatures, cooling must be provided. This paper discusses the first two classes - those which do not require cooling.

TESTS

Experiments have been conducted upon several devices which appeared likely to afford significant protection.

Solid Protective Covering

One short-time method involved a combination of insulation and heat storage. If the basic structure is of lightweight material incapable of

withstanding high temperatures, it can be protected for a short period by covering it with one or more layers of heavier material which can tolerate high temperature. Much of the heat which enters the structure during the first few seconds is stored in the covering material. Heat flow to the inner structure is delayed partly by the conductivity of the material and partly by thermal resistance of the joints. If the need for protection ends by the time a damaging amount of heat enters the basic structure, as it might in the case of a short-range missile, the objective is accomplished. Such a method was used to protect some tapered fins. With no protection, the leading edge of a magnesium fin melted in less than 2 seconds. With the leading edge covered with one layer of 0.008-inch-thick glass cloth and one layer of 0.031 Inconel, the temperature of the magnesium had risen to less than 125° F in 2 seconds. A heavier covering, in which one layer covered the entire fin and a second layer covered only the leading edge, was even more effective. Figure 1 shows that, while the temperature of the outer layer of Inconel rose rapidly and reached 1,750° F in 5 seconds, the temperature of the inner magnesium structure had risen to only 90° F in 2 seconds, when the unprotected fin had failed, and to less than 300° F in 5 seconds. During the first 2 seconds, less than 5 percent of the heat which entered the leading edge penetrated to the load-carrying structure.

Motion pictures of the test showed that, soon after the fin entered the jet stream, the cover became red near midspan, where the temperature of the gases from the jet were highest. Because the thickness of the covering varied between the leading and trailing sections, the temperature of the cover along the chord was fairly uniform. After 8.4 seconds, the jet pierced the protective cover and the fin failed almost immediately.

Double-Wall Construction

Two insulating configurations (fig. 2), designed to protect the airframe over a longer period of heating, were investigated. One was a single-faced, corrugated-core sandwich of Inconel X; the other was a stainless-steel honeycomb sandwich. The exposed surface was supported by the longitudinal corrugations in one case and by the core and inner face of the sandwich in the other; in both cases the sandwich was separated from the load-carrying structure by either bulk insulation or an air gap. Corrugated panels were constructed with and without bulk insulation; all honeycomb panels were made with only an air gap. Because of the very light weight of these panels, the possibility of flutter and failure existed; consequently, their structural integrity in a supersonic airstream, as well as their insulating qualities, was determined.

Corrugated panels.- The corrugated panels were designed and fabricated by the Bell Aircraft Corporation. Both the surface and corrugations were

of 0.005 Inconel X. A one-quarter-inch steel plate constituted the base or load-carrying structure. Retaining straps held the panel against the supports, and provision was made for expansion in both directions. Thermocouples on the under side of the outer face and at several locations in the interior measured the temperature during a test.

In order to determine the insulating capacity of this type of construction, the outer surface was heated, in a static test, at approximately 1/2 Btu/sq ft/sec until it reached 1,500° F, after which the skin was maintained at that temperature for about 50 seconds. Temperature histories are shown in figure 3. The temperature of the exposed surface rose at a constant rate for about 70 seconds and then was held steady until 2 minutes had elapsed from the start of the test. The temperature of the inner surface of the corrugation lagged behind that of the exposed surface and finally reached an equilibrium temperature about 150° F lower than that of the outer face. The combination of the radiation shield and bulk insulation protected the load-carrying structure so that it experienced only a negligible temperature rise.

Additional tests were made in a blowdown jet at a Mach number of 1.4, sea-level static pressure, and a stagnation temperature of 600° F. In some of the tests, added heat was supplied by a quartz-lamp radiator which faced the panel from just outside the jet stream and raised the surface temperature to nearly 1,000° F in some cases. Temperature histories for a test on a corrugated panel without bulk insulation are shown in figure 4. Surface temperatures of about 800° F were reached. The temperature of the inner part of the corrugation lagged several hundred degrees behind that of the exposed surface and the load-carrying structure experienced only a small temperature rise. The data terminate after 10 seconds because of the flutter and failure of the corrugated cover. Aerodynamic heating was augmented by the radiant heater and the combined effect of the heating and the air loads caused flutter to begin about 10 seconds after the test began. The panel was mounted as an extension of the tunnel wall and was divided into three bays by expansion joints. From motion pictures, flutter was first observed in the downstream bay. It spread quickly to the other bays and the panel was destroyed after about 12 seconds. High-speed pictures taken at 640 frames per second show the very high frequency of the flutter and indicate that the mode shape was much like that of corrugated metal. The corrugations were in the same direction as those of the supporting corrugations of the panel but appeared to have a longer wave length by a factor of perhaps two or three. Not all the tests of corrugated panels ended in this manner. A similar configuration, but with an improved design of the edges, survived the same test. However, the result emphasizes the need for careful experimental checking of such designs, at least until more adequate theoretical methods are available.

[redacted]

Honeycomb panels.- The honeycomb panels were fabricated of 0.005-inch-thick facing sheets brazed to both sides of a honeycomb core. All sandwich material was 17-7 PH stainless steel. The base or load-carrying structure was 1/8-inch-thick aluminum plate. The same type of static heating test was made on the honeycomb panels as on the corrugated panels. Temperature histories are shown in figure 5 for the outer and inner faces of the sandwich and for the base structure. The heating cycle is evident from the surface temperature and was very nearly the same as that for the corrugated panels. The inner-face temperature lagged behind and approached 1,250° F toward the end of the test. The aluminum base was heated to about 300° F, which is a higher temperature than that of the base plate behind the corrugated panel with bulk insulation, even when allowance is made for the difference in heat capacities of the two base structures. In the wind-tunnel tests, however, the bending stiffness of the honeycomb panels was sufficiently high to prevent flutter, and the only undesirable effect of the test was the pock-marked appearance of the outer surface. Thermal expansion of the heated skin caused the facing sheet to buckle over each cell of the honeycomb interior. This buckling reduced the smoothness of the aerodynamic surface but had the advantage of reducing the overall expansion of the panel.

DISCUSSION

Little difference in insulating value was found between the corrugated and honeycomb panels, so long as bulk insulation was not used between the sandwich and the base structure. The corrugated panels with bulk insulation were considerably better from an insulation standpoint than either type without it but, when bulk insulation was used, the protective covering was three times as thick as when it was omitted. The corrugated panels have certain advantages because they employ only one face; they can be fabricated by seam welding instead of brazing, which makes them easier to manufacture and, also, they can easily be bent around curved surfaces so long as the curvature is in only one direction. Similarly, the honeycomb panels have advantages because of their greater strength; they are considerably less susceptible to flutter and should require less supporting structure.

CONCLUDING REMARKS

These tests represent only a small effort in the field of insulated structures; many additional variations can be studied. Results so far indicate that effective short-time insulation can be achieved with fairly lightweight structures; however, it is emphasized that care should be given to design details in order to insure structural integrity.

[redacted]

ETHYLENE HOT-EXHAUST JET TEST

INCONEL-PROTECTED MAGNESIUM FIN

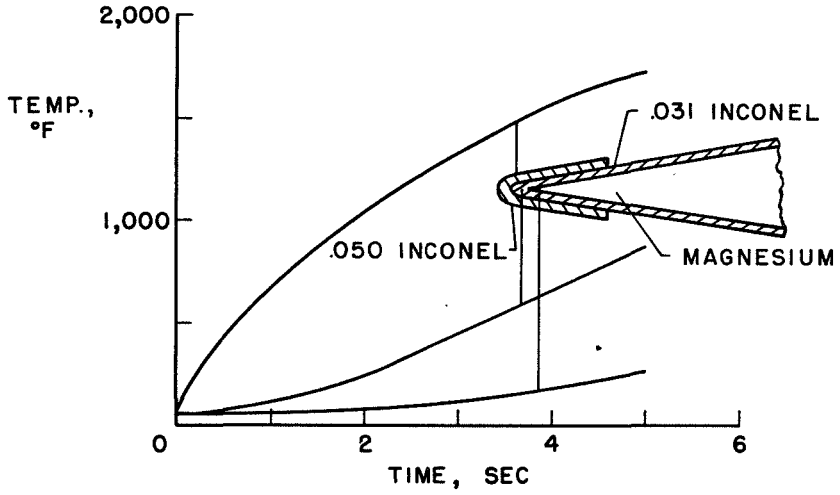


Figure 1

INSULATING PANELS

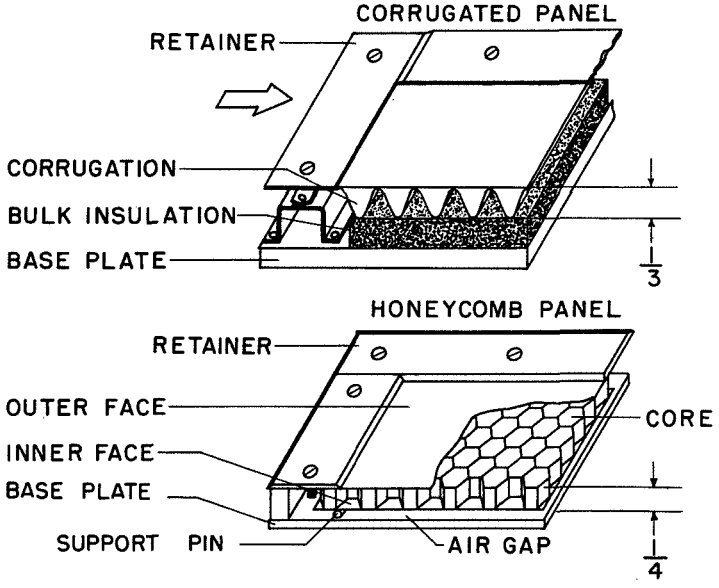


Figure 2



LABORATORY RADIANT-HEATING TEST
CORRUGATED PANEL

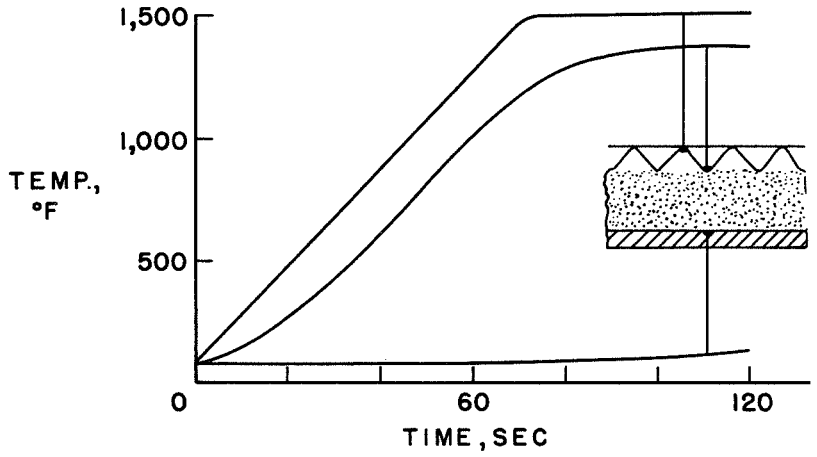


Figure 3

BLOWDOWN-JET TEST
CORRUGATED PANEL

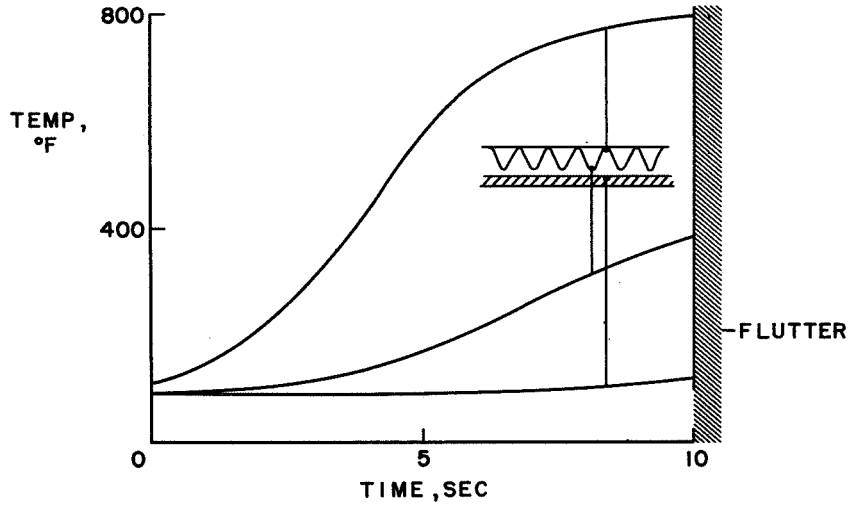


Figure 4



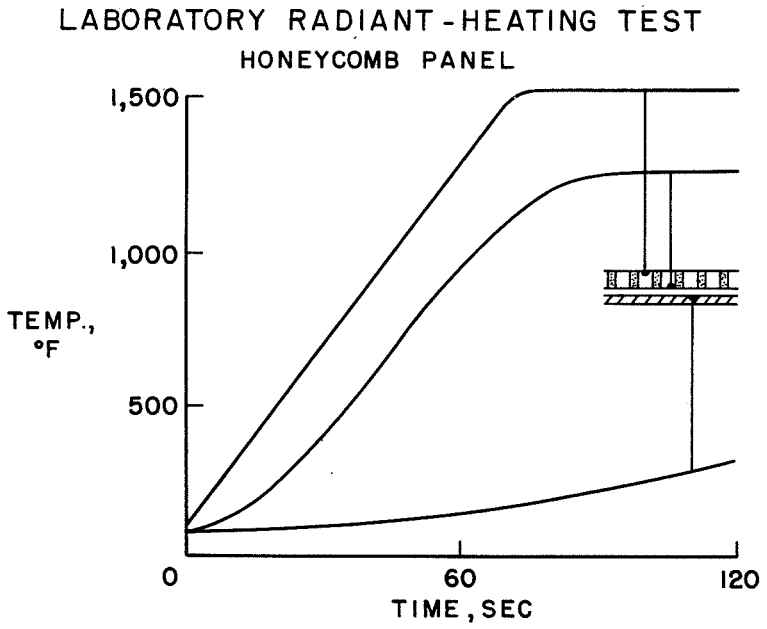

LABORATORY RADIANT-HEATING TEST
HONEYCOMB PANEL
1,500
1,000
500
0
TEMP., °F
60
120
TIME, SEC

Figure 5

N71-75410

F

SOME RESEARCH RESULTS ON SANDWICH STRUCTURES

By Melvin S. Anderson and Richard G. Updegraff

Langley Aeronautical Laboratory

SUMMARY

The results of compressive-buckling tests of steel sandwich plates are given, and the significant parameters which affect the strength of the plates are discussed. The various types of sandwich construction are shown to be comparable on a weight-strength basis with conventional high-strength aluminum-alloy construction.

INTRODUCTION

The use of high-density, heat-resistant materials in modern aircraft has served to reemphasize the need for lightweight methods of construction. One such method receiving wide attention is sandwich construction which permits almost full utilization of the strength of thin gages of materials. Success of this approach is to a large extent dependent upon advances in production techniques and practical engineering experience. For these reasons a number of sandwich configurations have evolved, some of which are shown in figure 1. The honeycomb sandwich has been produced by adhesive bonding, brazing, and welding techniques. In high-temperature materials there is considerable interest in the welding approach and attention has, therefore, been directed toward other configurations which are more amenable to welding. Representative of these configurations are the truss-core, tube-core, and web-core sandwiches also shown in figure 1. These configurations have the common characteristic that the core elements can be joined to the faces by welding along parallel longitudinal lines. Certain obvious differences exist between these configurations and the honeycomb; for example, they are more directional in their stiffness and strength properties. They require a heavier core to achieve comparable panel thicknesses, but the core carries direct loads and provides a high shear strength. The core also provides natural passages for the circulation of coolants in applications where this may be desirable. The behavior of the truss-core sandwich is typical of this group and is considered along with the honeycomb sandwich in this paper.

SYMBOLS

b	plate width
D	plate flexual stiffness per unit width
D_Q	plate shear stiffness per unit width
E	Young's modulus of elasticity
h	overall height of sandwich
k	plate-buckling coefficient
l	panel length
P_i	compressive load per unit width
t	plate-element thickness
η	plasticity reduction factor
θ	angle between face sheet and core element
μ	Poisson's ratio
σ	stress
σ_{cr}	buckling stress

Subscripts:

c	core
f	face sheet
1	upper face
2	lower face

EXPERIMENT

Honeycomb construction effectively increases the thickness of the sandwich plate which results in a high overall bending stiffness as compared with an equivalent-weight plate of solid material. At the same time, however, the light core tends to make a sandwich sensitive to concentrated loads and causes shearing deformations to play an important role in determining the stress that a sandwich plate can carry. Because of this effect, sandwich development has required considerable experimental work using special test techniques and fixtures.

Test Technique

A fixture that was found to be suitable for a simple test of the strength of a sandwich panel in compression is illustrated in figure 2. The panel is loaded on its ends by a testing machine, and the panel edges are alined by a fixture designed to give simple support. A cross-sectional view of the panel and fixture is shown in figure 3. The I-beam and knife edges prevent lateral deflection of the panel edges but permit rotation. They can be adjusted to accommodate panels of different thickness and width. Clearance between the fixture and the testing machine permits shortening of the panel without loading the fixture.

The sandwich plate shown in figure 2 has a honeycomb core. For this type of sandwich it was found necessary to reinforce the panel at the loaded ends to prevent end failures. The light areas of the test specimen are externally applied doubler plates which are adhesive-bonded to the panel. It is considered significant that in tests of truss-core sandwich no special end reinforcement was required. This is attributed to the higher shear strength of the core of this construction.

Test Results

Panels.- Test results for some honeycomb panels are compared in figure 4 with the buckling theory of reference 1. These panels varied in thickness from 1/4 inch to 3/4 inch with face-sheet thicknesses of 0.015 inch to 0.064 inch. The compressive buckling-stress coefficient is plotted as a function of a shear-flexibility parameter. Theory predicts a large loss in panel buckling strength as core shear flexibility increases. If the shear stiffness D_Q of the panel is large, the buckling-stress coefficient approaches the value of 4 which is associated with solid plates. Theory is capable of predicting the influence of the geometrical quantities which make up the shear-flexibility parameter as is illustrated by the open test points for both brazed and adhesive-bonded steel honeycomb panels. The core density associated with these points was

[redacted]

$8\frac{1}{2}$ lb/cu ft (1/4-inch cell with 0.002-inch foil) and 12 lb/cu ft (1/4-inch cell with 0.003-inch foil). However, when panels having a core density of $6\frac{3}{4}$ lb/cu ft (1/4-inch cell with 0.0015-inch foil) were tested, predicted strengths were not consistently obtained as indicated by the darkened test points. These low points are believed to be caused by the low shear strength associated with the lightest core. The influence of core shear strength is not included in buckling theory. The loss in buckling strength for these panels is much greater than the reduction in weight over a panel which had a heavier core but sustained the predicted load. Hence, on a weight-efficiency basis as well as from the standpoint of obtaining consistent and reliable results, these tests indicate that adhesive-bonded cores should have a density greater than $6\frac{3}{4}$ lb/cu ft. In the sandwiches with the heavier cores, the stresses in the face sheets varied up to 200,000 psi, the compressive yield stress of the material tested.

Beams.- Since the matter of core density is an important factor in determining the weight of honeycomb panels, further tests have been made in which sandwich panels were used as the compression covers of box beams in bending. Figure 5 is a photograph of one of the beams after a compression failure of the sandwich cover. Of the three beams tested to date, only the one having a sandwich with a core density of 12 lb/cu ft approached the load predicted by theory (14 percent less than theory). The remaining two beams had core densities of $8\frac{1}{2}$ and $6\frac{3}{4}$ lb/cu ft and failed at loads considerably less than the predicted ones. These results suggest that, to achieve adequate core shear strength, heavier cores may be required for a practical structure than for simple compression tests under more ideal conditions.

LOCAL BUCKLING OF TRUSS-CORE SANDWICHES

Plate-buckling theory has been applied to truss-core sandwich plates and the available test results indicate that the theory is again adequate. With the truss-core sandwich no problems with core shear stiffness or strength were encountered because of the higher core densities required to prevent local buckling of the individual plate elements of the sandwich configuration. The local buckling stress can be calculated with the aid of a diagram such as that shown in figure 6. By knowing the local buckling stress as well as the overall plate instability stress as a function of sandwich dimensions the proportions can be varied to obtain the most efficient sandwich for any given loading condition. In figure 6

[redacted]

the buckling coefficient for local instability of the sandwich configuration is plotted against the ratio of core-element thickness to face-sheet thickness over a range of values found to give efficient proportions. It should be noted that the core elements are of the same order of thickness as the face sheets in contrast to the foil in honeycomb cores which may be only a fraction of the thickness of the face sheets. Inasmuch as the sandwich is orthotropic, the buckling-stress coefficient is given for compression in both the longitudinal direction indicated by the upper curves and the transverse direction indicated by the lower curves. A lower strength is obtained for the transverse loading inasmuch as the face plates are subject to column failure between truss-panel points. In both cases, the buckling-stress coefficient is raised because of interference restraints caused by the triangular arrangement of the members. The values indicated in figure 6 have been substantiated by crippling tests on small specimens such as that shown in figure 7. This particular specimen is of welded construction, 17-7 PH stainless steel, and sustained a stress of 185,000 psi at failure.

By using figure 6, plate proportions can be adjusted so that local buckling of the sandwich elements is equal to or greater than the overall plate-buckling stress. For example, if it is desired to achieve a longitudinal-compression stress of 180,000 psi (a typical value for the yield stress of high-strength steel), the proportions given on the left-hand portion of figure 6 meet the requirements; also given is the critical compressive stress in the transverse direction which is almost two-thirds the value for the longitudinal direction. The overall height of the sandwich, indicated by the ratio $h/t_f = 15$, is such that a very favorable weight efficiency is obtained for panels of this sandwich loaded in edge compression.

EFFICIENCY OF SANDWICH CONSTRUCTION

The weight of unstiffened plates, sandwiches, and stiffened panels subjected to longitudinal-compressive stress is plotted as a function of the appropriate structural index in figure 8. The weight of these structures can be compared at identical values of the structural index inasmuch as the plate width b and panel length l are simply the support spacing in an actual structure. For this particular plot, the units are such that, if the ordinate is multiplied by the support spacing, the weight is given directly in pounds per square foot of surface. For example, at an ordinate value of 0.2, a plate 10 inches wide would weigh 0.2 times 10 (or 2 lb/sq ft).

The weight efficiency of the honeycomb-sandwich construction taken from reference 2 has been calculated by assuming that a core density of 10 lb/cu ft was necessary to obtain the stresses indicated by theory.

[redacted]

The most efficient proportions for the truss-core sandwich involve core densities varying from 30 to 50 lb/cu ft. Despite the greater core density for the truss-core sandwich, there is little difference in weight between the two types of sandwich construction; with the honeycomb sandwich more efficient at low values of the structural index and because of the load-carrying core, the truss-core sandwich is more efficient at the higher values. Also shown in figure 8 are the weight-efficiency curves for high-strength aluminum-alloy plates that would occur in multispar construction and for conventional stiffened-panel construction. It appears that under compressive loadings sandwich construction in steel is comparable in weight to efficient conventional construction in aluminum alloy.

THERMAL STRESSES IN SANDWICH PLATES

A consideration of the response of sandwich plates to transient heating indicates that certain adjustments to sandwich proportions may be desirable to minimize the effect of thermal stresses. For example, in figure 9 are shown the results of thermal-stress calculations for a typical sandwich which is heated on one face to 800° F at a rate of 8° F per second. Heat is transferred to the other face by conduction and radiation. The sandwich is assumed to be constrained to remain flat, and the resulting maximum thermal stress in the two faces is plotted against the thickness ratio of the two faces. This ratio was varied while holding the total weight of the sandwich constant.

For equal-thickness faces, the tension stress in the cooler face is equal to the compression stress in the heated face: As the thickness of the cooler face is decreased, relatively little change occurs in the tension stress while the compression stress in the heated face is reduced considerably. This favorable alteration in the thermal stresses is due partially to a reduction in the maximum temperature difference between the two faces and partially to the change in the relative areas of the faces. The decrease in compressive thermal stress permits an increase in load stress to be carried before buckling of the sandwich. In addition, the more even distribution of temperature through the thickness of the sandwich permits the absorption of a greater quantity of heat before the hotter face exceeds its allowable temperature.

CONCLUDING REMARKS

A few of the factors which affect the design of any particular sandwich configuration have been presented. For honeycomb construction, the core should be of sufficient stiffness to give a high buckling coefficient

 [redacted]

in order to obtain a minimum-weight sandwich. In addition, the core should be of adequate strength to prevent premature core failures and insure reliable results. For sandwiches such as the truss core, tube core, or web core, shear strength or stiffness is generally no problem; but the main consideration is proportioning the sandwich so that overall plate instability is not preceded by local buckling or crippling. Sandwiches of this type can be proportioned so that they compare favorably with honeycomb construction on a weight-strength basis. For elevated-temperature applications, a sandwich with a thicker outer face appears better able to cope with the effects of heating and restrained expansion.

REFERENCES

1. Seide, Paul, and Stowell, Elbridge Z.: Elastic and Plastic Buckling of Simply Supported Solid-Core Sandwich Plates in Compression. NACA Rep. 967, 1950. (Supersedes NACA TN 1822.)

2. Johnson, Aldie E., Jr., and Semonian, Joseph W.: A Study of the Efficiency of High-Strength, Steel, Cellular-Core Sandwich Plates in Compression. NACA TN 3751, 1956.

SANDWICH CONFIGURATIONS

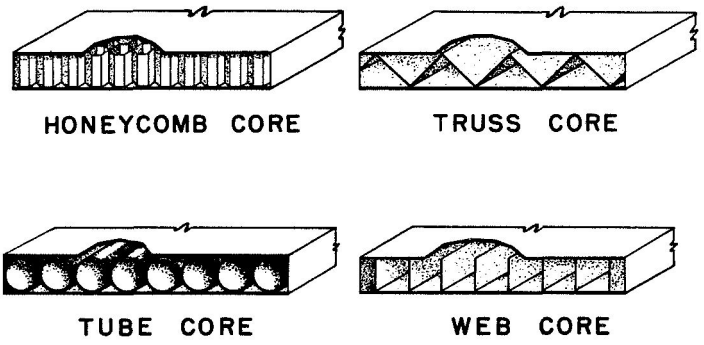


Figure 1

TEST SETUP

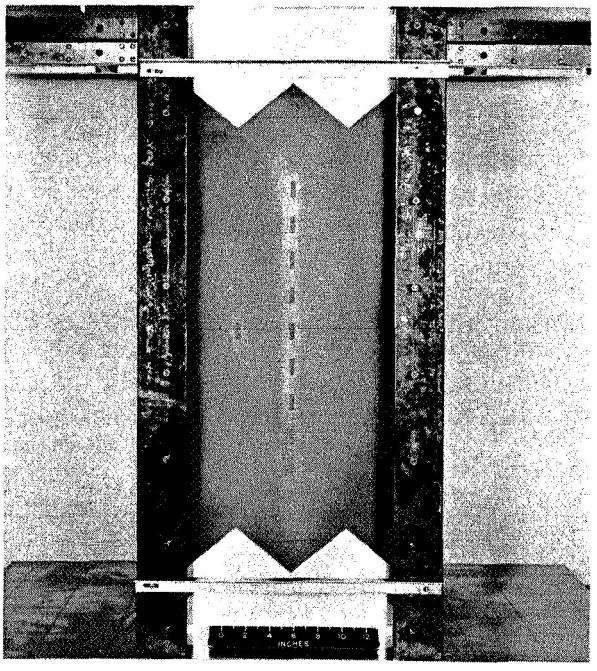


Figure 2

L-97141.1

CROSS SECTION OF FIXTURE AND SPECIMEN

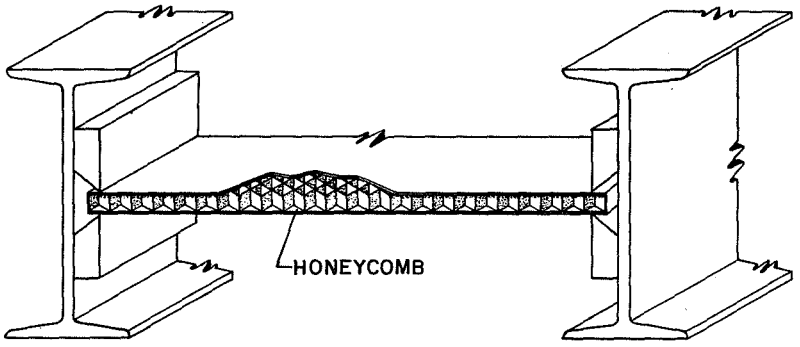


Figure 3

BUCKLING COEFFICIENTS FOR SANDWICH PLATES

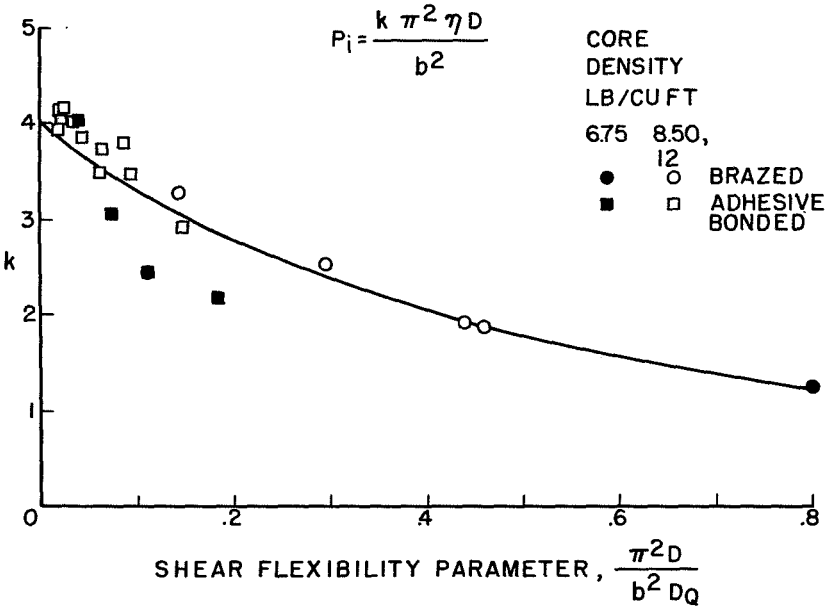


Figure 4

SANDWICH BOX BEAM AFTER FAILURE

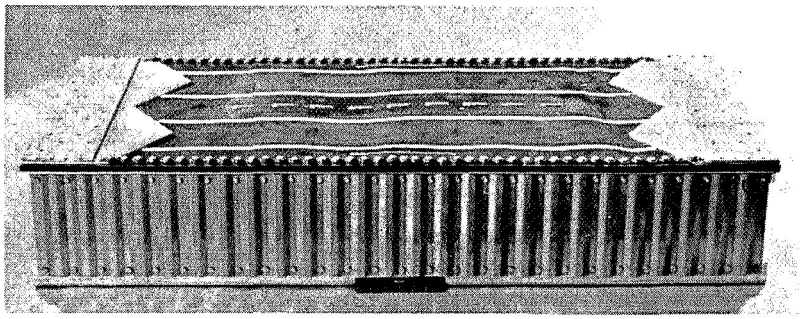


Figure 5 L-57-650.1

BUCKLING OF TRUSS-CORE SANDWICH ELEMENTS

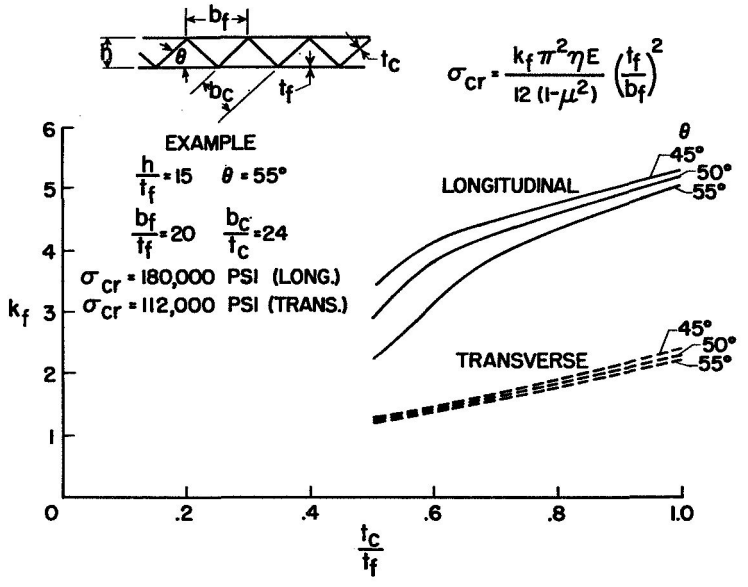


Figure 6

CRIPPLING SPECIMEN

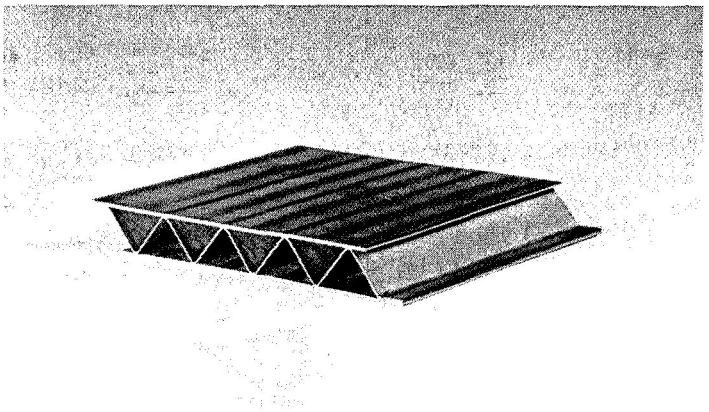


Figure 7 L-57-95.1

WEIGHT-STRENGTH CURVES

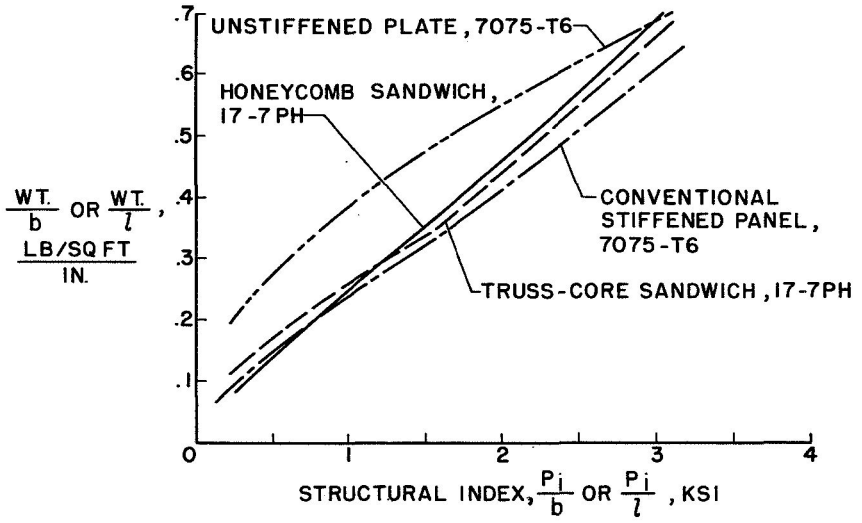


Figure 8

EFFECT OF SANDWICH DIMENSIONS ON THERMAL STRESSES

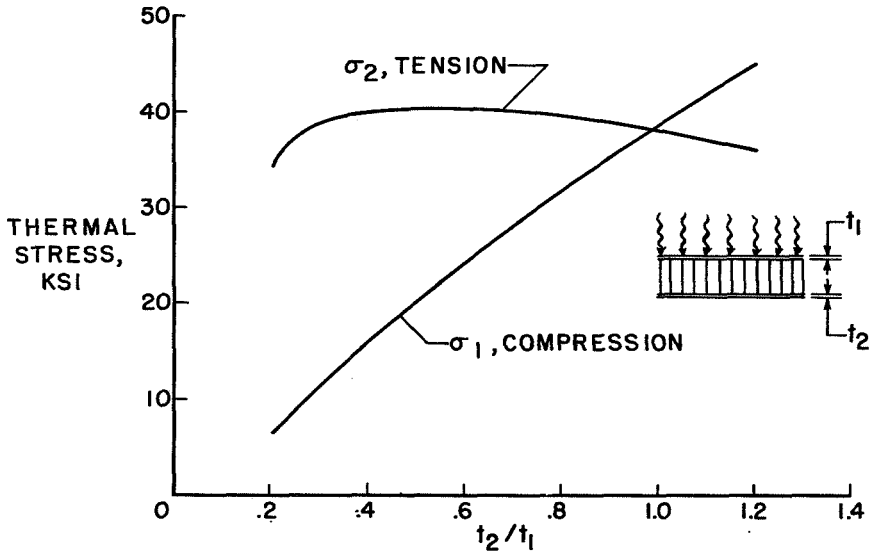


Figure 9

N71-75411

MATHAUSER, BERKOVITS & STEIN

RECENT RESEARCH ON THE CREEP OF AIRFRAME COMPONENTS

By Eldon E. Mathauser, Avraham Berkovits,
and Bland A. Stein

Langley Aeronautical Laboratory

SUMMARY

The results of recent research of the National Advisory Committee for Aeronautics on the creep of airframe components at elevated temperatures are summarized. Experimental lifetime data from creep tests of stainless-steel plates and aluminum-alloy unstiffened circular cylinders are presented and compared with results predicted from isochronous stress-strain curves. The results of a study to determine the magnitude of creep strains that produce significant structural deformations are included. A comparison of structural weight determined from assumed strength and creep criteria is made to establish temperature ranges in which creep is expected to influence structural design for various materials.

INTRODUCTION

Many studies have been made at the National Advisory Committee for Aeronautics during the past few years to obtain basic knowledge of the creep behavior of structural elements at elevated temperatures. These studies have ranged from analytical and experimental investigations of simple structural elements such as columns and plates (refs. 1 to 3) to the development of a variational theorem (ref. 4) suitable for application in many structural creep problems. Studies have also been made to establish approximate methods (for example, ref. 3) for predicting creep collapse of structural components. This paper presents comparisons between experimental and predicted lifetime results for stainless-steel plates and for aluminum-alloy unstiffened circular cylinders. The results of an analysis to determine the magnitude of creep strains that produce significant structural deformations are given. Temperature ranges in which creep is expected to influence aircraft structural design are indicated for various materials.

SYMBOLS

b	width, in.
E_s	secant modulus, ksi
E_t	tangent modulus, ksi
g	acceleration due to gravity, ft/sec^2
k	constant
r	radius, in.
t	thickness, in.
σ_{cr}	critical (buckling) stress, ksi
σ_{cy}	0.2-percent-offset compressive yield stress, ksi
$\bar{\sigma}_f$	average failure stress, ksi

DETERMINATION OF CREEP COLLAPSE

The approximate methods that have been investigated for predicting creep collapse of structural elements are based on the use of isochronous stress-strain curves in conjunction with methods established for predicting maximum strength. An example of isochronous stress-strain curves is given in figure 1. The dashed line indicates the material compressive stress-strain curve for 17-7 PH stainless-steel sheet (condition TH 1,050) at 800° F. The solid lines, designated as isochronous stress-strain curves, indicate the strain produced on application of a given stress plus the creep strain obtained at that stress for the various times. Curves such as these can be obtained by cross plotting compressive creep curves to give stress as a function of strain for different times. The isochronous stress-strain curves shown in figure 1 were obtained from compressive creep tests of the stainless-steel sheet at 800° F. The tick marks indicate the 0.2-percent-offset compressive yield stresses.

Plates

The use of isochronous stress-strain curves for the prediction of creep lifetime of plates will be considered first. A comparison between predicted and experimental lifetimes is shown in figure 2. Applied stress

is plotted against lifetime defined as collapse time for 17-7 PH stainless-steel plates (condition TH 1,050) at 800° F. The symbols indicate compressive-creep-test results from V-groove edge-supported plates for width-thickness ratios ranging from 15 to 60. The solid lines indicate plate life predicted from the following equation:

$$\bar{\sigma}_f = 1.60\sqrt{E_s \sigma_{cy}}\,\frac{t}{b} \tag{1}$$

where $\bar{\sigma}_f$ is the average applied stress to produce creep collapse of the plate, E_s is the secant modulus associated with $\bar{\sigma}_f$, σ_{cy} is the compressive yield stress, and t/b is the plate thickness-width ratio. Equation (1) gives maximum strength of V-groove edge-supported plates at elevated temperatures (ref. 3), if the material parameter $\sqrt{E_s \sigma_{cy}}$ is evaluated from the material compressive stress-strain curve. Evaluation of the material parameter from isochronous compressive stress-strain curves, in general, gives a satisfactory approximation for plate lifetime. This equation has been used to predict creep lifetime for both 2024-T3 and 7075-T6 aluminum-alloy plates. Similar agreement between experimental and predicted results was obtained.

Unstiffened Circular Cylinders

Prediction of creep lifetime of unstiffened circular cylinders using isochronous stress-strain curves will now be considered. In figure 3, bending moment is plotted against lifetime defined as collapse time for 5052-0 aluminum-alloy cylinders at 500° F. The symbols indicate experimental results obtained from reference 5 for radius-thickness ratios ranging from 125 to 250. Predicted lifetimes indicated by the curves were obtained by substituting materials data from isochronous stress-strain curves into the following relation:

$$\sigma_{cr} = k\sqrt{E_s E_t}\,\frac{t}{r} \tag{2}$$

where σ_{cr} is the critical or buckling stress, k is a constant assumed to be 0.6, E_s and E_t are secant and tangent moduli, respectively, and t/r is the cylinder thickness-radius ratio. The predicted buckling stresses were then converted to bending moments by using elementary beam theory. The isochronous stress-strain curves required for this study were obtained from compressive creep tests of 5052-0 aluminum-alloy sheet at 500° F. The experimental results shown in figure 3 are the only data available on the lifetime of cylinders subjected to bending. Although

the predictions are in good agreement with the experimental data, additional studies will be needed to determine whether equation (2) will predict lifetime satisfactorily for cylinders of other materials and to establish the appropriate value of k.

CREEP DEFLECTIONS

The results of the studies of creep of plates and cylinders and of other structural components investigated previously indicate that lifetime defined by collapse can be estimated in general by substituting material data obtained from isochronous compressive stress-strain curves into appropriate relations that define maximum strength of the structural elements. For some types of structures, it is realized that large creep deformations can be obtained in a fraction of the actual collapse time. Such deformations in many cases may determine the useful life of the structure. A study was made accordingly to determine the range of values for creep strain that would be expected to govern design of structures where deformation rather than collapse would be of primary interest.

The structure considered for this study was a constant-stress wing in which the stresses are assumed to be of the same magnitude at all stations along the wing. The deflections of a constant-stress wing are determined from the product of wing configuration and the strains produced by the applied stresses. The deflections that would be produced by creep over a complete range of stress for stainless-steel wings are shown in figure 4. In this figure, stress is plotted against the ratio of wing deflection produced by creep to wing deflection produced by load for 17-7 PH stainless steel at 800° F. Load deflection is defined as the static deflection of the wing obtained immediately upon application of any stress. At a stress of 50 ksi, for example, the creep deflection of the wing in 1 hour is equal to 0.1 of the static or load deflection obtained immediately upon application of the stress. If this stress is applied for approximately 300 hours, the creep deflection increases to a value equal to the static deflection. A shaded area is indicated for the range of creep to load deflection ratios from 0.1 to 1.0. This area is assumed to define the region of interest for structures such as aircraft wings. Creep deflections to the left of the shaded area would be practically negligible; whereas, to the right, the creep deflections would undoubtedly be considered excessive for most structural applications.

Creep strains that are associated with the range of deflection ratios shown in figure 4 are indicated in figure 5. The solid curves have been reproduced from figure 4. The dashed curves indicate creep strains produced in the specified times for the range of stresses shown. Note that creep strains of approximately 0.0002 to 0.002 are associated with ratios

of creep to load deflections ranging from 0.1 to 1.0. These results apply to bending deflections of any constant-stress wing regardless of structural configuration because the ratio of creep deflection to load deflection is determined from the ratio of creep strain to load strain.

This method of analysis which is used to determine the range of creep strains that are of interest for structures subjected to bending was applied to two other materials: 2024-T3 aluminum alloy at 400° F and Inconel X at 1,350° F. The results for the 2024-T3 aluminum alloy are shown in figure 6, and the results for Inconel X are shown in figure 7. For both materials approximately the same range of values of creep strain from 0.0002 to 0.002 was obtained for ratios of creep to load deflections from 0.1 to 1.0.

TEMPERATURE RANGES FOR CREEP

Consideration will now be given to the determination of temperature ranges in which creep will be expected to influence structural design for various materials. These temperature ranges are determined by comparing structural weight required for strength with the weight required for creep at different temperatures. The results obtained from this analysis for stainless steel are presented in figure 8. The required weight of a tensile member in arbitrary units is plotted against temperature for 17-7 PH stainless steel. The solid line indicates the weight required for strength based on ultimate load after 1,000 hours exposure to temperature. Ultimate load is assumed to be 3.75 times the 1 g load. The dashed curves indicate weight required for the three different creep criteria for 1,000 hours at 1 g load; namely, creep strains of 0.0002 and 0.002 and creep rupture.

The dotted curve for 0.0002 creep strain in figure 8 indicates that the tensile member can be designed on the basis of strength up to 650° F. Above 650° F, the weight of the tensile member would increase very rapidly in order not to exceed 0.0002 creep strain. The criterion of 0.002 creep strain would govern the design above 825° F. Above 825° F, significant deflections would be expected to occur in structures subjected to bending as discussed previously. The region between the curve for 0.002 creep strain and the curve for rupture defines the temperature range where creep would be a very important factor in structural design for this material. The region between the two creep-strain lines may be considered to be the temperature range in which creep strains become perceptible and gradually increase to a magnitude that produces significant structural deformations. It is of interest to note that design on the basis of a given creep strain requires a very large increase in weight for small increases in temperature. It appears that it will be more feasible to convert to a higher strength material than to add weight

[redacted]

in order not to exceed a given value of creep strain. If other creep and strength criteria are considered, the position of the creep lines is shifted relative to the strength curve; however, the temperature ranges defined by the distance between the various creep lines remain essentially constant.

This method of analysis of weight required for strength and creep to determine temperature ranges in which creep will be a design consideration was applied to two other materials which are shown in figure 9. The materials considered are 2024-T3 aluminum alloy, 17-7 PH stainless steel and Inconel X. The solid lines indicate the weight required for strength based on ultimate load. The shaded regions define the temperature range for each material where creep may be an important factor in structural design. The width of the shaded regions for each material was established by determining required weight for creep on the basis of several different creep criteria. These results indicate that creep problems will be restricted to a rather narrow range of temperatures for each material and that creep does not become a design consideration until temperatures are reached where the strength of the material deteriorates rapidly. Note that the weight required for creep increases very rapidly with small increases in temperature for all materials considered. It appears that, whenever a temperature is reached where creep is a design consideration, less structural weight will be required by converting to a higher strength material than by designing for creep with the original material. It is realized that conversion to a higher strength material introduces many new problems such as changes in production methods and consideration of availability and strategic importance of the higher strength material. Because of such factors, it is anticipated that the weight of some structural components will be increased to account for material creep rather than converting to a higher strength material.

CONCLUDING REMARKS

The results presented indicate that material creep will influence structural design over a rather narrow range of temperatures for each structural material. In this temperature range, lifetime or collapse time can be estimated satisfactorily for structural elements by using isochronous stress-strain curves in conjunction with established methods for predicting maximum strength. If useful life is determined by deflections rather than collapse, the simplified analysis of creep deflection of constant-stress wings indicates that creep strains ranging from approximately 0.0002 to 0.002 define the region of interest for structures subjected to bending.

[redacted]

[redacted]

REFERENCES

1. Libove, Charles: Creep-Buckling Analysis of Rectangular-Section Columns. NACA TN 2956, 1953.

2. Mathauser, Eldon E., and Brooks, William A., Jr.: An Investigation of the Creep Lifetime of 75S-T6 Aluminum-Alloy Columns. NACA TN 3204, 1954.

3. Mathauser, Eldon E., and Deveikis, William D.: Investigation of the Compressive Strength and Creep Lifetime of 2024-T3 Aluminum-Alloy Plates at Elevated Temperatures. NACA TN 3552, 1956. (Supersedes NACA RM L55E11b.)

4. Sanders, J. Lyell, Jr., McComb, Harvey G., Jr., and Schlechte, Floyd R.: A Variational Theorem for Creep with Applications to Plates and Columns. NACA TN 4003, 1957. (Prospective NACA paper.)

5. Hoff, N. J., Erickson, Burton, et al.: Creep Bending and Buckling of Thin Circular Cylindrical Shells. PIBAL Rep. No. 355 (Contract Nos. Naw-6392 and Naw-6447), Polytechnic Inst. Brooklyn, July 1956.

401

[redacted]

[redacted]

[redacted]

COMPRESSIVE STRESS-STRAIN CURVES
17-7 PH STAINLESS STEEL; 800° F

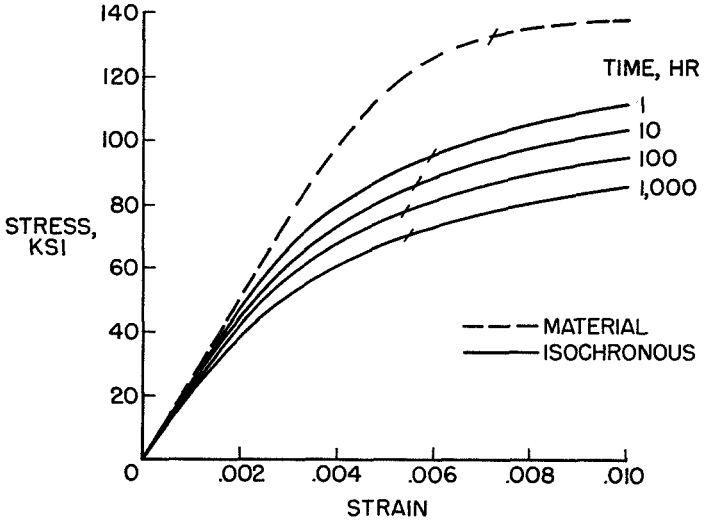
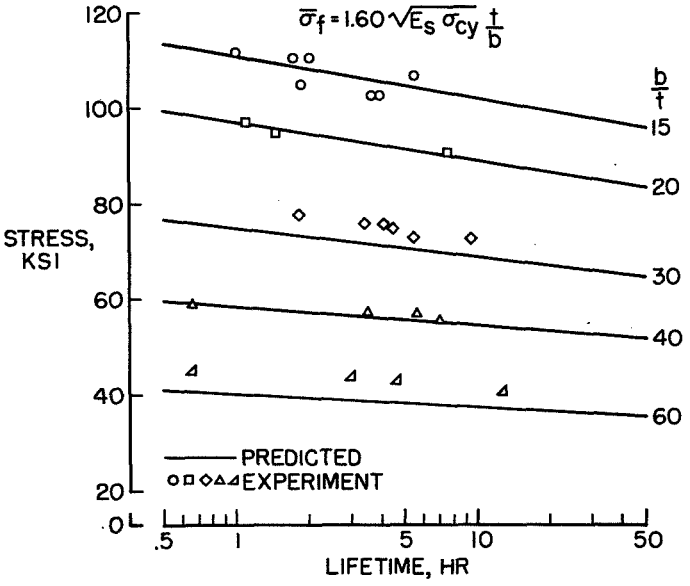


Figure 1

CREEP LIFETIME OF PLATES
17-7 PH STAINLESS STEEL; 800° F



402 [redacted] Figure 2

[redacted]

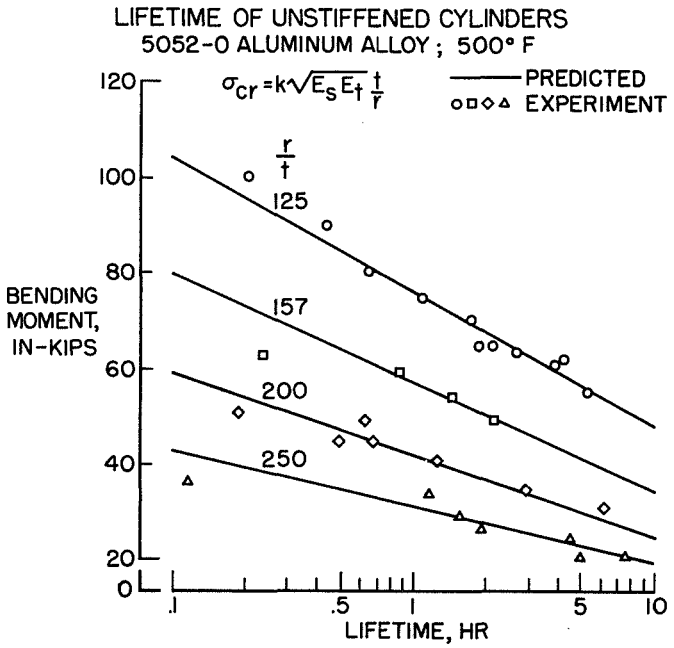


Figure 3

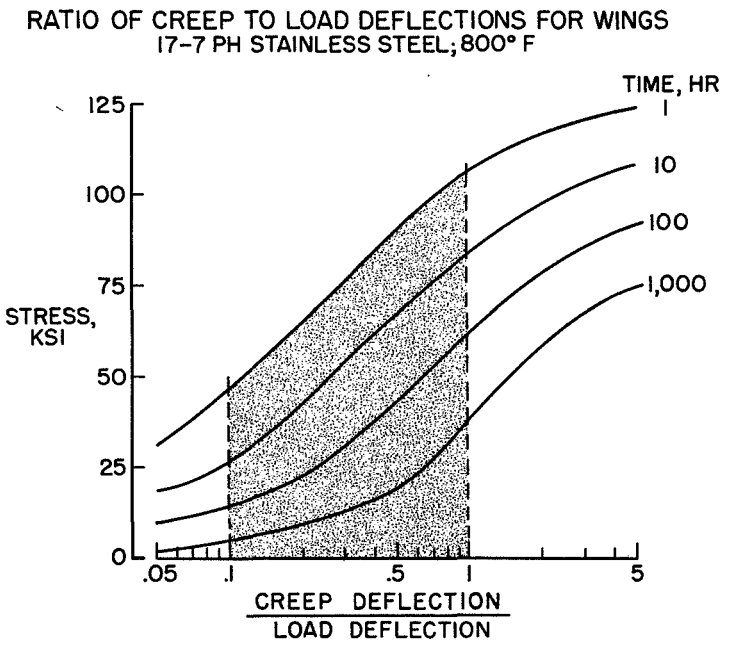


Figure 4

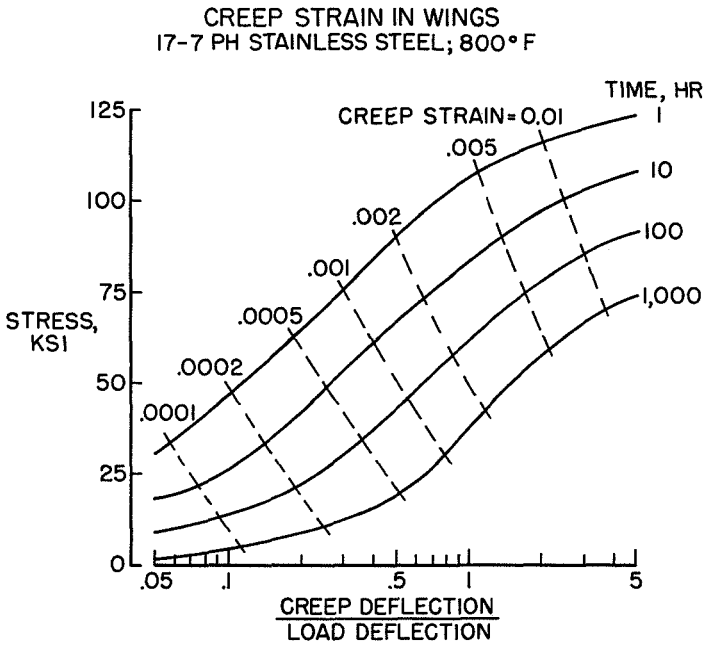
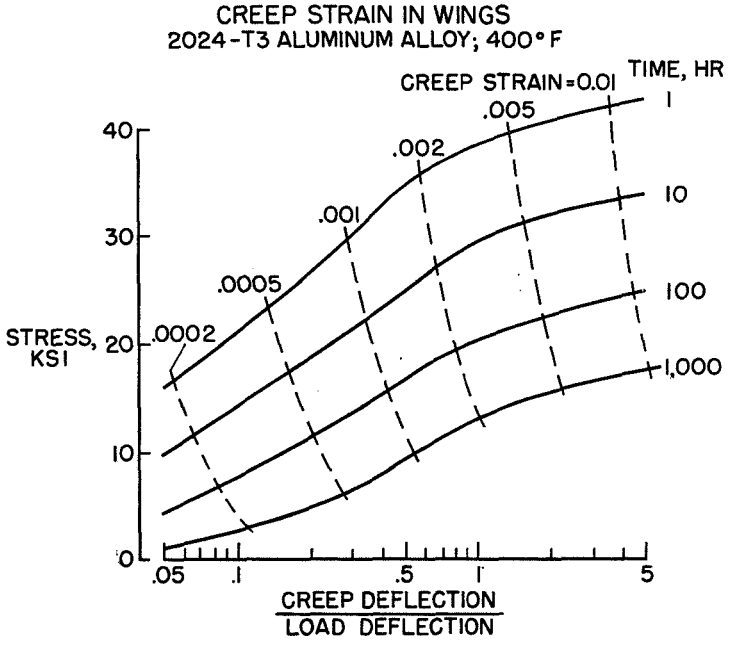


Figure 5



404

Figure 6

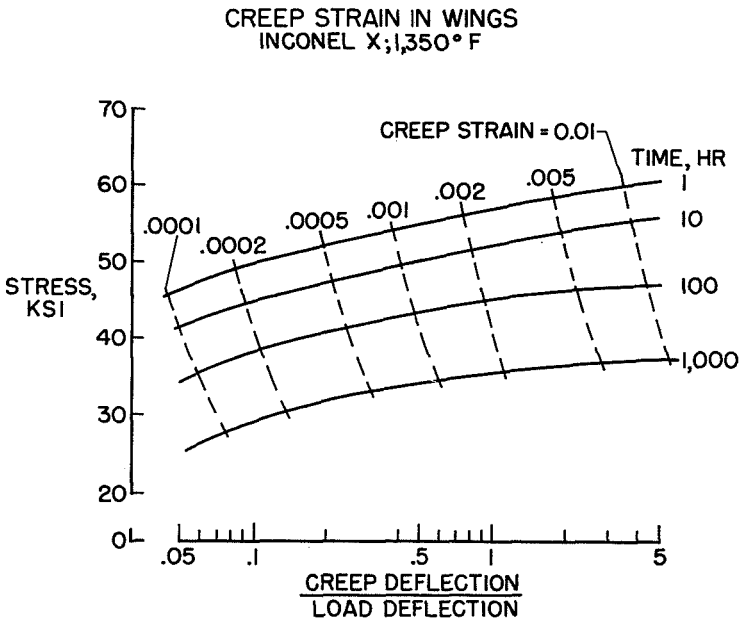


Figure 7

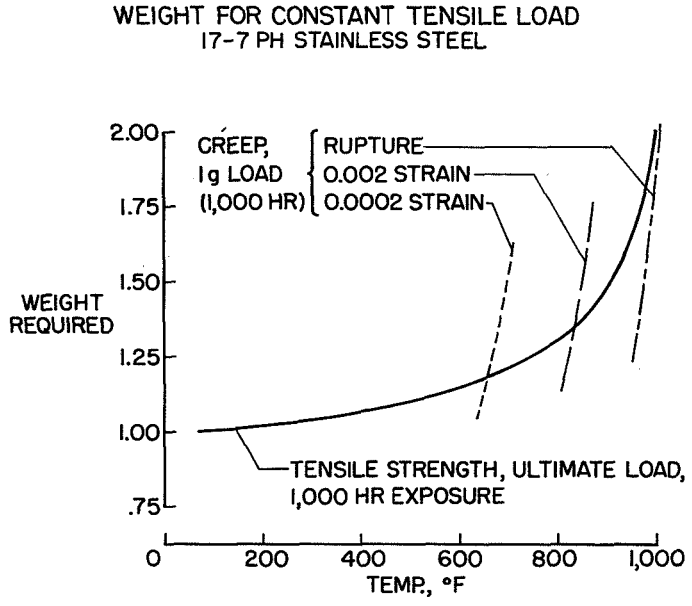


Figure 8

TEMPERATURE RANGES FOR CREEP

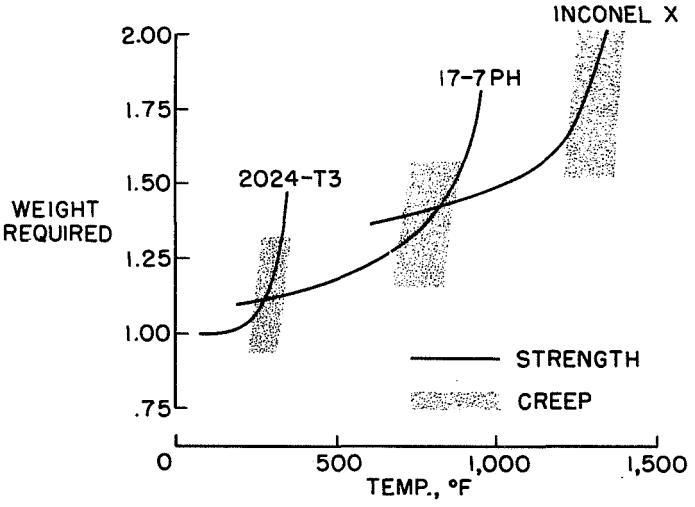


Figure 9

25F

N71-75412

A RELATION BETWEEN STRESS, STRAIN RATE, TIME, AND TEMPERATURE FOR METALS AT ELEVATED TEMPERATURES

By Elbridge Z. Stowell and George J. Heimerl

Langley Aeronautical Laboratory

SUMMARY

A relation between stress, strain rate, time, and temperature is suggested to account for the behavior of polycrystalline metals at elevated temperatures. The metal is assumed to have the basic properties of elasticity, thermal expansion, and viscosity. An appropriate combination of these three properties has been shown to account fairly well for the steady creep rate, time to creep rupture, stress-strain curves, and rapid-heating curves for 7075-T6 aluminum alloy. Similar calculations made for low-carbon steels show good correlation between ultimate tensile strength, time for creep rupture, and the steady creep rates. In the case of a complex alloy like Inconel X, fair correlation is also obtained provided one of the constants in the relation is permitted a slow variation with temperature.

INTRODUCTION

The need for knowledge of the behavior of metals at elevated temperatures is constantly becoming more and more important as flight speeds increase and as the effects of aerodynamic heating become more pronounced. Information is needed concerning -

(1) The creep of metals at these elevated temperatures

(2) The time at which rupture can be expected if the creep is allowed to continue

(3) The stress-strain characteristics at some particular temperature and strain rate

(4) The behavior of the metal when heated rapidly up to some high temperature

Evidently the job of providing this information would call for a great deal of testing, and it would be a useful achievement if some method of



calculation could be found which would simplify the task. Such a method follows from the relation between stress, strain rate, and temperature proposed in this paper.

SYMBOLS

ϵ	strain
$\dot{\epsilon}$	strain rate, per hr
t	time, hr
σ	stress, ksi
E	Young's modulus, ksi
α	linear expansion coefficient, per ^{o}K
T	temperature, ^{o}K unless otherwise indicated
s	constant, per hr per ^{o}K
ΔH	activation energy for creep, cal per mole
R	gas constant, taken as 2 cal per mole per ^{o}K
σ_o	constant, ksi
τ	time to rupture, hr
k_1, k_2	constants

STATEMENT OF THE RELATION

The strain rate $\frac{d\epsilon}{dt}$ at the absolute temperature T and the stress σ may be stated as follows:

$$\frac{d\epsilon}{dt} = \frac{d}{dt}\left(\frac{\sigma}{E}\right) + \alpha \frac{dT}{dt} + 2sTe^{-\Delta H/RT} \sinh \frac{\sigma}{\sigma_o} \qquad (1)$$

The first term to the right of the equal sign gives the contribution to the strain rate due to a change in stress σ; E is Young's modulus,



which is considered to be known as a function of temperature. The middle term gives the contribution due to a possible thermal expansion or contraction; α, the linear expansion coefficient, is assumed known as a function of the temperature. The last term on the right gives the contribution due to viscous flow. The exponential term, which describes the usual effects of temperature on viscous materials, contains ΔH, the constant activation energy for creep of the material, and R, the gas constant. The remaining constants in the viscous term are s and σ_o. The relation (eq. (1)) holds only for temperatures high enough for this viscous term to have an appreciable value, that is, for temperatures higher than about one-half the melting point.

Equation (1) may be integrated in various ways to provide information on such properties as steady creep, rupture time, stress-strain relations, and the effects of rapid heating. For example, at constant stress and temperature, $\frac{d\sigma}{dt} = \frac{dT}{dt} = 0$, and the relation (eq. (1)) becomes simply the equation for steady creep. If the creep is allowed to continue without interruption, the material will rupture in a time τ given by the relation $\tau \frac{d\epsilon}{dt} = \text{Constant}$. The stress-strain curve at any constant temperature T is obtained by setting the strain rate equal to the known constant testing rate and then solving the resulting equation for σ $\left(\text{with } \frac{dT}{dt} = 0\right)$ as a function of the time. And finally, if the material is held under a constant stress σ and heated rapidly, the resulting strain is found by integrating the expression $\left(\text{with } \frac{d\sigma}{dt} = 0\right)$ with respect to time.

The details of such applications to one material, 7075-T6 aluminum alloy, are given in reference 1.

APPLICATIONS

Creep and Rupture Parameters

In recent years, various empirical and semiempirical temperature parameters have been proposed for the creep of metals. Two of these parameters may be derived from the relation given by equation (1) when the stress σ is large enough to permit replacement of the hyperbolic sine by the exponential. Under this condition,

$$\sigma = \sigma_o\left[\left(\frac{\Delta H}{RT} + \log_e \dot{\epsilon}\right) + \log_e k_1\right] \tag{2}$$



where k_1 is a constant. Thus, if the stress is plotted against the parameter $\frac{\Delta H}{RT} + \log_e \dot{\epsilon}$, a single straight line with a slope equal to σ_o should be obtained.

If, in addition, use is made of the relation between creep rate $\dot{\epsilon}$ and rupture time τ

$$\dot{\epsilon}\tau = \text{Constant}$$

as found by Monkman and Grant (ref. 2), then equation (2) may also be written as

$$\sigma = \sigma_o\left[\left(\frac{\Delta H}{RT} - \log_e \tau\right) + \log_e k_2\right] \tag{3}$$

where k_2 is another constant. Thus, if the stress is plotted against the parameter $\frac{\Delta H}{RT} - \log_e \tau$, a single straight line with a slope equal to σ_o should be obtained.

In figure 1, which presents a correlation of creep and rupture data for 7075-T6 clad aluminum alloy, the parameters $\frac{\Delta H}{RT} + \log_e \dot{\epsilon}$ and $\frac{\Delta H}{RT} - \log_e \tau$ are plotted on the same abscissa scale against stress as ordinate. The data points, taken from reference 3, fall along two straight lines having the same slope. Since the temperature of 212° F is known to be too low for equation (1) to hold, the data points taken at that temperature do not fall on the lines but were included for comparison.

Steady Creep Rate

Figure 2 shows the steady creep rate per hour as a function of stress for two clad aluminum alloys: 7075-T6 on the left and 2024-T3 on the right. The solid-line curves represent actual data from reference 3 and it is seen that for the 7075-T6 alloy the solid-line curves are nearly parallel straight lines. The steady-creep law given by equation (2) requires that such curves be parallel straight lines; the dashed-line curves were computed from equation (2) with the use of the constants in table I. The data for the 2024-T3 alloy do not form parallel straight lines and for this material the relation does not apply.



Stress-Strain Curves

Figure 3 shows the stress-strain curves for the 7075-T6 aluminum alloy at three temperatures and for a strain rate of 0.002 per minute. The solid-line curves represent data taken from reference 4. The dashed-line curves were computed by using the constants in table I. The agreement is good at the two higher temperatures and is poor at the lowest temperature, which is below the temperatures at which the theory can be expected to hold.

Rapid-Heating Curves

Figure 4 shows the strains obtained when specimens of 7075-T6 aluminum alloy, held under three constant stresses as indicated, are heated rapidly at widely different temperature rates. The slant portions of the curves give mainly the effect of thermal expansion. The sharp upward turn at the right of each curve gives the effect of viscosity. The solid-line curves are data taken from reference 4, and the dashed-line curves are computed by using the constants in table I. Agreement is good at the higher temperatures.

The constants listed in table I for the different applications to 7075-T6 aluminum alloy are not quite the same. For a discussion of these small differences, see reference 1.

Low-Carbon Steels

In order to show how the relation works for materials other than aluminum alloys, an attempt was made to check the available data on low-carbon steels (ref. 5). The solid lines of figure 5 show the variation with temperature of the ultimate tensile strength, the stress to give creep rupture in 100 hours, and the stress to give a creep rate of 10^{-6} per hour. The dashed-line curves give the corresponding quantities computed by using the constants in table I. The agreement is good, especially above about 800° F.

Inconel X

The solid-line curves of figure 6 represent the same quantities as in figure 5 but are for the alloy Inconel X; the data are taken from reference 6. The corresponding dashed-line curves were computed by using the constants in table I; note that for this complex alloy the values of σ_o vary slowly with the temperature. It is believed that this variation reflects the microstructural changes which occur in Inconel X at elevated temperatures. The agreement with the data is fair and seems to



indicate that the proposed relation will be satisfactory even for a complex alloy, provided allowance is made for some instability with temperature.

CONCLUDING REMARKS

A relation between stress, strain rate, time, and temperature has been suggested for metals at elevated temperatures. The relation has been applied successfully to steady creep, creep rupture, stress-strain relations, rapid heating, and tensile strength for a few materials. The relation makes use of the elasticity, thermal expansion, and viscosity of the metal, and is an equation of state in rate form. The relation is inapplicable to metals which are markedly unstable or which undergo aging or changes in structure. The metal must be such that its steady creep is describable by the relation in order that the constants may be determined. With such a metal, however, the relation may be useful in the prediction of other properties from steady-creep data.

REFERENCES

1. Stowell, Elbridge Z.: A Phenomenological Relation for Metals at Elevated Temperatures. NACA TN 4000, 1957. (Prospective NACA paper.)

2. Monkman, Forest C., and Grant, Nicholas J.: An Empirical Relationship Between Rupture Life and Minimum Creep Rate in Creep-Rupture Tests. Paper No. 72, A.S.T.M. (Presented at Fifty-Ninth Annual Meeting of A.S.T.M., June 17-22, 1956.)

3. Anon.: Strength of Metal Aircraft Elements. ANC-5 Bull., Rev. ed., Depts. of Air Force, Navy, and Commerce, Mar. 1955.

4. Heimerl, George J., and Inge, John E.: Tensile Properties of 7075-T6 and 2024-T3 Aluminum-Alloy Sheet Heated at Uniform Temperature Rates Under Constant Load. NACA TN 3462, 1955.

5. Simmons, Ward F., and Cross, Howard C.: Elevated-Temperature Properties of Carbon Steels. Special Tech. Pub. No. 180, A.S.T.M., 1955.

6. Anon.: Inconel "X" - A High Strength, High Temperature Alloy, Data and Information. The International Nickel Co., Inc., Dev. and Res. Div., Jan. 1949.

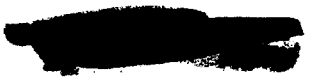


TABLE I

VALUES OF CONSTANTS USED IN APPLICATIONS

Metal	Application	ΔH, cal/mole	σ_o, ksi	at T, °F	s, per hr per °K	$\dot{\epsilon}_T$
7075-T6 clad aluminum alloy	Steady creep	35,800	4.3	All	1.62×10^8	0.0077
7075-T6 aluminum alloy	Stress-strain relations	34,700	4.3	All	1.50	
7075-T6 aluminum alloy	Rapid heating	34,700	4.3	All	3.60	
Low-carbon steels	All	72,000	2.0	All	9.15×10^8	0.025
Inconel X	All	108,500	4.9	1,000	$3,000 \times 10^8$	0.0095
			4.9	1,200		
			4.6	1,350		
			4.1	1,425		
			3.85	1,450		
			3.50	1,475		
			3.20	1,500		
			2.70	1,550		
			2.4	1,600		

413

CORRELATION OF CREEP AND RUPTURE DATA
FOR 7075-T6 CLAD ALUMINUM ALLOY

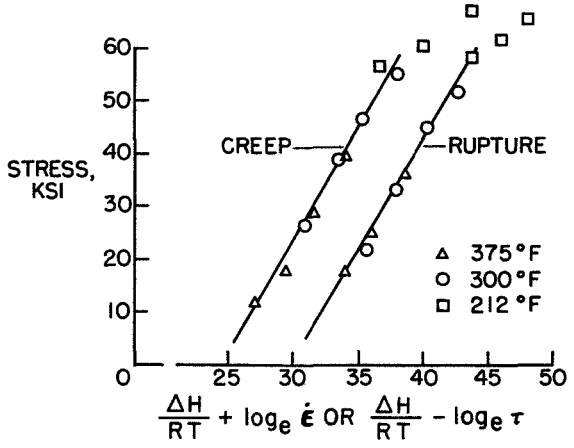


Figure 1

STEADY CREEP OF 7075-T6 AND
2024-T3 CLAD ALUMINUM ALLOYS

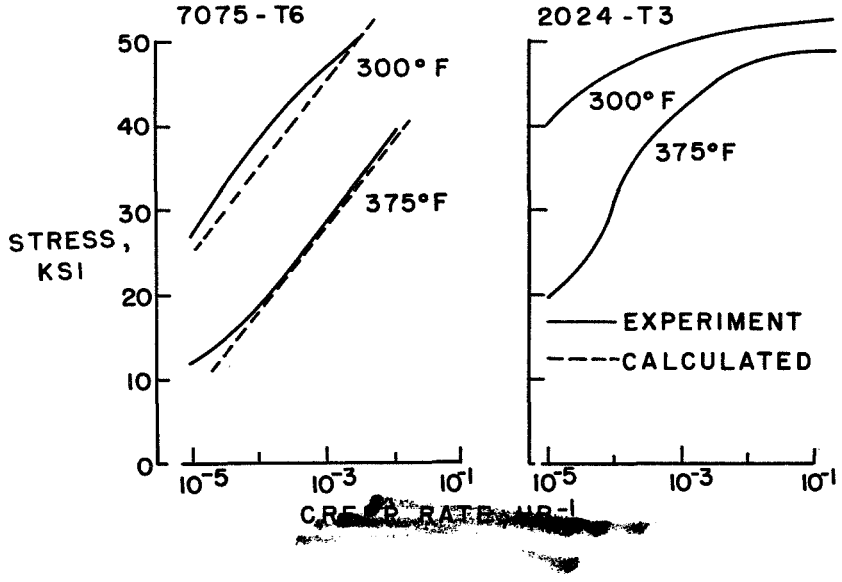


Figure 2

STRESS - STRAIN CURVES FOR
7075 - T6 ALUMINUM ALLOY

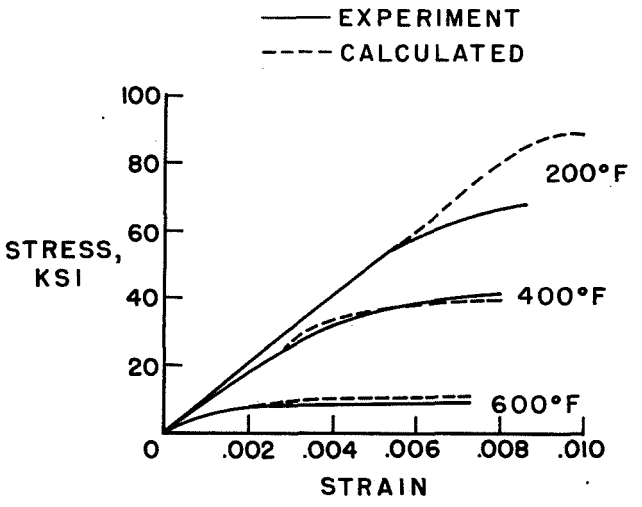


Figure 3

RAPID - HEATING CURVES FOR 7075 - T6
ALUMINUM ALLOY AT THREE STRESSES

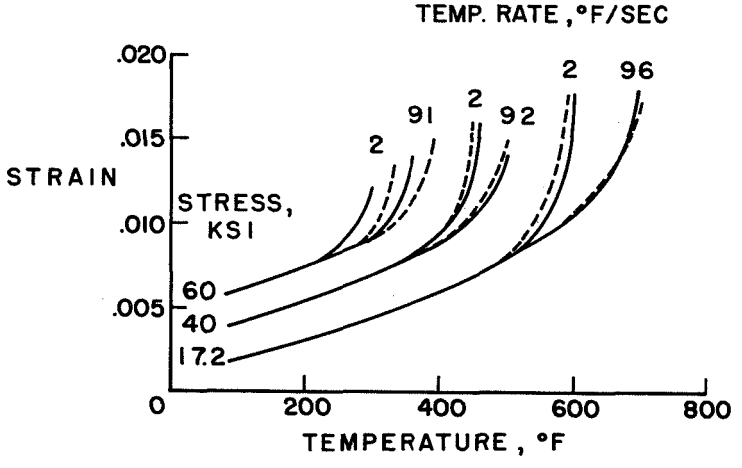


Figure 4



STRENGTH OF LOW-CARBON STEELS

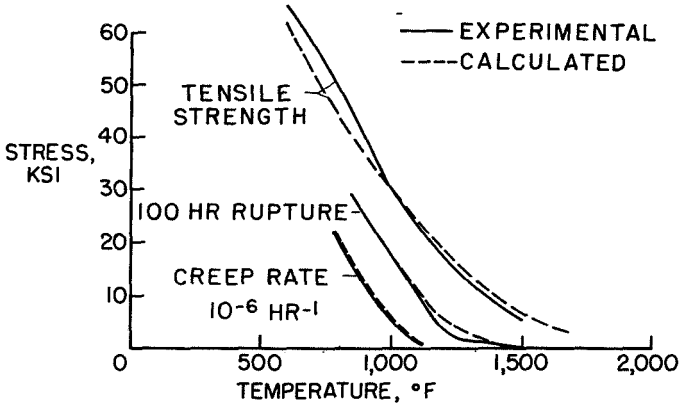


Figure 5

STRENGTH OF INCONEL X

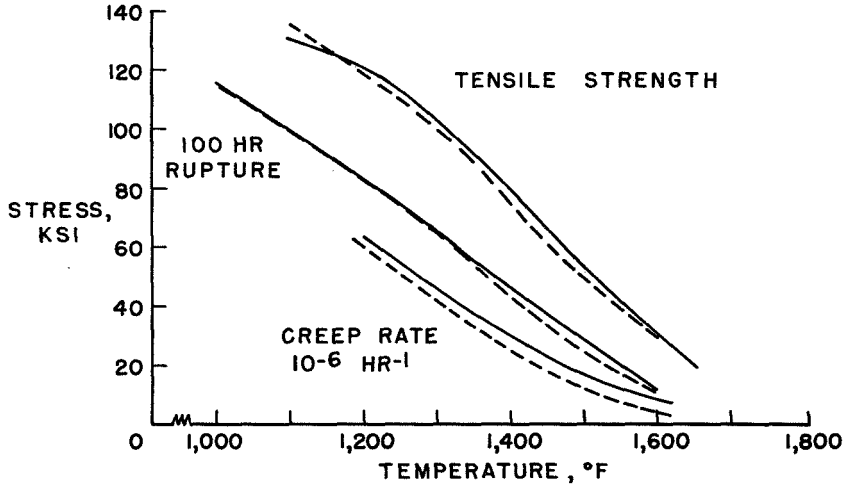
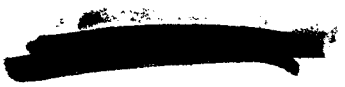


Figure 6



N71-75413

REACTIONS OF MATERIALS IN HIGH-TEMPERATURE AIR FLOWS

By Joseph G. Thibodaux, Jr., and Joseph N. Kotanchik

Langley Aeronautical Laboratory

SUMMARY

Ceramic-heated air jets and high-intensity arc-powered jets which are capable of duplicating some of the environmental conditions of hypersonic flight up to reentry velocities have been developed and are being operated. Initial tests of structural materials in these facilities at stagnation temperatures of 4,000° F and above indicate that these materials will be ignited, melted, or be severely oxidized. Surface heat inputs due to oxidation can be great enough to cause melting in high-velocity airstreams with stagnation temperatures several hundred degrees below the melting point of the materials. Laboratory experiments indicate that recombination of dissociated atoms on catalytic material surfaces can cause severe heating and greatly increased oxidation rates.

INTRODUCTION

In order to meet the current demand for high-temperature data, the National Advisory Committee for Aeronautics is now operating, or is putting into operation, many new high-temperature facilities. In these facilities, attempts are being made to duplicate environmental conditions which might be encountered by hypersonic airplanes and missiles in flying through and in reentering the earth's atmosphere. Current research programs are aimed, first, at furnishing sufficient data to insure the successful design and operation of hypersonic aircraft and, second, at furthering the understanding of high-temperature phenomena. Of particular interest at this time are reactions between structural materials and high-temperature environments. This paper will briefly describe two types of high-temperature air-jet facilities and discuss results of some materials tests conducted in them.

CERAMIC-HEATED AIR JET

Experience with rocket and combustion jets has shown that results were influenced by jet composition, that is, concentration of oxygen and steam, both of which oxidize most of the conventional aircraft structural

materials. In order to avoid this limitation, ceramic-heated air jets have been designed and put into operation. The general arrangement of this type of facility is shown in figure 1. It consists of a cylindrical steel pressure vessel which is lined with various types of refractories and interlocking ceramic refractory bricks. The central hole is filled with 3/8-inch-diameter lime-stabilized zirconia pebbles. A burner at the top supplies hot combustion gases which are drawn downward through the bed. When the required bed temperature and temperature distribution are reached, compressed air is blown back through the bed and expanded by a water-cooled nozzle.

Operating characteristics of two completed facilities are as follows:

Operating conditions	Laboratory model	Pilot model
Jet-exit diameter, in.	0.75 to 1.00	4.0
Stagnation pressure, lb/sq in. . .	To 100	To 1,600
Stagnation temperature, $^{\circ}$F	To 4,000	To 4,000
Jet velocity, ft/sec	3,500 to 5,200	4,300 to 6,100
Mass flow, lb/sec	0.2 to 0.5	6 to 10
Gas composition	Air or inert gas as desired	

The maximum operating temperature is now limited to 4,000° F because the pebble bed begins to soften and lose strength at slightly higher temperatures. Tests are now in progress which indicate that the maximum temperature may soon be increased to 5,000° F by the use of thoria bricks and pebbles.

MATERIALS TESTS

Up to the present time, materials tests were conducted to determine if the material reacted with the high temperature, high-velocity airstream, and, if so, to what extent the reaction contributed to the melting or the destruction of the material. These tests consisted of putting models of various materials into the jet and observing their behavior by means of high-speed color motion pictures. These pictures were carefully studied to determine if oxidation or ignition occurred and to determine the nature and severity of the reaction. Jet stagnation temperature is usually higher than the melting point of the materials, and, in this event, melting would occur even in the absence of any reaction.

Solid models of various shapes, having a maximum diameter of 1/2 inch, were used in all tests. Typical shapes were cones with different angles and nose radii, hemisphere cylinders, and flat-face cylinders. Initial

heating rates were greatly influenced by shape as well as by airstream properties. Tests of identical models of various materials were used to compare the relative behavior of the materials. Tests of identical materials of various shapes were used to compare the effect of shape and heating rate.

Results of tests of typical structural materials in the ceramic-heated air jet will now be discussed.[1] Operating conditions for the tests are as follows:

Stagnation temperature, °F	4,000
Stagnation pressure, lb/sq in. abs	105
Jet velocity, ft/sec	5,200
Jet Mach number	2
Jet-exit diameter, in.	0.8

Magnesium

The magnesium model was a solid 20° cone with a 1/32-inch nose radius. The material being tested formed only the first 3/8 inch of the cone. The remainder of the cone was a steel model support which was separated from the test specimen by a bakelite insulator. In the motion pictures, this insulator will be observed to ignite and burn before the model melts or ignites. This burning of the insulator plays no part in the behavior of the model and should be disregarded. This cone-shape model had a maximum initial heating rate of 2,000 Btu per square foot per second.

The magnesium began melting 0.2 second after entering the jet with no noticeable oxidation or ignition. Melting continued and the metal flowed back freely and froze on cooler portions of the model support. Intermittent ignition and combustion appeared in 0.6 second. The model was completely melted in 0.9 second. Downstream in the wake, out of the camera field, magnesium was vaporized and burned vigorously.

Aluminum

The aluminum model was of the same design as the magnesium model. The aluminum began melting 0.4 second after entering the jet. Melting was not accompanied by noticeable oxidation or ignition. Aluminum flowed freely and froze on the cooler portions of the model support. The model was completely melted in 1.5 seconds. Downstream in the wake, out of the view of the camera, aluminum ignited and burned in locations where the model support acted as a flame holder.

[1] A motion-picture film supplement (L-217) has been prepared and is available on loan from NACA Headquarters, Washington, D. C.

[redacted]

Steel

The steel model was the same design as the magnesium model. Steel began oxidizing immediately after entering the jet as evidenced by discoloration at the tip. The model heated to incandescence. Melting and simultaneous ignition were noted 0.7 second after entering the jet. The reaction rate increased rapidly and completely engulfed the model and model-support surface in flame. The model was completely destroyed in 3.5 seconds.

Stainless Steel

The stainless-steel model was the same design as the magnesium model. Stainless steel began heating up with the formation of oxides as evidenced by tip discoloration. The oxide began to build up and formed a hard, crusty, adherent deposit at the tip. This oxide afforded some protection from further oxidation until subsurface melting began 1.1 seconds after the model entered the jet. The oxide was blown away, new surface was exposed, and the oxidation process was then repeated. Soon, as the model heated up, the reaction became vigorous enough to cause continuous melting.

Copper

The copper model was the same design as the magnesium model. Copper began to form a black cupric oxide 0.5 second after entering the jet. This oxide continued to form at a relatively slow rate. It was very adherent and appeared to protect the copper from rapid oxidation. In 2.9 seconds, the cupric oxide began to decompose to the red cuprous oxide at the tip, and in 3.0 seconds melting began. The model was completely destroyed in 5 seconds.

Titanium

The titanium model was a 1/2-inch-diameter hemisphere cylinder. Initial heating rate was approximately 500 Btu per square foot per second. The cylindrical model required a much longer time to heat than the cone-shape models because of the lower heating rate and the larger surface-to-mass ratio. The model began oxidizing 2 seconds after entering the jet. This oxide formed until a stable coating protected the model from further oxidation. In approximately 13 seconds, at a temperature approaching the melting point, titanium suddenly burst into a violent reaction which completely destroyed the model in approximately 1 second.

 [redacted]

Molybdenum

The molybdenum model was the same design as the magnesium model except that the rear conical support was graphite and no bakelite separator was used. The melting point of molybdenum was approximately 600° F above the jet stagnation temperature. The model entered the jet and, in 0.2 second, a black oxide, probably the sesquioxide, was formed. In 1.3 seconds, a gray oxide, probably a mixture of the sesquioxide and trioxide, formed. In 2.5 seconds, a yellow oxide, molybdenum trioxide, formed. All these oxides were volatile and condensed out on portions of the model and support which were cooler than the sublimation temperature of the oxide. As the temperature increased, they all vaporized. In 3.1 seconds, a vigorous reaction began at the tip. In 3.2 seconds, ignition occurred and melting began. Vigorous oxidation and burning at the surface furnished sufficient additional heat input to cause and sustain melting.

Tungsten

The tungsten model was the same design as the molybdenum model. The melting point of tungsten was approximately 2,000° F above the stream stagnation temperature. Tungsten began to oxidize 0.5 second after entering the jet with the formation of a black oxide, probably the dioxide. In 2.5 seconds, a yellow oxide, probably the trioxide, was seen forming and condensing out on the cooler portions of the model support. This oxidation, although not vigorous, was steady. The tungsten oxidized with reasonable loss of mass of the model; however, oxidation was not sufficient to cause melting or ignition. The trioxide vaporized or reacted with the graphite model holder as the temperature increased. The graphite model holder was oxidized to a much greater extent than it would have been if it were tested alone; this fact indicates that tungsten or one of its oxides catalyzed the oxidation of graphite.

Graphite Coated With Flame-Sprayed Zirconia

The zirconia-coated graphite model was a 30° cone with a diameter of 3/4 inch and a nose radius of 1/8 inch. The model survived 10 seconds of test with no damage. The test was terminated by failure of the support system of the model.

HIGH-INTENSITY ARC-POWERED JETS

Ceramic-heated jets can produce temperatures which melt or severely oxidize most conventional structural materials. These temperatures are

considerably less than environmental temperatures which are associated with reentry. It is theoretically impossible to obtain reentry temperatures by chemical means, either directly or indirectly. For production of these high temperatures, the Langley Laboratory has been developing jets in which the energy is supplied by a high-intensity electric arc.

Initial operation of these arc-powered jets was conducted with water and liquid oxygen as the jet medium. More recently, they have been successfully operated with liquid and gaseous air as the jet medium. Operation with air is now being emphasized inasmuch as this medium more nearly reproduces the atmospheric environment at reentry velocities.

An arc-powered jet is shown schematically in figure 2. It consists of a pressure chamber that houses the arc and the jet medium which is to be heated. The anode enters the chamber through a hole in the bottom. The top forms the cathode and a hole in the top forms the nozzle. A high-intensity arc is struck and maintained between the anode and the cathode. Air enters the bottom of the chamber and flows into the arc chamber through an annular opening around the anode. It is then heated and expanded to high velocity through the nozzle. Power is supplied as indicated. This diagram shows a direct-current arc. Three-phase alternating-current arcs have also been operated successfully.

Characteristics of typical arc-powered jets which have been operated at this laboratory are as follows:

Jet-exit diameter, in.	0.25 to 1.00
Power, kw	60 to 1,000
Stagnation temperature, ^{o}F	>15,000
Stagnation pressure, lb/sq in.	3 to 30
Jet composition	Air (dissociated)
Heating rate (hemisphere nose), Btu/ft^2-sec	2,200

Temperatures and pressures indicated represent what has been achieved up to the present time and do not represent the maximum capabilities of this type of facility.

Materials tests similar to those conducted in the ceramic-heated air jets have also been run in the high-intensity arc-powered jets. For the purpose of comparing the relative severity of test conditions and behavior of materials in these two jets, results of tests of titanium, molybdenum, and graphite models will be presented. Jet conditions for these tests are as follows:

Stagnation temperature, ^{o}F	>15,000
Stagnation pressure, lb/sq in.	10
Jet velocity	Subsonic
Jet medium	Air
Jet diameter, in.	0.375
Initial heating rate, Btu/ft^2-sec	1,000 to 2,200

Titanium

The titanium model is a 1/2-inch-diameter flat-face cylinder. A hemisphere-cylinder model with one-half the initial heating rate withstood 13 seconds in the ceramic-heated air jet before ignition occurred. The model in the arc-powered air jet ignited in approximately 0.1 second. The reaction was violent. Heating rates were extremely high. Examination of the model afterward showed little penetration of heat into the model and indicates that most of the material was lost in a manner resembling ablation.

Molybdenum

The molybdenum model was the same shape as the titanium model. The molybdenum model having similar initial heating rates required 3.1 seconds to melt in the ceramic-heated air jet. The model in the arc-powered air jet began to react violently in 2 seconds. Examination of the model after the test also indicated that material was lost in a manner resembling ablation.

Graphite

The graphite model was a 1/2-inch-diameter hemisphere cylinder. Graphite was relatively undamaged by a 20-second exposure in the ceramic-heated air jet. In the present case, the graphite model suffered little damage due to a 5-second exposure to the arc-powered air jet. Some material was lost because of oxidation or sublimation, although the model was rapidly heated to incandescence.

The tests in both jets were contrived to produce rapid model heating so that materials reactions, if present, would begin soon after the models were introduced into the jets. Oxidation and ignition are complex phenomena which depend on many factors and conditions. Some of these are the temperature of both reactants, the thermal properties of reactants and products, the thermal and mass transport properties of reactants and products, the kinetics of reaction, the physical properties of reactants and products, and the surface-to-mass ratio of the model. Changes in the size and shape of models may well affect some of these

properties and conditions. Until a suitable explanation for the interrelation of these properties and conditions is found, results of these tests should be regarded as qualitative, and should not be applied directly to models of other sizes and shapes.

Both types of jets are being operated as free jets exhausting into the atmosphere. This type of operation allows reasonable duplication of stagnation conditions, and to some extent, velocity. It does not allow duplication of static conditions. Exact duplication of both static and stagnation conditions will require the use of vacuum chambers, diffusers, or auxiliary ejectors.

Both jets may be operated with inert gases, pure gases, and gas mixtures. Use of inert gases would allow determination of heat transfer in the absence of oxidation. Pure and mixed gases may be used to study reactions in controlled environments, and to study the aerothermochemical phenomena.

One such phenomenon, that of enhanced oxidation by oxygen atoms at elevated temperatures, has been studied and reported by Fryburg in reference 1. Platinum was chosen for this investigation because of its known catalytic activity in promoting recombination of oxygen atoms. Platinum strips were heated and their temperatures were maintained at temperatures of 1,000° C and above solely by recombination of oxygen atoms at the surface. The rates of oxidation of platinum were measured and found to be directly proportional to the number of atoms striking the surface. Oxygen atoms were 400 times more effective in oxidizing platinum than oxygen molecules, thereby indicating that extrapolation of low-temperature-oxidation data obtained in conventional environments to reentry conditions could cause serious errors.

CONCLUDING REMARKS

High-temperature air-jet facilities which can duplicate some environmental condition of hypersonic flight up to reentry velocities are now being operated.

Tests of materials in high-velocity airstreams at temperatures of 4,000° F and greater indicate that conventional structural materials undergo melting, ignition, or severe oxidation.

Oxidation and ignition characteristics of materials may be limiting properties rather than strength, creep, or fatigue.

Under certain conditions, recombination of dissociated atoms on catalytic surfaces can cause severe heating and oxidation.

The fact that materials undergo oxidation and ignition, and that these reactions can give rise to large surface heat inputs, suggests the use of caution in extrapolating low-temperature heat-transfer data to reentry conditions.

REFERENCE

1. Fryburg, George C.: Enhanced Oxidation of Platinum in Activated Oxygen. Jour. Chem. Phys., vol. 24, no. 2, Feb. 1956, pp. 175-180.

CERAMIC - HEATED JET

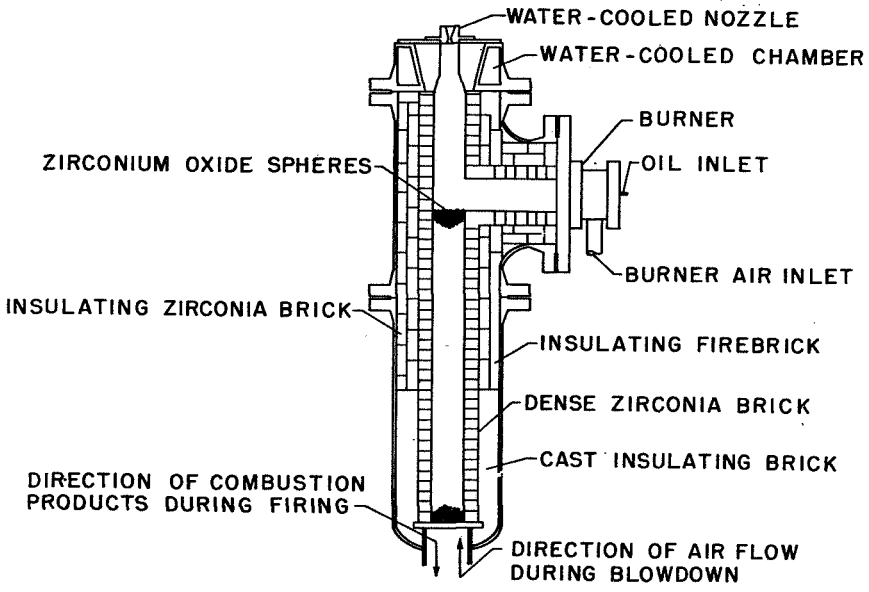


Figure 1

ELECTRIC-ARC AIR JET

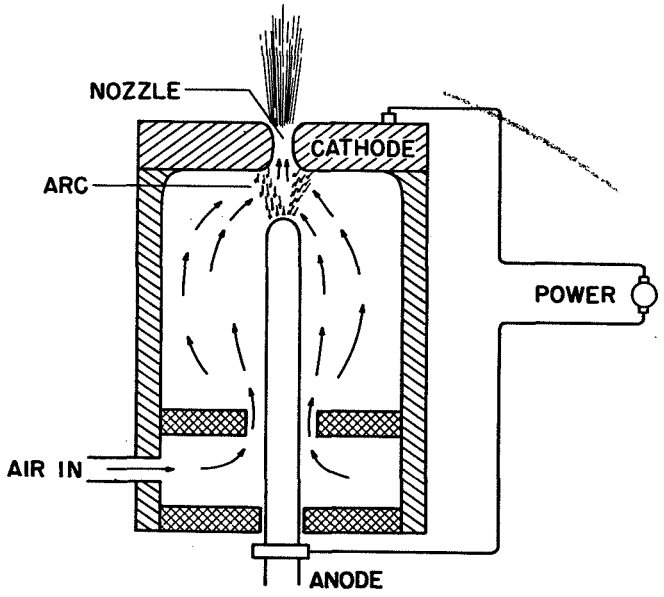


Figure 2

N71-75414

FATIGUE-CRACK PROPAGATION AND RESIDUAL STATIC STRENGTH OF BUILT-UP STRUCTURES

By Herbert F. Hardrath and Richard E. Whaley

Langley Aeronautical Laboratory

SUMMARY

Fatigue tests were conducted on box beams and tension panels in order to study some of the factors affecting fatigue-crack propagation. The box beams had essentially the same configuration except for the mode of connecting stringers to the tension cover. The beams with bonded stringers had the lowest rate of crack growth, and beams with riveted and integral stiffeners had successively higher rates of crack growth. Crack growth was slower in beams with close rivet spacing than in beams with greater rivet spacing. The tension panels were all of the same general configuration except that the proportions of cross-sectional areas of skin, stringers, and flanges were varied. Panels with heavy stringers and thin skin had lower rates of crack growth than did panels with heavy skin and light stringers.

Static tests were performed on box beams, on tension panels, and on two types of wings, all of which contained fatigue cracks. The comparison of results with predictions made by a simple theory indicates that test results were affected by a redistribution of loads among the various remaining elements and by whether cracks terminated at rivet holes.

INTRODUCTION

During the past several years the idea of "fail-safe" design has become a very popular topic for discussion among aircraft structural designers. Although the conditions for calling a given design fail-safe have not been clearly defined, almost all engineers concerned agree on several general conditions. First, the progress of a fatigue crack through a structure must be reasonably slow, preferably in a readily inspectable location. Second, the structure containing a crack must retain enough static strength to withstand some specified load.

The means for accomplishing these ends involve such factors as the selection of materials with satisfactory crack propagation and static

notch-strength properties, the arrangement of material to inhibit crack growth, the provision of multiple load paths, and others. The purpose of the present paper is to review current research which deals with the systematic study of some of these factors and their application to the design of structures used in wings.

CRACK PROPAGATION

Box Beams

One phase of the study of crack propagation involves fatigue tests of box beams such as those shown in figure 1. Two general configurations were tested. For the first configuration the tension cover had integral stiffeners and was machined from a plate. For the other configuration the stringers and skin were either bonded or riveted. The webs and compression covers on all beams were of identical built-up construction for simplicity in construction and analysis. All beams were 20 inches wide and 8 feet long. Identical beams were constructed in each of the aluminum alloys, 2024 and 7075. The beams were loaded as shown in figure 1 to produce tensile stresses of 13 ± 6.5 ksi in the carry-through bay. An oblong hole was made in the center of the carry-through bay to initiate the crack at that point. Cracks generally grew symmetrically across the chord. Although some of the data have been published previously (ref. 1), representative results are given in figure 2.

In figure 2 the percentage of the tension area lost by fatigue cracking is plotted as a function of the number of cycles of load applied after crack initiation. The curves are for beams with integral, riveted, and bonded covers. The material in each case was 7075 aluminum alloy. The results for 2024 aluminum-alloy beams are not shown, but the same general observations apply except that crack growth is appreciably slower in beams made of 2024 aluminum alloy.

As indicated by the curves, the cracks grew least rapidly in beams with bonded covers. The crack growth was confined to the skin and progressed at a reasonable rate, probably controlled by support from the stringers. Measurements of stringer stresses taken at intervals during the test indicated that these stresses increased more slowly than stresses in beams with other types of connections, probably because of the fact that the bond between the skin and stringers peeled back as the crack grew across the beam. Since there were no rivet holes in the stringers, no stress raisers were present, and no stringers failed before the crack had grown completely through the skin.

In riveted covers the stringers were somewhat more vulnerable to failure because stringer stresses increased more rapidly and stress

raisers due to rivet holes were present. The loss of stringers in the case of riveted beams contributes to the more rapid loss of tension material. In the case of the integrally stiffened covers the cracks grew at the fastest rate because no natural barriers to crack growth were present.

These observations indicate that crack propagation is very much a function of the effectiveness of connections between the sheet and stringers. An extension of this work to beams in which the rivet pitch was varied was therefore undertaken, and some of the results of this work are shown in figure 3.

In figure 3 the curves from figure 2 are replotted as solid lines. New curves for beams with rivet pitches of one-half and of twice the rivet pitch used in the previous beam are shown by dotted lines. The symbols represent the stage of the test when one or more stringers had completely failed. Crack growth was slower in beams with a rivet pitch of 3/4 inch than in those with a rivet pitch of $1\frac{1}{2}$ inches and was much slower than in beams with a rivet pitch of 3 inches. The stress measurements previously mentioned indicated that stresses in stringers straddling cracks increased more rapidly in beams with a rivet pitch of 3/4 inch than in other beams with riveted stringers. This increase in stresses had two effects: a slow rate of crack propagation in the sheet as indicated by the low initial slope of this curve, and increased probability of stringer failure as indicated by the fact that in this beam two stringers failed after only about 8 percent of the structure had been lost by skin cracking. On the other hand, in beams with a rivet pitch of 3 inches, the stringer stress increased more slowly and indicated that less support was given to the sheet; consequently, crack growth was very rapid in the skin. The results of these tests show that the closer the rivet pitch, the better the resistance to crack propagation. Fabrication limitations prevent decreasing the rivet pitch further. Integral construction, which might appear the same as rivets with a zero pitch, displays rapid crack growth. The reason appears to be that in integral construction only one crack needs to be started, and then that crack grows completely through the panel.

Tension Panels

Another phase of the investigation of crack propagation involves tension tests of stiffened panels. Some of the results are shown in figure 4. The panels tested were 30 inches wide and were composed of a skin, four stringers, and two flanges. The parameters varied were the percentages of the areas of skin, stringers, and flanges as indicated by values listed in the figure. Two of the configurations had 40 percent of the area in the skin, and one configuration had 80 percent of the

area in the skin. Many current aircraft have proportions within this range. Repeated tension loads were applied to produce nominal stresses of 14 ± 4.7 ksi. Fatigue cracks were initiated at cutouts with the shapes indicated in figure 4. Although only a few results are available, preliminary discussions are of interest.

The heavier stringers in panels with 40 percent of the area in the skin appear to have controlled the rate of crack growth more effectively than in the panels with 80 percent of the area in the skin. The result is an appreciably lower rate of crack propagation in panels with lighter gage skin. One configuration had a 5-inch-square cutout which was the width of one skin panel. This cutout removed approximately 7 percent of the original net section, and the beginning of the curve for this specimen is plotted at that value. In this case the growth of fatigue cracks was very slow in the initial stages of the test and illustrated the beneficial effect of framing members adjacent to cutouts.

RESIDUAL STATIC STRENGTH

The rest of this paper deals with the study of residual static strength in the specimens just described. The results which are preliminary in nature are discussed in order to indicate trends. These results are then compared with results of a simple analysis. Static tests of Convair 240 (designated herein as CV-240) and C-46 wings containing fatigue cracks are also discussed.

Box Beams

In figure 5 the ordinate represents the ultimate load producing static failure of beams with cracks expressed as a percent of the load calculated to produce failure of the tension covers in uncracked beams. The abscissa represents the length of the fatigue crack in the cover skin. The symbols represent the results of static tests of box beams which were made of 7075 aluminum alloy and which were identical except for the fastenings between the skin and stringers. The symbols represent either bonded covers or riveted covers as shown in figure 5. The dotted line represents the strength of the beam having a skin crack only, with no allowance made for stress concentration K due to the crack. The solid lines represent predictions made by calculations of the static strength of a specimen containing a fatigue crack in the skin only. The basis of this method is to compute a stress-concentration factor K_u for the sheet by the method outlined in reference 2. The residual static strength of a sheet containing a crack was added to the static strength of structural members such as stringers and flanges to produce the values for the upper curve. Each of the other curves was computed in a similar way

except that one or more stringers were assumed failed. Each test point is connected by a vertical line to the curve appropriate for the number of stringers failed in the specimen represented.

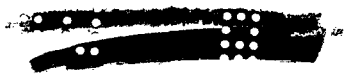
When the crudeness of the method used is considered, the agreement between predicted strength and actual strength of riveted beams is good. The beams with a rivet pitch of 3/4 inch fall farthest below the predicted curves, probably because of the higher stresses carried by stringers. Evidently the distribution of loads among the remaining members in the structure must be taken into account in order to improve the predictions. The strengths of beams with bonded covers are higher than the respective predicted strengths while other strengths are lower than predicted. No reason for this behavior has been found. One point fell above the dotted line which represents loss of strength equal to loss of area. This high strength was caused by the fact that the actual material strength was higher than the specification values used in computations. Adjustment of the computation for actual material proportions would affect all the results.

Tension Panels

Figure 6 gives results similar to those in figure 5 for static tests of the tension panels with 80 percent of the area in the skin. In this case the data were somewhat higher than predictions (shown by solid lines in the figure) made by the method previously used. The reason appears to be that in these panels the fatigue cracks ended at rivet holes. The computation of the stress-concentration factor should, therefore, allow for a radius of curvature ρ equal to the radius of the rivet instead of the effective radius at the root of a crack. Calculations based on this assumption are indicated by the dashed lines, and the test results fall below the predictions as before.

CV-240 Wings

Some CV-240 outer wing panels were subjected to repeated loading in order that crack growth might be studied, and then static tests were performed in order that the residual static strength might be determined. Figure 7 presents the results of three static tests of CV-240 wings containing fatigue cracks. The plot of figure 7 is similar to the plots of figures 5 and 6 except that the abscissa is the tension cross-sectional area failed expressed as a percentage of the total tension cross-sectional area. The dotted line represents reduction in static strength in the same proportion as the reduction in area. These wings were constructed of 7075 aluminum alloy, and the structure was somewhat more complex than that of the box beams discussed previously. As before, the stress concentration was computed for the skin only. Also, since cracks terminated at



rivet holes or grew to rivet holes at an early stage of the static test, the rivet radius was used in the calculations. The cracks in these wings originated in the rear spar caps and then grew across the chord. The calculation was, therefore, for a sheet with a notch on one side only. The test results fell slightly below the prediction as before.

C-46 Wings

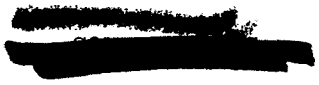
The fatigue tests of C-46 wings have been discussed in references 3 and 4. Thirteen wings were static tested after various amounts of the tension material were failed in fatigue tests. The results of the static tests have been presented in reference 4.

The results are also shown in figure 8 in the same type of plot as was used in figure 7. The predicted curve was computed on the assumption that the skin was continuous across the chord. The rivet radius was used in the calculation for the same reason as before. In spite of the fact that a wide variety of structural members failed during the fatigue tests on these specimens, the predicted strengths fell in a very narrow band which is represented in the figure as a single line. The discrepancy between results and predictions was somewhat greater than in the previous cases. This discrepancy was to be expected as a result of the much more complicated structure in the C-46 wings. Obviously, the redistribution of loads in this structure will have to be considered before more accurate predictions can be made.

The apparent large loss of strength with small cracks applies only to the tension surface. In compression-critical wings, such as the C-46 and CV-240, the loss in wing strength is very small until large cracks are present.

CONCLUDING REMARKS

Crack-propagation and static-strength tests in several types of built-up specimens and full-scale wings have been reviewed. The results, to date, indicate that the rate of crack propagation is influenced strongly by the mode of connecting the skin to stringers and by the proportions of areas of the skin and stringers. The analysis of residual static strength of complex structures indicates the feasibility of applying simple methods, but the results are subject to questions regarding the redistribution of loads, interactions between various members, and such seemingly trivial considerations as whether or not a crack terminates at a rivet. Much work remains to be done on these problems. Other configurations designed to improve both the rate of crack propagation and residual static strength should be investigated.



REFERENCES

1. Hardrath, Herbert F., Leybold, Herbert A., Landers, Charles B., and Hauschild, Louis W.: Fatigue-Crack Propagation in Aluminum-Alloy Box Beams. NACA TN 3856, 1956.

2. McEvily, Arthur J., Jr., Illg, Walter, and Hardrath, Herbert F.: Static Strength of Aluminum-Alloy Specimens Containing Fatigue Cracks. NACA TN 3816, 1956.

3. McGuigan, M. J., Jr., Bryan, D. F., and Whaley, R. E.: Fatigue Investigation of Full-Scale Transport-Airplane Wings - Summary of Constant-Amplitude Tests Through 1953. NACA TN 3190, 1954.

4. Whaley, Richard E., McGuigan, M. J., Jr., and Bryan, D. F.: Fatigue-Crack-Propagation and Residual-Static-Strength Results on Full-Scale Transport-Airplane Wings. NACA TN 3847, 1956.

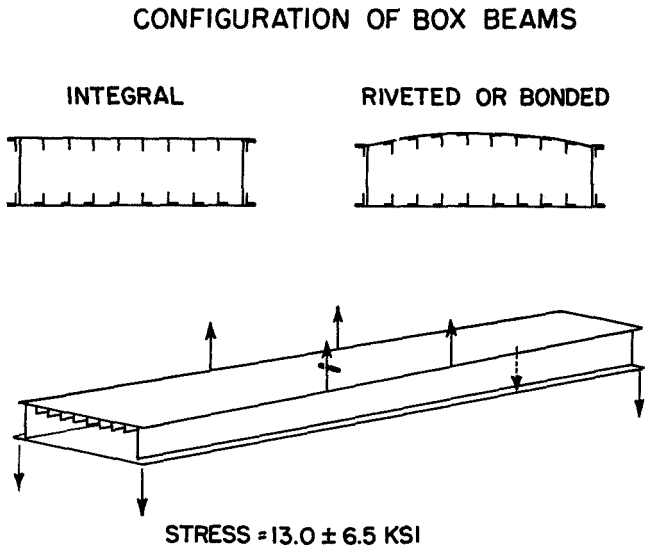


Figure 1

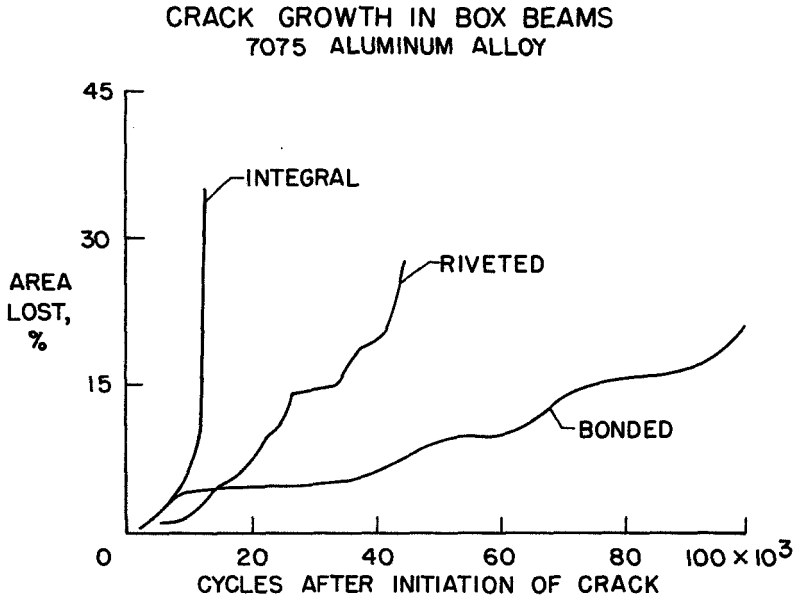


Figure 2

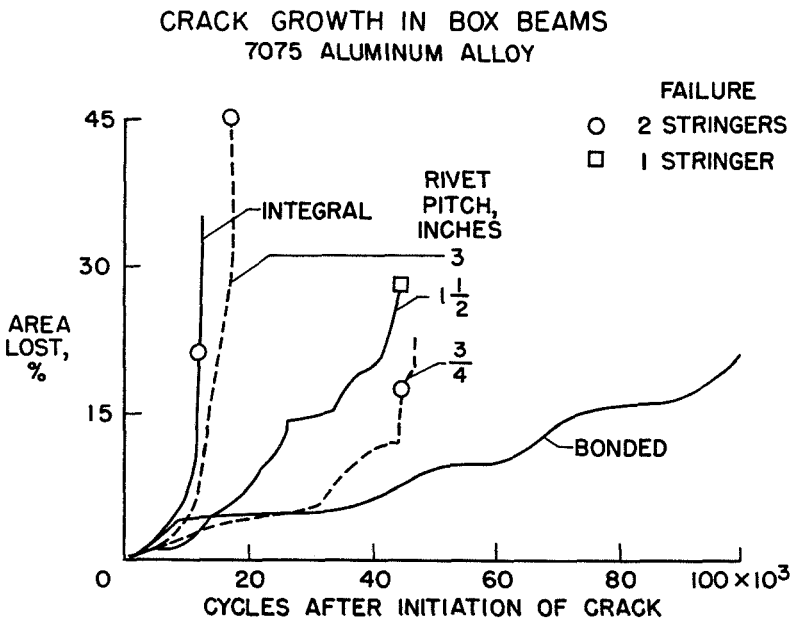


Figure 3

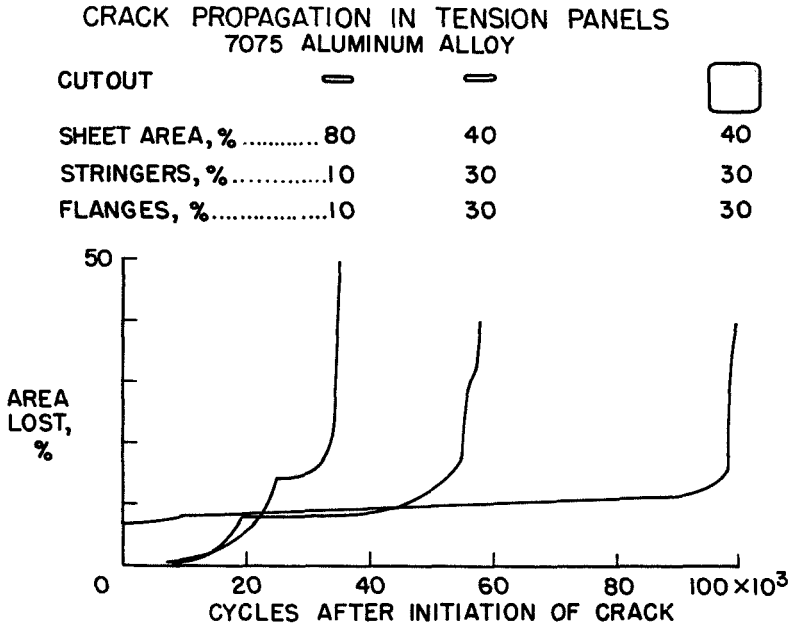


Figure 4.

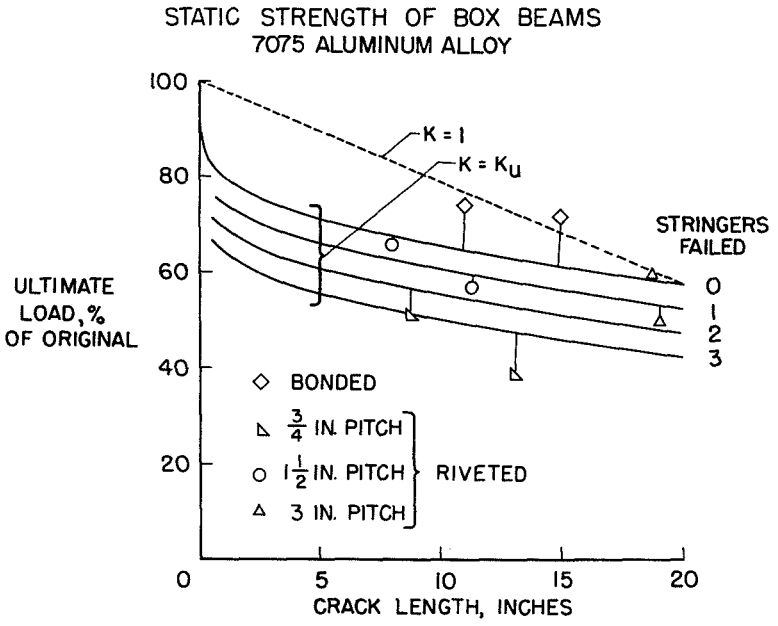


Figure 5

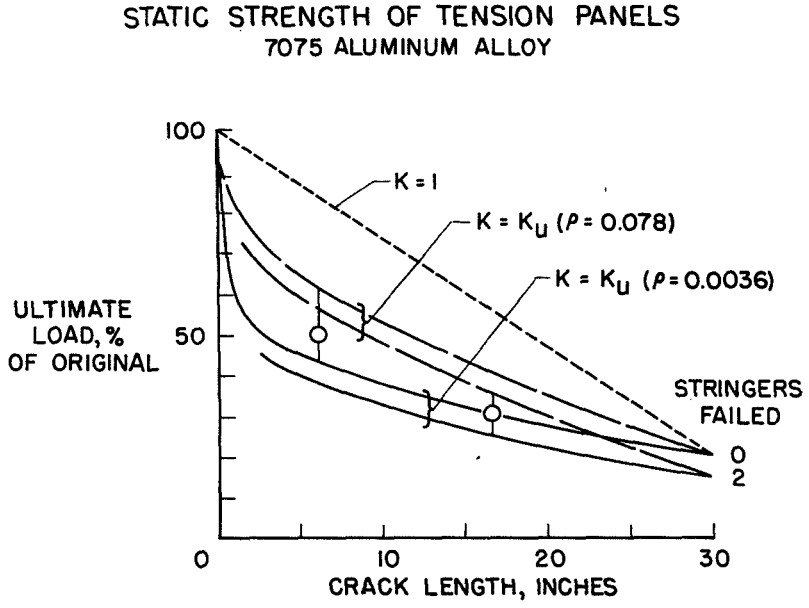


Figure 6

STATIC STRENGTH OF CV-240 WINGS
7075 ALUMINUM ALLOY

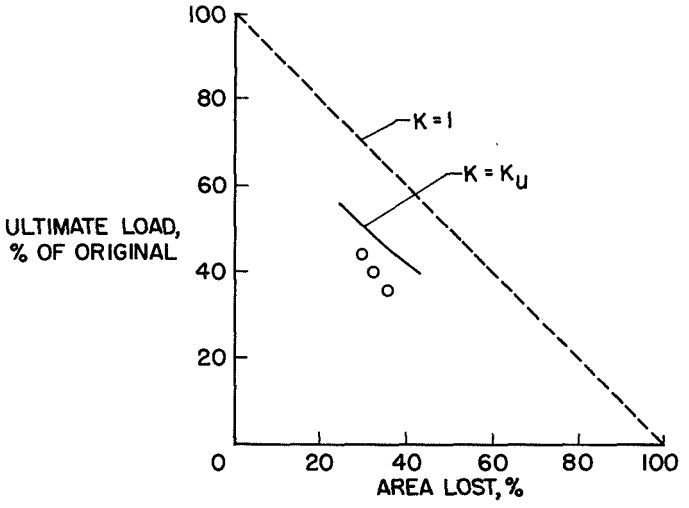


Figure 7

STATIC STRENGTH OF C-46 WINGS
2024 CLAD ALUMINUM ALLOY

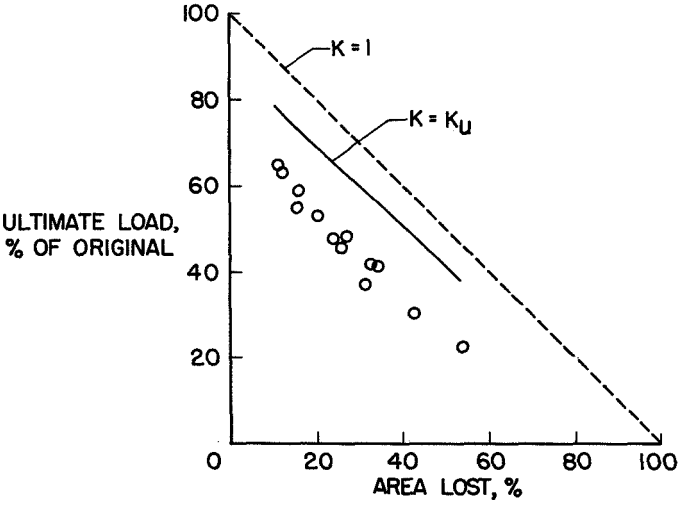


Figure 8

N(1-75412

F

KUHN & PETERS

SOME ASPECTS OF FAIL-SAFE DESIGN OF PRESSURIZED FUSELAGES

By Paul Kuhn and Roger W. Peters

Langley Aeronautical Laboratory

SUMMARY

Separate investigations have dealt with the critical crack length of flat sheets or of unstiffened cylinders and with the type of rupture experienced by stiffened cylinders. These investigations are correlated, supplemented by new tests, and combined into a uniform scheme for predicting critical crack length and type of rupture in stiffened pressurized cylinders.

INTRODUCTION

The fail-safe design of pressurized fuselages is a problem that has attracted much attention in the past few years. This paper is a progress report on work in this field and an attempt to correlate several lines of investigation.

SYMBOLS

A_{NET}	net area, sq in.
A_R	ring area (cross sectional), sq in.
K_u	stress-concentration factor for ultimate load
$K_{u,CYL}$	stress-concentration factor for cylinder
l	ring spacing, in.
P	load, ksi
r	radius of cylinder, in.
t_S	skin thickness, in.

[redacted]

δ	length of original slit, in.
σ	stress, ksi
σ_{MAX}	maximum stress, ksi
σ_u	ultimate tensile stress, ksi

DEFINITIONS

The problem is defined in a general way by two questions: If initial damage, such as a fatigue crack, is inflicted on a pressurized stiffened shell, how large can the damage be before the pressure causes a rupture of the shell, and what is the nature of the rupture? The only type of initial damage which is considered here is a longitudinal crack or slit of length δ as shown in figure 1. (For aluminum alloys, to which this discussion is confined, the difference between a fatigue crack and a fine slit is negligible.) For any specified pressure or hoop tension, a critical length of crack exists at which the pressure will rupture the skin. The term "confined rupture" in this paper will refer to a rupture which stops at the nearest rings, as indicated on the sketch at the left. The term "unconfined rupture" will refer to a rupture which extends into adjacent bays, as indicated on the sketch at the right. An unconfined rupture of the skin often results in failure of the rings and sometimes of the stringers.

SURVEY OF PREVIOUS INVESTIGATIONS

Critical Crack Length

Figure 2 shows schematically the first two steps in the investigation of critical crack length. At the top is shown a flat sheet under tension with a central crack of length δ. When the maximum stress σ_{MAX} in the sheet at the two ends of the crack becomes equal to the tensile strength of the material, the sheet will tear apart. At this instant, the maximum stress is equal to the product of the net-section stress P/A_{NET} and a stress-concentration factor K_u.

A method for calculating the factor K_u has been published in reference 1. The calculation involves the stress-strain curve and a size-effect constant which is determined from a tension test on a specimen with a sharp notch of known radius. The presence of this size effect

[redacted]

in problems involving cracks or sharp notches invalidates the mechanical law of similarity that geometrically similar structures fail at the same stress and makes it impossible to draw generalized curves based on dimensionless parameters.

The lower sketch in figure 2 shows a pressurized unstiffened cylinder with a longitudinal crack. The stress-concentration factor for such a cylinder is calculated by the formula shown. The quantity K_u is the stress-concentration factor calculated for the configuration obtained by unwrapping the cylinder into a plane. The term in parentheses is the "curvature correction," which was found empirically and applies to 2024-T3 aluminum alloy as well as 7075-T6 aluminum alloy. The experimental basis for the formula may be found in reference 2.

The importance of the curvature correction is shown in figure 3. For the two aluminum alloys, the critical crack length is shown as function of the tensile stress for flat sheet and for cylinders with a radius of 15 inches, which is a widely used size representing roughly a 1/4-scale model of a fuselage. For all but very short cracks, the drop in strength due to curvature effect is obviously substantial. Curves of critical crack lengths of unstiffened cylinders corresponding to the curves shown in figure 3 will be used later as a yardstick or reference basis for stiffened cylinders.

Type of Rupture

The initial investigation of the problem of type of rupture was conducted on cylinders with radii of 15 or 24 inches, stiffened by stringers and riveted-on rings. Subjecting these cylinders to a constant internal pressure and to repeated torsion loads resulted in fatigue cracks at 45° to the cylinder axis.

Figure 4 shows the results of the initial investigation on 2024-T3 cylinders. Hoop stress is plotted as the ordinate and ring-reinforcement ratio, the ratio of the cross-sectional area of a ring A_R to the area of the associated skin lt_s, is plotted as the abscissa. The dashed line, labeled "theoretical criterion," is based on elemetary considerations and gives the area which the rings must have to carry the hoop load if the skin itself cannot carry it because it is cracked or cut. The circles denote confined ruptures, the x-marks denote unconfined ruptures in the tests. The solid line, labeled "empirical criterion," is approximately the upper boundary of the confined ruptures. The ring-size criterion can thus be used as a basis for predicting the type of rupture. The data are taken from reference 3, except that the curve showing the empirical criterion is drawn here in a somewhat more conservative fashion than in the reference.



A few tests of the same nature have been made on cylinders of 7075-T6 material. The number of tests was too small to establish an empirical criterion for ring size, and the method of testing, pressure combined with cyclic torsion, has been replaced by pressure cycling.

NEW INVESTIGATIONS

Presented herewith are evaluations of more recent data. The presentation is aimed at answering two questions:

(1) What correlation exists between the critical crack length for unstiffened cylinders and that for stiffened cylinders?

(2) How reliable is the ring-size criterion for predicting the nature of the rupture of stiffened cylinders when the cracks are longitudinal rather than at 45°, as in the original investigation?

The majority of the tests discussed were actually made to obtain some preliminary information on the effect of parameters not considered previously, for instance, type of rings used. As a result, the tests available at this time are inadequate for giving definite answers to the two questions posed, but they do indicate trends.

The tests fall into three groups according to size of cylinder: small cylinders with a radius of 3.6 inches; medium-size ones with a radius of 15 inches; and full-scale ones with a radius of about 70 inches. All were stiffened by stringers and rings or hoops.

The small cylinders had precut slits and were brought to rupture by increasing the pressure steadily. The crack-length results are shown in figure 5. The curve, labeled δ_{REF}, gives the critical crack length of unstiffened cylinders having the same radius. The circles denote again confined ruptures; the x-marks, unconfined ruptures. Regardless of the type of rupture, all the critical crack lengths plot fairly close to the reference curve, which means that the critical crack lengths of the stiffened cylinders in this group of tests are equal to those of corresponding unstiffened cylinders.

Figure 6 shows the ring-size criterion plot for the same group of tests. Each test point represents the same specimen as the point at the same stress level in figure 5. The empirical criterion line is taken from figure 4. All ruptures observed are in agreement with the criterion: unconfined if above the curve, confined if below the curve. The cylinders in this test group had either rather light rings or else rather heavy rings; as a result this test group does not give a sensitive check on the



accuracy of the ring-size criterion. On the other hand, the fact that rather extreme ring sizes were used tends to increase the weight of the evidence regarding crack length shown in figure 5.

The next group of tests is on medium-size cylinders (15-inch radius) of 2024-T3 material. On these cylinders, the internal pressure was cycled to grow a fatigue crack, starting from an initial slit. Figure 7 shows the crack-length plot. The critical crack lengths for this group of tests are consistently longer than indicated by the reference curve, the excess length varying roughly from 40 percent to 100 percent. The result thus differs markedly from that obtained on the small cylinders.

Figure 8 is the ring-size plot for the medium-size cylinders. The types of failure are in agreement with the prediction, if the prediction for the border-line case on the line is made conservatively. This plot shows only 3 points, and thus no counterparts are shown for many of the points shown in figure 7; the missing points are discussed in the following paragraph.

On the small cylinders, and on the three medium-size cylinders discussed in the previous paragraph, the rings were riveted continuously to the skin. On the other medium-size cylinders, the rings were either floating, that is, not touching the skin at all, or they were touching the skin, but riveted to it only at the intersections with the stringers. Rings of either type are believed to have little if any power to confine rupture; therefore, the assumption is made that the presence of either type of ring justifies a prediction of unconfined rupture, and consequently, it is unnecessary to plot the point on the ring-criterion plot in order to arrive at a prediction of the type of rupture. So far, there appears to be no evidence that the assumption is unduly conservative.

Figure 9 shows the crack-length results for medium-size cylinders of 7075-T6. All the points plot close to the reference curve. Since the corresponding plot for 2024-T3 material (fig. 7) showed excess crack lengths ranging from 40 percent to 100 percent, it may be said that 2024-T3 has a "hidden margin of safety," under some conditions, which appears to be lacking in 7075-T6 material.

Figure 10 is the ring-size plot for the 7075-T6 cylinders. Only the theoretical criterion is shown, since no empirical criterion is established, as mentioned previously. The type of rupture is as expected in all cases, but the location of the points is such that the empirical criterion still remains undefined.

Figure 11 with data taken from references 4 and 5 shows two tests made by two aircraft manufacturers on full-scale models of fuselages with a radius of about 70 inches. The critical crack length is just above the



reference value for specimen A and about 60 percent larger for specimen B. This scatter suggests a scatter band somewhat similar to that obtained on the medium-size cylinders.

In specimen A, a saw slit had been made through the skin as well as through the ring underneath it. With one ring thus out of action, the ring-reinforcement ratio was marginal, which would lead to the prediction that the rupture will probably be unconfined. For specimen B, an unconfined rupture would be predicted because the rings were floating. The symbols indicate that both specimens had unconfined ruptures. It should be noted that both specimens served as starting points in the development of final designs.

CONCLUDING REMARKS

The crack-length criterion and the ring-size criterion appear to offer some promise as tools for putting some aspects of fail-safe design on a quantitative basis. The crack-length criterion in its present form states that the critical crack length of a stiffened cylinder is at least equal to that of an unstiffened cylinder of the same radius. The ring-size criterion, which is reasonably well established for 2024-T3 aluminum alloy but not for 7075-T6 aluminum alloy, appears to permit a prediction whether the rupture will be confined or unconfined when the rings are continuously riveted to the skin. When the rings are not so riveted (or otherwise fastened), the rupture will probably be unconfined.

Much work remains to be done, however. The conditions under which the critical crack length of the stiffened cylinder can be greater than that of the unstiffened cylinder should be established more fully. Only stray bits of information are available at present on a number of factors, such as effect of stringers, of load-carrying members bridging a crack, and of producing the initial damage very rapidly.



REFERENCES

1. McEvily, Arthur J., Jr., Illg, Walter, and Hardrath, Herbert F.: Static Strength of Aluminum-Alloy Specimens Containing Fatigue Cracks. NACA TN 3816, 1956.

2. Peters, Roger W., and Kuhn, Paul: Bursting Strength of Unstiffened Pressure Cylinders With Slits. NACA TN 3993, 1957.

3. Peters, Roger W., and Dow, Norris F.: Failure Characteristics of Pressurized Stiffened Cylinders. NACA TN 3851, 1956.

4. Sorensen, Arne: Some Design Considerations for Tear-Resistant Airplane Structures. Preprint No. 618, S.M.F. Fund Preprint, Inst. Aero. Sci., Jan. 1956.

5. Spaulding, E. H.: Observations on the Design of Fatigue-Resistant and 'Fail Safe' Aircraft Structures. Session 8. Paper 2. Presented at International Conference on Fatigue of Metals sponsored by British Inst. Mech. Eng. and A.S.M.E., Sept. 10-14 (London) & Nov. 28-30 (New York), 1956.



TYPES OF RUPTURE

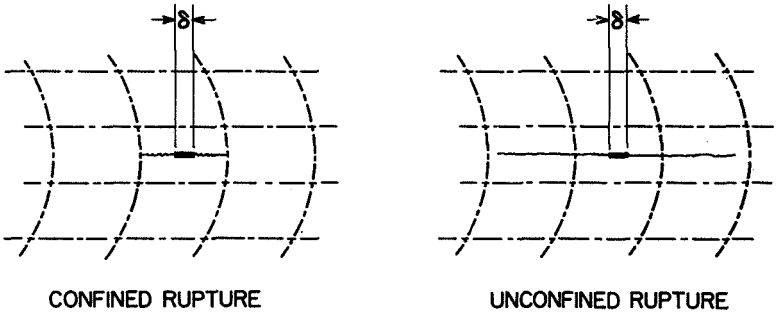
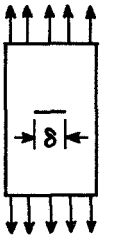


Figure 1

STRENGTH OF CRACKED SPECIMENS

$$\sigma_{MAX} = \frac{P}{A_{NET}} K_u = \sigma_u$$



$$K_{u,CYL} = K_u\left(1 + 4.6\frac{\delta}{r}\right)$$

FOR 2024-T3 AND 7075-T6 ALUMINUM ALLOY

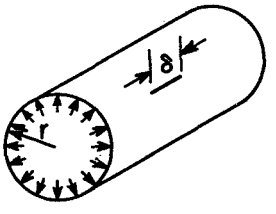
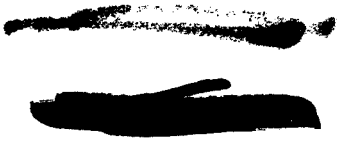


Figure 2



CRITICAL CRACK LENGTHS
UNSTIFFENED CYLINDERS

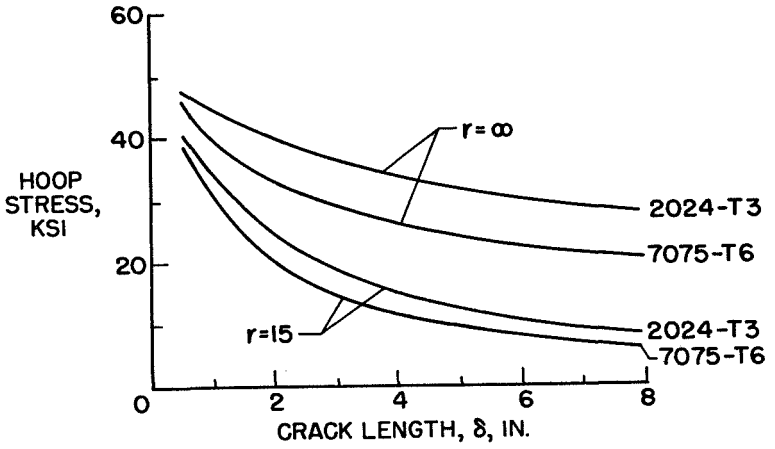


Figure 3

RING-SIZE CRITERION FOR 2024-T3
r=15 AND 24 IN.; PRESSURE AND TORSION

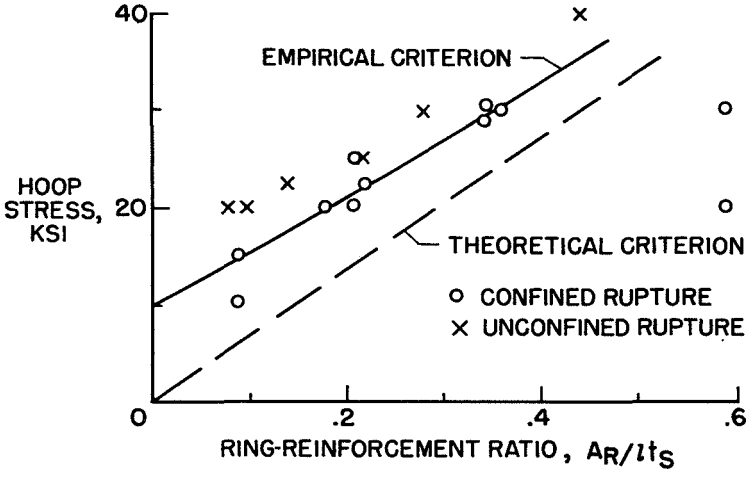


Figure 4

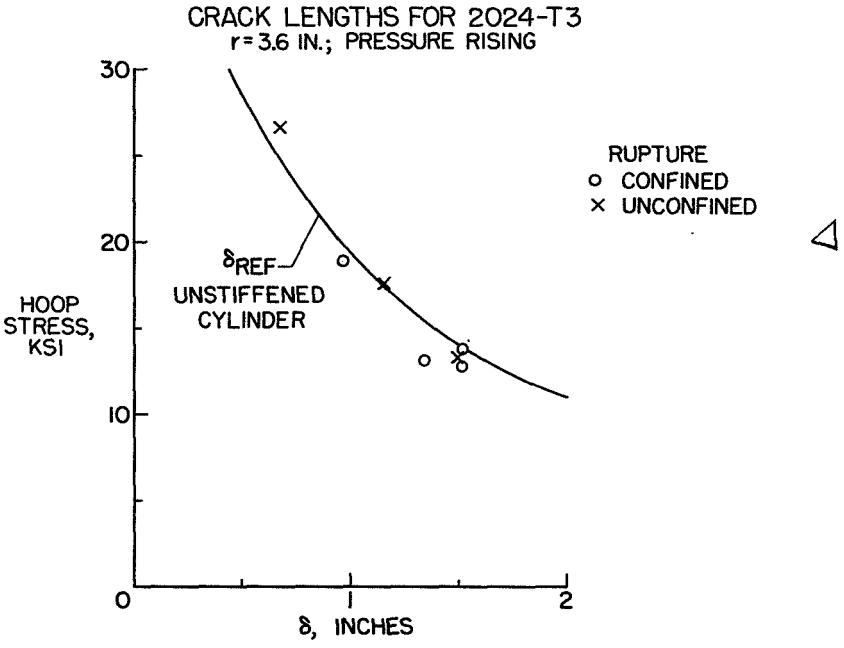


Figure 5

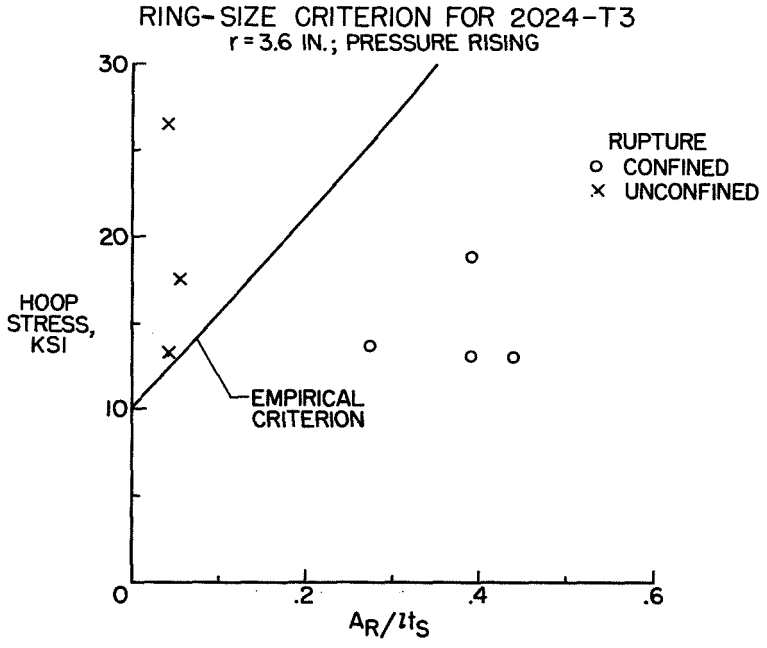


Figure 6

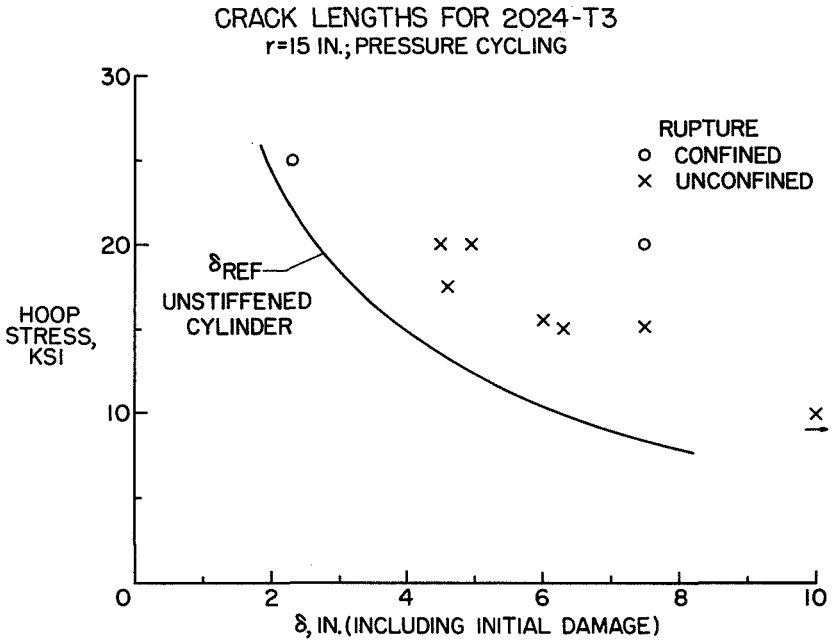


Figure 7

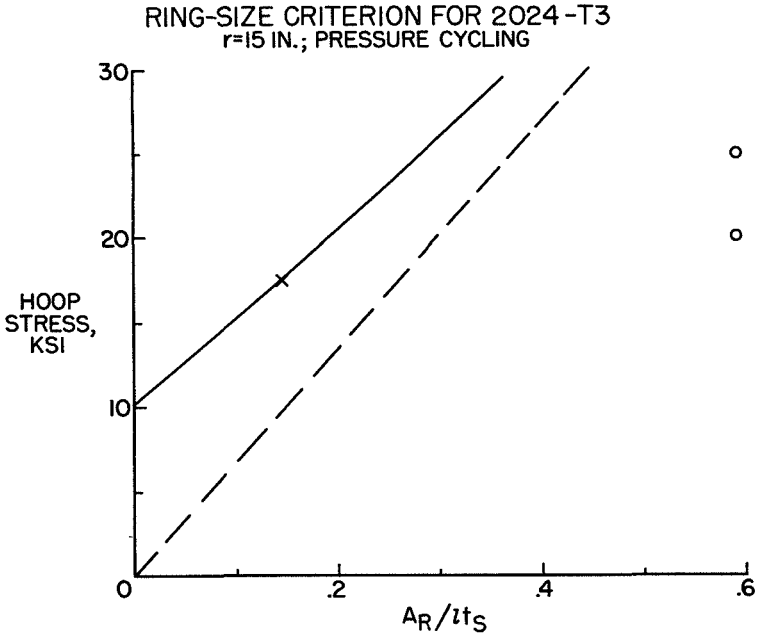


Figure 8

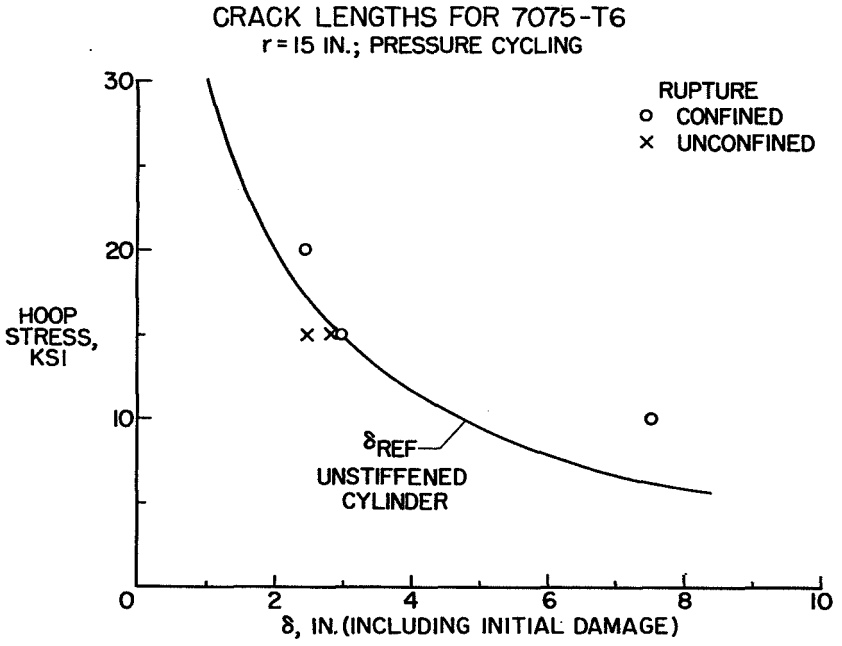


Figure 9

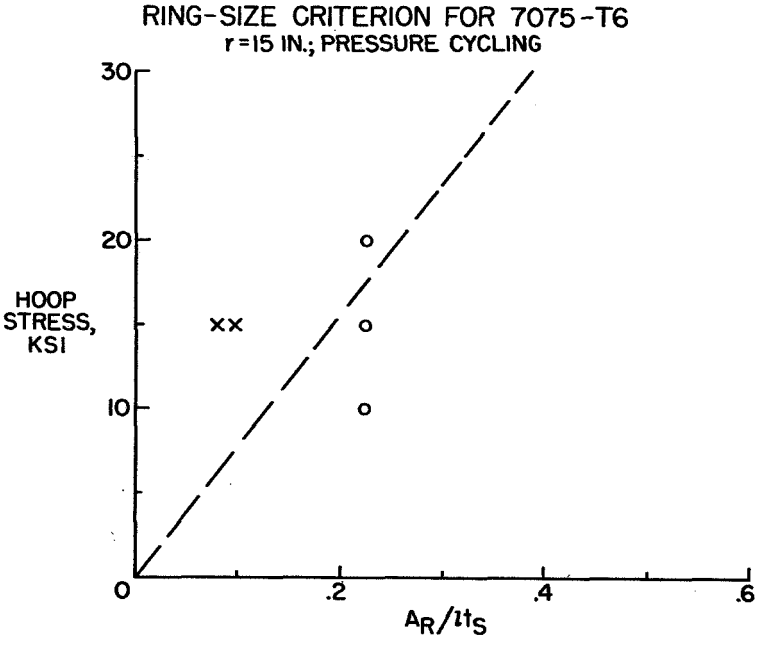


Figure 10

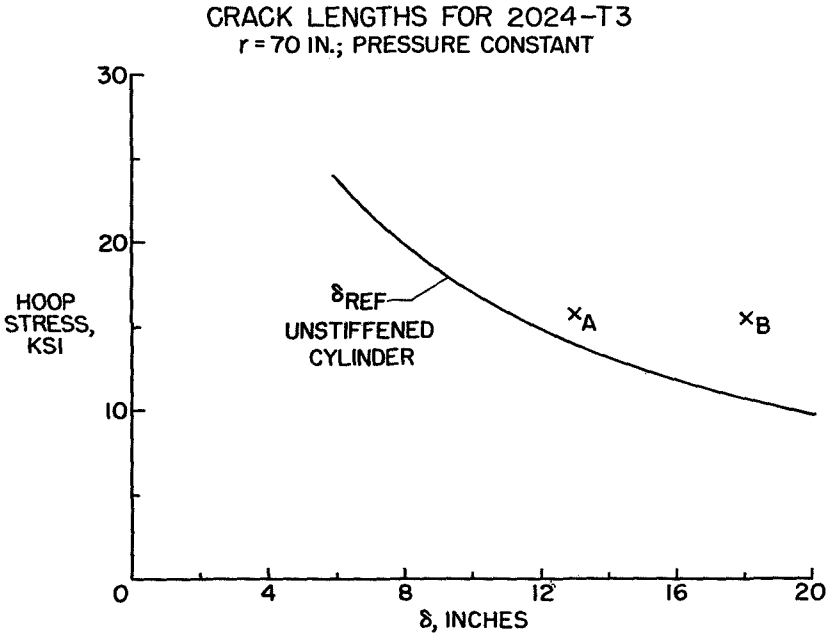

CRACK LENGTHS FOR 2024-T3
r = 70 IN.; PRESSURE CONSTANT
HOOP STRESS, KSI
30
20
10
0
4
8
12
16
20
δ, INCHES
δREF
UNSTIFFENED CYLINDER
×A
×B

Figure 11

RESULTS FROM RANDOM-LOADING FATIGUE TESTS OF A FULL-SCALE TRANSPORT WING

N71-75416

By John B. Garvin

Langley Aeronautical Laboratory

The importance of the "fail-safe" design concept with regard to fatigue in modern airplane structures is evidenced by the great attention which has recently been directed to this subject. Involved in this concept are a need to know something of the behavior of a fatigue crack as it starts and grows in an airplane component and, in addition, a need for knowledge of ability to estimate the fatigue life of the aircraft structure.

This paper presents results from an experimental investigation of full-scale-airplane fatigue. Crack behavior and fatigue life were studied during the application of random or variable-amplitude loads to the wings of a C-46 transport-type airplane. These wings were the same types of structures which were used in constant-amplitude fatigue tests reported in references 1 and 2. The fatigue tests of these wings provide the first opportunity to compare results from full-scale constant-amplitude loadings with those simulating actual flight.

The loading chosen for the variable-amplitude tests was the gust spectrum reported by Rhode and Donely for a wide sampling of transport operations in the United States. (See ref. 3.) The gust spectrum was selected because the loads due to flight maneuvers and ground operations were not considered to play a significant part in the fatigue life of this airplane.

Figure 1 presents the incremental loading spectrum for the C-46. The ranges of incremental load factor for each loading level are shown plotted against the number of loads applied at each level. Loads were applied at the mean of each of the 16 load ranges designated by the circled points. Thus, the lowest value of incremental load was 0.225g, representing the range from the threshold value of 0.15g to 0.30g. The numbers of cycles were established on the basis of a representative flight distance of 10 million miles. The maximum loading associated with a flight operation of this duration would, as is indicated by the position of the dashed line in the figure, be somewhat greater than limit load for this airplane.

In order to apply the loadings in such a way as to avoid putting on all one size load prior to any other, the spectrum of figure 1 was divided



by 100 which would correspond to a distance of 100,000 miles or about 500 flying hours under the assumed typical conditions of flight. The loads which appeared less than 100 times in the original spectrum would appear only occasionally in the reduced spectra.

For the purpose of introducing randomness into this method of loading, the actual order of application of the loading steps was established by reference to a table of random numbers. Such an arrangement has been called a "sequence." The random arrangements of the loadings in the reduced spectra for the first three sequences are illustrated in table I. The first incremental loading in the first sequence is the 0.525g load applied 3,510 times; this is followed by the 0.675g load applied 1,067 times. The load at 2.475g and all other loads in this sequence which appear with a zero value for the number of cycles applied are those loads which occur less than 100 times in the original 10-million-mile spectrum and thus only appear occasionally in the 100 sequences. It can be readily seen that the orders of application of the loads in the 3 sequences shown are different, and it may be of interest to note that none of the 100 sequences were identical with regard to order of load application to the specimen. Loading sequences greater than 100 repeated the original order; thus, the 101 sequence was the same as the first sequence.

The fatigue machine used for this investigation is seen in figure 2. This machine was basically a concentrated-eccentric-mass type of shaker capable of being operated at any frequency up to 4 cycles per second. The wing attached to a central portion of the fuselage can be seen inverted and mounted between two large supporting structures near the center of the picture. The eccentric weights can be seen under the wing tip; the gearbox and drive shafting are under the wing; and the necessary controls and cycle-measuring equipment were located centrally near the main support structures. Loads were applied dynamically up to incremental values of ± 1 g. Those loads above this level were applied statically by means of the hydraulic ram located directly over the eccentric weights. All loads applied during the tests were monitored by either internal structural strain gages or external load-measuring dynamometers which are located on top of the loading rams.

This program has, up to the present time, performed variable-amplitude tests on three complete wings, each composed of one center section and two outer panels. A total of 46 cracks have been observed, of which one crack on each of the six outer panels grew to such size as to indicate imminent failure of the wing. Actual final lifetimes accumulated by these wings ranged between 120 and 219 sequences of load corresponding to assumed flight times of from 62,000 to 114,000 flight hours.

Three subjects appear of interest from the results of these variable amplitude tests: the area of fatigue crack initiation, the rate of growth or propagation of the crack, and the [redacted]tion of fatigue damage in the structure during variable amplitude loading.



With regard to crack initiation, it was noted that fatigue cracks which grew to final failure in the variable-amplitude tests initiated in areas where cracks initiated only during the high-level constant-amplitude loadings. In other words, the serious cracks found under the random test conditions did not occur at the loadings which might be considered representative of that for greatest damage in the constant-level tests. Therefore, a constant-level fatigue test at the level of greatest fatigue damage might not reveal the proper area of crack initiation which would be of interest to operational inspection crews.

Crack-growth information is shown in figure 3. The abscissa scale is the percentage of final life for the specimen. This scale was chosen for convenience in displaying the results for specimens which were subjected to different values of constant-amplitude loading as well as those subjected to random loadings. This will be clear when it is realized that the specimen tested at a constant alternating load level of ± 1 g sustained only 100,000 cycles of load, while the variable-amplitude specimens accumulated about 10,000,000 cycles of load before final failure. The dashed curves show crack growth for two representative constant-amplitude specimens tested at a low and a high value of alternating load, and the solid curves show results for two representative variable-amplitude specimens. All curves appear to exhibit a characteristic shape denoting slow growth of the crack from initiation at about one-third to one-half of the final life until about 95 percent of the life had been spent, after which there was a very rapid growth of the crack until the entire specimen failed. This rapid growth initiated at a point where the crack had approached a value between 5 and 10 percent of the total tension material. The appearance of the step shown in the two upper curves at about 70 percent of the life is associated with the failure of a fairly heavy element of the structure. This failure characteristic appears to be associated with a particular configuration and might not be generally applicable to other structures. It would seem, however, from these results, that crack growth under variable-amplitude loading conditions is, in general, like crack growth under the constant-amplitude loadings.

An assessment of the amount of fatigue damage which an airplane wing might accumulate during the variable-amplitude loadings of flight may be determined in several ways. The cumulative-damage criterion, usually attributed to Miner, has been selected for a first comparison. (See ref. 4.) Since this damage criterion is based on an endurance curve from constant level testing and since such a curve was available from previous tests on an identical structure, having the same load distribution and corresponding load ranges, it was felt that this damage criterion might give an excellent prediction of life for both crack initiation and for final failure of the wing.

Figures 4 and 5 show the agreement obtained for the six outer wing panels tested under variable-amplitude loadings. A bar graph is used to show the relative life of these panels. The standard of comparison is the life calculated from the results of the constant-level tests. Figure 4 shows the relative life until initiation of the crack which grew to fail each specimen, and figure 5 shows the relative life until final failure. The calculated life for crack initiation was 17.4 sequences or about 8,700 flight hours while the calculated life to final failure was 37 sequences or about 18,500 hours. It can be seen in figure 4 that the average actual life to crack initiation is about $3\frac{1}{2}$ times the predicted life with a spread of about 5 to 1. Similar comparisons for all the 46 cracks which initiated in these wings would show that the average life would have been about $4\frac{1}{2}$ times the predicted life, while the overall spread would be about 33 to 1. The earliest crack which occurred in any of the wings was found to occur at about one-third of the life predicted by the cumulative-damage criterion.

Figure 5 shows that the actual final life of these specimens was about four times that predicted by this damage criterion and that the spread in the final failure values is slightly less than 2 to 1. It would appear from this that an estimation of a finite life either to crack initiation or final failure by the cumulative-damage method based on constant-level fatigue-test results would be uncertain.

Another method of analyzing fatigue life was performed on these data for comparison purposes. This method, known as the "intersect" method, makes use of the summation curve for the spectrum loading in conjunction with the appropriate endurance curves from the constant-level tests.

These results for the same specimens are shown in figures 6 and 7. In figure 6, the difference between predicted life and measured life has been reduced to a value of about 2 while the spread, as would be expected, remains the same as for the cumulative-damage method. In the case for final failure shown in figure 7, differences of about 2 to 1 are seen as were noted in the case for crack initiation by this method; here again the spread is the same as for the cumulative-damage method. Although the intersect method indicates closer values of life prediction than the cumulative-damage method, there appears to be little advantage of one method over the other because of the influence of spread in the data, particularly in the crack-initiation case.

The significance of any particular value of estimated life by either method would appear to be questionable; however, this would be the case in any attempt to use the results from one or several constant-level fatigue tests to predict the endurance of a similar component subjected to the variable loads of actual flight.

The apparent increase in life of the C-46 wings as indicated by the absolute values of both methods might be explained by the application of the higher loads of the spectrum. It is noted that these larger loads were of such a magnitude as to cause a considerable increase in life as indicated by results from constant-level tests on Meteor 4 tailplanes reported by Raithby and Longson in reference 5. Whether or not this effect fully accounts for the increase in life noted here is not known.

In summary, it appears that a constant-amplitude fatigue test might not reveal the area wherein a crack would initiate to cause failure of a structure subjected to the variable loadings of flight; crack propagation behavior based on the final life of the specimen appears to be similar under both constant- and variable-amplitude loadings; and, finally, the assessment of fatigue damage by either the cumulative damage method or the intersect method appears questionable when based only on constant-level fatigue-test results.

REFERENCES

1. McGuigan, M. J., Jr., Bryan, D. F., and Whaley, R. E.: Fatigue Investigation of Full-Scale Transport-Airplane Wings - Summary of Constant-Amplitude Tests Through 1953. NACA TN 3190, 1954.

2. Whaley, Richard E., McGuigan, M. J., Jr., and Bryan, D. F.: Fatigue-Crack-Propagation and Residual-Static-Strength Results on Full-Scale Transport-Airplane Wings. NACA TN 3847, 1956.

3. Rhode, Richard V., and Donely, Phillip: Frequency of Occurrence of Atmospheric Gusts and of Related Loads on Airplane Structures. NACA WR L-121, 1944. (Formerly NACA ARR L4I21.)

4. Miner, Milton A.: Cumulative Damage in Fatigue. Jour. Appl. Mech., vol. 12, no. 3, Sept. 1945, pp. A-159 - A-164.

5. Raithby, K. D., and Longson, Jennifer: Some Fatigue Characteristics of a Two Spar Light Alloy Structure (Meteor 4 Tailplane). Rep. No. Structures 195, British R.A.E., Jan. 1956.



TABLE I.- ORDER OF LOADING

First sequence		Second sequence		Third sequence	
Load, Δn	Cycles	Load, Δn	Cycles	Load, Δn	Cycles
0.525	3,510	1.725	0	0.225	39,312
2.475	0	2.175	0	1.125	21
1.875	0	.825	236	1.425	1
2.325	0	1.425	1	2.025	0
.675	1,067	1.275	5	2.475	0
2.025	0	1.575	1	.975	73
.975	73	1.125	20	1.875	1
1.575	1	2.475	0	.525	3,510
1.725	0	.375	15,444	1.575	1
1.275	6	.225	39,312	2.325	0
2.175	0	.675	1,067	.825	235
1.125	20	.525	3,510	.675	1,067
1.425	1	.975	73	1.725	0
.825	235	2.025	0	1.275	5
.225	39,312	2.325	0	2.175	0
.375	15,444	1.875	1	.375	15,444



C-46 LOAD SPECTRUM

10^7 MILES OF FLIGHT

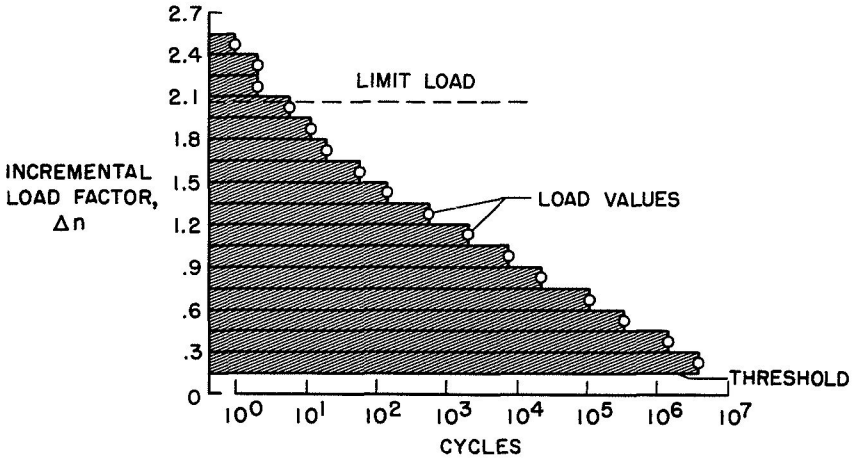


Figure 1

C-46 VARIABLE-AMPLITUDE FATIGUE MACHINE

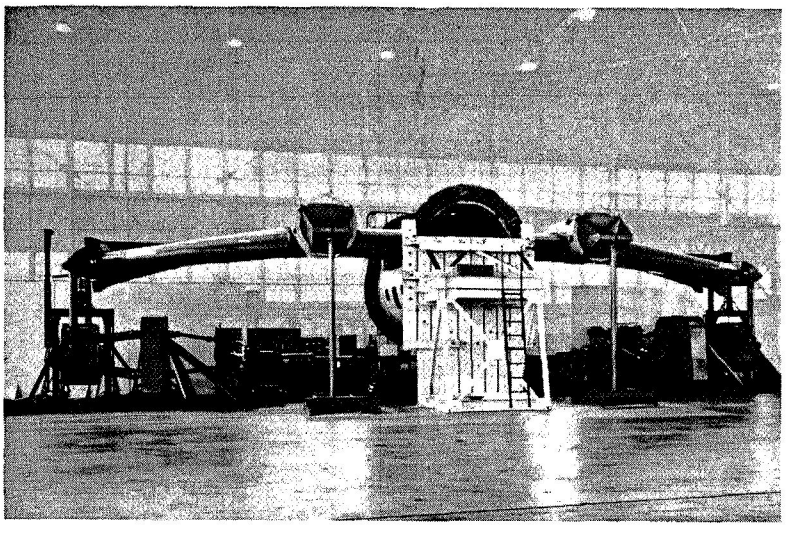


Figure 2

L-57-479.1

457

FATIGUE - CRACK PROPAGATION

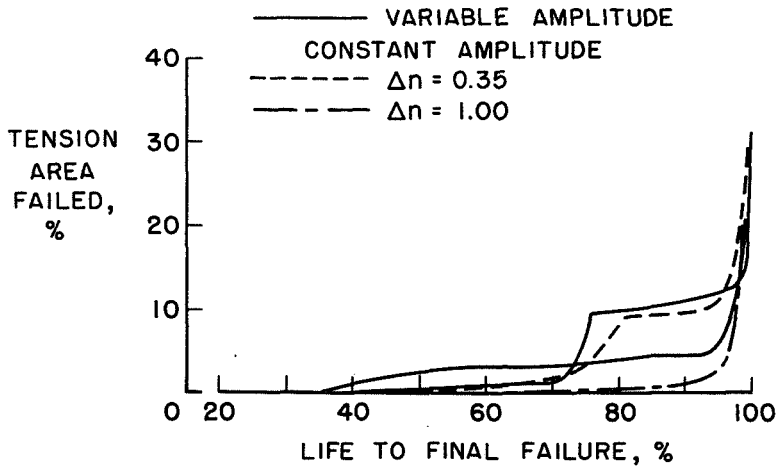


Figure 3

DAMAGE EVALUATION
CUMULATIVE DAMAGE METHOD; CRACK INITIATION

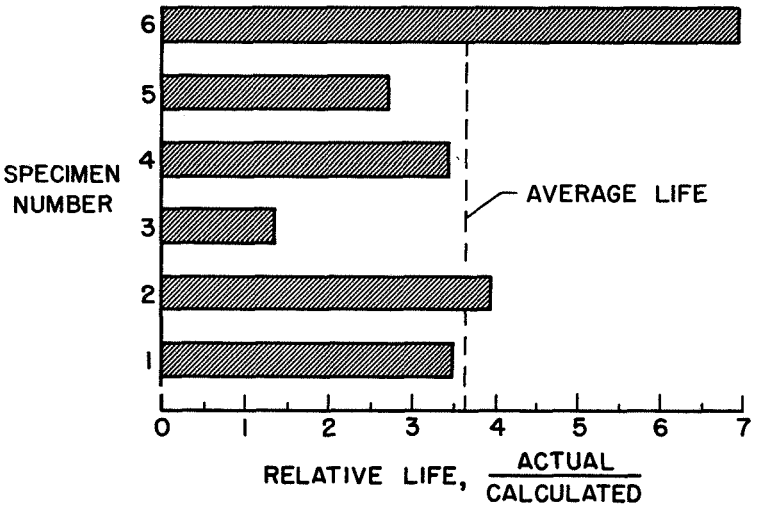


Figure 4

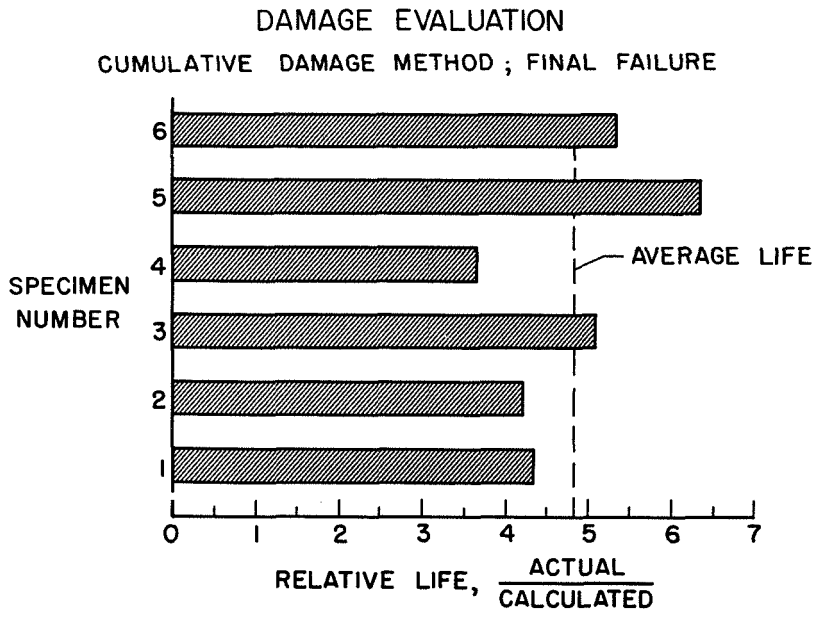


Figure 5

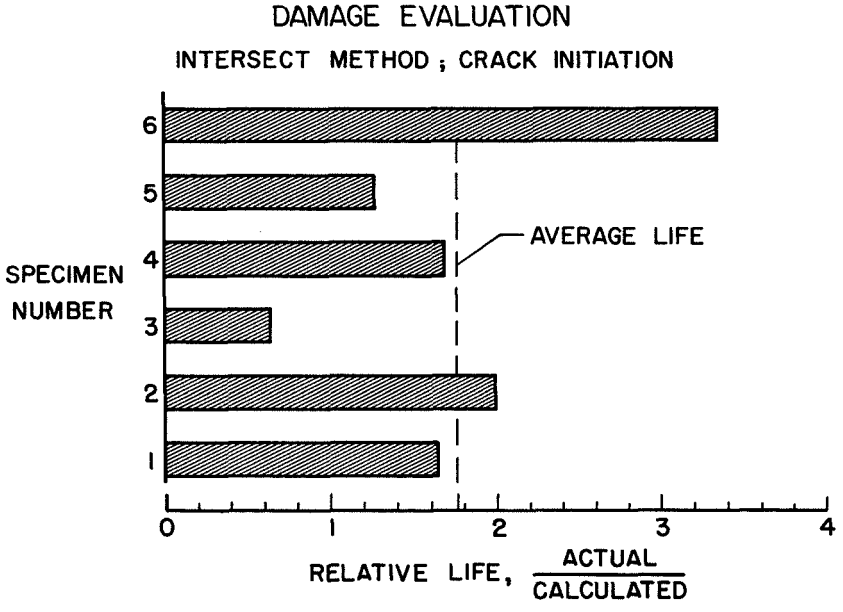


Figure 6

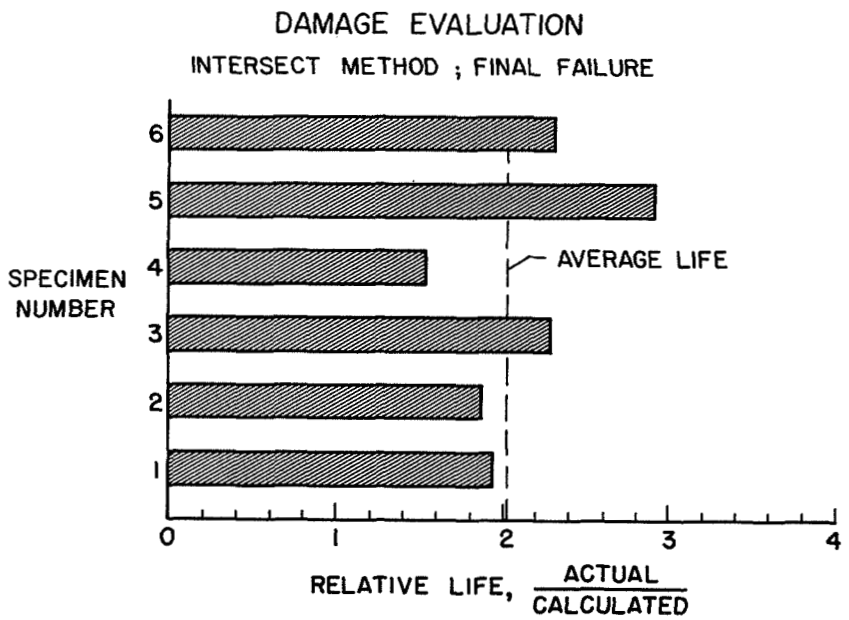

DAMAGE EVALUATION
INTERSECT METHOD ; FINAL FAILURE
SPECIMEN NUMBER
6
5
4
3
2
1
AVERAGE LIFE
0
1
2
3
4
RELATIVE LIFE, ACTUAL / CALCULATED

Figure 7

STUDIES OF STRUCTURAL FAILURE DUE TO ACOUSTIC LOADING

N71-75417

By Robert W. Hess, Robert W. Fralich,
and Harvey H. Hubbard

Langley Aeronautical Laboratory

SUMMARY

Some discussion of the acoustic fatigue problem of aircraft structures is given along with data pertaining to the acoustic inputs from some powerplants in common use. Comparisons are given for results of some fatigue tests of flat panels and cantilever beams exposed to both random- and discrete-type inputs. In this regard it appears that both the stress level of the test and the type of model are significant; hence, no generalization can be made at this time. With regard to increasing the fatigue life, it was noted that increased stiffening of a panel due to curvature and pressure differential is particularly beneficial.

INTRODUCTION

It is well-known that fatigue damage can occur to aircraft structures which are exposed to intense acoustic pressure loads. Damage usually occurs in the secondary structure of the aircraft as a result of a large number of relatively small loads applied at the rate of several hundred loading cycles per second. This paper presents information pertaining particularly to the problem of exposure to random noise such as that encountered from turbojets, ram jets, rocket engines, and aerodynamic boundary layers.

Some of the phenomena involved in this problem can be discussed with the aid of the block diagram of table I. Let us first direct our attention to the blocks themselves. The acoustic inputs are in the form of fluctuating pressures on the exposed surface of the structure. They impose loads that tend to vibrate the surface. Depending on its structural characteristics, such as geometry and method of construction, the surface will have a certain dynamic response. This dynamic response influences the stress patterns in the structure which, in turn, determine the fatigue life.

Analyses have been published (refs. 1 and 2) wherein the phenomena denoted as A in table I were made use of to calculate stresses on a simple panel. A knowledge of the noise spectra at an arbitrary point and the dynamic response to a uniform load have made it possible to calculate, by spectral techniques, the stresses at an arbitrary point on the panel. For more complex structures or inputs or both, this approach may not be sufficient and it may thus be necessary to use the quantities denoted as B in table I for the stress analyses. For instance, a knowledge of the correlation functions of the acoustic input and the complex dynamic influence coefficients of a panel surface might make it possible to calculate the stress distribution over the surface.

Thus, it is seen that the blocks in table I each represent rather complex phenomena. Detailed analyses of all parts of this problem would involve considerable effort and are beyond the scope of this paper. The rest of this paper will deal mainly with the fatigue life of structures exposed to noise and, in particular, will compare results of random and discrete frequency fatigue testing. The other parts of the problem are discussed only briefly.

SYMBOLS

d	nozzle diameter
x	axial distance measured from nozzle exit plane
$\Phi_N(\omega)$	power spectral density of noise input
$Z(\omega)$	mechanical impedance of panel
$\Phi_\sigma(\omega)$	power spectrum of stress in panel

ACOUSTIC INPUTS

The ingredient of this problem which differentiates it from other fatigue problems is the nature of the input function. This can be described briefly with the aid of figure 1. Shown here are the acoustic inputs for various powerplants in common use. The data shown are the noise pressure loads on a surface parallel to the thrust axis of the engine and four exit diameters distant from it. (Free space measurements were increased by 3 decibels to adjust them to conditions at the surface of the wall.) Both the noise pressure levels in decibels and the equivalent noise pressures in pounds per square foot are given on the vertical scale as a function of distance from the exit nozzle of

the engine. Surface pressure data are given for two turbojet engines and one rocket engine. It should be noted that the numbers associated with the coded legend are the pounds of thrust developed by the engine per square foot of nozzle exit area. The short solid turbojet curve applies to the J34-WE-22 turbojet engine whereas the curve of long dashes applies to the J57-P-3 engine for which free-space data are given in reference 3. These two curves illustrate the growing severity of the problem as the engine performance increases because of the increased engine pressure ratio. The curve of long-short dashes applies to a World War II rocket engine. It is seen that these pressures are of the order of 10 decibels higher than those for the J57 turbojet engine. For rocket engines operating at higher pressure ratios, there is some evidence that the acoustic pressure would also tend to be higher. All these engines generate intense noise in the range of frequencies that is detrimental to aircraft structures. For the type of random spectra generated by these engines, fatigue damage can occur at overall levels of the order of 140 decibels or higher. The amount of damage incurred at any given level, of course, is a function of the (1) detail design of the structure, (2) the length of exposure to the noise, and, also, (3) the spectrum of the noise.

DYNAMIC RESPONSE

The importance of the noise spectrum with relation to the dynamic response of a given structure is illustrated by the diagrams of figure 2. Conditions are defined for tests of flat panels exposed to discrete frequency noise from a siren and to random noise from a jet.

The input spectra of figure 2 are related to the stress spectra by the panel admittance. It can be seen that the noise from the siren was contained largely in the fundamental frequency, the harmonics being few in number and relatively weak. For these tests the siren was tuned until the fundamental frequency coincided with the first natural mode of the panel. As a result nearly all the energy accepted by the panel is in its first mode. A panel being excited by the broad-band spectrum of the jet, on the other hand, responds in some degree to all frequencies.

It can be seen from an inspection of the figure that a panel will accept essentially all the energy available from the siren whereas a large part of the energy available from the jet is not accepted. For these particular tests, the stress developed by a discrete-type excitation would be expected to be greater at a given overall noise pressure.

[redacted]

FATIGUE LIFE

Effects of Overall Noise Level

Some fatigue results obtained for panels exposed to both of these types of input are given in figure 3. Fatigue life as a function of the overall noise level is shown for an 0.032-inch gage flat panel 11 inches by 13 inches mounted over a rectangular cutout in a rigid frame. The panel was attached by small round head bolts tightened to a predetermined torque. This configuration was chosen for the reason that it facilitated assembly and disassembly of models while stress concentrations similar to those in a riveted structure were retained. For the solid points which represent fatigue data obtained with the siren, the curve has been sketched in through the available points to indicate a general trend of the data. Fatigue life is very strongly dependent on the level of noise excitation, since it varies from under a minute to several hours in the noise-level range of the tests.

Attention is called particularly to the open points which are data obtained with the jet. These data fall generally to the right of the curve in figure 3; thus, a longer fatigue life is indicated. This difference in fatigue life is due in part to the fact that the panel has a higher root-mean-square stress level when excited by the siren for a given overall noise level than when excited by the air jet.

Effects of Method of Mounting

During the discrete frequency tests with these simple panels, the opportunity was taken to change the manner of mounting to evaluate possible effects on fatigue life. These mounting configurations are shown schematically in figure 4 along with some of the test results in bar graph form. For all the mountings, the gage and size of panel were constant and the input noise levels were also constant. The basic configuration A is the same as that for which data were presented in figure 3. Failures in the skin panel occurred first near the bolt heads and the average fatigue life for this configuration is used as a reference in the figure.

Configuration B is the same as configuration A except that a layer of bonding material is placed between the panel and the rigid frame. During testing, the panel first peeled away from the bonding and then failure in the skin occurred near the bolt heads. This configuration lasted on the average about 50 percent longer than configuration A. An attempt was made to eliminate peeling by bonding both sides and clamping the panel between two rigid surfaces as in configuration C. In this case failure occurred at the edge of the frame and the average model lasted twice as long as configuration A.

[redacted]

In order to study the effects of curvature some panel models were rolled to an 8-foot radius and were fastened for testing to a curved rigid frame as indicated in configuration D. Failures were initiated near the bolt heads as in configurations A and B. This condition resulted in an average life about 15 times as long as for configuration A even though the frequency of the stress cycles increased by about 50 percent. A further increase of fatigue life was obtained by leaving the edges of the frame sharp instead of rounding as in the figure. This latter scheme caused the failures to occur at the edge of the frame instead of at the bolt head; by so doing the fatigue life was doubled as indicated by the bar of dashed lines. Configuration E is the same as configuration D except that tests were made with a pressure differential of 6 pounds per square inch across the panel. This high internal pressure caused the first panel frequency to nearly treble and the fatigue life was greatly increased as shown, in spite of the much faster rate of application of stress cycles.

As a matter of interest a 0.064-inch-gage panel was tested in a configuration similar to configuration A for comparison. It was found that doubling the gage thickness of the panel increased its fatigue life to about twenty times that of configuration A. This finding was confirmed in both the jet and siren tests.

A limited number of other tests have been made on larger and more complex panels. In all cases failures came first in the stiffener elements; thus, the importance of detail design of the panel supporting structure is emphasized. It was also noted that crack growth was markedly more rapid in bonded structures than in riveted structures.

Comparison of Random and Discrete Frequency Tests

Flat panels.- The rest of the paper will deal with comparisons of fatigue life under discrete and random loading at the same root-mean-square (RMS) stress levels. The results of flat-panel tests are given in figure 5. Time to failure in hours is shown for various root-mean-square stress levels for an 0.032-inch-gage panel. The solid points were obtained by means of discrete frequency excitation from a siren whereas the open points were obtained with random excitation from an air jet. The curve is a least-square curve through the solid points. It can be seen that at a given root-mean-square stress level, failure occurs in a shorter time when the panels are excited by the random jet noise. The fact that the random noise of the jet is more destructive may result from the fact that some of the peak stress responses are several times as great for a given root-mean-square value as they are for the constant-level siren tests. This phenomenon is particularly noticeable at the lower stress levels where the differences in fatigue life tend to be the greatest and the panel damping is relatively low. At

higher stress levels the panel damping is greater and the differences in fatigue life tend to be smaller.

Cantilever beams.- Similar fatigue tests have been made for notched cantilever beams at various stress levels for both random- and discrete-type inputs. A schematic diagram of the model along with some of the test results are illustrated in figure 6.

Here again the time to failure in hours is shown at various root-mean-square stress levels for the beams tested in bending. The specimens were 3 inches long, 1 inch wide, and 1/4 inch deep with 3/16-inch notches located 1/2 inch from the root. The open points were obtained by means of an amplified tape recording of jet noise fed into a shaker attached to the tip. The solid points were obtained by applying a sinusoidal load at the tip in a Sonntag bending fatigue machine. There is a tendency in these tests also for the random load to be relatively less destructive at the higher stress levels and more destructive at the lower stress levels than the sinusoidal load. For the data of figures 5 and 6 the strain-gage locations were arbitrary and hence the root-mean-square stresses shown in figures 5 and 6 are not necessarily comparable.

A theoretical prediction of the time to failure for the random loading is given by the solid curve. This theory is essentially one given by Miles (ref. 1) and is based on Miner's rule of linear accumulation of damage. It can be seen that this theoretical curve fits the data fairly well at low stress levels but is very conservative at the higher stress levels.

CONCLUDING REMARKS

The problem of acoustic fatigue of aircraft structures has been discussed with particular emphasis on a comparison of the fatigue life due to discrete- and random-type loadings. In this regard it appears that both the stress level of the test and the type of model are significant; hence, no generalizations can be made at this time. With regard to increasing the fatigue life, it was noted that increased stiffening of a panel due to curvature and pressure differential is particularly beneficial.

REFERENCES

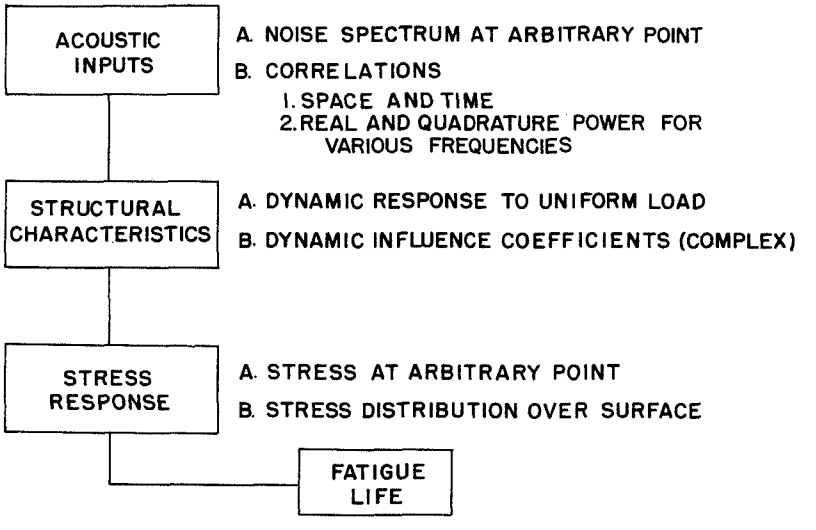
1. Miles, John W.: On Structural Fatigue Under Random Loading. Jour. Aero. Sci., vol. 21, no. 11, Nov. 1954, pp. 753-762.

2. Lassiter, Leslie W., Hess, Robert W., and Hubbard, Harvey H.: An Experimental Study of the Response of Simple Panels to Intense Acoustic Loading. Jour. Aero. Sci., vol. 24, no. 1, Jan. 1957, pp. 19-24, 80.

3. Howes, Walton L., and Mull, Harold R.: Near Noise Field of a Jet-Engine Exhaust. I - Sound Pressures. NACA TN 3763, 1956.

TABLE I

ACOUSTIC FATIGUE PROBLEM



ACOUSTIC INPUTS

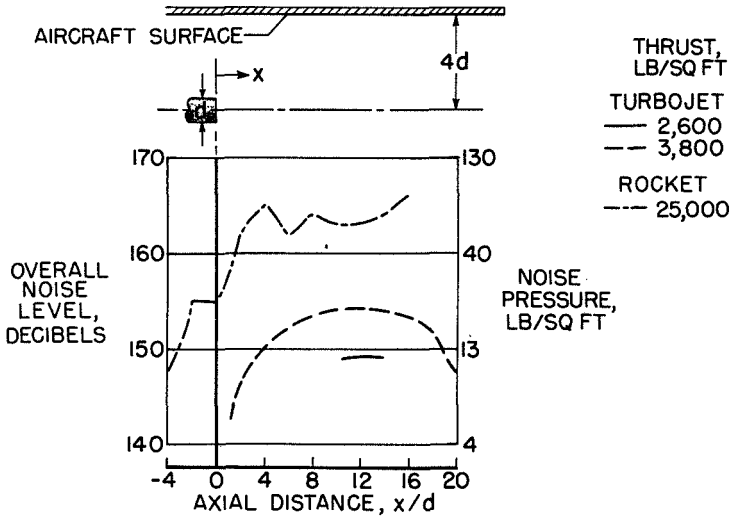


Figure 1

INPUT AND RESPONSE CHARACTERISTICS

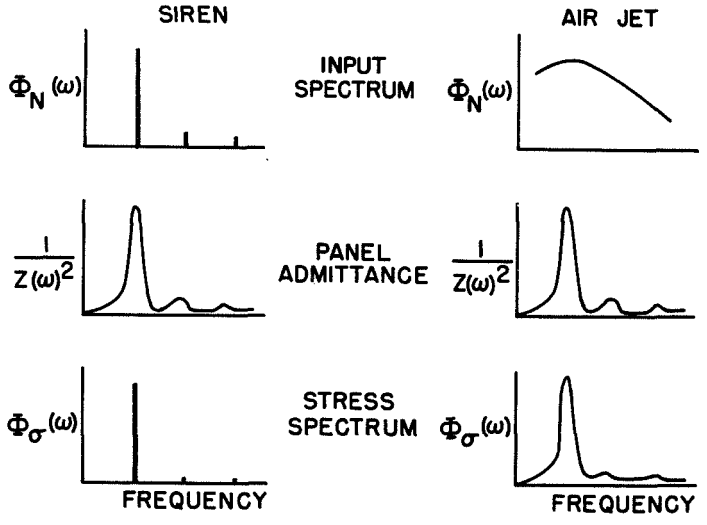


Figure 2

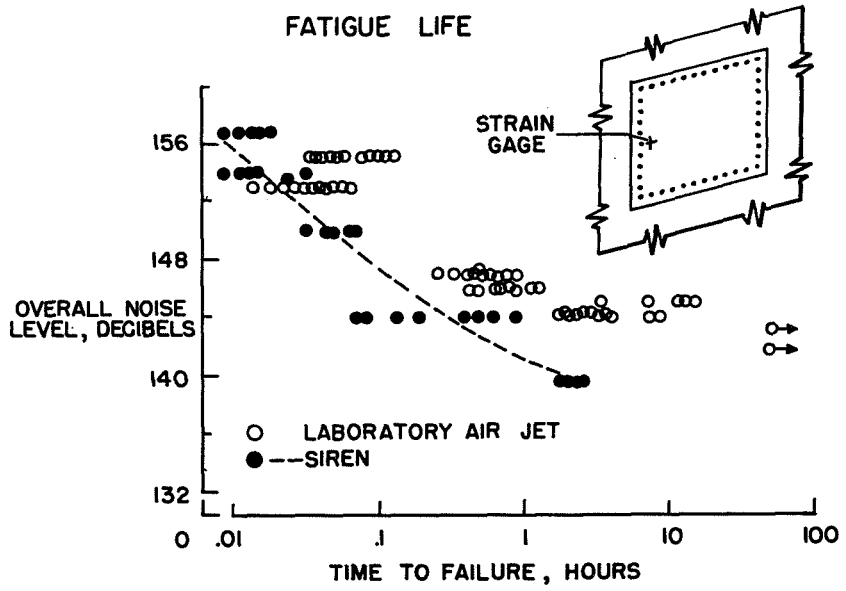


Figure 3

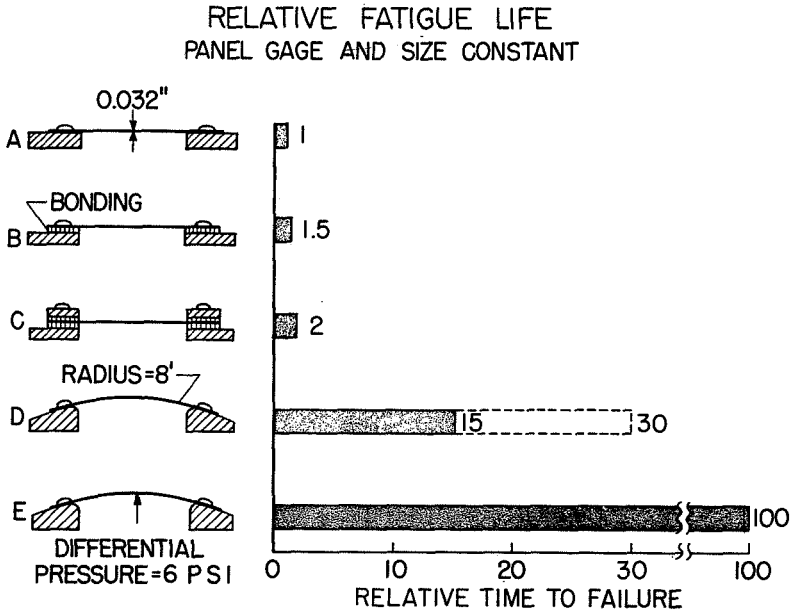


Figure 4

FATIGUE OF FLAT PANELS

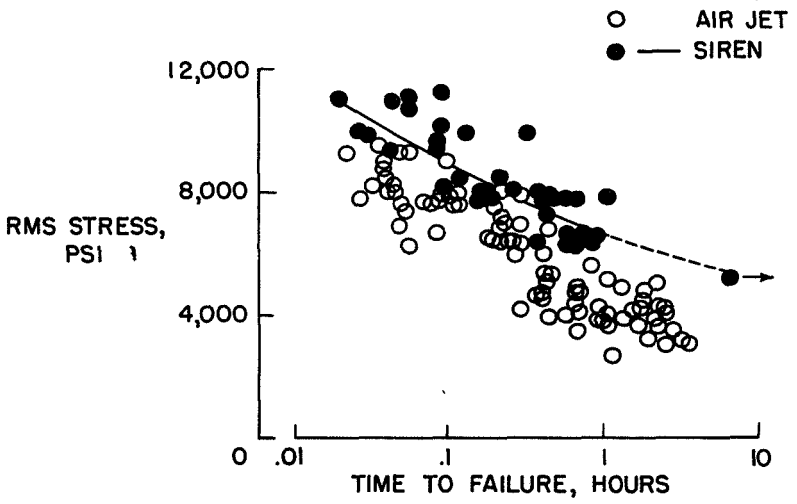


Figure 5

FATIGUE OF NOTCHED CANTILEVER BEAMS

FUNDAMENTAL FREQUENCY, 119 CPS

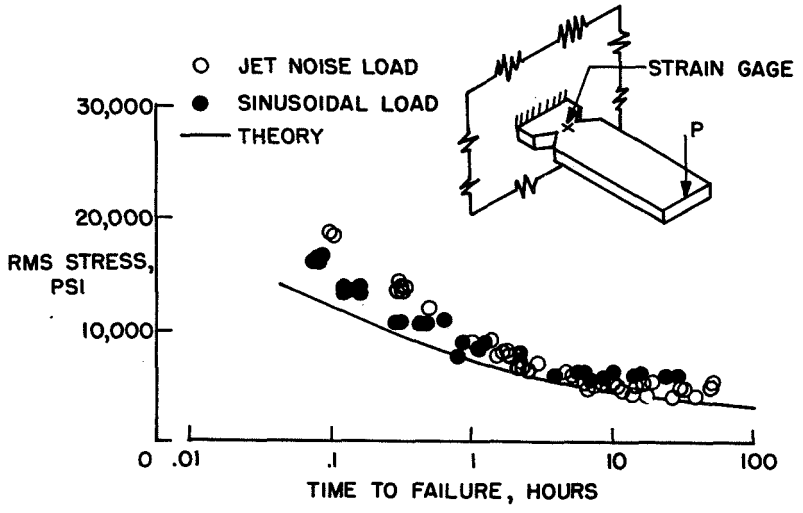


Figure 6

FLUTTER AND BUFFETING

[redacted]

THE USE OF WIND TUNNELS TO PREDICT FLIGHT BUFFET LOADS

By Don D. Davis, Jr., and Wilbur B. Huston

Langley Aeronautical Laboratory

N71-75418

SUMMARY

Methods and techniques developed for the study of buffeting by use of wind-tunnel models are described. Requirements on model damping and frequency characteristics, the model support system, and the effects of wind-tunnel turbulence on buffet tests are outlined. The results are shown of a recent comparison of buffet loads measured on a research airplane with thin unswept wings and on two different models of the airplane in two different wind tunnels.

INTRODUCTION

One objective of buffet research has been to learn how to predict flight buffet loads from wind-tunnel measurements. A method for meeting this objective is described in reference 1. Bending-moment measurements were made with electrical strain gages mounted near the wing root. By combining knowledge from two different fields, those of structural beam theory and statistical analysis, an equation was derived for predicting flight bending moments from the buffet measurements on the model. Results were presented for two specific cases, and they were encouraging.

Additional experience has been gained, since the publication of reference 1, with regard to test techniques and model requirements. The primary purpose of the present paper is to discuss these factors.

SYMBOLS

c_{AV}	average chord
$C_{I_{\alpha,1}}$	first-mode generalized lift-curve slope for damping component of aerodynamic force due to wing vibration
M	Mach number
V	velocity

[redacted]

[redacted]

474

α	angle of attack
ρ	air density
σ_M	root-mean-square value of bending moment due to buffet
$\Phi_{C_{N,1}}$	aerodynamic input parameter; power spectral density, at first-mode resonant frequency, of generalized normal-force coefficient for first-mode vibration
ω	circular frequency

Subscript:

MAX	maximum

DISCUSSION

Model Damping Requirement

One requirement for a buffet model concerns the damping of the buffet vibration. The question that arises is whether the damping is aerodynamic, structural, or some combination of the two. This question can be answered, in a given case, by studying the variation of buffet bending moment with air density as is done in figure 1. In order to facilitate comparison between different tests, the density values for a particular test have been normalized in figure 1 by dividing by the maximum density for that test. Similarly, the bending moments for a particular test have been normalized by dividing by the bending moment at the maximum density. The bending moment is herein defined as the root-mean-square value of the vibratory part of the wing-root bending moment; the static bending moment has been removed from the data.

If the damping is structural, the damping coefficient will be constant and the bending moment will be directly proportional to the exciting force and thus to the air density. This variation is shown by the dashed line in figure 1.

If the damping is aerodynamic, on the other hand, the damping coefficient and the exciting force will both be directly proportional to the density. By the methods of power spectral analysis, the root-mean-square bending moment is found to be proportional to the square root of the density. (See ref. 2.) This variation is shown by the solid line in figure 1.

Flight-test data indicate that the damping of the buffet vibration is primarily aerodynamic. (See refs. 1 and 3.) In order to illustrate this point, some flight results [redacted] th circular symbols in

[redacted]

figure 1. Such results led to the assumption of aerodynamic damping in developing the equation of reference 1 for scaling buffet bending moments from wind-tunnel models to full-scale airplanes. The equation is applicable, therefore, only when the damping is primarily aerodynamic for the model as well as for the airplane.

In order to determine whether the damping of models actually is aerodynamic, bending-moment data for three ordinary force-test models are plotted in figure 1. Model 1 is suitable for buffet loads tests because the damping is primarily aerodynamic. For models 2 and 3, on the other hand, the damping is largely structural; thus, the scaling equations of reference 1 do not apply to these models. The model data shown in figure 1 represent two extremes, and anything between these extremes is possible.

If the model is tested in a variable-density wind tunnel, a plot like figure 1 provides a means for learning, after the test is finished, whether the model was suitable for buffet loads tests. It would be better, of course, to know this before making the test. As a guide for that purpose, the following procedure is suggested. With tabulated flutter coefficients, make a rough estimate of the aerodynamic damping. In order to approximate the structural damping, measure the damping of the wing in a still-air vibration test. If the measured structural damping is as low as 1/10 of the estimated aerodynamic damping, the model will probably be satisfactory. Experience in transonic tunnels operating at atmospheric stagnation pressure has shown that solid metal wings are generally satisfactory if the wing-fuselage joints are tightly clamped. Difficulty has been experienced when insufficient joint fixity resulted in high structural damping and when tests were run at such low dynamic pressures that the aerodynamic damping was too low.

Model Frequency Requirements

Another requirement for the buffet model is that the vibratory mode shape and reduced resonant frequency be the same as those for the airplane. Of these two quantities, simulation of the resonant frequency probably is the more important. The power spectral density of the wing-root bending moment is plotted as a function of the reduced frequency in figure 2 for an airplane and for a 0.075-scale model of the airplane at the same Mach number. The vibration of the airplane wing is concentrated in the first symmetrical bending mode. This is also the case for the model; furthermore, the reduced resonant frequency for the model is about the same as that for the airplane. This comparison is interesting because the model has a standard solid-metal force-test wing. In the design of this model, there was no consideration whatever given to the resonant frequencies of the wing and yet frequency simulation of the first symmetrical bending mode was obtained. This seems to be a normal characteristic of solid-metal models of fighter-type airplanes (at least in the absence of

external stores); thus, the simulation of wing resonant frequency for such airplanes presents no serious model design problems.

In the case of the tail, however, the situation is very different. The power spectral density of the bending moment at the root of a horizontal stabilizer is plotted as a function of the reduced frequency in figure 3 for an airplane and for a 0.25-scale model of the airplane. Again there was no attempt in the model design to simulate the frequency characteristics of the airplane. For the airplane, the most prominent mode is associated with fuselage torsion but this mode is hardly visible on the model, presumably because the model fuselage is more rigid than that of the airplane. Note also that, for the model, the frequencies of the various vibration modes are very different from those for the airplane. Buffet bending moments measured on this model stabilizer would probably bear little relation to those measured on the airplane. It appears then that, although force-test models are usually satisfactory for the study of wing buffet loads, the scaling of tail buffet loads will require models specially designed for that purpose.

Support System

The vibration modes of the model may be influenced by the support system. Figure 4 shows power spectrums obtained with two different types of model supports. The spectrum at the left is for a floor-mounted semispan model that was tested in the Ames 12-foot pressure tunnel. The predominant mode is first symmetrical bending as it was in the case of the airplane wing in figure 2. The spectrum on the right is for a sting-mounted full-span model. Two new modes are evident in this spectrum. The antisymmetrical bending mode is actually a wing mode but the other new mode is essentially a rigid-body rolling vibration due to the torsional flexibility of the sting support. This mode has no counterpart in flight and therefore should be eliminated before an attempt is made to calculate flight bending moments.

At present, there are three methods of eliminating the mode due to the sting support. The first method is to determine the power spectrum and then subtract the response in this mode. The second method, which is the same in principle but less costly in practice, is to remove the sting mode with an electrical filter either at the time the data are taken or later. For some combinations of model and sting supports, the natural frequency of the sting mode is so close to that of the symmetrical bending mode that these two methods are not applicable. When these methods cannot be used, the third method can be used. The sting torsion response can be canceled by placing bending-moment gages on both wings and summing the outputs electrically. The dashed line in the plot at the right of figure 4 shows a spectrum that was obtained by this method.

Note, however, that not only the sting torsion mode but also the antisymmetrical wing mode is eliminated. The elimination of this antisymmetrical mode would be undesirable in a case where this mode contributed a large part of the total wing-root bending moment. Fortunately, however, the contribution of modes higher than the first-symmetrical bending mode is small for the fighter airplanes for which flight spectra are available.

Wind-Tunnel Turbulence

Experience has shown that wind-tunnel turbulence sometimes complicates the results of buffet tests. An example is illustrated in figure 5. The ordinate for the curves in this figure is a parameter that is proportional to the root-mean-square value of the wing-root bending moment. The numerator is associated with the input force that causes the wing to buffet and the denominator with the damping force that limits the amplitude of the buffet vibration. This parameter is plotted as a function of the angle of attack for three different Mach numbers. At a Mach number of 0.4, the flat portion of the curve at low angles of attack is the response due to wind-tunnel turbulence. The point where the curve rises steeply is considered to be the buffet boundary. At Mach numbers of 0.7 and 0.85, the response to turbulence is much higher. This increase has two effects. First, the turbulence tends to obscure the buffet boundary, as is the case at a Mach number of 0.7. In addition, the bending moments are higher because of the contribution of the wind-tunnel turbulence. The manner in which the turbulence and buffet inputs add to give the total is not yet completely understood. Any correction of the measured total for the effects of turbulence depends upon the frequency distribution of this input and on the degree of correlation between the two inputs, factors that have not yet been determined. A subtraction process is indicated schematically on the curve for a Mach number of 0.85 where the buffet response is considered to be only the part labeled "buffeting." Note that the results in figure 5 that were chosen for purposes of illustration are for a particularly bad case. The effects of turbulence are not always so severe as shown here. On the other hand, it is important to realize that because the wing is a resonant system with very little damping, a small exciting force due to turbulence may cause a sizable response.

For buffet tests, the important quantity is not the overall turbulence level in the wind tunnel but rather the power spectral density of the turbulence at the resonant frequency of the wing. There is little information available on the turbulence spectra of various wind tunnels in the frequency range of interest here. Wind-tunnel turbulence has been investigated rather extensively in connection with studies of boundary-layer transition. The frequencies of interest for boundary-layer transition, however, are much higher than the buffet frequencies.

[redacted]

At the present time, therefore, the best way to learn whether a given tunnel is suitable for buffet tests probably is to make such a test.

The effect of turbulence on buffet measurements is not a problem for the wind tunnels only. On occasion, turbulence has interfered with buffet tests of both rocket-propelled free-flight models and airplanes. In these cases, the solution to the problem is to avoid atmospheric turbulence when making buffet tests.

Instrumentation

With regard to instrumentation, tape recordings of the wing strain-gage output have been particularly useful. Power spectrums are obtained by recording the strain-gage output on magnetic tape and later analyzing the tape records (ref. 4). Root-mean-square bending-moment values can be obtained from the tape record or they can be obtained at the time of the test by means of a thermocouple meter, which is sensitive to the mean-square value of a random electrical current. The Ames Aeronautical Laboratory has developed an instrument that measures the peak buffet loads in successive 10-second intervals over a period of several minutes. The instrument is basically a condenser charged through a diode that conducts current only during a peak that is higher than any previous peak. Thus, the charge on the condenser is a measure of the highest peak. Either peak or root-mean-square measurements can be used to study buffeting. The measured peak values in the tests at the Ames laboratory were two to four times higher than the root-mean-square values and thus were about what would be expected for a Gaussian random process.

Additional Results Bearing on Validity of Theory

The experimental technique that is discussed in this paper is based on the assumption that buffeting is essentially a Gaussian random process and that the response of the wing can be treated as the linear response of a lightly damped single-degree-of-freedom elastic system. A recent analysis of flight-test data (ref. 5) has shown that wing buffet loads do indeed exhibit the characteristics of a Gaussian random process. For a representative stall maneuver, the loads are normally distributed, and the probability that a load peak will exceed a given level is in agreement with the theoretical results obtained in reference 6. For a representative pull-up into buffeting in the shock regime, the buffet intensity appears to vary linearly with penetration beyond the buffet boundary. The loads under maneuvering conditions are therefore not stationary and are thus non-Gaussian. By means of a simple linear transformation, however, the buffet loads in maneuvering flight can be treated as a Gaussian process.

[redacted]

Another result of theoretical interest has been established by an analysis (unpublished) of power spectrums of wing bending moments obtained in a wind tunnel. It was found that the relationship of the maximum value of the spectrum, the band width of the spectrum at the 1/2-power points, and the integrated mean-square bending moment is the same for the wing during buffeting as for a lightly damped linear single-degree-of-freedom system. This result is important not only as verification of a basic assumption but also because it implies that the magnitude of the wing damping forces can be evaluated, at least in principle, from the power spectrum.

Comparison of Flight and Wind-Tunnel Results

Wing-root bending moments during buffet have been measured in flight on a thin, unswept wing, research airplane (X-1E). They have also been measured on two models of different sizes in two different wind tunnels. The wind-tunnel results have been scaled up to flight conditions by using the equation presented in reference 1. The values obtained are compared with the flight bending moments in figure 6. When the fact that buffeting is inherently a random process is considered, the agreement between flight and wind-tunnel results shown in this figure is regarded as satisfactory. Apparently, flight buffet loads can be estimated from wind-tunnel results, at least for simple wings. It follows from this result that wind tunnels can also be used to study the effect of airplane modifications on the buffet loads.

CONCLUDING REMARKS

A description has been given of recent developments in the application of a method for predicting flight buffet loads from wind-tunnel model measurements. Model requirements have been outlined for proper scaling of the damping characteristics and vibration frequencies. These requirements appear to be easily met for wing loads, but special care will be needed in the construction of models for the study of tail loads.

The influence of the model support system and of the turbulence level in the wind tunnel on test results has been discussed, and the instrumentation for wind-tunnel studies has been described. A comparison has been made of the wing buffet loads on a research airplane with thin unswept wings and the loads that were measured on two models of the airplane built to different scales and tested in different wind tunnels. The comparison indicates that flight wing loads can be estimated from wind-tunnel results; thus, wind tunnels could also be used to study the effects of airplane modifications on buffet loads.

[redacted]

REFERENCES

1. Huston, Wilber B., Rainey, A. Gerald, and Baker, Thomas F.: A Study of the Correlation Between Flight and Wind-Tunnel Buffeting Loads. NACA RM L55E16b, 1955.

2. Liepmann, H. W.: Parameters for Use in Buffeting Flight Tests. Rep. No. SM-14631, Douglas Aircraft Co., Inc., Jan. 3, 1953.

3. Huston, Wilber B., and Skopinski, T. H.: Measurement and Analysis of Wing and Tail Buffeting Loads on a Fighter Airplane. NACA Rep. 1219, 1955. (Supersedes NACA TN 3080.)

4. Smith, Francis B.: Analog Equipment for Processing Randomly Fluctuating Data. Aero. Eng. Rev., vol. 14, no. 5, May 1955, pp. 113-119.

5. Huston, Wilber B., and Skopinski, T. H.: Probability and Frequency Characteristics of Some Flight Buffet Loads. NACA TN 3733, 1956.

6. Rice, S. O.: Mathematical Analysis of Random Noise. Pts. I and II. Bell Syst. Tech. Jour., vol. XXIII, no. 3, July 1944, pp. 282-332; Pts. III and IV, vol. XXIV, no. 1, Jan. 1945, pp. 46-156.

[redacted]

DAMPING

AERODYNAMIC OR STRUCTURAL

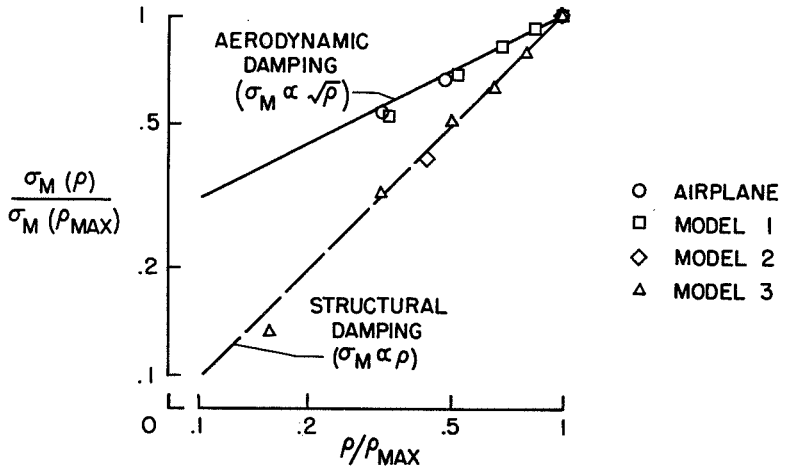


Figure 1

MODEL DESIGN

SIMULATION OF WING NATURAL FREQUENCY

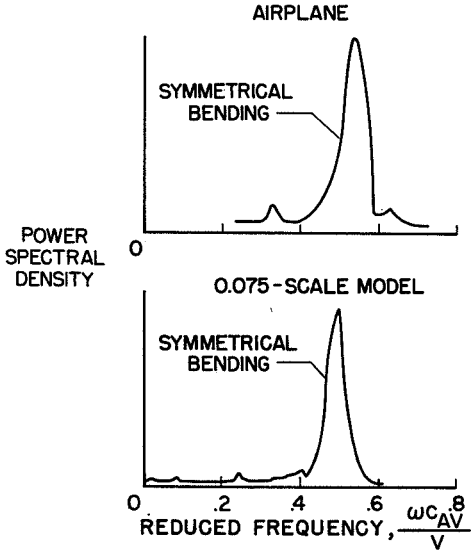


Figure 2

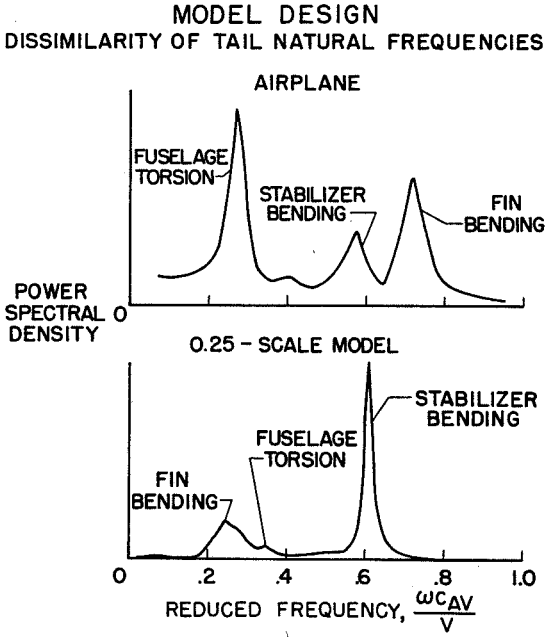
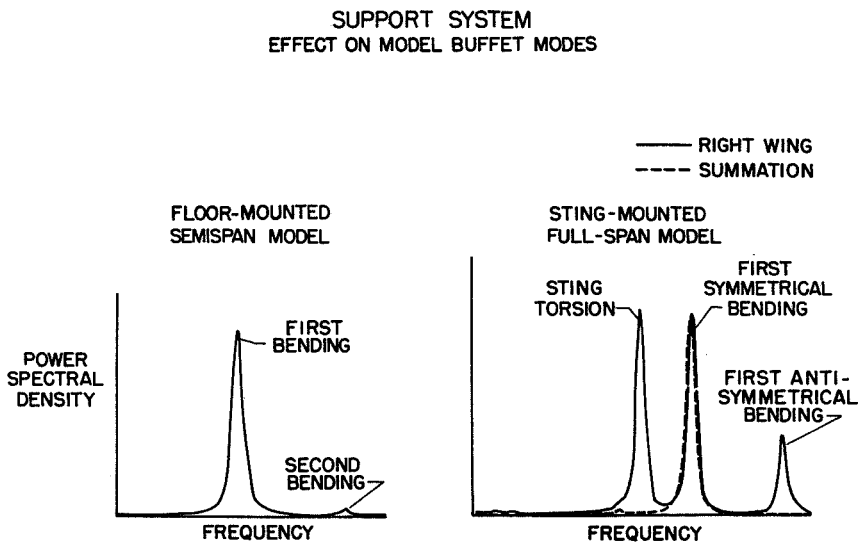


Figure 3



482

Figure 4

TURBULENCE COMPLICATES BUFFET TESTS

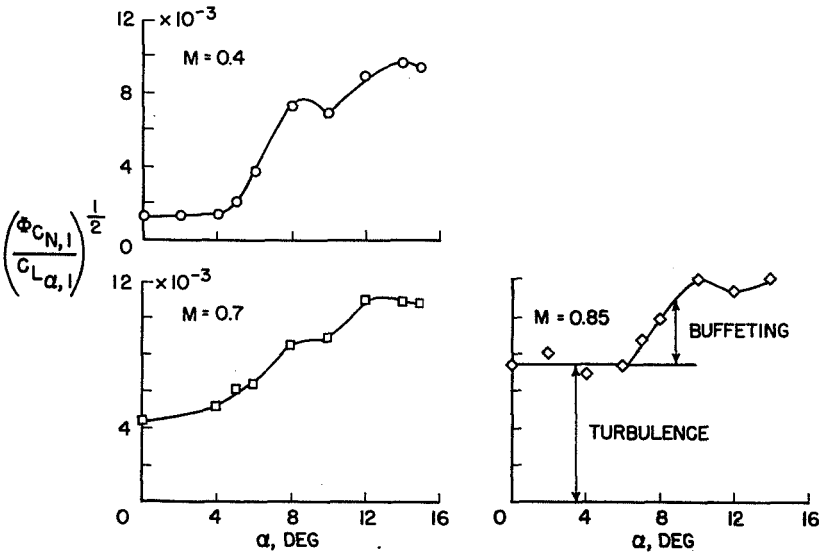


Figure 5

BUFFET LOAD
FLIGHT AND WIND-TUNNEL COMPARISON FOR X-1E

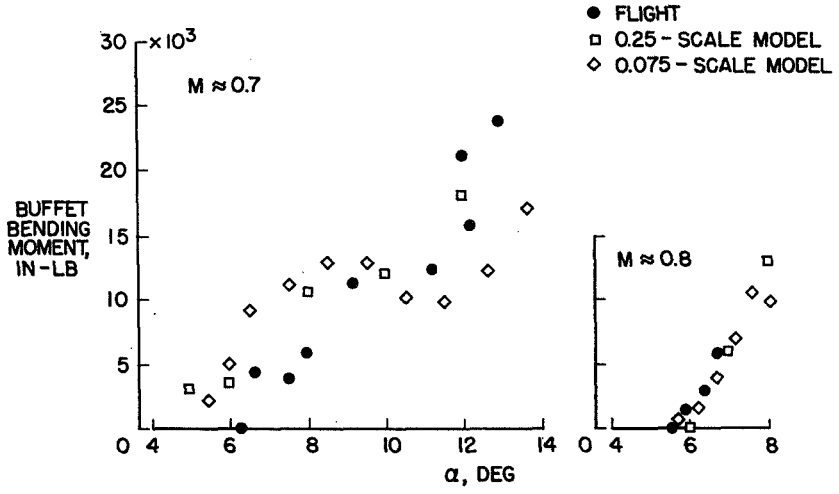


Figure 6

N71-75419

SUTTON & LAUTENBERGS

EFFECTS OF WING AND FUSELAGE MODIFICATIONS ON BUFFETING

By Fred B. Sutton and J. Walter Lautenberger, Jr.

Ames Aeronautical Laboratory

INTRODUCTION

The performance of many high-speed aircraft has been adversely affected by shock-induced separation encountered at moderate lift coefficients at high subsonic speeds. This phenomenon is usually evidenced by severe decreases in longitudinal stability, large increases in drag, and heavy buffeting. Much research has been directed toward the alleviation of the stability and drag difficulties, but little is known about the effects on buffeting of such stability and drag "fixes" as wing fences, wing leading- and trailing-edge modifications, and fuselage indentations. This paper presents some results of investigations in the Langley 8-foot transonic pressure tunnel and in the Ames 12-foot pressure tunnel to obtain an indication of the effects of these devices on buffeting.

DISCUSSION

The tests in the 8-foot tunnel were conducted with a model of a modified delta-wing airplane and some typical results of the tests in this tunnel are shown in figure 1. Fluctuating wing bending moments measured at the wing root of the model were reduced to show the relative buffeting input due to the aerodynamics of several model configurations. The apparent buffeting input at low lift coefficients is believed to be due to wind-tunnel turbulence. Test data are shown for a Mach number of 0.95, which corresponds to a flight speed at which buffeting is critical.

Figure 1 shows one-half of the sting-mounted full-span model used for the investigation. The heavy solid line is the outline of the basic configuration. The buffet inputs of the wing as a function of the lift coefficient are shown in this figure. When conical camber was added to the leading edge of the wing, the buffet intensity at the higher lift coefficients was reduced considerably. By further adding a swept trailing edge to the wing and a bump to the body in order to improve the area distribution of the airplane, the buffet intensity was still further reduced. These modifications, which were designed to improve the airplane performance, thus were quite effective also in reducing the buffet loads at transonic speeds.

The investigation in the 12-foot tunnel was made with a wing-fuselage-tail combination having a relatively thick sweptback wing with a high aspect ratio. This combination was typical of transport and bomber airplanes designed for long-range flight at high subsonic speeds. Reference 1 describes the semispan-model technique and the instrumentation employed in the investigation of buffeting in the 12-foot tunnel. Figures 2 and 3 illustrate the semispan-model setup and the model configurations used in this wind tunnel, respectively. Included in the investigation were studies of the effect of wing fences, a leading-edge extension, and a fuselage indentation of the Kuchemann type. The wing used in this investigation was twisted and cambered and had NACA 64A-series thickness distributions. A strain-gage bridge was mounted at the wing root to measure fluctuations of wing bending moment due to buffeting. The bridge output was fed into an electronic recorder-analyzer. This apparatus permitted the convenient recording and rapid analysis of data samples corresponding to several thousand fluctuations of bending moment and provided the maximum peak intensities as well as the usually measured root-mean-square intensities (refs. 2 and 3) of the fluctuating wing bending moments.

It has not been possible to deduce from the buffet outputs measured in the 12-foot tunnel the buffet inputs due to the model aerodynamics as was the case with the results obtained in the 8-foot tunnel. Instead, the measured fluctuating bending moments have been converted to approximate values of fluctuating normal-force coefficient ΔC_N. Because the dynamic characteristics of the model were essentially constant for the various configurations tested, these results do indicate relative buffeting.

The effects of wing fences and a leading-edge extension on the buffeting of the wing-fuselage-tail combination are shown in figures 4 and 5. Figure 4 shows the variation of $\Delta C_{N,MAX}$ with lift coefficient at a Mach number of 0.86, and figure 5 shows boundaries of lift coefficient and Mach number for heavy buffeting.

The intensity chosen for heavy buffeting, $\Delta C_{N,MAX} = \pm 0.08$, is strictly arbitrary and is intended only to indicate buffeting of relatively heavy degree. The boundaries shown were determined from maximum buffet intensities; however, boundaries from comparable root-mean-square intensities were very similar. The test results indicated that, at most Mach numbers, the wing fences generally reduced the erratic variation of buffet intensity with increasing lift coefficient and reduced buffet intensities at moderate and high lift coefficients. The wing leading-edge extension (figs. 4 and 5) was relatively ineffective as a means of reducing buffeting and, for some test conditions, increased buffeting. Figure 5 also shows that the fences greatly reduced the adverse effects of increasing Mach number on heavy buffeting. The combination was also

tested with a fuselage indentation which was designed to reduce the wing-fuselage interference effects. These results are not shown but they indicate that the fuselage indentation reduced buffeting for some test conditions; however, these effects were small compared with the improvements derived from the use of wing fences.

The lift coefficients for drag divergence and for pitching-moment-curve inflection or pitch-up are considered important design parameters in analyzing the static longitudinal characteristics of airplanes. These parameters are compared in figure 6 with boundaries of Mach number and lift coefficient for light buffeting and the previously described boundaries for heavy buffeting. The intensity selected for light buffeting, $\Delta C_{N,MAX} = \pm 0.02$, approximates the boundary for buffet onset. At the higher Mach numbers, the lift coefficients for drag divergence are close to the boundaries for buffet onset for both the model with and without wing fences. However, heavy buffeting was indicated at lift coefficients considerably lower than those for pitch-up. This is significant, inasmuch as the occurrence of heavy buffeting at these comparatively low lift coefficients indicates that the usable range of lift coefficients is probably much less than the lift-coefficient range for stability. Wing fences did much to lessen this difference, but heavy buffeting was still indicated at lift coefficients which were appreciably lower than those for pitch-up.

SUMMARY OF RESULTS

The results of these investigations may be summarized as follows:

1. Many modifications intended to improve drag and stability characteristics are also effective buffet alleviators.

2. For a model of a modified delta-wing airplane, a conically cambered leading edge, a swept trailing edge, and body bumps to improve area distribution all reduced buffeting.

3. For sweptback wings having high aspect ratios, fences were a very effective means of reducing buffeting. To a much lesser degree, a Kuchemann fuselage indentation also reduced buffeting. A wing leading-edge extension was ineffective as a means of alleviating buffeting and, for some test conditions, increased the buffeting.

4. At high subsonic speeds for sweptback wings having high aspect ratios, the lift-coefficient boundaries for buffeting onset are close to the lift-coefficient boundaries for drag divergence; however, heavy buffeting at these speeds usually occurred at lift coefficients which were considerably lower than the lift coefficients for pitch-up.

[redacted]

REFERENCES

1. Davis, Don D., Jr., and Huston, Wilber B.: The Use of Wind Tunnels To Predict Buffet Loads. (Prospective NACA paper.)

2. Polentz, Perry P., Page, William A., and Levy, Lionel L., Jr.: The Unsteady Normal-Force Characteristics of Selected NACA Profiles at High Subsonic Mach Numbers. NACA RM A55C02, 1955.

3. Huston, Wilber B., Rainey, A. Gerald, and Baker, Thomas F.: A Study of the Correlation Between Flight and Wind-Tunnel Buffeting Loads. NACA RM L55E16b, 1955.

[redacted]

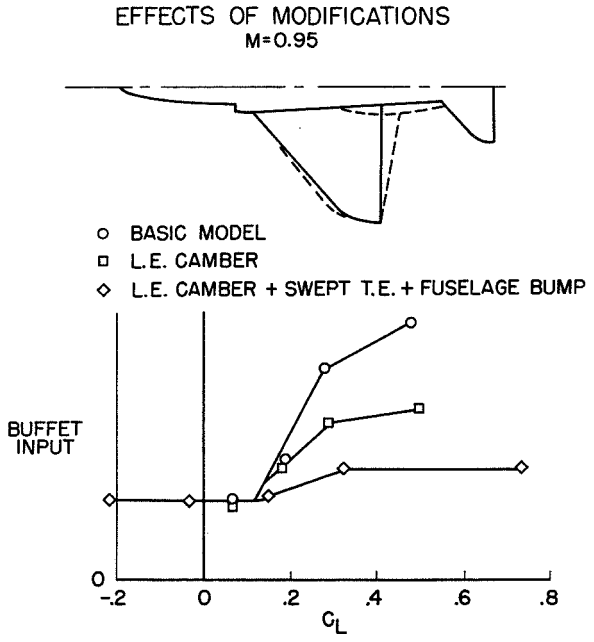


Figure 1

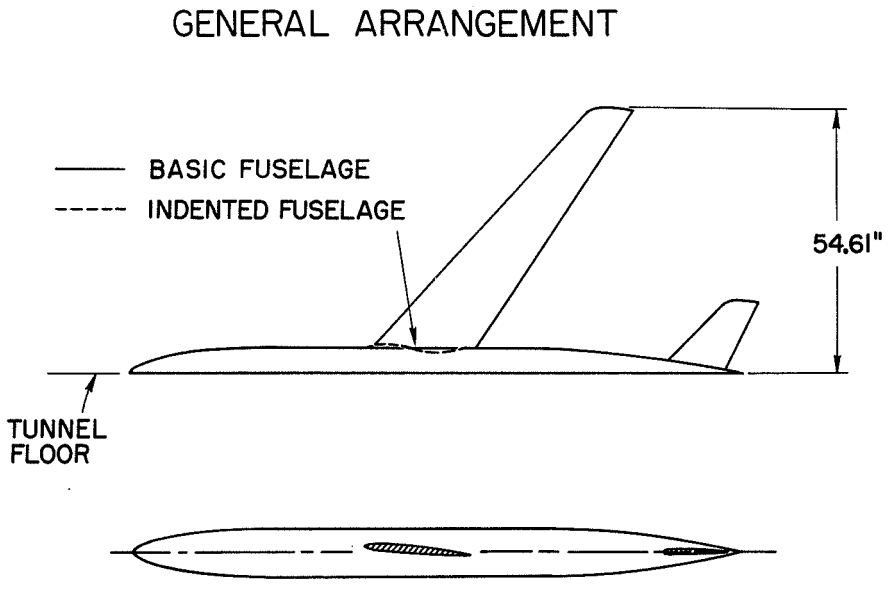


Figure 2

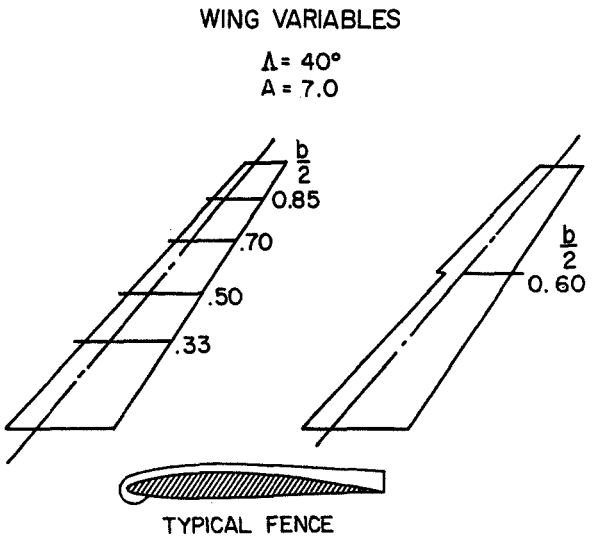


Figure 3

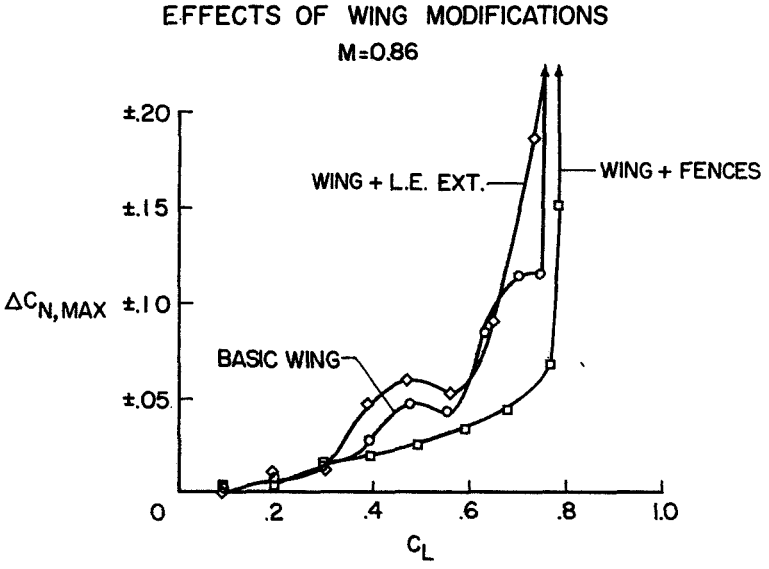


Figure 4

EFFECTS OF WING MODIFICATIONS
$\Delta C_{N,MAX} = \pm 0.08$

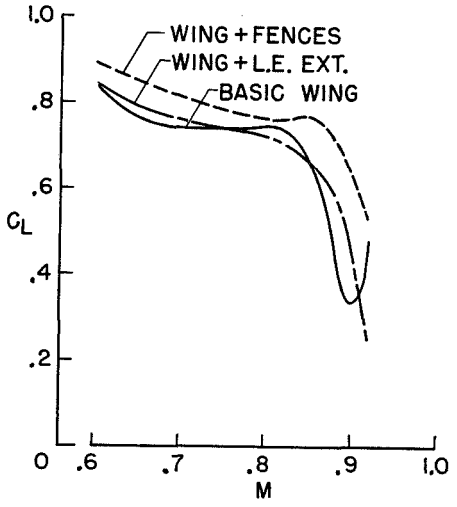


Figure 5

COMPARISON OF BUFFET BOUNDARIES WITH
STATIC LONGITUDINAL PARAMETERS

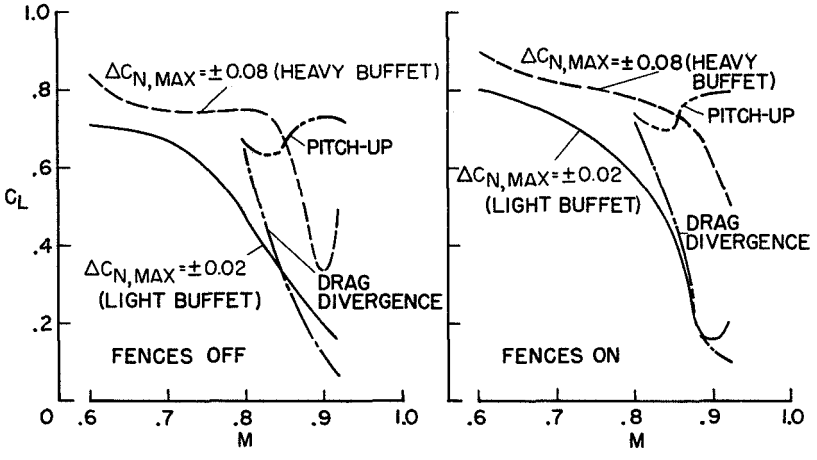


Figure 6

N71-75420

THEORETICAL AND EXPERIMENTAL INVESTIGATIONS OF DELTA-WING VIBRATIONS

By Edwin T. Kruszewski, Eldon E. Kordes, and Deene J. Weidman

Langley Aeronautical Laboratory

SUMMARY

The results of some theoretical and experimental investigations of delta-wing vibrations are discussed.

Nodal-line patterns and frequencies of a 45° built-up thin-skin delta-wing specimen obtained experimentally are compared with those calculated by two analytical methods - the idealized-structure type of method as described by Levy and a limited-deformation type of method proposed by Stein and Sanders. It is shown that when the effects of transverse shear are included into the Levy approach the agreement between calculated and experimental frequencies is exceptionally good.

Experimental nodal-line patterns and frequencies for a 60° thick-skin delta wing are also shown.

INTRODUCTION

The prediction of the vibrational characteristics of aircraft structures is a problem of importance to the designer of high-speed aircraft. As was discussed in reference 1, methods of predicting modes and frequencies for the large-apect-ratio box-beam type of structure are very successful. However, for low-aspect-ratio or delta wings, the problem is still of particular concern because of the analytical difficulties involved in predicting their stiffness characteristics.

An experimental investigation of the modes and frequencies of two large-scale built-up delta-wing specimens has recently been completed. The results of this experimental investigation are being used to evaluate theoretical methods of deflectional analysis. This paper will deal with the findings of this evaluation.

DISCUSSION

One of the delta-wing specimens used in the experimental investigation is shown in figure 1. It is a built-up large-scale 45° delta with a span of 18 feet 8 inches, a midchord of 8 feet, and a uniform carry-through section of 2 feet 8 inches. The wing is uniform in depth in the chordwise direction but varies in depth in the spanwise direction from $5\frac{1}{2}$ inches at the carry-through section to $1\frac{3}{4}$ inches at the tip. The covers are made up of a thin sheet stiffened by spanwise stringers. In order to facilitate construction, the stringers were placed on the outside of the covers. The internal construction consisted of four spanwise spars and a bent leading-edge spar with light streamwise ribs spaced at close intervals. A detailed description of the stiffness properties and weight distribution of the specimen is given in reference 2.

A general view of the vibration test setup is shown in figure 2. The delta wing is hung vertically by flexible aircraft cables from the gallows shown in the figure. The specimen was vibrated in the horizontal direction so that the wing could be considered to be essentially free-free. The vibrations were produced by four electromagnetic shakers (three of which can be seen in fig. 2). The mode shapes were obtained from pickups mounted at the intersection of the spars and ribs while the node-line locations were determined with a portable probe pickup. A total of 10 natural modes of vibration was established, five symmetrical and five antisymmetrical, with frequencies ranging from 43 to 216 cycles per second. Detailed descriptions of the vibration tests are given in reference 2.

In recent years a variety of methods of load deflectional analysis for low-aspect-ratio and delta wings has been proposed. (See, for example, refs. 3 to 6.) Two of these methods have been used for calculating the modes and frequencies of this specimen. One was described by Levy in reference 3 and the other was developed by Stein and Sanders in reference 4. Although both of these methods were discussed in detail in references 3 and 4, a recapitulation is thought to be worthwhile. Both of the methods are an influence-coefficient type of procedure; that is, the vibrational problem is set up through the use of static influence coefficients and the inertial characteristics of the structure. Furthermore, both methods neglect the effects of transverse shear.

The essential features of the two methods are shown schematically in figure 3. The Levy method deals with a simplified structure but allows arbitrary deflections of that structure. On the other hand, the Stein-Sanders method analyzes the actual structure but restricts the allowable deflection shape.

Consider first the Levy method. As shown in figure 3 the actual wing is idealized into a system of interconnecting beams and torque boxes. All the spanwise normal-stress-carrying material of the covers, both sheet and stringers, is concentrated into the spars of the idealized wing while all the chordwise normal-stress-carrying material is concentrated into the ribs. The shear-carrying capacity of the cover sheets is accounted for by torsion boxes in the spar-rib cells.

The stiffness influence coefficients for each component part of the idealized structure, that is, the spars, ribs, and torsion boxes, are superimposed to yield the stiffness influence coefficients of the complete structure. The flexibility influence coefficients are then obtained directly by inversion. Note that because of the nature of the idealization used, the Levy method is intended to be applied primarily to thin-skin structures, such as the particular 45° delta-wing specimen used in the experimental investigation.

The Stein-Sanders method deals with the deflections of the neutral surface of the actual wing. It is assumed that the chordwise variation of the deflection w is parabolic and can be expressed in the form shown in figure 3. In this case ϕ_0, ϕ_1, and ϕ_2 give the spanwise variation of the deflection, slope, and chordwise curvature at the trailing edge. Since the effects of transverse shear are neglected, the distortions of the various elements in the wing can be expressed in terms of the ϕ's. Further by taking a number of stations along the wing and by going through a straightforward calculation, the values of the ϕ's at the various stations can be expressed in terms of the loading at those stations.

Since the Stein-Sanders method deals with the actual structure, it should handle a thick-skin wing as well as a thin-skin wing. However, the restriction to parabolic deflections in the chordwise direction may lead to serious errors unless the center section is very stiff against chordwise bending.

The comparisons of the results of these two theoretical solutions and those obtained from the experimental investigation are shown in figure 4. In this figure the nodal-line patterns and frequencies are shown for the first five symmetrical modes.

As can be seen, the nodal-line patterns from the Stein-Sanders method agree quite well with the ones obtained experimentally. The frequency agreement, however, is poor; the errors ranging from 7 percent in the first mode to 38 percent in the fifth mode. On the other hand, the frequency agreement in the Levy method is much better. The largest error in the first four modes (which occurs in the third mode) is only $7\frac{1}{2}$ percent while the error in the fifth mode is 20 percent.

Some of the errors in the Stein-Sanders method are undoubtedly due to the assumption of parabolic chordwise deformation. This particular specimen had no extra chordwise stiffening in the center of the wing, such as would be furnished by a fuselage, for example. On the other hand, as previously noted, the Levy approach should be applicable to this specimen because of its relatively thin covers. Therefore, it is not too surprising that the Levy method gives better results.

Although the Levy method does give better results, the results are still somewhat unsatisfactory, especially for the fifth mode. For this reason, an investigation of the influence of transverse shear, which was neglected in the preceding calculations, was undertaken. This investigation dealt solely with the Levy method for which an approximate correction for transverse shear could be made with little additional labor. The effects of the shear deformations of the webs were simply included in the stiffness-coefficient calculations of the individual spars and ribs, but the torsion-box coefficients were left unchanged.

The results from this recalculation are presented in table I which summarizes the frequencies obtained by the different methods for the first five symmetrical modes. The frequencies as obtained experimentally are tabulated in the first row. The corresponding frequencies as calculated by the Stein-Sanders method and by the Levy method without shear are shown in the second and third rows, respectively. Shown in the fourth row are the results from the Levy method with the effects of transverse shear included. The frequencies shown in the last row will be discussed a little later in the paper. As can be seen, the frequencies calculated by the Levy method with shear are in excellent agreement with the experimental frequencies. The largest error, which occurred in the fourth mode, being slightly less than 4 percent. Furthermore, a comparison of the frequencies in the third and fourth rows shows that the effects of transverse shear can be appreciable; the largest effect being in the fifth mode where the inclusion of transverse shear causes an 18-percent reduction in the calculated frequency. The effects of transverse shear on the calculated nodal-line patterns were slight. The changes that did occur, however, tended to improve the comparison between theory and experiment.

Although only the symmetrical modes of vibration have been discussed, the antisymmetrical results indicate the same conclusions; that is, the Levy method predicts the modes and frequencies of thin wings with thin skins such as the 45° delta wing tested with more accuracy than the Stein-Sanders method and, secondly, the effects of transverse shear, which can be appreciable, are easily and accurately incorporated into the Levy method.

Now to digress a little, consider the frequencies shown in the last row of table I, which were calculated from influence coefficients determined experimentally. These results are of interest because a popular

method of obtaining frequencies is to measure influence coefficients either on a model or a full-scale structure and then to use these coefficients in a vibrational analysis. For the delta-wing specimen, this particular method yields results which are also very good. However, it must be remembered that the influence coefficients were measured on the actual wing; therefore, no errors due to modeling are involved. The advantage of the purely analytical method in the design stage is obvious.

An investigation of the vibrational characteristics of another delta-wing specimen of entirely different type of construction is being carried out. Although the calculations are not complete, the experimental information obtained should be of interest. A sketch of this specimen is shown in figure 5. It is a built-up 60° delta wing with a span of 8 feet and a midchord of 7 feet 4 inches. A chordwise cross section of the wing is shown in the figure. The covers are plates with integral waffle-like stiffening and are fastened to relatively light spars and ribs.

The sketches of the experimental nodal lines of the 60° delta wing for the first six modes (3 symmetrical and 3 antisymmetrical) are shown in figure 6. The corresponding natural frequencies are noted at the bottom of each sketch. The frequencies range from 82.5 cycles per second in the first mode (first antisymmetrical) to 207.9 cycles per second in the sixth mode (third antisymmetrical). Only six modes of vibration were obtained due to excessive panel vibrations of the covers. It is also believed that these panel vibrations could be partly responsible for the asymmetry of the nodal-line patterns.

The specimen is representative of thick-skin construction and thus will furnish an acid test for the Levy method. Although calculations have not been made, it is believed that the Levy method with correction for transverse shear will not predict the frequencies of the 60° delta wing as well as it predicted the frequencies of the 45° delta wing. The principal source of error in the Levy method is the neglect of the influence of the Poisson's ratio effect on the interaction of the chordwise and spanwise stresses. This effect, which is important in thick-skin wings, cannot be readily included into the Levy approach.

CONCLUSIONS

Comparisons of experimental and calculated modes and frequencies of a delta-wing specimen have shown that the idealized-structure type of method as proposed by Levy gives excellent results for thin-skin wings provided that corrections are made for the effects of transverse shear. The limitied deformation type of method proposed by Stein and Sanders is

apparently inapplicable to low-aspect-ratio wings when the center section is not very stiff against chordwise bending.

REFERENCES

1. Hedgepeth, John M.: Summary of Recent Theoretical and Experimental Work On Box-Beam Vibrations. NACA RM L55E09a, 1955.

2. Kordes, Eldon E., Kruszewski, Edwin T., and Weidman, Deene J.: Experimental Influence Coefficients and Vibration Modes of a Built-Up 45° Delta-Wing Specimen. NACA TN 3999, 1957. (Prospective NACA paper.)

3. Levy, Samuel: Structural Analysis and Influence Coefficients for Delta Wings. Jour. Aero. Sci., vol. 20, no. 7, July 1953, pp. 449-454.

4. Stein, Manuel, and Sanders, J. Lyell, Jr.: A Method for Deflection Analysis of Thin Low-Aspect-Ratio Wings. NACA TN 3640, 1956.

5. Schuerch, H. U., and Freelin, J. R.: Structural Analysis of a Delta Wing Structure by Elastic Coefficients. Rep. No. ZS-182, Convair, May 5, 1953.

6. Williams, D.: Recent Developments in the Structural Approach to Aeroelastic Problems. Jour. R.A.S., vol. 58, June 1954, pp. 403-428.

TABLE I

COMPARISON OF EXPERIMENTAL AND CALCULATED FREQUENCIES

Frequency determined by -	Frequency, cps, for -				
	1st mode	2d mode	3d mode	4th mode	5th mode
Experiment	43.3	88.8	122.8	164.2	179.7
Stein-Sanders method	46.4	105.3	150.0	202.0	248.0
Levy method (without shear)	44.6	94.7	132.0	172.0	216.0
Levy method (with shear)	42.8	88.9	120.1	158.0	184.0
Experimental influence coefficient . .	43.1	83.0	118.0	146.0	172.0

45° DELTA-WING SPECIMEN

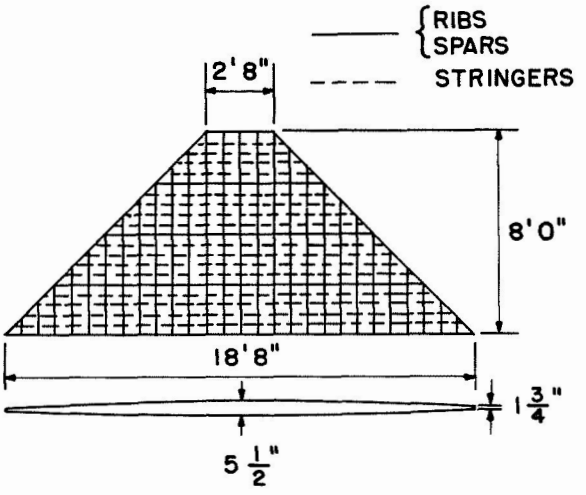
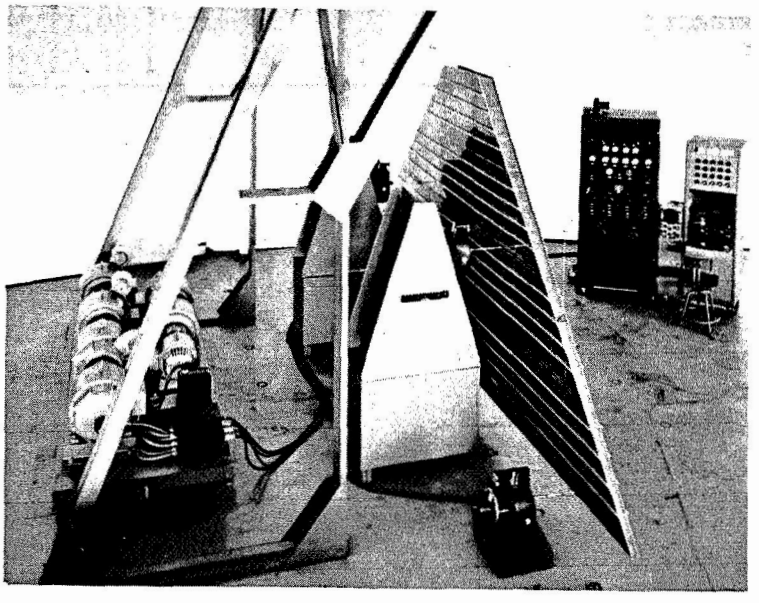


Figure 1

VIBRATION-TEST SETUP OF DELTA-WING SPECIMEN



L-88071

Figure 2

THEORETICAL APPROACHES CONSIDERED

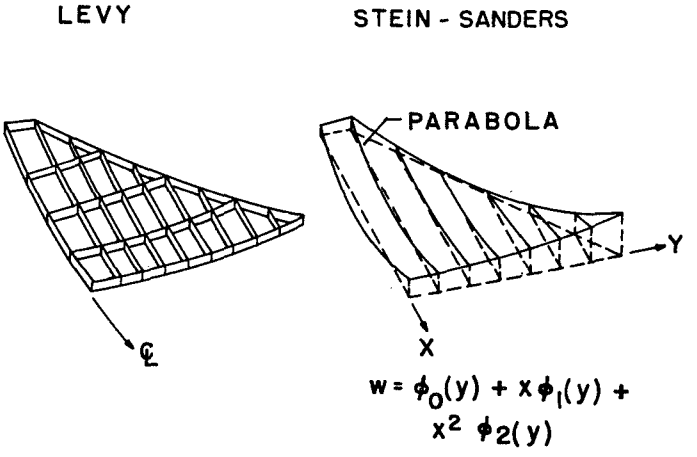


Figure 3

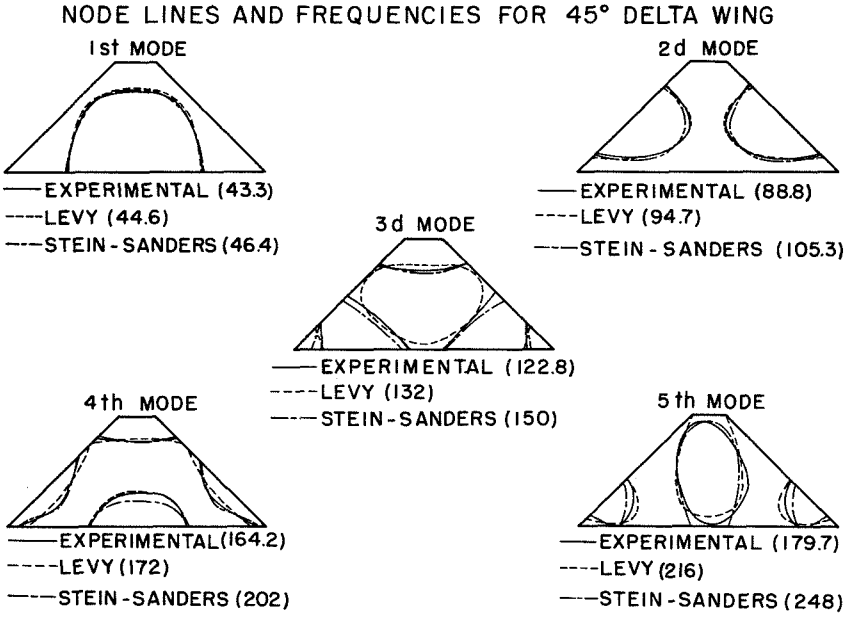


Figure 4

60° DELTA-WING SPECIMEN

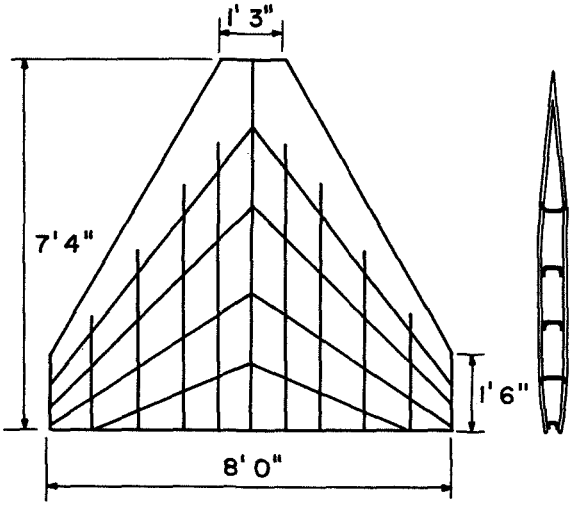


Figure 5

NODE LINES AND FREQUENCIES OF 60° DELTA WING

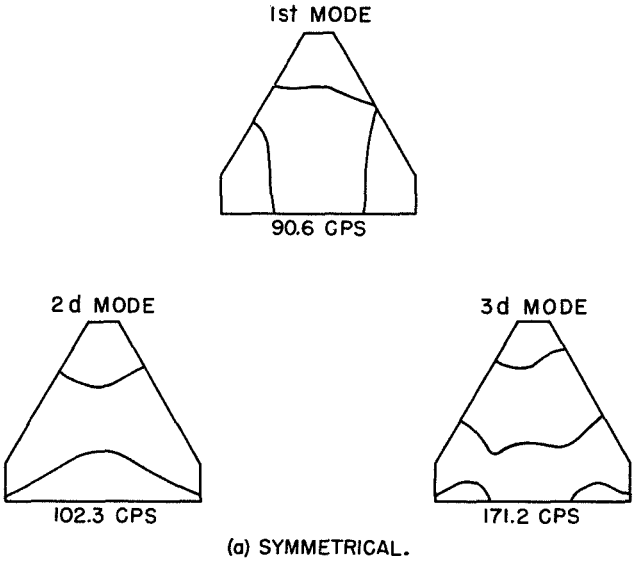


Figure 6

501

N71-75421

OSCILLATING AIR FORCES AND A PRESENTATION OF SOME FLUTTER CALCULATIONS

By Charles E. Watkins, Donald S. Woolston, and Herbert J. Cunningham

Langley Aeronautical Laboratory

INTRODUCTION

This paper is made up in two parts: the first part being a summary of the present status with regard to the calculation of aerodynamic forces necessary in aeroelastic problems, such as flutter; the second part being a presentation of some recent results of flutter calculations that are compared with experimentally determined results.

SYMBOLS

A	aspect ratio
$x,y;\xi,\eta$	Cartesian coordinates
φ	velocity potential
f,F_n	functions of ξ and η
a_n	constant coefficients
ρ	density
M	Mach number
ω	circular frequency
ω_1,ω_2	circular frequency of first and second vibration modes, respectively
V	velocity
c_r	root chord

k	frequency parameter, $\frac{\omega c_r}{2V}$
$w(x,y)$	amplitude of downwash velocity
$L(x,y)$	lift distribution
K	kernel function
S'	region of integration
$\lvert c_{l,h} \rvert$	amplitude of lift coefficient associated with translatory oscillations
$\lvert c_{l,\alpha} \rvert$	amplitude of lift coefficient associated with pitching oscillations
$\lvert c_{l,x^2} \rvert$	amplitude of lift coefficient associated with parabolic chordwise camber oscillations
$\lvert c_{l,y^2} \rvert$	amplitude of lift coefficient associated with parabolic bending oscillations
$\lvert c_{m,h} \rvert$	amplitude of moment coefficient associated with translatory oscillations
$\lvert c_{m,\alpha} \rvert$	amplitude of moment coefficient associated with pitching oscillations
$\phi_{l,h}$	phase angle associated with lift due to translatory oscillations
$\phi_{l,\alpha}$	phase angle associated with lift due to pitching oscillations
ϕ_{l,x^2}	phase angle associated with lift due to parabolic chordwise camber oscillations
ϕ_{l,y^2}	phase angle associated with lift due to parabolic bending oscillations
$\phi_{m,h}$	phase angle associated with moment due to translatory oscillations
$\phi_{m,\alpha}$	phase angle associated with moment due to pitching oscillations

$\frac{c_r \omega_1}{V}$	stiffness parameter
Λ	sweep
Λ_{TE}	trailing-edge sweep

AERODYNAMIC FORCES

An aeroelastic problem involves an elastic structure, such as an airplane wing or control surface, on which aerodynamic forces act. A solution to such a problem might imply a determination of the deformation that the structure undergoes because of aerodynamic loading or it might imply a determination of conditions under which the structure can vibrate or flutter in an undamped mode of oscillation.

The aerodynamic forces referred to herein are not the forces required to sustain flight but are superimposed forces generated by deformations or oscillations that the structure undergoes. This means that air forces and structural deformations are mutually dependent; that is, the air forces depend on the structural deformations and the structural deformations, in turn, depend on the air forces. Hence, in order to solve an aeroelastic problem, it must first be put in some form whereby the interaction between deformations and air forces can be accounted for. This can be done by various considerations, depending, of course, on the problem at hand.

With flutter problems the most common and perhaps most practical way of relating structural deformations and air forces is by resorting to a so-called modal analysis. This analysis involves an assumption that flutter modes of vibration can be satisfactorily represented by a superposition of a few known supplementary modes, for example, modes of the type illustrated in figure 1. The mode shapes used for this illustration are the first three natural modes of a tapered configuration that can be seen in outline in figure 1. They were determined experimentially by a photographic process and can be seen to involve considerable camber or curvature in both the chordwise and spanwise directions.

Before the aerodynamic forces necessary in this modal approach for solving flutter problems are discussed, perhaps a few words regarding its applicability are in order. This approach has proved to be very satisfactory for wings or configurations that are so constructed that they behave as simple beams. However, the behavior of thin, low-aspect-ratio wings of many current and future airplanes is more like that of a plate than of a beam. With configurations that behave as plates, a modal

approach for solving flutter problems becomes somewhat precarious because of the difficulty involved in choosing mode shapes that will unite satisfactorily to yield a flutter mode. The most logical modes to choose are the free vibration modes, if available, of the configuration under consideration. But even with these modes, it appears necessary to employ considerably more modes for plate-like structures than for beam-like structures.

The aerodynamic forces necessary in a modal approach are the forces associated with each chosen supplementary mode. It is of interest to note that the literature on unsteady aerodynamics deals mainly with this form of forces, although for the most part this literature pertains to special plan forms and very simple mode shapes. In recent years, however, considerable advancement has been made in calculating aerodynamic forces for arbitrary plan forms and mode shapes for both subsonic and supersonic speeds. These advancements will be discussed momentarily but first it is of interest to review briefly the pertinent plan forms and give some indication as to methods by which the aerodynamics for unsteady wings has developed. The plan forms for which oscillatory aerodynamic forces are known, roughly in order of development, are as follows:

I. Wings of infinite aspect ratio
 (a) Velocity potential
 (b) Indicial functions

II. Wings of vanishingly small aspect ratio
 (a) Velocity potential

III. Circular plate in incompressible flow
 (a) Pressure potential

IV. Finite wings for which flow normal to all edges is supersonic
 (a) Velocity potential
 (b) Indicial functions
 (c) Simple piston theory $\left(\frac{k}{M} = \frac{1}{M}\frac{\omega c_r}{2V} \ll 1\right)$

V. Rectangular and arrowhead plan forms in supersonic flow
 (a) Velocity potential expanded in powers of frequency

VI. Wings of any plan form
 (a) Lift distribution
 (1) Box method
 (2) Kernel function method

These will be dealt with very briefly in this paper. A good bibliography and accounting of developments can be found in reference 1.

The first item is the wing of infinite aspect ratio. The velocity potential, and hence the forces and moments, for this wing undergoing harmonic translation and pitching oscillations is now known for the complete Mach number range. In the past the theoretical aerodynamics of flutter has been based mainly on this two-dimensional theory. This theory has been employed in various strip-analysis methods and has been found to be very useful, particularly for high-aspect-ratio wings with beam-like behavior. In addition to the velocity potential for the infinite wing, the indicial response functions associated with sudden vertical and pitching motions are numerically known. These functions have applications in certain types of analog studies of flutter problems. They also have useful applications in such problems as determination of an airplane's response to gust.

The second plan form listed is a wing of vanishingly small aspect ratio. Results for this case are based on the assumption that all the forces arise from crossflows and that the trailing edge has no influence on the nature of the aerodynamic forces that act upon the wing. These results are of academic interest in that they correspond to the one extreme, $A = 0$; whereas the two-dimensional results correspond to the other extreme, $A = \infty$.

Results for the circular plate are based on a consideration of a pressure or acceleration potential. Aerodynamic coefficients associated with a few simple modes for this configuration have been tabulated. Corresponding results for other modes can, without very great difficulty, be obtained. It is not proposed that such results would ever be very useful in actual flutter studies, but they can be very useful in assessing other approximate procedures for obtaining aerodynamic forces.

The fourth plan form considered is a wing for which flow normal to all edges is supersonic. This case stands somewhat alone, because the velocity potential is known, at least in the form of a surface integral, for any given mode shape. In addition to this, indicial functions corresponding to instantaneous vertical and pitching displacements for such plan forms are explicitly known. In order to obtain the distribution of forces associated with the integral representation of the velocity potential, it is generally necessary to resort to approximate procedures for handling surface integrals. In this regard an approximation that applies when the Mach number is large and the reduced frequency is low has come to be known as "piston theory" and has created considerable interest in the past few months.

Large values of Mach number M and low values of frequency parameter k imply small values of the ratio k/M. When this ratio is small

enough, the velocity potential for this case can be explicitly expressed in a simple limiting form rather than as a surface integral. The forces obtained at a given point from such a limiting form depend solely on the motion of the structure at that point. Hence, each point of the surface can be imagined to behave as a small independent piston; thus, the name "piston theory." The word "simple" is used here to distinguish results, which are strictly linear, that are obtained from this limiting process from more elaborate second-order results that are also known as piston theory. For example, see the results of Hayes and Lighthill (ref. 1). The main concern here is the subsonic and low supersonic speed range wherein there is no basis for piston theory.

Item V in the list pertains to rectangular- and arrow-type plan forms. The velocity potential corresponding to fairly simple mode shapes for these plan forms can be derived in the form of a power series in terms of the frequency of oscillation. This procedure and certain applications thereof have been published for several years now. It is mentioned at this time for two reasons: First, because of some significant derivations and applications that have recently been made and are discussed later in this paper and second, because results of the expansion procedure are used as a yardstick by which other less restricted approximate procedures that are about to be discussed can be evaluated.

Item VI in the list pertains to arbitrary plan forms. It is for such plan forms that aerodynamic information has been critically lacking for a long time. It is also for these plan forms that significant advancements have recently been made. The advancements referred to are not based on new principles. The general methods on which they are based have been known for some time, but there has been a drawback to their application because of the enormous amount of calculation involved. With the high-capacity computing equipment that is now available, however, this phase of the work becomes simply a task of systemization. Such systemizations are being accomplished, and it appears that a point will soon be reached where the aerodynamics of linearized theory can be completely exploited.

The "box method" as used herein pertains only to wings with all supersonic edges. Basically, it is a method for numerically handling certain surface integrals to which the forces corresponding to a given mode can be reduced. The form of these integrals is shown in the following expression:

$$\int_{S'} \int f(\xi,\eta)\ \varphi(x,y;\xi,\eta)\ dS' \qquad (1)$$

The function f in the integral is related to a mode of oscillation and is known. The function φ is the potential for a source and is, of

course, known. The region of integration S' is indicated by shaded areas in the sketches in figure 2. This method was named by Pines and others at Republic Aviation Company, who proposed a procedure termed "box method" for obtaining generalized forces on flexible wings. As originally proposed, the wing plan form is replaced by a rectangular grid as indicated in the sketch at the left in figure 2. The leading edge is made jagged as shown. The integrations, in this original treatment, were effected by expanding integrands and approximating a term-by-term integration over the portion of each little box or rectangle that can affect the force at a given point x,y. When high-capacity computing equipment, such as an IBM 650 or higher capacity machine, is used very little is actually gained in computing time by approximating the plan form or by approximating the integrands. Therefore, this procedure has been programed for calculating forces for wings with supersonic edges without expanding the integrands and in such a way that the plan form is completely accounted for, as indicated in the sketch at the right in figure 2. The leading edge is not broken as in the sketch at the left. The present program is for an IBM 650 machine and has been tested by making a comparison with results for simple mode shapes calculated by the frequency expansion method. The two sets of results agree very satisfactorily. The program will probably be converted to an IBM 704 machine in the near future.

The kernel-function approach will now be considered. This method applies to either subsonic or supersonic speeds and is perfectly general with regard to plan form and frequency. It involves approximating solutions to an integral equation, namely,

$$w(x,y) = \frac{1}{4\pi\rho} \int_{S'} \int L(\xi,\eta)\ K(x,y;\xi,\eta;M,\omega)\ dS' \qquad (2)$$

In this equation $w(x,y)$ is the known amplitude of downwash or the normal velocity of points (x,y) of a wing; ρ is the fluid density; $L(\xi,\eta)$ is the unknown lift distribution acting on the wing; and $K(x,y;\xi,\eta;M,\omega)$ is the known kernel function of the integral equation. The region of integration S' extends over the portion of the wing that can affect the induced normal velocity or downwash at a given point (x,y). For subsonic speeds S' extends over the entire wing surface but for supersonic speeds it depends on Mach number. The region of integration for a triangular plan form and one particular supersonic speed and for all subsonic speeds is illustrated in figure 3.

The procedure for approximating solutions to the integral equation is to assume that the lift can be represented by a series of functions that are known except for certain constant coefficients. A general form of expression for the lift and the resulting downwash equation are indicated in the following equation:

[redacted]

$$w(x,y) = \sum_{n=0}^{N} a_n \int_{S'} \int F_n(\xi,\eta)\, K(x,y;\xi,\eta;M,\omega)\, dS' \qquad (3)$$

In this equation a_n represents unknown constants and the functions F_n are known expressions chosen to be combined so as to represent the lift distribution $L(\xi,\eta)$. Hence, when the coefficients a_n are determined, an approximate expression for the lift is known. In making a choice of the functions F_n, one must be guided by certain conditions that must be satisfied along the wing edges and the results for the few cases for which the lift distribution is known.

In order to determine the coefficients a_n, a system of linear algebraic equations in which these quantities are the only unknowns can be obtained by choosing $N + 1$ points at which to satisfy the known downwash. The coefficients of a_n in this system of equations however involve complicated surface integrals. These integrals, which must be evaluated to make the equations explicit, have to be handled by numerical methods and, because of strong singularities involved in the kernel function, the evaluations require special procedures. This is especially true in the neighborhood of the strip, shown darkened in figure 4, extending ahead of the point at which the downwash is being satisfied. Furthermore, the tremendous task of computations involved in evaluating the integrals make the task feasible only with the use of high-capacity computing equipment.

What makes the number of computations so great is the kernel function. It has to be evaluated many times in the process of determining the lift for one set of conditions and it is of such a nature that it can be evaluated quickly only by automatic high-speed equipment. In an effort to accelerate development and uses of this kernel function approach for treating aerodynamic problems, the Air Research and Development Command is sponsoring a tabulation of the kernel function for a few Mach numbers ($M = 0.6$, 0.8, and 1.0). This tabulation, which is now about complete, is being made at the Harvard University Computation Laboratory. These tables will have many uses but there now exist computing machines that are capable of handling the complete aerodynamic problem, including generation of the kernel function as it is needed, so that searching for these values in voluminous tables is not necessary.

With regard to evaluating the surface integrals involved in the kernel-function approach, several procedures have been considered. Runyan and Woolston (ref. 2) have developed a method of treating the case for subsonic speeds by a procedure similar to that of Falkner (ref. 3) for treating steady finite wings. Although this procedure

[redacted]

appears to give satisfactory results, it is not readily adaptable for systematically programing for machine calculation. Furthermore, there is no basis for its application when the speed is supersonic.

Nelson and Diederich (ref. 4) have developed a method for subsonic speeds that involves dividing the wing into many small elements in each of which the downwash is satisfied at the center of area. The lift in the elements bounded by the wing edges is represented by functions that have the proper behavior as the edge is approached. In all other elements the lift is represented by simple polynomials. Integrations are effected over each individual element. (See ref. 4.)

Recently, a method somewhat like that of Multhopp (ref. 5) for treating steady wings has been developed and programed for machine calculation at the Langley laboratory. It applies in principle to both subsonic and supersonic speeds but, since the kernel function differs for subsonic and supersonic speeds, a separate program is required for the two speed regimes. In order to describe this procedure briefly, the machine is instructed to calculate the spanwise distance over which the integrations extend and then to divide this distance into a specified number of intervals. Numerical integrating formulas are then applied along chordwise sections at each subdivision. Results of the chordwise integrations are then employed in the spanwise integrating formulas to complete the integrations. These integrations are simple and straightforward except in the neighborhood of singularities. In these neighborhoods, use of limiting forms and special formulas make it very easy to overcome the difficulties.

This setup for subsonic speeds has just recently been programed for an IBM 704 machine. Although the program is just being tested, this machine requires less than $1\frac{1}{3}$ minutes per control point to calculate the forces associated with five vibration modes for a given frequency value and Mach number. This means that, for 9 control points, which should be sufficient in most cases, the IBM 704 machine will require less than 15 minutes running time per frequency value and Mach number to calculate the forces associated with five different vibration modes.

The supersonic case has been recently programed for an IBM 650 machine and this machine requires about sixty times as much time as the IBM 704 to make the corresponding calculations. That is, it takes the IBM 650 machine about 15-hours running time per frequency value and Mach number to calculate the forces based on 9 control points for five different vibration modes. The program for the supersonic case will be converted to the IBM 704 machine in the near future and it is estimated that it will require less time on this machine than the subsonic case does.

[redacted]

In order to give some indication as to what might be expected with regard to accuracy of results calculated by this kernel function procedure, some comparisons are made for supersonic speeds by this method with results calculated by the frequency-expansion procedure for a triangular wing. In reference 6 the expansion procedure is applied to such wings deforming according to a general quadratic equation. The deformations considered for comparison are shown in figure 4. They include vertical translation and pitching of the wing considered as rigid, illustrated by section AA; a parabolic chordwise camber mode, illustrated by section AA; and a parabolic bending mode, illustrated by section BB. The particular plan form considered is a 60° delta wing. The reduced frequency parameter is 3/8 or 0.375 and the Mach number is 2. This is the Mach number condition for which the flow normal to edges swept 60° is sonic.

Amplitudes of the forces and associated phase angles have been calculated by the two methods. Results for the rigid modes are shown in figures 5 and 6. The magnitudes of lift and moment as well as phase angle are seen to be in very good agreement. Results for the camber and bending modes are shown in figure 7. The amplitudes are seen to be in almost perfect agreement, and the phase angles are in fair agreement. There is thus a good indication that the kernel-function procedure as programed is sound. Furthermore, there seems to be no reason why it would not give as good results for subsonic speed as these results indicate it does for supersonic speed. It therefore appears that there is a sound and feasible way of determining the linearized aerodynamic forces for any given plan form, mode shape, Mach number, and frequency. It is further pointed out that, by considering the mode shape in the form of a matrix of deflection functions, the kernel-function procedure can be handled so as to yield aerodynamic influence coefficients useful in a direct attack on the eigenvalue problem for the flutter mode.

SOME EXAMPLES OF FLUTTER CALCULATIONS

Consideration is now given to a few flutter calculations. The configuration for which results are first presented is a model of a 45° delta wing. Results for this model are shown in figure 8. The wing plan form is shown in sketch at the right of the figure. The modal lines corresponding to the first four natural modes of the model are shown. The necessary information regarding mode shapes for this particular model were obtained by fixing a small mirror at 24 different points on the surface and recording the trace of a reflected light source as the wing was forced to vibrate at a natural frequency. Unfortunately, only four modes were measured. The model was flutter tested in the Langley 8-foot transonic pressure tunnel and experienced flutter at a Mach number of 0.85 and a density corresponding to an altitude of about 35,000 feet.

511

[redacted]

Aerodynamic forces appropriate for this plan form and its mode shapes were determined by the kernel-function method and flutter calculations have been made for several altitude conditions employing first three and then four modes. Results of the three-mode analyses are indicated by squares and results for the four-mode analyses, by circles. The four-mode results may be noted to be within about 10 percent of the measured flutter speed. Although the results appear to have almost converged, it would be desirable to include additional modes to see the effect that they might have on the calculated results.

The next results are for the all-supersonic edge case. Cunningham (ref. 7) has recently employed the velocity-potential expansion procedure to develop aerodynamic forces associated with rolling and symmetric flapping modes for arrowhead wings with all-supersonic edges. The motivation for these derivations was that the results were needed for analyzing the flutter of some all-movable control surface models tested in the Langley 9-inch by 18-inch supersonic flutter tunnel.

From observation and measurement of the node lines of the natural modes, it was noted that the models had essentially all their flexibility concentrated in the supporting shaft. Two coupled modes were used in the analyses, and each coupled mode involved components of vertical translation, pitching, and flapping. The amount of each component could be determined by the location of the node lines because the control surface was essentially rigid.

A sample result of the analysis is shown in figure 9. This is for an all-movable 45° delta plan form with its supporting axis at 55.4 percent of the root chord. The Mach number is 1.6. The vertical coordinate for the figure is a stiffness parameter $c_r\omega_1/2V$ where c_r is root chord, V is the airspeed, and ω_1 is the frequency of the first natural mode. The horizontal coordinate is the ratio of the frequencies of the first and second natural modes. The calculated flutter boundary is a smooth curve with a large peak near a frequency ratio of 1. The flutter region is below the curve and the peak indicates that more and more stiffness is required to prevent flutter as the first and second frequencies approach one another.

Two experimental points are shown. The open point is a no-flutter point and the dark point denotes that flutter occurred after the shaft had been weakened by a certain amount. The critical flutter speed should then fall between the two points. The theory is on the conservative side for both points and agrees very well with experiment. Similar results were obtained for several other arrowhead wings for $M = 1.6$ and these are shown in figure 10. The plan forms are identified by leading-edge sweep and trailing-edge sweep. Sweepback is positive. Location of the supporting axis is given in percent root chord. In the upper left-hand

corner of figure 10 are results for the same configuration as that just discussed in figure 9 but with the pitch axis moved rearward to the 65.3 percent root chord. In the upper right-hand corner are results for a wing with the leading edge swept back 45° and the trailing edge swept forward 15°. In the lower left-hand corner are results for a 50° delta wing and in the lower right-hand corner are results for this 50° wing with the trailing edge swept back 15°. The theory is seen to be consistently conservative and to give results that are in reasonable agreement with the experimental data.

CONCLUDING REMARKS

Several approaches to the determination of the aerodynamic forces on oscillating wings have been briefly considered. These approaches take into account the actual plan form under consideration and the specific modes of oscillation. The few flutter calculations that have been discussed indicate that, when sufficient structural modes along with appropriate aerodynamic forces are taken into account, a reasonable correlation between theory and experiment can be obtained. It is emphasized that the kernel-function approach discussed is a highly versatile procedure and is currently being systematically programed for a high-speed calculator for both subsonic and supersonic speeds. Results obtained thus far indicate that, at least where linear theory is applicable, it should be a very powerful aid to the flutter analyst.

REFERENCES

1. Garrick, I. E.: Nonsteady Wing Characteristics. Aerodynamic Components of Aircraft at High Speeds. Vol. VII of High Speed Aerodynamics and Jet Propulsion, sec. F, A. F. Donovan and H. R. Lawrence, eds., Princeton Univ. Press, 1957, pp. 658-793.

2. Runyan, Harry L., and Woolston, Donald S.: Method for Calculating the Aerodynamic Loading on an Oscillating Finite Wing in Subsonic and Sonic Flow. NACA TN 3694, 1956.

3. Falkner, V. M.: The Calculation of Aerodynamic Loading on Surfaces of Any Shape. R. & M. No. 1910, British A.R.C., Aug. 1943.

4. Nelson, H. C., and Diederich, F. W.: A Numerical Integration Method for Calculating Pressure Distributions on Wings of Arbitrary Plan Form Deforming Harmonically in Subsonic Flow. (Prospective NACA paper.)

5. Multhopp, H.: Methods for Calculating the Lift Distribution of Wings (Subsonic Lifting Surface Theory). Rep. No. Aero. 2353, British R.A.E., Jan. 1950.

6. Watkins, Charles E., and Berman, Julian H.: Velocity Potential and Air Forces Associated With a Triangular Wing in Supersonic Flow, With Subsonic Leading Edges, and Deforming Harmonically According to a General Quadratic Equation. NACA TN 3009, 1953.

7. Cunningham, H. J.: Lift and Moment on Thin Arrowhead Wings With Supersonic Edges Oscillating in Symmetric Flapping and Roll and Application to the Flutter of All-Movable Control Surfaces. (Prospective NACA paper.)

[redacted]

MODES OF VIBRATION FOR A FLEXIBLE WING

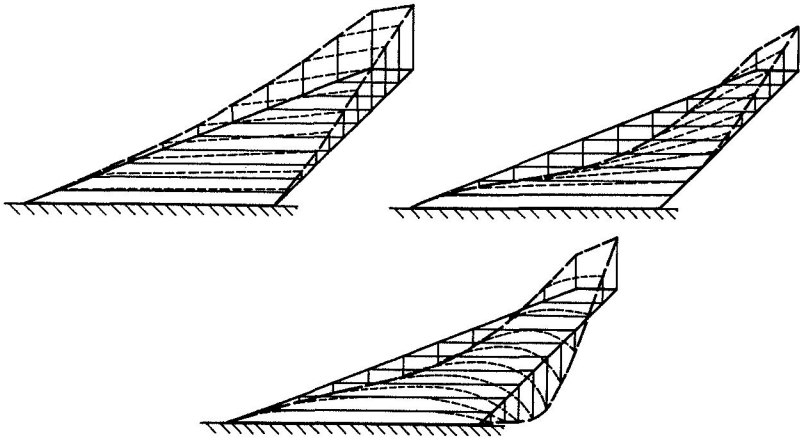


Figure 1

SCHEME OF CALCULATION BY BOX METHOD

SUPERSONIC EDGES

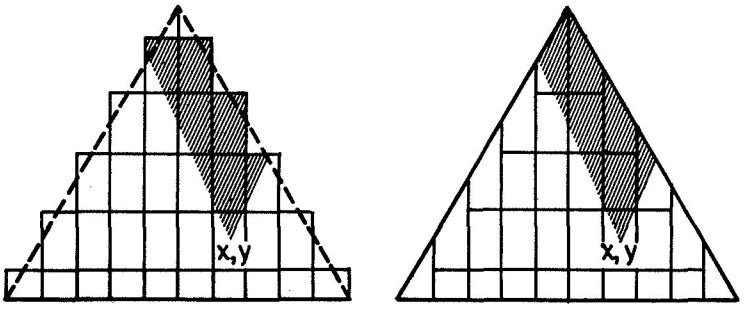


Figure 2

[redacted]

[redacted]

SCHEME OF CALCULATION BY KERNEL FUNCTION METHOD

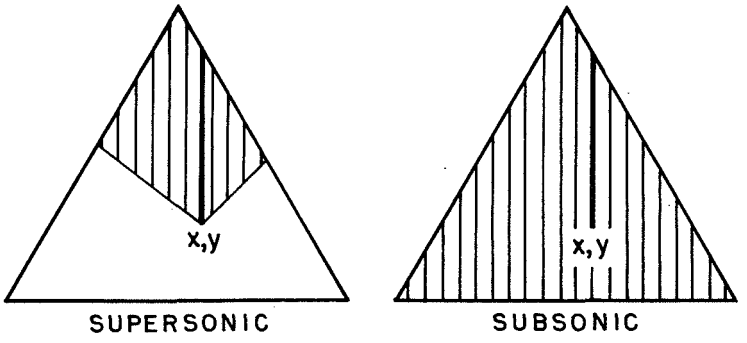


Figure 3

SOME DEFLECTION MODES TREATED BY FREQUENCY EXPANSION METHOD

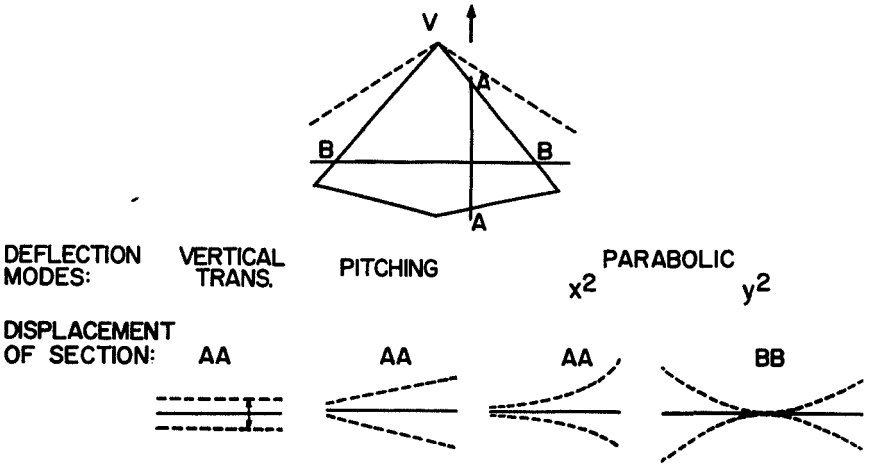


Figure 4

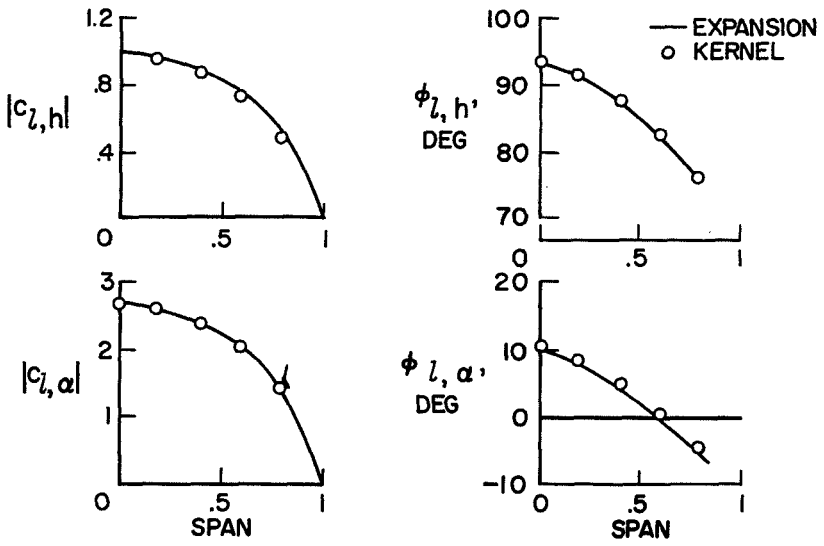


Figure 5

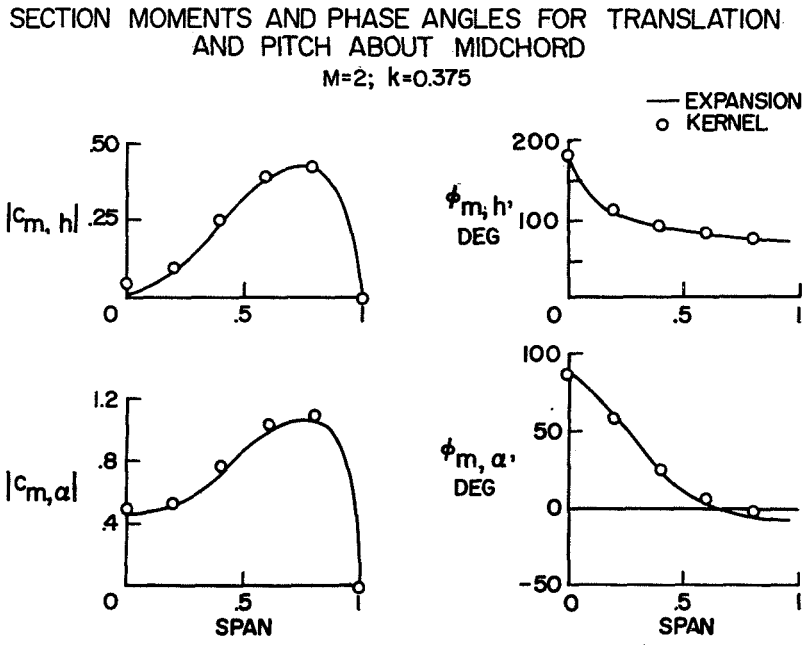


Figure 6

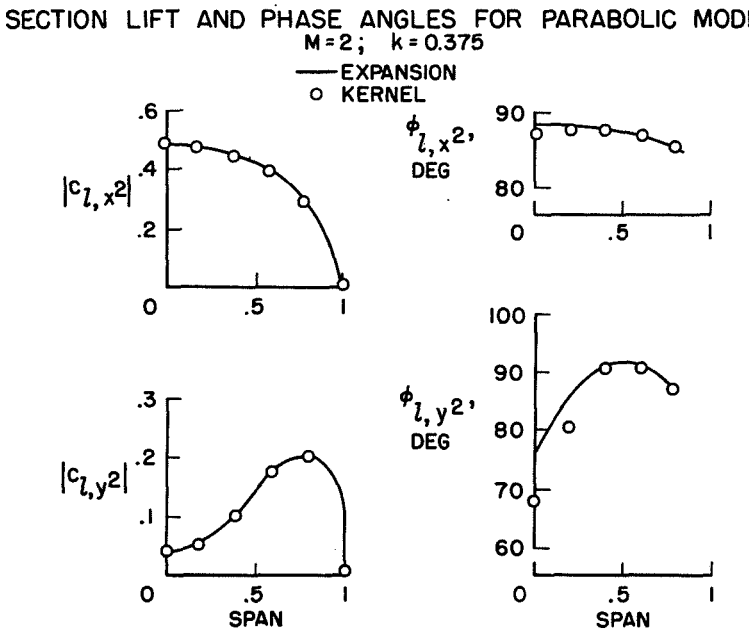


Figure 7

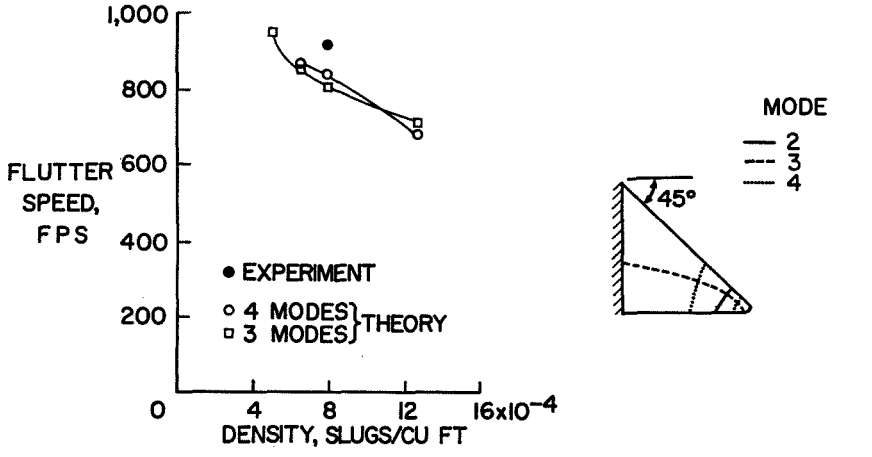


Figure 8

518

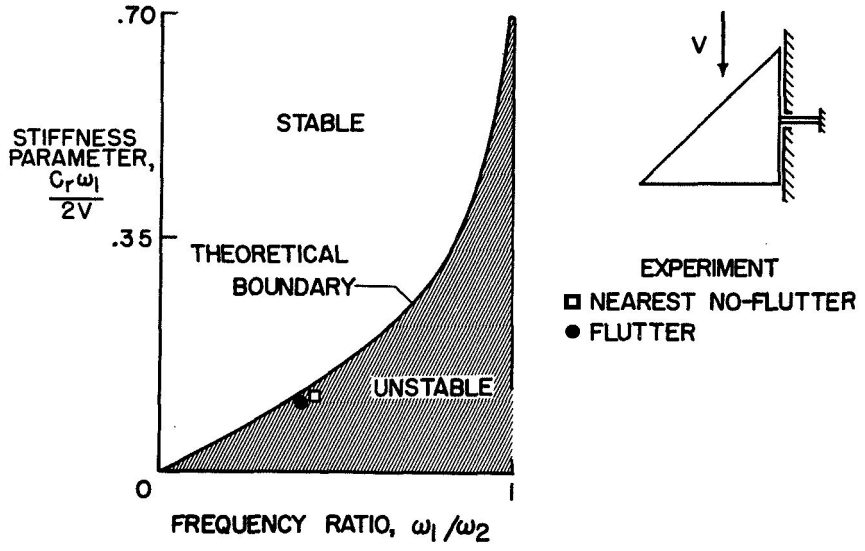
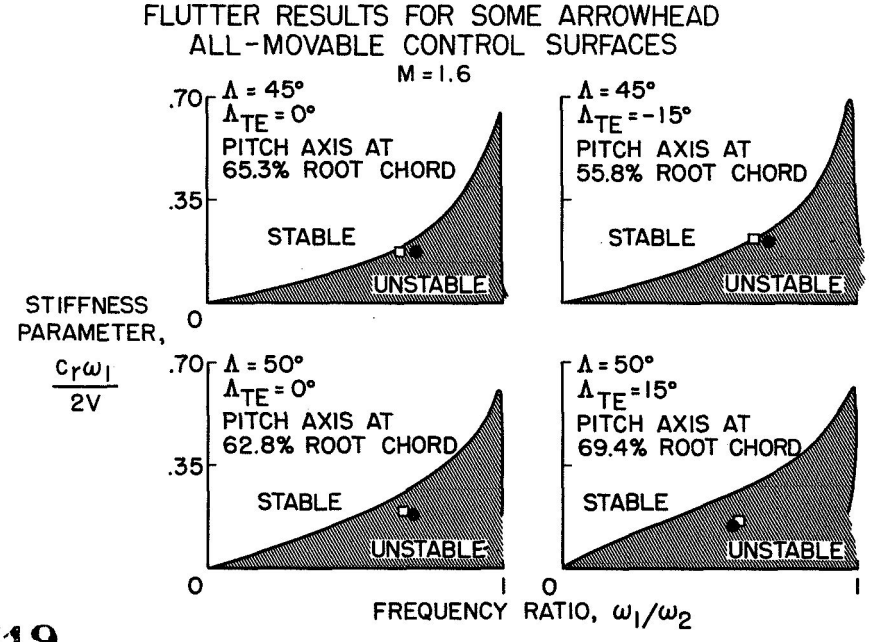


Figure 9



519

Figure 10

0G

[redacted] N71-75422

FLUTTER AT VERY HIGH SPEEDS

By Harry L. Runyan and Homer G. Morgan

Langley Aeronautical Laboratory

SUMMARY

This paper is concerned with a discussion of some of the problems of flutter and aeroelasticity that are or may be important at high speeds. Various theoretical procedures for treating high Mach number flutter are reviewed. Application of two of these methods, namely, the Van Dyke method and piston-theory method, is made to a specific example and compared with linear two- and three-dimensional results. It is shown that the effects of thickness and airfoil shape are destabilizing as compared with linear theory at high Mach number. In order to demonstrate the validity of these large predicted effects, experimental flutter results are shown for two rectangular wings at Mach numbers of 6.86 and 3. The results of nonlinear piston-theory calculations were in good agreement with experiment, whereas the results of using two- and three-dimensional linear theory were not.

In addition, some results demonstrating the importance of including camber modes in a flutter analysis are shown, as well as a discussion of one case of flutter due to aerodynamic heating.

INTRODUCTION

This paper is concerned with some problems of flutter and aeroelasticity at very high flight speeds. For this purpose high speeds will be defined as starting in the Mach number range of 2.5 to 3.

Some of the problems which are or may be important at high speeds are discussed according to the forces in the aeroelastic problem - aerodynamic, structural, and inertial. Under the aerodynamic part are:

(a) Nonlinear effect of airfoil shape, thickness, and angle of attack: There appears to be a very large effect of these factors on the flutter speed, which is discussed subsequently.

(b) Effect of shocks: Information is lacking and constitutes an area requiring research effort.

[redacted]

[redacted]

(c) Boundary layer and viscous effects: Here again information is lacking, (of course, even in the low speed case),but, with the thick boundary layers encountered at high-speed flight, the dynamics of the boundary layer could become important, particularly, interactions of the boundary layer with shocks.

(d) Plan form: Some of the new plan forms having sweep angles of the order of 75^{o} will pose special problems with respect to unsteady aerodynamics, and there arises the difficult problem of studying and developing theories that will take into account the effect of both airfoil shape and aspect ratio.

(e) Controls: Controls have always been a source of trouble for the flutter analysts. In the Mach number range of 10 to 20, the type of control that will prove to be satisfactory is not known. But from past experience, whatever type of aerodynamic control, if any, is found to be satisfactory, it will probably constitute a flutter problem.

Structures required for high-speed flight present another area of difficulty. Some of the problems are:

(a) Aerodynamic heating: An example of aerodynamic heating relating to flutter is briefly discussed.

(b) Panels and heat shields: For the flat-bottomed highly heated aircraft now envisioned for high-speed flight, it appears that the flutter of panels and heat shields will be a very real problem. Under high-temperature conditions, buckling will probably occur and will require nonlinear treatment.

(c) Plan form: For wings of high aspect ratio, the distortions of the wing involved mainly a twisting and bending of the wing, so that the elementary concepts of "beamology" could be used. However, the low-aspect-ratio wings now being considered behave more like plates and involve a large amount of chordwise deflection.

Inertial force is the third type of force in the aeroelastic problem. The aircraft structural weight is decreasing in comparison with the weight of the fuel, particularly with regard to missiles. Consequently, such nonlinear problems as fuel sloshing and swirl are becoming exceedingly important.

Three of these problems will be discussed: the effect of airfoil shape, structural plan form, and aerodynamic heating.

[redacted]

SYMBOLS

A	aspect ratio
a	speed of sound
b	half chord, in.
C_p	pressure coefficient, $\frac{p - p_o}{q}$
I_α	moment of inertia about elastic axis
M	Mach number
m	mass of wing per unit of span length, $\frac{\text{lb-sec}^2}{\text{in.}^2}$
p	pressure at point x,y
p_o	pressure in undisturbed stream
q	dynamic pressure
r_α	radius of gyration, $r_\alpha^2 = \frac{I_\alpha}{mb^2}$
t	thickness ratio
w	vertical induced velocity or downwash
V	stream velocity, ft/sec
x,y	Cartesian coordinates
α	angle of attack
γ	specific heat ratio
ω_h	bending frequency, radians/sec
ω_α	torsional frequency, radians/sec
ω_1	first bending frequency, radians/sec
μ	mass ratio, $\frac{m}{\pi\rho b^2}$

ρ fluid density

φ velocity potential

Subscripts:

L linear

NL nonlinear

ANALYTICAL METHODS

This section is concerned with a brief description of the theoretical methods available for high Mach number studies. The complete nonlinear partial differential equations for the potential and the pressure coefficient are shown by

$$\varphi_L + \varphi_{NL} = 0 \tag{1}$$

$$C_p = C_{p,L} + C_{p,NL} \tag{2}$$

and can be broken down into a linear part plus a nonlinear part. The linear solution now in general use is obtained from equations (1) and (2) by setting the nonlinear part equal to zero, as given by

$$\varphi_L = 0 \tag{3}$$

$$C_p = C_{p,L} \tag{4}$$

and then solving the equations with suitable boundary conditions.

Several approximate methods are available for obtaining nonlinear solutions. The first of these is the solution of Van Dyke (ref. 1). He first eliminated the third-order terms from these two nonlinear equations (this procedure, in effect, eliminates the effect of finite shocks) and then inserted the solution for the linear equation (3) in the nonlinear part of equation (1). This procedure resulted in a linear partial differential equation plus a known function as

$$\varphi_L + f(x,y,t) = 0 \tag{5}$$

$$C_p = C_{p,L} + C_{p,NL} \tag{6}$$

By a laborious technique, Van Dyke then solved these equations for the pressure on specific airfoils.

Another nonlinear method is the so-called piston theory. This procedure was originally suggested by Hayes (ref. 2), was used by Lighthill (ref. 3) to check the results of Van Dyke at high Mach number, and later was elaborated on and applied to the flutter problem by Ashley and Zartarian (ref. 4). The advantage of piston theory is its utter simplicity as compared with other theories. The pressure coefficient is easily derived on the basis of a piston moving in a one-dimensional channel. The expression for the pressure coefficient is given in

$$C_p = 2\left[\frac{1}{M}\left(\frac{w}{V}\right) + \frac{\gamma + 1}{4}\left(\frac{w}{V}\right)^2 + \frac{\gamma + 1}{12} M\left(\frac{w}{V}\right)^3 + \cdots\right] \tag{7}$$

where w is the instantaneous vertical velocity of a point on the wing, and V is the stream velocity. Note that, as M is increased, the first term would become less important, and the higher order nonlinear terms would begin to take an added importance.

Another method is use of the Newtonian concept. In this procedure it is assumed that the flow striking the exposed surface is compressed to a very thin boundary layer and the force exerted on the airfoil is due to the component of momentum perpendicular to the surface. The resulting pressure coefficient

$$C_p = 2\left[\left(\frac{w}{V}\right)^2 - \frac{1}{3} M^2\left(\frac{w}{V}\right)^4 + \cdots\right] \tag{8}$$

was obtained by expanding $\cos^2 \frac{w}{V}$. For a curved surface or an oscillating surface, additional terms due to centrifugal force could be added. Note that the first term is missing as compared with piston theory and the coefficient of the squared term has a factor of 1 as compared with 0.6 for $\gamma = 1.4$. Later, use will be made of the Van Dyke and piston-theory solution.

APPLICATION TO SPECIFIC EXAMPLES

Some applications and comparisons of the various theories are given. In figure 1 are shown the results of calculating the flutter of a rectangular wing of panel aspect ratio 1.5 throughout the Mach number range of 1.3 to 10. The airfoil section was 65 series, tapering from 4 percent at the root to 3 percent at the tip. Four theories have been used: linear two-dimensional theory, linear three-dimensional theory, nonlinear

piston theory, and Van Dyke theory. The results are plotted against the stiffness-altitude parameter, $\frac{b\omega_\alpha}{a}\sqrt{\mu}$. The flutter region is below the curves. Constant-altitude lines are horizontal and constant-dynamic-pressure lines are radial lines emanating from the origin. There are four points of interest in this plot. First, the large difference between the linear theories and the two theories which include the effect of thickness at the higher Mach numbers. This effect is primarily due to a forward shift in the center of pressure due to airfoil shape whereas the center of pressure for the two-dimensional linear theory is fixed at the 50-percent chord and the forward shift of the center of pressure in the three-dimensional tip does not predict as much forward movement as the nonlinear theories. Another point is the agreement of the more complicated Van Dyke theory with the simpler and more readily used piston theory at the higher Mach number. A third point of interest is the cross over of the two- and three-dimensional theory at $M = 1.6$. It has usually been assumed that inclusion of the three-dimensional effects is a relieving effect when compared with the two-dimensional theory. This is usually true at the lower Mach numbers but it is not necessarily true at the high Mach numbers. A fourth point is that the effect of airfoil shape and thickness is destabilizing. For instance, at an altitude corresponding to a value of the ordinate of 3.3, nonlinear theory indicates that flutter would be experienced at a Mach number of 5, whereas the linear theory would predict the airfoil to be flutter free.

In figure 2 is shown the calculated effect of thickness and airfoil shape on flutter at $M = 10$ obtained by using nonlinear piston theory. The stiffness-altitude parameter is shown plotted against the ratio of bending to torsion frequency. The flutter region is below the curve. Curves are presented for a flat plate, a 4-percent wedge, and a 4-percent biconvex airfoil. Let us focus our attention on the curves for the flat plate or zero-thickness airfoil and the biconvex airfoil. For low-frequency ratio, the zero-thickness airfoil gives no flutter solution whereas the biconvex airfoil shows a definite flutter solution. As the frequency ratio is increased, however, the curves tend to approach each other and at $\frac{\omega_h}{\omega_\alpha} = 1.2$ they actually cross. That is, the effect of thickness is destabilizing for low values of the frequency ratio and stabilizing for high values, at least for this case. Note that the wedge has a shape similar to the flat plate except it is slightly destabilizing.

In figures 1 and 2 are shown some rather large and disturbing effects of thickness and airfoil shape in reducing the flutter speed. The question is then "are these large effects, in fact, true." In an attempt to answer this question two wings have been fluttered at high speed. The frequency ratio selected for these wings was deliberately chosen so that as wide a spread as possible between the zero-thickness and the thickness solution could be obtained. For these cases the frequency ratio was

approximately 0.35. Although the parameters for figure 2 are not the same as those for the experiment, the trends are the same and at a frequency ratio of about 0.35 there is quite a difference between the zero-thickness and the thickness cases.

COMPARISON OF EXPERIMENTAL AND THEORETICAL RESULTS

Flutter at Mach Numbers of 6.86 and 3.0

Results for two rectangular wings are shown in figures 3 and 4, each having a panel aspect ratio of 0.8. One is an 11-percent double-wedge section and the other is a 4-percent flat wing. The properties of these wings are given in the following table:

	11-percent wedge	4-percent plate
b	2.55	2.57
m	0.0001276	0.000127
r_α^2	0.251	0.269
x_o	0.467	0.46
x_α	0.0545	0.0745
ω_h	110.9	106
ω_α	314	322
V at M = 3.0 . . .	2,110	2,120
V at M = 6.86 . . .	3,250	3,255

(The torsion mode for both wings was taken as unity across the span. The bending mode for the 11-percent wing was taken as $f_h = 0.23 + 0.1925x$ and for the 4-percent wing as $f_h = 0.335 + 0.186x$ where x varies from 0 to 4 inches.) The wings were very rigid and were mounted on flexible shafts so that, in effect, they corresponded to all-movable controls. The results are again plotted as the stiffness-altitude parameter against Mach number. The experimental results are shown as solid points and were obtained at Mach numbers of 6.86 and 3 in the Langley 11-inch hypersonic tunnel and the Langley 9- by 18-inch supersonic flutter tunnel, respectively. Let us examine first the double wedge. The solid line is the result of using nonlinear piston theory and fairly good agreement is indicated with the experiment. The two-dimensional, zero-thickness method gave no solution. The three-dimensional linear case indicated a flutter-free wing at a Mach number of 6.86 but gave a solution at a lower Mach number as indicated. For the 4-percent plate, similar [redacted] piston theory and

experiment was obtained. Again, two-dimensional zero thickness gave no solution and indicated the wing to be flutter free; whereas, inclusion of the three-dimensional tip effect gave a solution as indicated. The value of reduced frequency k for the $M = 6.86$ test was $\frac{1}{70}$ and a first-order theory in frequency such as the piston theory should be satisfactory.

Thus, it appears that the detrimental effect of thickness on flutter as predicted by piston theory is in fact true and that nonlinear theories must be used at the high flight speeds. One interesting fact is that lines drawn through the experimental points intersect the origin; thus a constant "q" flutter variation is indicated.

Flutter of Delta Wings

Now let us turn our attention to some flutter calculations of two low-aspect-ratio cantilever wings. In figure 5 the stiffness-altitude coefficient has been plotted against Mach number for 45° and 60° delta wings. The wings were flat plates with beveled leading and trailing edges. The circular points are the experimental results from reference 5 and the solid and dashed lines are analytical results. Piston theory was used for the aerodynamic input. A modal type of analyses which was based on experimentally measured mode shapes was used. Since these modes had a large amount of deflection in the chord direction, it did not seem that the deflection curves could be approximated by the usual procedure of bending and twisting of a straight line. Hence, analytical curves were fitted to the experimental deflection curves at each of 10 spanwise stations for use in the analysis. The results are shown by solid lines and show fairly good agreement with experiment. In order to assess the effect of chordwise deflection, the camber was arbitrarily eliminated from each mode and then recalculated. The results are shown by the dashed lines. For the 60° wing, the curve was shifted over to the nonconservative side, whereas for the 45° wing a very wide divergence is found. Thus the importance of including the camber deflection in the analysis of a low-aspect-ratio wing is demonstrated.

Flutter Due to Aerodynamic Heating

Another well-known problem of high speed is the effect of aerodynamic heating. With regard to flutter, the main effect of aerodynamic heating is to cause a loss in torsional stiffness, particularly during transient conditions. A solid duralumin wing has been tested at a Mach number of 2 in the preflight jet of the Langley Pilotless Aircraft Research Station at Wallops Island, Va. Two runs were made, a cold run during which the wing did not flutter and a hot run during which the wing fluttered. This phenomena can be explained with the aid of figure 1. These

calculations apply to this heated wing. In the cold condition the value of the stiffness-altitude parameter at a Mach number of 2 is 3.07 and is well in the stable region. During the fast start of the tunnel, the leading and trailing edges heated up much more rapidly than the thicker center section; this condition causes a momentary loss in torsional stiffness. Thus the torsional frequency was reduced; the stiffness-altitude parameter is correspondingly reduced and would follow a vertical line to an intersection of the flutter curve. Calculations of the loss in torsional stiffness have been made and show a reduction in the torsional frequency by 50 percent which is sufficient to intersect the flutter region. Thus, flutter which has been induced by aerodynamic heating, at least for a simple solid wing, can be calculated.

CONCLUDING REMARKS

New flutter and aeroelastic problems will appear at high flight speeds. Configurations dictated by high-speed requirements will probably also exhibit new problems in the lower speed ranges. An essential feature of many of these problems is their inherent nonlinearity. For accurate flutter prediction, inclusion of these nonlinearities, such as the effect of airfoil thickness and shape, is a necessity.

REFERENCES

1. Van Dyke, Milton D.: Supersonic Flow Past Oscillating Airfoils Including Nonlinear Thickness Effects. NACA Rep. 1183, 1954. (Supersedes NACA TN 2982.)

2. Hayes, Wallace D.: On Hypersonic Similitude. Quarterly Appl. Math., vol. V, no. 1, Apr. 1947, pp. 105-106.

3. Lighthill, M. J.: Oscillating Airfoils at High Mach Number. Jour. Aero. Sci., vol. 20, no. 6, June 1953, pp. 402-406.

4. Ashley, Holt, and Zartarian, Garabed: Piston Theory - A New Aerodynamic Tool for the Aeroelastician. Jour. Aero. Sci., vol. 23, no. 12, Dec. 1956, pp. 1109-1118.

5. Tuovila, W. J., and McCarty, John Locke: Experimental Flutter Results for Cantilever-Wing Models at Mach Numbers up to 3.0. NACA RM L55E11, 1955.

FLUTTER FOR VARIOUS AERODYNAMIC THEORIES

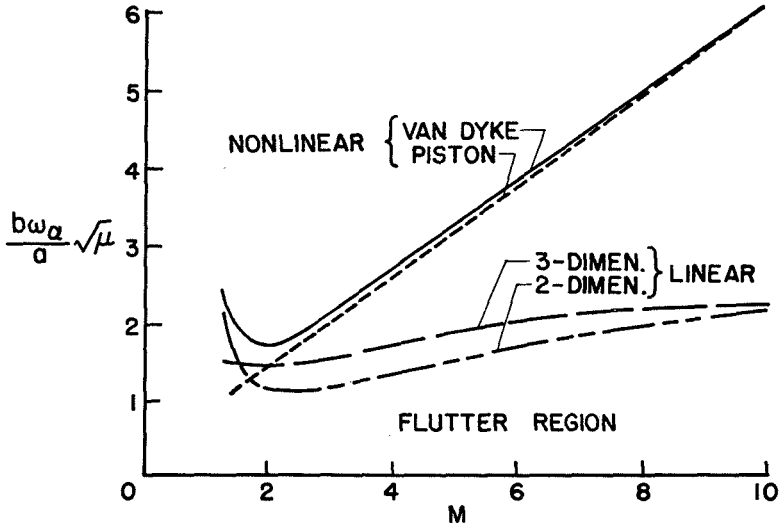
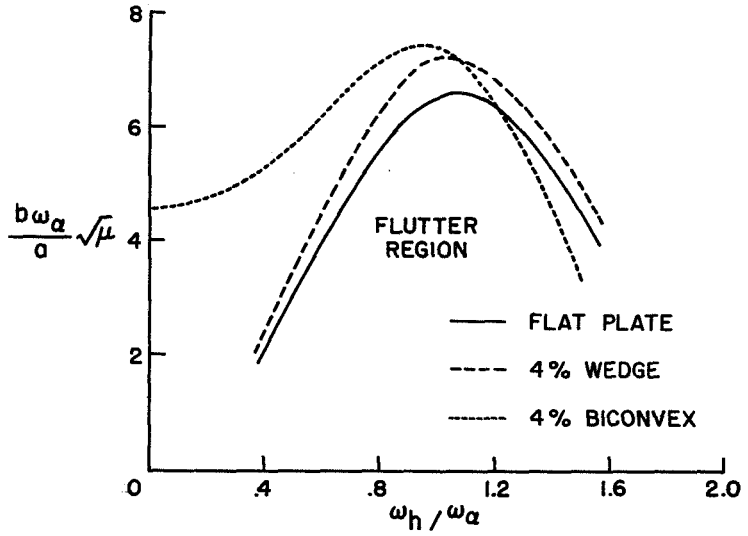


Figure 1

CALCULATED EFFECT OF AIRFOIL SHAPE

$M = 10; r_\alpha^2 = 0.25$; C.G. = 50%; E.A. = 40%



FLUTTER OF A DOUBLE WEDGE WING AT HIGH SPEED

E.A.=46.7%; C.G.=49.4%; A=0.8

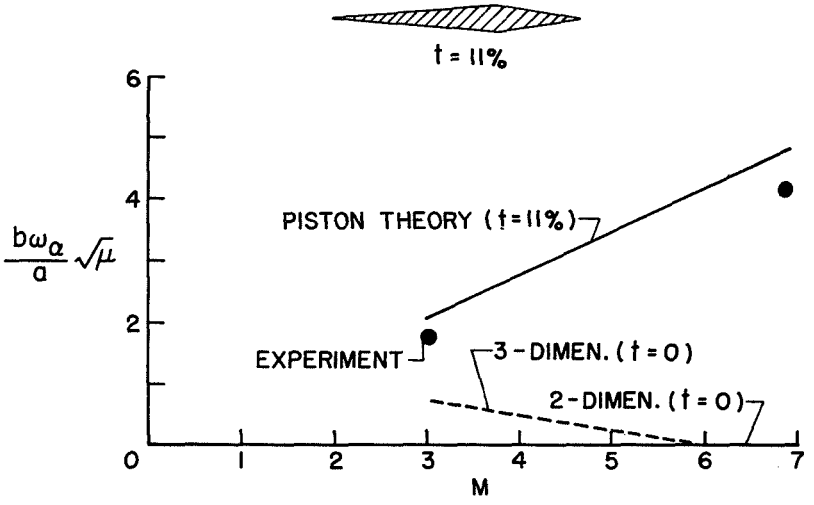


Figure 3

FLUTTER OF A THIN WING AT HIGH SPEED

E.A. = 46% ; C.G. = 50% ; A = 0.8

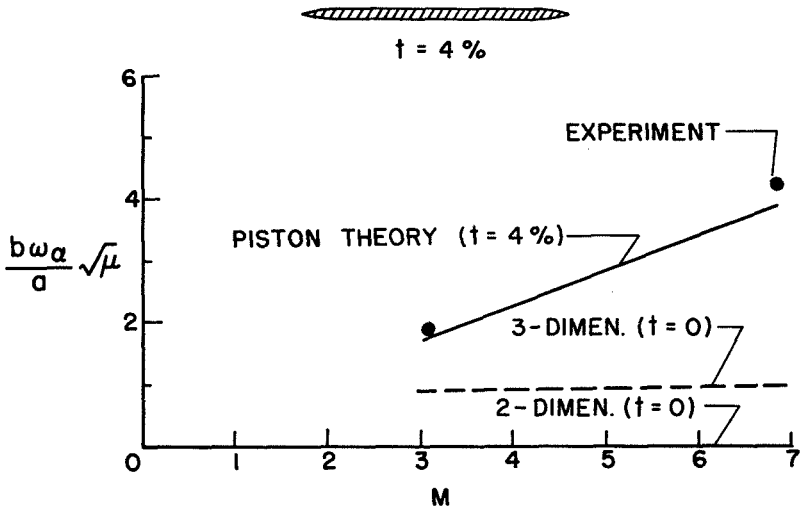


Figure 4

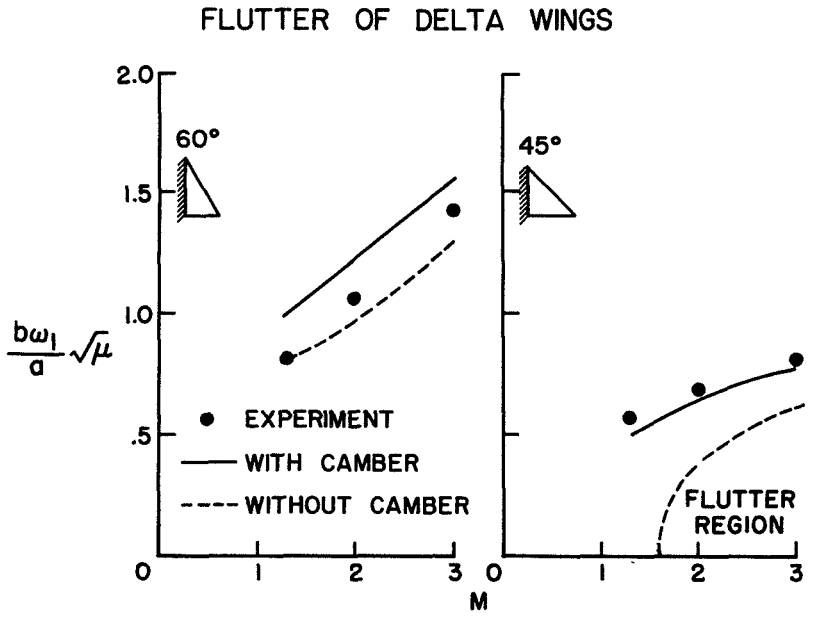

FLUTTER OF DELTA WINGS
2.0
1.5
1.0
.5
0
60°
45°
$\frac{b\omega_1}{a}\sqrt{\mu}$
EXPERIMENT
WITH CAMBER
WITHOUT CAMBER
FLUTTER REGION
1
2
3
M

Figure 5

N71-75423

LOFTIN & LAUTEN

FLUTTER OF WINGS WITH AND WITHOUT EXTERNAL STORES AT TRANSONIC AND SUPERSONIC SPEEDS

By Laurence K. Loftin, Jr., and William T. Lauten, Jr.

Langley Aeronautical Laboratory

INTRODUCTION

Much of the available experimental information on wing flutter at transonic and supersonic speeds deals with plain wings of moderate aspect ratio and taper ratio. In the present paper, some aspects of the flutter behavior at transonic and supersonic speeds of delta wings and highly tapered swept wings, and of wings with mass balance and external stores will be discussed. The Mach number range to be considered is from 0.8 to 3.0. The majority of the material to be presented was obtained recently, is rather fragmentary, and should be regarded as suggestive of possible leads or hints rather than as a basis for forming broad conclusions or design rules. Trends for the plain wings will be discussed first and then some results for wings with mass balance and stores will be presented.

SYMBOLS

A	aspect ratio
a	speed of sound, ft/sec
b	streamwise root semichord, ft
c	streamwise chord, ft
M	Mach number
q	dynamic pressure, lb/sq ft
q_0	dynamic pressure at flutter of wing without stores or bodies, lb/sq ft
q_s	dynamic pressure at flutter of wing with stores or bodies, lb/sq ft

Λ angle of sweep, deg

λ taper ratio

μ nondimensional density parameter (ratio of mass of exposed semispan wing to mass of air contained in the frustum of a cone whose upper and lower base diameters are equal to streamwise tip and root chords)

ω_α frequency of predominantly torsion mode, radians/sec

ω_θ uncoupled store pitching frequency, radians/sec

RESULTS AND DISCUSSION

Plain-Wing Results

The flutter trends to be discussed for wings without stores or balance weights are shown in figure 1. This is a plot of the stiffness-altitude parameter $\frac{b\omega_\alpha\sqrt{\mu}}{a}$ against Mach number. The flutter region is the region below the curve. Constant altitude is indicated by a horizontal line, constant dynamic pressure by a straight line through the origin. An increase in altitude for a given wing corresponds to an increase in the stiffness-altitude parameter. Trends are presented for a 60° delta wing, a 45° swept wing with a taper ratio of 0.2 and, for comparison, a 45° swept wing with a taper ratio of 0.6. The plan forms of the wings are indicated by the sketches on the left. The curves shown are based on data obtained in the 26-inch Langley transonic blowdown tunnel at Mach numbers from 0.8 to 1.4 and in the Langley 9- by 18-inch supersonic flutter tunnel from 1.3 to 3.0. The trends shown in this figure are thought to be particularly interesting in that the configurations investigated at transonic and supersonic Mach numbers are nearly the same and an acceptable basis for evaluating the relative severity of the flutter problem at transonic and supersonic Mach numbers is thus provided, at least for the plan forms considered. The trends show the existence of a critical flutter region around Mach number 1.0, after which the three wings are flutter-free at altitudes equal to or greater than that necessary to avoid flutter at transonic speeds, until the Mach number reaches values of the order of 2.0. No especial significance should necessarily be attached to the Mach number around 2.0, at which value the stiffness-altitude parameter becomes equal to the critical value around Mach number 1.0, except insofar as the particular configurations considered in the figure are concerned. Investigations at both transonic and supersonic Mach numbers indicate that the values of the stiffness-altitude parameter corresponding to flutter can be altered by

changes in wing plan form, center-of-gravity position, and perhaps other parameters. The trends of this figure, however, emphasize the necessity for careful consideration of the flutter boundaries at both transonic and supersonic speeds on any new high-speed aircraft.

An interesting detailed feature of the results shown in figure 1 is the behavior of the highly tapered wings at Mach numbers around 1.0. In contrast to the results for the wing with taper ratio of 0.6, the value of the stiffness-altitude parameter for the highly tapered wings is seen to drop suddenly to a lower value and then increase slowly as the Mach number is increased. Thus, a large stable region for these two wings is indicated at Mach numbers somewhat in excess of 1.0. The sudden decrease in stiffness-altitude parameter has been found to accompany an increase in flutter frequency by a factor of approximately 2, with the wing fluttering at about the natural torsional frequency. This change in flutter mode is felt to be of interest because the nature of a "fix" required to suppress flutter may be different for the different flutter modes. The combination of parameters responsible for the favorable decrease in the stiffness-altitude parameter with the accompanying increase in the flutter frequency is not understood; therefore, the range of application of the results cannot be assessed at this time.

Effects of Mass Balance

The results of some recent studies at transonic speeds of the effects of mass balance will now be discussed. The wing plan form employed was the same 45° swept wing with taper ratio of 0.2 discussed in figure 1. The configurations investigated are shown at the top of figure 2. The shaded areas shown at the leading edge represent the two positions of balance mass for which experiments were made. Balance masses of 6 and 12 percent of the wing mass were attached at each position and in each configuration the mass extended over 25 percent of the span. The results obtained from the four mass-balance configurations are shown in the bottom part of the figure. These results are plotted in the form of dynamic pressure required for flutter against Mach number. The area above the curve is the flutter region. The solid line represents data taken from figure 1 for the wing without balance. The dashed line is a fairing of data taken for all balance conditions since no significant difference existed between the data for the four configurations. The results show that in the critical flutter range between Mach numbers of 0.9 and 1.05, where the very pronounced peaks in stiffness-altitude parameter were evident in figure 1, the leading-edge balance mass increased the dynamic pressure required for flutter by as much as 100 percent. The hatched area labeled "no flutter" indicates that flutter could not be obtained beyond Mach number 1.1 for any of the mass-balance configurations up to the maximum dynamic pressure employed in the investigation. Obviously, substantial improvements in the transonic flutter characteristics of this wing can

[redacted]

be obtained by the use of mass balance. In this connection, it is perhaps of some interest to point out that an increase of approximately 100 percent in the plain-wing torsional stiffness would be required in order to achieve the effect produced by the addition of 6 percent of the wing weight as a mass balance. The fact that decreasing the amount of balance mass by a factor of 2, that is, from 12 percent to 6 percent wing mass, had no effect on the improvement shown leads to the question of just how little mass balance could be used in order to obtain a certain desired increase in dynamic pressure for flutter. There is no general criterion for the optimum amount and position of the balance mass and each case will probably have to be a subject for individual study.

Wings With External Stores

In contrast to the work just discussed on distributed mass, some exploratory studies have been made at Mach numbers from 0.8 to 1.3 on the effect on flutter of concentrated masses in the form of external stores. This work was aimed at gaining some insight into the nature of the problems encountered, and, if possible, what properties of the store might be significant to the flutter problem. Three configurations studied at transonic speeds are shown in figure 3. The wing was swept back 45°, had no taper, and had an aspect ratio of 4.0. The three stores employed were of the underslung type mounted on pylons, and had an aerodynamic shape consistent with current transonic design practice. The stores are labeled as A, B, and C. Stores A and B were nearly identical, except for a change in center-of-gravity position, and had a weight of about 70 percent of the wing weight. Store C was 40 percent heavier (approximately equal to the wing weight). The center of gravity of store A was located at the 38-percent-chord point at midsemispan and the center of gravity of store B was at the 12-percent-chord point, also at the midsemispan. The center of gravity of store C was 25 percent ahead of the leading edge at about 80 percent of the semispan.

The experimental results for the various store configurations are shown in figure 4 in which the ratio of the dynamic pressure at flutter of the wing with stores to that of the wing without stores is plotted against Mach number. No significant difference was found in the results for stores A and B, and the solid line in this figure represents a fairing of both sets of data. It may be seen that the dynamic pressure for flutter of the wing with stores A and B lies between 70 and 80 percent of that for the plain wing in the range of Mach number from 0.8 to about 1.3. The dashed line indicates the results obtained from the tests of configuration C. As can be seen, the dynamic pressure for flutter at $M = 0.95$ has been increased from about 75 percent to about 90 percent of that for the wing without stores as a result of this change in the weight position; outside the Mach number range of 0.88 to 1.05, the dynamic pressure required for flutter is larger for the wing with the store than for the wing without the store.

[redacted]

The fact that forward movement of the store center of gravity had no effect on the results obtained for stores A and B is perhaps not too surprising when consideration is given to the nodal patterns for the two store configurations. It may be seen in figure 5 that the shift in the center of gravity makes only a small change in the location of the nodal pattern and the uncoupled frequencies would not be expected to be much different. In regard to configuration C, it was assumed that a large forward movement of the predominantly torsion node line might, as previous investigators have suggested, be indicative of a favorable coupling effect with a corresponding increase in the dynamic pressure of flutter. Consequently, a vibration survey was made with the store located in numerous spanwise and chordwise positions. Configuration C was found to give the type of node line desired and yielded an increase in the flutter dynamic pressure. Any differences in the effects of the aerodynamic forces and moments of the store on the flutter condition as the store was moved from the location of A and B to C were assumed to be of second-order importance. The results shown in this figure indicate that, just as is the case at lower speeds, the addition of stores should not necessarily cause a serious flutter problem at transonic speeds and may perhaps be employed as a means for alleviating the problem.

A short exploratory study has also been made at transonic speeds of the effects of the introduction of flexibility into the store mount so as to give a pitching degree of freedom. The configuration and some of the results obtained are shown in figure 6. The same untapered wing used in connection with figures 4 and 5 was employed in these studies. A schematic diagram of the store mount is shown at the right of the figure. The store was mounted close to the under surface of the wing and was connected to the wing by a spring in such a manner that the store was essentially rigid in yaw and side bending but had flexibility in pitch. The spanwise position of the store was chosen to correspond approximately to the plain-wing second bending node line which was at about 75 percent of the semispan. The store mass was about the same as that of the plain semispan wing. The center of gravity was located at 31 percent of the wing chord. The data shown are in the form of the ratio of the dynamic pressure required for flutter for the wing with store to that for the wing without store, plotted against the ratio of the uncoupled store pitching frequency ω_θ to the uncoupled torsion frequency ω_α of the plain wing. The highest value of this ratio shown here represents about as near a rigid condition as could be obtained. The circled points represent values of the frequency ratio for which data were obtained. The results are for a Mach number of approximately 0.85. The trend of the data indicates a definite optimum value of the pitch flexibility. For the particular configuration studied, the optimum value of the ratio of pitching frequency to torsion frequency was about 0.6, with reductions in the dynamic pressure required for flutter accompanying either increases or decreases in the flexibility of the store mount. The results shown in this figure indicate the possibility of lessening the flutter problem with stores at transonic speeds by employing flexibility in the store mount.

[redacted]

Studies of the effects of external bodies on flutter at supersonic speeds are being carried out in the Langley 9- by 18-inch supersonic flutter tunnel. The plan forms for which these studies are being made include those shown in figure 1. Some of the results for the 60° delta wing and the 45° swept wing with taper ratio of 0.2 will be presented. The configurations investigated on the delta wing are shown in figure 7. The symbols indicate the 12 positions of the body center of gravity for which tests were made. The positions were -25, 0, 25, and 50 percent of the wing chord. The spanwise positions were 1/4, 1/2, and 3/4 of the semispan. The size and shape of the bodies are indicated by the outline drawings at the 50-percent-semispan station. The mass of the body was slightly more than one-half of the wing semispan mass. In all cases the body was equal in length to the wing chord at the 50-percent-semispan position and had a fineness ratio of 10. The shape of the body was rather crude; however, the slope of the lift and moment curves on a body of such high fineness ratio is relatively small and is not affected to any great extent by detailed changes in the shape. It was therefore assumed that the shape of the bodies was relatively unimportant in determining the flutter characteristics. A few tests with bodies of cleaner aerodynamic shape have indicated that this assumption is valid.

The effect of the center-of-gravity location on the flutter characteristics of the 60° delta wings is shown for Mach numbers 1.3 and 2.0 in figures 8 and 9, respectively. The ordinate is again the ratio of dynamic pressure necessary for flutter with body attached to that necessary for flutter with the plain wing. The abscissa is the fraction of the semispan. The circles indicate the center of gravity ahead of the leading edge, the squares indicate the leading-edge center-of-gravity position, the diamonds indicate the 25-percent-chord position, and the triangles indicate the 50-percent-chord position. The open points indicate that no flutter was obtained for these body locations up to the maximum dynamic pressure possible in the tunnel. Points above the solid line at a value of q_s/q_0 of 1 indicate an increase in the dynamic pressure required for flutter resulting from installation of the external body. Large increases in the dynamic pressure required for flutter are seen to accompany many body locations at Mach numbers of both 1.3 and 2.0. Although the results are not completely consistent, the far-forward, 3/4-semispan position of the center of gravity appears to be the most favorable.

The configurations investigated on the 45° swept wing with the taper ratio of 0.2 are shown in figure 10. The chordwise center-of-gravity locations were the same as for the 60° delta wing but the spanwise positions were at 1/3, 2/3, and full semispan. The effect of the installation of the bodies on the flutter characteristics of the 45° sweptback wing is shown in figures 11 and 12 for Mach numbers of 1.3 and 2.0, respectively. The ordinate and abscissa are the same as for the delta wing. As in the case of the 60° delta wing, large increases in the dynamic pressure required for flutter are seen to be associated with most of the

[redacted]

body installations. The far-forward position of the center of gravity seems to cause the greatest increase in the dynamic pressure for flutter. The most favorable spanwise position would appear to be near the 2/3-semispan position, particularly at the higher Mach number. At first glance, this may appear to contradict the results obtained on the delta wing but on the delta wing the outermost position was only 3/4 semispan.

The improvements shown in figures 8, 9, 11, and 12 to accompany the installation of external bodies on the delta and sweptback wings indicate that the increase in the stiffness-altitude parameter noted in figure 1 for the plain wings at the higher Mach numbers may be alleviated by the considered location of an external body.

CONCLUDING REMARKS

The trends which have been presented emphasize the necessity for careful consideration of wing flutter boundaries at both transonic and supersonic speeds on any new high-speed aircraft. The use of mass balance would seem to hold promise as a means for lessening the wing flutter problem. Large external bodies need not cause severe penalties from the flutter point of view and, in fact, hold promise as a possible means for alleviating the flutter problem at both transonic and supersonic Mach numbers.

EFFECT OF MACH NUMBER

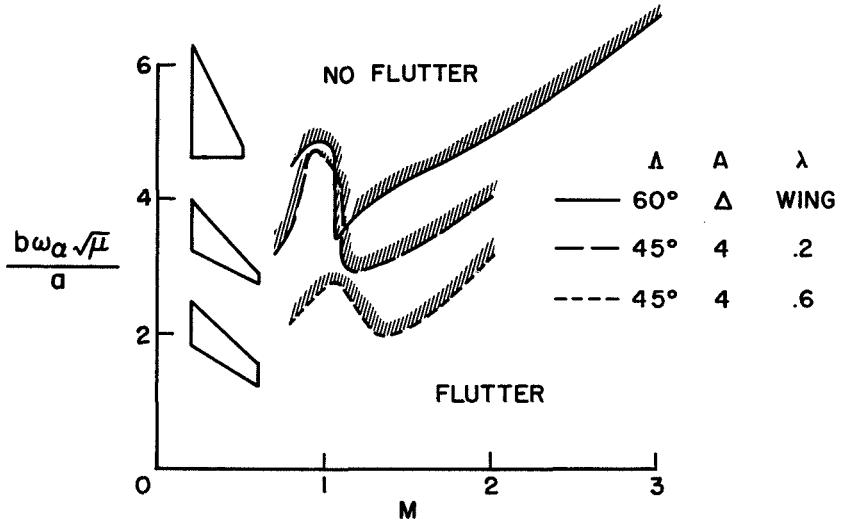


Figure 1

EFFECT OF MASS BALANCE
BALANCE MASS 6 AND 12 % OF WING MASS

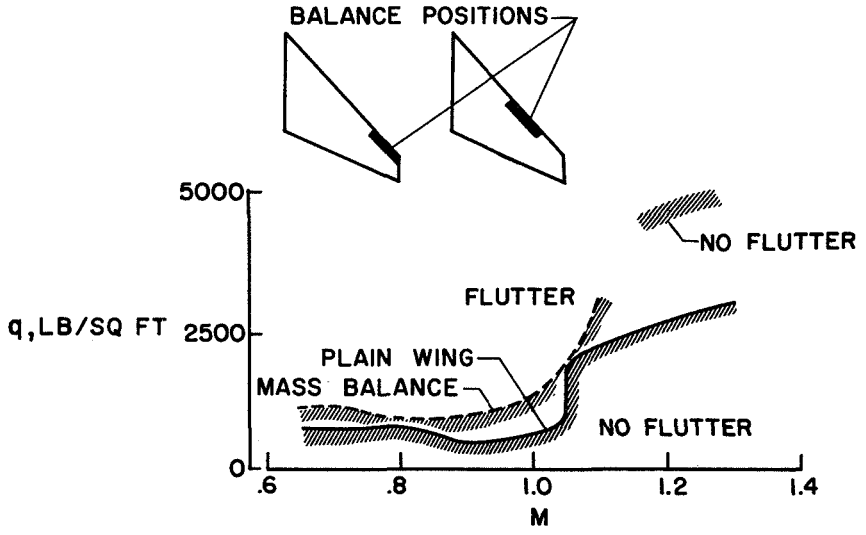


Figure 2

STORE CONFIGURATIONS

$\Lambda = 45°$; $A = 4.0$; $\lambda = 1.0$

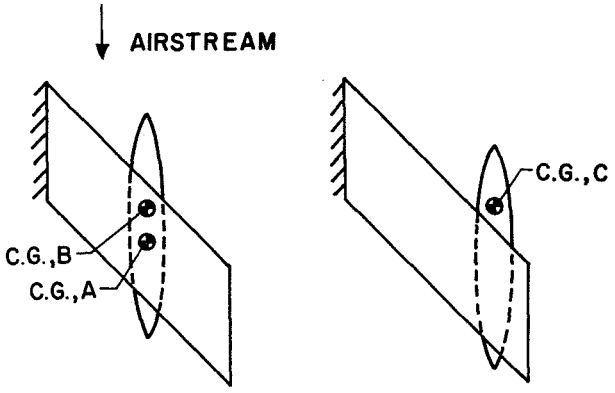


Figure 3

EFFECT OF STORES

$\Lambda = 45°$; $A = 4.0$; $\lambda = 1.0$

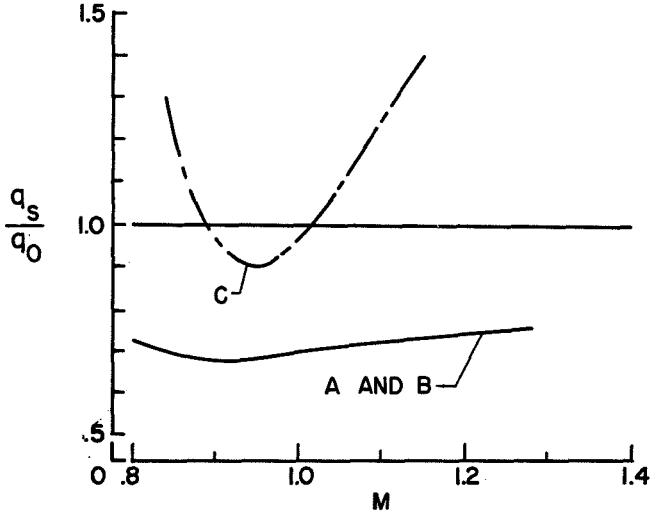


Figure 4

WING TORSIONAL NODE LINES

Λ=45°; A=4.0; λ=1.0

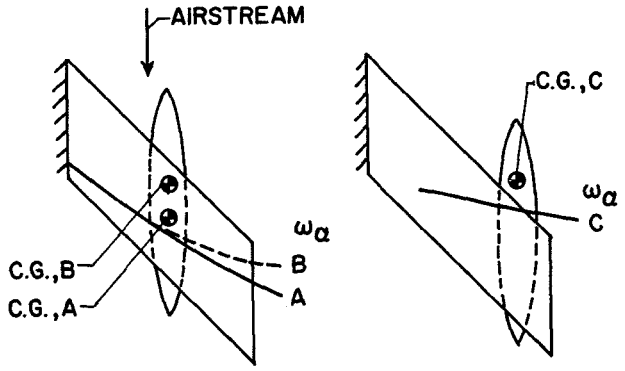


Figure 5

EFFECT OF STORE-MOUNT FLEXIBILITY
M=0.85

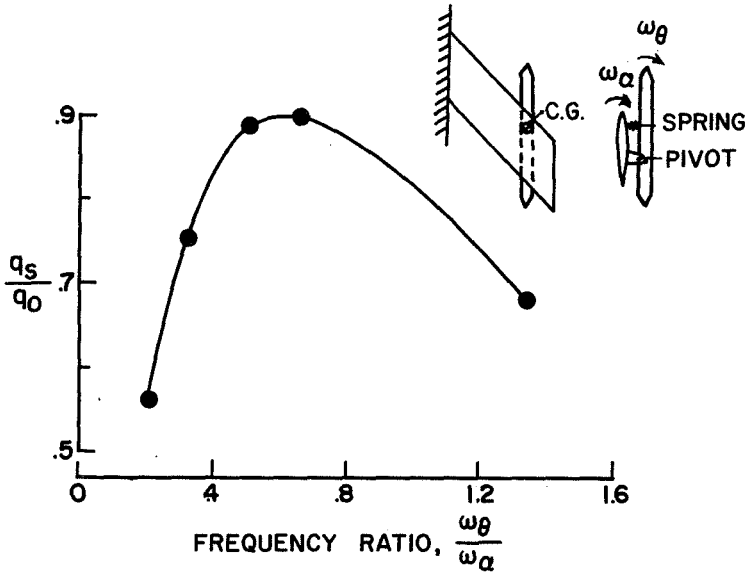


Figure 6

60° DELTA PLAN FORM SHOWING
C.G. LOCATION OF EXTERNAL BODIES

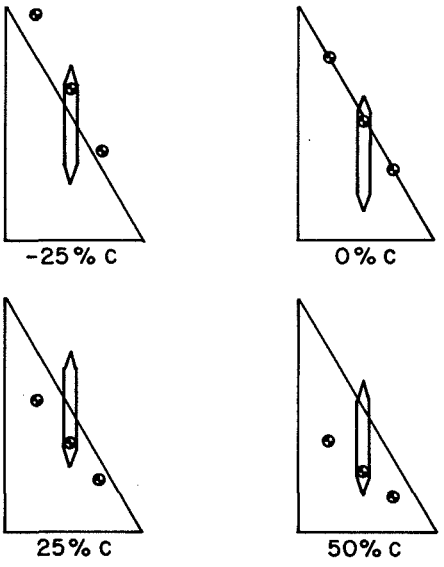


Figure 7

EFFECT OF C.G. SHIFT OF EXTERNAL BODIES
M=1.3 ; Λ=60°

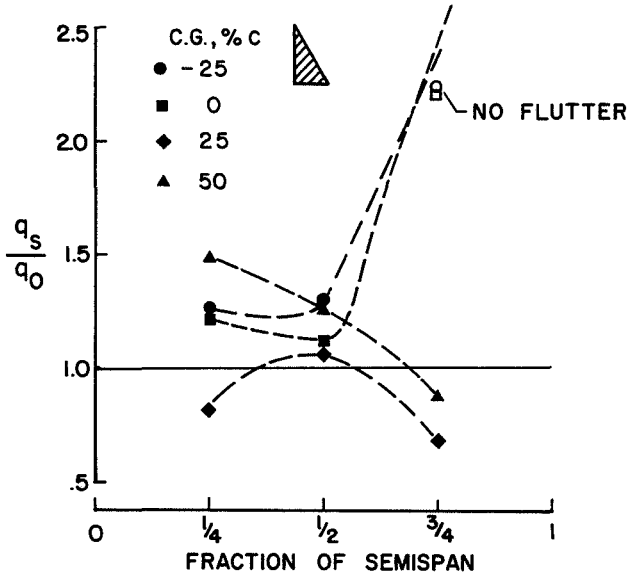


Figure 8

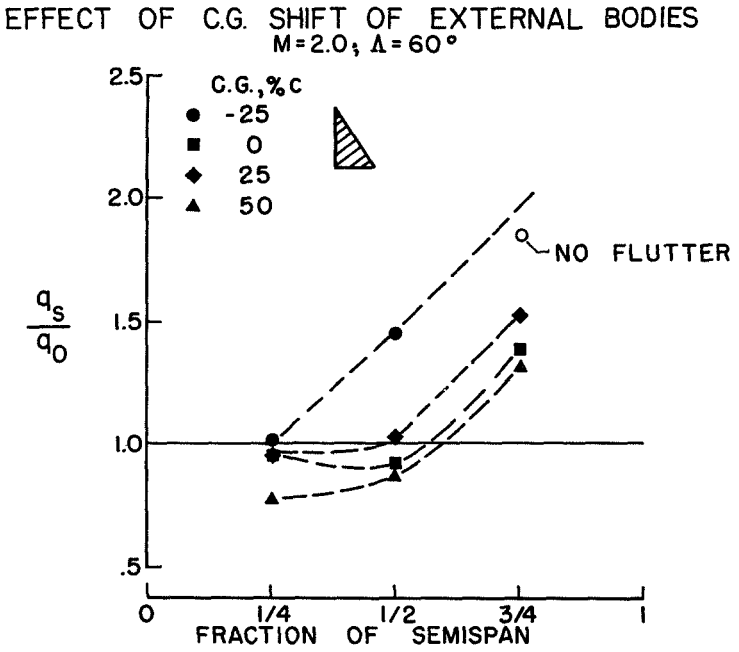
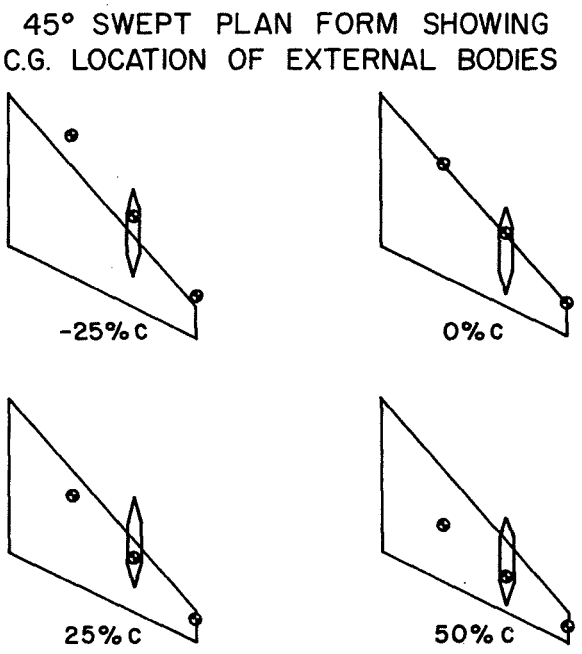


Figure 9



543

Figure 10

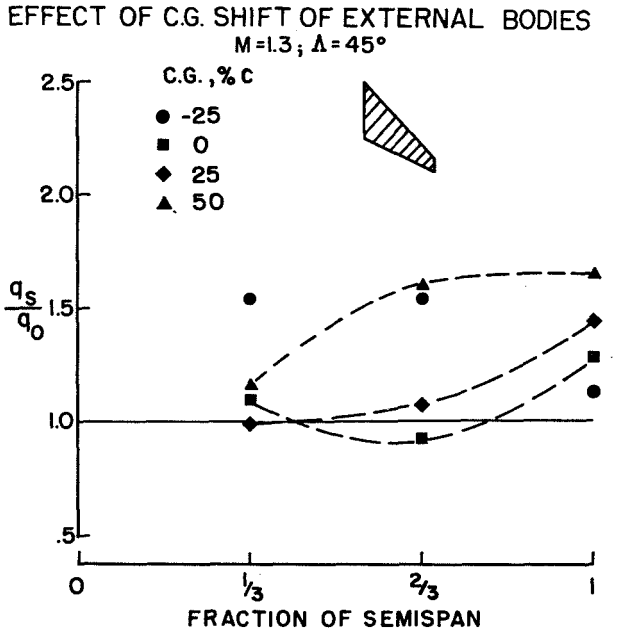


Figure 11

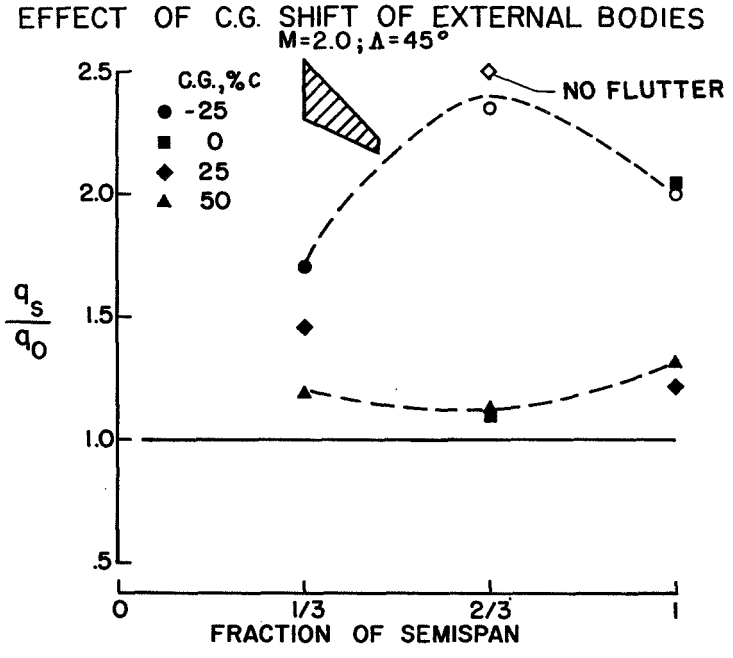


Figure 12

N71-75424

AERODYNAMICS OF OSCILLATING CONTROL SURFACES AT TRANSONIC SPEEDS

By Robert F. Thompson and Sherman A. Clevenson

Langley Aeronautical Laboratory

SUMMARY

Oscillating flap-type and all-movable controls are discussed with particular emphasis on the aerodynamic forces and moments at transonic speeds. Hinge-moment results from recent wind-tunnel and rocket-powered-model tests are summarized for trailing-edge flap-type controls to illustrate the effects of control hinge-line position and profile shape on one-degree-of-freedom flutter of this type of control. From a wind-tunnel investigation of a model considered representative of an all-movable control, the aerodynamic effects due to rigid-body-oscillation modes in roll and in pitch are presented.

The general magnitudes of the unstable aerodynamic damping moments for the flap-type controls tested are presented. No significant benefits toward alleviating the unstable aerodynamic damping in the control rotational mode at transonic speeds were obtained for a wide range of hinge-line positions tested. Of three control profile modifications tested, only a "wedge" modification to a 35-percent-overhang balanced control gave significant improvements in "buzz" stability. This wedge control gave stable aerodynamic damping in the control rotational mode up to the maximum speed tested. However, the stable damping and improvement in flutter characteristics were limited to oscillation amplitudes less than about 3°.

For an all-movable control, the oscillating aerodynamic derivatives which define the separate effects of rigid-body pitch and rigid-body roll have been presented through the transonic speed range. The aerodynamic damping for this low-aspect-ratio all-movable control was stable at all conditions tested.

INTRODUCTION

Oscillating aerodynamic forces and moments are needed in analyzing the dynamic or flutter characteristics of any airplane component. These aerodynamic values cannot be accurately computed for the mixed-flow

conditions at transonic speeds, and there is a current need for experimental data. The purpose of this paper is to summarize some recent tests on oscillating flap-type and all-movable controls, wherein the aerodynamic effects at transonic speeds have been measured. Flap-type controls are discussed first, and results pertain primarily to one-degree-of-freedon flutter or "buzz." Then, the aerodynamic effects due to rigid-body modes in pitch and in roll are presented for an all-movable control.

SYMBOLS

c_a	flap-type-control chord, distance from hinge line to trailing edge of control (see fig. 2), ft
c_b	flap-type-control balance chord, distance from hinge line forward to leading edge of control (see fig. 2), ft
c_r	root chord of all-movable control, ft
c_t	total control chord at midspan of control, $c_b + c_a$, ft
k_α	reduced frequency of all-movable-control pitch oscillation, $\frac{\omega c_r}{2V}$
k_δ	reduced frequency of flap-type-control oscillation, $\frac{\omega c_t}{2V}$
k_ϕ	reduced frequency of all-movable-control roll oscillation, $\frac{\omega c_r}{2V}$
M	free-stream Mach number
M'	area moment of flap-type-control area rearward of and about the hinge line, cu ft
q	free-stream dynamic pressure, lb/sq ft
S	semispan area of all-movable control, sq ft
V	free-stream velocity, ft/sec

C_h flap-type-control hinge-moment coefficient, $\frac{\text{Hinge moment}}{2M'q}$

C_L lift coefficient, $\frac{\text{Model lift}}{qS}$

C_l rolling-moment coefficient (fig. 7), $\frac{\text{Model rolling moment about roll axis}}{qS\frac{C_r}{2}}$

C_m pitching-moment coefficient (fig. 7), $\frac{\text{Model pitching moment about pitch axis}}{qS\frac{C_r}{2}}$

α amplitude of all-movable-control pitch oscillation, radians except as noted

δ amplitude of flap-type-control oscillation, measured in plane perpendicular to hinge line, radians except as noted

ϕ amplitude of all-movable-control roll oscillation, radians except as noted

ω angular frequency of oscillation, radians/sec

$C_{h_{\delta,\omega}}$, $C_{L_{\alpha,\omega}}$, $C_{m_{\alpha,\omega}}$, $C_{l_{\phi,\omega}}$ derivative with respect to δ, α, or ϕ as noted

$C_{h_{\dot{\delta},\omega}}$ derivative with respect to $\frac{\dot{\delta}c_t}{2V}$

$C_{L_{\dot{\alpha},\omega}}$, $C_{m_{\dot{\alpha},\omega}}$ derivative with respect to $\frac{\dot{\alpha}c_r}{2V}$

$C_{l_{\dot{\phi},\omega}}$ derivative with respect to $\frac{\dot{\phi}c_r}{2V}$

Subscript:

ω derivative obtained from an oscillation

DISCUSSION OF RESULTS

Flap-Type Controls

The aerodynamic hinge moment existing on the oscillating flap-type controls discussed herein is represented in complex notation by the relationship

$$\frac{\text{Resultant hinge moment}}{2M'q\delta} = C_{h_{\delta,\omega}} + ik_{\delta}C_{h_{\dot{\delta},\omega}}$$

where $C_{h_{\delta,\omega}}$ represents an aerodynamic spring-moment derivative proportional to the component of the total aerodynamic moment in phase with control position. The product $k_{\delta}C_{h_{\dot{\delta},\omega}}$ is an aerodynamic damping parameter, proportional to the component of the total aerodynamic moment in phase with control rotational velocity, and contributes the damping. The part $C_{h_{\dot{\delta},\omega}}$ represents an aerodynamic viscous-damping derivative.

Theoretical considerations.- Theoretical values for control aerodynamic damping are shown in figure 1. These two-dimensional-flow results were obtained from references 1 to 3 and are presented to provide a framework for evaluating the experimental flap-type-control data. Theoretical damping derivatives are plotted against Mach number for a 30-percent-chord flap-type control hinged at the leading edge. The dotted portion of the lines is an arbitrary fairing between the subsonic and supersonic theories, and the Mach number variation indicated is in general agreement with experiment. Theory shows the aerodynamic damping to be unstable for some values of reduced frequency at Mach numbers from about 0.9 to 1.5. In this region, control-surface flutter can occur unless sufficient nonaerodynamic damping is present in the control system to provide damping moments greater than the unstable aerodynamic moments. The subsonic and supersonic damping derivatives are fairly independent of Mach number and reduced frequency. However, large effects are indicated at transonic speeds, and the idealized theory indicates stable damping for reduced frequencies representing very high oscillating frequencies. Experimental damping results to date (refs. 4 to 11) have all been in the frequency range where theory indicates instability, and these experimental data show unstable damping in the control rotational mode at transonic speeds. The magnitudes indicated by test and theory are often in poor agreement, but this is not surprising considering the mixed-flow conditions which exist at transonic speeds and the possible influence from nonpotential sources. Based on these results, a fundamental approach in alleviating control-surface "buzz" would be to provide enough nonaerodynamic damping in the control system to overcome the unstable aerodynamic effects. This approach generally necessitates the addition of some type of artificial

damping to the control system, for example, the type provided by a hydraulic damper. This addition can often lead to mechanical complexities, especially when such factors as control free play are considered; and it would be desirable to stabilize the control aerodynamic damping by some change in geometric characteristics provided overall control efficiency can be maintained.

Control hinge position and profile shape are known to have large effects on static hinge moments, and some of their effects on dynamic hinge moments have recently been determined in the hope that stable control aerodynamic damping at transonic speeds can be achieved.

Effects of hinge position.- Studies of the effects of control hinge position and profile shape were made in the Langley high-speed 7- by 10-foot tunnel with the wing-control configuration shown in figure 2 (refs. 7 and 8). These tests were at a Reynolds number of about 2×10^6 based on the wing mean aerodynamic chord. Model plan form was held constant and the total control chord was 30 percent of the wing chord. The range of test conditions covered is indicated in figure 2. From figure 1 it can be seen that the test frequencies are in a range where two-dimensional-flow theory indicates unstable aerodynamic damping at transonic speeds for a 30-percent-chord control hinged at the leading edge. This paper first presents the effects of hinge-line position, as indicated by results for the three conventional control profiles shown in figure 2, and then summarizes the effects of the profile modifications indicated. The hinge line is located by the ratio of the balance chord c_b to the chord of the control rearward of the hinge line c_a, and 20-, 35-, and 100-percent-overhang balanced controls were tested.

In figure 3 the effects of hinge position on the control aerodynamic damping are summarized. These data are presented for a reduced frequency of 0.10 and an angle of attack of 0°; in general, the variations in angle of attack and reduced frequency covered in these tests had small effects on the control hinge-moment results. A free-oscillation test technique was used and the damping derivative is plotted against oscillation amplitude for representative test Mach numbers in figure 3(a) with the complete Mach number variation shown in figure 3(b) for low oscillation amplitudes. Positive values of $C_{h_{\dot{\delta},\omega}}$ indicate unstable aerodynamic damping. The flutter or buzz associated with the unstable damping shown for this model was a self-excited oscillation and built up in amplitude until the aerodynamic energy fed into the control system over a complete cycle was balanced by the energy dissipated due to structural and frictional damping. Steady-state flutter points for the test control system are indicated by the circular symbols in figure 3(a). The damping derivative for the 20- and 35-percent-overhang balanced controls at subsonic speed was stable and fairly constant to oscillation amplitudes of about 10°. Damping for the 100-percent-overhang balanced control was nonlinear with amplitude

at this speed and unstable at the higher oscillation amplitudes. In order to initiate the model flutter shown for this subsonic Mach number, it was necessary to displace initially the control to some intermediate amplitude and suddenly release it. This instability at a low Mach number is believed to be closely related to a stall-flutter type of phenomenon. Increasing the Mach number into the transonic speed range caused the control aerodynamic damping to become unstable for all hinge positions tested. For the 100-percent-overhang balanced control there was first a large stable increase in damping with increasing Mach number before the damping became unstable. Model flutter at these transonic speeds was initiated by random tunnel disturbances, and the flutter amplitude was markedly decreased at sonic speed with the hinge located at the control midchord. The damping at transonic speeds was nonlinear with amplitude for all hinge positions and indicated the influence of nonpotential effects which restrict the application of any potential theory.

Shown in figure 4 are recent control aerodynamic damping results obtained from a free-flight rocket-powered-model test by the Langley Pilotless Aircraft Research Division. These data were obtained by a free-oscillation test technique similar to that described in reference 10. Test Reynolds number, based on the wing mean aerodynamic chord, varied from 2×10^6 to 13×10^6. The delta-wing configuration is illustrated and the trailing-edge flap-type control was hinged slightly rearward of the control midchord. The experimental damping derivative evaluated for an oscillation amplitude of 1.8° is shown for Mach numbers from about 0.5 to 1.9, and the test reduced frequency varied as indicated through the Mach number range. For this midchord hinge position, there was a large increase in stable damping at high subsonic speeds and unstable aerodynamic damping in the transonic Mach number region, with the damping again becoming stable at the higher test supersonic speeds. These aerodynamic damping trends with Mach number, measured in free flight, are in agreement with the theoretical and wind-tunnel results presented. Based on the data shown in figures 3 and 4, reasonable hinge positions do not offer much promise in alleviating the unstable damping in the control rotational mode at transonic speeds.

The effects of hinge position and Mach number on the control in phase or stiffness derivative for the wind-tunnel model are presented in figure 5. Derivatives obtained from dynamic and static tests are compared to illustrate the effects of oscillating the control. Positive values of this derivative indicate overbalanced or statically unstable hinge moments. The balancing effect of shifting the hinge line rearward is shown, and the midchord hinge position overbalances the control throughout the speed range tested. The oscillating spring moments are approximately equal to the static values for the 20- and 35-percent-overhang balanced controls, and the differences shown for the 100-percent-overhang

balanced control can be attributed to the larger deflection range over which it was necessary to evaluate the stiffness derivative for the dynamic tests. This agreement indicates that, for a wide range of hinge positions, static hinge moments can be used to predict accurately the frequency of control buzz.

Effects of profile shape.- The profile modifications studied in the wind-tunnel investigation are illustrated in figure 2. For the 20-percent-overhang balanced control the thickness at the trailing edge was made equal to the hinge-line thickness, and the portion of the control forward of the hinge was not altered. Results for the oscillating hinge moments for this control were similar to the results for the original profile with the aerodynamic damping still unstable at transonic speeds. This modification caused a slight beneficial shift in the level of unstable damping and an increase in the aerodynamic spring stiffness; however, the flutter characteristics of the model were not appreciably improved. (See ref. 7.)

On the 35-percent-overhang balanced control two profile changes were made. For the lower modification shown, the rear half of the conventional control chord was replaced by a thin "splitter" plate over essentially the full span of the control. This control was similar to some controls tested in a flight investigation by North American Aviation, Inc. (For example, see ref. 12.) In the present tunnel tests, the oscillating hinge-moment and flutter results measured for this splitter-plate control did not show any significant differences relative to the original profile, and the aerodynamic damping indicated about the same level of instability at Mach numbers from about 0.92 to 1.01, the maximum speed tested. In reference 12 a trailing-edge splitter plate combined with a slight thickening of the forward portion of the control has given qualitative indication of improved buzz stability. Direct comparison of the model and flight results is not feasible since the aerodynamic damping was not measured in flight, and there are appreciable geometric differences between the configurations.

The "wedge" modification to the 35-percent-overhang balanced control did give some beneficial effects on control damping. The trailing-edge thickness was a little more than twice the thickness tested on the modified 20-percent-overhang balanced control. The leading and trailing edges were connected by a straight line which resulted in an increase in the hinge-line thickness relative to the original profile. Damping results for the wedge control are shown in figure 6 and are compared with the damping of the conventional profile. The aerodynamic damping of the wedge control was stable at low oscillation amplitudes for the complete-test speed range. However, at transonic speeds, stability is confined to oscillation amplitudes less than about 3°. Damping for the wedge control is unstable for amplitudes greater than about 3°; if the

model wedge control is manually displaced to these unstable amplitudes and released, it would flutter with characteristics very similar to those in the response of the conventional control.

All-Movable Control

The model used to measure some oscillating aerodynamic derivatives at transonic speeds for conditions of particular application to all-movable controls is shown in figure 7. These tests were made in the Langley 2- by 2-foot transonic flutter research tunnel at Reynolds numbers, based on the control mean aerodynamic chord, from 1.4×10^6 to 3.6×10^6. The rigid-body degrees of freedom in pitch and roll to be considered are illustrated. The pitch axis passes through the midchord at the root and the leading edge at the tip. The roll axis was arbitrarily chosen inboard of the model root, and the pitch and roll motion together with the angles describing the modes are illustrated. Nomenclature similar to that used in discussing the flap-type controls is also used for this all-movable control with the resultant aerodynamic forces and moments reduced to derivatives that are either in or out of phase with the motion. The aerodynamic forces and moments existing on the oscillating model are represented in complex notation for pitching motion as

$$\frac{\text{Resultant lift}}{qS\alpha} = C_{L_{\alpha,\omega}} + ik_\alpha C_{L_{\dot{\alpha},\omega}}$$

$$\frac{\text{Resultant pitching moment}}{qS\frac{c_r}{2}\alpha} = C_{m_{\alpha,\omega}} + ik_\alpha C_{m_{\dot{\alpha},\omega}}$$

and for rolling motion as

$$\frac{\text{Resultant rolling moment}}{qS\frac{c_r}{2}\phi} = C_{l_{\phi,\omega}} + ik_\phi C_{l_{\dot{\phi},\omega}}$$

Lift and pitching-moment derivatives are presented for the pitching motion, and the damping due to roll is shown for the rolling oscillation. These experimental data have not yet been compared with existing three-dimensional-flow theory (refs. 13 and 14).

Lift components due to pitch oscillation of the model are shown in figure 8, and these data were evaluated for a forced-oscillation amplitude of about 3° to each side of 0° angle of attack. The lift in phase with the motion is shown on the left and the out-of-phase component is shown on the right. Data were measured for a Mach number range from 0.6 to 1.2, and the curves represent values for various reduced frequencies.

For a constant reduced frequency, the in-phase derivative increases with Mach numbers from 0.6 to 1.0 and decreases with Mach numbers from 1.0 to 1.2. The out-of-phase derivative decreases with increasing Mach numbers from 0.6 to 1.0 and changes sign from positive to negative near a Mach number of 1.0. Increasing the reduced frequency decreases the in-phase component of the total lift at all test speeds and causes a positive increment in the magnitude of the out-of-phase component. Although it is not presented herein, experimental data have shown that the rolling moments due to pitch oscillation follow the same trends as those shown herein for the lift.

In figure 9 the pitch-damping parameter due to pitch oscillation of the control is plotted as a function of reduced frequency and Mach number. These aerodynamic data were evaluated from the free-oscillation response of the control following removal of the forcing function at an oscillation amplitude of about 3°. For additional information on the test technique used, see references 15 and 16. The aerodynamic viscous-damping derivative was essentially linear for amplitudes from 0° to 3°. The damping moments were stable throughout the complete Mach number range from 0.6 to 1.2, and there was a tendency for the damping parameter to become more stable up to $M \approx 1.0$ and then decrease. The damping increased as the reduced frequency was increased. For conditions roughly approximating those of the present tests, two-dimensional-flow theory (refs. 2 and 3) indicates unstable values for this parameter at transonic speeds. However, three-dimensional-flow theory (refs. 13 and 14) indicates a rather large stabilizing effect at these speeds due to aspect ratio; therefore, these experimental results showing stable damping appear to be in reasonable agreement with existing theory.

Figure 10 shows the roll-damping parameter due to roll oscillation of the control as a function of reduced frequency and Mach number. These data were evaluated from the free-oscillation response of the control following roll oscillations up to amplitudes ϕ of about 3°. The roll-damping moments were stable throughout the speed range tested, and the damping tends to become more stable as the test Mach number is increased. Increasing the reduced frequency also increases the stable damping-in-roll parameter.

CONCLUDING REMARKS

The aerodynamic forces and moments acting on oscillating flap-type and all-movable control surfaces at transonic speeds have been summarized. The discussion on flap-type controls has briefly reviewed what could be considered the fundamental approach in alleviating one-degree-of-freedom flutter of this type of control, namely, incorporating sufficient non-aerodynamic damping in the control system to overcome the unstable

aerodynamic moments. Experimental results were presented which establish the general magnitude of the unstable aerodynamic moments for the test models. However, it is desirable to have a control configuration with inherent aerodynamic stability; therefore, the aerodynamic effects of control hinge-line position and some profile modifications were studied. Based on these results, no significant benefits in control aerodynamic damping were obtained for a wide range of hinge positions. Of three control profile modifications tested, only a "wedge" modification to a 35-percent-overhang balanced control gave significant improvements in "buzz" stability. This wedge control gave stable aerodynamic damping in the control rotational mode up to the maximum speed tested. However, the stable damping and improvement in flutter characteristics were limited to oscillation amplitudes less than about 3°.

For an all-movable control, the oscillating aerodynamic derivatives which define the separate effects of rigid-body pitch and rigid-body roll have been presented through the transonic speed range. The aerodynamic damping for this all-movable control was stable at all conditions tested.

REFERENCES

1. Anon.: Tables of Aerodynamic Coefficients for an Oscillating Wing-Flap System in a Subsonic Compressible Flow. Rep. F.151, Nationaal Luchtvaartlaboratorium, Amsterdam, May 1954.

2. Nelson, Herbert C., and Berman, Julian H.: Calculations on the Forces and Moments for an Oscillating Wing-Aileron Combination in Two-Dimensional Potential Flow at Sonic Speed. NACA Rep. 1128, 1953. (Supersedes NACA TN 2590.)

3. Garrick, I. E., and Rubinow, S. I.: Flutter and Oscillating Air-Force Calculations for an Airfoil in a Two-Dimensional Supersonic Flow. NACA Rep. 846, 1946. (Supersedes NACA TN 1158.)

4. Reese, David E., Jr.: An Experimental Investigation at Subsonic and Supersonic Speeds of the Torsional Damping Characteristics of a Constant-Chord Control Surface of an Aspect Ratio 2 Triangular Wing. NACA RM A53D27, 1953.

5. Martin, Dennis J., Thompson, Robert F., and Martz, C. William: Exploratory Investigation of the Moments on Oscillating Control Surfaces at Transonic Speeds. NACA RM L55E31b, 1955.

6. Reese, David E., Jr., and Carlson, William C. A.: An Experimental Investigation of the Hinge-Moment Characteristics of a Constant-Chord Control Surface Oscillating at High Frequency. NACA RM A55J24, 1955.

7. Thompson, Robert F., and Moseley, William C., Jr.: Oscillating Hinge Moments and Flutter Characteristics of a Flap-Type Control Surface on a 4-Percent-Thick Unswept Wing With Low Aspect Ratio at Transonic Speeds. NACA RM L55K17, 1956.

8. Thompson, Robert F., and Moseley, William C., Jr.: Effect of Hinge-Line Position on the Oscillating Hinge Moments and Flutter Characteristics of a Flap-Type Control at Transonic Speeds. NACA RM L57C11, 1957. (NACA prospective paper.)

9. Tuovila, W. J., and Hess, Robert W.: Aerodynamic Damping at Mach Numbers of 1.3 and 1.6 of a Control Surface on a Two-Dimensional Wing by the Free-Oscillation Method. NACA RM L56A26a, 1956.

10. Martz, C. William: Experimental Hinge Moments on Freely Oscillating Flap-Type Control Surfaces. NACA RM L56G20, 1956.

11. Clevenson, Sherman A.: Some Wind-Tunnel Experiments on Single-Degree-of-Freedom Flutter of Ailerons in the High Subsonic Speed Range. NACA TN 3687, 1956. (Supersedes NACA RM L9B08.)

12. Anon.: Flight Test Progress Report No. 23 for Period Ending 7 October 1955 for Model FJ-4 Airplanes. Rep. No. NA 54H-374-23 (Contract NOa(s)54-323), North American Aviation, Inc., Oct. 20, 1955.

13. Nelson, Herbert C., Rainey, Ruby A., and Watkins, Charles E.: Lift and Moment Coefficients Expanded to the Seventh Power of Frequency for Oscillating Rectangular Wings in Supersonic Flow and Applied to a Specific Flutter Problem. NACA TN 3076, 1954.

14. Runyan, Harry L., and Woolston, Donald S.: Method for Calculating the Aerodynamic Loading on an Oscillating Finite Wing in Subsonic and Sonic Flow. NACA TN 3694, 1956.

15. Clevenson, Sherman A., and Widmayer, Edward, Jr.: Experimental Measurements of Forces and Moments on a Two-Dimensional Oscillating Wing At Subsonic Speeds. NACA TN 3686, 1956. (Supersedes NACA RM L9K28a.)

16. Widmayer, Edward, Jr., Clevenson, Sherman A., and Leadbetter, Sumner A.: Some Measurements of Aerodynamic Forces and Moments at Subsonic Speeds on a Rectangular Wing of Aspect Ratio 2 Oscillating About the Midchord. NACA RM L53F19, 1953.

THEORETICAL CONTROL DAMPING
TWO-DIMENSIONAL THEORY

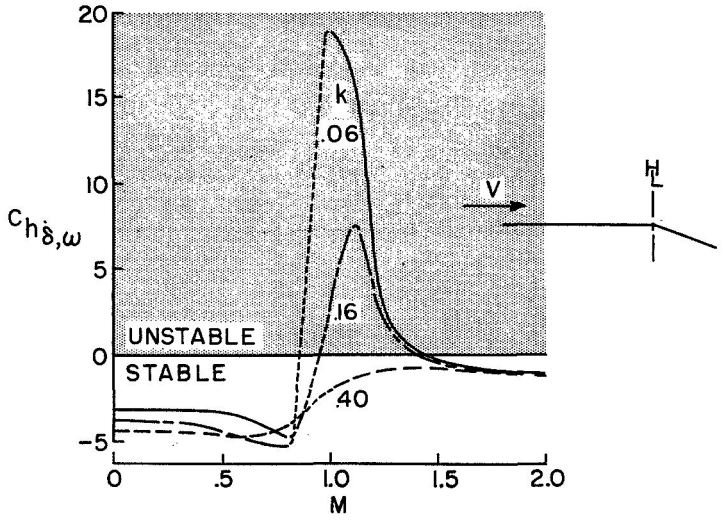
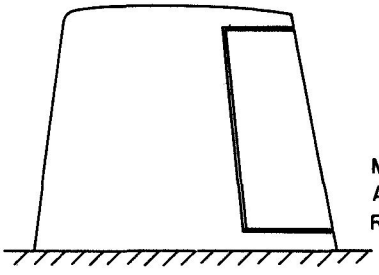


Figure 1

FLAP-TYPE CONTROL MODEL
WIND-TUNNEL TESTS



MODEL PARAMETERS

ASPECT RATIO 1.8
TAPER RATIO 0.74
NACA 64A004

SCOPE OF TESTS

M	0.6 TO 1.01
ANGLE OF ATTACK	0° AND 6°
REDUCED FREQUENCY	0.06 TO 0.13

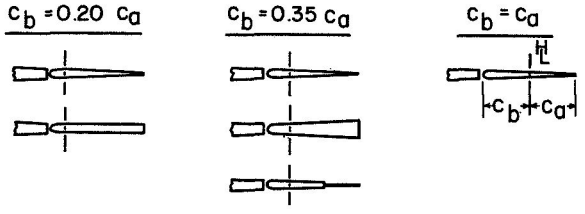


Figure 2

EFFECT OF HINGE POSITION ON CONTROL DAMPING

k=0.10 ; α=0°

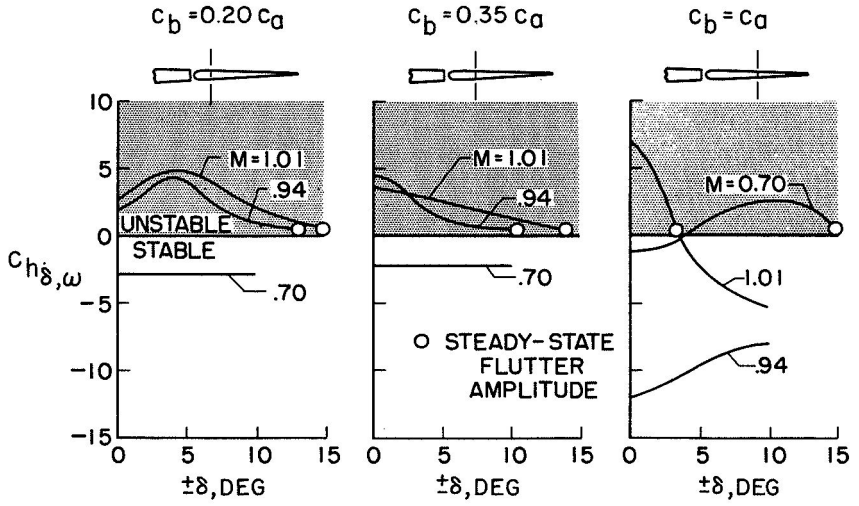


Figure 3(a)

EFFECT OF HINGE POSITION ON CONTROL DAMPING

k=0.10; α=0°; δ≈0°

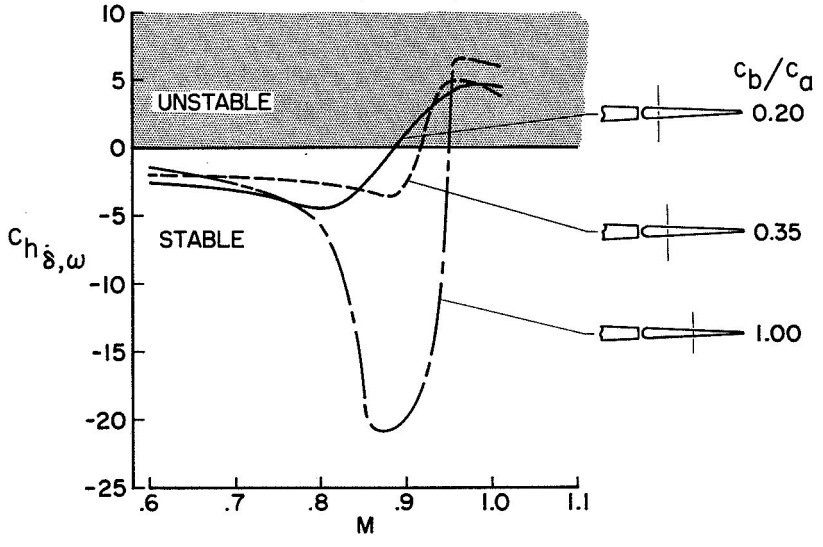


Figure 3(b)

EFFECT OF MACH NUMBER ON CONTROL DAMPING

ROCKET-MODEL TEST ; $\delta = \pm 1.8°$; $\alpha = 0°$

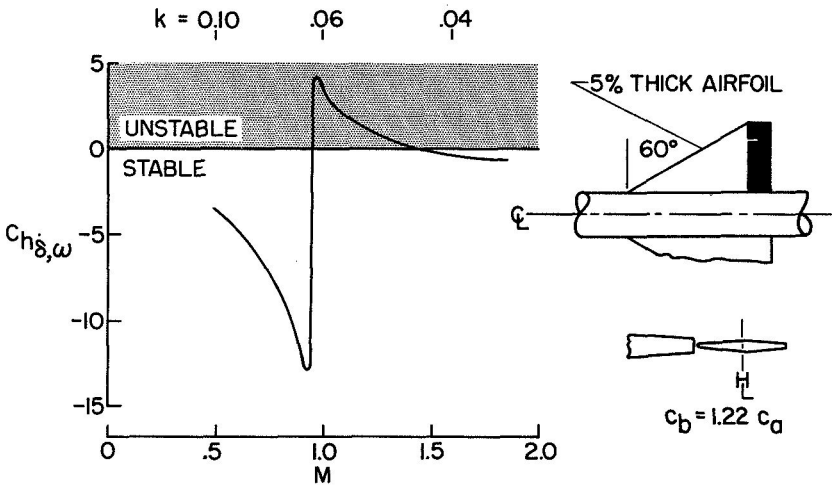


Figure 4

EFFECT OF HINGE POSITION ON CONTROL STIFFNESS

$k = 0.10, \alpha = 0°$

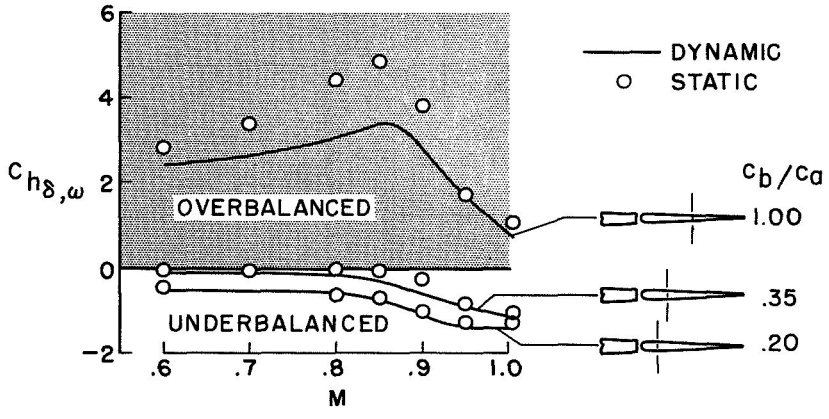


Figure 5

EFFECT OF WEDGE PROFILE ON CONTROL DAMPING

k=0.10 ; α=0°

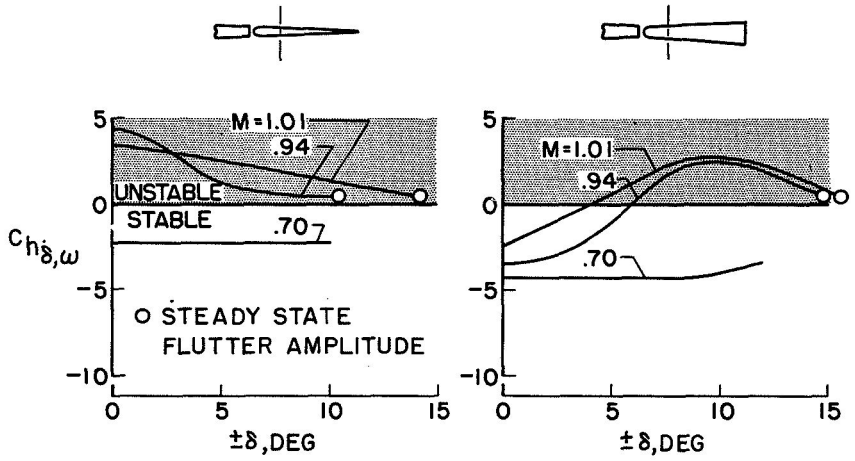
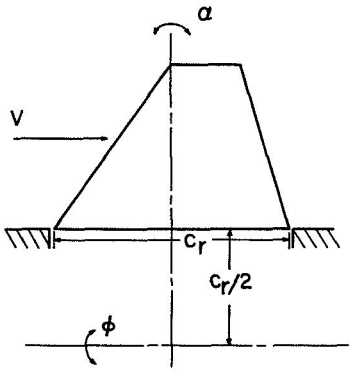


Figure 6

ALL-MOVABLE CONTROL SURFACE

RIGID-BODY DEGREES OF FREEDOM

PANEL ASPECT RATIO = 1.25
TAPER RATIO = 0.283
NACA 65A005



560

Figure 7

EFFECT OF MACH NUMBER ON LIFT COMPONENTS DUE TO PITCH OSCILLATION

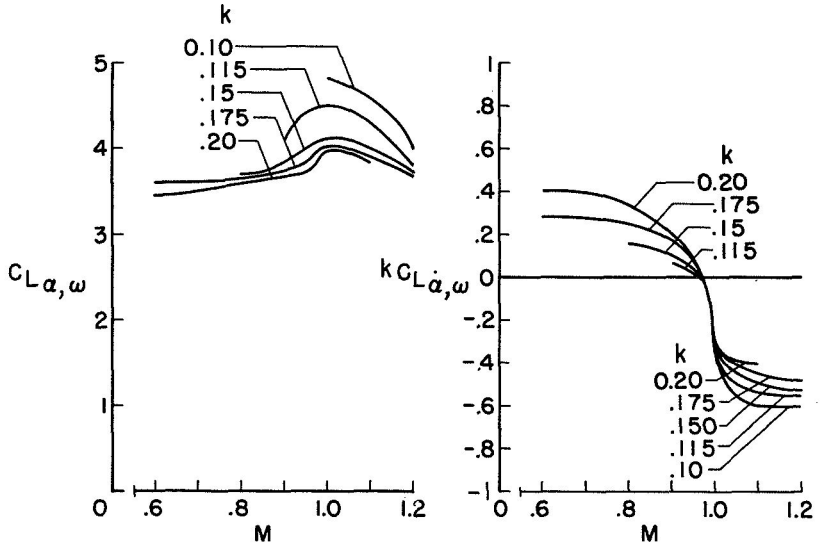


Figure 8

EFFECT OF MACH NUMBER ON PITCH-DAMPING COMPONENT DUE TO PITCH OSCILLATION

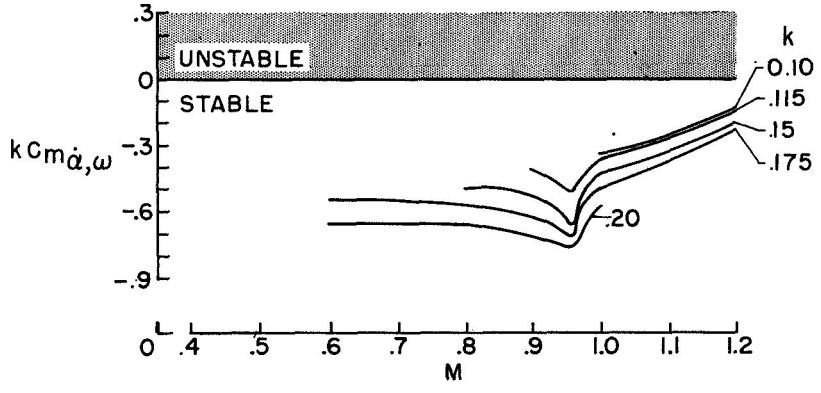


Figure 9

EFFECT OF MACH NUMBER ON ROLL-DAMPING COMPONENT DUE TO ROLL OSCILLATION

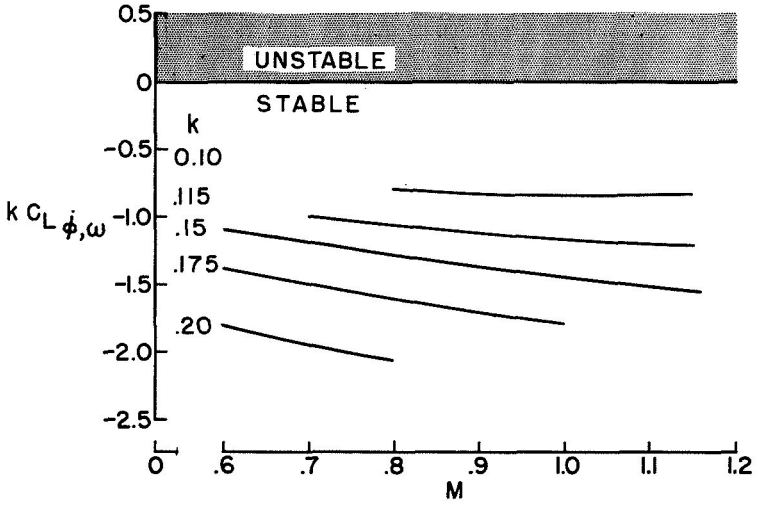


Figure 10

N71-75425

STATUS OF FLUTTER OF FLAT AND CURVED PANELS

By Robert W. Leonard and John M. Hedgepeth

Langley Aeronautical Laboratory

SUMMARY

Representative results are presented to show the current status of the panel flutter problem. The discussion includes flat panels with and without midplane stresses, buckled panels, and both unstiffened and stiffened infinitely long circular cylinders.

INTRODUCTION

The flutter of the skin panels of supersonic airplanes and missiles has aroused considerable interest in recent years. Numerous investigations (refs. 1 to 27) have determined that panel flutter may govern the design of at least very thin panels such as those used in fairings and in radiation shielding. Representative results of some of these investigations, which tend to illustrate the current status of the problem, are presented in this report. The discussion is divided roughly into three parts: First, the flutter of flat panels; second, the flutter of panels stressed beyond the buckling load; and third, the flutter of thin-walled circular cylinders.

SYMBOLS

$$A_p = \frac{P_x a^2}{D} + 2\left(\frac{a}{b}\right)^2 I_{pp}^{(2)}$$

a panel dimension in chordwise direction

$$B_p = \left(\frac{a}{b}\right)^2 I_{pp}^{(2)} \left[\frac{P_y a^2}{D} + \left(\frac{a}{b}\right)^2 \frac{I_{pp}^{(4)}}{I_{pp}^{(2)}}\right]$$

b panel dimension in spanwise direction

D panel stiffness, $\frac{Et^3}{12\left(1 - \mu^2\right)}$

E Young's modulus

$$I_{mj}^{(i)} = \int_0^1 \phi_m(\xi)\frac{d^i}{d\xi^i}\left[\phi_j(\xi)\right]d\xi$$

i,j,m,p integers

M Mach number

n integer, number of circumferential waves around the cylinder

P_x chordwise midplane load per unit spanwise length

P_y spanwise midplane load per unit chordwise length

q dynamic pressure

$R = \frac{P_y}{P_x}$

r cylinder radius

t thickness

w panel deflection

x chordwise coordinate

y spanwise coordinate

λ dynamic-pressure parameter, $\frac{2qa^3}{\sqrt{M^2 - 1}\,D}$

μ Poisson's ratio (taken equal to 1/3 throughout)

$\phi_m(\xi)$ mth mode of uniform clamped-clamped beam of unit length

ξ dimensionless coordinate

$$\nabla^4 = \frac{\partial^4}{\partial x^4} + 2\frac{\partial^4}{\partial x^2 \partial y^2} + \frac{\partial^4}{\partial y^4}$$

[redacted]

FLAT PANELS

Up to the present time, the largest research effort has been devoted to theoretical study of flat panels. Typical analytical results for flat panels are shown in figures 1 and 2.

The results in figure 1 apply to panels of infinite aspect ratio, that is, panels which extend to infinity in the spanwise direction and, hence, behave structurally like a beam. Figure 2 contains results for a panel with finite aspect ratio. Both plots give the panel thickness ratio t/a necessary to prevent flutter, at various Mach numbers, of steel panels at sea level. The results are restricted to panels which are unstressed; that is, they have no midplane tension or compression.

In both figure 1 and figure 2, the dashed curves at low supersonic Mach numbers are two-mode results based on the use of unsteady linearized air forces. (See refs. 8, 10, and 20.) The solid curves at high Mach numbers are two-mode results obtained by using much simpler "static" air forces in which no account is taken of unsteady effects. (See refs. 22 and 26.) Experience has shown that, for the high Mach numbers, the static approximation yields results in close agreement with those yielded by more refined theories. The smooth merging of the dashed and solid lines for each configuration illustrates this close agreement.

In figure 1, curves are shown for three different configurations: an array of panels continuous over equally spaced supports, a single panel with pinned ends, and a single panel with clamped ends. The general effect of panel boundary conditions may be seen from the relative positions of the curves at high Mach numbers. The most critical configuration, requiring thicker panels to prevent flutter, is the array of panels on equally spaced supports.

The effect of aspect ratio on required panel thickness is shown in figure 2. In this case, both curves are for a single panel with pinned edges. The upper curve applies to an infinite span panel and is the same as the middle curve of figure 1. The lower curve applies to a square panel. As would be expected, reducing the aspect ratio from infinity to one reduces the required thickness.

It should be pointed out that the moderate reduction in thickness ratio at high Mach numbers is due primarily to the structural effects of aspect ratio. (See ref. 26.) The aerodynamic effect is less than 2 percent throughout the range of the solid curves. Thus, the use of aerodynamic strip theory would give accurate boundaries for the square plate for these high Mach numbers.

[redacted]

The situation is apparently different for the low Mach numbers. In addition to the moderate structural effect, there is now a large aerodynamic effect of aspect ratio and a resulting large reduction in thickness in changing from the infinite-aspect-ratio panel to the square panel. It is interesting to note that, although the low supersonic Mach number range appears to be critical for infinite-aspect-ratio panels, this may not be the case for the simply supported square panel for which the results show a steady increase in thickness with increase of Mach number.

It should be pointed out that the dashed curves at the low Mach numbers in figures 1 and 2 are based on a rather limited number of calculations and this region has not yet been carefully explored. It is known, however, that structural damping is fairly effective in reducing the large thicknesses required for infinite-aspect-ratio panels. (See ref. 10.)

It is also worthwhile to note that a small amount of experimental data has been reported at Mach numbers of 1.3 and 1.56 for clamped panels which behave like the infinite-aspect-ratio panel. (See refs. 6 and 13.) The data are not shown in figure 1 because they apply to a different altitude and material. When compared with calculations made on the same basis, experiment and theory agree at Mach number 1.56. At Mach number 1.3, the data show an increase of thickness but not the large increase predicted by the theory. The difference may be due in part to structural damping.

So far, only panels with no midplane stress have been considered. However, the effect of midplane tension or compression stresses on the required thickness of flat panels has been investigated and is found to be important (ref. 26). This effect is illustrated by the results shown in figure 3.

Figure 3 is a plot of a modified-thickness-ratio parameter $\left(\sqrt{M^2 - 1}\,\frac{E}{q}\right)^{1/3}\frac{t}{a}$, containing both panel and air properties, against a chordwise compression parameter $\frac{P_x}{(\text{Buckling } P_x)_{P_y=0}}$. The coefficient of the thickness ratio contains the Mach number M, Young's modulus E, and the dynamic pressure q and allows the application of the plotted results to all Mach numbers above about 1.5. The compression parameter, which specifies stress in the chordwise direction, is the ratio of chordwise compression P_x to the buckling value of chordwise stress which corresponds to zero stress in the spanwise direction. Positive values of this parameter indicate chordwise compression and negative values imply tension. Curves are shown for two pinned-edge panels with aspect ratios of 0.5 and 1.

It must be remembered that the calculations apply to flat panels only. Hence, the curves in figure 3 are valid only up to the chordwise load which results in buckling. If the midplane stress in the spanwise direction is zero, the curves are therefore valid, by definition, only up to the compression parameter equal to one. If tension is applied to the panel in the spanwise direction, the chordwise load necessary to cause buckling is raised; the curves would then be valid to a higher value of the compression parameter. Spanwise compression would have the opposite effect. It should be noted that this is the only influence of spanwise stress on the flutter boundaries of flat panels. (See ref. 26.)

The influence of chordwise stress is shown by the variation of the curves themselves. Note especially that, for each aspect ratio, there is a critical value of chordwise compression for which the theory requires very large thicknesses to prevent flutter. In real panels, the required thickness in this range is dependent on the amount of structural damping. However, it is apparent that these critical combinations of aspect ratio and chordwise compression should be avoided in design.

The mode shapes of flutter of flat panels have an interesting feature that is illustrated in figure 4. Calculated chordwise variations of typical flutter-mode shapes are shown for panels with both pinned and clamped edges. The air flow is from left to right. Note that the motion is concentrated toward the rear of the panel for both panels. This "tail-wagging" type of motion is characteristic of the observed motion in actual instances of panel flutter.

BUCKLED PANELS

Consideration will now be given to the flutter of panels which have been buckled by heating or by the application of midplane loads. Buckled panels have been treated in a number of theoretical investigations, most of which are confined to panels of infinite aspect ratio. (See refs. 1, 2, 3, 9, 11, 23, and 26.) In addition, a few experimental studies have been made. (See refs. 13, 16, and 23.)

The effect of buckling may be seen from the results in figure 5. The required thickness ratio t/a is plotted against Mach number for steel panels of infinite span in air at sea level. Curves are shown at high Mach numbers for both pinned and clamped panels. The upper pair of curves (fig. 5) are calculated boundaries which apply to buckled panels of infinite span without regard to buckle depth. They result from closed-form solutions based on the so-called "transtability" concept. (See ref. 1.) The lower pair of curves (fig. 5) are the corresponding results for flat panels. Note that the buckled panels require much larger thicknesses to prevent flutter than do the unbuckled panels.

Experimental results for clamped buckled panels are also shown in figure 5. With the exception of the point at M = 2.18, these results were taken from reference 16. (They have been corrected to apply to steel at sea level.) The point at M = 2.18, which was obtained independently (ref. 23), appears to confirm the other experimental results. The dashed theoretical curve for clamped buckled panels differs on the conservative side by about 12 percent.

In references 13 and 16, some experimental results were presented for a group of clamped rectangular panels buckled by heating. These results are repeated in figure 6.

Figure 6 is constructed with modified-thickness-ratio parameters for both the ordinate and abscissa. One thickness ratio is based on the chord and the other, on the span. The data are applicable to all Mach numbers greater than about 1.3. The construction of the plot is such that data for panels of a given aspect ratio fall on a radial line from the origin. The aspect ratios and orientation of the test panels are shown by the small figures at the outer ends of the radial lines. In each case, node lines are shown to illustrate the observed buckle patterns. The distance outward from the origin of the plot is a measure of the panel thickness. Solid points designate panels that fluttered and open points indicate that no flutter was observed.

An attempt has been made to calculate a theoretical flutter boundary for this particular group of panels buckled by heating. Because the midplane stresses in the test panels had not been measured, it was necessary to estimate these stresses from the observed buckle patterns. Some details of this calculation are given in the appendix. The solid curve is the resulting approximate boundary. The curve has been shown dashed on the lower right because the calculation is a two-mode approximation which must be considered unreliable for the very low-aspect-ratio panels.

The agreement in figure 6 between the theoretical boundary and the experimental data encourages the viewpoint that successful analyses of rectangular buckled panels are possible. Of particular interest is the finding that, as in the case of flat rectangular panels, there are critical combinations of aspect ratio and stress for which even thick panels can flutter. One such critical point occurs in the calculated boundary near an aspect ratio of 0.5. Perhaps this explains why the test panels with an aspect ratio of 0.5 were more prone to flutter than the other test panels were.

It must be pointed out that the theoretical boundary is very sensitive to the type of buckling load, especially for aspect ratios between 0.5 and 2. Consequently, this boundary applies only to the particular series of tests shown. It should be emphasized that this boundary is not intended to be a universal flutter boundary for finite-aspect-ratio buckled panels. In fact, no such universal boundary exists.

CIRCULAR CYLINDERS

One other configuration which has received some preliminary attention is the infinitely long thin-walled circular cylinder with axial flow over its outer surface. (See refs. 14, 21, and 27.) Typical results, for empty steel cylinders, are shown in figure 7.

The ordinate in figure 7 is the ratio of wall thickness to cylinder radius t/r and the abscissa is the Mach number. The curves are theoretical flutter boundaries which apply to unstiffened infinitely long cylinders. The solid curves are boundaries that result when there is no static-pressure differential across the wall; the dashed curves, on the other hand, correspond to the existence of enough internal pressure to cause a circumferential tension near the ultimate.

It will be noted that the required wall thicknesses of unstiffened infinitely long cylinders increase rapidly with increase in Mach number and very quickly reach prohibitive values, even at very high altitudes. Internal pressure is seen to produce only small percentage reductions in these large thicknesses. Furthermore, it has been pointed out in reference 27 that negligible benefit can be expected if internal damping is taken into account.

On the other hand, an effect that shows promise of reducing the thicknesses to reasonable values is the effect of finite length. For the purpose of illustrating this effect, an approximate calculation has been made for a steel cylinder with rigid ring-stiffeners spaced a radius apart. The calculation is based on equation (42) of reference 21 with the air forces replaced, for simplicity, by their plane static approximation. This simplification imposes the requirements that the Mach number M be large and that $M\frac{r}{a} \gg \frac{n}{2\pi}$ where n is the number of full waves around the circumference of the cylinder (corresponding to the maximum required thickness for the prevention of flutter) and a is the distance between stiffeners. The resulting thickness ratio required to prevent flutter at $M = 6$ of the stiffened steel cylinder at an altitude of 35,000 feet with no internal pressure is shown by the small circle in figure 7. This result is only approximate because the above conditions are only approximately satisfied (maximum t/R corresponds to $n = 26$). However, it has the correct order of magnitude. Furthermore, in contrast to the extremely large thickness ratios predicted at $M = 6$ for the unstiffened infinitely long cylinder, the result for the stiffened cylinder has a reasonable order of magnitude. Thus, the large thicknesses predicted by analyses of infinitely long unstiffened cylinders apparently do not apply to practical configurations of finite length.

CONCLUDING REMARKS

It may be stated that much progress has been made in the solution and understanding of the panel flutter problem. Although, in general, panel flutter is of concern only in the design of very thin panels, there appear to be critical combinations of panel aspect ratio and midplane stress for which even very thick panels may flutter. It should be emphasized that there is a need for more work on certain phases of the panel flutter problem. In particular, there is a need for further consideration of cylinders of finite length and for more experimental results for assessing the validity of theoretical analyses.

APPENDIX

TRANSTABILITY ANALYSIS OF THE FLUTTER OF BUCKLED RECTANGULAR PANELS WITH CLAMPED EDGES

The application of the "transtability" concept (ref. 1) to rectangular buckled panels with pinned edges is discussed in reference 26. The corresponding results, for clamped panels, are presented in this appendix.

The transtability problem is governed by the plate equation

$$D\nabla^4 w + P_x w_{xx} + P_y w_{yy} + \frac{2q}{\sqrt{M^2 - 1}} w_x = 0 \tag{1}$$

where w is the panel deflection and the subscripts denote differentiation, and by the proper boundary conditions. The assumption is made that the panel deflection shape is adequately represented in the chordwise direction by a linear combination of the first two modes of a uniform clamped-clamped beam and in the spanwise direction by a single mode, the pth mode. Then, by the Galerkin method, the condition for the existence of a nontrivial solution is found to be

$$I_{12}^{(1)} I_{21}^{(1)} \lambda^2 = \left(I_{11}^{(4)} + A_p I_{11}^{(2)} + B_p\right)\left(I_{22}^{(4)} + A_p I_{22}^{(2)} + B_p\right) \tag{2}$$

where

$$\left.\begin{aligned} \lambda &= \frac{2qa^3}{\sqrt{M^2 - 1}\, D} \\ A_p &= \frac{P_x a^2}{D} + 2\left(\frac{a}{b}\right)^2 I_{pp}^{(2)} \\ B_p &= \left(\frac{a}{b}\right)^2 I_{pp}^{(2)}\left[\frac{P_y a^2}{D} + \left(\frac{a}{b}\right)^2 \frac{I_{pp}^{(4)}}{I_{pp}^{(2)}}\right] \\ I_{mj}^{(i)} &= \int_0^1 \phi_m(\xi) \frac{d^i}{d\xi^i}\left[\phi_j(\xi)\right] d\xi \end{aligned}\right\} \tag{3}$$

The function $\phi_m(\xi)$ is the nth mode for a beam of unit length. The beam modes and the integrals $I_{mj}^{(i)}$ are given conveniently in references 28 and 29.

As pointed out in reference 26, the critical value of the dynamic-pressure parameter λ depends on the midplane loads P_x and P_y applied to the panel at the boundaries or induced by heating a panel with fixed boundaries. Let $P_y = RP_x$. Substituting A_p and B_p from equations (3) into equation (2) yields a quadratic equation for the buckling loads P_x corresponding to given values of R and λ. As λ increases from zero, the buckling loads approach each other until at the critical "transtability" value of λ they coalesce and disappear. This condition is given by the vanishing of the discriminant of the quadratic and yields the result

$$\lambda_{cr} = \frac{\left\{\left[I_{22}^{(4)} + 2\left(\frac{a}{b}\right)^2 I_{pp}^{(2)} I_{22}^{(2)} + \left(\frac{a}{b}\right)^4 I_{pp}^{(4)}\right]\left[1 + \frac{I_{pp}^{(2)}}{I_{11}^{(2)}}\left(\frac{a}{b}\right)^2 R\right] - \left[I_{11}^{(4)} + 2\left(\frac{a}{b}\right)^2 I_{pp}^{(2)} I_{11}^{(2)} + \left(\frac{a}{b}\right)^4 I_{pp}^{(4)}\right]\left[1 + \frac{I_{pp}^{(2)}}{I_{22}^{(2)}}\left(\frac{a}{b}\right)^2 R\right]\frac{I_{22}^{(2)}}{I_{11}^{(2)}}\right\}}{2I_{12}^{(1)}\sqrt{\left[1 + \frac{I_{pp}^{(2)}}{I_{11}^{(2)}}\left(\frac{a}{b}\right)^2 R\right]\left[1 + \frac{I_{pp}^{(2)}}{I_{22}^{(2)}}\left(\frac{a}{b}\right)^2 R\right]\frac{I_{22}^{(2)}}{I_{11}^{(2)}}}} \qquad (4)$$

Calculations have been made of the quantities:

$$\left(\sqrt{M^2 - 1}\,\frac{E}{q}\right)^{1/3}\frac{t}{a} = \left[\frac{24\left(1 - \mu^2\right)}{\lambda_{cr}}\right]^{1/3}$$

and

$$\left(\sqrt{M^2 - 1}\,\frac{E}{q}\right)^{1/3}\frac{t}{b} = \left[\frac{24\left(1 - \mu^2\right)}{\lambda_{cr}}\right]^{1/3}\frac{a}{b}$$

for a series of test panels buckled by heating. The integer p, specifying the number of half-waves in the spanwise direction, was taken as the number of spanwise half-waves in the observed buckle patterns.

Furthermore, since the actual loads in the test panels had not been measured, the ratio $R = \frac{P_y}{P_x}$ was estimated from the buckle patterns with the aid of figure 5 of reference 30. Specifically, for each aspect ratio, the average longitudinal buckling load corresponding to the number of observed spanwise or chordwise half-waves was used along with the corresponding transverse load. For an aspect ratio of 1, it was assumed that $R = 1$ $(P_x = P_y)$. The resulting calculated boundary is shown in figure 6 along with the test results.

[redacted]

REFERENCES

1. Isaacs, R. P.: Transtability Flutter of Supersonic Aircraft Panels. U. S. Air Force Project RAND P-101, The Rand Corp., July 1, 1949.

2. Hayes, W.: A Buckled Plate in a Supersonic Stream. Rep. No. AL-1029, North American Aviation, Inc., May 10, 1950.

3. Miles, John W.: Dynamic Chordwise Stability at Supersonic Speeds. Rep. No. AL-1140, North American Aviation, Inc., Oct. 18, 1950.

4. Shen, S. F.: Non-Stationary Aerodynamics of a Two-Dimensional Bump in a Uniform Stream and Its Effect on the Vibration Characteristics of an Elastic Panel. M.I.T. Tech. Rep. (Contract No. N5ori-07833, NR 064-259), May 1952.

5. Shen, S. F.: Flutter of a Two-Dimensional Simply-Supported Uniform Panel in a Supersonic Stream. Contract No. N5ori-07833, Office of Naval Res., Dept. Aero. Eng., M.I.T., Aug. 6, 1952.

6. Sylvester, Maurice A., and Baker, John E.: Some Experimental Studies of Panel Flutter at Mach Number 1.3. NACA TN 3914, 1957. (Supersedes NACA RM L52I16.)

7. Goland, Martin, and Luke, Yudell L.: An Exact Solution for Two-Dimensional Linear Panel Flutter at Supersonic Speeds. Jour. Aero. Sci. (Readers' Forum), vol. 21, no. 4, Apr. 1954, pp. 275-276.

8. Hedgepeth, John M., Budiansky, Bernard, and Leonard, Robert W.: Analysis of Flutter in Compressible Flow of a Panel on Many Supports. Jour. Aero. Sci., vol. 21, no. 7, July 1954, pp. 475-486.

9. Fung, Y. C.: The Static Stability of a Two-Dimensional Curved Panel in a Supersonic Flow, With An Application to Panel Flutter. Jour. Aero. Sci., vol. 21, no. 8, Aug. 1954, pp. 556-565.

10. Nelson, Herbert C., and Cunningham, Herbert J.: Theoretical Investigation of Flutter of Two-Dimensional Flat Panels With One Surface Exposed to Supersonic Potential Flow. NACA Rep. 1280, 1956. (Supersedes NACA TN 3465.)

11. Fung, Y. C.: The Flutter of a Buckled Plate in Supersonic Flow. GALCIT Rep. No. OSR-TN-55-237, July 1955.

12. Eisley, J. G.: The Flutter of Simply Supported Rectangular Plates in a Supersonic Flow. OSR-TN-55-236, GALCIT, July 1955.

[redacted]

13. Sylvester, Maurice A., Nelson, Herbert C., and Cunningham, Herbert J.: Experimental and Theoretical Studies of Panel Flutter at Mach Numbers 1.2 to 3.0. NACA RM L55E18b, 1955.

14. Miles, John W.: Supersonic Flutter of a Cylindrical Shell. The Ramo-Wooldridge Corp., Guided Missile Res. Div.
I. General Theory. Rep. No. AM 5-2, Aug. 19, 1955.
II. Pressurization and Internal Fluid Effects. Rep. No. AM 5-11, Nov. 14, 1955.
III. Aeolotropic Shell. Rep. No. AM 5-12, Dec. 2, 1955.
IV. Effects of Non-Uniform Steady Flow. Rep. No. AM 5-16, Dec. 7, 1955.

15. Shen, S. F.: Remarks on "An Exact Solution for Two-Dimensional Linear Panel Flutter at Supersonic Speeds." Jour. Aero. Sci. (Readers' Forum), vol. 22, no. 9, Sept. 1955, pp. 656-657.

16. Sylvester, Maurice A.: Experimental Studies of Flutter of Buckled Rectangular Panels at Mach Numbers From 1.2 to 3.0 Including Effects of Pressure Differential and of Panel Width-Length Ratio. NACA RM L55I30, 1955.

17. Luke, Yudell L., St. John, Andrew, and Goland, Martin: An Exact Solution for Two-Dimensional Linear Panel Flutter at Supersonic Speeds. WADC Tech. Note 56-460 (Contract No. AF 33(616)-2897), Midwest Res. Inst., Mar. 15, 1956.

18. Luke, Yudell L., St. John, A. D., and Gross, Betty: Panel Flutter at Supersonic Speeds. Third Quarterly Progress Rep. (Contract No. AF 33(616)-2897), Midwest Res. Inst., Appl. Phys. Div., Mar. 29, 1956.

19. Luke, Yudell L., St. John, A. D., and Gross, Betty: Panel Flutter at Supersonic Speeds. Fourth Quarterly Progress Rep. (Contract No. AF 33(616)-2897), Midwest Res. Inst., Appl. Phys. Div., May 29, 1956.

20. Luke, Yudell L., and St. John, A. D.: Panel Flutter at Supersonic Speeds. Fifth Quarterly Progress Rep. (Contract No. AF 33(616)-2897), Midwest Res. Inst., Appl. Phys. Div., Oct. 31, 1956.

21. Leonard, Robert W., and Hedgepeth, John M.: On Panel Flutter and Divergence of Infinitely Long Unstiffened and Ring-Stiffened Thin-Walled Circular Cylinders. NACA TN 3638, 1956.

22. Hedgepeth, John M.: On the Flutter of Panels at High Mach Numbers. Jour. Aero. Sci. (Readers' Forum), vol. 23, no. 6, June 1956, pp. 609-610.

23. Eisley, J. G.: The Flutter of a Two-Dimensional Buckled Plate With Clamped Edges in a Supersonic Flow. OSR-TN-56-296, GALCIT, July 1956.

24. Miles, John W.: On the Aerodynamic Instability of Thin Panels. Jour. Aero. Sci., vol. 23, no. 8, Aug. 1956, pp. 771-780.

25. Ashley, Holt, and Zartarian, Garabed: Piston Theory - A New Aerodynamic Tool for the Aeroelastician. Jour. Aero. Sci., vol. 23, no. 12, Dec. 1956, pp. 1109-1118.

26. Hedgepeth, John M.: Flutter of Rectangular Simply Supported Panels at High Supersonic Speeds. Preprint No. 713, S.M.F. Fund Paper, Inst. Aero. Sci., Inc., Jan. 28-31, 1957.

27. Miles, John W.: Supersonic Flutter of a Cylindrical Shell. Jour. Aero. Sci., vol. 24, no. 2, Feb. 1957, pp. 107-118.

28. Young, Dana, and Felgar, Robert P., Jr.: Tables of Characteristic Functions Representing Normal Modes of Vibration of a Beam. Univ. of Texas, Pub. No. 4913, Eng. Res. Ser. No. 44, Bur. Eng. Res., July 1, 1949.

29. Felgar, Robert P., Jr.: Formulas for Integrals Containing Characteristic Functions of a Vibrating Beam. Cir. No. 14, Bur. Eng. Res., Univ. of Texas, 1950.

30. Libove, Charles, and Stein, Manuel: Charts for Critical Combinations of Longitudinal and Transverse Direct Stress for Flat Rectangular Plates. NACA WR L-224, 1946. (Formerly NACA ARR L6A05.)

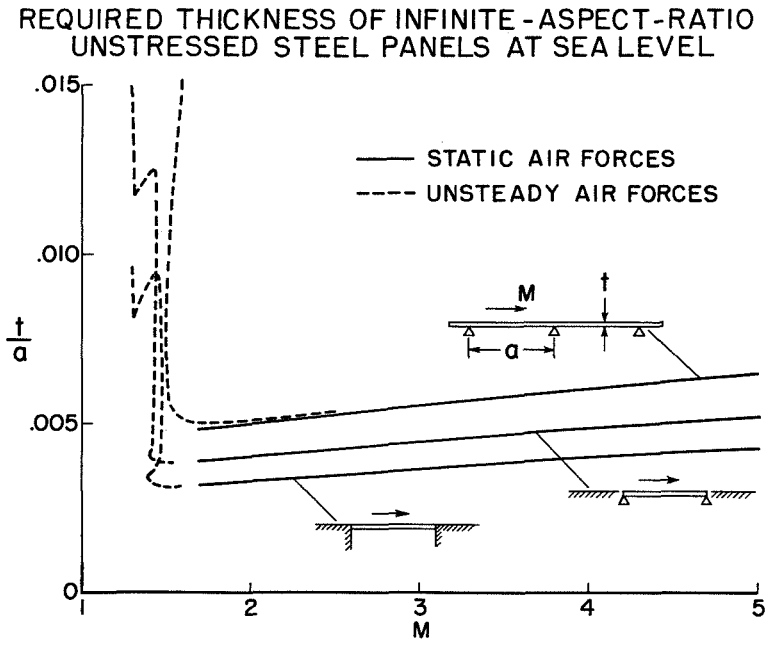


Figure 1

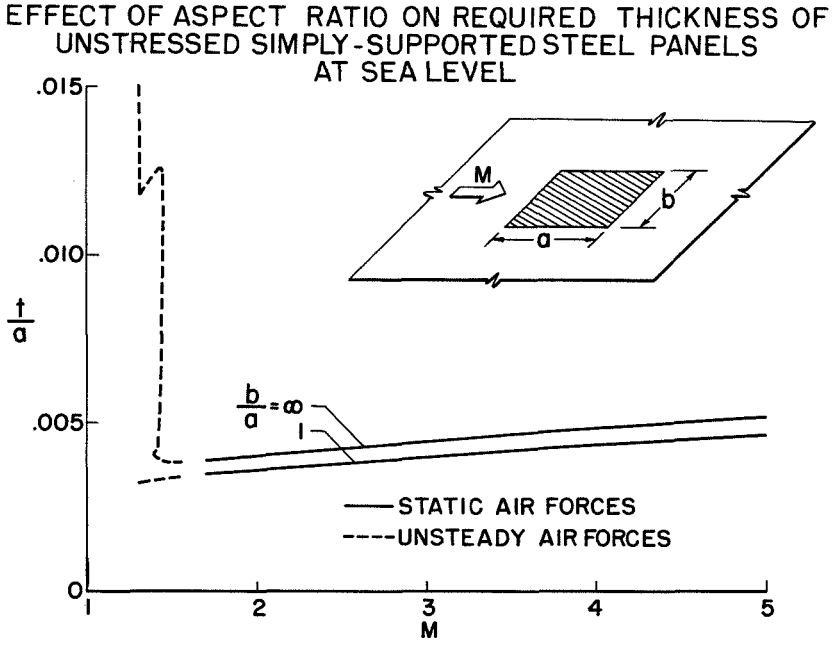


Figure 2

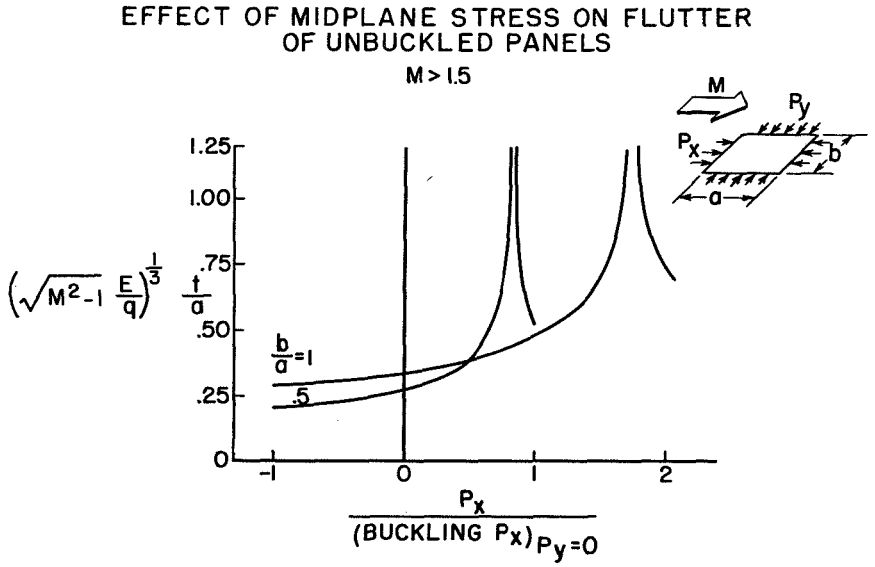


Figure 3

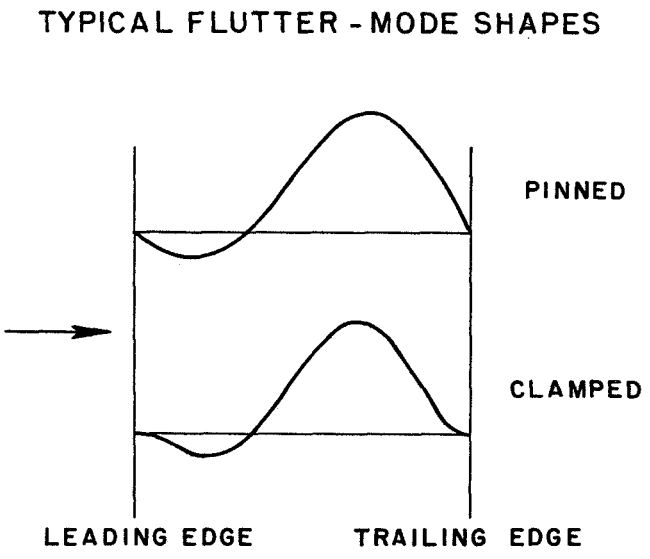


Figure 4

EFFECT OF BUCKLING ON REQUIRED THICKNESS OF INFINITE-ASPECT-RATIO STEEL PANELS AT SEA LEVEL

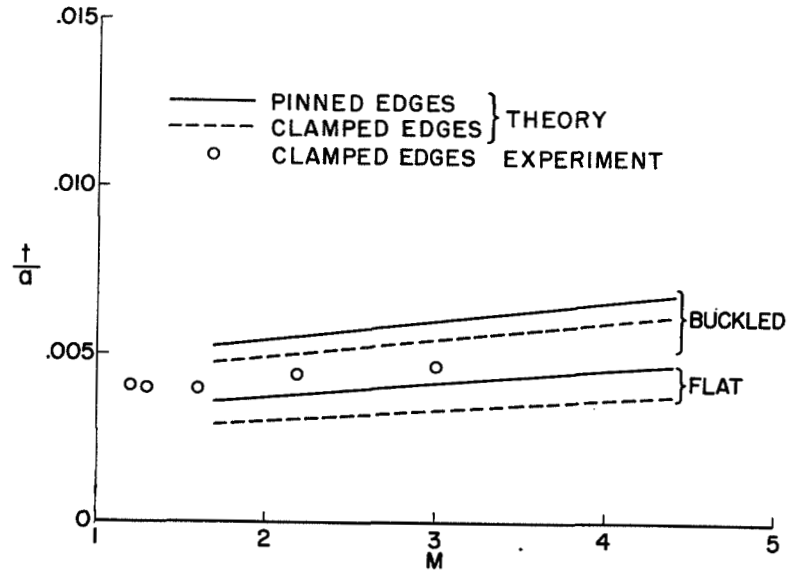


Figure 5

REQUIRED THICKNESSES OF A SERIES OF TEST PANELS BUCKLED BY HEATING

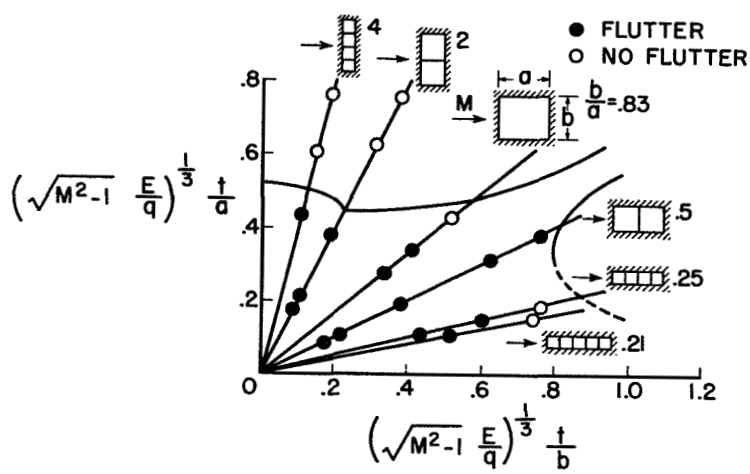


Figure 6

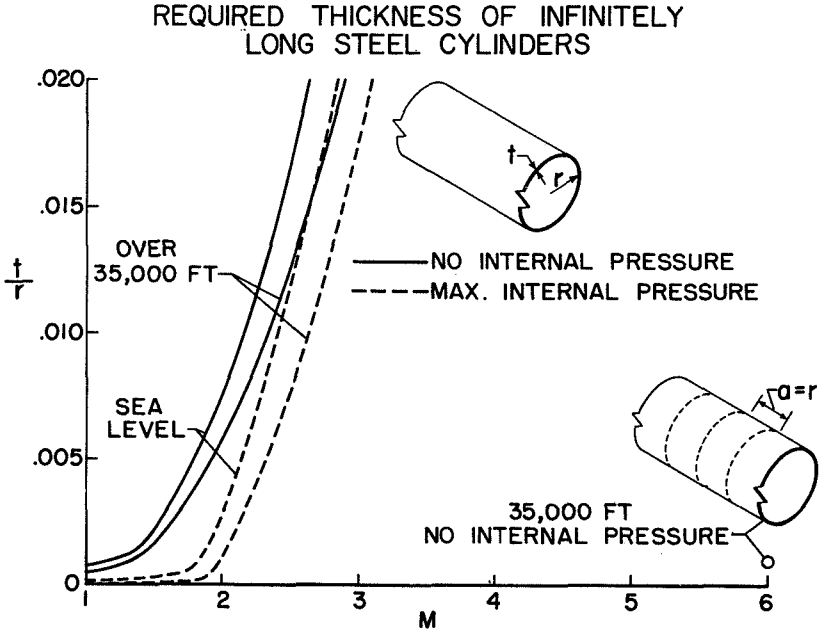

REQUIRED THICKNESS OF INFINITELY LONG STEEL CYLINDERS
.020
.015
.010
.005
0
t/r
OVER 35,000 FT
SEA LEVEL
NO INTERNAL PRESSURE
MAX. INTERNAL PRESSURE
t
r
a=r
35,000 FT
NO INTERNAL PRESSURE
1
2
3
4
5
6
M

Figure 7

N71-75426

FLUTTER AND DIVERGENCE OF RECTANGULAR WINGS OF VERY LOW ASPECT RATIO

By Robert W. Fralich, John M. Hedgepeth, and W. J. Tuovila

Langley Aeronautical Laboratory

SUMMARY

Slender-body aerodynamic theory is used in conjunction with thin-plate theory in the flutter analysis of low-aspect-ratio rectangular wings of constant thickness when chordwise variations of deflections are considered. The spanwise variation of deflection is given by a parabola, and the chordwise variation is allowed complete freedom. The results show the variation of flutter speed and mode shape with aspect ratio. Comparisons are made with results obtained by approximating the chordwise deflection shape by the first few terms of a power series. Comparisons with some preliminary experimental results are also included.

INTRODUCTION

The prediction of flutter of wing and tail surfaces of very low aspect ratio is a problem of some concern to aircraft designers. The difficulties in the flutter analysis of such surfaces are mainly connected with the presence of large amounts of chordwise curvature in the flutter mode. It is of interest to investigate the complexity of the chordwise deflection shape at flutter and to determine to what degree of accuracy the chordwise deflection must be represented in order to obtain good results. This paper is concerned with the flutter behavior, both theoretical and experimental, of the simple low-aspect-ratio configuration shown in figure 1. The analysis is similar to that of reference 1, which treated the static divergence behavior of the same configuration.

SYMBOLS

x,y,z	coordinate system (see fig. 1)
$w(x,y,\tau)$	wing deflection, positive in z-direction

V	free-stream velocity
t	wing thickness
c	wing chord
s	wing semispan
τ	time
$F(x,\tau)$	chordwise deflection shape
q	dynamic pressure, $\frac{\rho V^2}{2}$
E	Young's modulus of elasticity
ρ	free-stream density of fluid
ρ_m	density of material
T	period of oscillation
M	Mach number
$\varphi(x,y,z,\tau)$	perturbation-velocity potential
λ	flutter-speed parameter, $\frac{5\pi}{4}(1 - \mu^2)\frac{q}{E}\frac{s^3}{t^3}$
K	flutter-frequency parameter, $\omega\sqrt{\frac{\rho_m t s^4}{D}}$
ϵ	mass-ratio parameter, $\frac{\pi}{2}\frac{\rho s}{\rho_m t}$
μ	Poisson's ratio (taken as 1/3 in all computations)
D	plate stiffness in bending, $Et^3/12(1 - \mu^2)$
ω	flutter frequency

THEORETICAL APPROACH

The configuration analyzed in this paper consists of a rectangular plate of constant thickness cantilevered from a rigid wall. (See fig. 1.)

This plate may be thought of as representing one-half of a wing with a chord c and a semispan s. The plate is located in a fluid flow with a free-stream velocity V. The deflection shape of such a low-aspect-ratio plate can be expected to vary in a much more complicated manner in the chordwise direction than in the spanwise direction. For this reason the deflection w is assumed to vary as $w(x,y,\tau) = y^2F(x,\tau)$, where the spanwise deflection is given by a simple parabola and the chordwise variation F of the deflection is an arbitrary function of the chordwise coordinate x and time τ. The distortions of the plate are found through the use of ordinary thin-plate theory. The aerodynamic loadings are found most simply by using slender-body aerodynamic theory. In this theory streamwise perturbations are neglected in comparison with perturbations in the crossflow direction. The use of this approximate aerodynamic theory simplifies the aeroelastic problem to the extent that an exact solution is possible. A brief description of the analysis and the resulting equations are given in the appendix.

RESULTS AND DISCUSSION

Some results are given by the boundaries shown in figure 2. The ordinate is the dynamic-pressure parameter $\frac{q/E}{(t/s)^3}$, in which q is the dynamic pressure, E is Young's modulus of elasticity for the plate, and t/s is the ratio of thickness to semispan. The abscissa is the ratio of chord to semispan c/s. The variation of the dynamic-pressure parameter for flutter with the ratio of chord to semispan is dependent upon the mass-ratio parameter $\frac{\rho s}{\rho_m t}$ in which $\frac{\rho}{\rho_m}$ is the ratio of air density to plate density. The flutter boundaries are given for two values of mass-ratio parameter; the region above a particular boundary is unstable while that below is stable. Also shown is the result for static divergence obtained from reference 1. This result, which is, of course, independent of the mass ratio, is indicated by a single curve. Note that divergence is less critical than flutter for these particular mass ratios. Note also that, for the higher mass ratio, the flutter boundary consists of a series of loops approaching a constant value of dynamic-pressure parameter. The lower curve also has these characteristics; however, the loops are so elongated in this case that only one can be seen in this figure.

The kind of flutter mode shapes obtained from the analysis is shown in figure 3. The top set of curves shows the components of tip deflection which are in phase and out of phase with the maximum leading-edge deflection for a value of c/s corresponding to the tick mark on the bottom of the first loop on the flutter boundary in figure 2. The

tip deflection is given when the leading edge has its maximum amplitude and at one-quarter of a period later when the leading edge has zero deflection. The bottom set of curves gives the components of mode shape for a value of c/s given by the tick mark on the second loop of the flutter boundary of figure 2. The effect of increasing the chord is to add more waves to the mode shape.

In the results discussed so far, the chordwise variations of deflections were allowed complete freedom and an exact solution was possible. In a practical case, an exact solution would not be feasible, and some sort of approximation of the chordwise deflection shape would be necessary. Some flutter boundaries obtained by approximating the chordwise deflections by the first few terms of a power series are shown in figure 4. The dashed curve gives the results for parabolic deformations, and the long-and-short-dashed curve gives the results for cubic deformations. The exact boundary is also shown for comparison. Both approximations yield good results for the lower values of c/s. The cubic approximation is almost exact. For longer chords, however, both approximations yield poor results. Apparently, in order to analyze the flutter behavior of wings in this range, higher order terms in the deflection shape must be used.

It can be seen from figure 2 that for each value of mass ratio a limiting value of the dynamic-pressure parameter can be obtained by considering the values at the bottom of the loops as the chord becomes large. The variation of this limiting value with mass ratio is shown in figure 5. The results obtained so far indicate that this curve gives a conservative estimate of the flutter speed for thin rectangular plates of very low aspect ratio. It should be noted that the flutter speed is less than the divergence speed and seems to approach it asymptotically for high mass ratio.

Several preliminary tests of some low-aspect-ratio plates at supersonic Mach numbers have been run in the Langley 9- by 18-inch supersonic flutter tunnel. The results of these tests are shown in figure 6. The flutter speed of the various models is shown as a ratio of experimental flutter speed to calculated flutter speed, where the calculated flutter speed was obtained from the curve in figure 5. This ratio is plotted against the ratio of chord to semispan. The agreement between theory and experiment is fairly good in view of the approximations inherent in the theory and of the preliminary nature of the tests.

During the tests the flutter modes were observed, and it was noted that the specimens with the larger ratios of chord to semispan had the more complicated mode shapes as is predicted by theory.

CONCLUDING REMARKS

The flutter analysis of low-aspect-ratio rectangular plates indicates that the flutter-mode shape has an increasing number of waves in the chordwise direction as the aspect ratio is reduced; approximating the chordwise deflection shape by parabolic or cubic curves yields flutter speeds in fair agreement with those of the more exact theory, provided that the aspect ratio is not too low. The cubic curve gives somewhat better results. For lower aspect ratios, higher order approximations must be used. Experimental data indicate that the flutter speed and the type of mode shape yielded by the theory are in fair agreement with experimental results.

APPENDIX

ANALYSIS

In the application of slender-body aerodynamic theory to the present unsteady-flow problem, terms containing time derivatives in the velocity-potential equation for linearized flow are neglected in addition to those containing streamwise x-derivatives. The velocity-potential equation thus reduces to Laplace's equation in the crossflow plane. The boundary conditions on velocity and the pressure-potential relations are taken to be the same as those ordinarily used in unsteady linearized aerodynamic theory.

The potential φ and the aerodynamic loads resulting from the given deformation shape are calculated in a manner similar to that used in reference 1 for the static-divergence problem.

The principle of minimum potential energy is used to derive the differential equation of equilibrium for the function $F(x,\tau)$ in a manner analogous to that used in reference 1. Solution yields an eigenvalue equation which relates the flutter speed to the properties of the plate and the surrounding air:

$$0 = 64\alpha\beta\left[\left(D_1 \cos\frac{2\gamma c}{s} + E_1 \cosh\frac{\alpha c}{s}\cosh\frac{\beta c}{s} + \frac{F_1}{\alpha\beta}\sinh\frac{\alpha c}{s}\sinh\frac{\beta c}{s}\right) + i\left(D_2 \sin\frac{2\gamma c}{s} + \frac{E_2}{\alpha}\sinh\frac{\alpha c}{s}\cosh\frac{\beta c}{s} + \frac{F_2}{\beta}\cosh\frac{\alpha c}{s}\sinh\frac{\beta c}{s}\right)\right] \qquad (1)$$

where

$$i = \sqrt{-1}$$

$$D_1 = -\left[2A_1A_2 + A_1B_2 + A_2B_1\right]$$

$$E_1 = (A_3 + \lambda B_3)\left[2A_3 - (4\gamma^2 + \alpha^2 + \beta^2)A_4\right] + (A_4 - \lambda)\left[2\alpha^2\beta^2A_4 - (4\gamma^2 + \alpha^2 + \beta^2)A_3\right]$$

$$F_1 = (A_3 + \lambda B_3)\left[2\alpha^2\beta^2 A_4 - (4\gamma^2 + \alpha^2 + \beta^2)A_3\right] +$$

$$\alpha^2\beta^2(A_4 - \lambda)\left[2A_3 - (4\gamma^2 + \alpha^2 + \beta^2)A_4\right]$$

$$D_2 = -(A_1B_2 - A_2B_1)$$

$$E_2 = \gamma\left\{(A_3 + \lambda B_3)\left[\lambda\left(8\gamma^2 + 8a_1 - 8\lambda + \frac{K^2}{\gamma^2}\frac{5\epsilon}{12}\right) - 2(\gamma^2 - \lambda)\frac{K}{\gamma}\sqrt{\frac{5\epsilon\lambda}{12}}\right] -\right.$$

$$\left.\alpha^2(A_4 - \lambda)\left[\lambda\left(8\gamma^2 + 8a_1 - 8\lambda + \frac{K^2}{\gamma^2}\frac{5\epsilon}{12}\right) + 2(\gamma^2 - \lambda)\frac{K}{\gamma}\sqrt{\frac{5\epsilon\lambda}{12}}\right]\right\}$$

$$F_2 = -\gamma\left\{(A_3 + \lambda B_3)\left[\lambda\left(8\gamma^2 + 8a_1 - 8\lambda + \frac{K^2}{\gamma^2}\frac{5\epsilon}{12}\right) + 2(\gamma^2 - \lambda)\frac{K}{\gamma}\sqrt{\frac{5\epsilon\lambda}{12}}\right] -\right.$$

$$\left.\beta^2(A_4 - \lambda)\left[\lambda\left(8\gamma^2 + 8a_1 - 8\lambda + \frac{K^2}{\gamma^2}\frac{5\epsilon}{12}\right) - 2(\gamma^2 - \lambda)\frac{K}{\gamma}\sqrt{\frac{5\epsilon\lambda}{12}}\right]\right\}$$

in which

$$A_1 = -\frac{100}{9}(1 - \mu)^2 - \frac{10\mu}{3}\gamma^2 + \left(\gamma^2 - \lambda - \frac{K}{2\gamma}\sqrt{\frac{5\epsilon\lambda}{12}}\right)^2$$

$$A_2 = -\frac{100}{9}(1 - \mu)^2 - \frac{10\mu}{3}\gamma^2 + \left(\gamma^2 - \lambda + \frac{K}{2\gamma}\sqrt{\frac{5\epsilon\lambda}{12}}\right)^2$$

$$B_1 = \frac{20}{3}(1 - \mu)\lambda + (\gamma^2 - \lambda)\left(2\lambda + \frac{K}{\gamma}\sqrt{\frac{5\epsilon\lambda}{12}}\right)$$

$$B_2 = \frac{20}{3}(1 - \mu)\lambda + (\gamma^2 - \lambda)\left(2\lambda - \frac{K}{\gamma}\sqrt{\frac{5\epsilon\lambda}{12}}\right)$$

$$A_3 = \frac{100}{9}(1 - \mu)(1 - 2\mu) - \frac{20}{3}(1 - \mu)\lambda + \frac{10}{3}(1 - \mu)\gamma^2 + \lambda^2 - \frac{K^2}{4\gamma^2}\frac{5\epsilon\lambda}{12}$$

$$A_4 = \frac{10}{3}(1 - \mu) + \gamma^2$$

$$B_3 = \frac{10}{3}\mu - \gamma^2$$

$$\alpha^2 = \gamma^2 - 2(\lambda - a_1) + \frac{K}{\gamma}\sqrt{\frac{5\epsilon\lambda}{12}}$$

$$\beta^2 = \gamma^2 - 2(\lambda - a_1) - \frac{K}{\gamma}\sqrt{\frac{5\epsilon\lambda}{12}}$$

$$\frac{K^2}{\gamma^2} = \frac{4\left[\left(\gamma^2 - \lambda + a_1\right)^2 - 5\right]}{\frac{5\epsilon\lambda}{12} - \gamma^2\left(1 + \frac{5\epsilon}{12}\right)}$$

$$\lambda = \frac{5\pi}{4}\left(1 - \mu^2\right)\frac{q}{E}\frac{s^3}{t^3}$$

$$\epsilon = \frac{\pi}{2}\frac{\rho s}{\rho_m t}$$

$$K = \omega\sqrt{\frac{\rho_m t s^4}{D}}$$

$$a_1 = \frac{10}{3}\left(1 - \frac{3}{2}\mu\right)$$

In equation (1), α and β can be either real or imaginary quantities. Solution by trial yields the curves given in figure 2.

The divergence boundary obtained from reference 1 can also be obtained from the present analysis by setting the flutter-frequency parameter K equal to zero.

Mode Shapes

The flutter-mode shapes shown in figure 3 can be obtained from the following equation, where the real part gives the component in phase and

the imaginary part, the component out of phase with the maximum leading-edge deflection:

$$f(x) = \frac{C_1 e^{im_1 \frac{x}{s}} + C_2 e^{im_2 \frac{x}{s}} + C_3 e^{im_3 \frac{x}{s}} + C_4 e^{im_4 \frac{x}{s}}}{C_1 + C_2 + C_3 + C_4}$$

where

$$C_1 = \Big[(m_2 - m_4)(a_2 - m_3^2) A_{24} e^{-i(m_1+m_3)\frac{c}{s}} +$$

$$(m_3 - m_2)(a_2 - m_4^2) A_{23} e^{-i(m_1+m_4)\frac{c}{s}} +$$

$$(m_4 - m_3)(a_2 - m_2^2) A_{34} e^{-i(m_1+m_2)\frac{c}{s}} \Big]$$

$$C_2 = \Big[(m_3 - m_4)(a_2 - m_1^2) A_{34} e^{-i(m_1+m_2)\frac{c}{s}} +$$

$$(m_4 - m_1)(a_2 - m_3^2) A_{14} e^{-i(m_2+m_3)\frac{c}{s}} +$$

$$(m_1 - m_3)(a_2 - m_4^2) A_{13} e^{-i(m_2+m_4)\frac{c}{s}} \Big]$$

$$C_3 = \Big[(m_4 - m_2)(a_2 - m_1^2) A_{24} e^{-i(m_1+m_3)\frac{c}{s}} +$$

$$(m_1 - m_4)(a_2 - m_2^2) A_{14} e^{-i(m_2+m_3)\frac{c}{s}} +$$

$$(m_2 - m_1)(a_2 - m_4^2) A_{12} e^{-i(m_3+m_4)\frac{c}{s}} \Big]$$

$$C_4 = \left[(m_2 - m_3)\left(a_2 - m_1^2\right) A_{23} e^{-i\left(m_1+m_4\right)\frac{c}{s}} + \right.$$

$$(m_3 - m_1)\left(a_2 - m_2^2\right) A_{13} e^{-i\left(m_2+m_4\right)\frac{c}{s}} +$$

$$\left. (m_1 - m_2)\left(a_2 - m_3^2\right) A_{12} e^{-i\left(m_3+m_4\right)\frac{c}{s}} \right]$$

in which

$$m_1 = \gamma + i\beta$$

$$m_2 = \gamma - i\beta$$

$$m_3 = -\gamma + i\alpha$$

$$m_4 = -\gamma - i\alpha$$

$$A_{pq} = -4a_2a_3 - a_2\left(m_p^2 + m_pm_q + m_q^2\right) - 4a_3m_pm_q + m_p^2m_q^2$$

$$a_2 = \frac{10}{3}\mu$$

$$a_3 = \frac{10}{3}\left(1 - \frac{5}{4}\mu\right)$$

Approximate Solutions

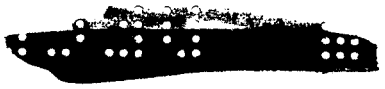
The approximate analysis used parallels the analysis for divergence presented in reference 1. Cubic approximation of the chordwise variation of deflection results in the following complex determinant:

$$\begin{vmatrix}
\left[A + 12K\sqrt{\frac{5\epsilon\lambda}{12}}\right] & \left[\frac{1}{2}A + 4\lambda\frac{s}{c} + 14K\sqrt{\frac{5\epsilon\lambda}{12}}\right] & \left[\frac{1}{3}A + \left(8\lambda + \frac{20}{3}\mu\right)\frac{s}{c} + 14K\sqrt{\frac{5\epsilon\lambda}{12}}\right] & \left[\frac{1}{4}A + (12\lambda + 10\mu)\frac{s}{c} + 14K\sqrt{\frac{5\epsilon\lambda}{12}}\right] \\
\left[\frac{1}{2}A\right] & \left[\frac{1}{3}A + \frac{40}{3}(1-\mu)\frac{s}{c} + 12K\sqrt{\frac{5\epsilon\lambda}{12}}\right] & \left[\frac{1}{4}A + \left\{4\lambda + \frac{10}{3}(4-3\mu)\right\}\frac{s}{c} + 1\frac{8}{3}K\sqrt{\frac{5\epsilon\lambda}{12}}\right] & \left[\frac{1}{5}A + \left\{8\lambda + \frac{20}{3}(2-\mu)\right\}\frac{s}{c} + 13K\sqrt{\frac{5\epsilon\lambda}{12}}\right] \\
\left[\frac{1}{3}A + \frac{20}{3}\mu\frac{s}{c}\right] & \left[\frac{1}{4}A + \frac{10}{3}(4-3\mu)\frac{s}{c} + 1\frac{4}{3}K\sqrt{\frac{5\epsilon\lambda}{12}}\right] & \left[\frac{1}{5}A + \left\{\frac{8\lambda}{3} + \frac{40}{9}(4-3\mu)\right\}\frac{s}{c} + 4\frac{s^3}{c^3} + 12K\sqrt{\frac{5\epsilon\lambda}{12}}\right] & \left[\frac{1}{6}A + \left\{6\lambda + \frac{20}{3}(3-2\mu)\right\}\frac{s}{c} + 6\frac{s^3}{c^3} + 1\frac{12}{5}K\sqrt{\frac{5\epsilon\lambda}{12}}\right] \\
\left[\frac{1}{4}A + 10\mu\frac{s}{c}\right] & \left[\frac{1}{5}A + \frac{20}{3}(2-\mu)\frac{s}{c} + 1K\sqrt{\frac{5\epsilon\lambda}{12}}\right] & \left[\frac{1}{6}A + \left\{2\lambda + \frac{20}{3}(3-2\mu)\right\}\frac{s}{c} + 6\frac{s^3}{c^3} + 1\frac{8}{5}K\sqrt{\frac{5\epsilon\lambda}{12}}\right] & \left[\frac{1}{7}A + \left\{\frac{24}{5}\lambda + 8(3-2\mu)\right\}\frac{s}{c} + 12\frac{s^3}{c^3} + 12K\sqrt{\frac{5\epsilon\lambda}{12}}\right]
\end{vmatrix} = 0 \quad (2)$$

where

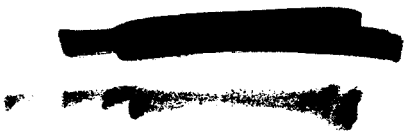
$$A = \left[20 - K^2\left(1 + \frac{5\epsilon}{12}\right)\right]\frac{c}{s}$$

This equation was solved by trial to obtain the long-and-short-dashed curve in figure 4. The equation for parabolic deformation is obtained from equation (2) by omitting the last column and last row. The results for parabolic deformation are shown by the dashed curve of figure 4.



REFERENCE

1. Hedgepeth, John M., and Waner, Paul G., Jr.: Analysis of Static Aeroelastic Behavior of Low-Aspect-Ratio Rectangular Wings. NACA TN 3958, 1957.



CANTILEVER PLATE OF VERY LOW ASPECT RATIO

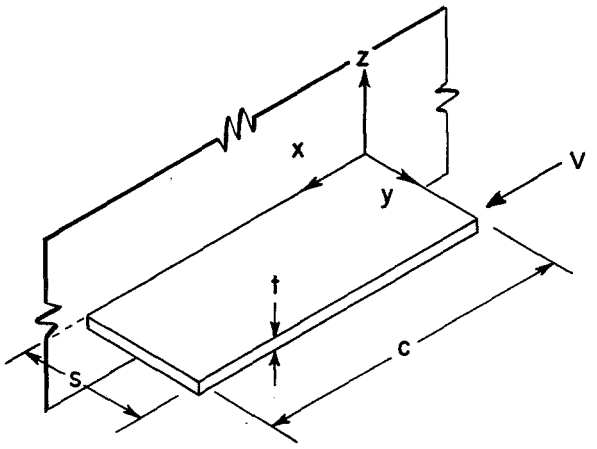


Figure 1

FLUTTER AND STATIC DIVERGENCE BOUNDARIES

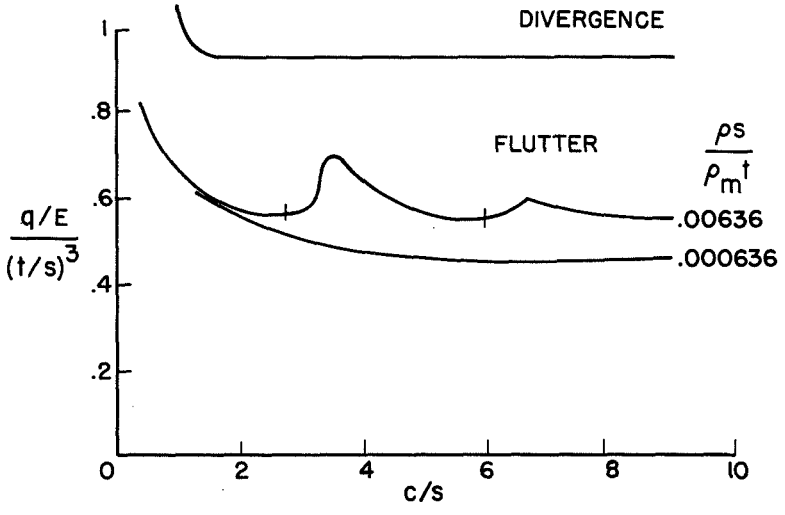


Figure 2

FLUTTER MODE SHAPES

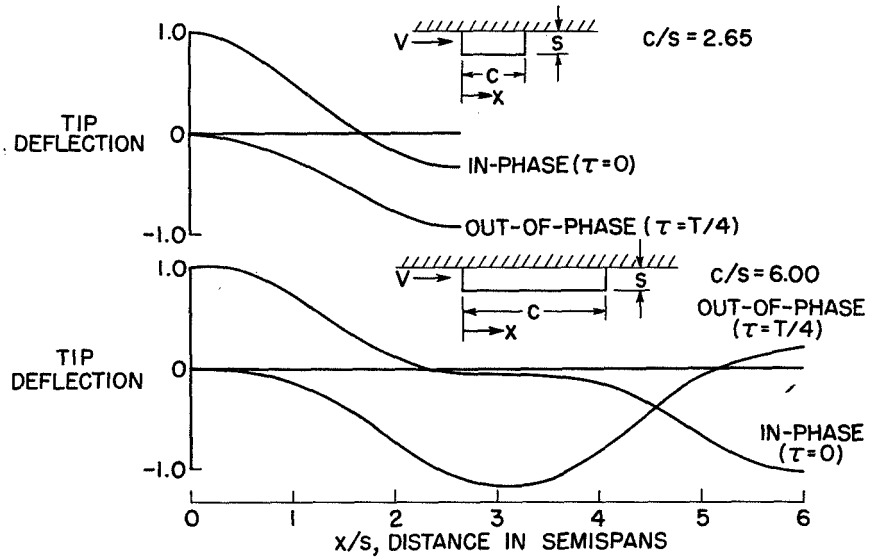
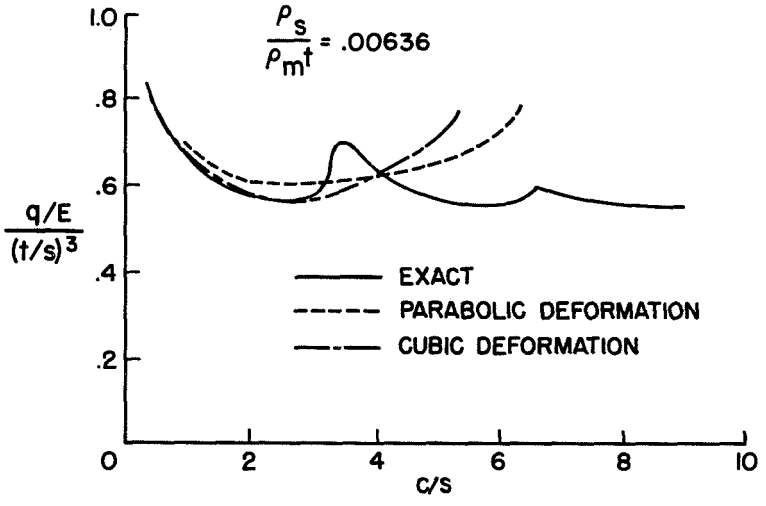


Figure 3

FLUTTER BOUNDARIES OBTAINED FROM APPROXIMATE DEFLECTION FUNCTIONS



594

Figure 4

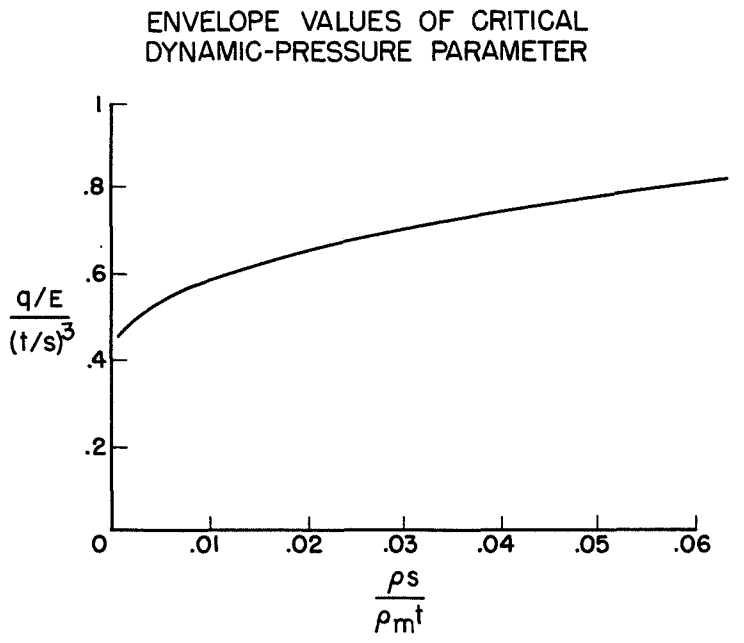


Figure 5

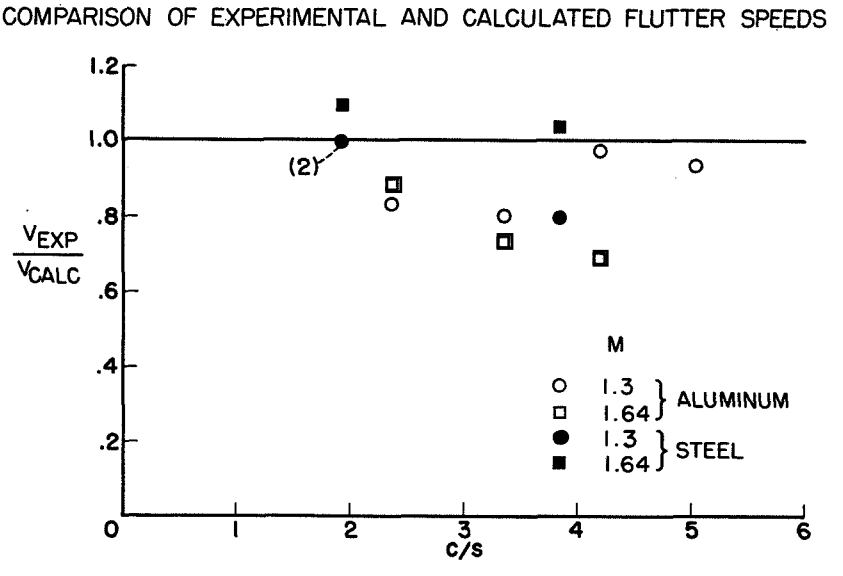


Figure 6

595

BOSWINKLE & MORGAN

N71-75427

FLUTTER EXPERIMENTS WITH VARIOUS CONTROL CONFIGURATIONS

By Robert W. Boswinkle, Jr., and Homer G. Morgan

Langley Aeronautical Laboratory

SUMMARY

The flutter characteristics of various control-surface configurations have been under study at the Langley Aeronautical Laboratory. Presented herein is a compilation of some of the more pertinent results. Most of the models studied were dynamically and elastically scaled from proposed aircraft. The flutter investigations were made in various facilities over both the transonic and supersonic speed ranges. Configurations tested included a wing with tip ailerons, all-movable elevators, vertical tails with trailing-edge rudders, and a T-tail.

INTRODUCTION

A large portion of the flutter problems which plague modern aircraft is associated with control systems. No really reliable analytical method is available for designing controls in the transonic zone. Such a variety of configurations arise that an overall trend study of characteristics is impractical. The alternative is to investigate experimentally the various specific configurations as they arise. Much of the work on controls at the Langley Aeronautical Laboratory has been of this type.

The Langley Laboratory has worked with various organizations on control-surface flutter problems of new aircraft. The work has included transonic and supersonic flutter tests of models. Most of the models used were both dynamically and elastically scaled from the prototype aircraft. Some of the more pertinent results of these investigations will be presented. The controls to be discussed are shown as configurations A to H in figure 1. They include a wing with tip ailerons, two all-movable controls, four vertical tails with trailing-edge rudders, and a T-tail.

SYMBOLS

a	speed of sound, ft/sec	596
b	root half chord, ft	

[redacted]

g structural damping coefficient

M Mach number

q dynamic pressure, lb/sq ft

V free-stream velocity, ft/sec

$$\mu = \frac{\text{Mass of wing}}{\text{Mass of air contained in truncated cone determined by wing}}$$

ω_f flutter frequency, radians/sec

ω_h bending frequency, radians/sec

ω_α torsional frequency, radians/sec

ω_β control-surface rotational frequency, radians/sec

ω_θ pitch frequency of all-movable control, radians/sec

ω_1 first coupled frequency, radians/sec

DISCUSSION

Configuration A - Wing With Tip Ailerons

Configuration A was a wing of arrowhead plan form, shown in figure 1, with trailing-edge flaps and all-moving tip ailerons. The leading edge of the wing was swept back 55° and the trailing edge was swept forward 10°. The aileron was about 20 percent of the exposed wing area and its hinge line was swept back about 4.5°. The hinge line was located at 56 percent of the aileron root chord (where the aileron root chord is the chord which contains the innermost parting line). The airfoil was 3 percent thick. The wing was cantilever mounted at the root. The trailing-edge flaps had a fixed rotational stiffness. Flutter points were obtained for different values of simulated aileron actuator stiffness.

The results are shown in figure 2, plotted as the stiffness-altitude parameter against Mach number. Increases in altitude correspond to increases in the value of the stiffness-altitude parameter. In this type figure, constant altitude occurs as a horizontal line, and constant-dynamic-pressure curves are straight lines through the origin. In figure 2, the frequency in the stiffness-altitude parameter is the torsion frequency of the wing. The actuator stiffness is the actual value divided by the original value.

Data for the original value of actuator stiffness are shown on the left side of figure 2. The no-flutter points correspond to about sea-level conditions. The mode of flutter which occurred at a Mach number of about 0.9 was predominantly bending and torsion of the wing, whereas the flutter mode at supersonic Mach numbers was predominantly aileron rotation.

These flutter points were considered to be too close to the airplane flight regime and an improvement in the conditions was sought by increasing the actuator stiffness to three times the original stiffness. This increased actuator stiffness was still a feasible value. The data obtained with the stiffer actuator are shown by the squares on the right side of figure 2. The no-flutter points at supersonic speeds so obtained were at lower altitudes than the flutter points previously obtained with the lower actuator stiffness. No-flutter points were also obtained at supersonic speeds with an infinite actuator stiffness. Infinite actuator stiffness was simulated by gluing the aileron to the wing so no relative motion could take place. It is interesting to note, however, that, even with infinite actuator stiffness, bending-torsion-type flutter was still obtained near a Mach number of 0.9 and occurred at about the same altitude as for the lowest value of actuator stiffness.

Increasing the actuator stiffness was one way to increase the aileron rotation frequency; another way was to reduce the moment of inertia of the aileron. Since there was considerable windup of the ailerons, a large reduction in effective moment of inertia was possible by cutting off the tips of the ailerons. Accordingly, the tips were cut off along the dashed lines shown in figure 1. Removal of these tips gave beneficial results at supersonic speeds but again left the subsonic flutter region essentially unaffected.

Increasing the actuator stiffness or cutting off the aileron tips reduced the altitude at which the aileron-rotation-type flutter occurred at supersonic speeds. These changes had no effect on the bending-torsion-type flutter obtained at subsonic speeds.

Configuration B - All-Movable Stabilizer

Configuration B, as shown in figure 1, was an all-movable stabilizer. The model had an aspect ratio of 3.3, a taper ratio of 0.42, 35° sweepback of the quarter-chord line, airfoil sections tapering from 6 percent thick at the root to 4 percent at the tip, a rounded tip, and a pitch axis at 78.9 percent of the center-line chord. Tests were made at a constant value of stabilizer twist stiffness and ratio of bending frequency to torsion frequency. The pitching frequency of the stabilizer on its spindle was the main test variable.

[redacted]

These test results are shown in figure 3 where the stiffness-altitude parameter is shown as a function of Mach number for various values of the ratio of bending frequency to pitch frequency. The frequency in the stiffness-altitude parameter is the torsion frequency of the stabilizer. The lower curve is for a frequency ratio of 0.50. As the Mach number is increased, the flutter boundary shifts to higher altitudes. This Mach number effect becomes more pronounced as the frequency ratio is increased toward 1.0, as shown by the slopes of the curves for frequency ratios of 0.62, 0.77, and 0.94.

The effect of frequency ratio at a Mach number of 0.8 is shown in figure 4. The flutter-speed coefficient $V/b\omega_\alpha$ is plotted as a function of frequency ratio for a given value of mass-density ratio. It should be noted that on this plot the flutter side of the boundary is above the curve. The experimental data are shown as a solid curve, cross-plotted from the previous figure. The other two curves are calculated results using two-dimensional incompressible aerodynamic coefficients and three uncoupled modes. The calculations were made at a fixed value of the ratio of bending frequency to torsion frequency, $\omega_h/\omega_\alpha = 0.305$. The lower dashed-line curves assume zero structural damping coefficient and the upper dashed-line curves use a structural damping coefficient in each of the three modes equal to the measured values. This calculation again shows the importance of damping on flutter speeds at frequency ratios near 1. The trend at frequency ratios below 1 appears to be predicted and the calculations are on the conservative side of the boundary. The calculations predict a favorable jump in flutter speed as the frequency ratio is increased above 1 although experimental data were not obtained at large enough frequency ratios for verification. For frequency ratios above 1, these calculations indicate that the flutter speed increases almost directly with the torsion frequency. Changes in ratio of bending frequency to pitch frequency would have practically no effect on the flutter speed. However, at frequency ratios between about 0.3 and 0.8, increases in torsion frequency may not result in proportionate increases in flutter speed. The flutter speed in this region varies in a much more complicated manner. For example, notice that an increase in torsion frequency ω_α while holding the ratio of bending frequency to torsion frequency constant would require increases in ω_h, the bending frequency. This, in turn, would increase the ratio of bending frequency to pitch frequency and lower the flutter-speed coefficient. A more complete discussion of this behavior is given in reference 1.

Configuration C - All-Movable Stabilizer

Configuration C, shown in figure 1, is a statically balanced all-movable stabilizer. The control was spindle mounted with the rotation

[redacted]

axis at 46 percent of the root chord. Its semispan aspect ratio was 1.56, leading-edge sweepback was 20°, the trailing edge was swept forward 24°, and the thickness ratio was 5 percent. Torsion frequency of the surface was very high, so that the predominant control-surface modes were pitch about the spindle axis and bending. Studies were made at various values of the ratio of bending frequency to pitch frequency. The results are shown in figure 5, with stiffness-altitude parameter plotted as a function of Mach number. The frequency in the stiffness-altitude parameter is the rotation frequency of the stabilizer. The upper curve is the flutter boundary established for an uncoupled bending-pitch frequency ratio of 1.02. When the frequency ratio was increased to 1.41 or decreased to 0.92, favorable shifts in the flutter boundary were obtained. For the higher frequency ratios the flutter mode involved both bending and torsion, whereas for the lowest frequency ratio the flutter mode involved primarily bending. These tests demonstrate that a change in frequency ratio which moves the frequency ratio away from 1 is beneficial and requires less stiffness to avoid flutter.

Mass balancing is a common method for increasing the flutter speed of controls. Such a method was studied for this case. The results are shown in figure 6. The plain-wing data for a frequency ratio of 1.02 are repeated from the previous figure. Also shown is the flutter boundary obtained when a heavy leading edge was added to the same configuration on the outboard 50 percent of the control, as shown by the sketch in figure 6. The added weight was about 7 percent of the plain-wing weight. The frequency ratio of the modified model dropped to 0.95. Adding the weight is seen to be beneficial so that less stiffness is required to prevent flutter. However, the increase in flutter speed may be due to the change in frequency ratio as well as the center-of-gravity shift.

Calculations have been made for comparison with the experimental data obtained with the plain wing at frequency ratios of 1.02 and 1.41. The calculated and experimental results are compared in figure 7. Experimental flutter points are shaded symbols and experimental no-flutter points are open symbols. The calculated results are shown as the curves. These calculations used the first two measured coupled modes of the system. Zero structural damping was assumed and the aerodynamic forces were obtained from piston theory (ref. 2) including the effect of airfoil thickness.

The calculated flutter boundary for a frequency ratio of 1.02 is seen to be in excellent agreement with the experimental data over the Mach number range investigated - 1.5 to 2.8. The agreement is not so good for a frequency ratio of 1.41. For this case, the calculated curve passes through experimental no-flutter points at Mach numbers of 1.6 and 2.0 and so predict more stiffness than necessary. Not enough stiffness is predicted at a Mach number of 2.2. These two examples give some

indication of the reliability of low supersonic flutter-speed calculations using piston theory. For one case, agreement between experiment and calculations is good and in the other case, not so good.

Configurations D and E - Vertical Tails With Trailing-Edge Rudders

Configurations D and E, shown in figure 1, were swept vertical tails with unbalanced trailing-edge rudders. Studies were made in two different facilities to obtain the flutter boundary for each configuration at both transonic and supersonic speeds. The models were cantilever mounted and had fairings to keep them out of the tunnel boundary layer. The models were flat plates that were tapered in thickness along the span. Both models had 60° sweptback leading edges. Vertical tail D had a panel aspect ratio of 0.72 and a taper ratio of 0.43. Its rudder hinge line was swept back 43° and its rudder was 24 percent of the exposed surface area. Vertical tail E had a panel aspect ratio of 0.77 and a taper ratio of 0.48, based on a plan form without a rounded tip. Its rudder hinge line had 50° of sweepback and its rudder was about 36 percent of the exposed surface.

The results for configuration D are presented in figure 8, where the stiffness-altitude parameter is plotted as a function of Mach number. The frequency appearing in the stiffness-altitude parameter is the rotation frequency of the rudder. This model was cantilever mounted along its entire root chord. These controls had a ratio of first bending frequency to rudder-rotational frequency of about 0.4. Also shown in figure 8 is the flutter frequency referred to the control rotation frequency. At a Mach number of about 1.2, an abrupt increase in stiffness is required to prevent flutter. At the same Mach number the flutter frequency also changes abruptly. At lower Mach numbers, the flutter frequency is less than the rudder-rotation frequency, whereas at higher Mach numbers the flutter frequency is greater than the rudder-rotation frequency. This change in flutter frequency is associated with a change in the flutter mode. Previously, flutter mode changes in wings without controls have been observed to produce more stable configurations in the transonic region. In the present case, however, the change is toward a less stable system.

Figure 9 shows the results for configuration E wherein the plan form was cantilevered from a stub. In this case, the ratio of first-bending frequency to rudder-rotation frequency is about 0.3. Again, the figure shows both the stiffness-altitude parameter and ratio of flutter frequency to rudder-rotation frequency as functions of Mach number. The flutter frequency again suggests a change in the flutter mode past a Mach number of 1 but the change is gradual as Mach number increases and not abrupt as

for configuration D. Also, no destablizing jump or discontinuity in the stiffness-altitude parameter occurs as Mach number increases. If a flutter-mode change does occur, the shift is gradual and produces no detrimental effects.

For vertical tail D, a destablizing jump was found in the flutter boundary at low supersonic speeds, whereas none was obtained for vertical tail E. A very different type of flutter boundary was obtained for somewhat similar vertical tails with rudders. However, for both controls, if the surface were designed with just enough stiffness to avoid flutter at transonic Mach numbers, a new flutter region would be encountered at the same altitude at a Mach number of about 2.5. This again shows the existence of two critical flutter regions - transonic and supersonic. A complete description and discussion of the tests on these two vertical tails will be found in reference 3.

Configurations F and G - Vertical Tails With Trailing-Edge Rudders

Configurations F and G, shown in figure 1, were swept vertical tails with statically balanced trailing-edge rudders. Static balancing was accomplished with overhanging-balance weights located at the top of the rudders. Vertical tail F had an aspect ratio of 1.33, taper ratio of 0.44, and its rudder was about 24 percent of the exposed surface area. Vertical tail G had an aspect ratio of 1.58, a taper ratio of 0.40, and a rudder which was about 20 percent of the exposed surface area. Both configurations had 45° sweep at the quarter-chord line, 29° sweep on their rudder hinge lines and tapered in thickness from about 6 percent at the root to about 4 percent at the tip. The models were cantilever mounted at the root.

The results for vertical tail F are presented in figure 10. The frequency appearing in the stiffness-altitude parameter is the torsion frequency of the fin. Fin properties remained essentially unchanged during the test, while the actuator and rudder twist stiffnesses were varied. The actuator and twist stiffnesses shown in the figure have been divided by the values of the stiffnesses for the original configuration. The flutter points obtained with the original vertical tail are indicated by the circles. This flutter boundary fell within the airplane flight regime. In an attempt to study the nature of this flutter, a new system was tried wherein the rudder twist stiffness was increased to 1.3 times the original value while actuator stiffness was reduced to 0.8 of its value. The squares show where flutter was obtained with the changed stiffnesses. They show that the change was quite detrimental to the flutter boundary; that is, with a stiffer rudder and a weaker actuator the flutter boundary shifted to higher altitudes. The coupled frequency

[redacted]

spectrum of the two models remained about the same: $\omega_\beta/\omega_\alpha = 0.33$ and $\omega_h/\omega_\alpha = 0.22$.

Some tests were made with viscous dampers on the original rudder in an attempt to eliminate the flutter from the flight envelope of the airplane. The dampers were mounted at about midspan on the rudder. Flutter was still obtained when the damping produced by the dampers was 60 percent of critical. The flutter was eliminated when the damping was 120 percent of critical. The damping values quoted here are based on an inelastic rudder and back-up structure. Since these assumptions yield high values of critical damping, the damping actually obtained was probably somewhat less than the stated value.

The circles for the original vertical tail are repeated as circles again in figure 11 where dynamic pressure is shown as a function of Mach number. For this plot the flutter side of the boundary is above the curve. Also shown in this figure are three no-flutter points and a flutter point obtained with vertical tail G which had a longer and stiffer fin than vertical tail F. As indicated in the figure, the rudder actuator and twist stiffness for vertical tail G were also somewhat greater than for vertical tail F, although ω_h/ω_α and $\omega_\beta/\omega_\alpha$ were about the same. These results indicate that the flutter boundary for vertical tail G would be at substantially higher dynamic pressures than for vertical tail F. However, the one flutter point for vertical tail G was still considered to be too close to the airplane flight regime. An adequate flutter boundary appeared to be obtained when viscous dampers were used. The dampers produced about 15 percent of critical damping.

An additional test was made without dampers but with the fin tip cut off along the dashed line indicated in figure 1. With the fin tip cut off, vertical tail G had about the same plan form as vertical tail F but the frequency ratios were reduced to $\omega_\beta/\omega_\alpha = 0.25$ and $\omega_h/\omega_\alpha = 0.18$. The one flutter point obtained with the fin tip cut off, shown in figure 11, reveals a large increase in dynamic pressure required to flutter this tail compared with vertical tail F. This increase in dynamic pressure required to flutter the clipped configuration G over that required for configuration F can be attributed to increases in the stiffness of the fin, actuator, and rudder. The rudder twist stiffness was 2.8 times that of the original configuration and the actuator stiffness was 1.5 times that of the original configuration.

Studies of vertical tails F and G in the transonic speed range have shown that their flutter boundaries are sensitive to changes in the rudder twist stiffness and rudder actuator stiffness. Flutter could be eliminated by using viscous dampers, but the amount of damping required varied greatly between the two configurations.

[redacted]

[redacted]

Configuration H - T-tail

Configuration H, shown in figure 1, is a T-tail which did not have any movable control surfaces. The torsion and side flexibilities of the fuselage were simulated in the tail mounts. The fin had an aspect ratio of 1.0, a taper ratio of 0.56, and 45° sweepback of the quarter-chord line. The stabilizer had an aspect ratio of 1.8, a taper ratio of 0.43, and 40° sweepback of the quarter-chord line. The ratio of cantilevered fin bending to fin torsion frequencies was about 0.55.

The results of the flutter investigation are shown in figure 12. Stiffness-altitude parameter is plotted as a function of Mach number and the frequency appearing in the parameter is the torsion frequency of the fin. The original stabilizer had 15° of positive dihedral and the flutter points obtained with this configuration are indicated by the circles. Models with zero stabilizer dihedral were also investigated and the flutter points obtained with this configuration are indicated by the squares. The results indicate that less fin stiffness is required for zero stabilizer dihedral and so stabilizer dihedral is indicated to be detrimental.

The detrimental effect of stabilizer dihedral can be explained qualitatively by considering the stabilizer as a yawing wing. When the fin twists, the stabilizer yaws. As a result of dihedral this yaw motion produces a rolling moment on the stabilizer so that fin twist results in fin bending.

Simple Models of All-Movable Controls

In addition to the previously discussed scaled models, some simple models of all-movable controls have been investigated at low supersonic speeds. As figure 13 shows, they had arrowhead plan forms - a 45° delta and one with a 45° sweptback leading edge and a 15° sweptforward trailing edge. The models were flat plates with beveled edges and were supported by a shaft mounted in a bearing. The flexibility was primarily in the shaft so that the control surface experienced only rigid-body torsion, flapping, and translation. The ratios of first coupled frequency to second coupled frequency varied from about 0.3 to about 0.7.

The results are presented as the stiffness-altitude parameter plotted against rotation-axis position in percent of root chord. The frequency in the stiffness-altitude parameter is the first coupled frequency of the system. The trend shown at a Mach number of 1.2 for both surfaces produces a more stable configuration as the rotation axis is moved forward. The two flutter points obtained at a Mach number of 1.6 indicate that, for rearward rotation axes, more stiffness is required to prevent flutter as

[redacted]

[redacted]

the Mach number increases. However, the stiffness required at a Mach number of 1.6 rapidly decreases as the rotation axis is moved forward so that, at the axis location shown in the figure, the controls were stable at a zero value of the stiffness-altitude parameter. This means the controls were flutter free when unrestrained in rotation and when free to float. Thus, these results show that movement of the axis location forward was beneficial on these plan forms at low supersonic Mach numbers.

CONCLUDING REMARKS

A compilation of flutter experiments with various control configurations at transonic and supersonic speeds has been presented. Some trends on specific configurations are indicated and improvements in flutter characteristics for various cases are shown. It would be risky to draw general conclusions from these results, but the discussion should be of value.

REFERENCES

1. Land, Norman S., and Abbott, Frank T., Jr.: Transonic Flutter Investigation of an All-Movable Horizontal Tail for a Fighter Airplane. NACA RM L56G06, 1957.

2. Ashley, Holt, and Zartarian, Garabed: Piston Theory - A New Aerodynamic Tool for the Aeroelastician. Jour. Aero. Sci., vol. 23, no. 12, Dec. 1956, pp. 1109-1118.

3. Hanson, Perry W., and Rainey, A. Gerald: Experimental Investigation of the Transonic and Supersonic Flutter Characteristics of the Upper and Lower Vertical Tails of an Air-to-Ground Missile. (Prospective NACA paper.)

[redacted]

TEST CONFIGURATIONS

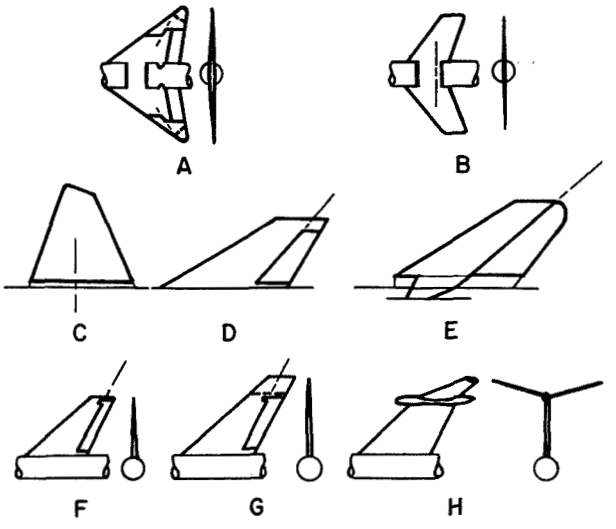


Figure 1

TEST CONFIGURATION A
WING WITH TIP AILERONS

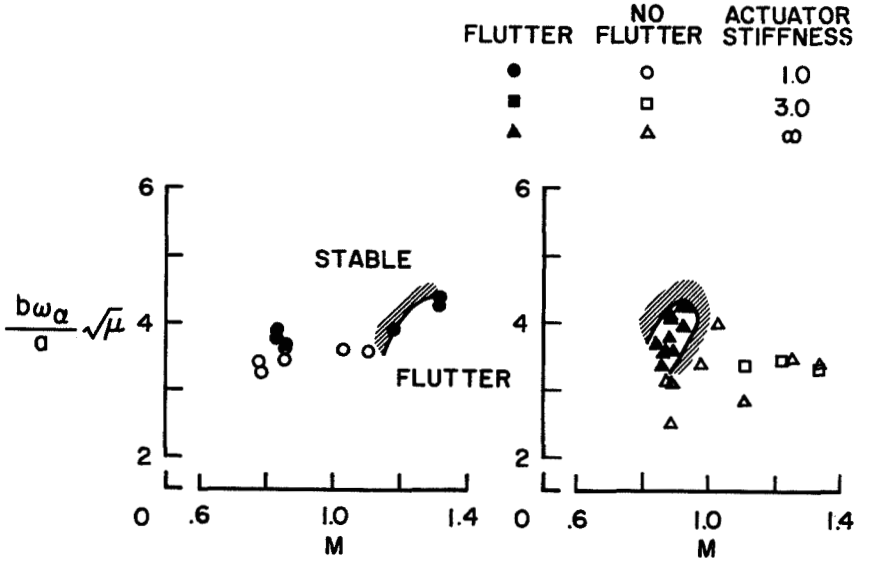


Figure 2

TEST CONFIGURATION B
ALL-MOVABLE STABILIZER

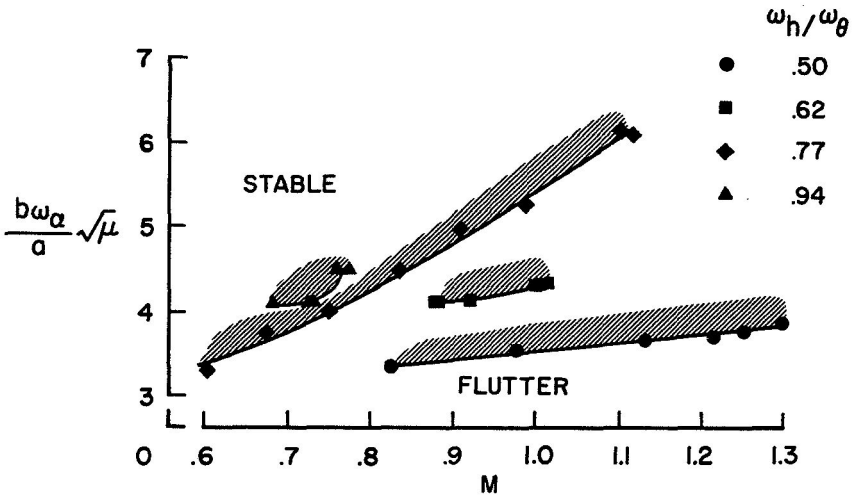


Figure 3

TEST CONFIGURATION B
ALL-MOVABLE STABILIZER

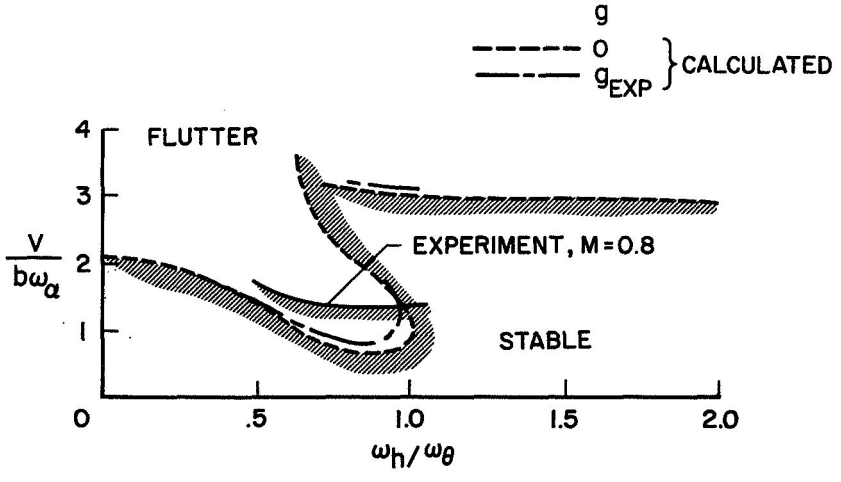


Figure 4

667

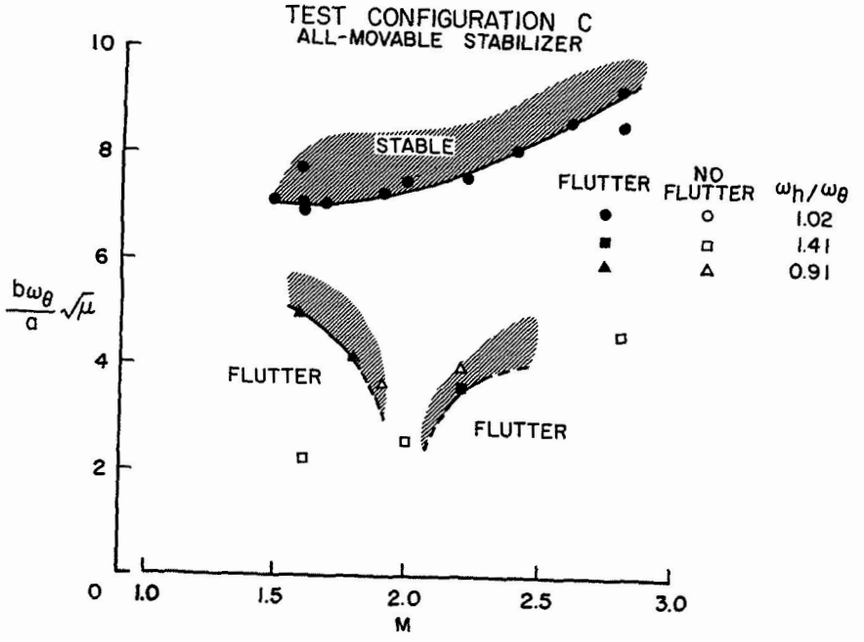


Figure 5

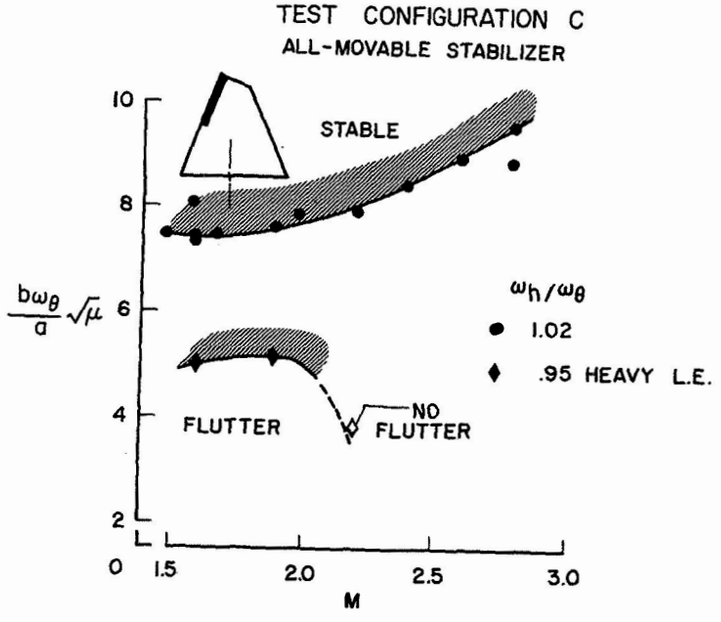


Figure 6

608

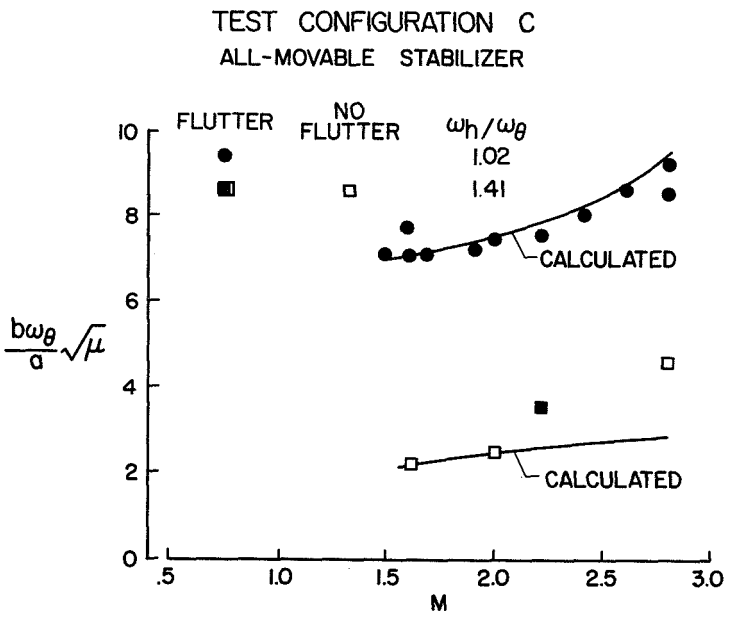


Figure 7

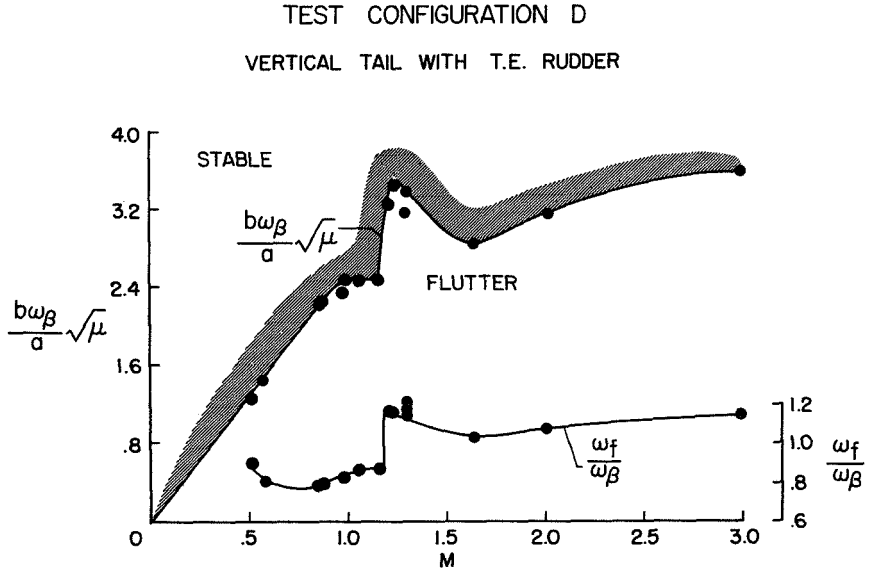


Figure 8

TEST CONFIGURATION E
VERTICAL TAIL WITH T.E. RUDDER

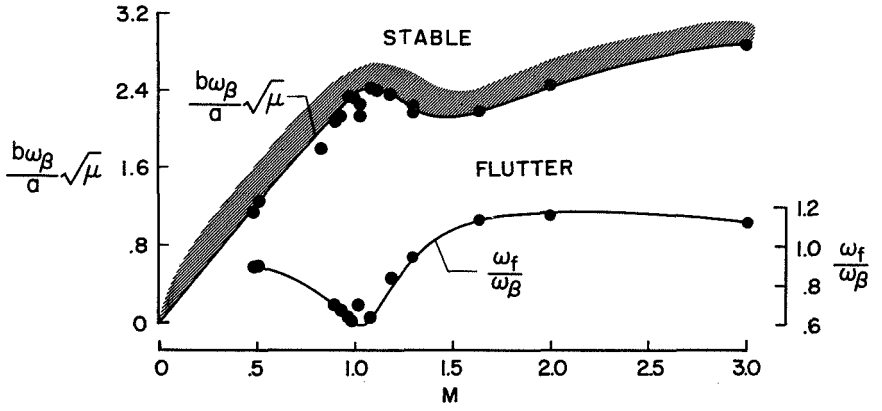


Figure 9

TEST CONFIGURATION F
VERTICAL TAIL WITH T.E. RUDDER

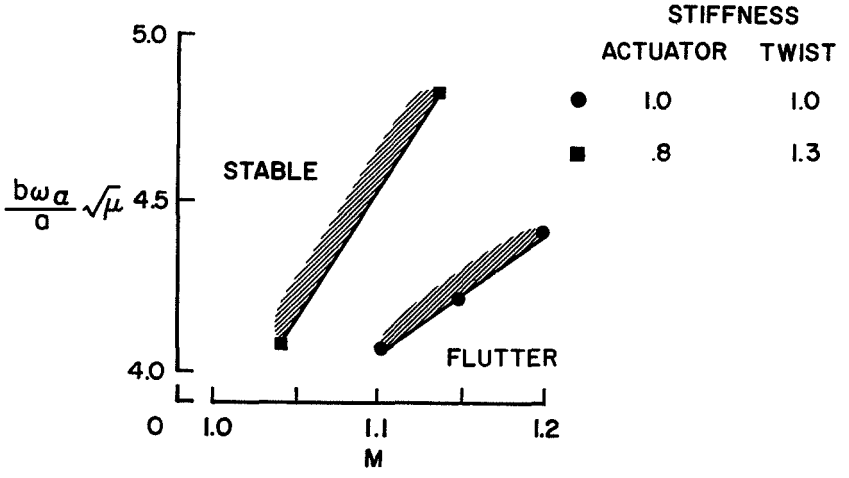


Figure 10

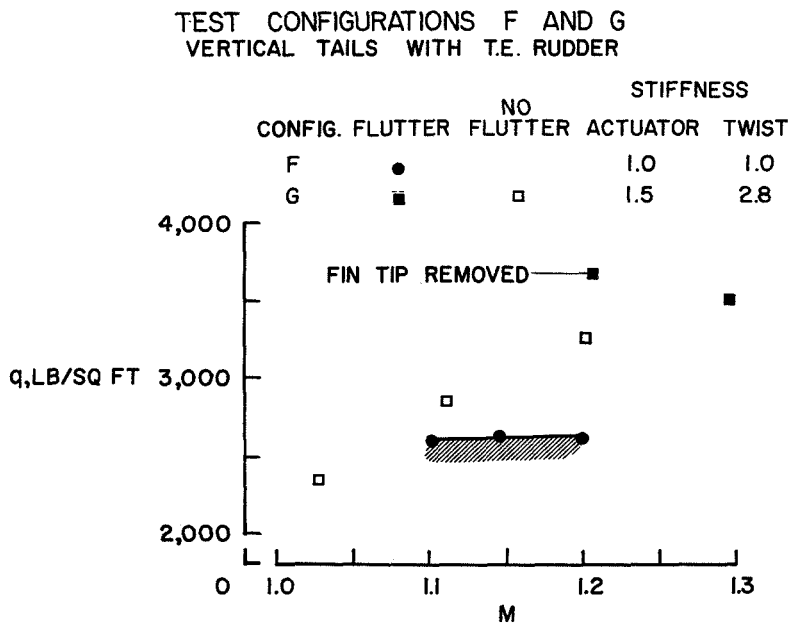
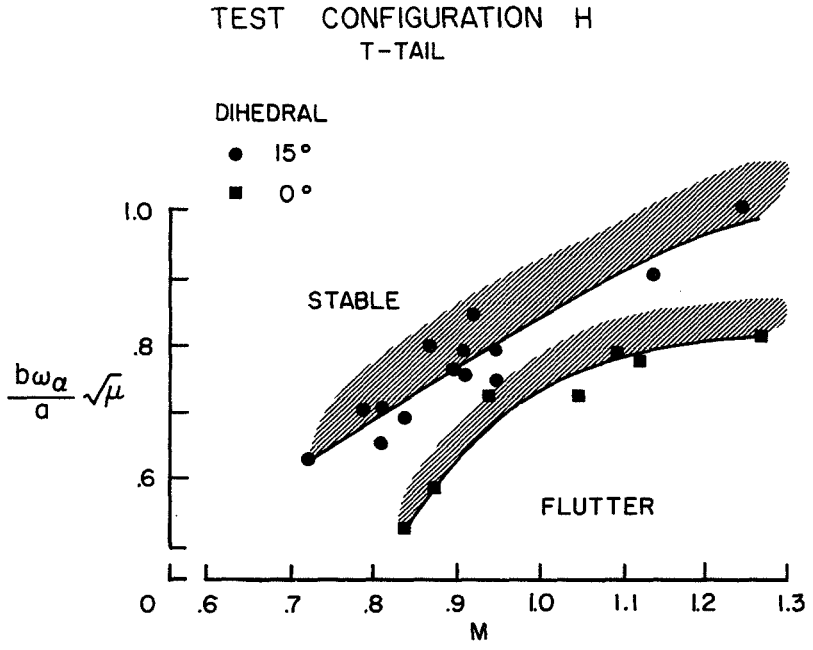


Figure 11



611

Figure 12

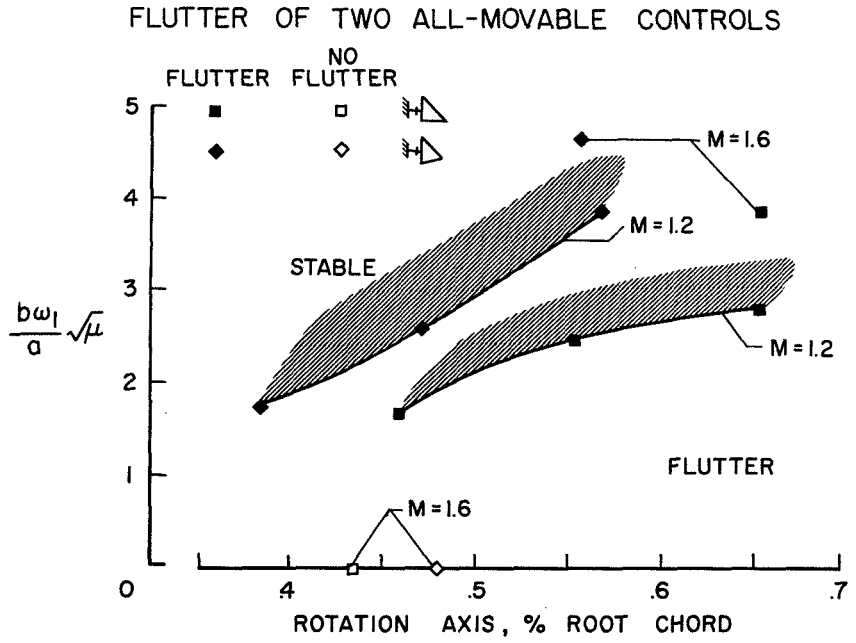


Figure 13

612

